ORGANIC CONDUCTORS IN EQUILIBRIUM AND NONEQUILIBRIUM STATES

The interaction with electric and light pulses

Von der Fakultät für Mathematik und Physik der Universität Stuttgart zur Erlangung der Würde eines Doktors der Naturwissenschaften (Dr. rer. nat.) genehmigte Abhandlung

Vorgelegt von

TOBIAS PETERSEIM GEB. KNOBLAUCH

aus Geislingen an der Steige

Hauptberichter: Professor Dr. Martin Dressel

Mitberichter: Professor Dr. Jörg Wrachtrup

Tag der mündlichen Prüfung: 21. 12. 2015

1. Physikalisches Institut
Fakultät 8 Mathematik und Physik
Universität Stuttgart
2016

Tobias Peterseim geb. Knoblauch: *Organic conductors in equilibrium and nonequilibrium states,* The interaction with electric and light pulses , © 2016

SUPERVISOR:
Professor Dr. Martin Dressel

″"Daß ich erkenne, was die Welt im Innersten zusammenhält"

— Faust I, Johann Wolfgang von Goethe

Dedicated to all the people who supported me over the last years.

ABSTRACT

Since the early days of mankind, the steady improvement of tools and objects are the basis of the triumphal procession of its evolution. Beginning with the usage of simple stones and natural materials as weapons and ancient tools in the Stone Age, old materials were continuously replaced by much more effective and efficient ones over the last 14,000 years. With each new material class mankind has always made one enormous leap of evolution. For instance, smelting and casting techniques were the basis of the Roman Empire, one of the first high technology societies. Until the middle of the 19th century, the interest of research was mainly focused on metals. However, with the beginning of the 20th century and the development of chemistry, a systematic study of materials, especially of alloys was initiated. By this, the number of newly discovered materials exploded. While at the beginning researchers were mainly interested in the improvement of the mechanical properties of the materials, completely new fields of applications were opened with the understanding of electromagnetism and its interaction with matter, mainly motivated by the research on semiconductors. However, silicon is still one of the most important materials in the electrical industry. During the last 60 years, organic compounds such as polymers (plastic), organic semiconductors, fullerenes, nanotubes, graphene and organic conductors have also been created in laboratories and went into the focus of fundamental and industrial research.

It was very fast recognized that their physical properties cannot be explained in the framework of classical band theory, since the theoretical predications do not match the experimental observations. Instead, the complex electron-electron and electron-phonon interactions, as well as their competition and interplay determine the physical ground state of these materials. By that they exhibit various magnetic and nonmagnetic ground states as superconductivity which can be tuned, for instance, by external parameters as pressure, temperature, magnetic as well as electric fields. Especially, the latter opens the possibility for new applications. In this regard, organic conductors play a special role since

1. The starting materials are very cheap, simple to produce and to handle.
2. The material composition can easily be adjusted and varied.
3. They can be produced in very high quality, i. e. purity.
4. Their physical properties can easily be tuned by external stimuli such as pressure.
5. Their physical properties are strongly anisotropic.
6. The electron-electron as well as electron-lattice are easily accessible by optical studies.

The disadvantage is that they are sensitive to high temperatures (>370 K) and fragile to mechanical force and tension which makes the experiments very challenging.

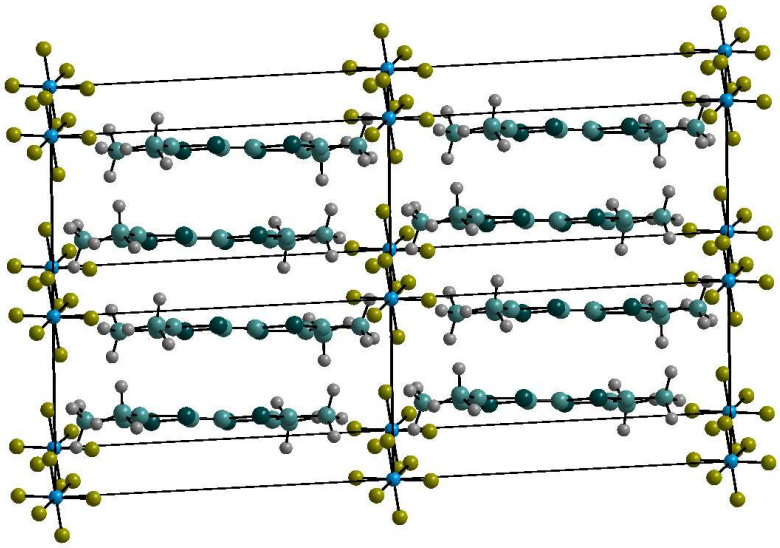

Figure 1: Exemplary illustration of the molecule arrangement of the one-dimensional organic conductor $(TMTTF)_2PF_6$. The organic molecules (gray, dark blue color) form layers which are separated from each other by the anions (bright blue and yellow color) along the long molecular axis [1].

In this context the aims of this thesis are:

1. A comprehensive and detailed optical study of the ground states of typical organic conductors. Additionally, transport measurements are performed whenever necessary.

2. Performing theoretical calculations and testing their capability to describe the physical properties of the examined systems.

3. Building up new experimental setups to study time-dependent effects in transport as well as in optical properties.

4. Examining of the interactions of the organic conductors with electric fields and short laser pulses to discover new effects and their characteristic time scales. The influence of external parameters is studied in detail.

5. Developing and applying models to describe the observed phenomena.

6. Better understanding of the ground state by comparing the equilibrium data with the externally induced state.

Therefore, one- and two-dimensional organic conductors have been studied by experimental as well as by theoretical techniques. Thereby, we have focused on the slightly dimerized quasi one-dimensional organic Fabre $TMTTF_2X$ (for example X=PF_6, AsF_6, ReO_4) family, the newly synthesized organic δ-(EDT-TTFCONMe$_2$)$_2$AsF$_6$ and δ-(EDT-TTFCONMe$_2$)$_2$Br, the mixed stacked organic charge transfer salts TTF-CA as well as the two-dimensional organic α-(BEDT-TTF)$_2$I$_3$ salt. All these compounds are composed of two organic and one inorganic molecule species. Within the crystal, the organic molecules form layers which are separated by inorganic ones, as depicted exemplary in Fig. 1. Concerning a unit cell, an electron is transferred from the organic layer to the inorganic counteranions. By that, the studied system gets quarter-filled, except TTF-CA.

Furthermore, the molecular orbital overlap of the organic molecules defines the properties and due to this anisotropy even the dimensionality of the systems. Therefore, all these compounds are very sensitive to electron-phonon interactions. Moreover, as the bandwidth is very small, electron-electron interactions play also an important role.

These interactions lead to a huge variety of different ground states, which can be optimally investigated by infrared spectroscopy:

1. Energy gaps and transfer integrals can be measured in the TMTTF family, α-(BEDT-TTF)$_2$I$_3$ and TTF-CA.

2. The molecular charge can be determined.

In our study, we have investigated the electrodynamic properties of all these compounds. Especially in the case of the Fabre salts TMTTF$_2X$ with X=PF$_6$, AsF$_6$, SbF$_6$, and ReO$_4$ we have performed an extensive characterization [2] of all three crystallographic axes. In this context, we have assigned most of the occurring vibrational modes. Together with our theoretical calculations of the molecular modes, we were capable to determine the temperature-dependent charge disproportionation between the molecular sites in the charge ordered state with highest achievable precision, which is shown in Fig. 2 for selected compounds. The temperature dependence of the charge imbalance reveals a crossover from a second to a first order phase transition, depending on the absolute value of T_{CO}. This suggests that the newest member in the Fabre family, TMTTF$_2$TaF$_6$ [3], should exhibit a very steep increase of the resistivity and the charge imbalance as T_{CO} is rather high. Furthermore, dip-like features in the reflectivity along the stacking direction could be attributed to the second harmonic of electron-molecular vibration coupled molecular modes which are strongly enhanced due to the asymmetry of the molecular energy potential in the charge order phase. With this important outcome, the charge order transition can be more effectively identified.

In total, our DFT calculations described the band structure as well as the electronic excitations and the anisotropy of the Fabre salts very well. From the calculations based on temperature-dependent crystal structures of different compounds, we derived that variations of the temperature must have the same impact as applying hydrostatic or chemical pressure. In addition, we predict elucidated fingerprints of the phase transition in the visible spectral range. By comparing the theoretical spectra with our experimental ones, it can be seen that electron-electron interactions play a very crucial role to describe the properties of organics. From a complex fitting procedure we could derive the temperature-dependent transfer energy t which agrees with the outcome of Hückel calculations.

Most importantly, within this thesis we present the first time-dependent photoconductivity investigations of the Fabre salts. For this, a new setup was developed and integrated in the existing FTIR-setup. The photocurrent appears below T_{CO} and reveals a superimposed oscillating behavior. We could show that the oscillating current is an intrinsic property of the compounds which does not fit any up to now known photocurrent phenomena. We attribute the effect to interactions between single excited charge carriers and the collective charge order state which destabilizes the latter.

While in the Fabre salts $2k_F$ Umklapp scattering can take place leading to an opening of a Mott gap due to half-filling, in the organic one-dimensional

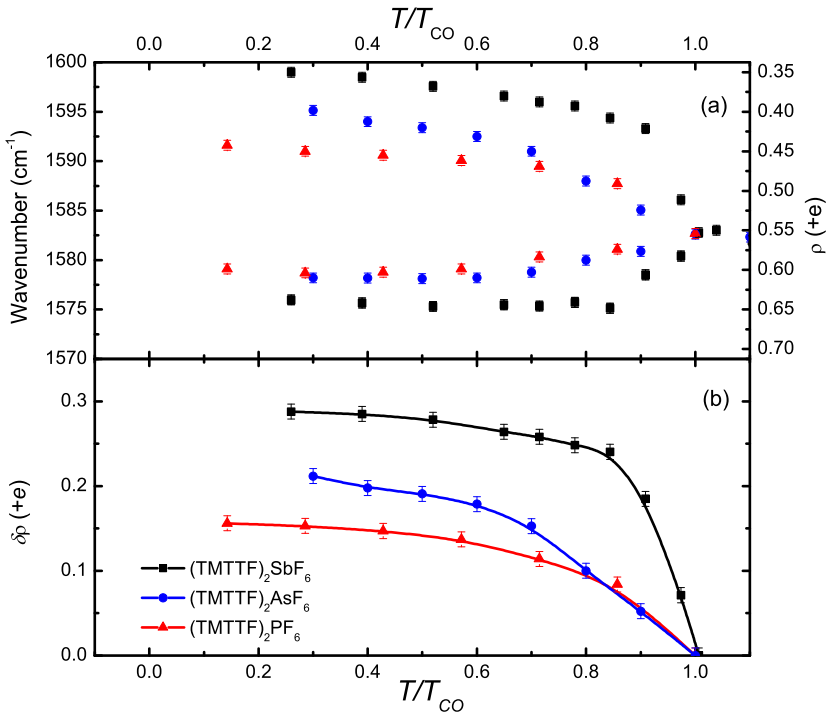

Figure 2: (a) Resonance frequency of a charge sensitive mode of various examined Fabre salts as a function of the normalized temperature T/T_{CO}. (b) The charge disproportionation was derived from the resonance frequency (a) which is plotted versus T/T_{CO} for three different $(TMTTF)_2X$ salts with X=PF_6, AsF_6, and SbF_6 with T_{CO}=67 K, 102 K, and 157 K.

δ-$(EDT\text{-}TTFCONMe)_2X$ salts with X=Br and AsF_6 the molecules are equally stacked and thus pure quarter-filled systems. Also for them, we present the temperature dependence of the optical properties of all crystallographic axis and compare them to simulations. Here, a large charge disproportionation of 1:9 exists already at room temperature. Furthermore, the structural transition can be identified by a modification of the vibrational resonance frequency [4]. In the high conducting state the strong shift of the mid-infrared band is attributed to the optical excitation of domain walls.

TTF-CA is completely different from the previously mentioned organic compounds, since the cation and anion molecules are arranged in an alternating way along all crystallographic directions. At room temperature it is neutral, whereas a first-order transition into an ionic phase takes place at T_{NI}=81.5 K. The high quality crystals were synthesized with a home-built setup, using the sublimation technique. Here, our theoretical calculations of the band structure excellently describe the temperature dependence of the optical energy gap as well as the temperature evolution of the electronic excitations. By our extremely precise optical study of the mid-infrared spectral range, we could for instance determine the variation of the molecular ionicity as well as the bandwidth, which agrees very well with our DFT calculations.

In this context, we have established for the first time the Step-Scan technique to study the temporal dynamics of the optical infrared response of a solid state material. In the case of TTF-CA we have concentrated on the photo-induced transition in the ionic phase and its development in the micro- and millisecond time range [5]. The spectral response resembles the spectrum of the neutral phase

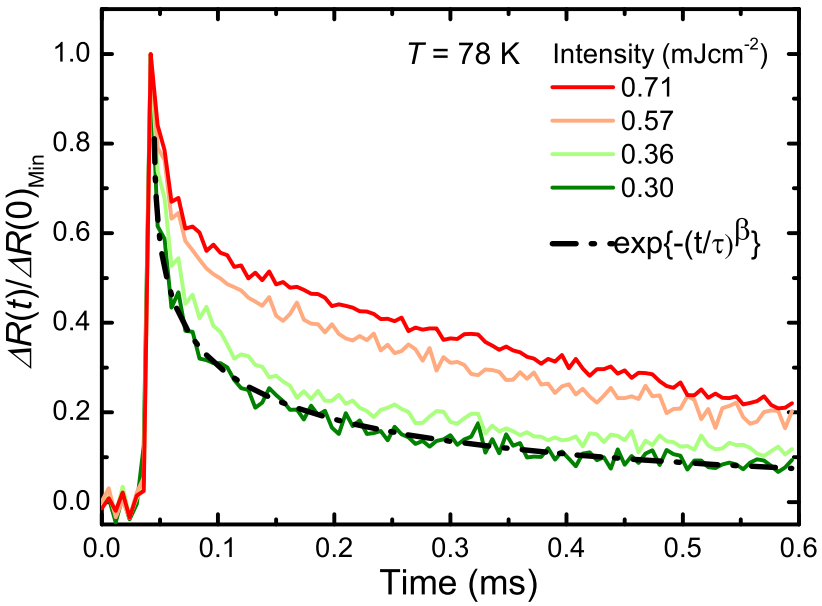

Figure 3: Time-dependent dynamics of the normalized reflectivity signal of TTF-CA after photoexcitation at 78 K for various laser intensities. The dashed-dotted black line marks an exemplary fit of a Kohlrausch-Williams-Watt function $e^{-(\frac{t}{\tau})^{\beta}}$ to the experimental data. (Reprinted with permission from Ref. [5].)

after the photo-excitation. However, the time-dependent evolution of the signals cannot be described by a simple exponential function, solely by a Kohlrausch-Williams-Watt function, as displayed in Fig. 3. We conclude that the relaxation process can be described by a 1D random-walk annihilation process of neutral-ionic domains walls, which is supported by numerical simulations. Furthermore, we determined the induced neutral domain size as a function of the laser intensity and temperature.

Besides the one-dimensional organic conductors, we have also studied the two-dimensional organic model system α-(BEDT-TTF)$_2$I$_3$ which reveals a metal-insulator transition at 136 K. The insulating state is accompanied by an unequal distribution of the charge carriers on the molecular lattice sites. Surprisingly, by our DFT calculations we could very well reproduce the metallic as well as the insulating state and the corresponding optical spectra. Up to now, it was always assumed that the transition can solely be described by taking electron-electron correlation effects into account. We also report on the very successful investigation of the electrically induced insulator-metal transition which was measured by a newly built setup to detect time-resolved transport properties. By that we were able to demonstrate resistivity switching from a low to a high conducting state after applying short voltages pulses. Related to that, a nonlinear transport behavior with a negative differential resistance regime appears. Additionally, we employed the time-resolved Step-Scan technique to trace any modification of the mid-infrared spectra due to the electrically induced phase transition. Indeed, a change of the infrared spectra takes place which is metallic at the vicinity of the phase transition, whereas at much lower temperatures it increases only slightly. We ascribe the observation to the excitation of non-equilibrium charge carriers which is perfectly described by our numerical simulations of the hot electrons. By that we are capable to determine the lattice temperature which differs from the temperature of the electronic system. The theoretically determined lattice

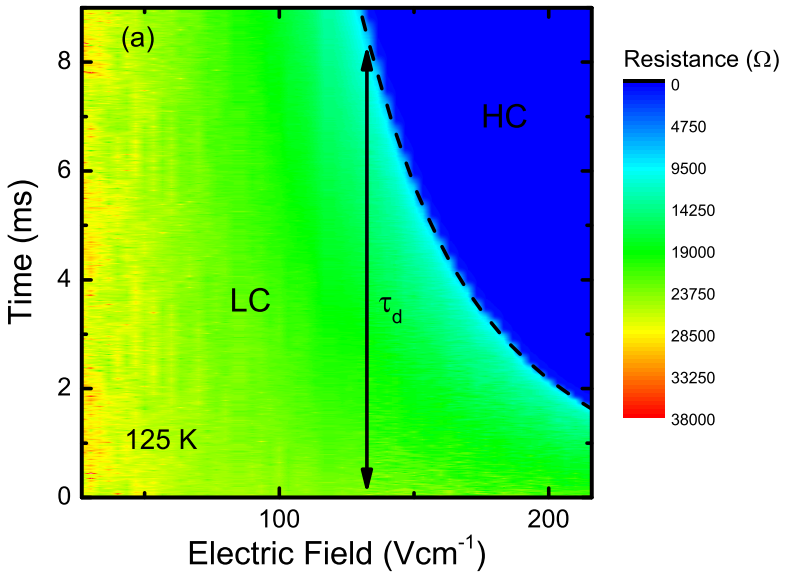

Figure 4: Contour plot of the time-dependent sample resistance of α-(BEDT-TTF)$_2$I$_3$ for different electric fields. Voltage pulses with a length of 9 ms were applied to the sample. The yellow, green area corresponds to the low conducting, insulating state whereas the blue region marks the high-conducting state. With increasing electric field the switching time τ_d decreases nonlinearly.

temperature agrees excellently with our estimation of the sample temperature from the infrared measurements.

In summary, the applied theoretical methods and calculations have delivered very important information about the impact of electron-electron interactions and dimensionality on the electronic system of the various investigated compounds. The excellent agreement with our optical studies provides us for the future the unique possibility to predict the optical properties of other organic compounds and other materials. Furthermore, advanced normal mode analysis was established as a very powerful tool to determine the vibrational frequency, the infrared as well as Raman activity and the assignment of the experimentally detected molecular vibrations.

A further milestone of this thesis was the first successful application of the infrared time-resolved Step-Scan technique to study externally perturbed solid state materials. Moreover, we have combined this technique with newly developed and home-built setups to excite the samples under investigation by short electric fields and pulses. This opens the incredible possibility to study the materials out of equilibrium in a time range from nanoseconds to minutes, which cannot be reached by classical ultrafast pump-probe experiments. This allows us to discover unexpected new effects. With all that, we set the cornerstones for further fruitful experiments to examine possible applications in molecular electronic devices, i.e memories, optical switches. Therefore, we hope that our investigations stimulate further studies on the temporal behavior of other organic and inorganic compounds, for instance the dynamics of magnetic properties after perturbations with electric fields or light.

PUBLICATIONS

Publication related to this thesis
Some of the result presented in this thesis have been published in or submitted to the following scientific journals:

- **Knoblauch, T.**; Dressel, M., Charge disproportionation in $(TMTTF)_2X$ (X=-PF_6, AsF_6, SbF6) investigated by infrared spectroscopy, Phys. Status Solidi C, **9**, 1158-1160 (2012)
- Dressel, M.; Dumm, M.; **Knoblauch, T.**; Masino, M., Comprehensive optical investigations of charge order in organic chain compounds $(TMTTF)_2X$, Crystals, **2**, 528-578 (2012)
- Dressel, M.; Dumm, M.; **Knoblauch, T.**; Kohler, B.; Salameh, B.; Yasin, S., Charge Order Breaks Magnetic Symmetry in Molecular Quantum Spin Chains, Advances in Condensed Matter Physics 2012, 398721 (2012)
- Ivek, T.; Kovacevic, I.; Pinteric, S.; **Knoblauch, T.**; Schweitzer, D.; Dressel, M., Cooperative dynamics in charge-ordered state of α-$(BEDT\text{-}TTF)_2I_3$, Physical Review B, **86**, 245125 (2012)
- **Peterseim, T.**; Ivek, T; Dressel, M., Time-dependent infrared measurements of the nonlinear conductivity in α-$(BEDT\text{-}TTF)_2I_3$, in preparation
- **Peterseim, T.**; Antal, Á.; Dressel, M.; Batail, P.; Drichko, N., Characterization of the quasi-one-dimensional compounds δ-$(EDT\text{-}TTF\text{-}CONMe_2)_2X$, X = AsF_6 and Br by vibrational spectroscopy and DFT calculations, Journal of Chemical Physics, **140**, 064504 (2014)
- Antal, Á.; **Knoblauch, T.**; Dressel, M.; Batail, P.; Drichko, N., Infrared spectra of the one-dimensional quarter-filled Wigner lattice compounds δ-$(EDT\text{-}TTF\text{-}CONMe_2)_2X$ (X = AsF_6, Br): Domain-wall excitations, Physical Review B, **87**, 075118 (2013)
- **Peterseim, T.**; Haremski, P.; Dressel, M., Random-walk annihilation process of photo-induced neutral-ionic domain walls in TTF-CA, Europhysics Letters, **109**, 67003(2015)

Publication not directly related to this thesis

- Dvorak, M.; Müller, M.; **Knoblauch, T.**; Bünermann, O.; Rydlo, A.; Minniberger, S.; Harbich, W.; Stienkemeier, F, Spectroscopy of PTCDA attached to rare gas samples: clusters vs. bulk matrices. I. Absorption spectroscopy, Journal of Chemical Physics, **137**, 164301 (2012)
- Dvorak, M.; Müller, M.; **Knoblauch, T.**; Bünermann, O.; Rydlo, A.; Minniberger, S.; Harbich, W.; Stienkemeier, F., Spectroscopy of PTCDA attached to rare gas samples: clusters vs. bulk matrices. II. Fluorescence emission spectroscopy, Journal of Chemical Physics, **137**, 164302 (2012)

- Antal, Á.; **Knoblauch, T.**; Singh, Y.; Gegenwart, P.; Dressel, M., Optical properties of the iron-pnictide analog $BaMn_2As_2$, Physical Review B, **86**, 014506 (2012)
- Dengl, A.; Beyer, R.; **Peterseim, T.**; Ivek, T.; Untereiner, G.;Dressel, M., Evolution of ferroelectricity in tetrathiafulvalene-p-chloranil as a function of pressure and temperature, Journal of Chemical Physics, **140**, 244511 (2014)
- De Zuani, S.; **Peterseim, T.**; Berrier, A.; Gompf, B.; Dressel, M., Second harmonic generation enhancement at the percolation threshold, Applied Physics Letters, **104**, 241109 (2014)
- Pinterić , M.; Culo, M.; Milat, O.; Basletić, M.; Korin-Hamzić, B.; Tafra, E.; Hamzić, A.; Ivek, T.; **Peterseim, T.**; Miyagawa, K.; Kanoda, K.; Schlueter, J. A.; Dressel, M.; Tomić, S., Anisotropic Charge Dynamics in the Spin-Liquid Candidate κ-(BEDT-TTF)$_2$Cu$_2$(CN)$_3$, Physical Review B, **90**, 195139 (2014)

CONTENTS

Part I

INTRODUCTION

1 INTRODUCTION

Since the early 70's of the past century organic charge transfer salts attract enormous attention in scientific research which has multiple reasons. Historically the story of organic conductors starts with the basic idea proposed by W. Little [6] that it must be possible to synthesize an organic high-temperature superconductor by arranging organic molecules in a one-dimensional chain. That proposal motivated more than one generation of chemists to create hundreds and thousands of organic compounds which finally lead to the first organic superconductor $(TMTSF)_2ClO_4$[1] with a transition temperature of 1.4 K [7]. Although the critical temperature was pushed consequently to higher temperatures, since several years it resides at about 30 K for a doped full fullerene [8].

Besides superconductivity this material class reveals many different states as metallic, semiconducting or insulating phases, in combination with para-, ferro, or anti-ferromagnetic states which leads to a very rich phase diagram. The ground states can be tuned in general by chemical substitution or hydrostatic pressure opening the possibility to control the physical properties by external parameters. This makes them very attractive for industrial applications. Moreover, the interplay and competition of different phases can be studied and hence opens the route to disentangle their physical driving mechanism. It is to note that they additionally reveal different dimensionalities influencing the development of the ground states which can be examined as well. Moreover, the reduced dimensionality allows to test and compare theoretical models which can be easily solved analytically in low dimensions. However, more interestingly, these systems deviate from standard materials as copper or silicon which can be described in the framework of the Drude-Sommerfeld model or simple band structure theory depending solely on the strength and position of the nuclei potential within the crystalline structure. It became very fast clear that electron-electron and electron-phonon interactions play a crucial role in defining the ground state.

The combination of the possibility to tune the physical properties by simple chemical engineering, the amount of different ground states as well as its interplay with the dimensionality makes them to a very interesting and hot area of research over more than 40 years.

Since the last 20 years ultrafast laser spectroscopy was developed and significantly improved to open the door to study temporal dynamics taking place on the (sub-)femtosecond and nanosecond time regime by what electron-electron as well as electron-phonon interaction can be examined delivering important, normally not accessible information about the driving mechanism of the ground states [9]. So, it is possible to study optically induced hidden metastable states and to control this metastable state externally. It also turned out that the ground state can be manipulated by electric fields short in time which expresses as a suddenly occurring resistivity change in the experiment. Also, first tentative studies were undertaken to study the interplay of electric fields and light pulses and their influence of the physical quantities and states [9]. A new perspective opens multiferroic organic salts [10] where the order parameters are coupled to

1 Under ambient pressure.

each other and can be controlled by their external fields which is normally not the case.

Especially since different branches of industry are looking intensely for new materials with chemical and physical properties outperforming the characteristics of the well-established silicon and inorganic semiconductors, the research on organic conductors and their application in micro- and nanoelectronic devices attracted more attention and receives more stimuli. Moreover, it is also important that i.) the opportunity to easily tailor the material properties in the laboratory as well as in industrial dimensions and ii.) the starting materials are very cheap in purchase and available in large quantity. The future vision is to build, for instance, (ultra-) fast optical switches, (non-)volatile electronic devices out of organic conductors.

Therefore, the combination of industrial interest and the first small fainthearted steps towards molecular nanoelectronics on the bench-scale are the source of this thesis whose aim is to explore the capability of organic correlated materials to be used in daily live applications and to extend our knowledge about the important physical properties.

The most famous model systems of one-dimensional organic salts are the Fabre and Bechgaard families (TMTCF)X with X standing for different anions, for example centro-symmetric or non-symmetric anions as PF_6 or ReO_4, respectively, and C stands for S or Se atomic types. While in the past decades the Bechgaard salts (TMTSF) have been studied extensively, more studies have been performed on the Fabre salts (TMTTF) for the last ten years.

In contrast to the Bechgaard salts, which reveal a dimensional crossover from a two-dimensional to a three-dimensional metal and superconducting ground state at low temperatures, the Fabre salts exhibit a bunch of different electronic and magnetic phases. The most interesting phenomena is the insulating charge ordered state which appears between 50 K and 250 K depending on the chosen counteranion X. There, the charge becomes unequally localized on the lattice sites within the unit cell. It manifests itself as a sharp rise of the resistivity and makes it therefore especially interesting as the charge ordered state can be probably transferred in a metastable state by an external electric-field or light pulses. Therefore, we performed the most comprehensive optical study on the Fabre salts [2, 11] disentangling the amplitude of charge disproportionation, electronic excitations as well as the participating molecular vibration in the optical spectra. Moreover, advanced theoretical calculations were conducted to determine on the one hand the band structure and on the other hand the optical spectra which we compared with our experimental results. Based on the experimental and theoretical characterization we progressed and performed the first time-resolved photoconductivity measurements.

Related to the material class of the Fabre salts, we have examined the non-dimerized δ-(EDT-TTFCONMe$_2$)$_2$AsF$_6$ and δ-(EDT-TTFCONMe$_2$)$_2$Br compounds systematically by optical infrared spectroscopy [5, 12]. While the Fabre salts are dimerized, the donor molecules in the present case are equally stacked in the unit cell. Amazingly, they exhibit a charge order phase already established at room temperature. The experimental results were additionally supported by theoretical calculations of the molecular vibrations [4], band structure and electronic excitations.

In contrast to the previously mentioned compounds, in TTF-CA the donor and acceptor molecules are arranged in a mixed-stack configuration leading to a one-

dimensional system. It reveals a neutral-ionic phase transition at about 80 K becoming noticeable as an increase of the ionicity of the constituting molecules and an abnormal dip in the transport curve. It is the prototypical system for a neutral-ionic phase transition. We have grown the crystals with an in-house setup developed in the framework of this thesis. The extensive characterization was conducted with a detailed optical examination assisted by extended theoretical calculations. The main perspective of this subproject was on the photo-induced phase transition which we demonstrated by time-resolved infrared spectroscopy [5]. The observations showed excellent agreement with a numerical model of the 1D random-walk annihilation process of neutral-ionic domain walls NIDW.

Also, to account for two-dimensional organic salts, α-(BEDT-TTF)$_2$I$_3$ was chosen since it exhibits similar as the Fabre salts a metal-insulator transition at 136 K with a unequally distributed charge localization in a horizontal charge pattern. Since the optical characteristics are well-known, we have concentrated on the simulation of the optical spectra and the electrically induced resistivity switching which was examined by time-resolved resistance as well as by time-dependent infrared measurements supported by a theoretical model based on non-equilibrium charge carriers [13].

Moreover, by the search for other correlated materials, we selected the strongly electron-electron correlated transition metal VO_2 which we examined in great detail with various techniques, as AFM, optical spectroscopy, (time-resolved) transport measurements and DFT calculations. Interestingly, it exhibits a metal-insulator phase transition above room temperature at 340 K which is easily accessible and thus perfectly suitable for application. Therefore, we used our gathered expertise on temporal dynamics and focused on the study on the electrically induced phase switching because of its promising prospect for applications.

Besides the study of correlated materials, we have conducted several preliminary studies on the electrically induced switching behavior of liquid crystals which we originally used to test the built-up time-resolved infrared setup.

According to the above mentioned topics, this thesis is organized into several chapters as follows:

1. Chapter: Here, we give a brief introduction into the basic concepts of molecular materials and carve out the difference of organic molecular conductors to organic semiconductors. As a variety of phases appear in organic charge transfer salts, they will be explained in detail and in this relation the experimental quantities and methods will be mentioned to detect them. This comprises the (Spin-)Peierls transition SP, charge density wave CDW, charge order CO, Mott insulator, and metallic-like states. In this regard the main theoretical model is introduced briefly to explain and describe the phases occuring in correlated materials. With the gathered basic information and with this knowledge in mind, the optical properties of organic conductors are presented and clarified.

2. Chapter: Besides the equilibrium phases, non-equilibrium phases are studied in the framework of the thesis like photo-induced phenomena as well as electrically induced phase transitions. Therein, a chronological summary of the experimental results as well as the theoretical concepts to explain the occurring observations are presented.

3. Chapter: This chapter is dedicated to the employed experimental methods and is therefore split into two parts. In the framework of this thesis several experimental setups were built up and tested. In this context the FTIR-technique will be introduced in detail and the difference of the Rapid-Scan method to the Step-Scan technique is highlighted. Furthermore, a setup for time-resolved photoconductivity and transport measurements was developed. For this purpose, a laser system was built-up and incorporated in the existing setup.

   Since we support most of the experimental results by theoretical calculations based on DFT, we introduce the main concepts and show how the physical quantities are determined theoretically.

4. Chapter: This chapter is devoted to the experimental results of the one-dimensional and two-dimensional organic salts. In the first sections, we discuss the physical properties of the Fabre salts $(TMTTF)_2X$, (X=PF_6, AsF_6, SbF_6, and ReO_4), δ-(EDT-TTFCONMe$_2$)$_2X$, (X=Br and AsF_6) and TTF-CA. In general, each section contains a discussion on the theoretically determined results performed in the framework of this thesis and a comparison of them with the experimental outcomes. In relation to that, comprehensive optical studies are presented in detail for all compounds. The last subsections embody the study of photo- or electric-induced phenomena and explaining theoretical models.

   Apart from the aforementioned 1D materials, we examined the 2D organic conductor α-$(BEDT\text{-}TTF)_2I_3$. Besides the basic physical properties we mainly focus on the theoretical calculations of the electronic properties and the agreement with our experimental results. This is followed by discussing the electrically induced switching resistivity.

5. Chapter: In this part, all the previous received results, conclusions and gained knowledge are summarized briefly. Outgoing from the acquired findings within this thesis, we will draw a possible roadmap for future projects and research studies on organic conductors. The focus will be on possible material candidates to study non-equilibrium phenomena as well as other experimental techniques to study such effects.

6. In the appendix, all the calculated resonance frequencies and infrared intensities are listed up for the CA, TTF, EDT-TTFCONMe$_2$, and TMTTF molecules in the neutral as well as in the cationic state. Additionally, the comprehensive results of the side project being about the correlated material vanadium dioxide VO_2 and the test measurements of the electrically induced switching of liquid crystal cells are summarized here.

Part II

CORRELATED MATERIALS

2 ORGANIC SOLIDS-GROUND STATES

2.1 ORGANIC SOLIDS

At the beginning of this thesis we want to make the reader familiar with the concept of organic salts. In the upcoming chapter the material class of the organic conductors will be introduced and shortly classified in the context of the other organic based materials. The different ground states emerging in these materials are explained in detail as well as the main theoretical concepts, for instance the (extended) Hubbard model. The chapter will be finalized by a section about non-equilibrium states induced by light and electric fields.

Since more than 60 years solid state physics has been the largest research area in physics. Beginning with the enormous interest in the physical properties of simple metals at the beginning of the 20th century, the focus was redirected on inorganic semiconductors in the early 50's. They attracted more attention because of the possibility of tuning the Fermi level by doping and hence building fast, robust and cheap electronic devices building-up the modern electronic industry. At the same to the research on semiconductors, a large part of the scientific community focused on the disentanglement of the driving force of superconductivity occurring in various material classes. Throughout the years the mysterious effect of superconductivity has still been an active research area revitalized by the discovery of iron based superconductors in 2008 [14]. Most of the aforementioned effects have been studied in inorganic compounds, but since the 70's of the past century, the large class of organic solids has gained more and more interest because of the low production costs and the opportunity to tune their physical properties by slight variation of the chemical components and composition. Therefore, they take up a place among the established inorganic material classes, as for instance transition metal oxides.

In principle, the class of organic compounds can be divided into two main subclasses which have in common that they consist of organic molecules or polymers containing carbon atoms in the most cases , but also sulfur, selenium, hydrogen, or oxygen.

In the first class, the organic compounds contain only one type of constitution which can be an organic molecule or polymer. Here, the conjugated π electron systems attract the main interest due to their large electronic excitation energy between the highest occupied HOMO and the lowest unoccupied LUMO molecular orbital depending on the size of the molecular building blocks of the crystal. The energy gap is between 1 eV and 4 eV. The most prominent representatives are, for instance, benzene, naphthalene, anthracene, and tetracene (with increasing optical energy gap). The dominant force keeping these organic solids together is the dispersive Van-der-Waals force. They are promising candidates for light-emitting devices, organic field-effect transistors or organic solar cells [15, 16].

The second subclass, which is solely treated in this thesis, are the donor-acceptor complex systems whose physical properties are discussed extensively in the following sections. In that category the crystals are composed of two different molecular components. At least one of them has to be an organic

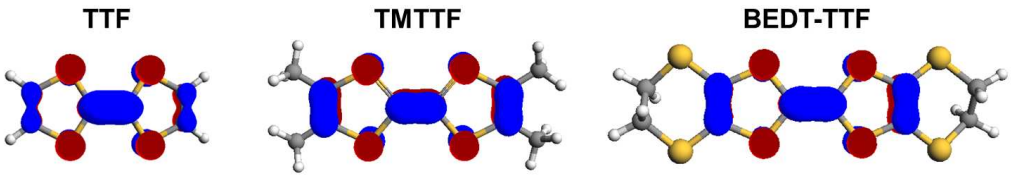

Figure 2.1: Highest occupied molecular orbital of (a) TTF, (b) TMTTF, and (c) BEDT-TTF mainly composed of the p_z-orbitals of the sulfur and carbon atoms. The calculation was performed with the semi-empirical ZINDO method.

molecule. The most common stoichiometric ratios are 1:1, as in the case of TTF-CA or TTF-TCNQ, or 1:2, as it is the case for the Fabre- and Bechgaard salts $(TMTYF)_2X$ with Y = S or Se and X corresponding to different types of covalent anions [1]. One of the building blocks is a donor with a small ionization energy E_{ion} and transfers a hole or a fraction of an electron charge to the acceptor which has a high electron affinity E_A. The energy ΔE which is necessary for the charge transfer

$$\Delta E = E_{ion} - E_A - E_B < 0 \tag{2.1}$$

depends not only on E_{ion} and E_A, but also on a third term E_B containing for example the exchange energy. The Coulomb force (i. e. ionic bonds, charge) between the different structural units defines the crystal structure in charge-transfer complexes whereas the Van-der-Waals or inductive forces play only a minor role. This material subclass can be further divided in two subcategories: the radical-cation as well as the radical-anion salts and the radical-ion salts. In the first one the cation or the anion is a radical, respectively.[2] The Bechgaard- and Fabre-salts on which will be reported extensively in chapter 5.1.2 as well as most of the two-dimensional organic salts, i.e. α-$(BEDT\text{-}TTF)_2I_3$. (see chapter 5.4.1), fall into this category. In these mentioned cases, the anions have a closed shell which means that they have no unpaired spin and the charge is closely bound. Hence, they do not account to the transport conduction. This conclusion is supported by theoretical calculation. Concerning the intermolecular forces, they typically form separated stacks of anions (acceptors) and cations (donors) creating layers explaining the anisotropy of the physical properties in these complexes. This packing configuration leads to the overlap of the partially filled molecular orbitals. The filling of the bands is a function of the charge transfer between the acceptor and donor components and their number in the unit cell. The overlapping orbitals cause a delocalization of the charge carriers between the molecules and an enhanced conductivity along the direction of the highest molecular overlap. The molecular orbitals are constructed by a linear combination of atomic orbitals leading to σ and π-orbitals whereas the first ones are strongly localized and responsible for the bonding and the latter ones are weakly bond and therefore higher in energy in comparison to the carriers in the σ-orbitals. Hence, when talking about the charge carriers we mean the carriers in the π-orbitals. In Fig. 2.1, the HOMO of the three neutral TTF, TMTTF, and BEDT-TTF molecules are exemplarily visualized. The HOMO mainly consists of the p_z-orbitals of the sulfur and carbon atoms sticking out of the molecular plain leading to the π-

1 TMTTF contains sulfur and TMTSF selenium.

2 A radical means that an atomic or molecular unit has an open shell and therefore an unpaired spin additionally to its charge.

character of the molecule orbital. Molecular orbitals at lower energies have a higher contribution of the p_x and p_y-wavefunctions and hence, the charge carriers are strongly localized along the atomic bonds and in the molecular plain. The overlap of these orbitals between adjacent molecular sites exactly determines the conducting behavior and the dimensionality of the compounds. The overlap integral $S_{ij} = \int \Phi_i^* \Phi_j \mathrm{d}V$ between two sites j and i strongly depends on the distance and the orientation of the molecular sites to each other. The modulation of S_{ij} is nicely demonstrated in a theoretical model by Mori et al. [17]. The overlap integral is closely connected to the transfer integral $t_{ij} = \int \Phi_i^* |H_{ij}| \Phi_j \mathrm{d}V$, where H_{ij} is the Hamiltonian of a dimer system, which defines the electronic conductivity of a material. The transfer integral is a measure of the conductivity of the system. As both quantities are sensitive to the intermolecular distance, the properties can be tuned by an external stimuli like temperature or pressure, causing a variety of different ground states by competing with correlation effects. By tailoring the organic molecular units and enlarging them, the overlap can be further enhanced by what the dimensionality is increased. The molecular packing motif of one-dimensional organic salts is a simple stacking of the organic cations along one crystal direction, which we will be discussed in more detail in Sec. 5.1.2. Especially in the case of two-dimensional conductors, the molecular arrangement within the plane can be manifold as it is depicted in Fig. 2.2 for the BEDT-TTF salts. The different orientation and arrangement of the molecules, labeled by Greek letters, lead to different ground states and hence, physical properties. Here, for more information, it is referred to the literature [8, 18, 19]. Sec. 5.4.1 is especially dedicated to the α-(BEDT-TTF)$_2$I$_3$ compound.

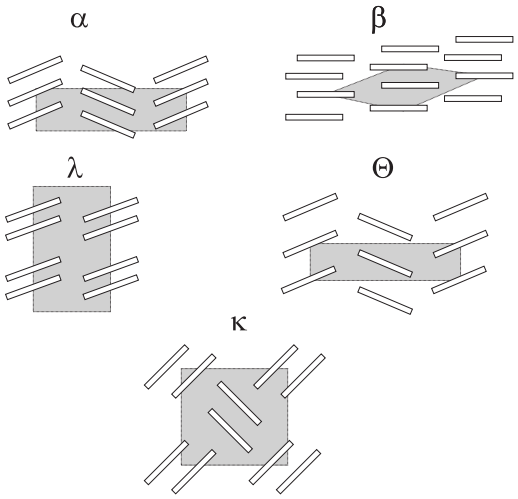

Figure 2.2: The most important packing patterns of organic charge-transfer salts labeled with Greek letters α, β, λ, Θ, and κ are depicted. The view is perpendicular to the molecular plane. Among the shown ones several other variations can be found.

In the before mentioned class, the radical-ion salts, both building blocks have a closed shell and the charge is transferred between them, leading to the situation that both units, here this means molecules, are radicals and hence both carry unpaired spins. In chapter 5.3 we face the material TTF-CA which belongs to this group. It is often also called weak charge transfer compound as only a fraction of the charge is assigned. In TTF-CA the two building blocks, TTF and CA, are arranged in a mixed stack leading to a low conductivity even at elevated temperatures (room temperature) along all three crystal axes.

Due to the low-dimensionality and the anisotropy of the Fermi surface of these material classes, they are sensitive to electron-phonon and electron-electron interaction as well as any kind of external perturbation. Therefore, the phase diagrams of these materials are very rich of different electronic and magnetic phases which give the unique opportunity to study and to compare them with partly analytically-solvable theoretical models.

2.2 THEORETICAL DESCRIPTION: HUBBARD-MODEL AND DFT

In organic systems and, more general, in correlated materials, a huge variety of thermal equilibrium ground states can emerge whose driving force are not always certainly known, for example in high-T_c materials, magnetic [20] or also charge fluctuations [21] are treated as possible candidates as the driving force of superconductivity. Therefore, to gain further insights besides the experimental results, several theoretical models are developed to describe the appearing states. The first approach is to solve the Hamiltonian of a solid state material which in general consists of nuclei and electrons periodically arranged in real space which form complex many-body systems[3]:

$$\begin{aligned}\mathcal{H} = &-\frac{\hbar^2}{2m_e}\sum_i \nabla_i^2 - \sum_I \frac{\hbar^2}{2M_I}\nabla_I^2 - \sum_{i,I}\frac{Z_I e}{|\vec{r}_i - \vec{R}_I|} \\ &+\frac{1}{2}\sum_{i\neq j}\frac{e^2}{|\vec{r}_i - \vec{r}_j|} + \frac{1}{2}\sum_{I\neq J}\frac{Z_I Z_J}{|\vec{R}_I - \vec{R}_J|}\end{aligned} \tag{2.2}$$

The first two terms describe the kinetic energy of the electrons i and the nuclei I, which are interacting with each other via Coulomb interaction expressed by the third term. The last two terms describe the electrostatic electron-electron and the nucleus-nucleus interaction. Since this Hamiltonian is very complicated and cannot be solved exactly, several approximations and methods have been introduced in the recent five decades [22, 23] ranging from simple semi-emperical methods to advanced *ab initio* methods as DFT or Möller Plesset perturbation theory to name only a few of them. In Sec. 5.1.1, 5.2, 5.3, 5.2, and D we have successfully used DFT to explain not only the optical properties, but also the band dispersion and assign the experimentally resolved vibrational modes occurring in a variety of organic conductors.

In 1963, a much simpler model was developed by J. Hubbard [24] based on the second quantization of the Hamiltonian which is used mainly for systems with a single narrow band near the Fermi surface. It works well for one- and two-dimensional systems and has demonstrated to describe magnetic properties, metal-insulator transitions, and metallic states accurately [25, 26]. In the simplest case it takes into account the on-site Coulomb interaction U and a hopping term t which is also known as the transfer integral which deflects the kinetic part of the electron. In Fig. 2.3 a schematic view of a one-dimensional site chain is depicted with the Hubbard model parameters. By assuming that an electron wants to be transfered from one site to a neighboring site, it has to overcome the Coulomb repulsion U. Therefore, the Hubbard model can be written in the following form:

$$H = \sum_{\langle ij\rangle,\sigma} t_{\langle ij\rangle}\left(c^\dagger_{i,\sigma}c_{j,\sigma} + c^\dagger_{j,\sigma}c_{i,\sigma}\right) + U\sum_i n_{i,\uparrow}n_{i,\downarrow} \tag{2.3}$$

i and j denote the lattice site with the $\langle ij\rangle$ pairs. σ is the spin index with the values $\uparrow$ and $\downarrow$. t_{ij} is the transfer or hopping integral between the two sites i and j and U is the on-site Coulomb repulsion. The advantage of defining a site-pair depending transfer integral is for instance that dimerization can be considered in this notation. $n_{i,\uparrow}$ and $n_{i,\downarrow}$ are the number operators of the site i with the

3 Some interactions are neglected, for instance magnetic interactions as spin-orbit coupling.

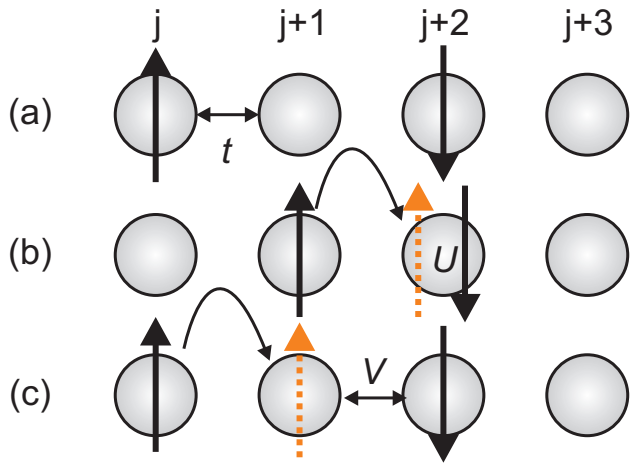

Figure 2.3: (a) One-dimensional chain of lattice sites j which is quarter-filled. For simplicity we have assumed a non-dimerzied system. The orientation of the arrows mark the spin state of the free carriers. t is the transfer/hopping energy. (b) displays the influence of the on-site Coulomb energy on the hopping of the charge carriers to the next site. (c) Illustration of the inter-site interaction V.

creation and annihilation operator $c^{\dagger}_{i,\sigma}$ and $c_{i,\sigma}$, respectively. The competition between t and U defines which state the system captures[4]. For the case U=0, the considered system is metallic, but in the other extreme case when $U \gg t$ the charge stays equally distributed and localized on the lattice sites which leads to the Mott insulator which additionally depends on the band filling (i.e half-filling, see Sec. 2.6.1). When dimerization is taken into account, a gap opens at the Brillouin zone boundary, forming two split bands. For a three-quarter filled band, the upper band becomes half-filled and by switching on U>0 a gap opens at the Fermi energy and the system is transformed to a Mott insulator.

The Hubbard model can be further extended by taking into account inter-site Coulomb repulsion interactions V which is crucial to derive the charge order state [25, 27, 28]. By that, Eq. 2.3 is modified accordingly:

$$H = \sum_{\langle ij\rangle,\sigma} t_{\langle ij\rangle} \left(c^{\dagger}_{i,\sigma} c_{j,\sigma} + c^{\dagger}_{j,\sigma} c_{i,\sigma} \right) + U \sum_{i} n_{i,\uparrow} n_{i,\downarrow} + \sum_{\langle ij\rangle} V_{ij}\, n_i n_j \tag{2.4}$$

where V_{ij} is the Coulomb interaction between the sites i and j. This Hubbard model can be further extended by electron-phonon interaction, i.e modulating the on-site energy and the transfer integral.

The transfer integral was previously determined by extended Hückel calculations. Nowadays, they are determined by DFT calculations. The transfer integral is a function of the molecular or atomic distance and the angular-dependent orientation of the lattice sites with respect to each other. It decays exponentially with increasing molecular distances r_{ij}. In the case of organic conductors the transfer integral is in the range of $\sim$ 100 meV [29]. In contrast, U is on the eV scale [30] and hence, larger than the hopping parameter. It differs from molecule to molecule (from atom to atom). The inter-site interaction V is a function of the lattice distance and decays with $\propto \frac{1}{r_{ij}}$ and is on the same scale as the on-site Coulomb interaction U [30]. Up to that point, we have only considered the one-dimensional case, however, the extended Hubbard model (Eq. 2.4) can be easily

4 U-t defines the energy which has to be paid if one lattice site is doubly occupied.

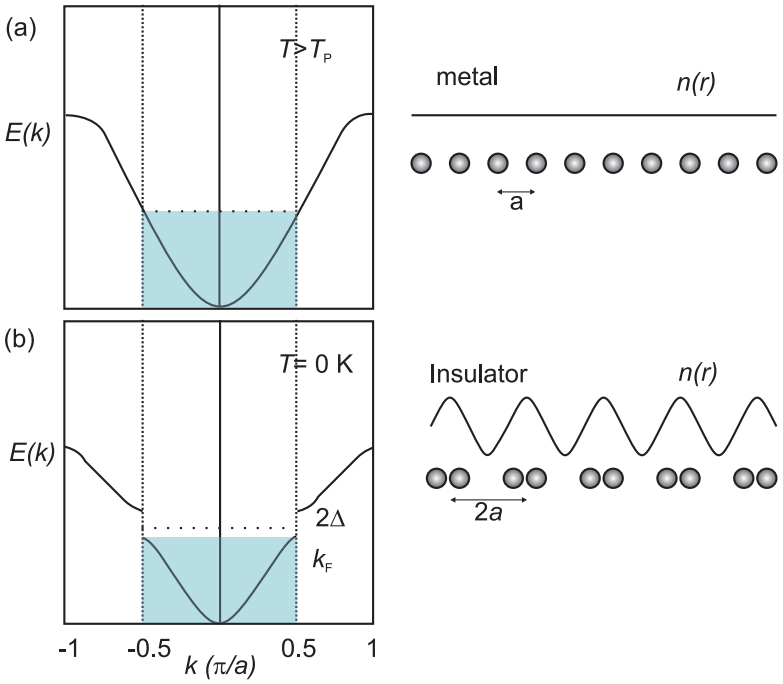

Figure 2.4: (a) A one-dimensional lattice of atomic or molecular potentials with the lattice constant a. Energy dispersion of the conducting electrons in a half-filled band with a Brillouin zone ranging from $-\frac{\pi}{a}$ to $+\frac{\pi}{a}$. (b) Distortion of the 1D lattice due to electron-phonon interaction leading to the modulation of the charge density. Because of the half-filling of the band, a gap of size 2Δ opens at $\pm\frac{\pi}{2a}$.

employed for two-dimensional materials by simply defining further off-chain elements V_{ij} and t_{ij}.

2.3 (SPIN)-PEIERLS-TRANSITION

Many organic charge-transfer complexes undergo a metal-insulator transition at a certain temperature, which is in general below room temperature, although it is expected that they stay metallic or even become superconducting down to the lowest temperature, as for example for TTF-TCNQ. The Peierls phase transition is dominantly triggered by the interaction of the crystal lattice and the electronic system leading to a static and periodic distortion of the lattice accompanied by a fluctuation of the charge density solely in the k-space. This effect occurs predominantly in one-dimensional systems. But why? To answer this, we should start with a gedankenexperiment. The basis is a one-dimensional lattice consisting of nuclei creating potentials with a regular lattice spacing a which is illustrated in Fig. 2.4 (a). Beginning with the parabolic band dispersion of a free electron with

$$E = \frac{\hbar^2 k^2}{2m} \tag{2.5}$$

which is shown in Fig. 2.4 (a). We further assume that the band is half-filled up to the Fermi energy with the corresponding energy dispersion shown in Fig. 2.4 (a) where the electrons move in a lattice with a periodically modulated potential. The weak amplitude of the potentials lead to a splitting of the bands at the zone boundaries of the Brillouin zone BZ at $\pm\frac{\pi}{a}$. As in this example, only one electron or hole, respectively, is contained in the unit cell so that the band is filled up

until $k_F = \pm\frac{\pi}{2a}$ and, hence, it becomes half-filled leading to a metallic behavior and the charge density $n(r)$ is equally distributed. On the other hand, if two free charges resided in the unit cell the system would be already an insulator as the band is filled up to the Fermi energy. If the electron-phonon interaction is now switched on, the free carriers undergo inelastic scattering processes with lattice vibrations. As only the carriers close to the Fermi level at k_F participate in the electric conductivity and as their energy is low in comparison to the total energy of the electronic system, the total change of their wave vector must be $q = 2k_f$. In the one-dimensional case, in principle only one phonon wave vector exists which fully satisfies the law of energy and momentum conservation. This leads to a doubling of the unit cell with the crystal constant of $2a$ where the building blocks form dimers which is depicted in Fig. 2.4 (b). Therefore, a gap opens at $\pm\frac{\pi}{2a}$ in the $E(k)$-k-diagram. The energy cost of the lattice distortion is compensated by the energy gain of the electronic system due to the opening of the gap of which both, the electronic and the lattice, are a function of the displacement of the atoms or the molecules, respectively. Due to the displacement the electron density undergoes also a modification which is called a charge density wave CDW being explained more extensively in Sec. 2.4. The modulation of the charge density is a direct consequence of the divergent behavior of the Lindhard response function which directly connects the change of the charge density with the modulation of the atomic or molecular potentials. Note, the divergence of the Lindhard function is absent in higher dimensions. In this specific case, the lattice distortion and the charge density wave are commensurate, with any other random filling [31, 32] they are incommensurate. The transition occurs only at low temperatures as the thermal excitation of the electrons across the gap prevents the interaction of the electronic system and the lattice subsystem. Furthermore, the Peierls transition is most pronounced in one-dimensional electronic systems as the Fermi surfaces in a theoretically perfect 1D conductor are parallel to each other and the nesting vector is therefore exactly $2k_F$ [32], but as soon as the anisotropy decreases and the coupling of the carriers in other directions to neighboring stacks increases, the possibility of the occurrence of a fitting nesting vector and, hence, of the phase transition is reduced. The transition can also be explained by solving the Hamiltonian of a one-dimensional system in the framework of the mean-field theory leading to a BCS-like gap:

$$\Delta(T = 0\,\mathrm{K}) = 2We^{\frac{-1}{g}} = 1.76k_B T_P \tag{2.6}$$

with g_P the electron-phonon coupling constant, W the bandwidth and T_P the Peierls transition temperature. Due to the large bandwidth the transition usually appears at higher temperatures than the superconducting transition[5]. According to the BCS theory, the phase transition is usually of second-order and the gap Δ reveals the same square-root dependence of the temperature. Mean-field theory does not take into account any fluctuations which lead especially in low-dimensional systems to strong modifications of the phase transition which is therefore observed at lower temperatures in real systems. Hence, the determined coefficients 3.52 or 1.76 from Eq. 2.6, respectively are altered and in common higher. At a later point in this thesis, it will be talked about quarter-filled, one-dimensional systems which lead to a $4k_F$ charge density wave CDW. When

5 In the case of superconductivity, the phonon energy is the crucial quantity being in general significant smaller than the bandwidth.

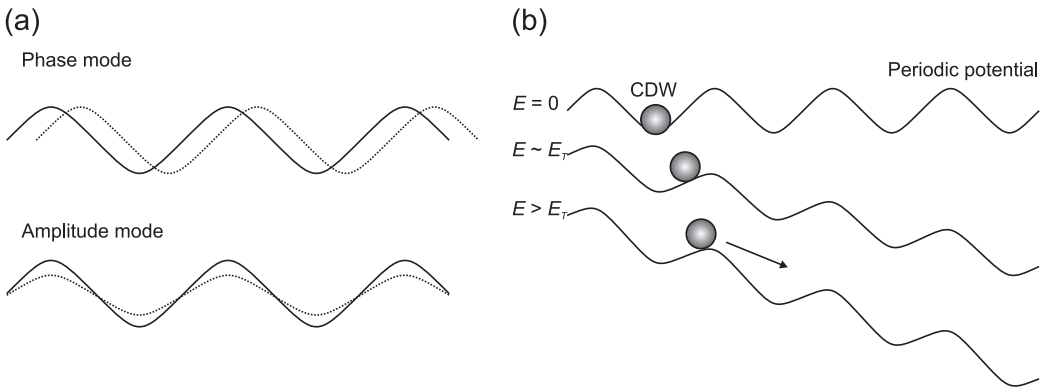

Figure 2.5: (a) The phason mode is related to a change of the phase of the gap Δ, $u(r)$ or charge density $n(r)$ for $q = 0$. In general, this mode is infrared active, while the amplitude mode, which is connected to an oscillation of the amplitude, is Raman active. (b) Simplified picture of the CDW transport. The filled circle symbolized the quasiparticle CDW in a periodic potential. For $E > E_{\text{th}}$ the CDW starts to slide and contribute to the conductivity of the single particles. Adapted from [32].

it is commensurate with the underlying lattice, it is also often called a Wigner crystal[6] or a charge order state. However, in this meaning the state is purely electronically driven.

SPIN-PEIERLS TRANSITION The difference to the Peierls transition is that the electron spins are involved in the phase transition. There, the total energy of the system is reduced due to the magneto-elastic coupling. Starting point is again a 1D chain of atoms or molecules, which forms an anti-ferromagnetic spin chain whose intra-chain exchange coupling is larger than the inter-chain coupling. Via the magneto-elastic coupling effect, the lattice is distorted and, hence, the magnetic exchange alternates leading to the formation of spin singlets which are non-magnetic. The main feature is a sharp decrease of the magnetic susceptibility because of the formed spin singlet. The transition temperature is a function of the external magnetic field.

2.4 CHARGE DENSITY WAVE

Over the last 50 years, charge density waves CDW have been observed in several, especially inorganic, compounds, as for instance $NbSe_3$, TaS_3, and $Ko_{0.3}MoO_3$. It was assumed that the sliding of the charge density wave, induced by an electric field, can lead to a kind of superconductivity. This idea was originally proposed by Fröhlich [8]. The dynamic of the CDW or collective mode depends on the order parameter Δ being directly related to the more demonstrative lattice distortion $u(r)$. The collective mode $u(r) = u_0 \cos 2k_F x + \phi$ depends on the modification of the phase Φ and of the amplitude, as it is illustrated in Fig. 2.5. Due to the electron-phonon interaction, amplitude (amplitudon) and phase mode (phason) appear which are decoupled from each other. The amplitudon exhibits a gap, depending on g_P, with a quadratic dispersion. It is Raman-active and with increasing temperature the mode softens below T_{CDW}. On the other hand, in first approximation neglecting any screening effects, the phason reveals a linear

6 Named after the physicist Eugene Wigner who predicts the crystallization of electrons in a uniform pattern.

dispersion with $\omega_{\mathrm{Ph}}(q = 0) = 0$ and corresponds to a translation motion of the charge density. In principle, it should be infrared active, but as $\omega_{\mathrm{Ph}}(q = 0) = 0$ for a sample with high purity, it can only be detected by neutron scattering experiments. As in both modes the ions are involved, the resonance frequencies are normalized according to the effective collective mass. The effective mass of the charge density wave $m^\star$ is in the range between 100 and 1000 m_e. Under an external alternating electric field and solving the corresponding equation of motion, one determines a zero frequency mode which occurs beside the single-particle gap. This was the reason why it was expected that CDW materials exhibit a supercurrent under an applied voltage similar to BCS superconductors, but in real materials impurities are present causing a pinning of the collective mode to the lattice and thus shift the resonance frequency to a finite frequency within the energy gap Δ.

The most interesting feature is the nonlinear collective charge transport. If the pinning energy is small, above a certain small threshold field (< 1 V/cm) the conductivity leaves the Ohmic regime and reveals a nonlinear behavior. In this context, it was demonstrated that the threshold field is also a function of the pinning center concentration. The conductivity consists of two different current contributions: i.) one arises from the thermal excited charge carriers in the conduction band and ii.) the other one from the sliding of the CDW dominating the conductivity above E_{th}. For much higher electric fields the current saturates. A simple model describes this effect very well which bases on a stiff density wave being pinned to impurity potentials which forms for simplicity a periodic potential landscape. The solution of the damped equation of motion yields the value for the threshold field. A more pictorial explanation is illustrated in Fig. 2.5 (b) . At $E = 0$ V/cm, the collective state is pinned to the potential, with increasing E the pinning energy can be overcome and above E_{th} the CDW starts to move. In the nonlinear regime when the time-resolved current is Fourier transformed, sharp resonance features appear in the frequency spectrum. The resonance frequency and amplitude increase with increasing electric field. Many interesting phenomena are connected to the CDW, which are summarized in the following briefly:

- A metal-insulator transition occurs which can be observed as an abrupt increase of the resistivity as well as by the opening of a single-particle gap Δ in optical experiments.
- Above a certain electric threshold field nonlinear conductivity sets in.
- A narrow- and broad-band noise is connected to the sliding of the CDW.
- Dielectric spectroscopy reveals a strong frequency dependent feature.
- In the microwave and terahertz regime collective modes occur.
- Due to the electronic screening and the diverging Lindhard function at $q = 2k_{\mathrm{F}}$, the acoustic phonons at $q = 2k_{\mathrm{F}}$ soften while approaching the transition temperature $T \to T_{\mathrm{CDW}}$. The softening of the mode can be detected by neutron scattering experiments and follows a square-root temperature-dependent behavior for $T > T_{\mathrm{CDW}}$ and tends to zero for $T = T_{\mathrm{CDW}}$.
- The superstructure due to the lattice distortion leads to additional peaks in X-ray scattering experiments. The reflection intensity obeys the same temperature-dependent modification as the single-particle gap Δ.

- A finite anomaly in the specific heat C_p appears at T_{CDW}.

In all mentioned effects any fluctuations or deviations from the perfect one-dimensional case lead to a modification of the observed features, for example the Bragg reflections as well as the transition in C_p broaden or the soft mode does not tend to zero.

2.5 METALLIC STATES

Metallic behavior is observed in various material classes. In standard metals as copper, gold or aluminum the optical as well as the DC conductivity can be described in the framework of the Drude model (free electron gas) [7]. There, it is assumed that the charge carriers only interact with the underlying lattice (phonons) as well as with impurities and not with each other. The interaction with the lattice is taken into account by a scattering rate which depends on the free mean path and the Fermi velocity.

FERMI-LIQUID However, when the bands are narrow or the dimensionality is low, the density of the states is enhanced at the Fermi energy and electron-electron interactions become important. Therefore, Landau [33] suggested that the electron-electron interactions can be mapped on a free electron gas by renormalizing the band mass. The main idea behind these calculations is that the excitation of an interacting system resembles the behavior of the excitation of quasi-particles in a non-interacting system by adiabatically switching on the interactions. This "Fermi liquid theory" implies several consequences:

1. Only particles close to the Fermi surface participate. Thus, the Fermi liquid behavior becomes dominating at low temperatures.
2. The Drude response becomes renormalized by an effective scattering time τ^*_{Sc} and effective mass $m^\star$.
3. The scattering rate of the quasi-particles becomes

$$\frac{1}{\tau^*_{Sc}} \propto T^2 \text{ and } \omega^2 \tag{2.7}$$

4. The DC conductivity σ_{DC} is proportional to $\frac{1}{T^2}$.

The Fermi liquid theory is valid for systems with the dimensionality $d \geqslant 2$. When the dimensionality is further reduced, a Luttinger liquid appears.

LUTTINGER-LIQUID In the case of one-dimensional interacting systems as nanotubes, semiconductor wires or quasi-one-dimensional conductors the Fermi-liquid model breaks down. In a one-dimensional system the Fermi surface consists of points. This leads to the Peierls instability as different parts of the Fermi surface can be mapped on each other by a $2k_F$ vector, meaning that perfect nesting conditions are present. By that, the response function obeys a singularity at the Fermi energy. Considering solely excitations close to the Fermi surface, the energy dispersion in momentum space can be assumed to be linear. Therefore, only collective excitations are allowed in a one-dimensional system, in contrast

7 The optical response of a Drude component is discussed in Appx. F.

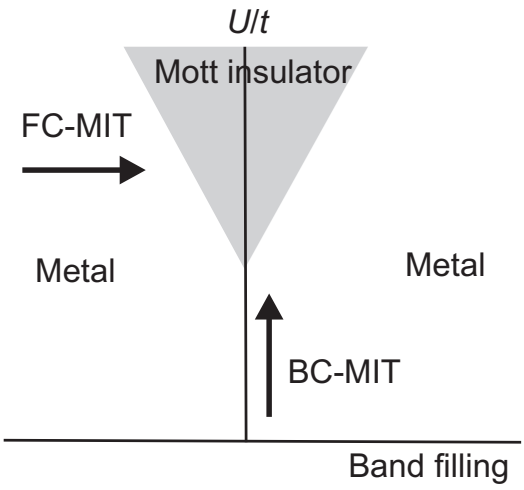

Figure 2.6: Phase diagram containing the metallic (white) and insulating (gray) phase. The metal-insulator transition can be controlled either by the band filling (FC-MIT) or by the bandwidth of the system (BC-MIT).(Adapted from [26])

to a high-dimensional system where single excitations can occur. The Luttinger liquid is characterized by some key features:

- The spin and charge are separated from each other.
- Gapless excitations.
- Fluctuations of spin and charge degrees of freedom.
- Power low behavior of certain quantities such as conductivity or density of states, depending on the Luttinger interaction parameter appearing in the exponent.

2.6 INSULATING STATES

It is known from the theory of noninteracting electrons in a solid that the band filling decides if the system is metallic or insulating. When the band is just partially filled, the material is a metal while for a completely filled band the material becomes insulating. In this framework the physical properties are only determined by the spatially periodic arrangement of the atoms in the crystal structure. Moreover, we define a system with an energy gap larger than 3 eV as an insulator and below as a semiconductor as a rule of thumb.

2.6.1 *Mott insulator*

In the first part of the 20th century many transition metal oxides were studied for which a metallic behavior was predicted due to the partially filled bands, but very often an insulating behavior was experimentally discovered. Thus, Mott [34] proposed that electron-electron interaction is the driving force and that the competition of the on-site Coulomb repulsion U with the kinetic (transfer) energy t controls, besides the band filling, the physical ground state. The Mott-insulator and the very often observed metal-insulator transition can be described successfully in the framework of the introduced Hubbard model (see Sec. 2.2).

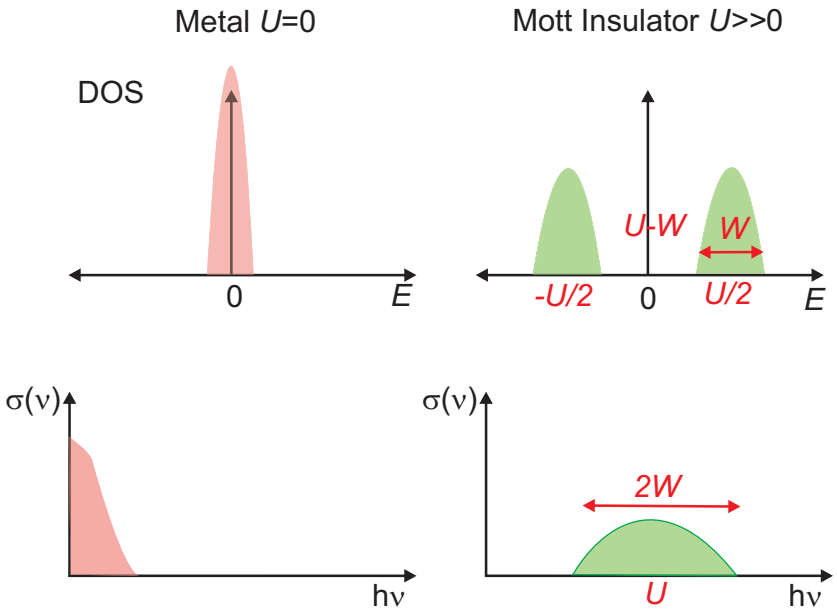

Figure 2.7: (a) DOS for a half-filled band which is intersected by the Fermi energy with weak electron-electron interaction $U \approx 0$. The DOS is concentrated around E_F. The charge carriers at E_F are excited and lead to a Drude component in the optical response. (b) With $U \gg W$ a Mott-insulator is established by what the band is separated into a lower and upper Mott-Hubbard band with the energy spacing of U. The bands have a bandwidth of W. In the corresponding optical spectrum one broad feature appears at U with a width of $2W$.

As we pointed out that the two important ingredients for a Mott insulator are i.) the ratio U/t and ii.) the band filling n. By that, a simple phase diagram can be drawn depending on these two parameters, which is depicted in Fig. 2.6. On the most left side of the x-axis the band filling is zero whereas on the most right side the site is doubly occupied. The y-axis accounts for the ratio U/t. At half-filling (n=1) the metal-insulator transition can be induced by varying the bandwidth W, correspondingly, the transfer energy t of the system which can be tuned by the intrinsic coupling to the lattice or by applying hydrostatic or chemical pressure. It is assumed that the transition is of the first order type. In contrast, by doping the materials with holes or electrons, the band filling can be controlled, so that the system can be driven away or towards the metal-insulator transition in a continuous way.

Furthermore, for instance at 1/2 filling, the charge carriers can be localized in an alternating pattern which we will discuss in detail in Sec. 2.6.2. Additionally, the Mott insulator is often accompanied by magnetic ordering like an AFM state.

The spectral response of a transition from a metal to a Mott insulator can be understood by considering the density of states, as depicted in Fig. 2.7. Here, the system consists, for simplicity, only of one band at the Fermi energy which is set to zero in the sketch. There, the DOS state is maximum at the Fermi energy and the on-site Coulomb energy is $U \approx 0$. Only the states or charge carriers close

to the Fermi energy E_F can contribute to the optical response. Thus, the optical conductivity contains only one single Drude component with a finite σ_{DC} value and a certain scattering rate τ_{Sc}. In the insulating state, U captures a finite value by what the system is driven in the Mott insulating state where the single band is split into the so-called lower and upper Mott-Hubbard bands. The optical excitation can only take place across the created energy gap from the occupied to the unoccupied Mott Hubbard band which corresponds to the transfer of a charge carrier to a neighboring lattice site which becomes doubly occupied. The bands have a bandwidth of W. This is reflected in the optical spectrum as a broad feature centered around U with the width of 2W.

2.6.2 *Charge order*

The basic concept on charge ordering CO goes back to the ideas of Wigner [35] in the 1930's. He proposed that by considering the interaction of free electrons with opposite spins, their wave function must be strongly modified and deviates from the initial form. By taking this interaction into account, it leads to the so-called crystallization of the electrons in a regular pattern within the crystal, which is called Wigner crystal.

Therefore, charge order and Wigner crystal are often mentioned in the same context. We have mentioned previously in Sec. 2.4 that charge ordering is called very often commensurated $4k_F$ CDW. Indeed, one has to distinguish that in the case of CDW and Peierls instability a nesting of the Fermi surface is necessary, which is mainly satisfied in one-dimension, as well as the interaction with the lattice system is important whereas the CO is established independently on the shape of the Fermi surface and hence, the dimensionality, and mainly triggered by electronic interactions. Furthermore, it was stated in Sec. 2.2 that besides the on-site Coulomb interaction U the inter-site V plays a crucial role for developing the charge ordering [25] in one-dimensional as well as in two-dimensional organic compounds.

In the same decade, Verwey [37] observed a sharp metal-insulator phase transition below T_{CO}=120 K in the transport data of magnetite Fe_3O_4. The conductivity is reduced by less than 2 orders of magnitude. He proposed that the valence states of the iron atoms Fe^{+3} and Fe^{+2} are statistically distributed in the solid in the high conducting phase. They exchange electrons rapidly leading to a hopping conductivity [38]. Below T_{CO} the Fe^{+3} and Fe^{+2} ions are arranged in a regular pattern which suppresses the electron hopping by what the conductivity decreases. However, this transition was and is still called Verwey transition in literature.

Over the last decades, charge ordering was discovered in many material classes as transition metal oxides or organic conductors, as discussed in this thesis, for instance in manganates [26, 39, 40], nickelates [26], and cuprates [41] where it attains great attention because of its appearance in the phase diagram in the vicinity of the superconducting phase. It is also supposed that charge fluctuations occurring often close to the charge ordered phase can mediate superconductivity in organic conductors [19, 21, 42, 43, 44] which cannot be explained solely by simple coupling to the phonon bath or by magnetic fluctuations.

Here, we focus on the organic conductors with a charge-ordered phase. One of the most famous subclass of charge ordered materials are the Fabre salts $(TMTTF)_2X$ with different types of anions X. They are quarter-filled, one-di-

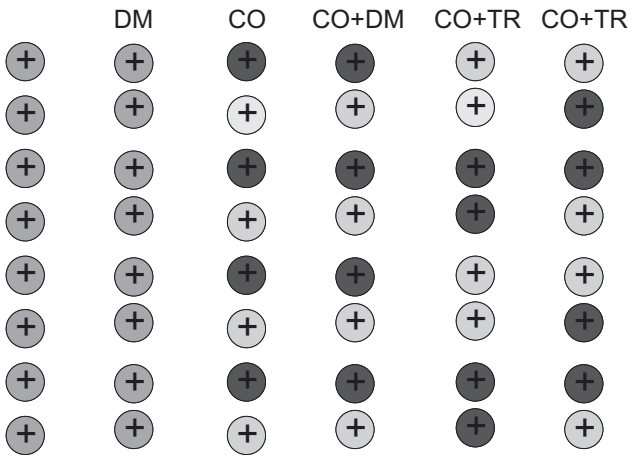

Figure 2.8: Here, we consider a quarter-filled, one-dimensional system (going from left to right). i.) Equally distributed charge and equally spaced lattice sites. ii.) Dimerization leads to a "paring" of the sites and together with U to a Dimer-Mott (DM) state where the charge is localized on bonds between the dimer. iii.) and iv.) For with and without dimerization the charge becomes unequal distributed in an alternating way for $V>0$. v.) and vi.) Due to a further potential, for example caused by anion ordering, the charge pattern can be rearranged in two different ways. (Adapted from [19, 36].)

mensional conductors where the TMTTF molecules form a 1D chain. Their physical properties can be explained very well in the framework of the extended Hubbard model ([27] Eq. 2.4) presented in Sec. 2.2. Depending on the ratio of U/t and V/t as well as on the dimerization for a quarter-filled system, different charge and structure patterns can be found in the 1D case, as depicted in Fig. 2.8. For no dimerization and $U \neq 0$ and $V=0$ the system is metallic. However, when dimerization is switched on, a gap opens at the Brillouin zone and the band is split into one completely filled and one half-filled band separated from each other by an energy gap. Furthermore, when $U \neq 0$ a Dimer-Mott state can be established where a gap opens at the Fermi energy leading to a splitting of the DOS and the charge is equally distributed.

In a next step, V captures a finite value and above a certain critical inter-site Coulomb repulsion charge ordering occurs independently of the dimerization state. For a non-dimerized system the transition is of the first order kind. Finally, the chain can undergo a tetramerization leading to further gaps in the band dispersion and a rearrangement of the charge pattern into different configurations as it is observed for Fabre salts with non-centrosymmetric anions. In the Hubbard model the possible influence of the anions and their potential via electronic polarization on the electronic properties of the conducting cation chain is not considered.

Also, two-dimensional quarter-filled organic conductors reveal charge ordering, for example α-(BEDT-TTF)$_2$I$_3$ or the Θ-(BEDT-TTF)$_2MN$(SCN)$_4$ with M=Rb and Tl, and N=Zn and Co. It can be as well described by the extended Hubbard model by defining two different inter-site interaction parameters V. From that three charge patterns can be deduced: horizontal, vertical as well as diagonal stripes, as displayed in Fig. 2.9. The main difficulty is to take into account the different structural types. However, when the band filling deviates from quarter-filling, the material becomes conducting.

Nonlinear conductivity under high electric fields is observed in several charge ordered materials [45, 46, 47, 48, 49] which opens the possibility to use these

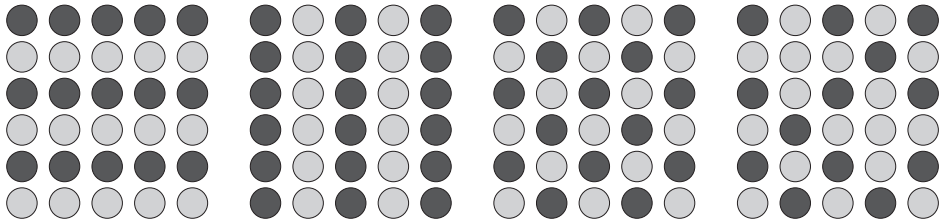

Figure 2.9: Schematic charge pattern for a square lattice. Depending on the interaction terms and directional kinetic energy of the charge carriers i.) horizontal ,ii.) vertical, or iii.) diagonal charge patterns can develop. For a band filling, which is different from quarter-filling, the charge carriers can find a lattice site where they can hop leading to a finite conductivity.

materials at one point as new materials in electronic micro- and nano devices, for instance, as a thyristor, (non-)volatile memory devices. Moreover, controlling the charge-ordered state by light is a very active research field. It has already been demonstrated that the charge ordered phase can be melted by photo-excitation resembling the characteristics of metallic as well as superconducting phases [50, 51, 52, 53]. In the future, more attention will be paid to photo- and electrically stimulated phenomena in charge-ordered compounds considering optical switches and the entanglement of the physical origin of superconductivity since there are indications that charge fluctuations mediate superconductivity [21].

There are several techniques available to detect charge order:

- Vibrational spectroscopy as FTIR- and Raman spectroscopy can be applied to trace the temperature- or pressure-dependent modifications and splittings of the resonance frequencies of vibrational modes which are charge sensitive [19].
- Similar, the NMR method detects the changes of the chemical environment of the differently occupied lattice sites which is caused by the unequal charge localization [54].
- Charge order is very often accompanied by a broken symmetry activating ferroelectricity which is demonstrated by a diverging dielectric response at the phase transition [55].
- X-ray scattering experiments can observe modifications of bond lengths within organic molecules. These bonds are sensitive to the amount of localized charge [56].
- Second harmonic generation can deliver additional information about charge order and ferroelectricity when the structural symmetry is broken [57].
- Spatially resolving methods with atomic resolution like STM can visualize the charge pattern [58].
- Parallel to the charge localization, the DC conductivity reveals in general a decrease of several orders of magnitude which was demonstrated by transport measurements [59].

ANION ORDERING Besides the charge ordering mentioned within this thesis, the reader will face an anion ordering AO which can be found in specific compounds of the TMTSF as well as of the TMTTF family. It always appears in systems where non-centrosymmetric anions are used, as the tetrahedal ReO_4 and BF_4. In the unit cell of the Bechgaard and Fabre salts, the anion resides on an inversion center in a molecular cavity formed by the methyl end groups of the cation (TMTTF and TMTSF, respectively). The non-centrosymmetric anions can capture two or more orientations. At room temperature, they are disordered [8, 18, 60] and can be thermally excited to capture the other configuration by what they are statistically equally distributed. This is only the case at high temperatures. Upon cooling, the anions are confined to one orientation and long-range order is realized. However, by fast cooling the AO can be quenched. The AO has strong influence on the electronic and structural properties: opening of a gap at the Fermi surface and doubling of the unit cell expressed by an anion ordering wave vector q_{AO}. In the case of the anion ReO_4, the wave vector is $q_{AO} = (1/2, 1/2, 1/2)$. AO becomes noticeable as an increase of the resistivity and a drop of the spin susceptibility. In addition, the charge pattern can be redistributed, as shown in Fig. 2.8.

2.7 OPTICAL PROPERTIES OF ORGANIC CONDUCTORS

In the previous section we have seen that many different phases occur in correlated low-dimensional organic salts. Each of these thermal equilibrium states modifies the energy landscape and dispersion of the materials, not only close to the Fermi energy, but also on a wider energy range depending on the driving force and the involved interactions. Therefore, any phase and especially phase transition has its own impact on the optical properties and fingerprints which can be used to identify the present state and to learn something about the internal physical mechanisms and interactions. Furthermore, electron-electron correlations lead to some deviations from the standard concepts leading to redefinition of some optical features, for instance the optical response of free charge carriers. On the basis of the theoretical concept of the Hubbard model introduced in Sec. 2.2, the optical spectra can be interpreted within this framework. However, we are not going to discuss the mathematical expressions describing the occurring optical features at that point. Therefore, the reader is referred to Appx. F where more detailed information can be found as well as in Ref. [19, 44] and in the literature there within.

Here, we want to give the reader just an idea and impression of a typical optical spectrum which can be encountered while studying an organic conductor. Such a frequency-dependent reflectivity and optical conductivity spectrum is depicted in Fig. 2.10. The total spectrum consists of three parts. At low frequencies the optical response is dominated, in the case of a metal, by the free charge carriers which are excited by the external electromagnetic wave. It influences the spectrum up to the mid-infrared spectral range (4000 cm^{-1}) and also beyond in the case of standard metals, as gold. In the case of an insulator, the spectral weight of the free charge carriers is shifted to higher frequencies which leaves an optical gap in the spectrum at low frequencies. Therefore, the vanishing of the contribution of the free carriers can be accounted for a metal-insulator transition. In the case of strongly correlated materials the response of the carriers cannot be modeled in a strict sense by the Drude model which must be extended therefore.

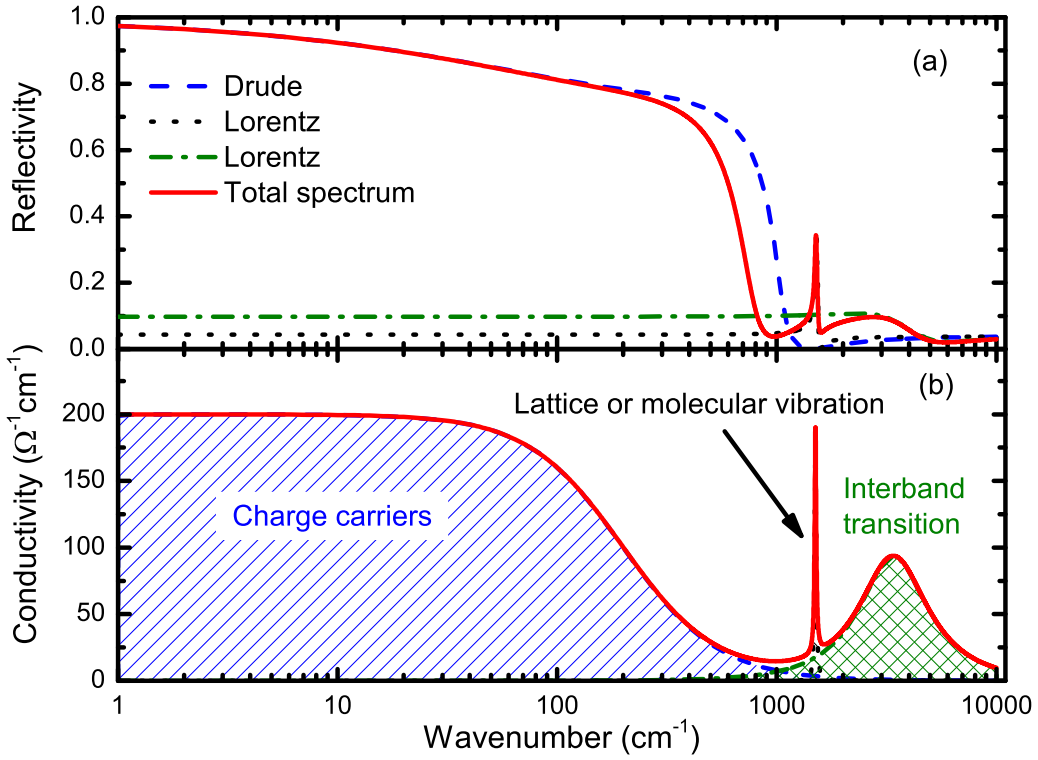

Figure 2.10: (a) Simulated reflectivity spectrum (red line) of an organic conductor as it can be observed in an experiment. The spectrum consists of three contributions: a Drude feature (blue dashed line) caused by the optical response of the free charge carriers to the electromagnetic wave with a plasma frequency of ν_p=1550 $cm^{-1}$and a scattering rate of γ_{Sc}=200 cm^{-1}, emv-coupled vibrational mode (black dotted line) expressed by the Lorentz-like resonance located at 1500 $cm^{-1}$with a width of 30 cm^{-1}. The interband transition (dashed dotted green line) causes the broad peak located at 3400 $cm^{-1}$and a damping of 3000 cm^{-1}which is described in the framework of the Lorentz-model. (b) Frequency-dependent optical conductivity corresponding to the reflectivity data from (a) where the optical components simply sum up to the total spectrum. The different contributions are highlighted by the shaded areas. (Adapted from [19].)

Thus, the carrier mass and the scattering rate must be renormalized and become frequency-dependent quantities by which the spectral response can be modeled accurately [44].

Besides the Drude feature, further excitations can be found in an optical spectrum. They occur typically in the kHz and GHz frequency regime. For instance collective excitations, as of a charge density wave, or the excitation of permanent electric dipoles in a ferroelectric material can be detected in this energy range if there are not screened by free carriers and the view is not obscured by the Drude component. Further excitations as solitons, domains-walls or excitons are possible which would appear as a Lorentz-like feature in the spectrum. Naturally, due to the different molecular and atomic building blocks of the bulk material lattice vibrations occur in the frequency range between 10 $cm^{-1}$and 500 cm^{-1}[8]. Due to the larger mass of the molecules in the organic conductors, their resonance frequency mainly appears below 200 cm^{-1}according to our study [2].

The resonance frequency of the fundamental molecular vibrations spans from 30 cm^{-1}up to 3500 cm^{-1}. Depending on their symmetry, the modes can cou-

8 Within this manuscript we refer to it as "phonons" to keep a consistent definition of expressions for the reader.

ple to the electronic background by what their spectral shape deviates from the Lorentz form and becomes antisymmetric or Fano-like (see Appx. F). The vibrational modes are a perfect probe for the charge state of the molecules. That is why we use specific modes to determine the charge order state CO. Furthermore, as the phonons are sensitive to any modification of the crystal structure or the molecular environment which makes them a feasible tool to study structural transitions. With the assistance of theoretical normal mode analysis the different vibrational frequencies can be assigned to certain bonds and angles of the molecule. By emv-coupled modes any change of the electronic background and excitations between different bands can be checked and traced.

In a frequency range from 1000 cm^{-1} to 5000 cm^{-1} mainly broad and strong features appear which can be ascribed to the excitation of a transition between an occupied and an unoccupied band whose strength depends on the transition dipole moment, band dispersions and the joint density of states. They are often referred to the Hubbard band or mid-infrared band. They deliver information about the correlations in the regard of U (in the case of a Mott insulator, see Ref. 2.6) and V and charge or hopping transfer t between the lattice sites.

3 NON-EQUILIBRIUM STATE

3.1 PHOTO-INDUCED PHENOMENA

Besides the examination of the various physical ground states, the study of non-equilibrium states has become a very active research field for the last three decades as it is promising to discover new hidden, metastable states whose physical properties are different from the ground states at thermal equilibrium[1]. Furthermore, it is the hope and expectation to gain information about the driving mechanism of these states, for instance superconductivity or metal-insulator transitions and to use this attained knowledge to find external control parameters as electric field or light. This approach can also pave the way to new ultrafast electronic devices for applications in data processing and telecommunication not based on standard semiconducting materials as silicon. It is known that metastable states can be induced by thermal quenching/rapid cooling of disordered materials leading to a transition into a glassy state. In this case its lifetime can be between seconds and years. However, these metastable states cannot be used for applications and really controlled in a proper, controlled way, in general.

Most review articles and textbooks state that the history of photo-induced phase transitions PIPT started in the late 80's and early 90's with the examination of polydiacetylenes (PDAs) [61, 62] and the one-dimensional organic mixed-stacked salt TTF-CA [63], but in the 70's first studies on the interaction of electromagnetic waves with superconductors have been performed. There, also a breakdown of the superconducting state was observed and attributed to a photon-driven transition with a negligible thermal contribution [64]. Therefore, the cornerstones were put in principle with the availability of high power photon sources such as lasers which were developed in the early 60's.

Based on the pioneer work on the photo-induced phase transition in TTF-CA by Koshihara et al. [63], further experiments were stimulated on other material classes, especially on correlated electron materials, like transition-metal oxides [51, 53, 65, 66], organic conductors [67, 68, 69, 70, 71], pnictides [72], and CDW systems [73]. Simultaneously to the experimental successes, theoretical models were developed to explain the experimental results. In this context, K. Nasu [74] and K. Yonemitsu [75, 76] significantly influenced this research area by their theoretical work from the beginning.

In the early days, the materials were excited by photons with an energy of >1 eV by what, in general, a transition between the valence band VB and the conduction band CB is induced. This is also known as photodoping. Also, to that time the laser pulse length was limited to the picosecond range. Due to the rapid development of the ultrafast pump-probe spectroscopy technique the time resolution was improved down to the sub-femtosecond range making it feasible to record electron-electron and electron-phonon interactions. Furthermore, in the last decade the energy range of the laser systems was extended from the visible

1 In this context we do not consider the tuning of the ground state by static external parameters, for example, pressure or magnetic field to create hidden states.

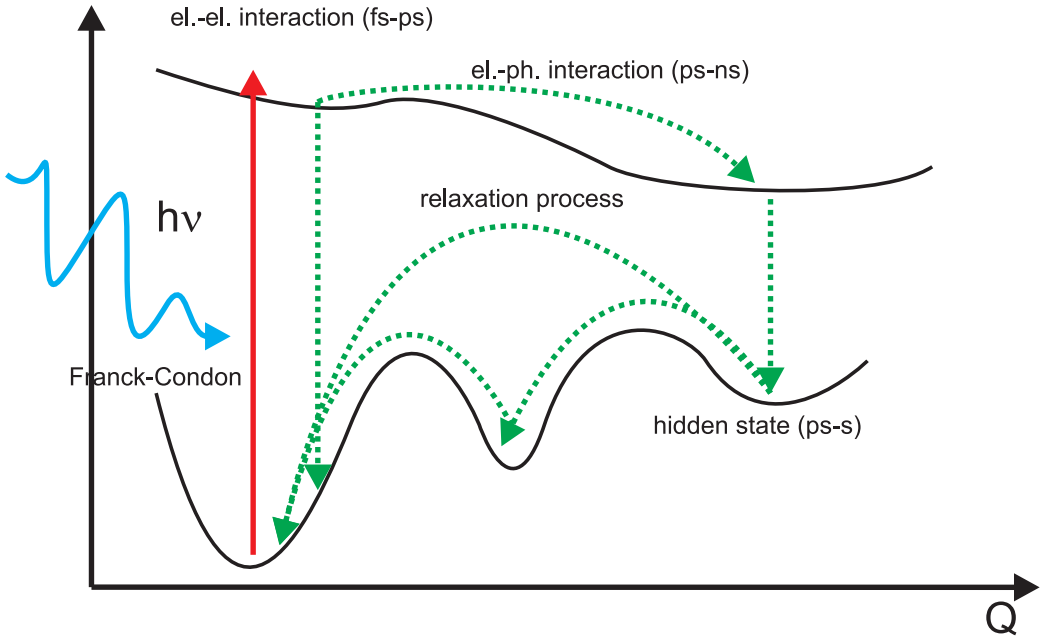

Figure 3.1: Schematic sketch of the generation of hidden metastable state by photons with a certain energy. Potential energy surface of the ground and excited states (black solid lines) for a certain order parameter Q. The blue arrow symbolizes a photon with the energy $h\nu$ exciting vertically the ground state into a higher energy level. Different relaxation channels (green dotted lines) are possible which can result in a metastable hidden state with a different value of the order parameter from the ground state. It is separated from the initial state by energy barriers.

range to x-ray and also down to the THz regime. While photons in the visible range lead to transitions between different electronic bands which is a multiple of the energy barrier between the different energetically separated phases[2] it was shown that with low-energy photons a phase transition can be triggered as well. For example, Fausti et al. [53] have demonstrated that a striped-ordered non-superconducting cuprate can be transformed into a superconductor by exciting certain vibrational modes with mid-infrared light. A further achievement, which has to be mentioned at this point, is the creation of a metastable quasi-superconducting state at room temperature above the superconducting dome in a cuprate compound [77]. In addition, the study was extended to Mott insulators where the on-site Coulomb energy U was modified by exciting the vibrational modes of the organic molecules which influences the molecular orbitals. By that it opens a strategy to gain control over electron-electron interactions [78]. To our best knowledge, the ultrafast pump-probe experiments are limited to a time range of a few hundred picoseconds. However, the induced states can survive up to the microsecond as well as the millisecond regime. While the focus is still on the extension of the time resolution to the attosecond regime, it also becomes more important and interesting for the future to study the slow dynamics and the recovery processes of the metastable states concerning the importance for future applications, as optical switches.

Many materials undergo a variety of different phases by either cooling or heating them up. At each temperature the free energy of the system takes its global energy minimum which can be separated from other local minimum by an en-

2 For instance, the superconducting gap is in the range of a few meV.

ergy barrier which cannot be reached by pure thermal energy. They can differ from the global minimum in certain physical quantities and order parameters. In principle, the potential energy surface is a multidimensional landscape with various hills and valleys which can be reached by the right chosen route. Therefore, in the context of photo-induced phase transitions it is very often talked about hidden "multi-stabilities" or "false ground" states.

A schematic illustration of a PIPT suggested by Nasu [74] is depicted in Fig. 3.1. We assume that the material is in thermal equilibrium and the free energy is in the global minimum whereas several false ground states exist in parallel. Now, the system is excited by a photon of a certain energy. By the Franck-Condon principle the excitation is vertical since the reaction of the electronic system to the perturbation is in the as/fs-regime whereas the lattice reacts in the ps-range. The electronic and lattice systems are decoupled from each other in the first few fs/ps and, hence, the lattice is not affected by the excitation. The occurring modification due to electron-electron correlations, taking place in the first hundred attoseconds up to one femtosecond, can hardly be resolved by the state-of-the-art techniques. The single excited electron can now interact with the left hole alternating the surrounding electronic system and orbitals. This takes place in the first few femtoseconds. One route back is decay and recombination of the electron-hole (exciton) pair which leads to a direct relaxation into the initial state. Furthermore, the created exciton can break up and create several low-lying excited states, for instance charge transfer excitons or collective excitations, by many-body scattering mechanisms or Auger decay leading to a cooperative effect. In addition, energy is dissipated and the electronic system couples to the lattice subsystem by which energy is transfered and phonons are excited. They appear as damped oscillation in the time-dependent signal of pump-probe experiments. By a FT the resonance frequency can be determined and assigned to lattice modes in thermal equilibrium. However, the low-lying excited states trigger the phase transition by relaxation to the hidden "false ground" state. The created metastable domain can further proliferate with a long lifetime and finally decays back to the equilibrium ground state across the energy barrier. The lifetime can be on the nanosecond, but also on the millisecond time range.

3.2 ELECTRIC-INDUCED PHENOMENA

Under this overall term we summarize all effects which deviate from a standard ohmic behavior and are induced by high electric fields, for instance nonlinear conductivity or electrically induced phase transitions. Such phenomena have been known since the early days of inorganic semiconductors where, for example, in the case of the direct gap semiconductor GaAs [79, 80, 81] a negative differential regime exists where the mobility nonlinearly depends on the electric field and decreases above a certain threshold field. The effect is known in this context also under the expression "hot electrons" or Gunn effect which means that the electrons are out of equilibrium and a thermal electron temperature can be defined which is different from the lattice temperature. The carriers can be excited and by that out of equilibrium [81] or scattered by phonons into other k-points in the conduction band with a different effective mass affecting the carrier mobility. However, the expression is not defined precisely and is used in different contexts. Related to this is the Gunn effect in GaAs in which the current starts to oscillate and emits microwaves or the avalanche effect in semicon-

ducting devices. Additionally, artificially constructed heterogeneous structured devices as quantum wells reveal nonlinear conductivity and current oscillations. On the opposite, under high electric fields the charge carriers can be captured easier by impurities or traps which therefore reduces the mobility. From standard semiconductors, as silicon, it is well-known that, for instance, the current flow across a metal-semiconductor interface depends nonlinearly on the applied electric field as well as on the temperature [80, 82] and we should not forget the tunneling effect which depends additionally on the barrier height and width.

Indeed, these effects are not limited to semiconductors since also band insulators can reveal nonlinear conductivity under very high electric fields >10 $MVcm^{-1}$, which is known as dielectric breakdown. This occurs, for instance, in thin insulating oxide films [82] which is mainly related to a highly conducting filament which can destroy a fraction of the film. There are different models to explain this effect:

- The existence of an impurity band between the valence and conduction bands created by the ionization of the impurities by which a highly conducting state is promoted [83].
- Injections of ions through the metal-insulator interface cause a conducting impurity band.
- Irregularities at the metal-insulator interface lead to a local field enhancement and a modification of the insulator structure. It is speculated that the conducting path is formed by vacancies in the material leading to a hopping conductivity or alternatively in the case of metal oxides a pure metallic path is formed.

Furthermore, as discussed in Sec. 2.4 in materials exhibiting a charge density wave phase, as for instance $NbSe_3$, a highly conducting state arises under a moderate electric field (< $1Vcm^{-1}$) which is accompanied by current oscillations in the upper kHz and MHz range whose resonance frequency is a function of the applied voltage. The increase of conductivity is caused by the depinning of the charge density wave from impurities, as described in Sec. 2.4.

Nonlinear conductivity together with resistivity switching also appears in transition metal oxides [45, 46, 84, 85, 86] as VO_2 (for much more details see Appx. D, etc.). In these materials clear models are still missing which can describe the electrically induced effects accurately. It is mainly attributed to a depinning and sliding of a charge ordered state or dielectric breakdown similar to the band insulators.

In ferroelectric materials, domains of different polarization can emerge which are separated from each other by domain walls. These domain walls can be excited by an electric field causing a current flow being expressed as a short, well-defined increase of the current. As soon as the domain wall[3] reaches the opposite contact the current signal drops to zero[87].

In the following we are going to discuss the nonlinear conductivity which is connected to the negative differential resistance (NDR) regime often emerging in the previous listed material classes. There, two different current-voltage curves can be observed which are depicted in Fig. 3.2. The first one is the so-called

3 A single polarized domain is created.

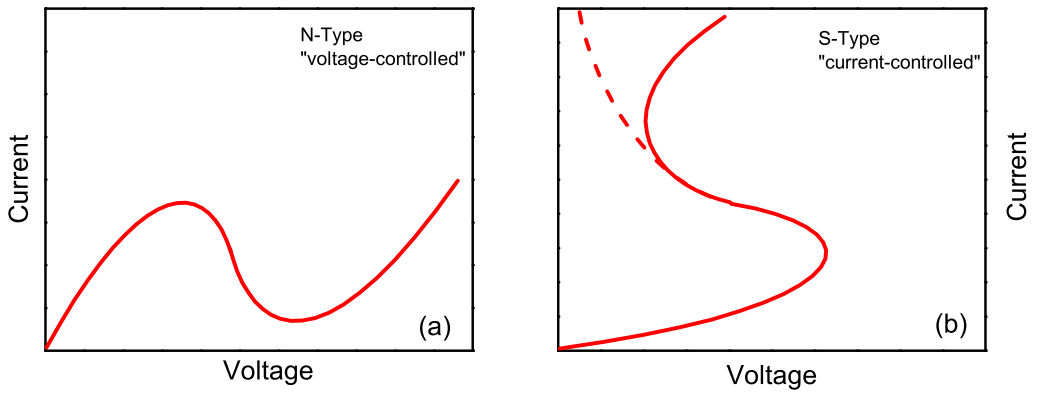

Figure 3.2: (a) N-type current-voltage curve where the current drops above a certain threshold voltage. (b) S-type current-voltage curve. At one point the current is increased significantly whereas parallel to that the voltage is dramatically reduced. Two different final current states can be reached. In one case the current rises steeply (dashed red line) and in the other one the current resembles the resistivity behavior at very low voltages.

N-type current-voltage curve[4] which is very often observed in high electric field experiments on inorganic semiconductors where the mobility drops due to an enhanced effective charge carrier mass.

The other observed current-voltage characteristics is called current controlled or S-type E_{ion}-V curve where at low voltages the current follows a simple ohmic behavior and above a certain threshold voltage the current jumps to a much higher value whereas the voltage reduces simultaneously. Afterwards two different cases can be distinguished i.) the current increases steeply while the voltage stays almost constant which marks that the final state differs from the initial state or ii.) the current evolution resembles the initial ohmic-like behavior. The first case is mainly observed in organic conductors as α-(BEDT-TTF)$_2$I$_3$ presented in Sec. 5.4.1 whereas the latter appears for instance in VO_2 (see Appx. D). This development is related to a resistivity switching from a low conducting state into a high conducting state. Besides that a bistable state can be established by implementing external resistors and capacitors in the electronic circuit leading to an oscillating current. It is noticeable that the switching does not happen immediately after the electronic perturbation and often appears together with a certain delay time τ_d.

The first studies on organic conductors were performed in the 70's and 80's on Cu(TCNQ) [88] and TTF-CA [89] (see Sec. 5.3). Later, this was extended to further organic systems as K(TCNQ) [90] the switching was as well recorded optically, expressing a stripe structure of alternating insulating and metallic domains between the two contacts. In the two-dimensional organic salt Θ-(BEDT-TTF)$_2$CsZn(SCN)$_4$ [91] and its sister compounds [47] the charge order was melted by applying a current to the crystal [92].

A concept or model which can explain all these observations in organic salts is still not established. There exists solely one phenomenological explanation proposed by Iwasa et al. [93, 94] which relates σ_{DC} with the temperature and electric current.

$$\sigma_{DC}(T, J) = \sigma_1(T) + \sigma_2 J^n \tag{3.1}$$

4 It is also well-known as voltage controlled type since for each voltage value there is only one corresponding current value.

where the first term on the right side describes the thermal activated linear ohmic behavior and the second term accounts for the nonlinear conductivity.

In the two-state model it is assumed that "hot electrons" are generated in the conduction band similar to the case in inorganic semiconductors. This was successfully applied by Ozawa et al. [95] and Mori et al. [96] to β″-(BEDT-TTF)$_3$(HSO$_4$)$_2$ and (TMET-TTP)$_4$PF$_6$. Furthermore, it is assumed that the electron system is decoupled from the lattice by which an effective electron temperature T_e can be defined [5]. These excited electrons or quasi-particles follow the heat balance equation:

$$nC_p \frac{dT_e}{dt} = P + \nabla(\lambda_{therm} \nabla T) \tag{3.2}$$

which can be simplified by assuming a linear spatial heat transfer, expressed by the last term, leading to:

$$nC_p \frac{dT_e(t)}{dt} = P(t) - \lambda_{therm}(T_e(t) - T_0) \tag{3.3}$$

The left side of the equation is the energy stored in the excited electronic system. The first term on the right hand side is the electric input power P in Wcm^{-3} created by the externally applied electric field or current, which can be expressed as follows:

$$P(t) = E \times J(t) = \sigma(T_e(t))E(t)^2 \quad \text{or} \quad = \frac{J(t)^2}{\sigma(T_e(t))} \tag{3.4}$$

and the second term describes the linear heat transfer from the electronic system to the lattice system which is kept at the initial temperature T_0 in Kelvin. λ_{therm} is the thermal conductivity in WK^{-1}m^{-1}. nC_p is the electron heat capacity per volume with JK^{-1}m^{-3}. Eq. 3.3 is solved numerically for a certain starting electric field or current pulse. $\sigma(T_e)$ is in general determined from the conductivity curve of the corresponding material as it is assumed that the excited carriers are responsible for the DC conductivity. From this model, a delay time τ_d can be estimated which also accounts for current oscillations.

Summarizing, we define now the following five classes of electrically induced nonlinear phenomena in solid state materials:

1. Non-equilibrium charge carriers: modification of the charge carrier number or the mobility.
2. Space-charge distribution: for instance impurity bands.
3. Electrically induced phase transitions: modification of the electronic system or the crystalline structure.
4. Ionic motion in the host material: forming of conductive filaments.
5. Sliding charge density waves or charge order.
6. Domain wall motions or excitations of solitons.

Although exotic electrically induced effects emerge in almost every material class, it is almost impossible to draw a conclusive picture due to the fact that

5 This is just a hypothetical temperature and does not mean that the sample is heated up.

the diversity of the involved ground states is enormous. Nevertheless, in regard to future electronic devices and applications, more effort has to be put in the experimental studies on electrically induced phenomena as well as in the development of accurate models explaining a wide range of these effects occurring in various material classes.

For the more interested reader we refer to the review articles [82, 92], textbooks [80, 81], and further literature there within.

Part III

EXPERIMENT

4

EXPERIMENTAL SETUP

This chapter is dedicated to the various measurement methods which are used to study the organic crystal. Most of the methods were developed, constructed and tested within this thesis. The main focus is on the FTIR-spectroscopy in which one has to distinguish between the well-known standard Rapid-Scan method (see Sec. 4.1.1) and the time-resolved Step-Scan technique (see See. 4.1.3). Besides the specific differences of both methods, the occurring problems, their solution as well as the analysis methods are discussed.

The Rapid-Scan mode of the FTIR-spectrometer was used to study the steady-state temperature-dependent reflectivity of the samples to gain information about their physical properties and phases. Additionally, the FTIR-setup was extended to measure the electric transport properties simultaneously to the static infrared measurements (see Sec. 4.2). With this configuration it is also possible to examine the time-dependent behavior of the conductivity (see Sec. 4.2) under the influence of short voltage pulses. A Nd:YAG laser system (see Sec. 4.3) was additionally implemented in the setup to perform time-resolved photoconductivity (see Sec. 4.4) and reflectivity measurements. In this case the FTIR-spectrometer operates in the Step-Scan mode (see Sec. 4.1.3).

Besides the various experimental methods, quantum chemical calculations on the basis of density functional theory were performed which are described in Sec. 4.5 and the following. The simulations include the determination of the normal modes of different organic molecules and their resonance frequency, and infrared intensity. Furthermore, the band structure of the studied compounds and the optical spectra were calculated by DFT. At the end of this chapter the related theoretical basics as well as some convergence tests are introduced.

4.1 FTIR-SPECTROSCOPY

4.1.1 *Rapid-Scan technique*

In the simplest case a FTIR-spectrometer consists of a light source and a two-beam interferometer which is arranged in the Michelson configuration. It was invented in the 19th century by A. A. Michelson [97, 98]. A schematic drawing of such an interferometer arrangement is depicted in Fig. 4.1. In a Michelson interferometer the light beam emitted from a light source with a certain intensity $S(\nu)$ is separated by a beam splitter into two beams. They interfere after the reflection on the mirrors M_1 and M_2 and repeated pass through the beam splitter. It depends on the optical path difference δ between two interferometer arms whether the two beams interfere constructive or destructive at the detector position. Since one of the mirror is movable, which is M_1 in Fig. 4.1, the path difference δ can be dynamically adjusted so that the intensity $I(\delta)$ is modified at the detector. Such a situation is illustrated in Fig. 4.2 (a) for a monochromatic light source like a mono mode laser with a finite line width whereas the Lorentz shape of the laser spectrum (see Fig. 4.2 (b) leads to an exponentially decaying envelop of $I(\delta)$. The beams interfere constructive in the case of a monochromatic light source

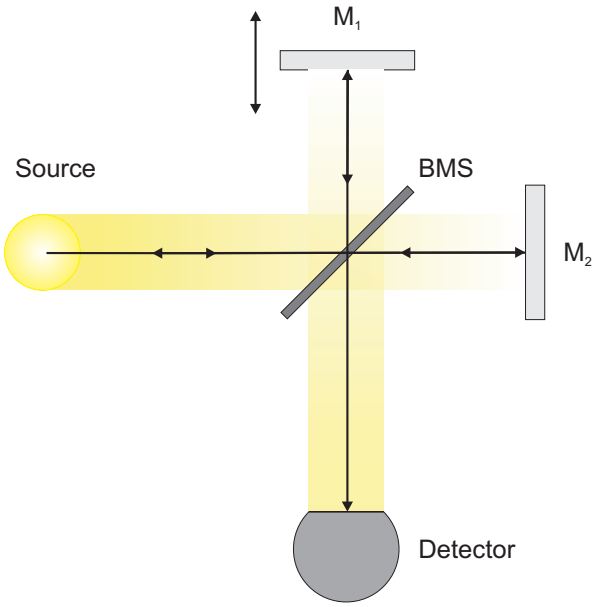

Figure 4.1: Setup of a Michelson-interferometer which consists of a light source, a beam splitter BMS, a fixed (M_2) and a movable (M_1) mirror as well as a detector.

with the wavelength $\lambda = \frac{1}{\nu}$ and under the condition of $\delta = n \cdot \frac{1}{\nu}$ with $n \in \mathbb{N}_0$. The intensity measured at the detector is $I(\delta) = 0.5S(\nu)(1 + \cos 2\pi\nu\delta)$. In general, the position x_{ZPD} of the mirror M_1 is called zero path difference ZPD at which all wavelengths λ interfere constructive and are in-phase. This is pronounced for a broad band source, as depicted in Fig. 4.2 (c) and (d). Since the position of the movable mirror has to be known accurately, its location is determined in commercial FTIR-spectrometer by the interference pattern of a helium-neon laser with a precision in the sub-nanometer range. There are two different kinds of motion for the mirror M_1:

1. The mirror moves with a constant velocity v_{Mi} causing a time-dependent variation of the intensity $I(\delta(t))$ with $\delta(t) = 2tv_{Mi}$ at the detector position. This mode is called Continuous-Scan or Rapid-Scan mode being the common operation.

2. In contrast, in the Step-Scan mode the mirror is stopped at fixed equally spaced points x_i within the interferometer arm. With it, a time-dependent change of the intensity $I(t, x_i)$ is recorded for the different x_i mirror positions and can be transformed in a time-resolved spectrum. Therefore, this method is the best choice for time-resolved measurements in the infrared region capturing reactions in the time range from nanoseconds to seconds. An explanation and description of the method can be found in detail in Sec. 4.1.3.

The intensity $I(\delta)$ in a continuous scan is a function of the path difference δ and consists of a constant DC- and variable AC- component. However, only the alternating part of the intensity is important as it contains the spectral information. Thus, the DC -component is removed in general by an electronic high pass filter. This has the advantage that the AC-part can be more amplified by what the bit range of the A/D-converter can be filled completely. This has the positive effect that the signal-to-noise ratio (SNR) is improved significantly. Also,

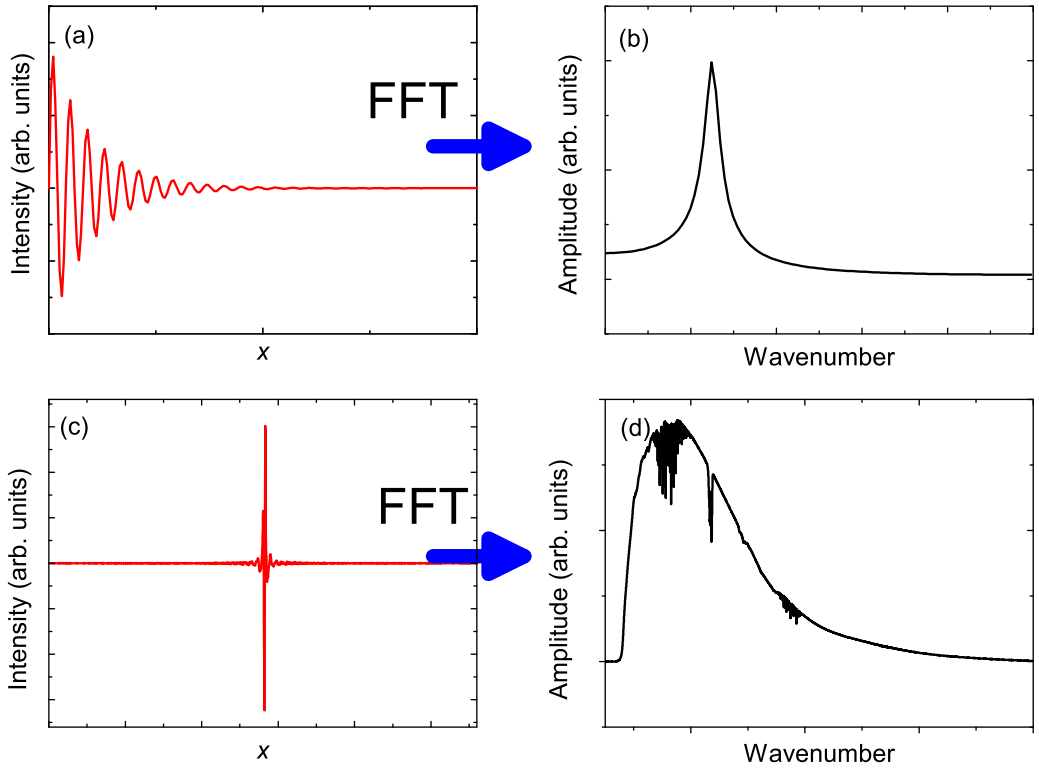

Figure 4.2: (a) Single-sided interferogram of a monochromatic light source with a finite line width reflected in the exponential decay of the signal. (b) A Fourier-transformation of (a) results in a Lorentz-shaped peak. In (c) the interferogram of a broadband light source is visualized as it is usually observed in a FTIR-spectrometer. There, the ZPD can be clearly identified where all wavelengths overlap constructively. In (d) the FFT-spectrum of c.) is illustrated and reflects the broadband spectrum of a black body radiation source. The fine structures originate from the vibrational modes of water and CO_2, being present in air.

the A/D-converter does not saturate due to an additionally amplified DC- component. Furthermore, the measured intensity $S(\nu)$ at the detector depends on the optical as well as on the electronic parts, for instance the beam splitter, mirror, amplifier, etc. The original intensity $I(\delta)$ recorded by the detector becomes modified to $I^*(\delta) \propto S(\nu) \cdot H(\nu) = S^*(\nu)$.[99] $H(\nu)$ is a wavelength-dependent correction factor containing the modifying parts influencing the intensity, for instance mirror, beam splitter, detector etc.. By a Fourier-transformation FT $I^*(\delta)$ can be transformed into the spectrum $S^*(\nu)$[1] [100]:

$$S^*(\nu) = 2 \int_0^{+\infty} I^*(\delta) \cdot e^{2\pi i \nu \delta} d\delta \tag{4.1}$$

Due to the varying intensity at the detector, the moving mirror, the response time of the detector, and the electronic components, the signal cannot be recorded continuously. Thus, the intensity is recored in discrete intervals $I^*(\delta) = I(n \cdot \Delta x)$. ν and δ are replaced by discrete values $j \cdot \Delta\nu = j \cdot \frac{1}{N \cdot \Delta\delta}$ and $n \cdot \Delta\delta$, respectively, leading to a reformulation of Eq. 4.1 :

$$S^*(j \cdot \Delta\nu) = 2 \sum_{n=0}^{n=N-1} I^*(n \cdot \Delta\delta) \cdot e^{2\pi i j \frac{n}{N}}. \tag{4.2}$$

1 In this consideration the apodization function is neglected for simplification of the equation. It is used to compensate the arising effects of the finite travel way of the mirror.

The spectral resolution $\Delta\nu$ of the spectrometer is proportional to the inverse of the maximum distance δ_{max} of the mirror.

The sampling rate of the signal $f = 2v_{Mi}\nu_{max}$ has also to be considered in a rapid scan measurement as the distance $\Delta\delta$ between two measurement points must be smaller than $\frac{1}{2\nu_{max}}$, so that no information is lost. This is the so-called *Nyquist criterion*. If the distance between two data points $\Delta\delta$ can be enlarged, the total number of recorded data points $N = \frac{2\nu_{max}}{\Delta\nu}$ is reduced. In the case of the Step-Scan experiment the total measurement time can be minimized remarkably by that. However, it must be guaranteed that above ν_{max} no intensity exists. Otherwise the signal above ν_{max} is back folded into the spectrum and causes artifacts. This effect is prevented by the utilization of an optical band pass or an electronic filter by what the intensity is suppressed in the specific frequency range. This procedure to reduce the amount of data is named *undersampling*.

To apply Eq. 4.1 or 4.2, the interferogram must be symmetrical around ZPD. This is not satisfied in reality because of

- the digitalization of the data since it cannot be ensured that directly at the ZPD a data point is recorded.
- Electronic parts, for example filters, amplifiers as well as optical parts cause a frequency-dependent phase shift.

To eliminate these disturbing effects, a phase correction has to be performed otherwise this results in a complex spectrum

$$K^*(\nu) = R(\nu) + iI(\nu) = S^*(\nu)e^{i\Phi(\nu)}. \tag{4.3}$$

However, the quantity of interest is the amplitude $S^*(\nu)$. The phase spectrum can be derived by the equation

$$\phi(\nu) = \frac{I(\nu)}{R(\nu)}. \tag{4.4}$$

The amplitude $S^*(\nu)$ [101] is now calculated by a transformation of Eq. 4.3 with the phase determined in Eq. 4.4. While in a standard Rapid-Scan measurement this determination of $S^*(\nu)$ is executed automatically, an additional data treatment has to be performed in a Step-Scan measurement (for details see Sec. 4.1.3).

The standard infrared measurements presented in the framework of this thesis were performed in the Forward-Backward Double-Sided scan mode[2]. The advantage is that the signal-to-noise ratio (SNR) is improved by a factor of $\sqrt{2}$ as well as the error in the phase correction is minimized. However, by that the measurement time is increased.

A further important technical aspect is the dynamical range (small resolution) of the analog-to-digital (A/D)-converter. It is important because the side bands of the interferogram contain the spectral information of vibrational modes, for instance. Their intensity can be up to 100,000 smaller than the signal intensity at the ZPD. In the case of a too small dynamical range the intensity of the side bands is stored together with the noise signal in the lowest bits and hence, the information is lost in the noise. Therefore, the signal must be amplified to use

2 In this driving mode the mirror starts at a certain distance to the zero path difference (ZPD) and completes one interferogram with the ZPD in the center. Afterwards it drives back to its initial position while acquiring the second interferogram.

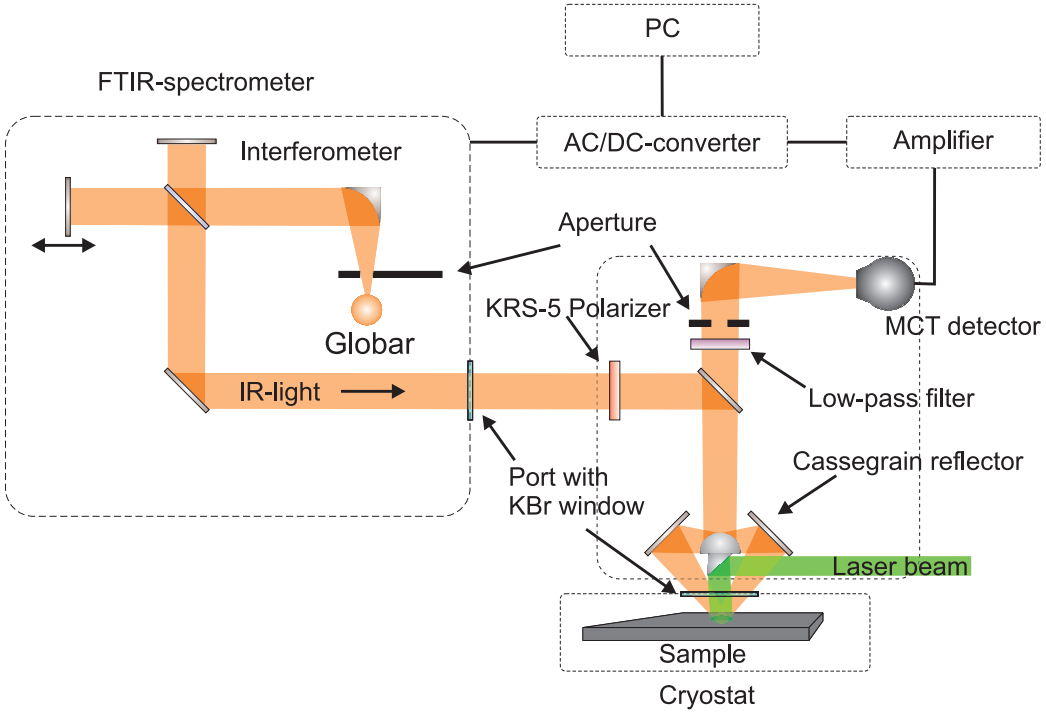

Figure 4.3: Sketch of the optical setup including the laser beam to excite the sample. The setup consists of three main parts (dashed lines). The centerpiece of the setup is the spectrometer containing the electronics as the A/D-converter and amplifier, but also the Globar light source, the interferometer with the BMS and several mirrors to deflect the light beam. The second part is the infrared microscope which is attached to the spectrometer. There, the light is focused on the sample by a Cassegrain reflector. Furthermore, a polarizer and band pass filter can be mounted in the microscope. The MCT detector is placed at the end of the light beam. The data are transferred to a PC. The setup of the cryostat is described in detail in Fig. 4.4.

the total dynamical bit range. Thus, the noise is solely stored in the lowest bits and minimized in the spectrum by averaging. As an example the standard A/D-converter implemented in the spectrometer has a resolution of 24-bit ($16,7 \cdot 10^6$), meaning that by a voltage range of $\pm 10\,\mathrm{V}$ each Bit-level has a distance of $1.1\,\mu\mathrm{V}$ corresponding to the *Bit noise*.

In general, a FTIR-spectrometer has some unbeatable properties and advantages in comparison to a monochromator which were partly denoted in the last paragraphs and will be here briefly summarized:

1. In the case of a monochromator the intensity is measured for a fixed frequency ν while a FTIR-spectrometer records the whole spectrum within one scan (*Fellget or Multiplex advantage*).

2. The mirror can travel with different velocities between $0.1\,\frac{\mathrm{cm}}{\mathrm{s}}$ and $11.4\,\frac{\mathrm{cm}}{\mathrm{s}}$, so that the full spectrum is captured within a few seconds.

3. Since the complete spectrum of a broad band source is measured, a very high light intensity hits the detector in contrast to a monochromator (*Jacquinot-advantage*).

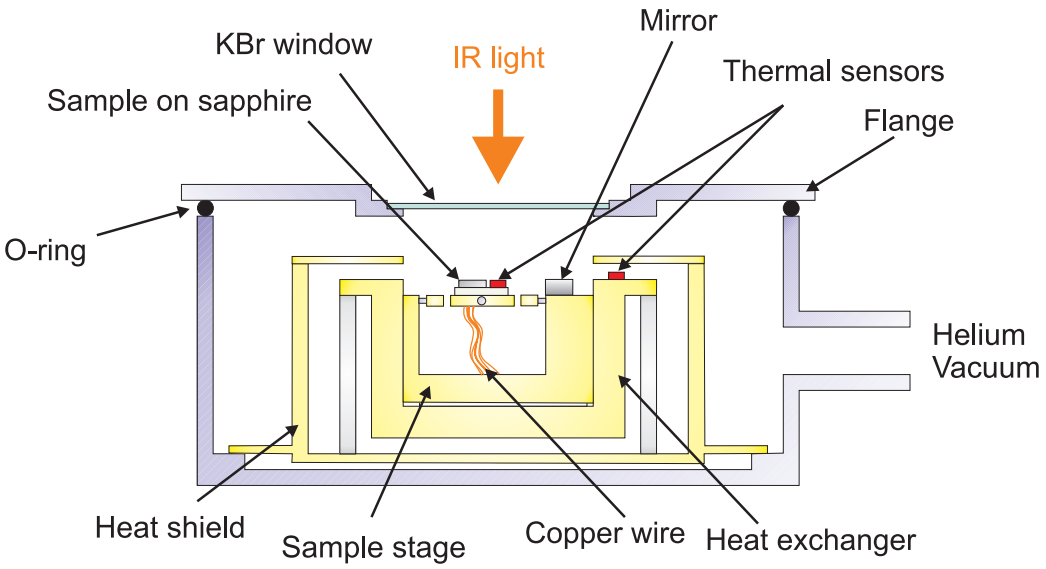

Figure 4.4: Sketch cross of the flow cryostat which is used for the infrared and *in-situ* static as well as time-resolved transport measurements. The outer jacket (grey) separating the pumped compartment from the lab environment is illustrated together with KBr window (light blue) glued on the cover. The sample holder and the main inner parts as the heat shield consist of brass. The two temperature sensors(red) are used to check and control the temperature. The sample and the reference mirror are drawn in as well. Copper wires are soldered to improve the thermal contact.

4.1.2 *Experimental FTIR-setup*

In Fig. 4.3 the setup to measure the infrared spectrum of the materials under consideration is sketched. It consists of a Vertex 80/v FTIR-spectrometer from the Bruker Optics GmbH whose compartment is pumped by an oil-free scroll pump. The final pressure in the compartment is $p < 1.3$ hPa. By pumping the spectrometer, disturbing influences on the infrared active vibrational modes of water and carbon dioxide are reduced. The measurable frequency range is from 10 cm^{-1} to 30000 cm^{-1} depending on the chosen detector, light source, and beam splitter. In the present work the mid-infrared spectral range was examined ranging from 500 cm^{-1} to 8000 cm^{-1}. Therefore, a black body radiation source made out of silicon carbide was used as light source, which is also known as Globar [101]. For the beam splitter KBr was employed which transmits about 90% of the light in the spectral range between 400 cm^{-1} and 40000 cm^{-1} [102].

An Hyperion 3000 (Bruker Optics GmbH) infrared microscope is attached to the right output of the spectrometer to examine the small organic crystals. They are separated from each other by a KBr window. With the microscope it is possible to study samples with a minimum diameter of about 30 µm. In addition, it is possible to perform polarization-dependent measurements in reflection as well as in transmission. The spot size of the infrared light on the sample can be chosen variably between 30 and 300 µm. The light reflected from the sample hits a Mercury-Cadmium-Tellurium MCT-detector located within the microscope. Depending on the measurement, two different detectors have been used which operate in two different modes: the photovoltaic and the photo current mode which have advantages as well as disadvantages. They are discussed in detail in Sec. 4.1.3. The voltage signal of the detector is sent directly to the amplifier and then to the A/D-converter of the spectrometer. The amplification can be freely ad-

justed by the software program between a factor of 1 and 16. The A/D-converter possess a 24-Bit resolution. The intensity $I(\delta)$ or the voltage signal, respectively, is transformed after the digitalization process by a Fourier-transformation to the sample reflection spectrum $S_{\text{Sam}}(\nu)$.

For the temperature-dependent study the sample is placed on a two-axis tiltable sample holder in an optical flow cryostat (Cryovac GmbH), as sketched in Fig. 4.4. This kind of table is used to align the sample such that the incident light beam is perpendicular to the sample surface. Therefore, it is guaranteed that the maximum of the reflected light hits the detector.

The samples are thermally coupled to the sample holder with carbon paste or GE-glue. It is noticeable that solvents contained in the glue do not corrode the organic crystalline samples. Both glues exhibit a high thermal conductivity and hence, ensure a good thermalization of the sample with the environment while the cooling process. The temperature is checked and controlled during the cooling and heating cycles by two temperature sensors (silicon diode, model DT-670, Lake Shore Cryotronics). A temperature controller (model 340) from Lake Shore Cryotronics was employed to read out the sensors, regulate the heater in the cryostat and stabilize the temperature. One of the sensors is placed directly on the heat exchanger which is used to control the temperature T_{Cryo} of the cryostat. Due to the construction of the goniometer a temperature gradient evolves between the heat exchanger and the sample. Therefore, the second temperature sensor is placed next to the sample to capture the actual temperature of the sample T_{Sam}. The maximum temperature difference between the sample and the heat exchanger temperature is a function of T_{Kryo}: close to room temperature the difference is less than 0.5 K and below 100 K it increases significantly to $\Delta T = 4\,\text{K}$ at $T_{Krypo} = 5\,\text{K}$.

The cryostat is capped by a cover in which a KBr-window is glued. The sealing is carried out by a rubber O-ring. To improve the thermal isolation, the whole sample chamber is pumped by a turbo pump including a pre-pump. The final pressure is $p = 9 \cdot 10^{-7}$ mbar.

The cryostat is cooled by liquid helium. Besides the heater in the cryostat the temperature can be adjusted by the helium flow via a needle valve. The cooling rate depends on the amount of evaporated helium since the liquid helium evaporates in the warm inner pipes of the cryostat and thus, cool down the heat exchanger (not shown in Fig. 4.4) .

To determine the absolute reflectivity $R(\nu) = \frac{|\vec{E}_{\text{Sam}}|^2}{|\vec{E}_{\text{Ref}}|^2}$ of the sample, the sample spectrum $S_{\text{Sam}}(\nu) = \mid \vec{E}_{\text{Sam}} \mid^2$ has to be normalized by the intensity spectrum $S_{Mi}(\nu) = \mid \vec{E}_{\text{Ref}} \mid^2$ of a perfect mirror.[3] For this purpose, self-manufactured aluminum mirrors with a thickness between 500 and 1000 nm are used. They are optically dense for mid-infrared light and exhibit a constant reflectivity. The mirror is aligned independently from the sample so that the maximum signal reaches the detector.

Data processing and analysis

To determine the complex response functions $\sigma(\nu)$ or $\epsilon(\nu)$ of the sample under investigation, first the phase $\theta(\nu)$ must be derived from the reflectivity $R(\nu)$ by a

3 $\mid \vec{E}_{\text{Sam}} \mid^2$ and $\mid \vec{E}_{\text{Ref}} \mid^2$ are the reflected wavelength-dependent intensities of the sample and the reference mirror.

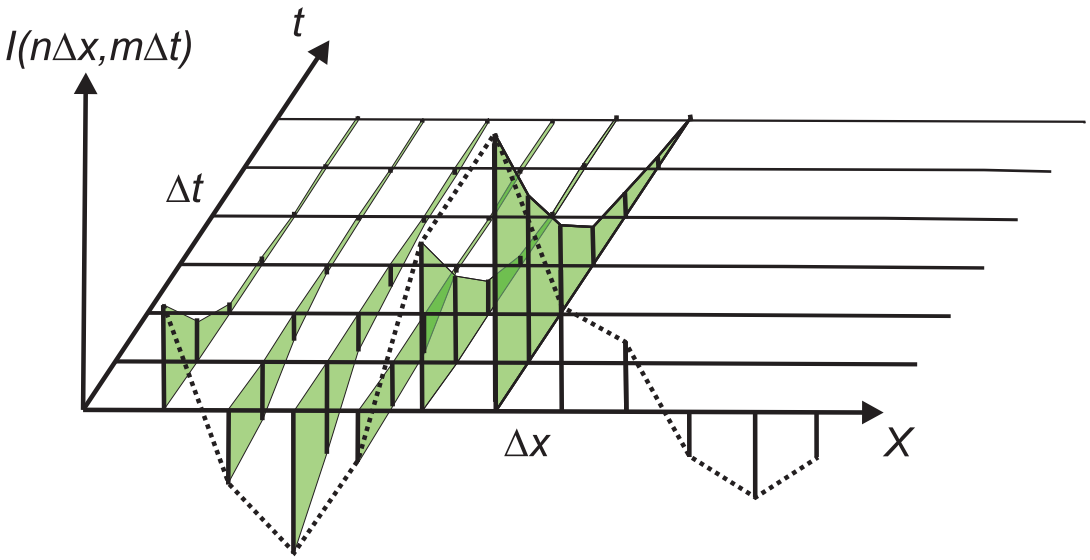

Figure 4.5: (a) At each mirror position $n\Delta x$ the detector signal $I^*(n\Delta x, m\Delta t)$ is recorded as a function of time. After all mirror positions were passed through, the time-dependent signal is recieved by the execution of a FT for each measured time point $m\Delta t$.

Kramers-Kronig transformation as the electromagnetic wave experiences a phase shift $\theta(\nu)$ by transmission or reflection [102, 103, 104]. The complex reflectivity function is related to the quantity $R(\nu)$ by the relation $\mathbb{R}(\nu) = \sqrt{R(\nu)}e^{i\theta}$ and can be rewritten as:

$$\ln \mathbb{R}(\nu) = \ln \sqrt{R(\nu)} + i\theta. \tag{4.5}$$

By the KKT the phase $\theta(\nu)$ is associated with the reflectivity $R(\nu)$ as follows:

$$\theta(\nu_i) = -\frac{2\nu}{\pi} P \int_0^\infty \frac{\ln \sqrt{\mathbb{R}(\nu)}}{\nu^2 - \nu_i^2} d\nu \tag{4.6}$$

whereas P is the Cauchy principal value. From the determined phase $\theta(\nu)$ all further optical functions can be derived [103]. Since the data are discretely recorded, the integration in Eq. 4.6 is converted into a numerical integration. Such a numerical transformation is performed by computer programs. The code of a self-written script is documented in the Appx. G which can be executed with Scilab. One necessary precondition is a large measured frequency range to perform the KKT accurately. As this is not satisfied in most of the cases the reflectivity data has to be extrapolated. The chosen low frequency extrapolation depends on whether the material is an insulator, a semiconductor or a metal. In the first two cases a constant extrapolation is taken, but for a metal a Hagen-Rubens extrapolation $\sim 1 - (\frac{2\nu}{\pi\sigma_{DC}})^{0.5}$ has to be applied. For the high frequency part normally a $\sim \nu^{-2}$ or $\sim \nu^{-4}$ is applied also in combination with a constant value. The high frequency extrapolation has to be carried out at least to 300000 cm^{-1}.

4.1.3 *Step-Scan technique*

As mentioned in Sec. 4.1.1, the Step-Scan technique differs from the standard Rapid-Scan technique in the kind of driving the interferometer mirror. The Rapid-Scan method can as well be used for time-resolved experiments, but

mainly for not repeatable and slow dynamic experiments and reactions. The time resolution depends on the spectral resolution $\Delta t \propto \frac{1}{\Delta\nu}$ and the mirror velocity v_{Mi}. The minimum time resolution is 10 ms which can be achieved on the expense of the spectral resolution.

In contrast, the Step-Scan method has the advantage that the reaction and processes taken place on the nanosecond to the millisecond time range can be detected with a high spectral resolution (> 1 cm^{-1}) since the mirror is only moved stepwise. However, the reaction must be repeatable.

The Step-Scan technique is mostly applied in biophysics and polymer chemistry where, for instance, the photolysis processes of chemical reactions [105], bacteria systems [106, 107, 108, 109, 110] and the time-dependent reorientation of liquid crystals under the influence of a short electric field [111, 112, 113, 114, 115] (for more details see Appx. C) are studied. Furthermore, it is used to examine the characteristics of lasers and their mode spectra [105] and for photo-reflection measurements of semiconducting materials as well as quantum wells [116, 117]

In Fig. 4.5 the data acquisition of a Step-Scan measurement is schematically depicted. At each new mirror position $n\Delta x$ along the traveling distance of the mirror the temporal varying reflection signal $I^*(n\Delta x, t_i)$ is recorded. The complete interferogram is sampled for various times and retardations by successive stepwise moving of the mirror. A subsequent FT for each measured time point $m\Delta t$ in the intensity "matrix" $I^*(nx, mt)$ derives the time-resolved spectrum $S^*(j\Delta\nu, m\Delta t)$. The process can be repeated several times to improve the SNR whereas at each $n\Delta x$ position the time-dependent signal is averaged. It is recommended to average between 10 and 50 spectra. Additionally, the stability of the mirror influences the SNR significantly [106, 118], therefore, one must take care that the spectrometer is located on a vibration-free and silent environment. For this reason the FTIR-spectrometer was put on a heavy optical bench mounted on air attenuators. Thus, the system is decoupled from the environment. Furthermore, the vacuum pumps were placed in a separated room. Hence, the reached mirror stability is better than 3 nm.

Since the data acquisition at each mirror position $n\Delta x$ has to start always at the same time, the data recording must be synchronized with the external stimulation source (laser or pulse generator). Thus, the trigger signal sequence is very important and crucial in a Step-Scan measurement. In Fig. 4.6 the temporal sequence of the TTL control signals is visualized. An external or an internal trigger signal T1, which is correlated with the beginning of the reaction, controls the data acquisition. Yet, before the recording starts, the spectrometer sends a signal T2 to the interferometer, so that the mirror is moved to the next position. There, it is stabilized for a few milliseconds. After the stabilization procedure (~ 20 ms) the next arising trigger signal T1 is used as a starting signal for the record window T3. The signal T3 stays high for the total recording time $T = N \cdot \Delta t$ (N total number of time slices) which is defined at the beginning of each measurement. As soon as the signal T3 is on, at each TTL-signal T4 the detector signal is captured. Depending on the number of averaging spectra this procedure is repeated several times starting again with the T3 signal. Subsequently, the mirror moves to the next position. The time resolution Δt depends mainly on the response time of the detector. Standard PC-MCT-detectors, operating in the photocurrent mode, have a minimum response time of 1 µs. Their disadvantage is that the measured current becomes nonlinear above a certain incident threshold intensity. A PV-Detector has a two order of magnitudes smaller response time

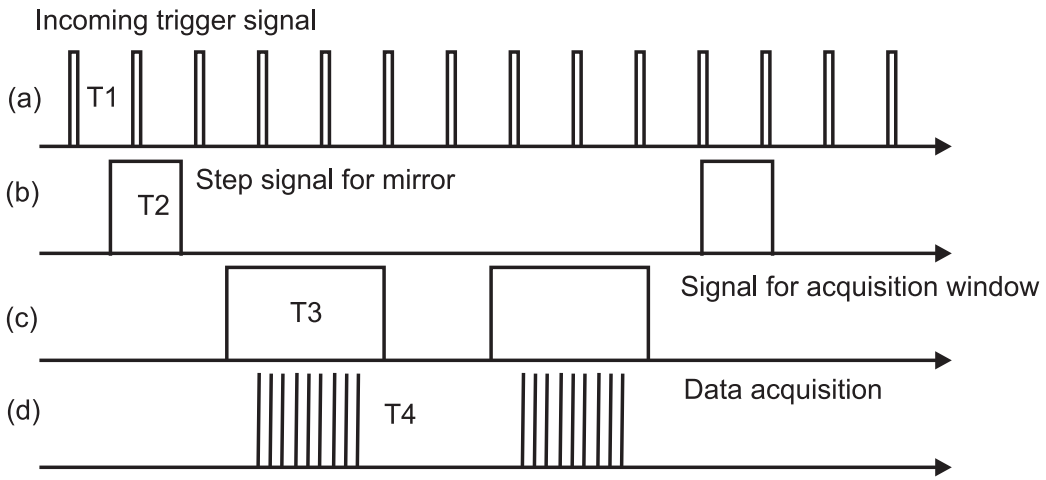

Figure 4.6: Illustration of the signal sequence within a Step-Scan experiment. (a) These pulses are the external trigger signals T1 which are correlated with the external perturbation source, for example a pulse generator or laser. (b) The second signal T2 is generated by the spectrometer and is sent to the interferometer motor to move the mirror to the next position. (c) After a certain predefined stabilization time the third signal T3 waits for the next external trigger signal T1 and rises afterwards immediately. It stays high as long as all data points are captured. (d) Signal T4 corresponds to each recorded time point within the signal T3.

due to the small detector area and the applied bias voltage of about 100 mV. Furthermore, the measured signal is always proportional to the incident light intensity. For the measurement a PC-MCT of the model D316 (Bruker Optics GmbH) with a time resolution of about 1 µs and a PV-MCT KMPV11-11-1-J1 from Kolmar Technologies with a theoretical rise time of 25 ns are available. The time resolution also depends on the amplifier and the A/D-converter. There are two amplifiers, the build-in amplifier of the spectrometer and the KA100-A1 from Kolmar Technologies with a band width of 250 MHz. As an A/D-converter the internal converter of the spectrometer with its time resolution of 6 µs, with a dynamical range of 24 Bit and a maximal input voltage of $V_{pp} = 20\,V$, can be used, or a transient recorder M3i.4142 from Spektrum GmbH with a bandwidth of 400 MHz at 16 Bit and $V_{pp} = 10\,V$. In Sec. 4.1.1 it was demonstrated that the interferogram consists of an AC- and DC-component while only the AC-signal contains the important spectral information. The phase correction can only be performed directly for a Rapid-Scan measurement. In a Step-Scan experiment the spectrum can include positive as well as negative features. Thus, a phase correction with the raw time-resolved AC-signal does not work. Two options exist to solve this difficulty, as schematically depicted in Fig. 4.7. The first one is the simultaneously recording of the DC-signal and the AC-signal. The DC component provides the right phase correction $\theta(\nu)$ for the AC-component. The second possibility is to use the phase of a previous Rapid-Scan measurement.

Since the technique has never never been used before at the institute and firstly established within this thesis, test measurements were performed by studying the electric switching behavior of liquid crystals. The aim was to examine the possibilities and limits of this technique. Therefore, liquid crystals were placed between two infrared transparent CaF_2-windows. By applying a voltage, the liquid crystals orient. This time-dependent rearrangement can be traced by following the polarization-dependent vibrational modes of the liquid crystals. For

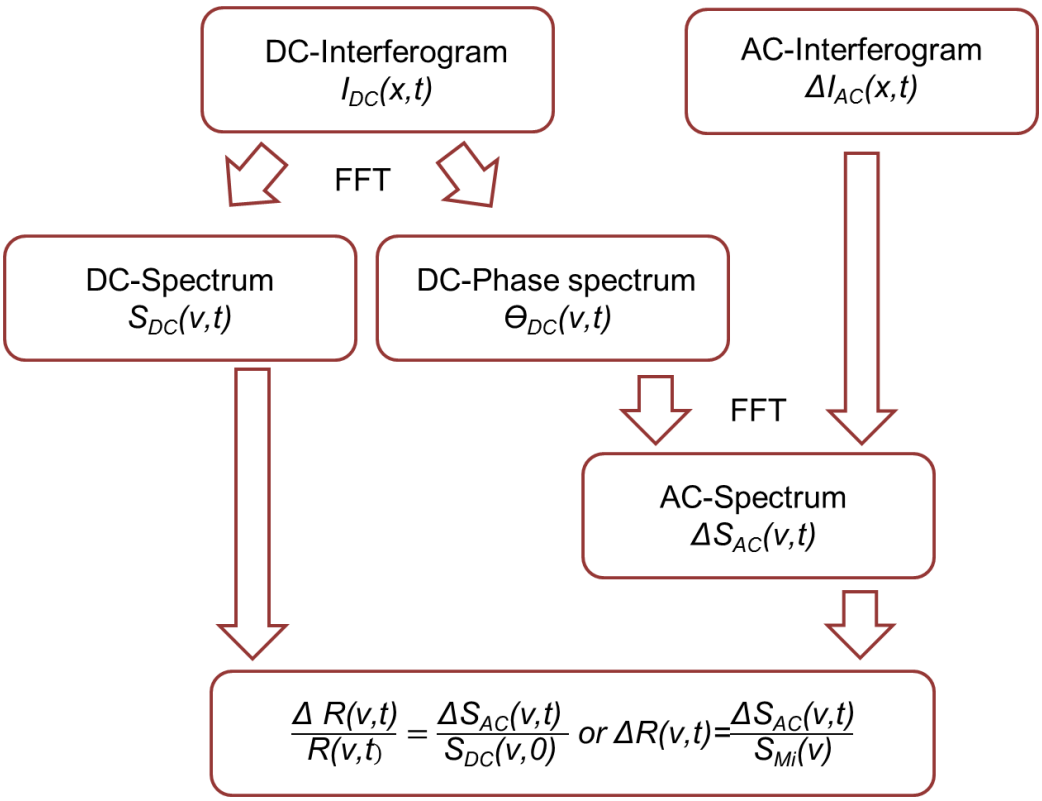

Figure 4.7: Flow diagram of the data post processing procedure which explains how the normalized as well as the absolute change of the reflectivity, $\frac{\Delta R(\nu,t)}{R(\nu,0)}$ and $\Delta R(\nu,t)$, are calculated. From the DC-interferogram ($I_{\mathrm{AC}}(n\Delta x)$ or $I_{\mathrm{DC}}(n\Delta x,t)$) of the Rapid-Scan or the Step-Scan measurement the phase spectrum $\theta(\nu)$ is calculated by a FT. This is used for the phase correction of the time-dependent AC-interferogram $\Delta I_{\mathrm{AC}}(n\Delta x,t)$ to determine the spectrum $\Delta S_{\mathrm{AC}}(j\Delta\nu,t)$.The relative and absolute modification of the reflectivity $\frac{\Delta R(\nu,t)}{R(\nu,0)}$ or $\Delta R(\nu,t)$ can be derived from the spectrum.

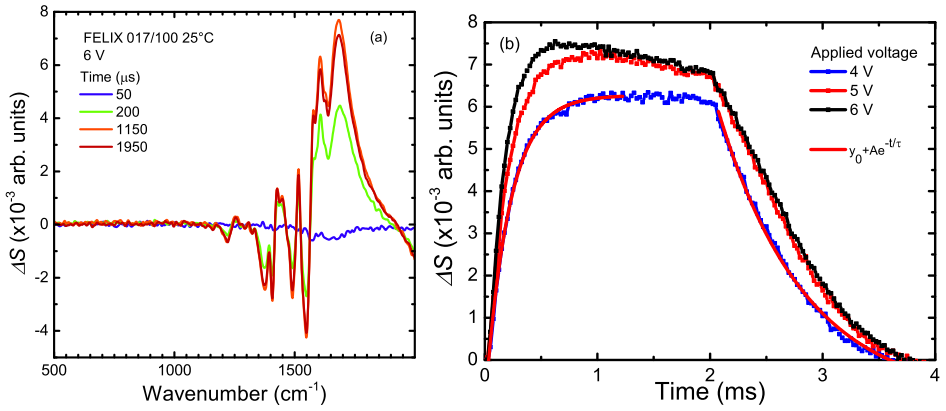

Figure 4.8: (a) Modification of the liquid crystal spectrum for four different points in time after applying a voltage pulse of 6 V. (b) Variation of the intensity $\Delta S(\nu,t)$ is illustrated for the resonance frequency 1606 cm^{-1} for three different voltages.

a detailed description of the experiments and results we refer to Appx. C. The results of such a switching experiment are exemplary displayed in Fig. 4.8. In the spectrum several vibrational modes (see 4.8 (a)) are visible exhibiting an electric-induced modification of their intensity due to a rotation of their rigid

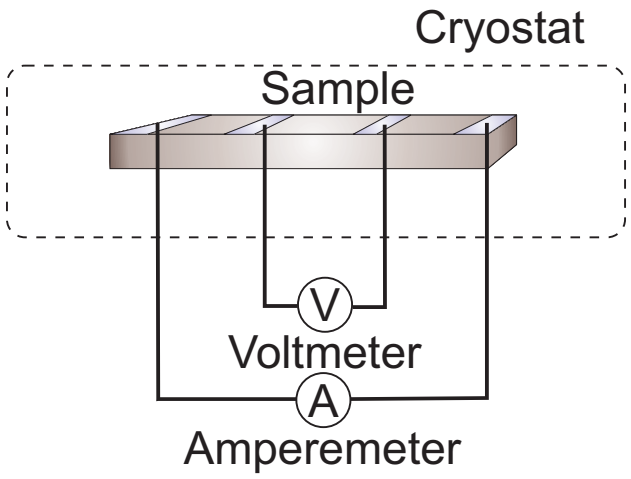

Figure 4.9: For the determination of the sample resistance the 4-point-method was applied. The current is created at the outer contacts while at the inner contacts the voltage drop is measured by a voltmeter.

molecular body. The liquid crystal is rearranged within a few hundred microseconds, as depicted in Fig. 4.8 (b) for 1606 cm^{-1}. This example nicely shows that it is possible to easily detect changes taking place on a microsecond time scale.

Singular value decomposition

The singular value decomposition SVD is used in various fields, for instance, in imaging processing to compress pictures or in statistics to analyze multivariate data sets in the principle component analysis. In this thesis we used it to improve the SNR of the 2D time-dependent spectra and to check how many different processes are involved.[119, 120]

In general, every matrix S $(n \times m)$ can be expressed in a product of three matrices which are related to determination of the eigenvalues of an $n \times n$ matrix.

$$S = UVW^T. \tag{4.7}$$

V contains the positive singular values of S on the diagonal of the matrix. The columns of U and W are called the left and right singular vectors. The number r of singular values sorted descended and with $v_i > 0$ of the Matrix V defines the rank of S. The first r columns of U form an orthonormal basis. Furthermore, UVW^T is the best approximation of S. For example, if the spectra S contain only one relaxation rate and one initial state[4] without any noise, the rank is 1 as only one singular value exists. However, real spectra always are contaminated by noise. Thus, the rank is m. Sorting the columns of U and W according to the highest singular values of matrix V, neglecting the residual of v_i below a chosen threshold value as well as the corresponding columns in U and W, the matrix $S^\star = U^\star V^\star W^{\star T}$ can be formed which resembles the original matrix S, but with less noise.

4 This means that W and U contain only one non-zero column vector.

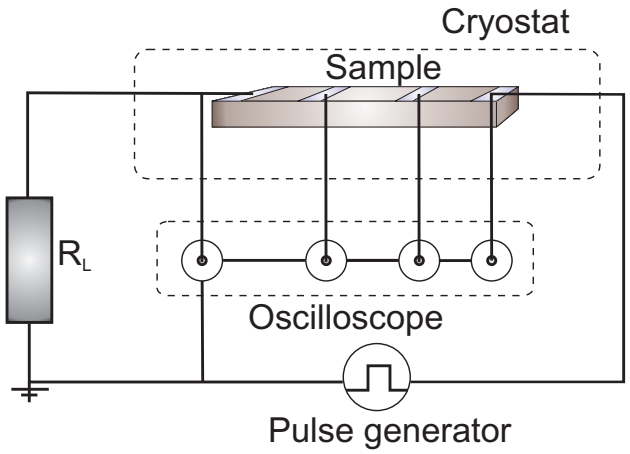

Figure 4.10: For the time-resolved transport measurement either the 4 point or 2 point configuration was employed. It can be switched between the steady-state and the time-resolved transport measurement. The voltage pulses are created by a pulse generator. An oscilloscope records the applied voltage U_S, the voltage drop U_{23} across the inner contacts as well as the total current of the circuit by the voltage drop U_L across the load resistor in series.

4.2 DC- AND TIME-RESOLVED TRANSPORT SETUP

It is very interesting to measure the transport properties of the organic compounds for various reasons. The different phases and the occurring phase transitions can be characterized more precisely considering the electronic system and the corresponding transition temperatures can be correlated with the transition temperatures determined by optical experiments. Since electrically- and photo-induced processes are studied, it is also of interest to compare the non-equilibrium values with the one in the thermodynamic equilibrium.

For this reason the FTIR-spectrometer was extended by a transport setup. A schematic sketch of the transport setup is depicted in Fig. 4.9. For the static measurements a Keithley Nanovoltmeter 192 A was used to measure the voltage and a Keithley Sourcemeter 2611 was used as a current source. The resistivity was determined with the 4 point method. There, the current is applied on the outer contacts[5], and on the inner contacts the voltage drop is measured. Thus, the contribution of the contact resistance is eliminated and only the sample resistance is recorded. Gold wires with a diameter of $d = 15\,\mu m$ were directly glued on the sample surface or on previously evaporated gold stripes. The organic crystals were glued on a sapphire plate with GE vanish to electrically insulate them from the conducting sample holder. Sapphire was chosen because of its high thermal conductivity and its insulating properties.

The resistance was recored by a self-modified Labview program[6] which controls the cooling and measurement procedure. The current as well as the voltage were applied depending on the phase of the material (between 10 µA and 0.01 µA). To avoid possible cracks of the sample due to thermal contraction, the cooling rate was set between 0.2 $\frac{K}{min}$ and 0.5 $\frac{K}{min}$.

To change between the static and time-dependent transport measurement a switch box was used. To study electric-induced switching processes occurring,

5 The applied current value was adjusted depending on the conductivity state of the studied material.

6 The original version was written by Eva Rose.

a load resistor R_L is connected in series to the sample, as depicted in Fig. 4.10. It protects the sample from high current burst appearing after switching into a high conducting state. In addition, the current of the circuit can be measured by the voltage drop across R_L. An Avtech AV-1010-B pulse generator or a HP pulse generator is employed to create voltage pulses with a maximum length of 10 ms at a minimum repetition rate of 10 Hz. The rise time of both pulse generators is less than 10 ns. For an inner resistance of 50 Ω and a high load impedance the overshoot or ringing decays within 30 ns. Solely, 50 Ω BNC-cables were used for the pulse measurements.

For the Step-Scan measurements the Sync-output of the pulse generators were connected to the trigger input (signal T1 in Fig. 4.6) of the spectrometer. The applied voltage pulse was recorded by one of the four channels of the Tektronix 744 A oscilloscope. The other ones were employed to log the voltage drop across the sample and the voltage drop across R_L. The measurements were fully controlled by a self-written Labview program which sets and loops through all the parameters of the voltage pulse and reads out the channels of the oscilloscope at the same time.

4.3 OPTICAL SETUP

For the photoconductivity measurements and the photo-induced phase transition a refurnished pulsed Nd:YAG laser (B.M Industries/Thales, YAG-502DNS-DPS920) was implemented in the setup. The length of the laser pulse is 8 ns. The samples were excited by the second harmonic 532 nm (2.35 eV) of the fundamental wavelength (1064 nm). Therefore, a temperature stabilized nonlinear crystal is heated up to 35 °C to satisfy the phase matching conditions. The repetition rate can be freely selected internally and externally between 1 Hz and 20 Hz. The laser intensity is adjusted roughly manually and continuously by a Brewster plate in which the intensity depends nonlinearly on the Brewster angle, as depicted in Fig. 4.11. However, neutral density filters between 0.1 optical density (OD) and 0.5 OD were used to attenuate the laser beam. The laser intensity was checked by a power and energy meter in front of the sample. The long term stability of the laser power is better than 5 %.

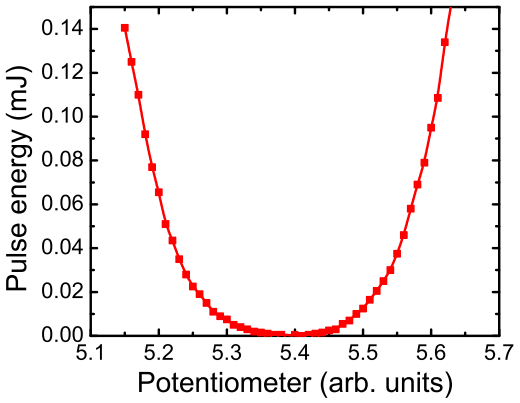

Figure 4.11: Laser pulse energy as a function of the potentiometer, respectively.

The laser beam has a diameter of about 1 cm. A telescope was installed in the beam path to demagnify the beam diameter by a factor of 2, illustrated in Fig. 4.12. The laser beam is directed from the optical bench to the infrared microscope (see Fig. 4.3) via several mirrors. There, it is deflected on the sample by a 45° aluminum coated mirror being mounted below the Schmidt-Cassegrain objective. A lens ($f = 400$ mm) focused the beam on the sample, by varying the focal length. The light is circular polarized. The whole laser system and optical setup are spatially decoupled from the FTIR-spectrometer and mounted on an optical table to suppress possible external vibrations.

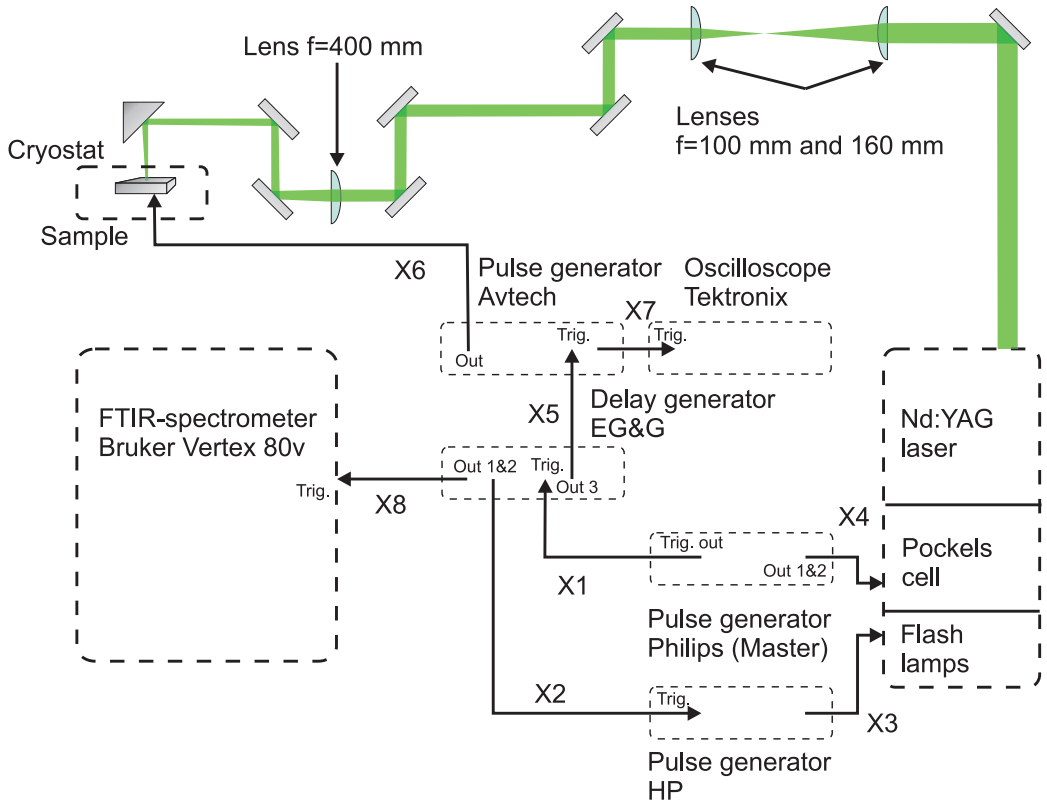

Figure 4.12: Sketch of the laser setup. The centerpiece is the pulsed Nd:YAG laser which is externally controlled by two synchronized pulse generators. A delay generator is additionally implemented in the setup to guarantee synchronization between the laser pulse and the voltage pulse generator as well as the oscilloscope. It also triggers the spectrometer to acquire the infrared data. The laser beam (green) is collimated, directed and focused on the sample via several mirrors and lenses. X1 ... X8 label the signal which are used to trigger the various instruments.

The laser pulse sequence is controlled externally to ensure the temporal synchronization between the laser, the pulse generators as well as by the FTIR-spectrometer, as depicted in Fig. 4.13. The charging of the flash lamps is triggered by an external signal as well as the Pockels cell generating the laser pulse. Therefore, a HP pulse generator (PM 5786 B) sends the trigger signal X1 to the delay generator (EG&G Princeton Applied Research Model 4144). One of the delay generator output signals X2 is forwarded to a second pulse generator (HP 214B) which releases a further delayed pulse X3 with a minimum length of 150 µs and minimum height of 5 V. It initializes the charging of the flash lamps of the laser system. After signal X3 drops to zero the lamps are charged with a delay of 1.5 ms. It also activates the discharge of the lamp with a delay of 15 µs. About 30 µs after the end of the charging and discharge pulse X3 a further voltage signal X4 from the first HP PM 5768 B pulse generator (length 6 µs, 6 V) is sent to the Pockels cell generating the laser pulse. In the case of the photoconductivity measurements the delayed trigger signal X5 from the delay generator activates the Avtech pulse generator to apply a voltage pulse X6 to the sample. The sync. pulse X7 of the Avtech device goes to the Tektronix oscilloscope to start the acquisition of the photocurrent. The third signal X8 from the delay generator is used to initialize the time-resolved infrared measurement of the FTIR-spectrometer.

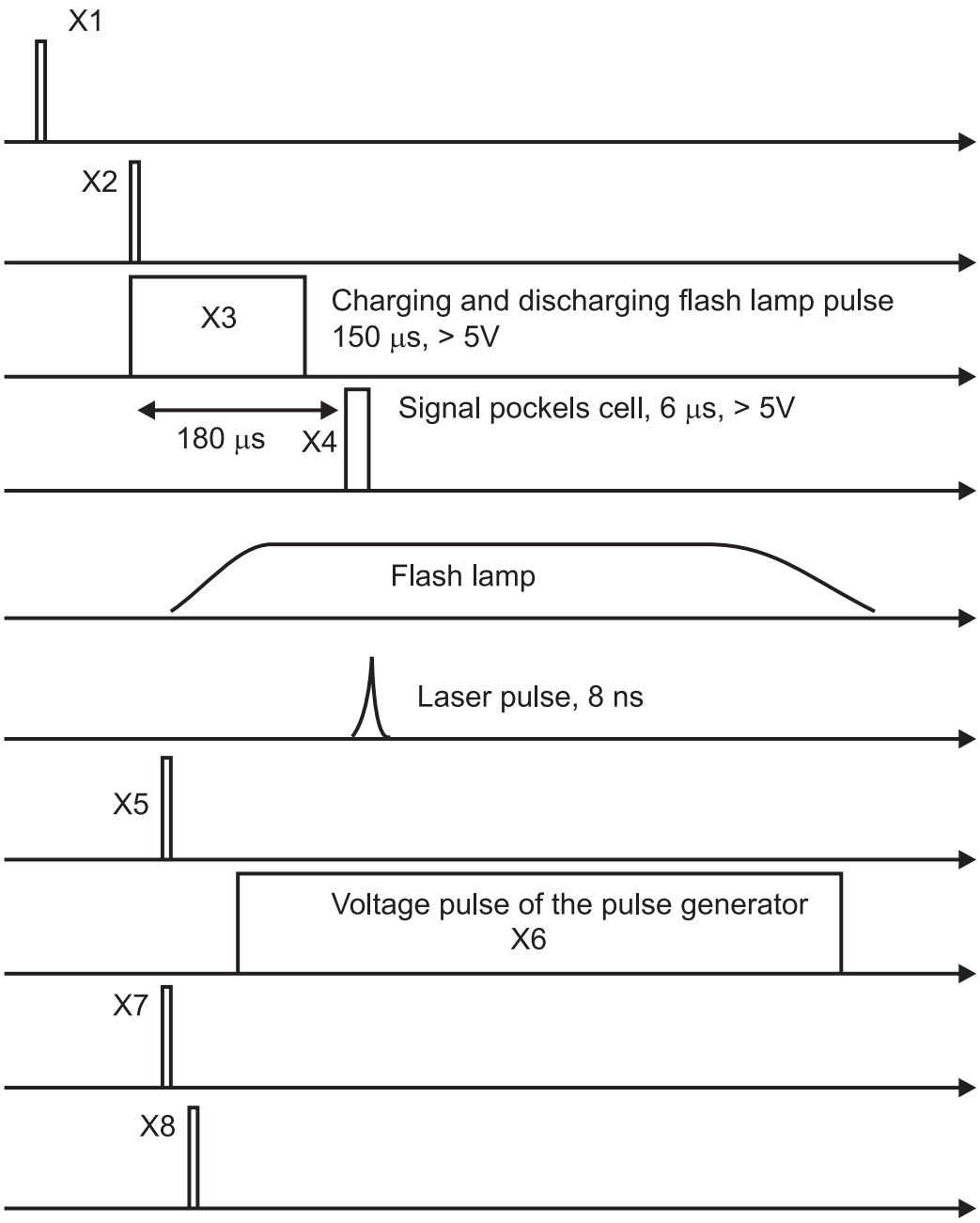

Figure 4.13: Pulse sequence to control a laser-induced experiment. X1 is the master trigger pulse triggering the delay generator. It synchronizes the flash lamps (X2 and X3), the voltage pulse generator (Avtech) (X5) and the FTIR-spectrometer (X8) with each other. X4 controls the Pockels cell in the resonator with a minimum length of 6 µs. The pulse X6 is the voltage pulse which is applied to the sample for the photoconductivity measurements, for instance. The oscilloscope records the variation of the sample current or resistance and is synchronized with the other instrument via the signal X7.

4.4 PHOTOCONDUCTIVITY SETUP

Information can be collected about optically excited free or bound electron-hole pairs, like the so-called excitons, defects and impurities by photoconductivity studies. The setup for the photocurrent measurements consists of two contacts on the sample. Gold wires are attached to samples by conducting glue or carbon paint. A voltage pulse with variable width is created on the contacts by one of the previously introduced pulse generators. The applied voltage U_S is measured

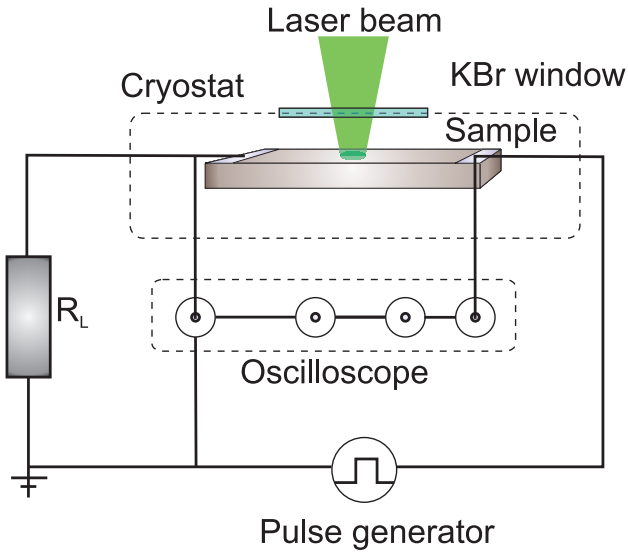

Figure 4.14: Schematic drawing of the photoconductivity setup. It consists of a pulse generator creating the voltage U_S at the sample, an oscilloscope, and a load resistor. R_L is used to determine the current in the circuit.

by an oscilloscope. It logs indirectly i.) the photocurrent as a voltage drop U_L across the load resistor R_L or ii.) the oscilloscope is connected in series to R_L. In this case the current is measured across the inner 50 Ω input resistance of the oscilloscope. The load resistor also protects the circuit from current peaks. If the oscilloscope is parallel to R_L, the input impedance of the oscilloscope must be higher than R_L so that the main current flows through R_L. Thus, the maximum value of R_L was set to 100 KΩ.

Since the laser has a low repetition rate between 1 Hz and 20 Hz it is ensured that also long living states decay before the next pulse arrives and hence, accumulation effects can be excluded.

The generated photo current $I_{Ph}(t)$ can be derived from the following physical relation. The electronic circuit consists of a voltage source, the sample and the load resistance. The dark current $I_D(t)$ is defined as

$$I_D(t) = \frac{U_S}{(R_L + R_{Sam,D})} \tag{4.8}$$

with U_S the source voltage, R_L the load resistance, and $R_{Sam,D}$ the dark resistance of the sample. The total current under illumination $I_{Ill}(t)$ is respectively

$$I_{Ill}(t) = \frac{U_S}{(R_L + R_{Sam,Ill})} \tag{4.9}$$

with $R_{Sam,Ill}$ Thus, the measured photo current is

$$I_{Ph}(t) = I_{Ill}(t) - I_D(t) = U_S \left(\frac{1}{(R_L + R_{Sam,Ill})} - \frac{1}{(R_L + R_{Sam,D})} \right) \tag{4.10}$$

In a photocurrent measurement the contact resistance plays a crucial role since they influence the transport of the charge carriers to the contact. The materials, i.e metal, semiconductor or insulator, meeting at the interface form different types of contacts. At the boundary the band structure is deformed due to the difference in work function and electron affinity of the materials. Therefore, a barrier is created at boundary surface leading to a depletion area [80, 121]. By

that, additional carriers can be transferred or the charge carrier can be blocked at the contacts. There are typically two kinds of contacts: the Schottky-contact and the ohmic contact. Generally, several process participate in the charge transport across the barriers. The dominating processes are the thermal emission of charge carriers across the energy barrier and tunneling of the carriers, being temperature-independent. However, it is supposed that ohmic contacts are formed in the organic crystals. During the transport measurements (see Sec. 4.2) the temperature-dependence of the contacts was checked by measuring the contact resistance at specific intervals. Their resistance value normally changes at a phase transition when a gap opens in the electronic system.

4.5 THEORETICAL CALCULATIONS

Besides the experimental methods described in the previous chapter, quantum chemical calculations were performed to determine and understand the physical properties of the organic salts and compared to the experimental results. The calculations were performed on the level of density functional theory DFT. Thus, several programs were employed:

1. The Quantum Espresso package (Version 4.3.2 and 5.1) [122] was used to determine the band structure and the optical functions. The program is installed on two workstations. The first server is equipped with one Pentium i7 CPU with 8 cores and 8 GB memory and the second one is a workstation with 2 x Xeon E5-2650 with 16 cores in total and 64 GB main memory. The software runs under Linux Ubuntu 12 and 14.

2. The determination of the normal modes of the organic molecules, their resonance frequency as well as their infrared intensity was calculated with the Gamess-US [123, 124] and Spartan 13 software packages. For the first one, the calculations were computed on servers of the BwGRID[7] [125]. Further simulations were performed locally on a standard laptop.

4.5.1 *Band structure and optical functions*

For the band structure calculations only crystal structures were used determined by x-ray, Neutron- or muon-scattering experiments. Based on previous experimental results, like transport measurements, the materials are treated as a metal or an insulator, respectively. To determine the physical properties, the total energy of the system has to be regarded:

$$\begin{aligned}\mathcal{H} = &-\frac{\hbar^2}{2m_e}\sum_i \nabla_i^2 - \sum_{i,I}\frac{Z_I e}{|\vec{r}_i - \vec{R}_I|} + \frac{1}{2}\sum_{i\neq j}\frac{e^2}{|\vec{r}_i - \vec{r}_j|} \\ &- \sum_I \frac{\hbar^2}{2M_I}\nabla_I^2 + \frac{1}{2}\sum_{I\neq J}\frac{Z_I Z_J}{|\vec{R}_I - \vec{R}_J|} \\ &= \mathcal{T}_e + \mathcal{V}_{ext} + \mathcal{V}_{int} + \mathcal{T}_I + \mathcal{V}_{II}\end{aligned} \tag{4.11}$$

The first term describes the kinetic energy of the electrons, the second one the Coulomb-interaction of the electrons with the positive charged nuclei and the third one the interaction of the electrons with each other. The last two components take into account the kinetic energy of the atomic cores and their interaction with each other. The cores are more than a factor of 1000 heavier than the electrons. Therefore, the kinetic energy of the nuclei can be neglected. Since the electrons move much faster than the atomic nuclei, the atomic core potential for them is frozen. On the other hand the atomic cores move in an electronic potential since the electrons adapt themselves instantaneously to any new atomic

7 The bwGRID was an association of seven universities in Baden-Württemberg providing the scientific staff with several server clusters for free. The calculations were mainly performed on the HLRS-cluster of the University of Stuttgart. The operating system was Scientific Linux 5.5 and the hardware consists of 500 nodes each with 2 Intel Xenon E4550 (4-cores) and 16 GB. The University of Stuttgart stopped the collaboration in spring of 2013.

nuclei configuration. This consideration is known as the Born-Oppenheimer approximation. The goal is to solve the Schrödinger equation

$$i\hbar\frac{\partial\Psi(\vec{r},t)}{\partial t} = \mathcal{H}\Psi(\vec{r},t) \tag{4.12}$$

to find the minimum energy of the system. It is achieved by determining the eigenstates and eigenfunctions of the total Hamiltonian $\mathcal{H}$ by the variational principle.

At the moment DFT is the standard technique to solve Hamiltonians $\mathcal{H}$ and thus, to calculate the physical quantities of a many body system. In DFT, it is assumed that the ground state energy and each term in the Hamiltonian can be expressed by functionals of the electronic density $n(\vec{r}) = n(\vec{r})_\downarrow + n(\vec{r})_\uparrow$ with the spin states $\sigma = \uparrow$ and $\downarrow$ instead of the wave function $\Psi(\vec{r})$:

$$\mathcal{E}[n] = \mathcal{T}_e[n] + \mathcal{V}_{ext}[n] + \mathcal{V}_{int}[n] + \mathcal{V}_{xc}[n] \tag{4.13}$$

In this representation the kinetic energy of the nuclei T_I and their Coulomb interaction $\mathcal{V}_{II}$ are neglected. The last term is the so-called exchange-correlation term $\mathcal{V}_{xc}$ containing all not respected interactions, for example self-interaction, correlations, etc. The main task in DFT is to find the accurate $\mathcal{V}_{xc}$ which describes the system properly.

Functional

There are different approaches which are classified by Jacobs ladder [126] which has five steps differing in accuracy:

- Level 1: the most famous $\mathcal{V}_{xc}$ is the so-called local density approximation (LDA) or local spin density approximation (LSDA) functional. It is assumed that $\mathcal{V}_{xc}$ corresponds to the known exchange-correlation energy of a homogeneous electron gas which is directly related to the electron density. LDA describes metallic systems very well as they can be approximated by an undisturbed electron gas. However, it fails to model systems in which the electron density strongly varies in space as semiconductors or insulators.

- Level 2: a significant improvement of the precision and results is achieved by taking into account the spatial variation of the electron density. It can be considered as an additional correction parameter for LSDA. These functionals are summarized under the keyword generalized gradient approximation (GGA). The most famous GGA functionals are: B88[127], BLYP[128], PW91[129], and Perdew-Burke-Enzerhof (PBE)[130, 131].

- Level 3: when higher derivatives of the electron density are included then they are called meta-GGA functionals (Level 3).

- Level 4: furthermore, in the meantime hybrid-GGA functionals (Level 4) are used to describe atoms as well as molecules with a much higher precision. Different exchange and correlation functionals are mixed and combined with each other depending on their coefficient. If they are determined by fitting experimental data, they are called semiemperical functionals, or they have to satisfy certain predefined conditions. The most used representative are B3LYP [132, 133, 134], and PBE1PBE [135] functionals. For more detail it is referred to the relevant literature [23].

- Level 5: random phase approximation (RPA).

In the framework of this work only the PBE-functional was employed for the band structure and optical spectra calculations since the considered organic salts are strongly anisotropic and the electrons or holes are more localized in comparison to pure metals as copper. Van der Waals force play an important role in organic compounds which is not described accurately by LDA, but better by a GGA functional. Nevertheless, this is a future task to implement the Van der Waals interaction into the upcoming functionals. In addition, GGA as PBE yield better estimations of the band gaps than LDA which generally underestimates it.

In contrast, the B3LYP- or the EDF2[136] functionals were used for the normal mode analysis. They yield very good results for organic molecules and their results agree very well with experimental data [137, 138, 139, 140]. Therefore, they are widely-used and tested.

Basis set

The main task of all *ab-initio* methods is to solve the Schrödinger equation 4.12. Thereto, one has to know the wave function of the system, which can be a single atomic orbital, a molecular orbital or the periodic wave function of a bulk material. In the case of DFT, at the beginning of each calculation the wave functions are constructed by a linear combination of predefined wave functions at which the precision depends on the chosen basis set and its size. A complete basis set would in principle be capable to describe the system entirely, but this would be related to an extreme large effort of computational time and capacity. Therefore, one has to find a compromise between precision and CPU time. Over several decades a few approaches were developed:

- One possibility is to start with localized orbitals which can be divided in two subgroups: Slater-orbitals and Gauss-orbitals. Considering only the last ones, they are build of polynomial functions multiplied with Gaussian functions (e^{r^2}). The main advantage of this mathematical construction is that the matrix element, i.e. integrals, can be solved analytically and hence, computing time can be reduced. The precision can be increased by enlarging the size of the basis function. Furthermore, diffuse and polarization function can be added to the standard basis set because they describe molecular bonds and charged states of molecules much better.

  The Gaussian or Pople basis sets are mainly used for calculations of isolated molecules or structures, because the wave functions decay with increasing distance to the atom or molecule and thus the electron density $n(\vec{r})$ is only calculated there where also charge is present. In addition, the region close to the nucleus is also described well by a Gaussian basis set.

- Instead of approximating the wave functions by a linear combination of Gaussian functions, they can be constructed from the linear combinations of plane waves:

$$\Psi_{\vec{k},n}(\vec{r}) = \frac{1}{\sqrt{N_{eff}}} e^{i\vec{k}\vec{r}} \cdot \sum_m c_{n,m}(\vec{k}) \cdot e^{i\vec{G}_m\vec{r}}. \tag{4.14}$$

  This construction is perfectly suitable for the description of any periodic crystal structure. Typically, the valence electrons are responsible for the

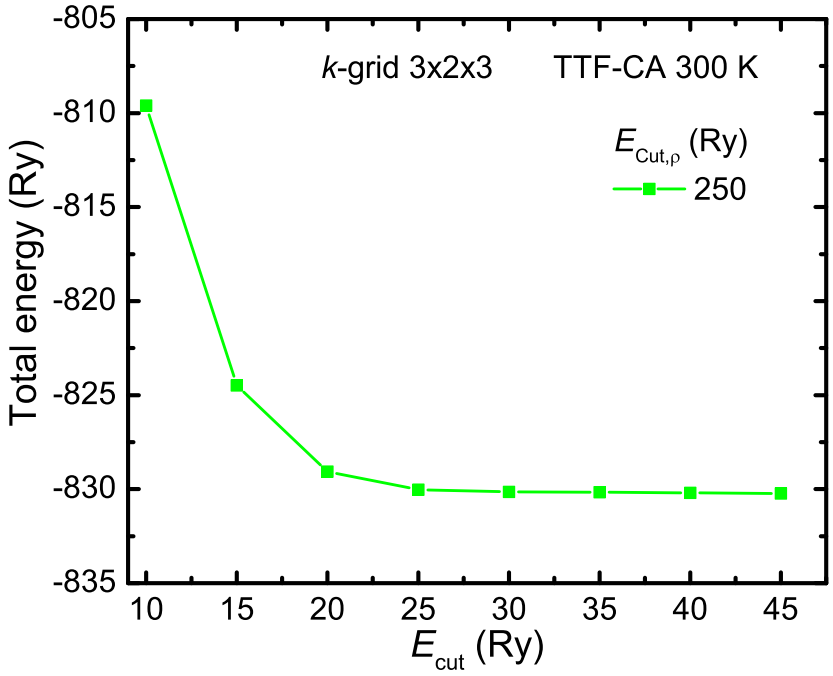

Figure 4.15: Total energy of TTF-CA at 300 K for a $3 \times 2 \times 3$ k-grid for an electron density cutoff energy of $E_{\text{cut},\rho}$=250 Ry as a function of E_{cut}. Above $E_{cut} = 25$ Ry the total energy varies barely.

bindings and the core electrons can be regarded as an additional correction. Since close to the atomic cores the wave function oscillates very strongly they have to be described by large wave vectors $\vec{k}$. According to Schrödinger's Eq. 4.12 the kinetic energy of the electrons E_{Kin} is a quadratic function of the $\vec{k}$-vector. Therefore, the kinetic energy of the core electrons is very large. In general, this leads to an extremely large number of wave functions and makes it necessary to define a cutoff energy of the electrons in consideration of the precision. Thus, to limit the number of wave functions, the pure atomic potential is approximated by pseudo potential PP.

The minimum cutoff-energy must be identified in respect to the total energy of the system. In Fig. 4.15 the total energy of the organic compound TTF-CA is plotted as a function of the wave function cutoff energy E_{cut} for a cutoff energy of the electron density $E_{\text{cut},\rho}$ of 250 Ry. For the convergence test ultrasoft pseudo potentials were used (see for more details the following section). Above E_{cut}= 25 Ry the total energy converges and does not change anymore significantly. Therefore, E_{cut}= 30 Ry is a good value for the calculations. The cutoff energy of the electron density $E_{\text{cut},\rho}$ should be by a factor of four larger than E_{cut} for norm-conserving pseudopotential (PP). In the case of ultrasoft PP $E_{\text{cut},\rho}$ must be between 8 and 12 times larger than E_{cut}.

Moreover, the number of plane waves $N_G \propto \Omega_{Cell} \cdot E_{cut}^{\frac{3}{2}}$ depends on the maximal defined kinetic energy $\frac{\vec{G}_{max}^2}{2} = \frac{(\vec{k}+\vec{G})^2}{2} \leqslant E_{cut}$ and the volume of the unit cell Ω_{cell} [8]. Hence, the necessary number of wave functions

8 The volume of the plane waves in the reciprocal space is $V_{max} = \frac{4\pi}{3} G_{max}^3$ at which the volume of a single plane wave is $V_{PW} = \frac{2\pi}{\Omega_{cell}}$.

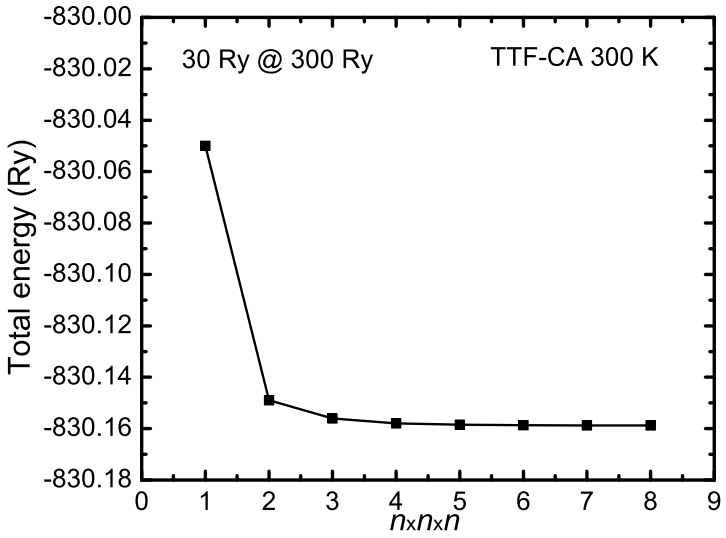

Figure 4.16: Illustration of the total energy of TTF-CA at 300 K as a function of k-grid size for $E_{cut} = 30\,\text{Ry}$ and $E_{cut,\rho} = 300\,\text{Ry}$. The total energy is converged above a grid size of $3 \times 3 \times 3$.

increases with increasing the unit cell size and is much larger in contrast to the localized approach with Gaussian functions, for instance. However, plane waves can also be used for isolated molecules, but for this purpose a very large super cell has to be defined so that the plane waves decay very fast within the cell and do not interact with their mirror image of the neighboring cells.

Pseudo potential

The number of plane waves can be substantially reduced by modeling the potential near the atomic core by a simple mathematical function. By that, the number of nodes and oscillations diminishes and hence, $\vec{k}$ and E_{cut} decrease as well. The crucial point is that the valence electrons are modeled accurately since they are mainly responsible for the chemical bonds. The simplified function is called effective core potential or pseudo potential.[9] To construct a PP, the full potential is split into two regions at a selected cutoff radius r_c, as depicted in Fig. 4.17. For the calculation of a PP for an element of the periodic system r_c must be defined and afterwards tested.

There are two classes of pseudo potentials. The norm-conserving PP and wave functions form an orthonormal system. They have to satisfy four conditions:

1. The eigenvalues of the PP must agree with the ones of the real potential.
2. Above the cutoff radius r_c the wave functions of the PP must be equal to the true total electron wave function.
3. The total charge within r_c corresponds to the charge of the real total wave function.
4. The derivative of the PPs wave functions at r_c and $r_c > r$ must agree with the real derivatives.

9 The expression pseudo potential will be used throughout this thesis.

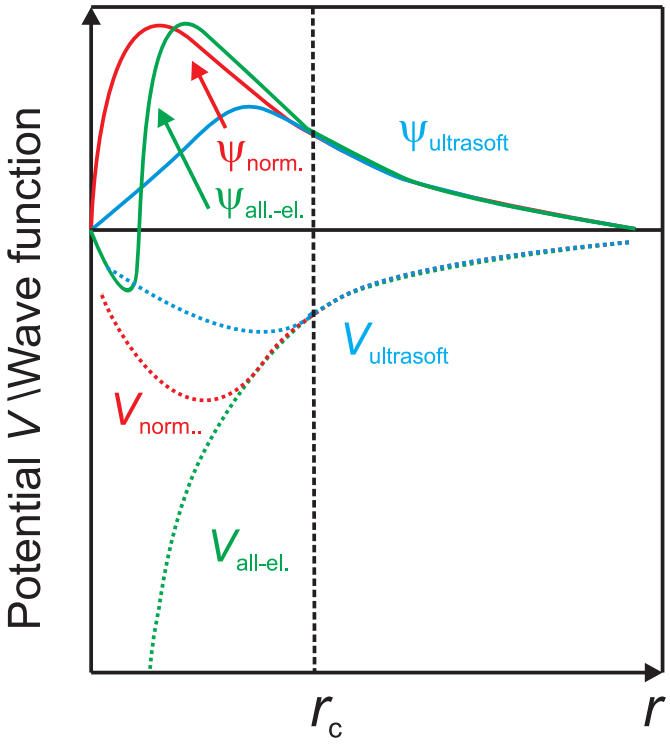

Figure 4.17: Exemplary comparison of the real wave function $\Psi_{all.el.}$ with the constructed norm-conserving and ultrasoft wave function $\Psi_{norm.}$ and $\Psi_{ultrasoft}$. The artificial wave function does not exhibit nodes and allows to simulate them with less plane waves, especially for the ultrasoft wave function. Above r_c all wave functions show the same spatial evolution. Below r_c the electron density $n(\vec{r})$ of $\Psi_{ultrasoft}$ differs from the true electron density, which must be renormalized. In contrast, $\Psi_{norm.}$ is considered to be norm conserving since its $n(\vec{r})$ is equal to electron density of $\Psi_{all.el.}$. To create the artificial wave function, the core potential has to be approximated by a corresponding $V_{norm.}$ or $V_{ultrasoft}$ potential being soften in the core region. This is actually the reason why the total wave function can be modeled by less plane waves.

The second alternative, ultrasoft PP, which was developed by Vanderbilt [141], violates the third condition of the norm-conserving PP and has a larger r_c. There, the core potential for $r < r_c$ is stronger weakened so that the wave function oscillates less. Thus, the cutoff energy can be decreased and hence, the number of plane waves as well as the computing time are reduced. In the case of Quantum Espresso they are limited to calculations of the band structure, density of states, and the total energy. Therefore, the optical spectra as well as the band structure are calculated solely by norm-conserving potentials.

Band structure

Before the band dispersion along a specific k-path can be determined, a self-consistent calculation has to be conducted on a dense equally spaced k-grid within the Brillouin zone to obtain the exact wave functions of the system. This is necessary to guarantee that the derived band dispersions and energies are valid. For the calculation we chose an automatic generated regular Monkhorst-grid [142] $a \times b \times c$. One can utilize the fact that the number of k-points scales reciprocally with dimension of the unit cell. This allows to diminish the number of k-points for the long axis of an anisotropic unit cell. The studied k-path was generated with visualization software Xcrysden [143].

Besides the convergence of the total energy with respect to the cutoff energy, its development as a function of grid size has to be checked as well. In Fig. 4.16 such an evolution of the total energy of TTF-CA is studied as a function of the k-grid size. The total energy drops steeply and reveals no significant change above $3 \times 3 \times 3$. The calculation of the k-points was parallelized in QE and distributed between several cores. Afterwards several post-processes have to be performed to receive a simple text file containing the information about the band structure.

Insulator and metals have to be treated differently within the calculations. In the case of insulators the lowest bands $N = \frac{N_{elec}}{2}$ are filled up to the band gap according to the Pauli-principle and the occupation is set to "fixed" in QE. However, it is important to add few empty bands to determine the wave function and the band gap accurately.

While insulator are, in principle, easy to handle, complications with metals occur because DFT-calculations are always performed at $T = 0\,\mathrm{K}$ and therefore, the bands are always filled up to the Fermi energy. This leads to a discontinuous jump of the wave function and their integrals, for instance the electron density, at the Fermi edge. Additionally, band-crossing can occur there during the calculations. Firstly, a larger number of k-points as for insulators are necessary to determine the dispersion of the bands at the vicinity of the Fermi energy precisely. Secondly, a finite temperature has to be introduced in the way of a smearing of the occupancy by a broadening function at the Fermi energy.

Dielectric function

The Hamiltonian $\mathcal{H}$ of a system interacting with electromagnetic radiation consists of two parts:

$$\mathcal{H} = \mathcal{H}_0 + \mathcal{H}_{int} \tag{4.15}$$

The first $\mathcal{H}_0$ is the unperturbed Hamiltonian and contains, for example, the electron-electron, the electron-ion and the electron-phonon interaction. The second term considers the interaction with an external vector potential $\vec{A}$ with the electrons:

$$\mathcal{H}_{int} \propto \sum_i^N [\vec{p}_i \cdot \vec{A}(\vec{r}_i) - \vec{A}(\vec{r}_i) \cdot \vec{p}_i], \tag{4.16}$$

at which a scalar potential field Φ is not considered being responsible for the longitudinal response. Also the quadratic term $\vec{A}^2(\vec{r})$ describing two-photon processes are not considered. $\mathcal{H}_{int}$ can be expressed by the electric current density $\vec{j}(\vec{r})$ [103]:

$$\mathcal{H}_{int} \propto \int \vec{j}(\vec{r}) \cdot \vec{A}(\vec{r}) d\vec{r} \tag{4.17}$$

$$\text{with } \vec{j}(\vec{r}) \propto \sum_i^N [\vec{v}_i \delta(\vec{r} + \vec{r}_i) - \delta(\vec{r} - \vec{r}_i)\vec{v}_i]\,. \tag{4.18}$$

The optical functions can be derived via Fermi's golden rule by the total absorbed power per volume $P \propto |\langle n^* | \mathcal{H}_{int} | n \rangle|^2 = \omega \epsilon_2 \vec{E}^2(\vec{r}) = \sigma_1 \vec{E}^2(\vec{r})$ in which the transverse electric field is connected to the vector field $\vec{A}(\vec{r})$ through the relation $\vec{E}(\vec{r}) = i\frac{\omega}{c}\vec{A}(\vec{r})$.

The imaginary dielectric tensor $\epsilon_{2,a,b}(\omega)$ can also be deduced from perturbation theory within the adiabatic and electric dipole approximation $A(\vec{r}) \propto \vec{E}e^{-i\vec{q}\cdot\vec{r}} \propto \vec{E}$ as a response function [103, 144]. Finally, after several transformation the Drude-Lortenz function is derived:

$$\epsilon_{2,a,b}(\omega) = \frac{4\pi e^2}{\Omega N_{\vec{k}} m^2} \sum_{n,\vec{k}} \frac{\Delta\omega \hat{M}_{a,b}}{\omega^4 + \Delta^2\omega^2} + \cdots + \sum_{n^*,n} \sum_{\vec{k}} \frac{\hat{M}_{a,b}}{E_{\vec{k},n^*} - E_{\vec{k},n}} \tag{4.19}$$

$$\cdots\cdots \frac{\Gamma\omega f(E_{\vec{k},n})}{[(\omega_{\vec{k},n^*} - \omega_{\vec{k},n})^2 - \omega^2]^2 + \Gamma^2\omega^2}. \tag{4.20}$$

The dielectric function $\epsilon_{1,a,b}$ is obtained by a Kramers-Kronig transformation. Γ is the life time of the excited state while Δ is the scattering time of the excited free charge carriers. The matrix transition element $\hat{M}_{a,b}$ is defined as follows:

$$\hat{M}_{a,b} = \left\langle \Psi^\star_{\vec{k},n^*} \middle| \hat{p}_a \middle| \Psi_{\vec{k},n} \right\rangle \left\langle \Psi^\star_{\vec{k},n} \middle| \hat{p}^\dagger_b \middle| \Psi_{\vec{k},n^*} \right\rangle \tag{4.21}$$

$$\hat{M}_{a,b} = \left\langle \Psi^\star_{\vec{k},n^*}(\vec{r}) \middle| \frac{\partial}{\partial x_a} \middle| \Psi_{\vec{k},n}(\vec{r}) \right\rangle \left\langle \Psi^\star_{\vec{k},n}(\vec{r}) \middle| \frac{\partial}{\partial x_b} \middle| \Psi_{\vec{k},n^*}(\vec{r}) \right\rangle. \tag{4.22}$$

$\left|\Psi_{\vec{k},n^*}\right\rangle$ is the Bloch wave function of the band n^* being determined by the previous DFT calculation and $\hat{p}$ is the dipole transition operator. Only vertical transitions, in which $\vec{k}$ does not change, are taken into account.

The complex dielectric function $\hat{\epsilon}(\omega)$ was calculated by the subroutine epsilon.x of QE. Prior to this a self-consistent calculation of the total energy has to be performed and after all $\hat{\epsilon}(\omega)$ is ascertained by the determined eigenvalues and eigenfunctions. It is important that a dense grid of k-points is set to guarantee that all transitions are equally included.

4.5.2 *Normal mode analysis*

Lattice and molecular vibrations can be determined by the variation of the total energy in the thermodynamic equilibrium. Since the nuclei are much heavier than the light electrons, they move slower so that the contribution of the electrons can be neglected. Therefore, the total energy $E(\vec{R})$ of the system can be regarded as a function of the atomic nucleus coordinates $\vec{R} \equiv \{\vec{R}_I\}$ being called as the potential energy surface PES. The equation of motion for the nuclei I is:

$$M_I \frac{\partial^2 u_I(t)}{\partial t^2} = -\frac{\partial}{\partial \vec{R}_I} E(\vec{R}) \tag{4.23}$$

leading to a system of equations of coupled harmonic oscillators. $E(\vec{R})$ can be developed as a Taylor series at the global minimum of the PES. The first order is zero due to the minimum of the total energy at the equilibrium and only the second order term is considered:

$$C_{I,a;J,b} = \frac{\partial^2 E(\vec{R})}{\partial R_{I,a} \partial R_{J,b}} \tag{4.24}$$

$C_{I,a;J,b}$ corresponds to the force constant. The equation of motion 4.23 can now be expressed as

$$-\omega^2 M_I u_I(t) = -\sum_{J,b} C_{I,a;J,b} u_{J,b} \tag{4.25}$$

$$\det \left| \frac{1}{\sqrt{M_I M_J}} C_{I,a;J,b} - \omega^2 \right| = 0 \tag{4.26}$$

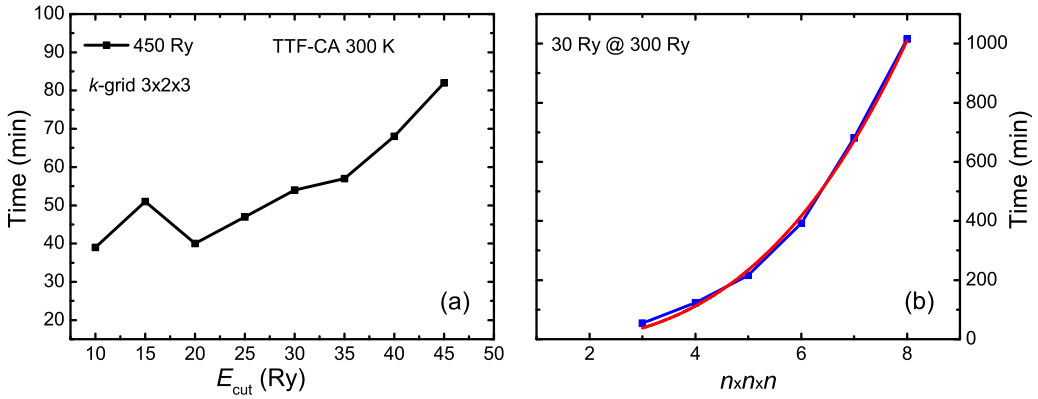

Figure 4.18: (a) Dependence of the computing time of TTF-CA for a crystal structure at 300 K for different cutoff energies E_{cut} for $3 \times 2 \times 3$ grid and $E_{cut,\rho} = 450\,\text{Ry}$. (b) Computing time (green) as function of the grid size. E_{cut} and $E_{\text{cut},\rho}$ were set to 30 Ry and 300 Ry. The computing time increases cubic with the grid size. The red lines shows the fit of the cubic function.

with the displacement $u_{I,\alpha}(t) = u_{I,0,\alpha}e^{i\omega t}$ of the nucleus I.

For the normal mode analysis the molecular structures were drawn by chemical drawing software (i.e. Gabedit, Avogadro) or taken from existing structural data sets derived by scattering experiments. In general, the B3LYP[132] or the EPF2[136]-functional were used in connection with a Gaussian basis set. To get the normal modes, it is necessary to optimize the structure by finding the global minimum of the PES of the molecule. For this, the coordinates of the atoms are relaxed and the gradient of the total energy determined which has to be zero. Furthermore, the second derivative, the Hesse matrix $\mathbf{H}$, must be positive in all elements. It is assumed that in first approximation the PES is quadratic for small displacements.

4.5.3 *Speed test of the DFT-calculations*

Speed tests were performed to get an estimation of the length of a typical calculation and its dependence on selected parameters like grid size or cutoff energy. Only one parameter was always varied in the test while the others kept fix. Fig. 4.18 (a) displays the necessary computing time for a self-consistent calculation of the total energy of TTF-CA as a function of E_{cut}. The grid size was fixed to $3 \times 2 \times 3$ for $E_{cut\rho} = 450\,\text{Ry}$. As expected, the computing time increases nonlinearly with increasing E_{cut}. However, the largest impact on the computing time has the selected $\vec{k}$-grid size. In Fig. 4.18 (c) it is plotted for various $n \times n \times n$ values for E_{cut} = 30 Ry and $E_{\text{cut},\rho}$ = 300 Ry. The computing time increases cubic. This outcome is important concerning the calculations of metals which need many k-points. Therefore, the optimum combination of grid size and cutoff energies has to be allocated.

Part IV

RESULTS

5 EXPERIMENTAL RESULTS

This chapter is dedicated to the experimental results of the various types of organic conductors studied within this thesis, i.e. the one-dimensional organic conductors of the Fabre-Salts, the newly synthesized δ-(EDT-TTFCONMe$_2$)X (X =Br and AsF$_6$) compounds, the one-dimensional mixed-stacked TTF-CA, and the two-dimensional α-(BEDT-TTF)$_2$I$_3$ system. The different sections are arranged in such a way that first, a brief introduction of the physics of the compounds and the current state of research are given. Subsequently, the experimental results and the studies of the thermal equilibrium state are presented which are derived mainly by optical and transport measurements. The experimentally determined data were compared to extensive theoretical quantum chemical calculations mainly based on DFT.

One of the main goals was to study electrically- and light-induced transitions and related effects in the aforementioned organic conductors. Therefore, the non-equilibrium behavior of most of the compounds were examined by time-resolved infrared photoconductivity and optical measurements. A large diversity of exotic effects were observed and explained by theoretical models.

5.1 FABRE-SALTS: TMTTF$_2X$ (X=SBF$_6$, ASF$_6$, PF$_6$, AND REO$_4$)

5.1.1 *Scope of the study on the one-dimensional Fabre salts*

The Fabre salts are one of the model systems in solid state physics to study physical effects occurring solely in one dimension. Although they have already be known for almost 40 years, they are still an active field of research since the appearance and the trigger mechanism of several phases is still not understood. Therefore, we have performed a comprehensive study of the optical properties of (TMTTF)$_2X$ (X=PF$_6$, AsF$_6$, SbF$_6$, and ReO$_4$) allowing us to determine the temperature dependence of the charge disproportionation in the charge ordered state with a very high precision for the first time. Furthermore, we compared our experimental optical results with *ab initio* calculated optical spectra. This reveals also a temperature-dependent evolution of the electronic excitations above 8000 cm^{-1}(1 eV) which was disregarded in the past, but is actually an attractive energy range for further investigations. Photoconductivity measurements reveal unexpected current oscillations occurring only in (TMTTF)$_2$SbF$_6$ in the charge order phase. This compound differs from its sister salts, since the transition is more first order-like. Parts of our results were published and incorporated in several publications [2, 11, 145].

5.1.2 *One-dimensional organic conductors*

The first examined class material is the so-called Fabre salt family (TMTTF)$_2X$ (X=Br, PF$_6$, AsF$_6$, SbF$_6$, etc.) which was firstly synthesized in the late 70's of the twentieth century [146].

In general, their unit cell contains two organic TMTTF molecules stacked along the crystallographic a-direction and one inorganic anion, as depicted in Fig. 5.1. For all here considered systems, the space group of the unit cell at RT is the trinclinic $P\bar{1}$. A further look at the unit cell directly reveals the origin of the quasi-one-dimensional character of the transport properties: while the TMTTF molecules are stacked along the a-axis which ensures a good orbital overlap, the interstack interaction is much weaker along the other directions. Along the b-axis, interstack interactions are reduced due to the side-to-side orientation of the TMTTF molecules, which cannot be completely neglected. Therefore, the systems are quasi-one-dimensional salts. The anion occupies an inversion center of the unit cell and separates the cation layer in the ab-plane from each other along the c-direction (see Fig. 5.1). The reduced overlap of the molecules along the b- and c-direction and the directional transfer integrals cause a strong anisotropy in the physical properties. For instance, the resistivity exhibits an approximated ratio between the three directions of $\rho_a : \rho_{b'} : \rho_{c^\star} \approx 1 : 10 : 1000$. The exact ratios at room temperatures are specified in Tab. 5.1. Their quasi-1D character makes them attractive to test the reliability and precession of theoretical models which can be often solved analytically only in one dimension.

Due to the stoichiometry of the compounds half of an electron is transfered from each of the cations to the single anion. Hence, the anion is negatively charged and has a closed shell as mentioned in the introductory of Sec. 2.1. Thus, the energy of the highest molecular orbital of the anion is located far below the Fermi energy and on the first view does not play any important role concerning the physical properties of the Fabre salts. The charge transfer leads to a three-quarter filled system with respect to the electrons, and a quarter-filled one in respect to the holes[1]. It appears that the TMTTF molecules are weakly dimerized along the stacking direction. Therefore, the transfer integrals are altered and a gap opens at $2k_f$. This leads to two bands: a completely filled lower band separated from the upper half-filled band by a dimerization gap.

In Tab. 5.1 the transfer integral between the TMTTF molecules along the stacking direction are listed for the studied compounds X=PF_6, AsF_6, SbF_6, and ReO_4.[29]. By comparing the two transfer integrals t_1 and t_2 between two neighboring molecules, it is obvious that with decreasing temperature the dimerization becomes smaller and the molecules get equally arranged. In addition, the intradimer transfer integral t_1 decreases for the symmetric anions with increasing size, which resembles the temperature behavior of the transfer integral.

In general, the transfer integral is mainly determined by the distance of the TMTTF molecules and hence, by the overlap of the adjacent sulfur atoms. Thus, the most apparent possibility to tune this parameter is to substitute the sulfur atom by an element with an extended orbital or apply hydrostatic pressure by which the transfer integral increases. Jérome et al. [147] and Bechgaard et al. [7] were the first to replace the sulfur atoms by selenium atoms, laying the cornerstones for the Bechgaard salts $(TMTSF)_2X$. Thereby, the transfer integral as well as the coupling to neighboring chains are increased which modifies the dimensionality. In 1980, $(TMTSF)_2PF_6$ was the first discovered organic superconductor with a transition temperature of $T_C = 1.3\,K$ under a hydrostatic pressure of 6 kbar [147]. Already one year later the first organic superconductor $(TMTSF)_2ClO_4$with $T_c = 1.3\,K$ at ambient pressure was synthesized by Bech-

1 Throughout the whole text we will stick to the first notation.

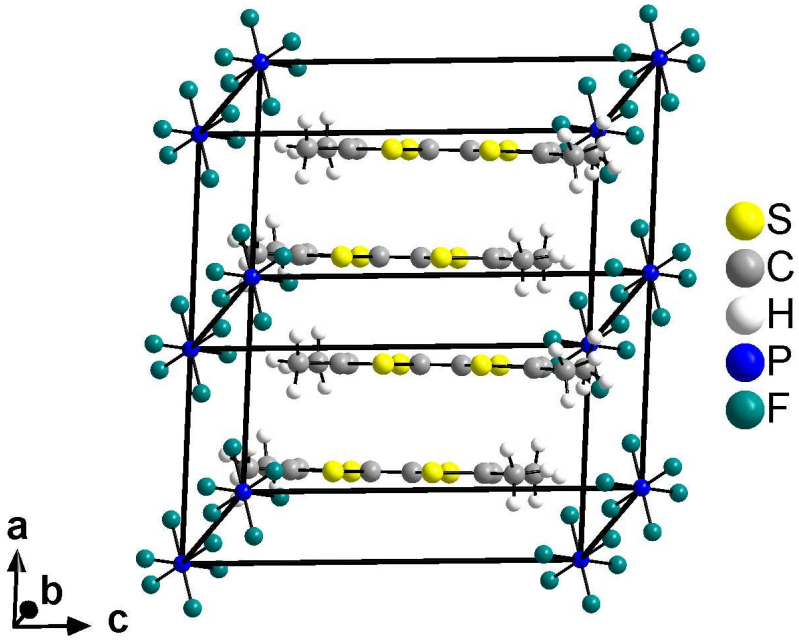

Figure 5.1: Crystal structure of (TMTTF)$_2$PF$_6$ oriented along the b-axis at 4 K. Two unit cells are visualized. The TMTTF molecules are stacked along the a-direction in a zigzag configuration leading to an optimal molecular overlap between them. In the c-direction the cations are separated from each other by the anions (in the present case by PF$_6$). [1]

gaard et al. [7], following Little's idea [6] of an organic room temperature superconductor. The occurrence of the superconducting state provided solely in the TMTSF salts that the dimensionality plays a crucial role. Nowadays, many different compositions of the TMTTF and TMTSF salts with various centro- and noncentro-symmetric anions are available. As aforementioned, low-dimensional organic compounds are a great playground for theorists giving them the chance to test their theories and compare them directly with the experimental data. At low dimensionalities, electron-electron and electron-lattice interactions become more important and cause phenomena which only appear under these circumstances (see Sec. 2.3 and 2.4). Hereby, several ordering phenomena as charge ordering (CO), CDWs or SDWs can occur together with a symmetry breaking. As stated in Sec. 2.3, fluctuations prevent in pure one-dimensional systems any long-range order, but in real materials a certain coupling of the one-dimensional chains can stabilize these novel phases.

In Fig. 5.2 (a) the resistivity of (TMTTF)$_2X$, X=PF$_6$, AsF$_6$, SbF$_6$, and ReO$_4$ along the stacking direction is depicted as a function of temperature [59]. All these compounds are bad conductors at room temperature. At lower temperatures, a minimum appears in the resistivity which can be attributed to the opening of a Mott gap due to enhanced electronic correlations. Thus, the correlations are strong enough at low temperatures to localize the charge equally. Furthermore, a suddenly increase[2] of the resistivity follows when cooling to different critical temperatures T_{CO} (for PF$_6$ at 67 K, AsF$_6$ at 102 K, SbF$_6$ at 156 K, and for ReO$_4$ at 230 K) indicating that the transition into an insulating state is caused by the unequal distribution of the charge carriers on the molecular cationic sites. In the case of ReO$_4$, a second kink is present in the resistivity curve, being caused

2 More pronounced for SbF$_6$ and ReO$_4$.

Table 5.1: Intrastack transfer integrals t_1 and t_2 [29] for the Fabre salts at various temperatures as well as the ratios of the direction-dependent resistivity $\rho_a : \rho_{b'} : \rho_{c^\star}$ [59] at room temperature.

Fabre salts: $(TMTTF)_2X$					
X	T (K)	t_1 (eV)	t_2 (eV)	$2(t_1-t_2)/(t_1+t_2)$	$\rho_a : \rho_{b'} : \rho_c^\star$
PF_6	4	0.1912	0.1686	0.126	
	300	0.1976	0.1569	0.231	1: 50: 2000
AsF_6	4	0.1943	0.1759	0.1	
	300	0.1951	0.1568	0.218	1: 30: 1000
SbF_6	100	0.1823	0.1747	0.042	
	300	0.1925	0.1426	0.298	1: 40: 600
ReO_4	300	0.14[148]	0.1	0.33	1: 7: 70

by an anion ordering at T_{AO}= 156 K that leads to a tetramization and doubling of the unit cell. Below 200 K, the temperature dependence of the resistivity cannot be described in all cases by a typical thermally activated transport behavior with a constant gap, but rather by the combination of the variable-range-hopping[3] and a mean-field model [59, 149]; the latter is based on a temperature-dependent gap consisting of at least a temperature-independent gap and a charge order gap. In the case of compounds with non-symmetric anions like ReO_4, the anion ordering gap has to be added to the aforementioned gap contributions.

The temperature dependence of the real part of the dielectric permittivity is illustrated in Fig. 5.2 (b) [55, 153, 154]. All compounds show a divergent behavior of ϵ_1(T) at T_{CO}, where also the resistivity increases steeply (see Fig. 5.2). For ReO_4 the signal drops sharply at the anion ordering temperature of T_{AO}= 157 K, indicating the transition into an antiferroelectric phase. The evolution of ϵ_1 at the vicinity of the phase transition resembles the behavior of a second order ferroelectric phase transition [87], as it follows a Curie law $\epsilon_1 \sim \frac{1}{T-T_{CO}}$. The same temperature-dependent behavior of the relaxation rate is observed from the position of the resonances in ϵ_2, supporting the idea of a ferroelectric charge order phase.

In order to investigate the magnetic phases, the spin susceptibility at constant volume is displayed in Fig. 5.2 (c) for all studied components along the stacking direction. In all four cases, it demonstrates the behavior of a spin-1/2 antiferromagentic Heisenberg chain at high temperatures which can be described excellently by the well-known theoretical model suggested by Bonner and Fisher [155]. While the charge localization and the charge order phase transition appear as a kink in the DC-curve, no sign of it is present in the temperature dependence of the spin susceptibility [150, 151, 156]. This means that the charge and the spins are well separated from each other, which is the hallmark of a strongly interacting one-dimensional electron system, a so-called Luttinger liquid. In the case of SbF_6, $[\chi_S]_V$ shows a minimum at the antiferromagnetic transition temper-

3 It only contributes significantly to the conductivity at low temperatures and along the b'- and $c^\star$-direction.

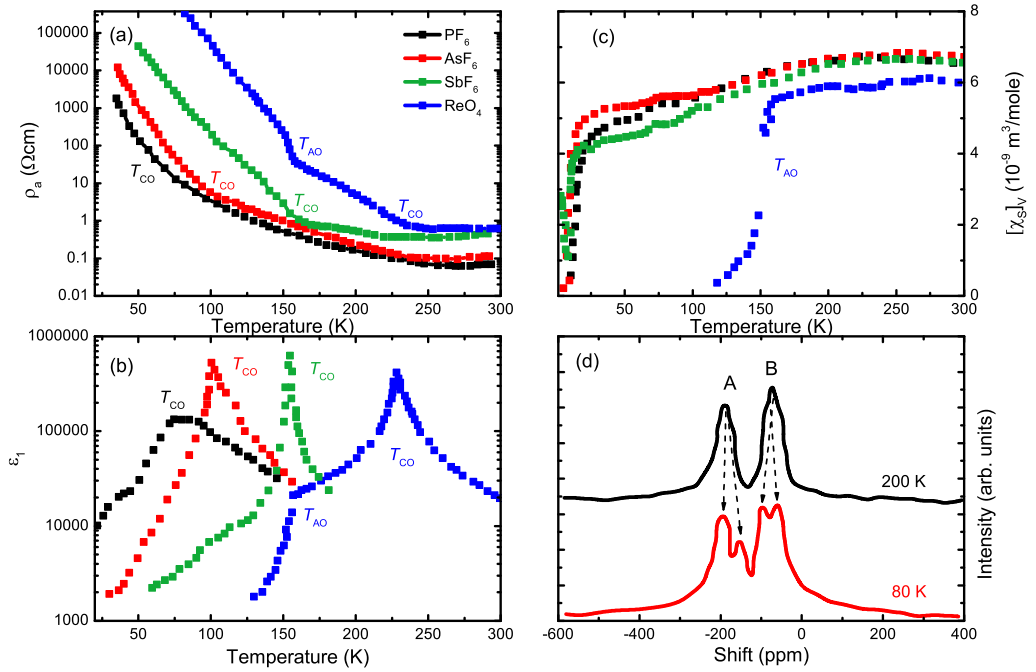

Figure 5.2: Experimental data of (TMTTF)$_2X$, X=PF$_6$ (black), AsF$_6$ (red), SbF$_6$ (green), and ReO$_4$ (blue). (a) Temperature-dependence of the resistivity along the a-direction [59]. The labels mark the charge order transition temperature T_{CO}, and the anion ordering temperature T_{AO} in the case of X=ReO$_4$. (b) ϵ_1 at 100 kHz as a function of temperature. All compounds reveal a Curie-law behavior. [55] (c) Temperature-dependence of the spin susceptibility (constant volume). X=PF$_6$ and AsF$_6$ undergo a Spin-Peierls transition at 19 K and 13 K, respectively. X=SbF$_6$ exhibits an antiferromagnetic state below 8 K causing an increase of $[\chi_S]_V$. (TMTTF)$_2$ReO$_4$ exhibits a spin paring due to the anion ordering and the related tetramerization of the TMTTF, leading to a nonmagentic ground state. Above the transition $[\chi_S]_V$ can be described by a model of a 1/2 antiferromagnetic Heisenberg chain. [150, 151] (d) ^{13}C NMR spectra of (TMTTF)$_2$AsF$_6$ at 200 K and 80 K. Above T_{CO} two distinct features A and B can be identified which split into a total of 4 peaks, as depicted by the arrows. [152]

ature of 8 K, while the downturn in the case of the symmetric anions AsF$_6$ and PF$_6$ is caused by the creation of a spin-singlet due to a Spin-Peierls transition (see Sec. 2.3) at 13 K and 19 K, respectively. In contrast, $[\chi_S]_V$ drops sharply for ReO$_4$ due the first-order anion ordering transition at T_{AO}=157 K. The wave vector of the anion ordering Q=(1/2,1/2,1/2) indicates a tetramerization of the TMTTF molecules along the stacking direction. The charge pattern changes from an alternating arrangement in the CO phase of o-O-o-O to o-O-O-o (O: charge rich site, o: charge poor site).

Recently, first evidences were found in the charge ordered phase that the charge degree and spin degrees of freedom are coupled. The charge imbalance and the symmetry breaking in the CO phase influences the g-tensor, leading to two inequivalent molecular sites on adjacent chains. The two different magnetic sites induce a doubling of the periodicity of the ESR linewidth.

In Fig. 5.2 (d) the ^{13}C NMR spectra of AsF$_6$ is exemplarly depicted for a temperature above and below T_{CO} [152]. Above the phase transition, two peaks are present in the spectrum due to the inequivalent positions of the inner and outer ^{13}C atoms. At the phase transition the lines are split into four features. Indeed, the charge order was firstly confirmed by NMR [54, 158] with the charge

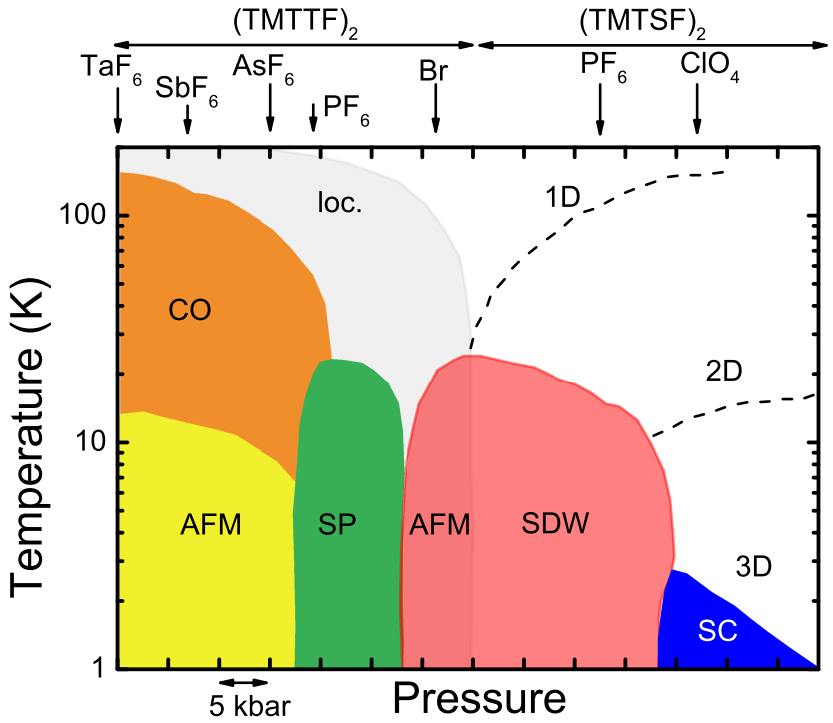

Figure 5.3: Unified temperature-pressure phase diagram of the Fabre and Bechgaard salts [2, 157]. The physical properties can be tuned by applying hydrostatic pressure or by substituting the anions (chemical pressure). By exchanging TMTTF with its selenide analogue TMTSF or applying hydrostatic pressure, a dimensional crossover from a 1D to a 3D metal can be attained. At low temperatures several ground states emerge: charge ordering (CO), charge localization (loc.), antiferromagnetism (AFM), Spin-Peierls (SP), spin-density wave (SDW), and superconductivity (SC). The arrows mark the position of the chemical substituted compounds in the phase diagram at ambient conditions.

disproportion being proportional to the inverse ratio of the spin-relaxation rates or of the Knight shift [159]. Both methods yield slightly different results for the charge imbalance. In the Spin-Peierls state as well as in the anion ordered phase, the four lines merge into one single line, indicating a possible redistribution of the charges between the molecular sites [152, 160].

For many years, the charge ordered state has been considered as a structureless transition [161] since structure resolving methods like x-ray scattering could not detect any modification of the crystal structure (an overview can be found in Ref. [60]). However, it was discovered later that irradiation destroys the charge order state, preventing the detection of a related structural transition [162]. Recently, neutron scattering discovers a weak modification of the lattice due to the charge ordering. Furthermore, thermal expansion reveals a feature at the phase transition, providing first hints that the charge order is accompanied by a modification of the structure [163, 164]. Therefore, the idea that the anions stabilize or even trigger the charge order transition [165], for instance via static electronic polarization, with the methyl-groups of TMTTF or TMTSF, experience a revival [60] to explain the occurrence of the charge order phase. Up to now, no evidences were found for this assumption. However, some observations point towards the importance of the anions, as for example T_{CO} increases with the

Table 5.2: Table of the various transition temperatures and charge order energy gaps derived by various methods of (TMTTF)$_2X$, X=PF$_6$, AsF$_6$, SbF$_6$, and ReO$_4$. (Trans: transport measurements, Optic: optical measurements, Div.: other techniques.)

Fabre salts: (TMTTF)$_2X$							
X	T_{CO} (K)	T_{SP} (K)	T_N (K)	T_{AO}	$\Delta_{Trans.}$ (K)	Δ_{Optic} (K)	$\Delta_{Div.}$ (K)
PF$_6$	67	19	-	-	440[59]	1150 [166]	1160 [167], 860 [166]
As$_6$	102	13	-	-	710 [59]		
SbF$_6$	157	-	8	-	875 [59]		
ReO$_4$	230	-	-	157	1255 [59]		

anion size. To clarify this question, extended neutron diffraction experiments could be performed in the future to detect any deformation of the methyl group and shift of the anions within the crystal cavity formed by the methyl groups of the surrounding TMTTF molecules.

In Tab. 5.2 the transition temperatures and the energy gaps derived from the experiments are summarized.

Collecting all the information from a large amount of studies, a unified phase diagram of the Fabre- and Bechgaard [2, 157] salts can be drawn, which is depicted in Fig. 5.3. On the left site the Fabre-salts are located, starting with the centrosymmetric anion X=TaF$_6$ [3] which was newly synthesized in 2009. Going to the right, the anion size decreases from SbF$_6$, AsF$_6$, PF$_6$, towards Br, resembling hydrostatic pressure. It is known from transport measurement that these compounds exhibit a metallic behavior at room temperature, visible as an increase of the DC conductivity with cooling. Between 300 K and 200 K, the conductivity exhibits a minimum which is ascribed to the localization of the charge carriers due to the opening of a Mott-Hubbard gap. On further cooling, the charge ordered state CO develops which is at low temperatures accompanied or suppressed by an antiferromagnetic or Spin-Peierls phase SP. By applying hydrostatic or chemical pressure the horizontal position in the phase diagram can be controlled, which was demonstrated by various measurement techniques [169]. Eventually, a crossover from a one-dimensional to a two- and a three-dimensional metal takes place being related to the transition from a Luttinger to a Fermi liquid. The pressure and substitution of the anions as well as of the cations increase the interchain interaction and hence, the influence of the correlation effects are attenuated. Therefore, further ground states develop as a spin-density wave (SDW) or superconducting state (SC). It should be emphasized

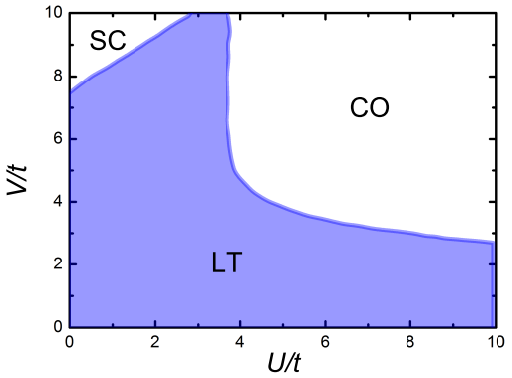

Figure 5.4: Phase diagram of a one-dimensional quarter-filled system derived from the extended Hubbard model without any dimerization. (Adapted from [168])

that $(TMTTF)_2ReO_4$ does not fit into the phase diagram; there is still no phase diagram which combines all Fabre and Bechgaard compounds.

The various ground states can be modeled theoretically in the framework of the extended Hubbard model (see Sec. 2.2). At first, it was solved exactly by Mila *et al.*[170] for a three-quarter filled one-dimensional system in the absence of dimerization. By that, they could derive a phase diagram as a function of U/t and V/t, yielding an insulating phase for large U/t and V/t values, as depicted in the schematic phase diagram in Fig. 5.4. For small U/t and V/t, the simulation reveals a metallic state; at low U/t and large V/t, a superconducting state appears. Hydrostatic and chemical pressure lead to a decrease of U/t and large V/t and hence, changing the position within the phase diagram. Further attempts were undertaken to include the dimerization, first with V=0 [171] and later for $V \neq 0$ [172]. The conclusion was that the dimerization competes with the charge order phase. Furthermore, phonon-electron interactions were also taken into account resulting in an additional SP state. Further details can be found in Ref. [25, 173] and references there within.

5.1.3 *Ab initio calculations: band structure, optical spectra and normal modes*

The combination of theoretical calculations and experimental results are very powerful to understand the physical properties and the underlying mechanism in solid state materials. Therefore, we have performed quantum chemical calculations to determine the band structure, optical properties, as well as the normal modes, and have compared them to our experimental results.

BAND STRUCTURE The band structure of $(TMTTF)_2X$ (with X=PF_6, AsF_6, and SbF_6) were determined by *ab initio* DFT calculations which is standardly implemented in the software package Quantum Espresso [122]. In contrast to the well-established Hückel theory with its molecular orbitals, it is based upon plane-waves and it is not semi-empirical; instead, it uses the advantage of the crystal periodicity and can be applied to almost every material. Moreover, it is fast, reliable and robust. Furthermore, we used a norm-conserving PBE GGA functional for all atom types, up to a certain level taking into account the exchange correlation as well as the spatial variation of the charge density. The crystal structure for the calculations were taken in the case of $(TMTTF)_2PF_6$ from [174] for 300 K, for $(TMTTF)_2AsF_6$ from [146] for 300 K, and for $(TMTTF)_2SbF_6$ from [174] for temperatures from 300 K to 100 K; the structures were not relaxed within the calculations. Due to the stoichiometry of the organic salts, they are treated as metals. Thus, a smearing factor of 0.005 Ry was applied. Furthermore, the cutoff energy of the plane waves and the electron density were set to 30 Ry and 120 Ry, respectively. The wave functions were determined in a self-consistent way on a Monkhorst $8k \times 8k \times 4k$ grid. The band structure was calculated on the k-path: $\Gamma(0,0,0) \rightarrow X(0.5,0,0) \rightarrow U(0.5,0.5,0) \rightarrow \Gamma(0,0,0) \rightarrow Y(0,0.5,0) \rightarrow T(0,0.5,0.5) \rightarrow \Gamma(0,0,0) \rightarrow Z(0,0,0.5) \rightarrow R(0.5,0.5,0.5) \rightarrow \Gamma(0,0,0)$.

The resulting band structure close to the Fermi energy is depicted in Fig. 5.5 for 300 K.[4] The HOMO of the Fabre-salts is three quarter-filled. Due to the dimerization between the $TMTTF^{+0.5}$ molecules, the HOMO is split into a lower com-

4 The very small deviation between the $(TMTTF)_2AsF_6$ band structure and the other ones is mainly caused by different definitions of the angles of the unit cell. However, this does not hinder us to compare them with each other.

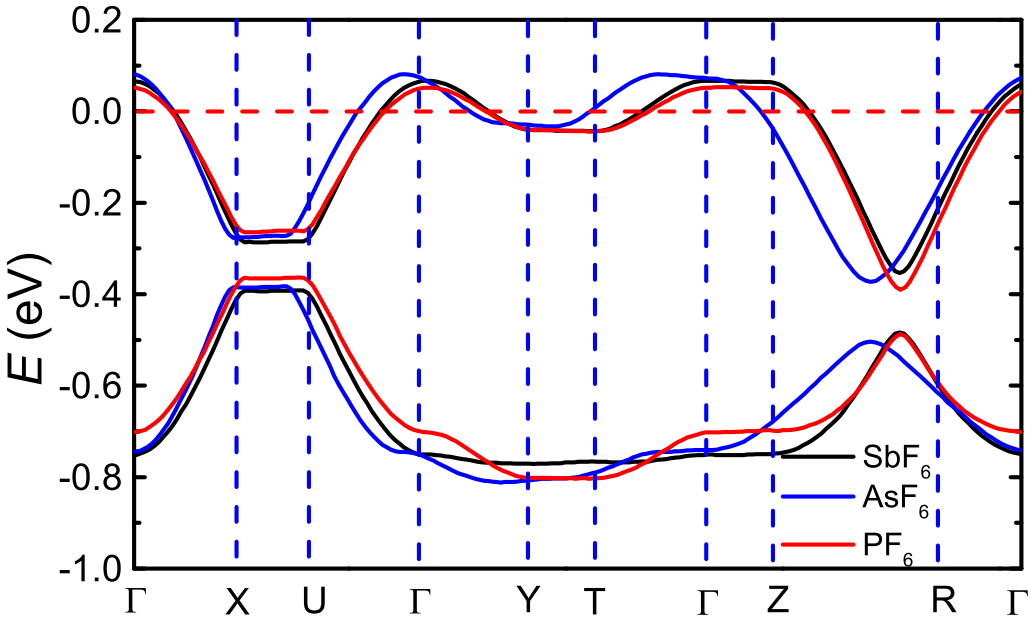

Figure 5.5: Comparison of the band structure of (TMTTF)$_2X$, X= PF$_6$ (red), AsF$_6$ (blue), and SbF$_6$ (black) at room temperature along the k-path: $\Gamma\,(0,0,0) \rightarrow X\,(0.5,0,0) \rightarrow U\,(0.5,0.5,0) \rightarrow \Gamma(0,0,0) \rightarrow Y\,(0,0.5,0) \rightarrow T\,(0,0.5,0.5) \rightarrow \Gamma(0,0,0) \rightarrow Z\,(0,0,0.5) \rightarrow R\,(0.5,0.5,0.5) \rightarrow \Gamma(0,0,0)$.

pletely filled band and a half filled upper band. These bands are well separated from the other bands which are located at -2 eV below and about 1.5 eV above the HOMO band (not shown here). The anion layer does not contribute to the bands near the Fermi energy due to the closed shell of the anions. The occupied and unoccupied bands of the anions reside far below and above the HOMO band.

The dimensionality of the compounds is reflected by the band dispersion. The band shape is similar for all compounds; the main deviations occur for the paths corresponding to the b-direction ($\Gamma \rightarrow Y$ or $T \rightarrow \Gamma$). They reveal an enhanced dispersion going from the large SbF$_6$ to the smaller PF$_6$ anion. This is consistent with the increase of the overlap between neighboring TMTTF molecules along the b-direction, being caused by the reduced spacing between the adjacent stacks due to the smaller anion size when going from SbF$_6$ to the smaller PF$_6$. Therefore, the compounds become more two-dimensional. The largest dispersion appears for the paths: $\Gamma \rightarrow X$ which is along the stacking direction, $U \rightarrow \Gamma$ and $Z \rightarrow R$ containing contributions of the a-directions as well. The bandwidth for the three materials is about 350 meV for the upper as well as for the lower band, being in excellent agreement with previous studies [29, 175]. For the b-direction, the bands are weakly warped and intersect the Fermi energy. In contrast, there is no energy dispersion for the c-direction ($\Gamma \rightarrow Z$), since the adjacent cation chains are separated from each other along the c-axis by the anion layer. The dimerization gap at the X-point decreases from about 110 meV for AsF$_6$ and SbF$_6$ to 81 meV for PF$_6$.

Moreover, also the temperature-dependence of the band structure was studied within this thesis which is visualized for SbF$_6$ over a temperature range between 300 K and 100 K in Fig. 5.6. With decreasing temperature the band width along the stacking direction ($\Gamma \rightarrow X$) slightly decreases whereas it increases for the path ($\Gamma \rightarrow T$) and ($T \rightarrow \Gamma$). This implies that the compounds become more two-dimensional on cooling. This behavior is similar to applying chemical pressure,

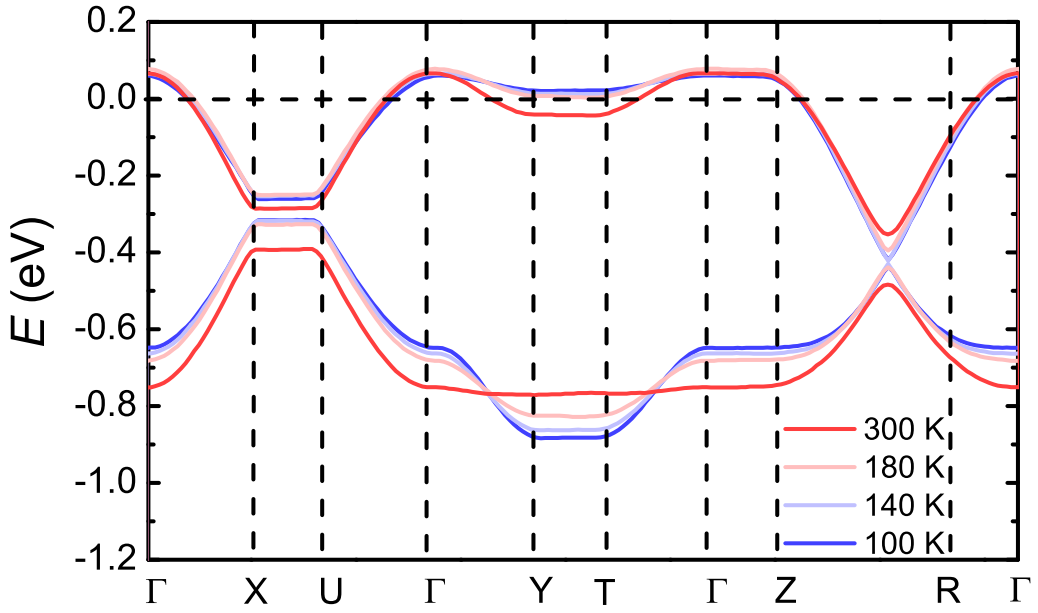

Figure 5.6: Band structure of $(TMTTF)_2SbF_6$ in a temperature range from 300 K (dark red) to 100 K (dark blue) on the selected k-path: $\Gamma\,(0,0,0) \rightarrow X\,(0.5,0,0) \rightarrow U\,(0.5,0.5,0) \rightarrow \Gamma(0,0,0) \rightarrow Y\,(0,0.5,0) \rightarrow T\,(0,0.5,0.5) \rightarrow \Gamma(0,0,0) \rightarrow Z\,(0,0,0.5) \rightarrow R\,(0.5,0.5,0.5) \rightarrow \Gamma(0,0,0)$.

already discussed in Fig. 5.5. This observation is supported by calculations of Jacko et al. [29] who also observed an increase of the dimensionality when the crystal structure of $(TMTTF)_2PF_6$ under hydrostatic pressure was taken for the calculations. Concerning the dimerization, the corresponding gap at the X-point obviously diminishes from 110 meV at 300 K to 55 meV at 100 K, again resembling the effect of pressure as demonstrated in Fig. 5.5.

In summary, the decrease of temperature should, in principle, have the same effect on the dimensionality and on the dimerization as hydrostatic or chemical pressure. However, it is well-known that the metallic state does not persist down to 0 Kelvin. Instead, a phase transition occurs at finite temperature into a charge ordered state which is triggered by electron-electron correlations.

OPTICAL SPECTRA To our best knowledge the optical spectra of the Fabre salts have not yet been theoretically calculated before. Thus, in the framework of this thesis DFT calculations were performed to derive the optical constants for all three crystallographic axis. While the excitation spectra were calculated for a regular spaced grid of 132 k-points, the same functional, smearing factor, and cutoff energies were used as reported in the previous paragraph. The inter-band transition were folded with a Lorentz function with a width of 100 meV, in contrast, for the Drude a width of 10 meV was assumed.

Fig. 5.7 displays the optical conductivity of $(TMTTF)_2SbF_6$ in a frequency range between 1000 cm^{-1} and 30000 cm^{-1} for temperatures between 300 K and 100 K. Below 5000 cm^{-1}, the a-direction is dominated by a Drude component (marked by an **A**). While it is less pronounced in the b-direction, the c-direction does not reveal any Drude component and drops to zero at $\omega \rightarrow 0$. The ratio of

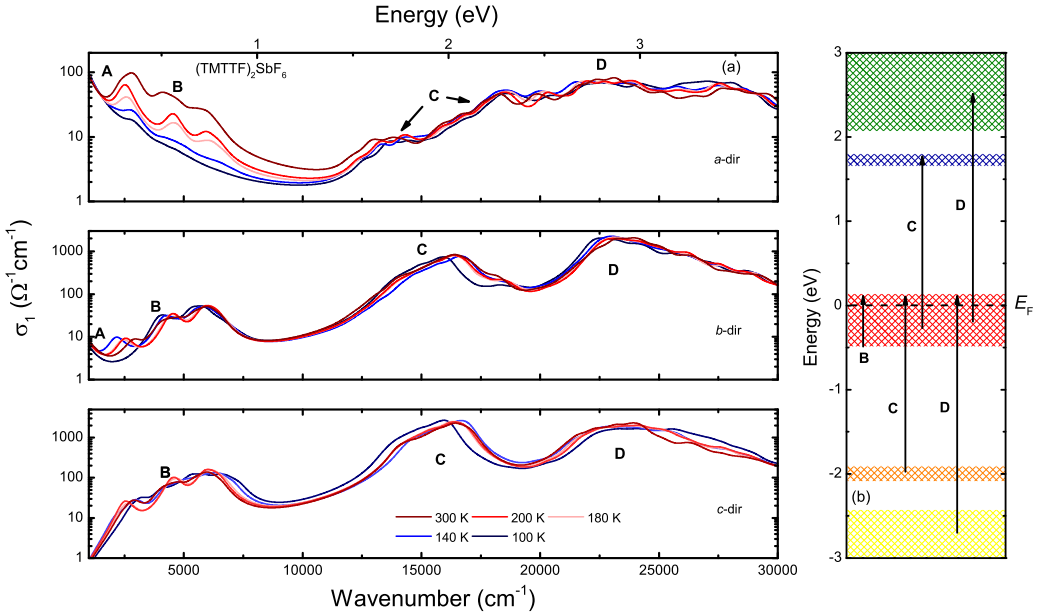

Figure 5.7: (a) Calculated optical conductivity of $(TMTTF)_2SbF_6$ between 300 and 100 K in a frequency range from 1000 cm^{-1} to 30000 cm^{-1} for the a-, b-, and c-direction. (b) Schematic diagramm of the transition between the occupied and unoccupied bands which are labeled by the corresponding markers from the optical conductivity spectra in (a).

the optical DC resistivity[5] is $\rho_a : \rho_b : \rho_c = 1 : 10 : 6500$ which agrees well with the result of the transport measurements (see Tab. 5.1 [59]).

On top of the Drude feature several resonances **B** are superimposed which can be found as well in the c-direction. These are excitations from the completely occupied band near the Fermi energy E_F into the empty states above E_F, being the strongest for the b- and c-direction.[6] The weaker and broader interband transitions (**C**) occur for the a-, b-, and c-direction between 12000 cm^{-1} and 20000 cm^{-1}. They can be attributed to the excitation from the half-occupied band to the lowest unoccupied band LUMO which is located 1.7 eV above E_F, as depicted in Fig. 5.7 (b). Moreover, also the excitations from the full occupied bands -2 eV below E_F to the half-filled band contributes to this feature. The smeared features **D** resides above 20000 cm^{-1} and can be assigned to the transition from the HOMO to the unoccupied bands located at 2 eV in the band structure and from the occupied bands being located -2.5 eV below E_F to the half-occupied band at E_F.

By comparing the intensity of the features **C** and **D** for the various directions, it is evident that the bands in the stacking direction are by a factor of 10 less intense. This is because these transitions are caused by intramolecular electronic transitions of the cation molecule TMTTF$^{+0.5}$, whose dipole moment is along the molecular axis. From the crystal structure it can be deduced that the long molecular axis of the TMTTF molecules is mainly oriented along the c-axis. For instance, the transition from the occupied band at the Fermi energy to the band at 1.7 eV corresponds to the transition from the HOMO of the TMTTF$^{+0.5}$ molecule

5 For a better comparison with the literature values, the resistivity ratio is used instead of the conductivity ratio.

6 Since no correlations effect are taken into account in the DFT calculations, the mid-infrared **B** band is not determined correctly. In the case of electron-electron correlations, the spectral weight of the Drude component is transferred to the mid-infrared band, leading to an enhancement of it. For more details see Sec. 5.1.4

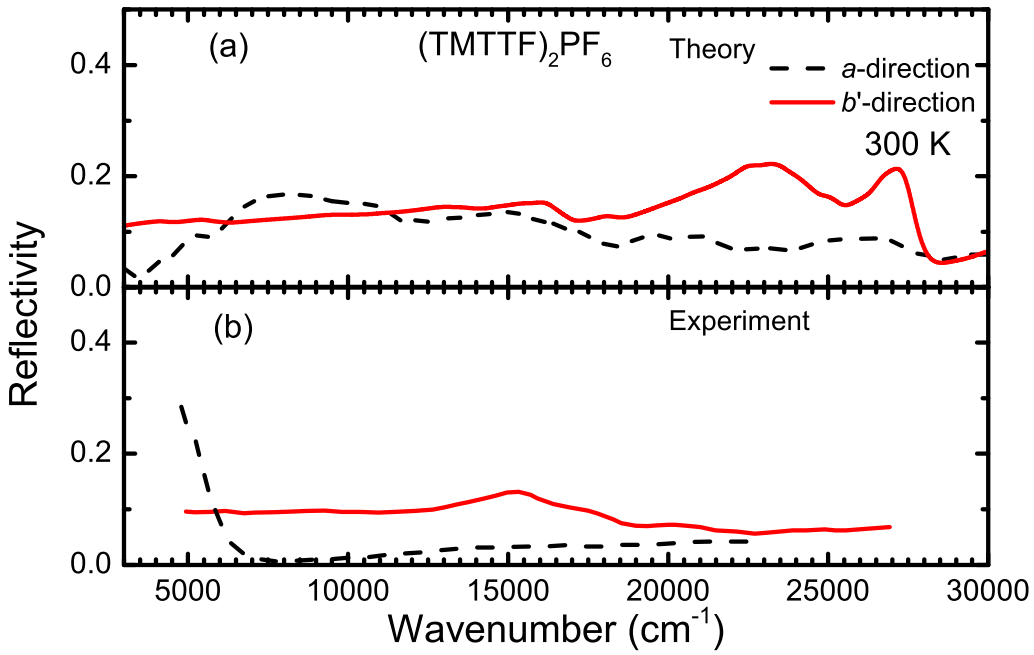

Figure 5.8: (a) Theoretically calculated optical spectra of $(TMTTF)_2PF_6$ at 300 K from 3000 cm^{-1} to 30000 cm^{-1} for the a- and b-direction. (b) Experimentally determined NIR and VIS spectra of $(TMTTF)_2PF_6$ recorded at 300 K for the a- and b'-direction (black dashed and red solid lines,respectively, adapted from [176].)

in the LUMO. The excitation energy of this transition decreases with increasing molecule size. In the case of $TTF^{+0.5}$ this excitation is located at 24000 cm^{-1} (see Fig. B.1 b- and c-direction) whereas for $TMTTF^{+0.5}$ it is at about 16000 cm^{-1}, and for $EDT\text{-}TTFCONMe_2$, and BEDT-TTF it is in the range between 8000 cm^{-1} and 10000 cm^{-1} (see Fig. B.8, and Fig. B.7 c-direction).

Besides the overall shape of the spectra and the assignment of the features it is very interesting to track the temperature evolution of the spectra and compare it to the experimental measurements. The **B** band reveals the largest temperature dependence. In the a-direction, its intensity decreases on cooling and vanishes in the Drude component, while for the b- and c-direction it only shifts to lower and to higher frequencies, respectively. In addition, also the **C**- and **D**-bands exhibit a temperature-dependent modification. Therefore, also the electronic excitations into higher energy levels can be used to track thermal effects. This is also true for phase transitions which are accompanied by a strong transfer of spectral weight.

In order to investigate how realistic our calculations are, we compare the theoretically calculated reflectivity spectra of $(TMTTF)_2PF_6$ with published reflectivity spectra from Ref. [176] in Fig. 5.8. The calculated reflectivity of the a-direction agrees excellent with the experimental reflectivity, even the absolute value as well as the slope of the reflectivity above 5000 cm^{-1} fits nicely. It is noteworthy that the steep increase below 5000 cm^{-1} is caused in the case of the theoretical spectra by the Drude component and the interband transitions, however, in the experimental data it originates from interband transitions across the charge gap which is not taken into account in the calculation.

For the b'-direction, the simulation describes the reflectivity very well in the sense of the absolute reflectivity. Merely, the feature between 20000 cm^{-1} and 30000 cm^{-1} cannot be found in the experimental reflectivity. It is not reported how the sample was oriented in respect to the polarized infrared light. Thus,

Table 5.3: Table of the most important vibrational modes of TMTTF^0 and TMTTF^{+1} with their scaled resonance frequency (in cm^{-1}), infrared intensity (in D^{2}amu^1 Å^{-2}) and the frequency difference (in cm^{-1}). The labeling is according to [177]. In brackets the frequency difference determined by Meneghetti et al. [177] is shown.

		TMTTF^0		TMTTF^{+1}		
Symmetry	label	ν_{sca}	Int.	ν_{sca}	Int.	Shift
a_g	ν_3	1636	0.0036	1570	0	66 (76)
	ν_4	1545	0.0036	1444	0.0021	101 (112)
	ν_5	1454	0.2444	1400	0	54 (-2)
	ν_6	1388	0.006	1391	0.0015	-3 (-2)
	ν_{10}	500	0.0197	530	0	-30 (-29)
b_{1u}	ν_{28}	1628	1.547	1551	8.6833	77 (80)
	ν_{31}	1112	0.6616	1108	0.0616	3 (-6)
	ν_{32}	950	0.0842	939	1.2806	11 (3)
	ν_{33}	786	0.9168	829	0.6553	-43 (-48)
b_{2u}	ν_{48}	1203	0.5125	1209	0.0754	-6 (-7)
	ν_{49}	1120	0.3985	1120	0.2273	0 (-13)

it is possible that this specific transition could not be captured. On the other hand, the position and the amplitude of the interband transition located at about 15000 cm^{-1}is reproduced accurately.

NORMAL MODE ANALYSIS Additionally to the electronic properties and spectra, the molecular vibrations of the TMTTF$^{+0.5}$ molecule were calculated to assign the vibrational features in the experimental spectra in Sec. 5.1.4. Therefore, the GAMESS package [123, 124] was used to perform *ab initio* normal mode analysis. The hybrid DFT-B3LYP functional and the 6-31+G(d,p) basis [138] set were applied to optimize the molecule structure. The C_1 symmetry was supposed for the gaseous molecule as the symmetry of the molecule is broken within the crystal. However, for the labeling and assignment of the vibrational modes the D_{2h} symmetry suggested by Meneghetti et al. [177] was assumed. The symmetry of the cation and the neutral molecule after the optimization was C_2 within restrict boundaries. All received vibrational frequencies are positive for the C_1 symmetry verifying that the equilibrium structure has been obtained.

The neutral molecule distorts in a boat-like configuration and the cation is flat similar to the molecular structure of the EDT-TTFCONMe$_2$ molecules depicted in Fig. 5.43. The same distortion is observed for other organic molecules [178, 179, 180] (see Sec. 5.2.2). Since the TMTTF molecule consists of 26 atoms, we expect in total 72 normal modes. For a better comparison with the results of [177], we distributed the normal modes according to the 8 irreducible representations of the D_{2h} group:

$$\Gamma = 12a_g + 6b_{1g} + 7b_{2g} + 11b_{3g} + 7a_u + 11b_{1u} + 11b_{2u} + 7b_{3u} \tag{5.1}$$

The a_g, b_{1g}, b_{2g}, and b_{3g} are Raman active whereas the b_{1u}, b_{2u}, and b_{3u} are infrared active. The a_u is neither infrared nor Raman active. In Tab. 5.3 the

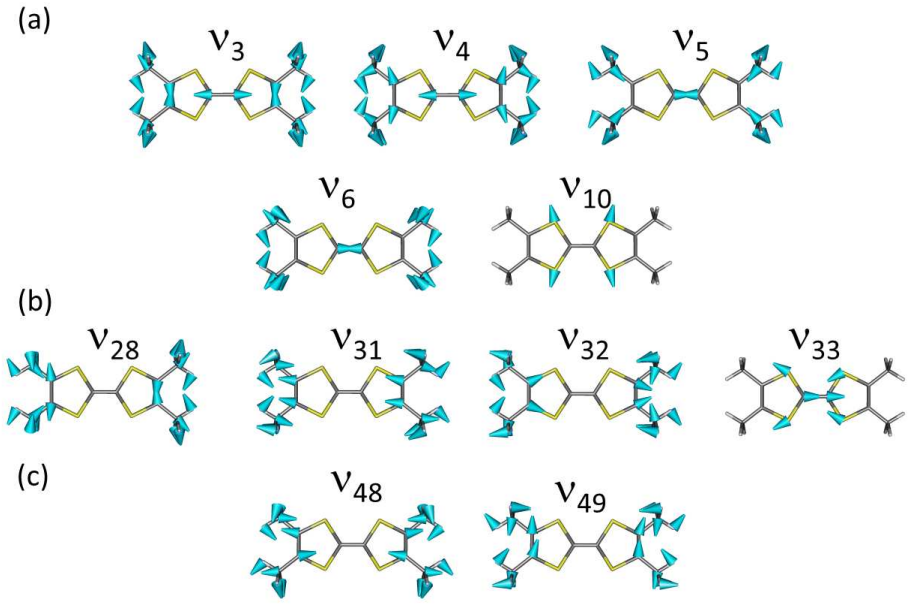

Figure 5.9: (a) The most important molecular vibrations of TMTTF with the irreducible representative a_g. (b) Sketch of four unsymmetric b_{1u} modes. (c) Illustration of the unsymmetric b_{2u} modes. (Published in Dressel et al. [2].)

most important and strongest modes for $TMTTF^0$ and $TMTTF^{+1}$ are listed with their resonance frequencies[7] and infrared intensity. The table contains mainly the symmetric a_g modes and the infrared ungerade b_{1u} and b_{2u} modes. The modes with the symmetry a_g are interesting because they become infrared active via electron-molecular vibration (emv) coupling which is explained in detail in Appx. F.

In Fig. 5.9 the molecular vibrations listed in Tab 5.3 are visualized. Here, we want to highlight the ν_3, ν_4, ν_{10}, ν_{28}, and ν_{33} modes, as they exhibit the largest frequency shift going from the neutral to the positive charged stated. This is caused by the fact that C=C double bonds dominate these molecular vibrations. Thus, they are very sensitive to a modification of the electron density which influences the bond length as well as the bond angles. Therefore, these modes can be used to determine the charge distribution between the molecular sites in the unit cell. While a linear behavior can be assumed between the charge and the resonance frequency for the infrared active ν_{28} and ν_{33} mode , it was shown in Ref. [181, 182, 183] that the strongly emv-coupled modes reveal a nonlinear shift of the resonance frequency as a function of molecular charge. Thus, the frequency of the infrared active ν_{28} (b_{1u}) mode will be studied to derive the charge imbalance between the molecular sites.

While the normal modes of the TMTTF molecule can be calculated, the vibrational eigenmodes of the anions could not be determined since the anions contain to heavy elements. Their electronic configuration cannot be described accurately by any basis sets. However, for all anions in the gaseous phase experimental data exists which can be used to assign the corresponding features in the experimental spectra since the resonance frequencies experience only a slight shift due to the crystal field. The free centro-symmetric, octahedral ions,

7 To scale the resonance frequencies, two factors were used i.) 0.9679 for resonances above 1300 cm^{-1} and ii.) 1.01 for vibrational modes below 1300 cm^{-1} [137].

Table 5.4: Table of the infrared active vibrational modes of PF_6 [186], AsF_6 [187], SbF_6 [185], and ReO_4 [188] with their resonance frequency (in cm^{-1}) and symmetry representative in brackets.

Anion	ν_1 (a_{1g})	ν_2 (e_g)	ν_3 (t_{1u})	ν_4 (t_{1u})	ν_5 (t_{2g})	ν_6 (t_{2u})
PF_6^-	756	585, 570	865, 835	559, 530	480 468	-
AsF_6^-	689	573	700	385	375	252
SbF_6^-	668	558	669	350	294	-
Anion	ν_1 (a_1)	ν_2 (e_2)	ν_3 (t_2)	ν_4 (t_2)		
ReO_4^-	-	-	920±4	322±10		

like PF_6^-, exhibit the O_h point group symmetry. The 15 modes are distributed on the 5 irreducible representatives [184, 185] as follows:

$$\Gamma = a_{1g} + e_g + 2t_{1u} + t_{2g} + t_{2u}. \tag{5.2}$$

The gerade ν_1 (a_{1g}), the ν_2 (e_g), and the ν_5 (t_{2g}) are Raman active at which the antisymmetric t_{1u} ν_3 and ν_4 modes are infrared-active. The ν_6 (t_{2u}) mode is Raman as well as infrared silent.[8] In Tab. 5.4 the infrared active modes are presented. The resonance frequency shifts by trend to lower frequency with increasing mass of the central atom. The tetrahedral ReO_4^- anion has the T_d symmetry with 9 vibrational modes which are sorted into the 5 irreducible representatives:

$$\Gamma = a_1 + e + 2t_2. \tag{5.3}$$

All modes are Raman active and only the ν_3 (t_2) and ν_4 (t_2) mode are also infrared-active. The resonance frequencies of ReO_4^- can be found as well in Tab. 5.4. In Fig. 5.10 the centro-symmetric, octahedral and tetrahedral anion vibrations are sketched which are mainly visible in the mid- and far-infrared spectra range.

8 In the symmetry notation "e" and "t" means two-fold and three-fold degenerated, respectively.

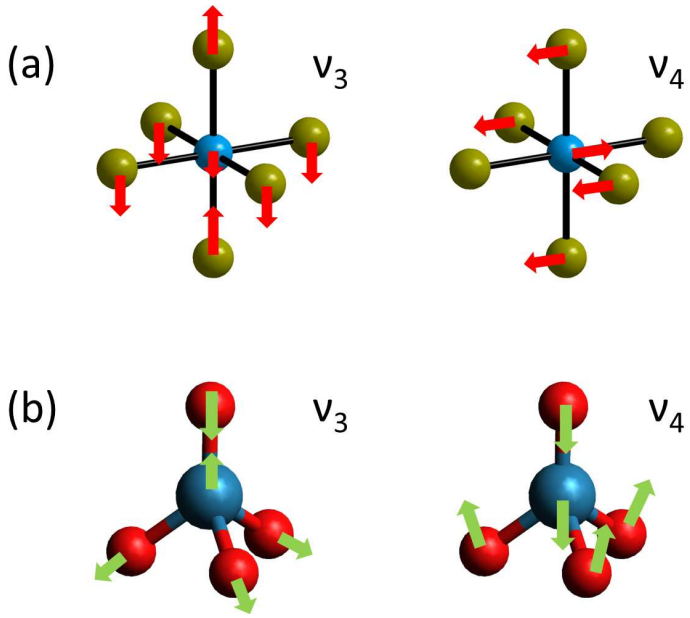

Figure 5.10: (a) Sketch of the infrared three-fold degenerated ν_3 (t_{1u}) and ν_4 (t_{1u}) of the NF_6^- anion with N=As, P, and Sb. The central blue spot and the greenish dots represent the N=P, As, and Sb and the fluorine atoms, respectively. (b) Illustration of the ν_3 (t_2) and ν_4 (t_2) of ReO_4 with the blue dot as the Re atom in the molecule center and the red dots as the oxygen atoms. The red and the green arrows mark the moving direction of the atoms within the vibrations.

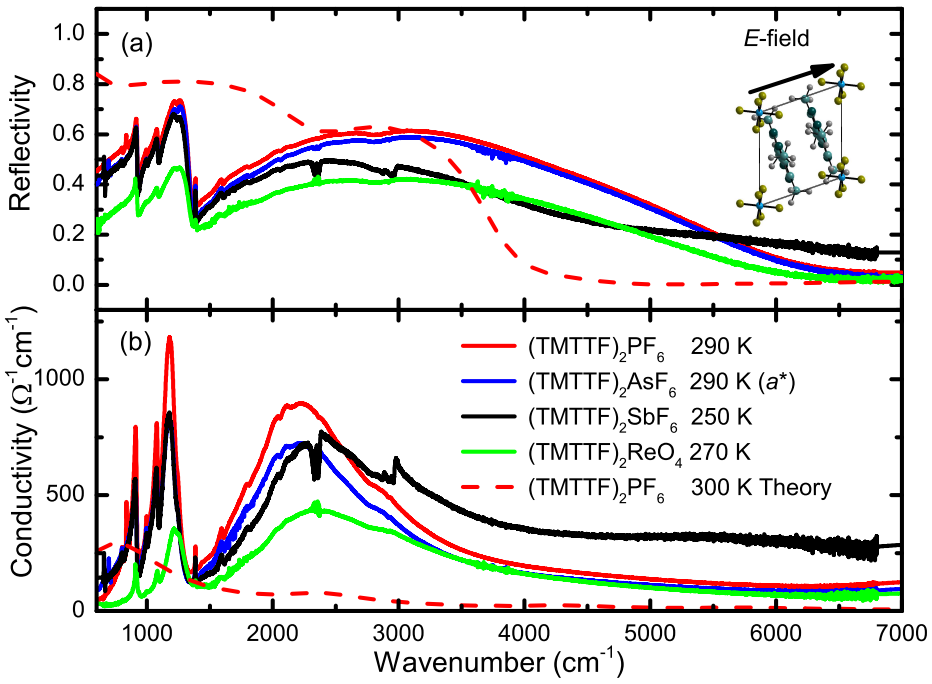

Figure 5.11: (a) Frequency-dependent reflectivity of (TMTTF)$_2X$ (X=PF$_6$ (red), AsF$_6$ (blue), SbF$_6$ (black), and ReO$_4$ (green)) close to room temperature. The dashed red line presents the simulated reflectivity of (TMTTF)$_2$PF$_6$. The inset displays the polarization of the infrared light in respect to the orientation of the unit cell axis. (b) Corresponding experimental and theoretical optical conductivity.

5.1.4 *Infrared measurements*

In this section we present the results of one of the most comprehensive optical studies on one-dimensional organic conductors, in which all three crystallographic axis of the four compounds (TMTTF)$_2X$, X=PF$_6$, AsF$_6$, SbF$_6$, and ReO$_4$ were examined between 10 K and 300 K in a frequency range from 600 cm^{-1}to 8000 cm^{-1}. First, the optical conductivity and reflectivity of the a-direction will be discussed, followed by the b- and c-direction, respectively.

5.1.4.1 *Optical properties of the a-direction*

As a reminder we know from previous experimental results and our theoretical calculations that the Fabre salts are one-dimensional conductors with the highest DC conductivity along the stacking (a-) direction. Therefore, we also expect that the optical conductivity as well as the reflectivity of this direction are large compared to the other two orientations, which was indeed demonstrated in literature for the TMTSF salts [166].

In Fig. 5.11 the reflectivity and optical conductivity of the four salts is depicted between 800 cm^{-1}and 7000 cm^{-1}at room temperature. The optical conductivity was determined from a KKT of the reflectivity data in the case of X=PF$_6$, AsF$_6$, SbF$_6$, and ReO$_4$. The far-infrared part from 70 cm^{-1}to 650 cm^{-1}was taken from the experimental data in Ref. [189]; for the other compounds, a similar extrapolation was taken. At even lower frequencies, a constant value was assumed for the extrapolation, since the systems are semiconducting. From theoretical and experimental spectra we know that the reflectivity is constant above 7000 cm^{-1}(see Fig. 5.8). Therefore, the high frequency part was first extrapolated with a con-

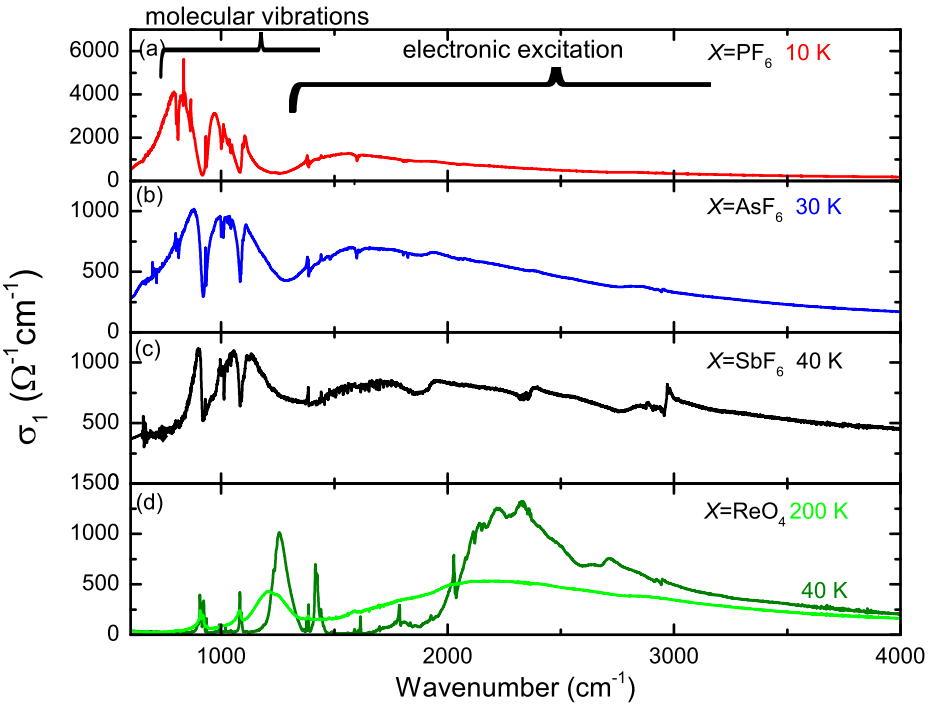

Figure 5.12: (a), (b), (c), and (d) show the frequency dependence of the optical conductivity of $(TMTTF)_2X$ (X=PF_6, AsF_6, SbF_6, and ReO_4) at the lowest measured temperatures between 600 cm^{-1} and 4000 cm^{-1}. Additionally, the spectrum of the asymmetric anion ReO_4 is displayed in the charge ordered phase at 200 K (light green line).

stant value up to 40,000 cm^{-1} and finally with a ω^{-4} decaying function up to 1,000,000 cm^{-1}.

The spectral shape of the reflectivity and the optical conductivity of all compounds are in principle the same, only the spectrum of the $(TMTTF)_2AsF_6$ deviates as it was recorded in the $a^\star c$-plane. However, it does not hinder us to compare it with the other compounds. Interestingly, with decreasing anion size and decreasing sulfur anion distance (going from PF_6 to SbF_6 and ReO_4) [59], the overall reflectivity and optical conductivity decreases continuously.

Below 2000 cm^{-1} the spectra are dominated by vibrational features originating mainly from emv-coupled a_g modes, since our normal mode analysis shows that only three infrared b_{3u} modes occur in the considered frequency range in accordance with our normal mode analysis (see Tab. A.1). In contrast, the high reflectivity and conductivity above 2000 cm^{-1} stems from electronic interband transitions between occupied and unoccupied bands.

In addition to the experimental data, the optical response (red dashed line) derived from the DFT calculations is also displayed. It reveals two resonances located at about 900 cm^{-1} and 2400 cm^{-1} which resemble the mid-infrared broadband feature. Therefore, we attribute them to the interband transition between the occupied and unoccupied bands at the vicinity of the Fermi surface. The Drude component is not shown here, but appears below 500 cm^{-1} and dominates the optical properties, causing a rise of the reflectivity up to 1 for $\nu \to 0$. One should note that the response of the free electrons reflected in a Drude component is not present in the real material since it is insulating below 250 K. The present Drude component is responsible for the low conductivity of the interband transition in the simulation since all the spectral weight is "shifted" in the unbound charge carriers. Qazilbash et al. [190] have proposed the idea when the

Table 5.5: emv-coupling constants of the TMTTF molecule which were theoretically determined by Pedron et al. [191].

	ν_3	ν_4	ν_7	ν_8	ν_9	ν_{10}	ν_{11}	ν_{12}
ω_i (cm^{-1})	1636	1545	1114	949	558	500	316	213
g_i (cm^{-1})	242	968	242	242	161	484	81	81

ratio of the experimentally determined kinetic energy which is equal to the area under the Drude component and the kinetic energy derived from band theory tends towards zero, the material becomes electron correlated. This is the case here while the theory yields a Drude component, the experiment shows no response of the free charge carriers leading to a ratio of zero meaning the systems are strongly correlated. Besides that, the calculation describes the optical properties reasonably well. Also the mid-infrared bands are slightly shifted to low frequencies which is due to the absent of the optical gap.

In the following, we focus on the vibrational features and on the low-temperature behavior of the optical response of the stacking direction which is plotted in Fig. 5.12. In the case of ReO_4, the optical conductivity in the charge ordered phase at 200 K as well as in the tetramized anion ordered state at 40 K are presented. For all compounds, several dips and antiresonances can be recognized on top of the mid-infrared band. The very weak features located at 2950 cm^{-1} are assigned to the antisymmetric ν_{66} (b_{3u}) mode of the TMTTF molecule as well as to the symmetric CH_3 ν_1 and ν_2 (a_g) mode. More surprising and fascinating is the very broad dip located between 2700 and 2900 cm^{-1} which cannot be assigned directly to the fundamental molecular mode and is in general not discussed in literature. This was in the past wrongly attributed [43] to an artifact or resonance caused by the KBr window, but we will demonstrate later that these features (and many more) originate from an inharmonic PES of the TMTTF molecules in the unit cell. Therefore, we assign it to the first overtone of the ν_4 (a_g) mode which has the highest coupling constant to the electronic background (see Tab. 5.5). For ReO_4, it shifts towards 2500 cm^{-1} in the anion ordering phase. This has multiple reasons: i.) The PES is further deformed in the tetramized state, ii.) the charge order pattern changes from o-O-o-O to o-O-O-o and iii.) the position of the resonance depends on the location of the electron band as well as on the transfer integral which is modified in the AO phase of $(TMTTF)_2ReO_4$.

Importantly, the feature at 2300 cm^{-1} which sometimes appears as dip, hump or is completely absence, is caused by carbon dioxide which is always present in the atmosphere. As its concentration depends on different environmental factors, it reveals a time dependence which always causes the variation of intensity in non-vacuum experiments. In order to minimize the effect, the optical path is continuously purged by dry nitrogen.

Focusing now on the spectral range rich of vibrational features, displayed in Fig. 5.13, we find clusters of symmetric dips and peaks which can be reliable assigned by our calculations. We start again with the higher frequencies. Between 1800 cm^{-1} and 1900 cm^{-1} we find a pronounced dip structure which stems from the combination of the emv-coupled ν_4 and ν_{10} (a_g) modes. Here, one can recognize that the intensity exhibits a dependence on the anion and the charge disproportionation. In the nearest neighborhood two antiresonances are identi-

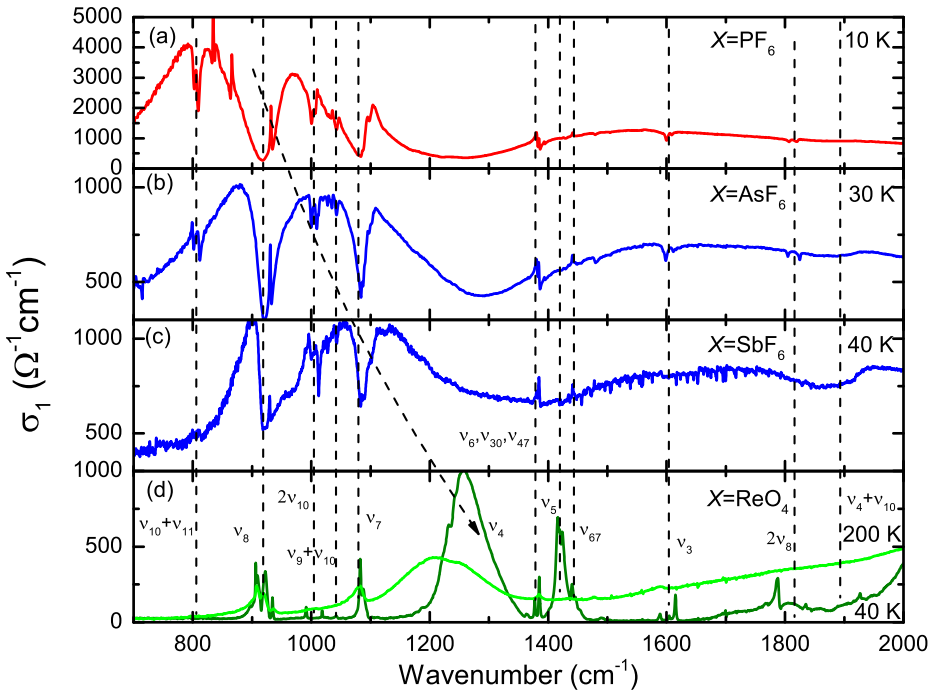

Figure 5.13: (a), (b), (c), and (d) show the optical conductivity of $(TMTTF)_2X$ (X=PF_6, AsF_6, SbF_6, and ReO_4) focusing on the spectral range asserted by the vibrational features. The vertical dashed lines mark the position of the identified molecular vibrations.

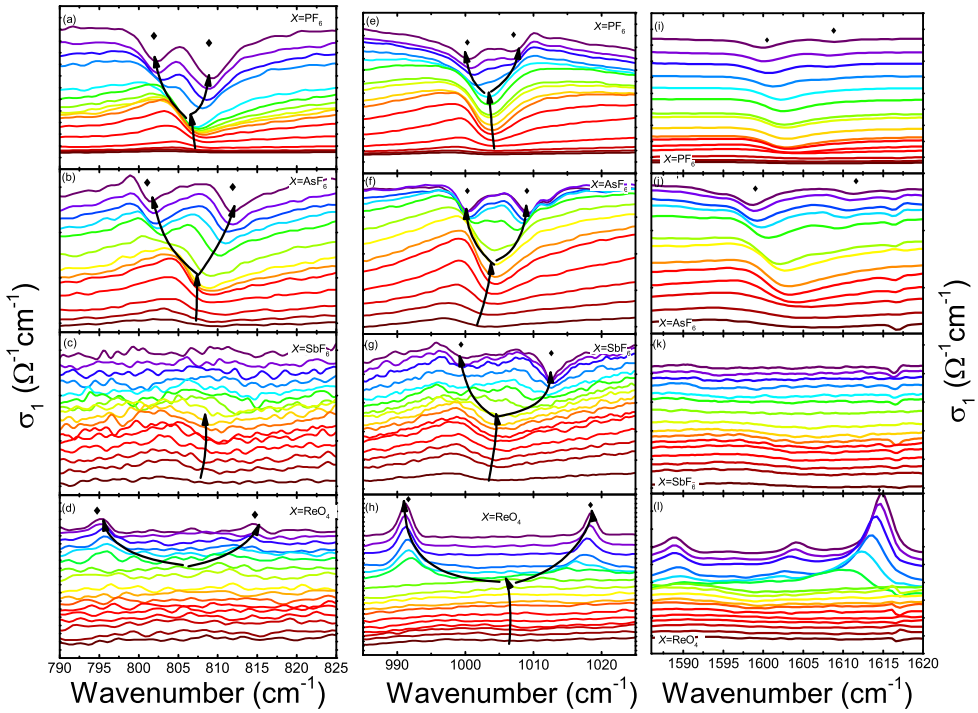

Figure 5.14: (a)-(d) Temperature-dependent optical conductivity of the ν_{10} and ν_{11} modes for the anions PF_6, AsF_6, SbF_6, and ReO_4. (e) - (h) Spectral evolution of the $2\nu_{10}$ overtone on cooling for the four examined compounds. (i) - (l) Optical conductivity of the fundamental charge sensitive ν_3 mode displayed for different temperatures. The black arrows are guides to the eyes to follow the temperature evolution of the resonance frequency. All modes reveal a splitting due to charge or anion ordering, respectively. The diamond symbol marks the final position of the resonance frequency (if present).

fied which we attribute to the second harmonic of the ν_8 (a_g) mode. The splitting is caused by the charge imbalance of the two TMTTF molecular sites in the unit cell. At 1600 cm^{-1}we find, besides the high energy vibrations of the CH_3 end group, the first molecular vibration of the C=C double bond of the TMTTF skeleton, which is highly sensitive to a modification of the molecular charge. The so-labeled symmetric ν_3 (a_g), which is depicted for all compounds in Fig. 5.14 (i), (j), (k), and (l), was used to trace the molecular charge, since it reveals a large difference between the resonance frequency of the neutral and cationic molecules of about 66 cm^{-1}(as shown in Tab. 5.3). One advantage of this mode is its weak coupling to the electronic background. As a result the resonance frequency is less disturbed.

In the case of the asymmetric ReO_4, we could not see in the CO state a clear separation of the mode into two features due to the thermal broadening of the resonances at high temperatures and disturbing water lines. However, at the lowest measured temperature of 40 K, which is far below the anion ordering temperature of T_{AO}=157 K, we observe three very narrow modes with the weakest resonance located at 1604 cm^{-1}, visualized in Fig. 5.14 (l). The next strongest one is located at 1588 cm^{-1}, whereas the strongest resides at 1615 cm^{-1}. At the moment we can only speculate about the origin of the weakest mode. First of all, an absorption line of water molecules can be excluded since it exhibits a temperature-dependence. Instead, a possible explanation is that the doubling of the unit cell and tetramerization of the cations leads to a further splitting of the modes.

From the position of the other modes we determined the charge imbalance $\delta\rho$ by assuming a linear relation between the charge imbalance and the difference of the resonance frequency as follows:

$$\delta\rho = \frac{\Delta\nu}{66\,\mathrm{cm}^{-1}}. \tag{5.4}$$

We derive from the resonance of the mode a charge disproportion $\delta\rho$ of +0.41 e, which deviates 35 % from the value +0.63 e estimated from the antisymmetric ν_{28} (b_{1u}) mode (see Sec. 5.1.6).

In Fig. 5.14 (i), (j), and (k) the optical conductivity of the ν_3 mode is displayed between 1555 cm^{-1}and 1620 cm^{-1}as a function of temperature. For PF_6 and AsF_6, a clear splitting of the ν_3 (a_g) mode is visible. From this, we determine a charge disproportionation $\delta\rho$ of +0.12 e and 0.19 e, respectively, which is lower than our published result of the ν_{28} (b_{1u}) mode. This is a further evidence that the symmetric a_g modes underestimate the charge imbalance. In the case of the SbF_6 anion, the splitting could not be resolved due to the high noise in the spectra and the disturbing water absorption lines.

The next mode which appears very weakly and only at low temperatures is the molecular out-of-plane ν_{67} b_{3u} vibration. Only in the case of ReO_4, next to this mode a very broad and pronounced feature appears in the AO. One could ascribe it to the ν_5 (a_g) mode, which is very weakly coupled to the electronic background, since mainly the CH_3 groups are involved. This would explain its absence in the other compounds. However, it is more plausible that this mode originates together with the strongest mode at 1250 cm^{-1}from the ν_4 (a_g) mode due the AO state.

Very impressively, in the direct comparison of the compounds, it becomes obvious how the position of the strongly emv-coupled ν_4 depends on the position

of the electronic mid-infrared band [182, 183]. The double occurrence appears due to the tetramization and the rearrangement of the charge pattern in the AO phase. As a consequence two different resonances of the same origin become infrared-active.

The weak modes at lower energies appear typically along the c- and b-direction and contain the end groups of the TMTTF molecules which form the molecular cavity for the anions. Thus, they are sensitive to a deformation or shift of the anion towards one of the molecules. As further explained later in this chapter, the modification of these modes appears always already above the CO. This indicates that the two TMTTF molecules in the units are slightly unequal, although x-ray measurements claim that they are related with each other via an inversion center. However, x-rays cannot resolve the spatial position of the light hydrogen atoms accurately.

As mentioned previously, the strong antisymmetric feature extending from 800 cm^{-1} to 1300 cm^{-1} is caused by the ν_4 mode, whose Fano shape is ruptured by antiresonances of several emv-coupled a_g modes, such as the ν_7 at 1080 cm^{-1}, the sum frequency of the $\nu_9 + \nu_{10}$ mode at 1040 cm^{-1}, and the overtone of the ν_{10} at 1000 cm^{-1}. The latter is, similar to its related fundamental mode, very sensitive to the molecular charge and also visible in Raman spectra [2, 177]. Therefore, we have plotted its temperature dependence together with the combined mode of $\nu_{10} + \nu_{11}$ in Fig. 5.14. Above the T_{CO} and T_{AO}, no strong modification appears. However, below the phase transition they exhibit a splitting. We calculated from the $2\nu_{10}$ mode a charge imbalance $\delta\rho$ of +0.14 e for PF_6, +0.19 e for AsF_6, +0.26 e for SbF_6, and +0.47 e for ReO_4. These results support our above determined outcome.

A further strong emv-coupled mode is the ν_8 mode, which appears in the spectra as a very strong antiresonance at 911 cm^{-1}.

The appearance of the usually forbidden a_g modes can easily be understood in the framework of emv-coupled modes, which is discussed extensively in Appx. F. However, in the last decades, in the Bechgaard salts, mainly the electronic excitations [166] were studied, whereas the vibrational features were completely neglected. Especially, an interpretation of the modes above 1500 cm^{-1} was neglected.

In the following, we want to focus on the optical properties of these modes, one immediately recognizes that these modes appear very often and most strongly in the charge-ordered state in more detail, for instance in α-(BEDT-TTF)$_2$I$_3$ (see Sec. 5.4.2) [192], Θ-(BEDT-TTF)$_2$RbZn(SCN)$_4$[193], and the new one-dimensional organic salt EDT$_2$Br and EDT$_2$AsF$_6$ discussed in Sec. 5.2. These dip-like structures occur solely in the spectra of the high conducting directions, where the mid-infrared bands appear. The features cannot be attributed to an electronic origin and were related to vibrational overtones which were activated by the anharmonicity of the molecular potential energy surface PES.

Yamamoto *et al.* [194, 195] developed a model to explain this phenomenon which they originally identified in two dimensional organic conductors. The suggested model is based on a molecular dimer, which is described by the following Hamiltonian:

$$H = H_e + H_{ext.} \tag{5.5}$$

with (5.6)

$$H_{ext.} = H_{vib.} + H_{emv} \tag{5.7}$$

The first term H_e contains the pure electronic contributions, whereas $H_{ext.}$ summarizes the independent molecular vibrations. They contain the $H_{vib.}$ term that account for the odd molecular vibrations and the emv-coupling H_{emv} term, considering the coupling of the molecular vibrations to the electronic background. In the following, we want to focus on the last one which contains not only linear coupling terms, but also higher order terms[9] which is written according to Ref. [194] as:

$$H_{emv} = \sum_{1,2} \left(g_i n_i Q_i + \frac{1}{2} g_2 n_i Q_i^2 \right) \tag{5.8}$$

n_i is the charge density on the i^{th} molecule with the Q_i normal coordinate, g_i and g_2 are the linear [196] and quadratic coupling parameter to the electronic background. The considered Hamiltonian can be further modified by introducing special symmetry coordinates[10] which lead to higher terms in H_{emv}:

$$H_{emv} = \cdots - A_{CT} Q_+ Q_-^2 + \cdots - A_{CD} Q_-^3 + \ldots \tag{5.9}$$

The two parameters, A_{CT} and A_{CD}, denote for the two most important prefactors of the cubic terms. The first term

$$A_{CT} = \left| \frac{g_i g_2 \delta n_{eg}^2}{\sqrt{2} E_{eg}} \right| \tag{5.10}$$

is a measure how much the PES deviates from the harmonic approximation due to the intrinsic charge transfer between the two participating molecules. Therefore, its strength depends on the transfer matrix element δn_{eg}. E_{eg} is the energy gap between the ground and excited state, g_i the linear emv-coupling term and g_2 the quadratic term.

The second term

$$A_{CD} = \left| \frac{g_i^3 \delta n_{eg}^2 \delta \rho}{\sqrt{2} E_{eg}^2} \right| \tag{5.11}$$

is a function of the charge disproportionation $\delta\rho$. Since both terms can appear at the same time, it is possible that the spectral structures of the vibrational overtones even occur in non-charge ordered systems, where they are caused by A_{CT} and the transfer matrix element δn_{eg}. To get a first estimation which term dominates and, hence, causes the vibrational feature in the spectra, we have calculated the ratio A_{CD}/A_{CT} with $g_i = 120$ meV as the value for the emv-coupling constant of the ν_4 (a_g) mode of the TMTTF [191].[11] The ratio is depicted as a function of $\delta\rho$ in Fig. 5.15 for the studied compounds. We determine from the difference of the resonance frequency of the positively charged (ω_{cat}) and the neutral (ω_{neu}) molecule:

$$g_2 = \frac{1}{2}(\omega_{cat} - \omega_{neu}) \tag{5.12}$$

9 Only the second order term is included in this consideration.

10 $Q_+ = \frac{1}{\sqrt{2}}(Q_1 + Q_2)$ and $Q_- = \frac{1}{\sqrt{2}}(Q_1 - Q_2)$.

11 g_i rises with increasing molecule size from 117 meV for TTF [197] via 120 meV for TMTTF [191] to 132 meV for BEDT-TTF [198].

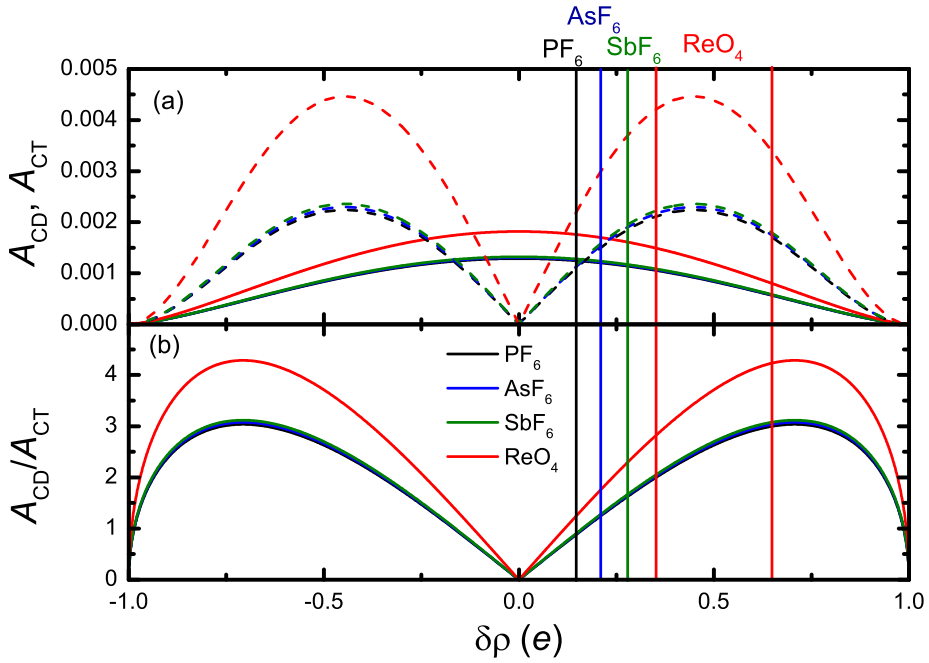

Figure 5.15: In the upper panel (a) the two different anharmonic prefactors A_{CD} (dashed lines) and A_{CT} (solid lines) are displayed as a function of charge disproportionation for $(TMTTF)_2X$ with X=PF_6 (black), AsF_6 (blue), SbF_6 (olive), and ReO_4 (red). (b) The ratio of the two parameters A_{CD}/A_{CT} in dependence of the charge disproportionation $\delta\rho$. When the values are below 1, A_{CT} dominates. The vertical lines mark the actual charge imbalance of the considered compounds represented in the corresponding color.

which is 6 meV in the case of the ν_4 mode [177]. The transfer matrix element δn_{eg} and the energy gap E_{eg} are a function of the charge imbalance $\delta\rho$ and the transfer integral t in the case of E_{eg}:

$$\delta n_{eg} = \sqrt{1-\delta\rho^2} \tag{5.13}$$

$$E_{eg} = \frac{2t}{\sqrt{1-\delta\rho^2}} \quad . \tag{5.14}$$

In Fig. 5.15 the ratio of A_{CD} (dashed line) and A_{CT} (solid line) is illustrated as a function of the charge disproportionation $\delta\rho$ for the four Fabre salts with the anions PF_6 (black), AsF_6 (blue), SbF_6 (green), and ReO_4 (red). The values for the transfer integral t were taken for the centrosymmetric anions from Ref. [29] and for ReO_4 from Ref. [148] at room temperature[12]. For the unordered phase, the charge transfer prefactor A_{CT} dominates the considered nonlinear term with increasing charge disproportionation, A_{CT} decreases monotonously. In contrast, A_{CD} is zero at $\delta\rho = 0\,e$, whereas its maximum resides at about $\pm 0.5\,e$. From that it can be deduced that as soon as a weak charge imbalance is present in the material, A_{CD} determines the cubic term. This becomes more obvious when the ratio $\frac{A_{CD}}{A_{CT}}$ is considered. The ratio is only smaller than 1 for smaller than $\pm 0.15\,e$ or larger than $\pm 0.98\,e$. The highest value is 4.5 for ReO_4, caused by t of only 0.14 eV, which is smaller than the average value of $t = 0.195$ eV for the centro-symmetric anions.

12 The values were determined by DFT calculations combined with a tight binding model or by extended Hückel calculations. Since the compounds are dimerized, we have taken the hopping integral between the molecules forming the dimer.

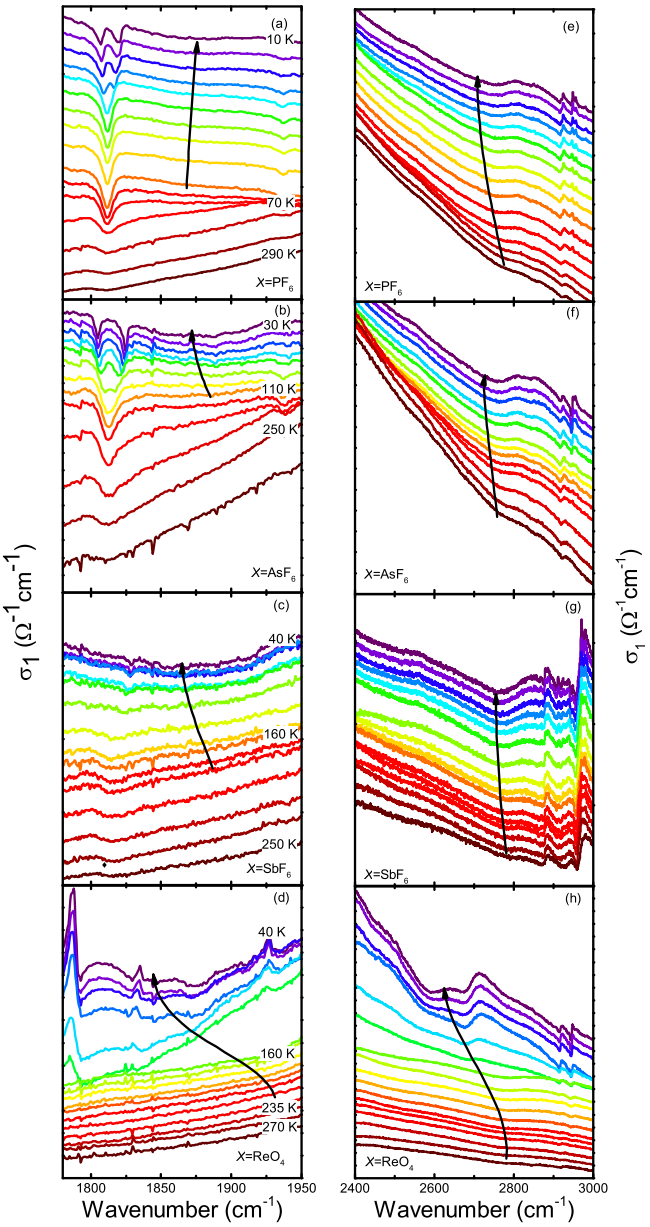

Figure 5.16: On the left side the temperature-dependent spectra of $(TMTTF)_2PF_6$ (a), $(TMTTF)_2AsF_6$ (b), $(TMTTF)_2SbF_6$ (c) and $(TMTTF)_2ReO_4$ (d) is displayed between 1775 cm^{-1} and 1950 cm^{-1}. This dip-like vibrational structure is ascribed to the combination mode of ν_4 and ν_{10}. Accordingly, in the right panels (e)-(h) the first overtone of the ν_4 mode is depicted for PF_6 (e), AsF_6, SbF_6, and ReO_4. The arrows are guides to the eyes highlighting the temperature evolution of the resonance frequency.

In Fig. 5.15, $\delta\rho$ is visualized for the compounds by the vertical colored bars. In the case of PF_6 with $\delta\rho = 0.15\,e$ the prefactors are equal, meaning that the overtones are activated above as well as below the charge ordered phase with the same strength. For X=AsF_6 and SbF_6 the charge disproportionation increases accompanied by an increase of A_{CD}. Therefore, the intensity of the overtones is enhanced. Interestingly, we expect from Fig. 5.15 that the overtones of ReO_4 are especially strongly enhanced in the charge ordered as well as the anion ordered phase which is indeed the case (see Fig. 5.16).

It should be furthermore mentioned that since the structural parameters of the compounds as the intermolecular distance are a function of temperature, chemical or hydrostatic pressure, these quantities also influence the transfer integral as well as the dimensionality of the systems [29] and therefore also A_{CD} and A_{CT}. Moreover, also the resonance frequency of the overtones depends on t, g_i and $\delta\rho$. Because of that we expect a shift of the overtones in the charge ordered state, which was indeed demonstrated by Yamamoto et al. [194].

To proof that assumption we take a closer look at the spectral range where we do not expect fundamental modes, but overtones. This range is in principle located between 1700 $cm^{-1}$and 3000 cm^{-1}. In Fig. 5.16 (a) and (b), we have selected two spectral windows ranging from 1775 $cm^{-1}$to 1950 $cm^{-1}$and from 2400 $cm^{-1}$to 3000 cm^{-1}, respectively. There, strong dip-like features can be observed. We assign the first one to the combination mode of the ν_{10} and ν_4 mode and the second one to the first overtone of the ν_4 mode. In the past, they were incorrectly attributed to some impurities or absorption bands in the spectrometer window [43] in our eyes, as vibrational bands of atmospheric CO_2 are present at about 2300 cm^{-1}.

In the case of ReO_4, the anti-resonances are clearly visible and, especially in the anion ordered state where the charge imbalance is larger, they are extremely pronounced. This is also related to the opening of the energy gap and the related shift of the mid-infrared band to higher energies. From a theoretical perspective, it is not clear which influence the tetramerization has on the activation of the overtone and how the features evolve.

However, we find that the considered features exhibit a temperature-dependence in the experiments and mainly become activated or enhanced when a charge imbalance is present. Therefore, we ascribe them to an anharmonicity of the PES due to unequal distributed molecular charge. Furthermore, the features are almost not visible above T_{CO} and become enhanced below T_{CO}. The intensity increases from PF_6 to SbF_6, since $\delta\rho$ increases by the factor that A_{CD} becomes larger than A_{CT}. It is also obvious that resonance frequencies shift with temperatures because of the temperature-dependence of the charge transfer integral t. With decreasing t the resonance shifts to lower energies whereas it can be assumed that g_i is not changing and for increasing $\delta\rho$ it should move to higher energies so that it finally competes with t.

ELECTRONIC CONTRIBUTIONS Besides the vibrational features, the following paragraph is dedicated to the electronic excitations[13]. Due to the anisotropy of the molecular orbitals and, hence, their overlap, the highest conductivity occurs along the (stacking) a-direction of the TMTTF molecules. In Fig. 5.17 the fitted function to the reflectivity and optical conductivity is exemplarily illustrated for $(TMTTF)_2AsF_6$ at room temperature between 800 $cm^{-1}$and 7000 cm^{-1}. For the fit we used a Lorentz-Fano fitting function (see Sec. F for a detailed description).

In our consideration, we have employed two Lorentz functions to fit the broad electronic band. Whereas the first one is very strong and broad, describing the true electronic contributions of the a-direction, the second one is weaker and accounts for the contribution of the electronic bands along the b- and c-directions due to imperfect alignment and polarizers. They occur at higher energies at

13 In the following we will call it Mott-Hubbard band since the systems can be considered as a single band system.

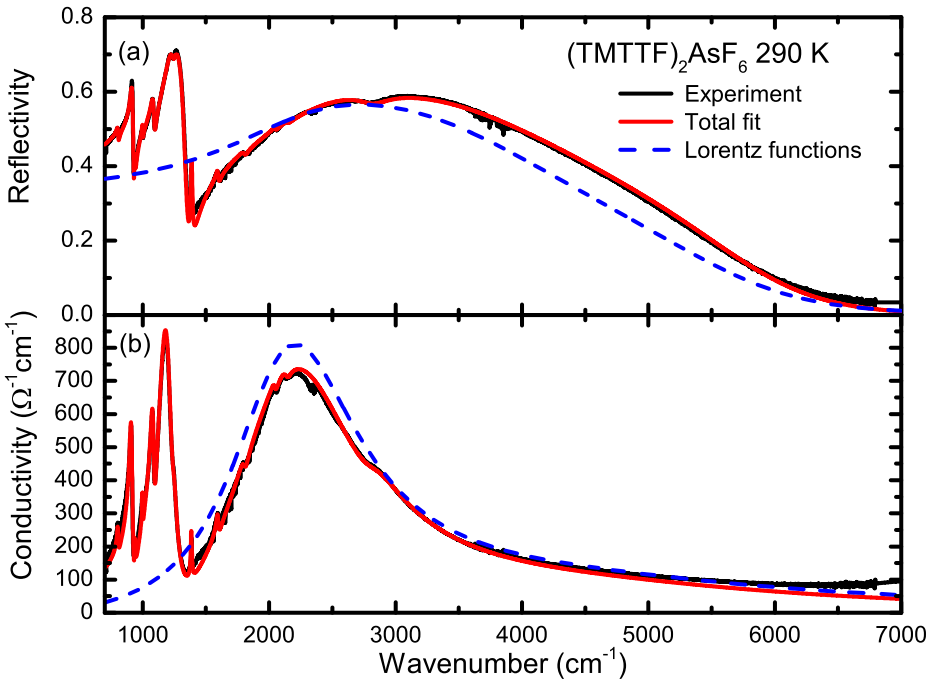

Figure 5.17: The reflectivity (a) and optical conductivity (b) of (TMTTF)$_2$AsF$_6$ (black solid line) at room temperature is compared with the fit (red solid line) between 800 cm^{-1} and 7000 cm^{-1}. The dashed blue lines display the pure, undisturbed electronic contribution.

about 4500 cm^{-1} (see Sec. 5.1.3). This is nicely demonstrated in Fig. 5.11 for (TMTTF)$_2$AsF$_6$ which is recorded for infrared light polarized within the ac-plane. Therefore, along the a^*-direction the electronic band of the b-direction contributes stronger to the spectrum than for the a-direction. According to the theory of a Mott insulator, the peak position depends on the on-site Coulomb repulsion U. As, U is larger than $4t$, the peak should be located above 1 eV [170, 172]. Therefore, we consider the mid-infrared peak as the excitation (transfer) of a charge carrier from one molecular lattice site to its neighboring site.

In the following we only consider the strong mid-infrared band and its specific parameters. We used up to 20 Fano functions to fit the emv-coupled vibrational features. As can be seen in Fig. 5.17 (b) the original Lorentz shape of the Hubbard band is strongly modified by the emv-coupled vibrational modes. We can deduce from Fig. 5.17 that the fitted reflectivity and optical conductivity excellently reproduce the experimental data.

From the Lorentz function we have extracted several parameters such as the position of the resonance frequency ω_{CT} and plasma frequency ω_p, which are depicted for the Fabre salts with centro-symmetric anions in Fig. 5.18. At 250 K, the resonance frequency ω_{CT} is 2400 cm^{-1} for SbF$_6$, 2100 cm^{-1} for PF$_6$ and AsF$_6$. On cooling, ω_{CT} shifts linearly to lower energies for all compounds. In general, AsF$_6$ and PF$_6$ exhibit almost the same values. The total shift is about 600 cm^{-1} for SbF$_6$ and 500 cm^{-1} for PF$_6$ and AsF$_6$ with the lowest temperature of 40 K.[14]

Interestingly, no jump of the peak resonance occurs above and below T_{CO}, although one expects that at least ω_{CT} resides at a constant value or increases again due to the opening of the charge order energy gap.

14 Keeping in mind that the total change in EDT$_2$AsF$_6$ and EDT$_2$Br is about 800 cm^{-1}.

The plasma frequency ω_p reveals a similar behavior as it increases continuously between 250 K and 40 K from about 8000 cm^{-1} for AsF_6 and 8600 cm^{-1} for PF_6 to 9500 cm^{-1} for AsF_6 and 11500 cm^{-1} for PF_6. The values of SbF_6 are located between these values. The room temperature value of PF_6 is in full agreement with a previous optical study [199]. The plasma frequency contains the charge carrier number and is related to the oscillator strength of the band. This means that upon cooling, the number of localized charge carriers increases. The unexpected jump of the plasma frequency in the case of PF_6 at 75 K can be in principle related to the charge ordering phase transition with T_{CO} = 67 K, causing an enhanced charge localization. The "abruptness" is within the rather large error bars of PF_6 and should thus not be over interpreted.

Rice et al. [196] developed a model to describe an unpaired electron in a molecular dimer including emv-coupling. This model was successfully applied to $(TMTSF)_2ReO_4$ [176, 200]. According to that model, the resonance frequency of the mid-infrared band ω_{CT} can be used to estimate the charge transfer t since $\omega_{CT} \geqslant 2t$. Based on that model the transfer integral decreases with temperature from about 130 meV for PF_6/AsF_6 and 148 meV for SbF_6 to 110 meV and 99 meV, respectively. These values are too small in comparison with the theoretically determined averaged results [29]. Furthermore, the hopping depends on the molecular arrangement and distance, we would expect in contrast a continuous increase of the transfer integral. Therefore, this model is not sufficient to estimate the transfer integral.

The transfer integral can be alternatively estimated by another approach which is based on a one-dimensional conductor and a tight binding approximation [19, 176]. From that, the transfer integral is related to the plasma frequency ω_p as:

$$\omega_p^2 = \frac{4td_{\mathrm{Dim}}^2 e^2}{\pi\epsilon_0\hbar^2 V_m} \sin\left(\frac{\pi\rho}{2}\right) \tag{5.15}$$

with the interdimer distance[15] d_{Dim} and the unit cell volume V_m [29]. In Fig. 5.18 (d) the temperature-dependence of the transfer integral t is displayed. The transfer integral increases from 0.15 eV (AsF_6) and 0.18 eV (PF_6) at room temperature to 0.22 eV (AsF_6) and 0.32 eV (SbF_6) at 40 K. As the transfer integral is proportional to ${\omega_p}^2$, it also increases with decreasing temperature. Furthermore, it should decrease with anion size. The latter is not true for SbF_6, which can be explained by an imperfect alignment. t increases on cooling since the molecular distance decreases in the same rate leading to a larger overlap of the molecular orbital. This means that these compounds become more metallic. However, t depends exponentially on the intermolecular distance so that t should rise steeper with diminishing temperature. This deviation can be explained by the fact that the modification of the molecular distance is very small in the examined temperature range, leading to an almost linear behavior in the considered narrow energy range. Furthermore on the first consideration, this observation contradicts the theoretical prediction that the ratio $\frac{V}{t}$ and $\frac{U}{t}$ (see Sec. 5.1.2) should rise so that the charge ordered state can be established. While U is constant, V is reciprocal proportional to d_{Dim} [28, 30]. Therefore, we suggest that V varies stronger with d_{Dim} than t it does.

15 We have taken half of the unit cell along the a-direction for the calculation. The values were taken from Ref. [29].

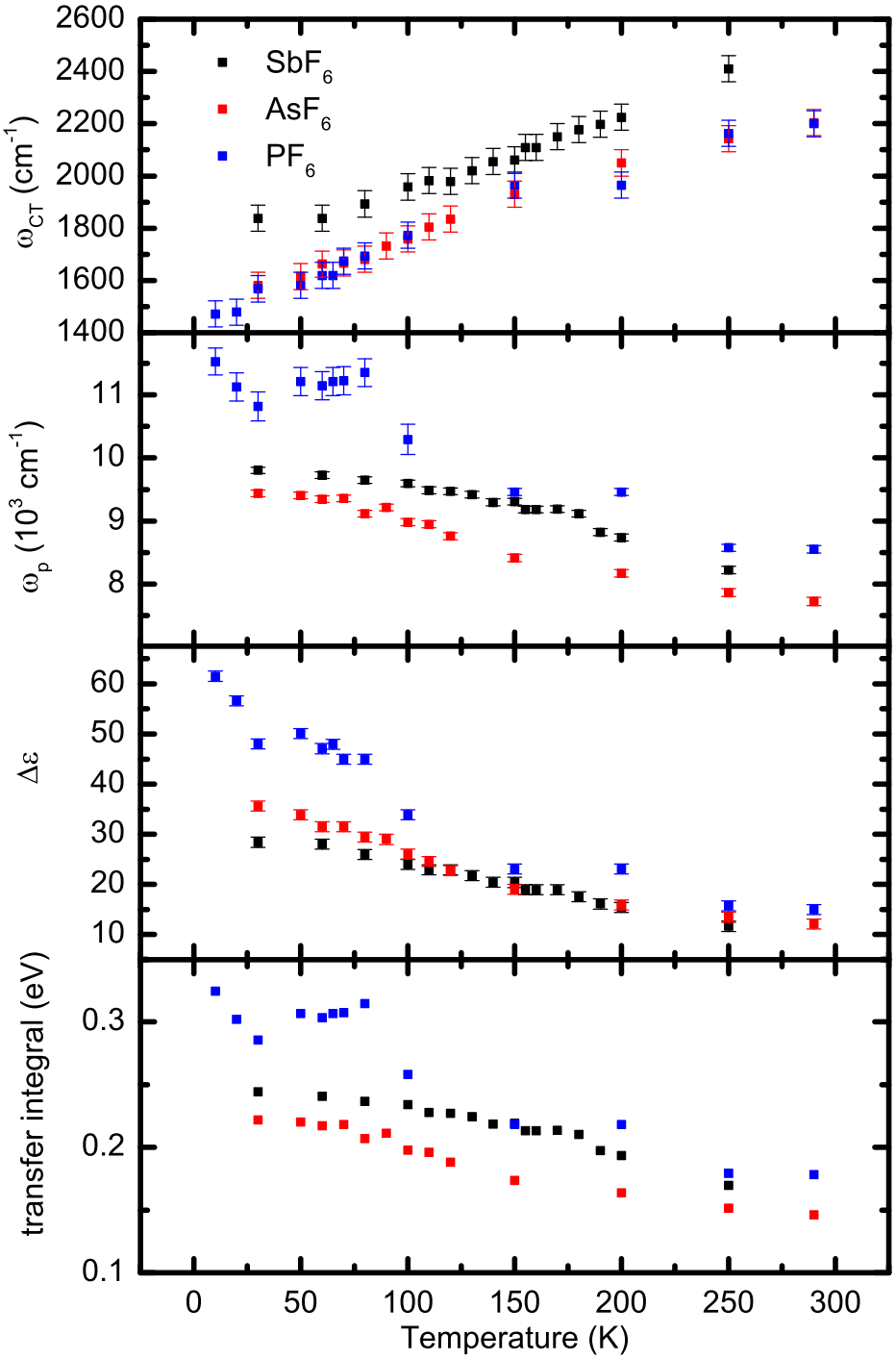

Figure 5.18: Temperature dependence of the resonance frequency (a) of the mid-infrared band (electronic excitation), plasma frequency (b), strength (c), and transfer integral (d) of the TMTTF salts with centro-symmetric anion PF_6, AsF_6, and SbF_6.

In the following we discuss the electronic contributions in $(TMTTF)_2ReO_4$. In Fig. 5.19 (a) the position of the resonance frequency of the mid-infrared band is illustrated as a function of temperature. As a reminder, at 230 K $(TMTTF)_2ReO_4$ crosses over into a charge ordered state and below 157 K, anion ordering occurs. Similar to the Fabre salts with centro-symmetric anions the resonance frequency decreases above all orderings continuously with temperature to lower frequencies. Also the initial value of ω_{CT} is comparable to the above discussed positions. At T_{CO} no clear change can be observed, while below T_{AO} ω_{CT} rises again until

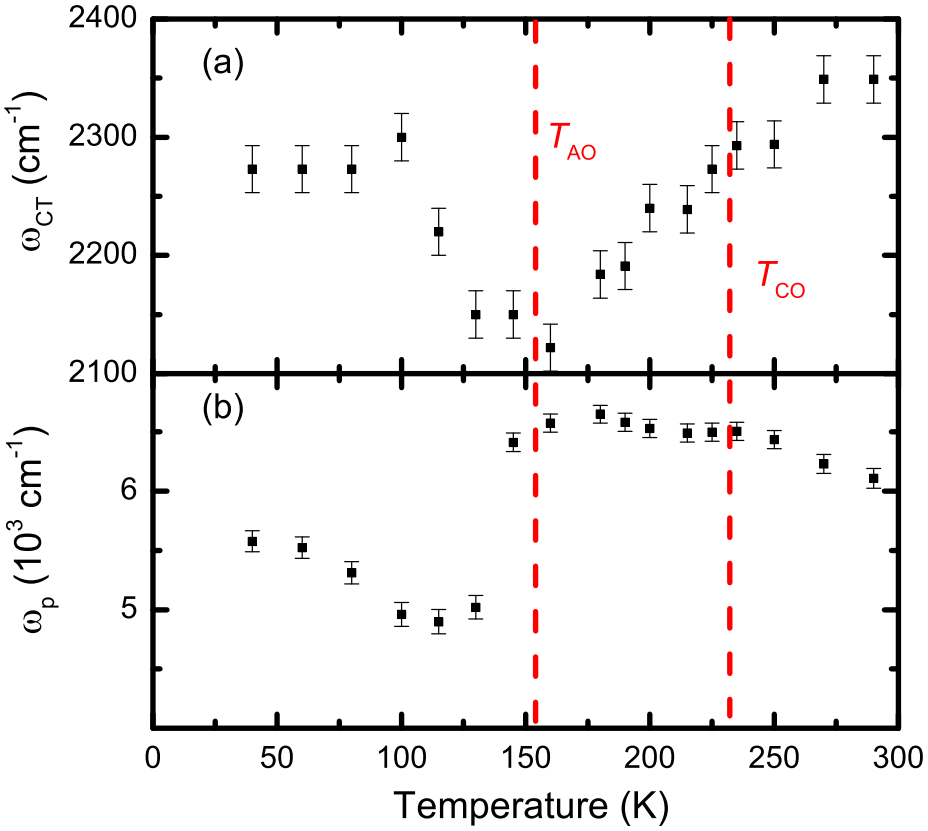

Figure 5.19: Resonance frequency (a) and plasma frequency (b) of $(TMTTF)_2ReO_4$ as a function of temperature. The red vertical lines mark T_{CO} and T_{AO}.

it saturates below 100 K. The sudden jump of ω_{CT} below T_{AO} is related to the opening of the anion ordering energy gap which is about 220 meV large, being estimated from the mid-infrared band in Fig. 5.12 (d).

In contrast to the plasma frequency of PF_6, AsF_6, and SbF_6, in the case of ReO_4 the slope of ω_p changes at high temperatures only slightly from 6000 cm^{-1} to 6500 cm^{-1} and the absolute values are below these of the symmetric anions. At T_{CO} ω_p flattens and stays almost constant. At the anion ordering transition, the plasma frequency drops abruptly from about 6500 cm^{-1} to 4900 cm^{-1} and increases slightly to 5500 cm^{-1} at 40 K. An increase of ω_p indicates an increase of the localized charge carriers. However, the drop of ω_p at T_{AO} can be attributed to the tetramerization. From these results one can determine together with Eq. 5.15 the transfer integral t, which is above T_{CO} between 0.09 eV and 0.1 eV[16], in well agreement with the theoretically determined value of 0.14 eV [148]. As expected, it is below the values of PF_6, AsF_6, and SbF_6. Moreover, this outcome fits to the DC conductivity measurements, as the conductivity of ReO_4 is lower than that of the other compounds [59]. Below T_{AO} it is not possible to make any reliable prediction about the transfer integral, since the unit cell is doubled and the molecules are tetramized.

16 The values for V_m and d_{Dim} are extracted from Ref. [201].

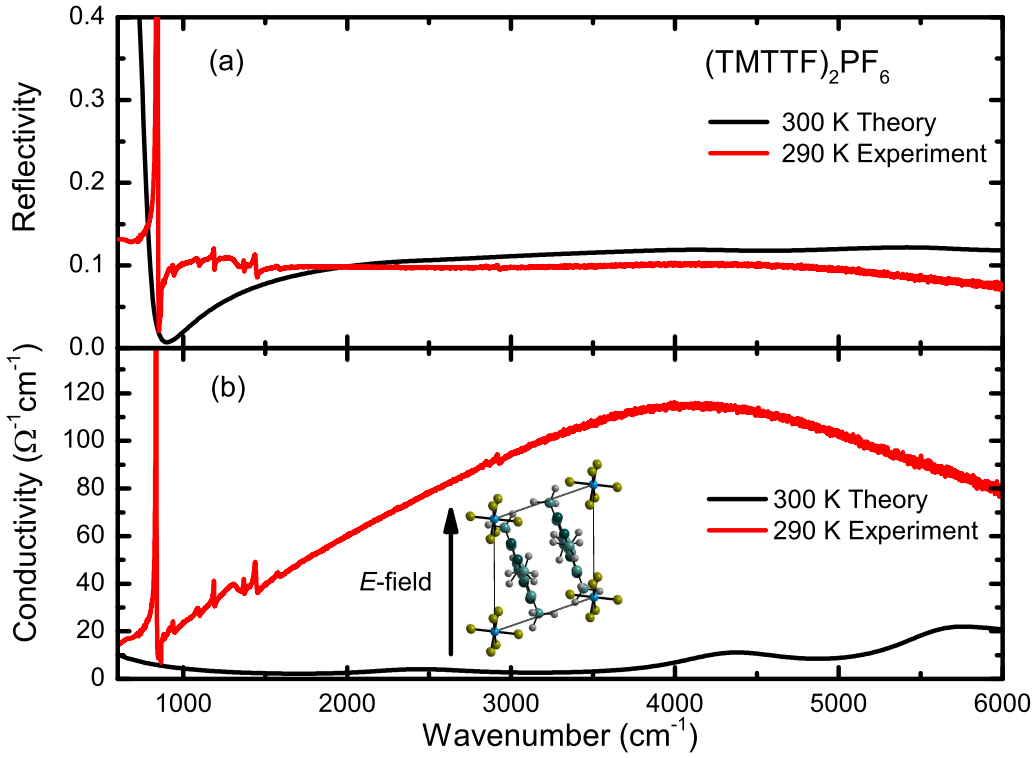

Figure 5.20: (a) Experimental and theoretical reflectance (red and black) of (TMTTF)$_2$PF$_6$ at room temperature along the b-direction between 800 cm^{-1}and 6000 cm^{-1}. (b) Kramers-Kronig consistent experimental optical conductivity of (TMTTF)$_2$PF$_6$ derived from the reflectivity in (a). The optical conductivity determined by quantum chemical calculations is illustrated in black. The inset shows the polarization of the infrared light with respect to the unit cell orientation.

5.1.5 *Optical properties of the b-direction*

While the optical spectra of the a-direction have the highest optical conductivity, due to the anisotropy of the Fabre salts we expect a flat and low optical response for $E \parallel b$. Therefore, the vibrational features should not be screened by electronic excitations and deliver undisturbed information about molecular motions. By that possible intermolecular interactions and changes of the structure can be detected.

In Fig. 5.20 the experimental reflectivity and optical conductivity of(TMTTF)$_2$PF$_6$ is compared to our theoretically calculated spectra between 800 cm^{-1}and 6000 cm^{-1} at room temperature. The reflectivity (red) is constant at 10 % and only disrupted by intermolecular vibrations. The strongest vibrational feature is ascribed to the ν_3 (t_{1u}) mode, whose degeneracy is lifted due to the point symmetry P-1 of the molecular site. The theoretical determined spectrum yields exactly the same trend and agrees quantitatively with the experimental results. The increase of the theoretical reflectivity below 800 cm^{-1}can be attributed to a weak Drude component due the neglect of the correlation effects.

From this, we derived the optical conductivity by a Kramers-Kronig transformation. For that, we have extrapolated the low-frequency part to zero, since the b-direction is insulating. For the high-frequency region a ω^{-4} function was used from 6000 cm^{-1}to 10^6 cm^{-1}. The result is displayed in Fig. 5.20 (b). The experimental conductivity reveals a maximum at about 4000 cm^{-1}, which is small in

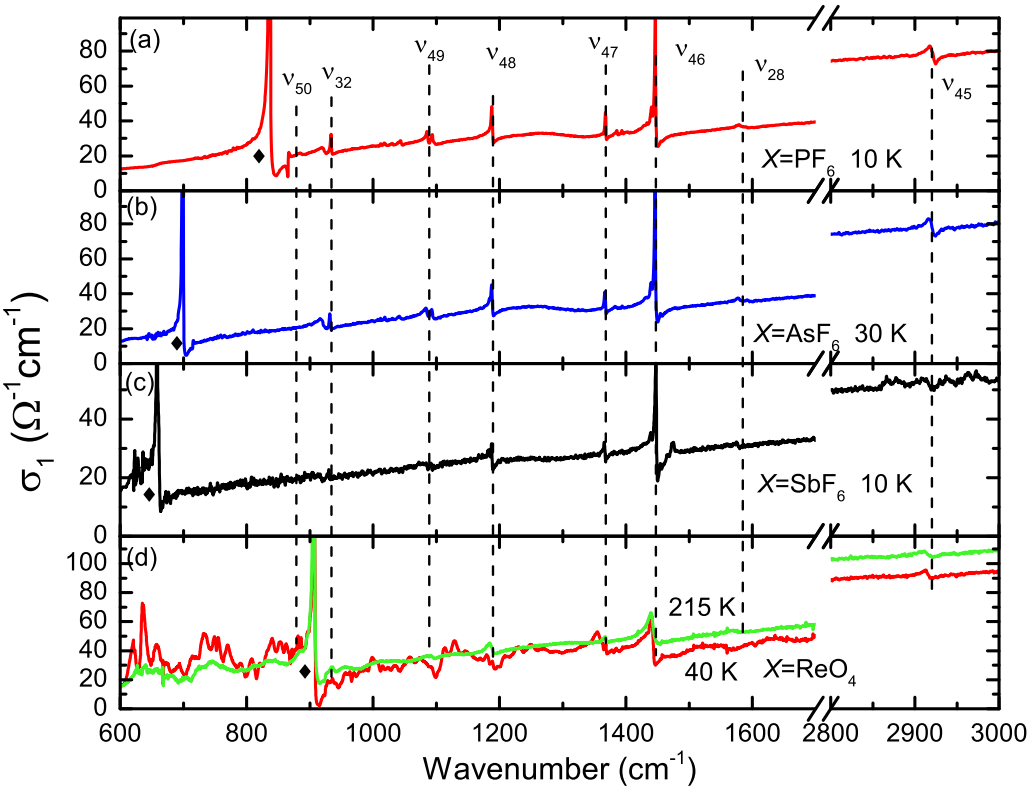

Figure 5.21: Optical conductivity of $(TMTTF)_2X$, (X=PF_6 (a), AsF_6 (b), SbF_6 (c), and ReO_4 (d)) along the b-direction at the lowest measured temperature between 600 cm^{-1} and 1700 cm^{-1} as well as from 2800 cm^{-1} to 3000 cm^{-1}. The dashed vertical lines mark the assigned vibrational modes, whereas the diamonds highlight the anion modes.

comparison to the electronic excitations along the a-direction. The theoretical curve is lower and exhibits several maximums which are attributed to interband excitations from the fully occupied band (below the Fermi energy) to a partially occupied band intersected by the Fermi edge. The transitions were broadened by a Gaussian function with a width of about 800 cm^{-1} (100 meV) to mimic this excitations to the broad feature in the experimental spectrum. Therefore, the vibrational features reveal a slight asymmetry. Since the theoretical spectra reveal a Drude part which is absent in the experimental ones due to the energy gap along the b-direction, the spectral weight of the Drude component is transferred to the interband transitions, yielding a higher optical conductivity.

In Fig. 5.21 a closer look is taken at the vibration modes of all examined compounds at the lowest measured temperatures. Here, the strongest features belong to the ν_3 (t_{1u}) mode of the centro-symmetric anions and the ν_3 (t_2) mode of ReO_4, which we will discuss later in this and the subsequent paragraph. The mode located at 865 cm^{-1} is the strongest in PF_6 and can be assigned to the ν_{50} (b_{2u}) mode, involving the C-S bond and the methyl groups. However, its total infrared intensity is very low for the $TMTTF^{+0.5-\frac{\delta\rho}{2}}$. This explains why the overall appearance is weak and possibly only visible for the positive charged $TMTTF^{+0.5+\frac{\delta\rho}{2}}$ molecular site. The following features at higher frequencies are assigned to the emv-coupled ν_8 (a_g) mode located at 920 cm^{-1} and the odd ν_{32} (b_{1u}) mode; indeed, they can be found in the spectra along the out-of-plane c-direction as well (see Fig. 5.25). It behaves similarly like the ν_7 (a_g), and

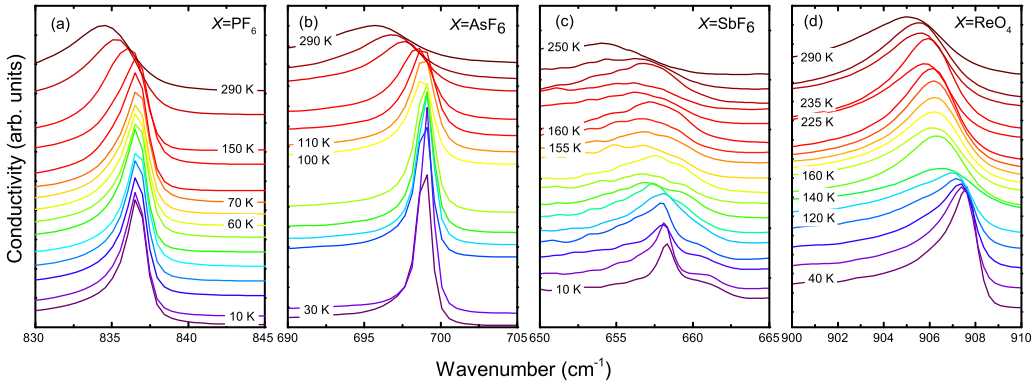

Figure 5.22: Illustration of the temperature-dependent evolution of the anion modes of X=PF$_6$ (a), AsF$_6$ (b), SbF$_6$ (c), and ReO$_4$ (d) for infrared light polarized along the b-direction.

ν_{49} (b_{2u}) modes located at 914 cm^{-1}and 934 cm^{-1}, which include mainly the vibrations of the methyl end groups, interacting with the neighboring anions and their fluorine nucleus. The strongest modes at 1120 cm^{-1}, 1368 cm^{-1}, and 1445 cm^{-1}are the ν_{48} (b_{2u}), the ν_{47} (b_{2u}) and the ν_{46} (b_{2u}) modes, including also solely the methyl groups. At about 1580 cm^{-1}a weak trace of the ν_{28} (b_{1u}) mode is found which is most strongest along the out-of-plane c-axis. A very weak signal of the asymmetric stretching of the CH_3 groups can be found at 2920 cm^{-1}, which we attribute to the ν_{45} (b_{2u}) mode.

In a next step, we are going to focus on the anion modes as we hope to find hints of a temperature-dependent distortion of the anion configuration, which should be expressed as a modification of the resonance frequency, that precedes the charge ordering. The corresponding frequency ranges of the ν_3 (t_{1u}) and ν_3 (t_2) modes is displayed in Fig. 5.22. In (a) only one mode is visible for PF$_6$, which indicates that the polarization of the infrared light is exactly parallel to one of the dipole moments of the vibrational mode. At room temperature the feature is broadened and sharpens upon cooling. Furthermore, it shifts from 835 cm^{-1}to 837 cm^{-1}at 150 K where it resides down to 10 K. The anion mode of AsF$_6$ reveals exactly the same behavior; it hardens from 696cm^{-1}to 699 cm^{-1}. In comparison, in SbF$_6$ the mode at 658 cm^{-1}does not exhibit any observable sharpening down to 40 K. At lower temperatures, a shoulder evolves at the high-energy side, which can be attributed to one of the vibrational modes whose degeneracy is lifted, being invisible due to large mode width at elevated temperatures. In the case of ReO$_4$ an obvious modification sets in below the first-order anion ordering transition. The shape of the mode (907 cm^{-1}) becomes asymmetric and the resonance frequency shifts towards higher energies. However, the Fano-like shape of the mode is not caused by emv-coupling. Thus, we do not find indications in any of the investigated compounds for a geometry change at T_{CO}. This is further confirmed by high-energy x-ray experiments [60].

In summary, we do not find any hint for any alternation of the anion configuration, caged in the molecular cavity of the TMTTF methyl groups, below CO. Changes above CO can be correlated to the thermal contraction of the unit cell, which is completed in all considered cases above 100 K. The thermal effect hinders the anions to rotate within the cavity. This causes on the one hand a decrease of the mode width and on the other hand the anions are locked in a certain position, creating weak F-H bonds. In the case of ReO$_4$, the occurrence of

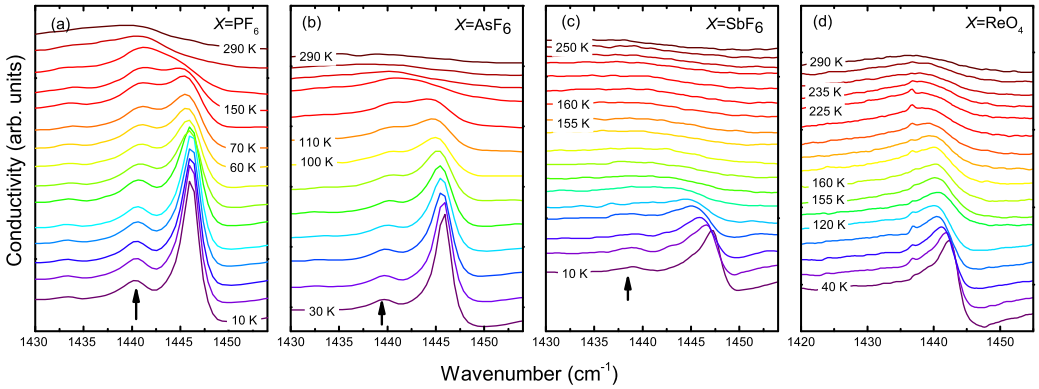

Figure 5.23: The temperature-dependent spectral evolution of the ν_{46} mode of $(TMTTF)_2X$: X=PF_6 (a), AsF_6 (b), SbF_6 (c), and ReO_4 (d) for $E \parallel b$. The satellite feature is marked by a black arrow. The spectra are shifted by a constant value for a better overview.

the two modes below T_{AO}=157 K is caused by the ordering of the anions capturing two possible configurations. Furthermore, this leads to a mode sharpening and shift of the vibrational frequency.

Any interaction of the anions with their environment takes place via the fluorine and methyl group. Therefore, we have plotted the strongest features, the ν_{46} (b_{2u}) mode located at about 1440 cm^{-1}, more in detail in Fig. 5.23. This vibration is dominated by the CH_3 group, performing an asymmetrically scissoring of the H-C-H bonds. In all compounds the signal is smeared out at 300 K. On cooling, a second very sharp feature appears at about 1460 cm^{-1} for PF_6, AsF_6, and SbF_6, accompanied by a weak satellite peak at about 1440 cm^{-1}. While for PF_6 and AsF_6 these peaks are already visible far above the CO transition, for SbF_6 the feature is only observable below 40 K. We assume that these features are in all cases already present at room temperature, which suggests, that far above the charge order transition two inequivalent molecular cationic TMTTF sites are present. Such an effect cannot be detected by standard structural resolving methods, as x-ray scattering experiments, since they are not sensitive to hydrogen atoms and destroy the charge ordered state (see Ref. [60] and references therein). Amazingly, we are sensitive to them by the FTIR-method. We conclude that the outer part of the TMTTF molecules is distorted by the anions, removing the inversion center (with respect to the symmetry of the end groups). An analog behavior was recently observed in the quasi one-dimensional organic salts o-$(DMTTF)_2X$ (X=Cl, Br, and I) by Jankowski et al. [202]. These materials exhibit a semiconducting-metal transition at 50 K as well. In the past, the transition could not be related to a charge ordering, although one of the charge sensitive mode reveals a clear shoulder below the transition in the Raman spectra. Only recently, it was proven by a comprehensive study of various methods that in the insulating state, the CO state coexists with a dimerized Spin-Peierls state. As our investigations now show a similar behavior, the question raises whether this modification of the vibrational modes of methyl-groups is a universal behavior and as a precursor or trigger of the charge ordering. In order to solve this fundamental question, we propose optical studies on systems where charge ordering is absent such as $(TMTTF)_2ClO_4$.

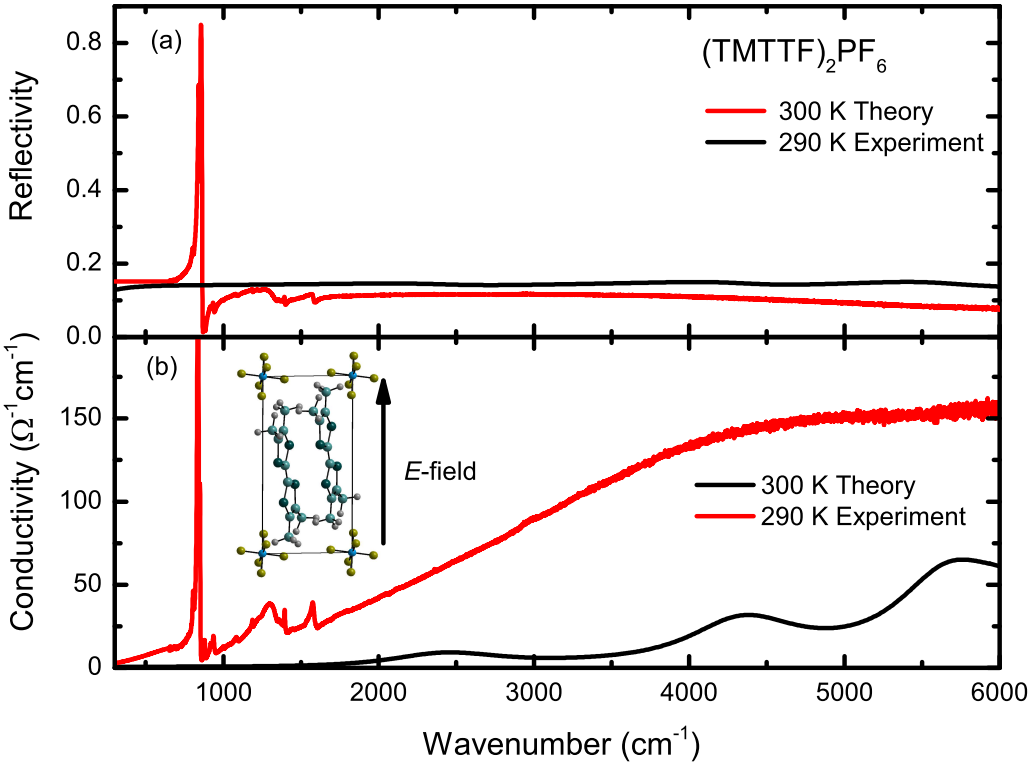

Figure 5.24: (a) Experimental (red) and theoretical (black) reflectivity of $(TMTTF)_2P_6$ for $E \parallel c$ at 290 K in a frequency range from 300 cm^{-1} to 6000 cm^{-1}. The flat reflectivity background is accompanied by vibrational features below 2000 cm^{-1}. (b) Kramers-Kronig consistent optical conductivity (red) and the theoretical one (black). The incorporated picture displays the polarization direction of the mid-infrared light with respect to the unit cell orientation.

5.1.6 *Optical properties of the c-direction*

While in the last two paragraphs the optical properties of the high conducting a- and the low conducting b-direction were presented and discussed extensively, the following section is dedicated to the optical response of the c-direction. In Fig. 5.24 the measured and theoretically calculated reflectivity and optical conductivity of $(TMTTF)_2PF_6$ are shown at room temperature between 300 cm^{-1} and 6000 cm^{-1} for a polarization of $E \parallel c$. The experimental reflectivity is almost constant throughout the whole displayed frequency range, with an average reflectivity of about 10%. It reveals a slight downturn at about 3500 cm^{-1}. Below 2000 cm^{-1}, the reflectivity is superimposed by some vibrational features, which originate from vibrations of the cationic TMTTF molecules and the negative charged anion. The strongest feature located at about 840 cm^{-1} can be ascribed to the ν_3 (t_{1u}) mode of the SbF_6^- anion. Due to the low reflectivity, the view on the vibrational modes is not obscured as it is the case for the a-direction, and the spectra reveal many similarities to the b-direction. The theoretical reflectivity is also constant in the selected frequency window and exhibits some weak minimum and maximum above 2000 cm^{-1} which can be attributed to electronic interband transitions from the highest fully occupied band to the half-filled band at the Fermi edge. The excitations were broadened by a Gaussian function with a width of 800 cm^{-1} (100 meV), still allowing the resolution of single features.

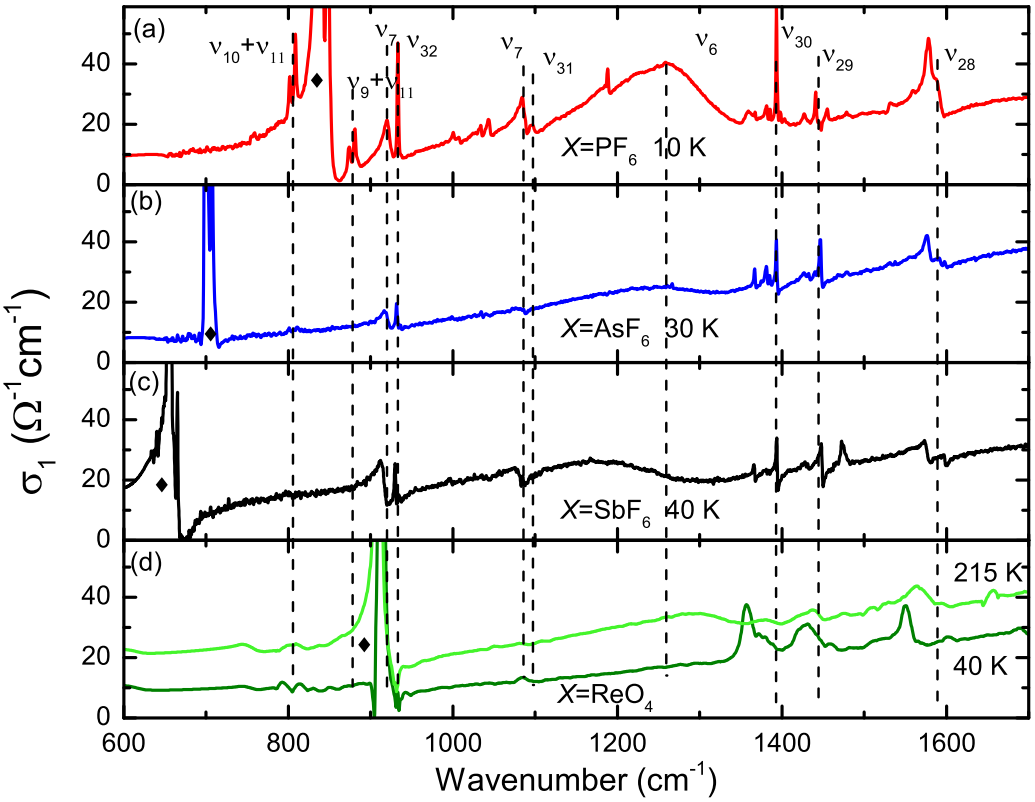

Figure 5.25: Optical conductivity of $(TMTTF)_2X$, X=PF_6 (a), AsF_6 (b), SbF_6 (c), and ReO_4 (d) along the c-direction. The vertical lines together with the vibrational mode labels mark the different vibrational features occurring in all compounds. The diamond symbols highlight the position of the vibrational modes of the anions which is the ν_3 (t_{1u}) mode for the centro-symmetric anions and for ReO_4 the ν_3 (t_2) mode, respectively. (d) The spectra are shifted by a constant value for better clarity.

This becomes more obvious when we take a closer look at the theoretical optical conductivity which exhibits three electronic features in this range.

The optical conductivity can be derived from the recorded sample reflectance by performing a Kramers-Kronig transformation. Therefore, the reflectivity was extrapolated for the low-frequency range until o cm^{-1} by a constant value, since the c-direction is insulating. For the high-frequency part a ω^{-4} function was applied to extrapolate the data from 6000 cm^{-1} up to 10^6 cm^{-1}.[17] This is also in full accordance with our calculations where conductivity and reflectivity, both decrease at frequencies higher than the interband transitions. The experimental and theoretical results agree qualitatively well. From this we conclude that the steady increase of the experimental conductivity can be attributed to some interband transitions, which was until now an unanswered question. Thus, it is not surprising that some of the modes exhibit an asymmetric (Fano-like) line shape, as explained in Appx. F.

As the electronic background was discussed in the last section, we concentrate now on the vibrational features occurring in this organic salt family. They can provide information about the temperature dependence of the charge state of the molecules and (as for the b-direction) about any redistribution of the anions within the molecule cavity formed by the neighboring TMTTF cations.

17 This extrapolation procedure was earlier used for other compounds and temperature yielding very good results and simplifies the comparison of the data.

Therefore, we compare the c-axis conductivity of all examined compounds at the lowest measured temperature in the charge ordered state in Fig. 5.25; in the case of X=ReO$_4$, we also show the anion ordered phase. All compounds reveal a low conductivity between 10 Ω^{-1}cm^{-1} and 40 Ω^{-1}cm^{-1} in the displayed frequency range from 600 cm^{-1}to 6000 cm^{-1}. Due to the interband transitions the conductivity increases slightly with increasing frequency. The diamonds tag for each compound the anion mode which is the ν_3 (t_{1u}) mode for the centrosymmetric anions and the ν_3 (t_2) mode for ReO$_4$. They are located in the case of PF$_6$, AsF$_6$, SbF$_6$, and ReO$_4$ at 840 cm^{-1}, 700 cm^{-1}, 655 cm^{-1}, and 915 cm^{-1}, respectively. Similar to the b-direction, they are by far the strongest vibrational features and will be discussed in more detail later in this section.

The other features can be ascribed solely to the cation TMTTF. At about 800 cm^{-1} we observe the $\nu_{10}+\nu_{11}$ (a_g) splitted combination mode which we already know from the a-direction, indicating that some contributions of the stacking (a-) direction is captured. It is noteworthy that the optical axis are determined by a polarization-dependent measurement. This means that the c-axis is defined by the lowest reflectivity measured in the ac-plane for different polarizer settings. However, we used only naturally grown single crystals without any further treatment so that the crystal surfaces do not have to coincide with the unit cell planes. This leads to the effect that some other directions can contribute to the optical response of one chosen direction. Also the $\nu_9+\nu_{11}$ (a_g) mode can be observed at 875 cm^{-1}solely in PF$_6$ which is splitted due to the charge imbalance.[18] The feature at 920 cm^{-1}can be assigned to the ν_8 (a_g) mode which becomes infrared-active by emv-coupling. It is present in all compounds, however, in ReO$_4$ it is superimposed by the anion mode. Close to it, a very sharp resonance is located at 937 cm^{-1}which is ascribed to the antisymmetric ν_{32} (b_{1u}) mode. The subsequently weak split feature at about 1000 cm^{-1}is the emv-coupled second harmonic $2\nu_{10}$ mode which is also observed in Raman spectra [2] and for light polarized parallel to the a-direction. Furthermore, emv-coupled modes occur at 1087 cm^{-1}between 1200 cm^{-1}and 1300 cm^{-1}, which we assign to the ν_7 and out-of phase ν_4 vibrations, respectively. The last one is observed in Raman spectra as a broad feature at room temperature as well. The strength of these features along the c-direction depends on the contribution of the a-direction, for example for AsF$_6$ they are very weak. We want to point out that the coupling for the ν_4-mode is especially strong, as our calculations indicate for it an undisturbed position of 1495 cm^{-1}. Such enormous shift of the resonance frequency of an emv-coupled mode was theoretically proven for the BEDT-TTF molecule by Yamamoto and Yakushi [182] [183]. They have discovered that with increasing emv-coupling constant, the fundamental resonance frequency of the out-of-phase (infrared active) mode shifts to lower frequency and the relation between the resonance frequency and the ionicity is strongly nonlinear. When we now use this finding for the ν_4 mode of the TMTTF molecule[19], we recognize immediately by comparing the emv-coupling constants of the various a_g modes that the ν_4 mode has the largest emv-coupling constant. Hence, it must undergo a very strong frequency shift to lower frequencies. The two most prominent features between 1350 cm^{-1}and 1500 cm^{-1}can be ascribed to the ν_{30} (b_{1u}) and ν_{29} (b_{1u}) mode.

18 Due to a slight misalignment of the polarizer with respect to the a-direction.

19 The same C=C double bonds in the BEDT-TTF molecule are involved in the considered molecular vibration

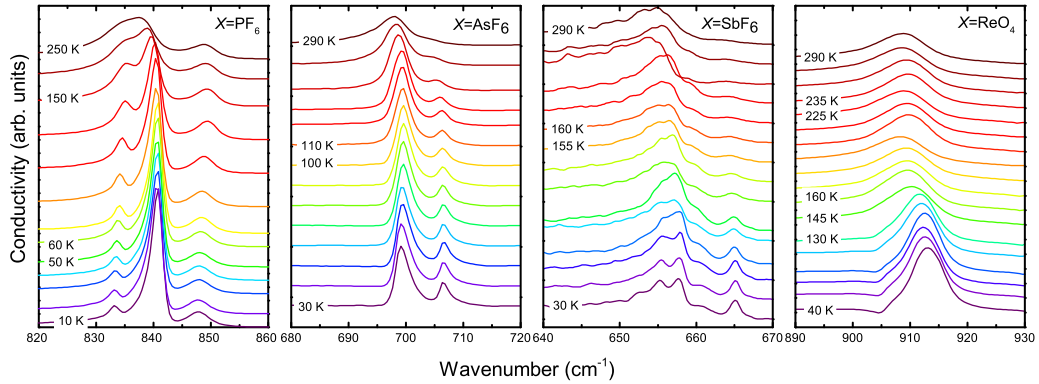

Figure 5.26: Illustration of the temperature-dependent evolution of the anion modes of X=PF_6 (a), AsF_6 (b), SbF_6 (c), and ReO_4 (d) for light polarized along the c-direction.

The other side features and bands originate from b_{2u} modes like ν_{47} or further a_g modes like the ν_5 and ν_6.

However, the most interesting mode is the odd ν_{28} mode which is located at room temperature at about 1575 $cm^{-1}$and reveals a splitting into two resonances in the charge ordered phase due to the charge disproportion between the two cations. Since it is antisymmetric, it does not couple to the electronic background. Therefore, its resonance frequency is not altered by the emv-coupling and changes linearly with the ionicity of the cations. Hence, it is the perfect choice to determine the charge imbalance in the charge ordered state with a very high accuracy.

Besides, other interesting features are the modes of the anion which were also examined in the previous paragraph about the optical properties of the b-direction. The possible role of the anions in the organic salts will be recalled again. It is assumed that the anions, which experience strong oscillations at room temperature due to thermal activation, lock-in a certain configuration within their molecular cavity created by the surrounding methyl groups and hence, trigger the charge ordering transition. Since the symmetry of the t_{1u} mode is lifted due the P-1 space group of the unit cell and their molecular site symmetry is -1, three different resonance frequencies occur in the expected frequency range. As depicted in Fig. 5.24 (b), we expect to observe three modes; one should be by far the strongest, since the connecting line of the central pnictide to one of the fluorine nuclei is parallel to the electric field of the incident light and the dipole moment. In Fig. 5.26 the temperature dependence of the resonance frequency of the anion ν_3 is displayed in the corresponding frequency range.

In the case of X =PF_6 we find at 250 K three resonances at 834 cm^{-1}, 837 cm^{-1}, and 849 cm^{-1}which is in perfect agreement with the frequency (835 cm^{-1}) of a free anion. A small shift of about 2 $cm^{-1}$of the strongest central peak to higher frequency can be detected for decreasing temperatures which is attributed to the thermal contraction of the crystal. Below 100 K the left peak sharpens, separates from the main peak and slightly redshifts on cooling while the right peak softens by 1 cm^{-1}. No influence of the charge order transition on the anion vibration can be recognized.

The other two compounds with the centro-symmstric anions X=AsF_6 and SbF_6 exhibit a similar temperature evolution. In contrast to PF_6 we detect only two features in AsF_6, which is caused by a slightly different polarization state of the infrared light that couples solely to two dipole moments. Therefore, the

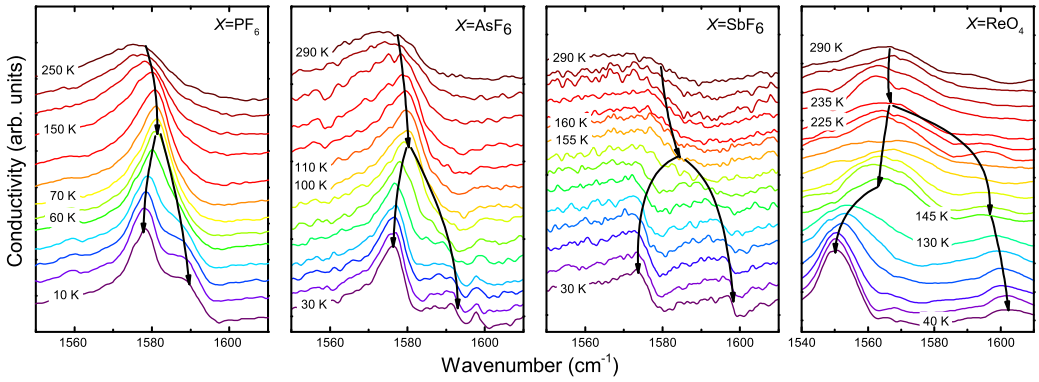

Figure 5.27: Temperature-dependent evolution of the ν_{28} mode of the Fabre salts with the anions, PF_6 (a), AsF_6 (b), SbF_6 (c), and ReO_4 (d). The vibrational frequency of the TMTTF^{+0} and TMTTF^{+} are 1628 cm^{-1}and 1551 cm^{-1}.

high-frequency feature is more intense compared to PF_6 more. The resonance position of the main peak is 698 cm^{-1}at 290 K and hardens to 700 cm^{-1}within the first 100 K. The frequency is in excellent agreement with measurements of AsF_6^- in the gaseous phase (see Tab. 5.4). The SbF_6 spectrum at 290 K reveals one broad peak at 655 cm^{-1}, accompanied by a shallow broad feature at 664 cm^{-1}. Both resonances do not exhibit any temperature-dependent modification.

In the case of ReO_4, a single broad mode appears at 908 cm^{-1}which is slightly lower than the 920 cm^{-1}of the free molecules. The width of the peak is caused by the disorder of the anions which can capture randomly two possible configurations at room temperature [201]. Upon cooling the resonance frequency resides at the same position and does not show any modification at the charge order transition. However, at the first order anion transition where the ReO_4 molecule orders and the unit cell doubles, the feature jumps to 912 cm^{-1}and becomes much sharper. By that a shoulder becomes apparent at 908 cm^{-1}. We attributed it to the second configuration, causing the tetramerization.

Admittedly, no evidence was found from the c-axis measurement that the orientation of the anion triggers or influences the charge order transition. However, recent theoretical and experimental studies on the magnetic properties of Fabre salts demonstrate a modification of the g-factor due to an interaction of the anion potential and the cation. Moreover, the authors performed additional theoretical calculations where they found that the electronic wavefunction of the TMTTF molecule is modified by the anion potential [203] .

Light polarized parallel to the c-axis mainly measures the antisymmetric b_{1u} modes which have their dipole moment along the long molecular axis. According to Tab. 5.3 the ν_{28} mode obeys the largest shift of frequency as a function of molecular ionicity. Furthermore, since it is not emv-coupled the resonance frequency depends linearly on the charge on the molecule [2, 177]. Similar to the ν_3 mode along the a-direction, this also offers the possibility [183] to study the charge disproportion in charge ordered systems.

In Fig. 5.27 the temperature dependence of the optical spectra is illustrated for all examined compounds in the frequency range of the ν_{28} (1550 cm^{-1}/ 1540 cm^{-1}(ReO_4) and 1610 cm^{-1}). In PF_6, a broad feature is observed at high temperatures which slightly shifts with temperature to higher frequency due to the thermal contraction. Below T_{CO} it starts to gradually evolve into two features, which is not completed at 10 K. This is the direct proof that the two molecular

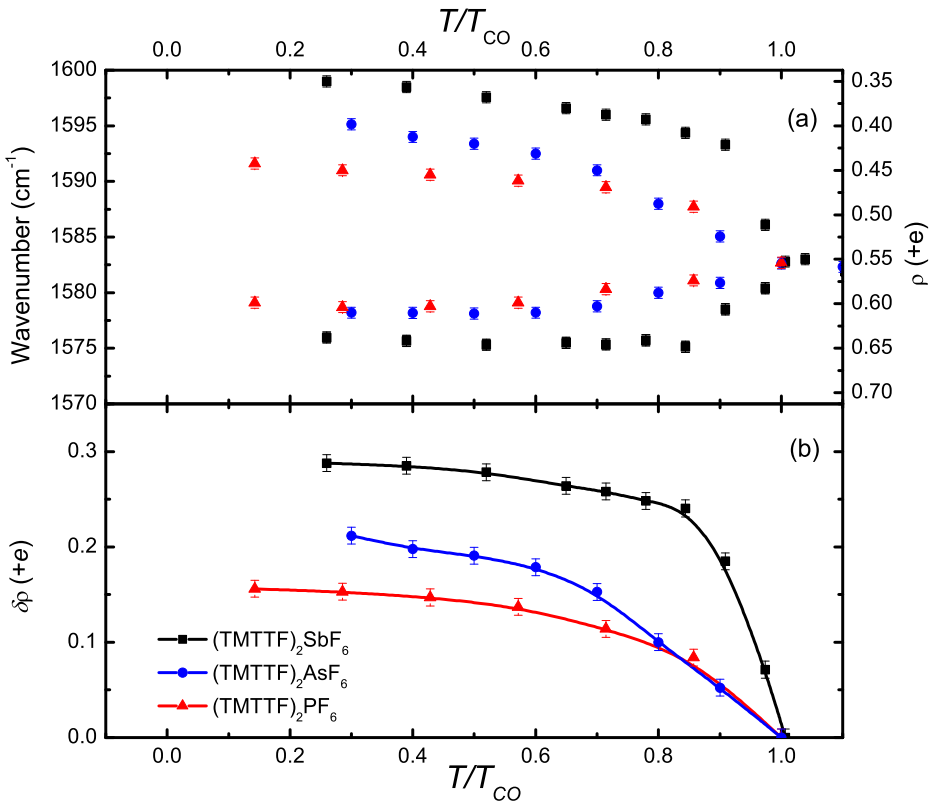

Figure 5.28: (a) Vibrational frequency of the ν_{28} (b_{1u}) mode of the TMTTF as a function of the normalized temperature T/T_{CO} for $(TMTTF)_2X$ (X=SbF_6 (black), AsF_6 (blue), and PF_6 (red)) with T_{CO}=67 K, 102 K, and 156 K, respectively. (b) Charge disproportionation $\delta\rho$ plotted versus T/T_{CO} for $(TMTTF)_2X$ (X=SbF_6 (black), AsF_6 (blue), and PF_6 (red)) below T_{CO}.

sites have a different charge state and become inequivalent, meaning that the symmetry is broken and the point inversion is lost. This leads to the ferroelectric nature of the charge order state in the Fabre salts. A similar behavior is noticed for AsF_6, and where the mode splits immediately below the transition into two components. However, here the splitting is obviously larger than in PF_6. In this context, SbF_6 exhibits the largest mode separation of the studied organic materials with centro-symmetric anions.

Since ReO_4 has two transitions we expect also two times a modification of the ν_{28}. Indeed, while from 290 K to 235 K no change happens, below T_{CO}=230 K two features appear whose distance further increases below the anion ordering transition (157 K). While in the three previous compounds the splitting was symmetric, for ReO_4 this is not the case. This asymmetry is attributed to the disorder of the anions which influences the frontier molecular orbital of the two TMTTF molecules differently and hence, also the Coulomb interaction that induces the charge ordering. Furthermore, below T_{AO} only the lower feature undergoes a clear redshift accompanied by a sharpening that indicates a vanishing structural disorder and a redistribution of the charge order pattern from o-O-o-O to o-O-O-o.

We have fitted the optical spectra by one single Fano function above T_{CO} and two below the transition and determined from that the resonance frequencies which are displayed in Fig. 5.28 (a) for PF_6, AsF_6, and SbF_6 as a function of the normalized temperature T/T_{CO}. All features exhibit the same resonance fre-

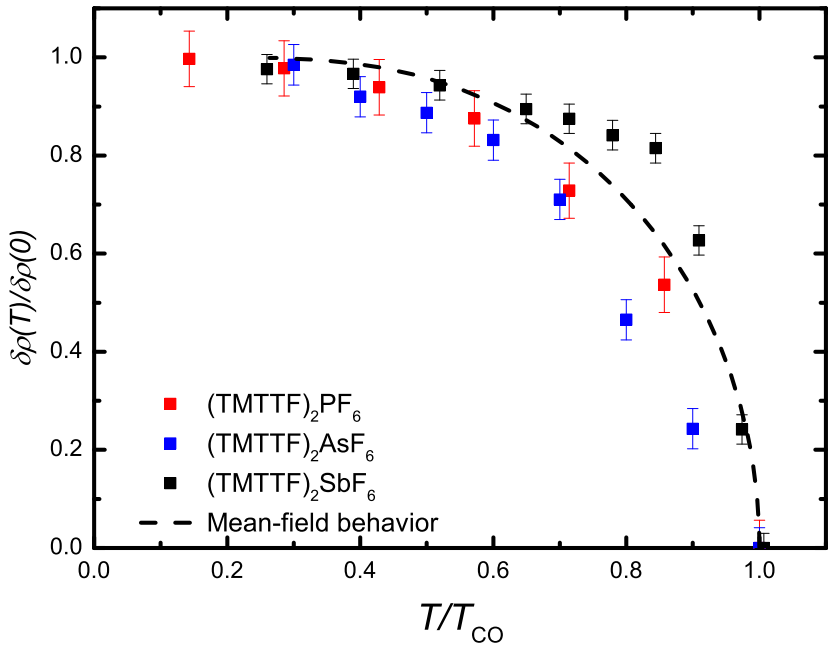

Figure 5.29: Normalized charge imbalance of (TMTTF)$_2X$ (X=SbF$_6$, AsF$_6$, and PF$_6$) as a function of T/T_{CO}. The dashed line displays the mean-field like temperature dependent evolution of the charge disproportionation.

quency of about 1583 cm^{-1}at room temperature, which is lower than the calculated value of 1590 cm^{-1}for +0.5 e per molecule. This deviation is caused by the molecular environment[20] which shifts the resonance frequency of the gaseous molecule. Below T_{CO} the mode splits equally and gradually into a lower and upper mode which hardly reveal any temperature dependence.

The charge disproportion $\delta\rho$ between the two molecular sites can be calculated by the resonance frequencies and the following linear function (with a maximum difference of 80 cm^{-1}[177] between the resonance frequency of a neutral and a cationic molecule):

$$\delta\rho = \frac{\Delta\nu}{80\,\mathrm{cm}^{-1}} \tag{5.16}$$

The results are plotted in Fig. 5.28 (b) as a function of T/T_{CO}. PF$_6$ reveals the smallest charge disproportion of about +0.16 e which increase to +0.22 e for AsF$_6$ and about +0.3 e for SbF$_6$. In the first two cases $\delta\rho$ increases slowly with temperature and resembles the behavior of a second order transition, whereas the transition of SbF$_6$ is abrupt and limited to a small temperature range which suggests a first-order transition. Thermal expansion [164] as well as transport measurements [59] support this observation.

In Fig. 5.29 we normalize the charge imbalance to 1 and assume that $\frac{\delta\rho(0)}{\delta\rho(T)}$ is proportional to the energy gap Δ. Furthermore, we assume a temperature-dependent mean-field like behavior of $\frac{\delta\rho(0)}{\delta\rho(T)}$ [204], which is plotted as a dotted line. In the case of PF$_6$ and AsF$_6$ it nicely describes the experimentally determined data. However, SbF$_6$ deviates from this behavior, pointing towards a first order phase transition.

Finally, the question remains whether a structural modification occurs at the phase transition which alters the electronic energy such as the transfer energy.

20 Similar to the solvent shift of electronic excitations.

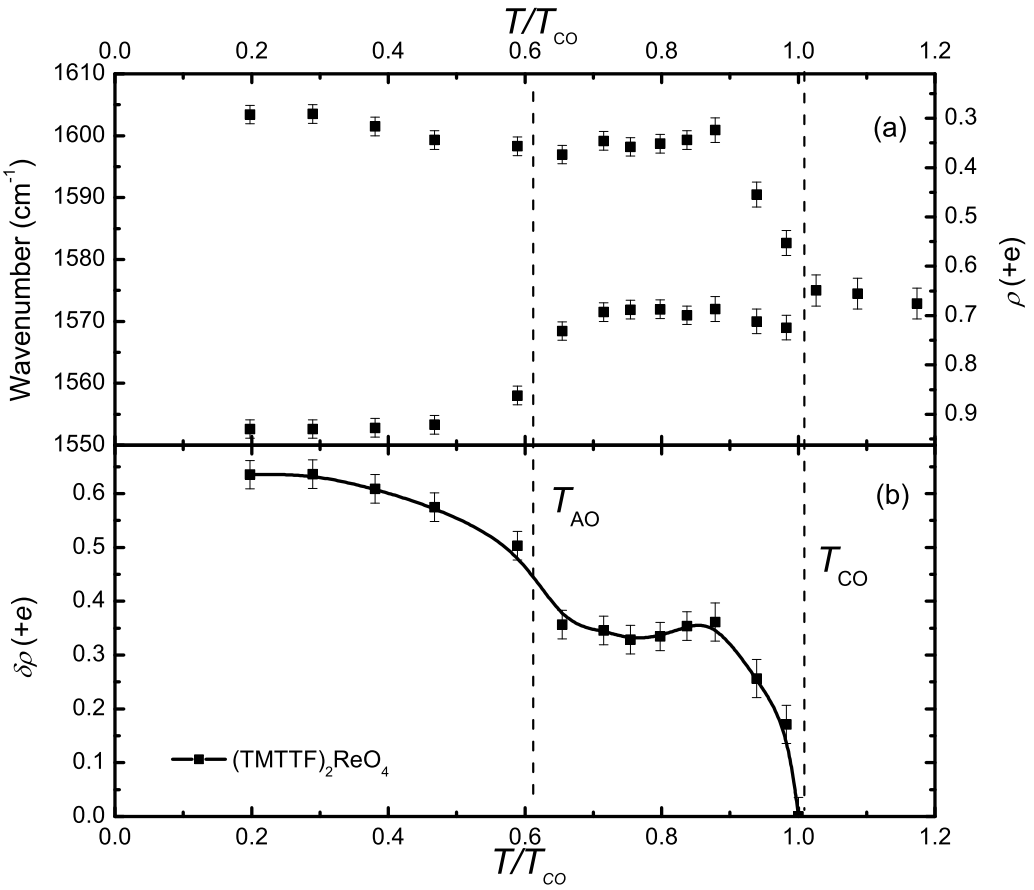

Figure 5.30: (a) Vibrational frequency of the ν_{28} mode for the organic compound $(TMTTF)_2ReO_4$ and the corresponding molecular charge as a function of T/T_{CO}. (b) Temperature-dependence of the charge imbalance $\delta\rho$ in the charge and anion ordered phase. The dashed line marks the anion order transition at 157 K.

However, we could not find any hints in our study of the electronic excitation in the a-direction for a modification of t. While the compounds with the centrosymmetric anions only exhibit one transition, $(TMTTF)_2ReO_4$ reveals a second transition due to the anion ordering. Therefore, we have plotted the resonance frequency separately in Fig. 5.30. The vibrational frequency is in the conducting phase 1572 cm^{-1}, which is lower than the previously observed value of 1582 $cm^{-1}$and deviates strongly from the calculated value (see Tab. A.1). As stated before, the vibrational feature of the ν_{28} is broader in comparison to the other ones, which is a hint for the large disorder of the anion. By that, the molecular environment is stronger modified than in the other studied Fabre salts, leading to an enhanced alteration of the resonance frequency. That is why it can be assumed that on each molecular site +0.5 e resides. At T_{CO}=230 K the mode splits into two features and strongly shifts to about 1600 cm^{-1}, whereas the other one only slightly shifts to 1570 $cm^{-1}$where it stays constant. Supposing a resonance frequency of 1582 cm^{-1}as in the other compounds at 300 K means that the mode splits symmetrically. When further lowering the temperature at T_{AO}, the lower features reveals an enormous shift within a narrow temperature range, while the other one stays constant. This can be ascribed to the tetramerization and modification of the charge order pattern which effects the electronic structure of the TMTTF molecules and hence, changes the resonance frequency.

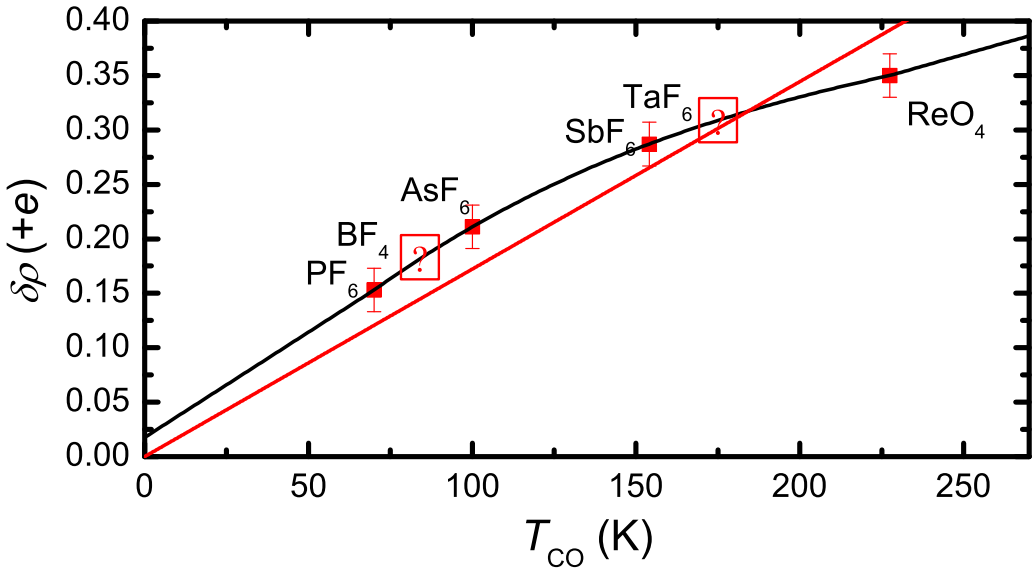

Figure 5.31: Charge imbalance as a function of the transition temperature T_{CO} for (TMTTF)$_2X$ (X=SbF$_6$, AsF$_6$, PF$_6$, and ReO$_4$). The black curve is a guide for the eye whereas the red line is a linear fit to the data. The question marks designate the possible charge imbalance for BF$_4$ and TaF$_6$.

Fig. 5.30 (b) summarizes the determined charge imbalance $\delta\rho$. The charge disproportionation jumps within a narrow temperature range to about +0.35 e and stays constant until the T_{AO} transition which is of the first-order kind. Below the anion transition, it first increases steeply to +0.52 e and further to +0.63 e. This is in good agreement with x-ray studies [205] which reveal an increase of the charge disproportionation at the anion ordering from about +0.3 e at the transition to +0.5 e at 100 K. Moreover, it is in agreement with the temperature-dependence of the optically determined ω_p (see Sec. 5.1.4.1). Furthermore, an NMR experiment has yielded a value of +0.33 e in the charge ordering [206]. This means that due to the anion ordering not only the unit cell is doubled, but also the charge disproportionation is significantly increased.

As we already know infrared spectroscopy is one of the most sensitive techniques to determine the molecular charge. In the following, we want to compare our results with literature values. In Tab. 5.6 all published values are listed together with ones determined within this thesis. The optical studies agree well with each other, while the results determined by NMR are in general too large. This deviation of NMR experiments can be understood, when considering that the charge disproportionation is derived by the spin relaxation rate which are suppressed in the low temperature phases, for instance in the Spin-Peierls phase. In addition, we could not find any indication of a further phase transition within or below the charge order phase despite in the case of (TMTTF)$_2$ReO$_4$. In the past, a decrease of the ν_3 (a_g) mode splitting in (TMTTF)$_2$AsF$_6$ was detected below 10 K (in the SP[2]) which implies a relation between SP phase and the charge imbalance. However, a similar behavior could not be observed for (TMTTF)$_2$PF$_6$ which has a much higher SP transition temperature of 19 K. This can be explained by the fact that the emv-coupled modes are sensitive to the SP.

Therefore, we exclude an influence of the SP phase on the charge disproportionation since the ν_{28} mode does not interact with the electronic background.

Recently, the different intensities of the modes at temperatures below T_{CO} attracted attention for BEDT-TTF-based compounds. Therefore, we have also plotted the optical conductivity in the concerned frequency range as a function of temperature in Fig. 5.27. Similar to Ref. [210], we clearly observe a dependence of intensity on the molecular charge. This trend can also be noticed in our calculations of the vibrational modes briefly summarized in Tab. 5.3. In the calculation, the intensity of the ν_{28} of $TMTTF^{+1}$ is by a factor of 6 larger than the one of the neutral molecule. Girlando [210] has shown that the molecular orbital is not modified by changing the charge of the molecule; instead, the charge distribution between the constituting atoms is altered which causes the enhancement of the infrared intensity of the cationic vibrations.

In Fig. 5.31 the charge disproportionation $\delta\rho(0)$ is plotted as a function of the transition temperature T_{CO}. In the mean-field theory the energy gap at T=0 K is a linear function of the transition temperature. Indeed, the charge disproportionation which depends on the energy gap depends almost linear on the transition temperature. Additionally, the possible charge disproportionation of BF_6 and newly synthesized TaF_6 is added to the plot. We suppose that further compounds with YF_6 and ZF_4 anions follow this trend[21]. Coming back to the question of the influence of the anion, one should further note that [59] tried to find a dependence of the transition temperature T_{CO} on external parameters as the distance between the anions and the TMTTF molecules. Actually, the transition temperature is decreasing with increasing F-S distance. However, in this context it cannot be concluded that the anion is triggering the phase transition, but influences definitely the dimensionality and the spacing between the cations. By that, the transfer integral t and next-nearest neighbor Coulomb repulsion V is mainly modified, further driving the compounds according to the extended Hubbard mode into the charge ordered state.

21 Y and Z are indefinite atoms from the periodic table.

Table 5.6: Charge disproportionation derived from different experimental techniques with the lowest measured temperatures in brackets. In the case of the values derived from NMR measurements the different results stem from different methods of determination.

Material	$\Delta\rho$ ($+e$)				
	$\nu_{28}(b_{1u})$ IR	$2\nu_{10}$ (a_g) IR	ν_3 (a_g) IR	ν_3 (a_g) Raman	NMR
PF_6	0.15 (10 K)	0.14 (10 K)	0.12 (30 K)	0.10 (20 K)	0.28 [160]
AsF_6	0.21 (30 K)	0.19 (30 K)	0.26 (20 K) [207, 208] 0.19	0.17 (20 K)	0.33 [152]
					0.50 [158]
	0.11 [159]				0.16 [159]
SbF_6	0.29 (40 K)	0.26 (40 K)			0.50 [209]
ReO_4	0.35 (CO)/0.63 (AO)	0.47 (AO)	0.41 (AO)		0.33 [206] (CO)

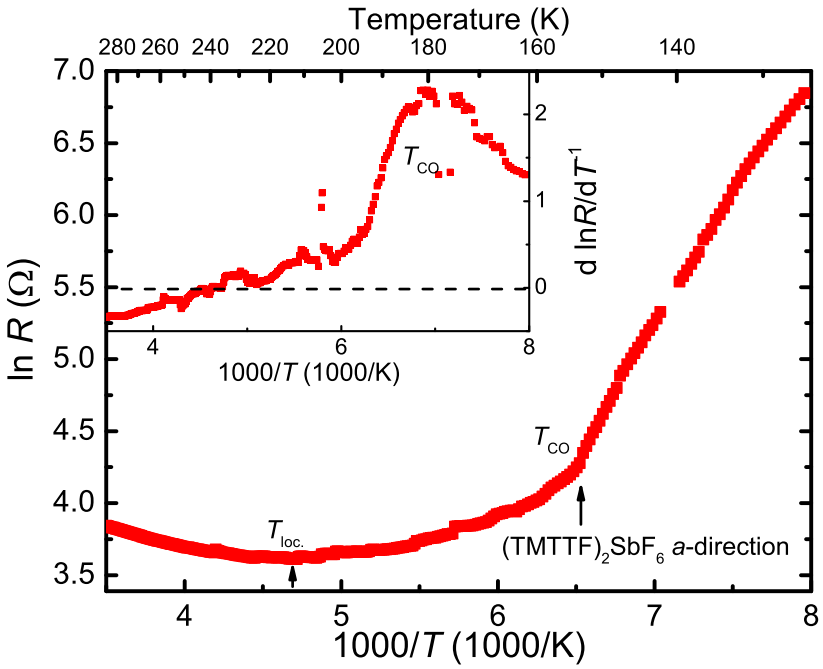

Figure 5.32: Logarithm of the resistance of $(TMTTF)_2SbF_6$ as a function of the inverse temperature. At about 215 K a minimum appears, marking the transition to the localized state related to the opening of a Mott gap. The resistance increased slightly and at 158 K a kink is observed in the curve. It is caused by the charge order transition. Inset: derivative of the logarithm of the resistance vs. $1/T$. The charge localization leads to a change of the sign from negative (metallic) to positive (insulating). Also the slope changes at T_{CO} leading to a rather flat curve at low temperatures.

5.1.7 *Response to electric pulses*

Since nonlinear behavior was observed in several different inorganic as well as organic compounds (see Sec. 3.2) at the vicinity of a metal-insulator transition, we expect to discover similar phenomena in the quasi one-dimensional salts $(TMTTF)_2X$, X=PF_6, AsF_6, and SbF_6. However, only for the compound with the centrosymmetric anion X=SbF_6 a surprising response due to illumination was observed. As depicted in Fig. 5.2 (a) $(TMTTF)_2SbF_6$ reveals the steepest slope at the phase transition, while PF_6 and AsF_6 exhibit a smooth transition. Therefore, we conclude that for the 1D salts strong resistivity changes [59] at the transition temperature are a good indication that nonlinear behavior can be observed. Otherwise, the difference is too small and the photo-induced effect is absent.

Before the response of SbF_6 on electric pulses is presented, its temperature-dependent resistance from room temperature to 125 K has to be discussed. It serves two purposes: the determination of the phase transition temperature by resistivity measurements is more precise as it would be possible with optics and furthermore, the contact resistances need to be deduced. In Fig. 5.32 the logarithm of the resistance of SbF_6 is illustrated for the a-direction in a temperature range from room temperature down to 125 K. When increasing the temperature, the resistance decreases down to a minimum at 215 K, which corresponds to the sign change of its slope (see inset Fig. 5.32). This is caused by electron-electron interactions which open up a Mott gap at the middle of the upper half-filled band and Umklapp scattering. Thus, the resistance further increases with de-

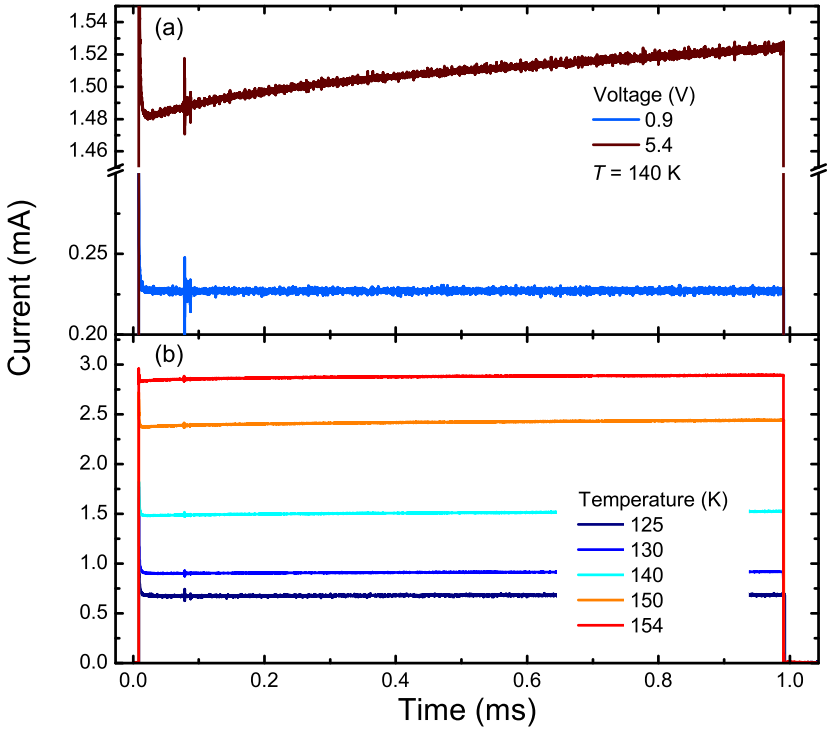

Figure 5.33: (a) Response of the current, when 1 ms pulses of two different voltages are applied at 140 K on $(TMTTF)_2SbF_6$. (b) Current response plotted for various temperatures below T_{CO}.

creasing the temperature down to the charge order transition, corresponding to a linear slope of the derivative. At T_{CO} a kink arises and the resistance increases above nonlinearly. In the inset it is obvious from the temperature-dependent derivative below the charge order transition that the slope of $\ln R$ is not linear and hence, it is not strictly thermally activated.

Furthermore, SbF_6 reveals an anomaly in the thermal expansion coefficient at the CO transition. In contrast, in its sister compounds no feature appears at the corresponding transition temperature. A similar behaviour also appears in the temperature-dependent evolution of the charge disproportion, as depicted in Fig. 5.28. While PF_6 and AsF_6 a mean-field behavior appears, a first-order like transition takes place in SbF_6. The latter is probably related to the enhanced dimerization (see Tab. 5.1) and the charge localization state at elevated temperatures.

In Sec. 3.2 it was presented that electric-induced resistivity switching or nonlinear conductivity appears in many organic compounds, paving the route for devices based on organic salts. Since these phenomena are mostly related to materials with a metal-insulator transition, it is obvious to assume a similar behavior for the quasi one-dimensional Fabre salts. The experimental setup described in Sec. 4.2 was used to trace a possible electrically induced effect. Therefore, voltage pulses of 1 ms length were created at the sample and the total current was measured by the voltage drop across the load resistor (1 kΩ) connected in series to the sample. The repetition rate was fixed to 4 Hz to avoid heat accumulation.

In Fig. 5.33 the time-dependent current response of SbF_6 at 140 K is plotted for two different voltages. At the beginning of the pulse, an overshoot of the measured current is present due to the parasitic capacity and resistance in the circuit (see Fig. 5.33 (a)). Afterwards, the current decays to a constant value. The

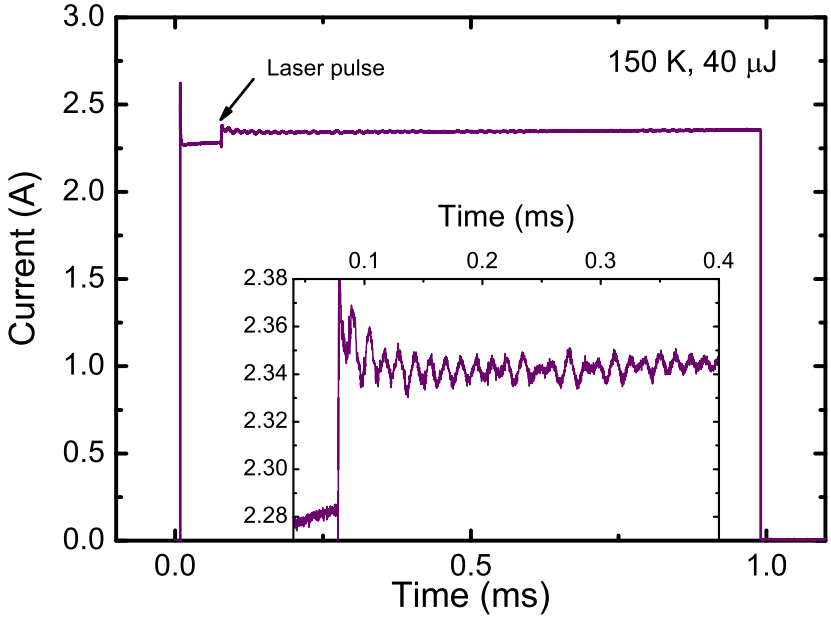

Figure 5.34: Current response on a 1 ms 5 V voltage pulse applied at 150 K on $(TMTTF)_2SbF_6$. At about 0.75 ms, an additional laser pulse (black arrow) illuminates the sample. This induces a photocurrent, visible in the steep, weak jump of the current signal. In the inset the first 400 µs of the photocurrent response are magnified. Interestingly, the signal is dominated by oscillations.

oscillating signal located at 100 ms is caused by a parasitic current induced by the switching of the Pockels cell of the laser system[22]. For low voltages the current signal stays constant during the whole pulse. However, when increasing the amplitude of the pulse, the current increases linearly obeying an ohmic behavior. However, following the temporal evolution further reveals a nonlinear increase of the current, which can be attributed to a thermal modification of the contact resistance.

Fig. 5.33 (b) also shows current pulses for different temperatures. The current signal decreases for the same applied voltage as the total resistance increases with temperature. Independent of the applied voltage or examined temperature no switching behavior or current oscillation can be detected, which would indicate a sliding of the $4k_F$-CDW/CO.

5.1.8 *Response on laser pulses*

The photo response of $(TMTTF)_2SbF_6$ was studied by illuminating a fraction of the space between the two contacts by a laser pulse. The contact distance was about 1.1 mm. In Fig. 5.34 the recorded current pulse is illustrated exemplarily at 150 K for a 5 V voltage pulse and a laser pulse with the energy of 40 µJ. Similar to Fig. 5.33, an overshoot is present at the beginning. Additionally, 750 µs after onset of the voltage pulse, the current suddenly shoots up within a few nanoseconds. Strikingly, this onset is correlated with the incident laser pulse. The signal decays barely and stays almost constant over the entire pulse length. In the inset of Fig. 5.34 an enlarged detail of the first 300 µs of the photocurrent is visualized. Surprisingly, current oscillations are superimposed on top of the

22 The laser is later used to create the photocurrent.

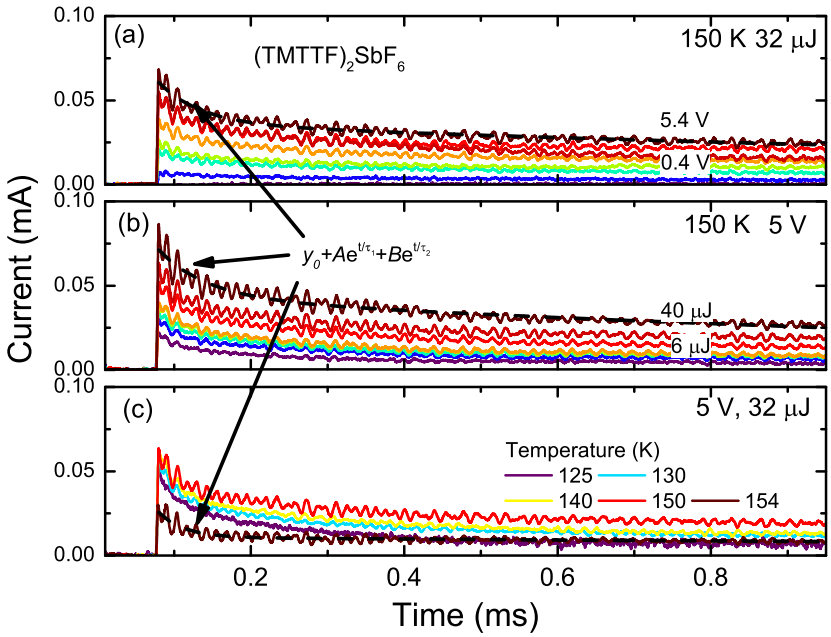

Figure 5.35: Time-dependent photocurrent for various voltages (a), laser pulse intensities (b) and temperatures (c). The temporal dynamic is fitted by a double exponential function (dashed black lines).

signal, whose amplitude decays with time. The inset further reveals a slight signal decay within the first 59 µs.

We examined the photocurrent signal for various voltages below the phase transition T_{CO} = 158 K, as presented in Fig. 5.35 (a) for 150 K and 32 µJ. Above T_{CO}, no change was observed. There, the photocurrent was extracted by subtracting the current without any light (see for example Fig. 5.33) from the total current signal. By that, we also get rid of the nonlinear transport behavior of the device, consisting of the contact resistance and the sample. By increasing the applied voltage the signal increases linearly. Similarly, the photocurrent increases with increasing pulse energy and the temporal behavior is the same as for the voltage-dependent current curves, as depicted in Fig. 5.35 (b). Finally, also the temperature dependence of the transient photocurrent is plotted for a fixed pulse energy 32 µJ and voltage amplitude 5 V in Fig. 5.35 (c). The photocurrent is the smallest at the vicinity of the phase transition (154 K) and than stays almost constant below 150 K. One should note that all curves in the latter three graphs exhibit the same temporal dynamics which can be fitted by a double exponential decay function $f(t) = y_0 + e^{\frac{t}{\tau_1}} + e^{\frac{t}{\tau_2}}$. Between 154 K and 125 K, the first time constant τ_1 decreases from 30 µs to 16 µ and τ_2 diminishes by a factor of 2 from 300 µs to 170 µs. y_0 is the background which can be considered as a third extended living state, decaying at least on a millisecond time range. Such relaxation dynamics were as well observed in other photo response experiments on organic conductors [211, 212, 213, 214] taking place between the microsecond regime and far above the millisecond time scale.

However, a very amazing phenomenon is the interference patterns which are superimposed on top of the exponentially decaying current signal. To our best knowledge, this has never been detected before in a photoconductivity experiment on organic conductors. To analyze the oscillations in detail, the frequency components were extracted from the decaying current by a FFT. The amplitudes

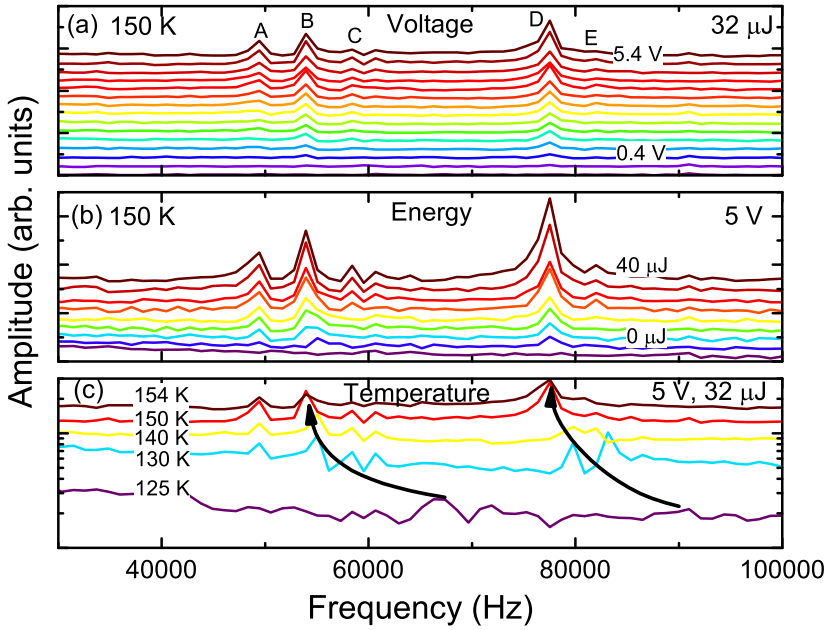

Figure 5.36: Amplitude spectra of the current oscillations in $(TMTTF)_2SbF_6$ obtained by FFT. The curves are shifted by a constant value for better visualization. (a) Amplitude spectrum in a frequency range from 30 kHz to 100 kHz plotted for various voltages from 0.4 V to 5.4 V and for a pulse energy of 32 µJ at 150 K. (b) Same temperature and frequency range as in (a), however, the amplitude spectra are shown for different pulse energies at a fixed voltage of 5 V. (c) Temperature-dependent amplitude spectra from 154 K to 125 K for 32 µJ and 5 V.

of the frequency components from the curves, depicted in Fig. 5.35, are visualized in Fig. 5.36. Five resonance frequencies can be identified: 49000 Hz (A), 54000 Hz (B), 58500 Hz (C), 77500 Hz (D), and 82000 Hz (E). Varying the voltage does not influence the resonance frequency, although the amplitude increases linearly. The same is true for the laser intensity dependence of the oscillation amplitude; it increases linearly without any modification of the maximum position, as shown in Fig. 5.36 (b) for 150 K and 5 V. It is important to note that the dark current is independent of the applied voltage, as it is exemplarily displayed in Fig. 5.33; no oscillations occur, resulting in a flat amplitude spectrum. While the resonances display only an amplitude-dependence on the voltage and pulse intensity, both the amplitude as well as the resonance frequency depend on temperature.

From these observations, several questions arise.

1. What is the origin of the photocurrent and its dynamic?

2. Why does the current start to oscillate after illumination?

To understand the involved processes, the excitation of the sample by light has to be discussed. In the case of $(TMTTF)_2SbF_6$, the photons with the energy of 2.35 eV excite either i.) the transition from the quarter-filled HOMO band to the LUMO+1 band of the $TMTTF^{+\delta}$ molecules or ii.) the transition from a fully occupied band far below the Fermi energy to the quarter-filled unoccupied mid-infrared band, as depicted for the transitions labeled in Fig. 5.7 with the letter **C**. After the vertical electronic excitation into the unoccupied bands several decay channels are open.

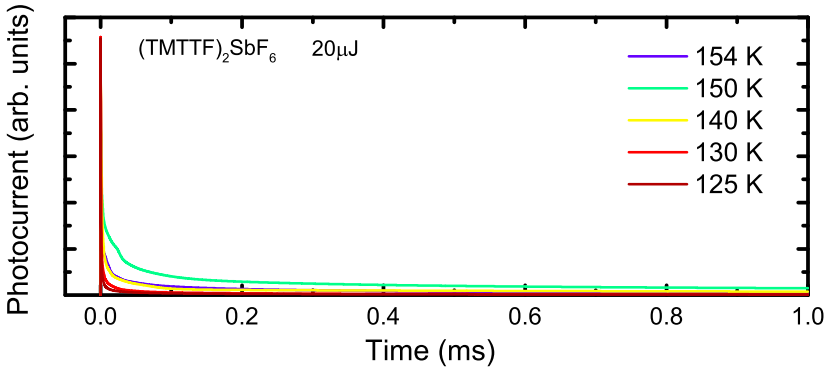

Figure 5.37: Simulation of a thermally induced photocurrent by a short laser pulse for five different temperatures. A steep current peak slowly relaxing to zero.

- A free electron and hole can be created, which gets separated from each other by an electric field, leading to the photocurrent signal. However, they can recombine before they reach the electrodes or become trapped. In general, the lifetime of the free carries is between nanoseconds and microseconds.
- After a few picoseconds the excited electronic states couple to the lattice phonons and intramolecular vibrations. By this, energy is transferred to the lattice subsystem and the sample is warmed up.
- Afterwards, the excited electrons decay back into their initial state by emitting a red-shifted photon. The latter can be reabsorbed or detected as a photoluminescence signal, for instance in Raman scattering experiments. Also, a radiation-free decay is possible for the decay into the lowest excited (mid-infrared) band.
- Otherwise, the excited charge can relax into a low-lying unoccupied band, triggering a charge transfer from one cation to its neighbor molecule in the picture of a molecular chain. This can induce a phase transition from the charge ordered to the metallic state.
- Recently, in photoluminescence spectra of a two-dimensional organic Mott insulator the creation of an exciton was observed [215]. In addition, in the theory of photo-induced transitions [216] it is supposed that the excitation of higher excited states and the generation of excitons and that the breaking up of excitons may also stimulate a light-induced transition. Especially in low dimensional system fluctuations, as well as electron-electron and electron-phonon interactions play a crucial role, eventually destabilizing the equilibrium state. This picture is similar to the suggested model for the photo-induced phase transition in TTF-CA presented in Sec. 5.3.6.

In the following, the influence of thermal effects on the induced current will be discussed. For this purpose, Eq. E.4 in Appx. E will be used to calculate the temporal behavior of the sample temperature and correlate it with the temperature-dependent sample resistance depicted in Fig. 5.32. The result of the simulation is visualized in Fig. 5.37 for various temperatures. We assume that the whole pulse energy is absorbed and transferred at the surface of the sample into Joule heat as the penetration depth is only a few hundred of nanometers.

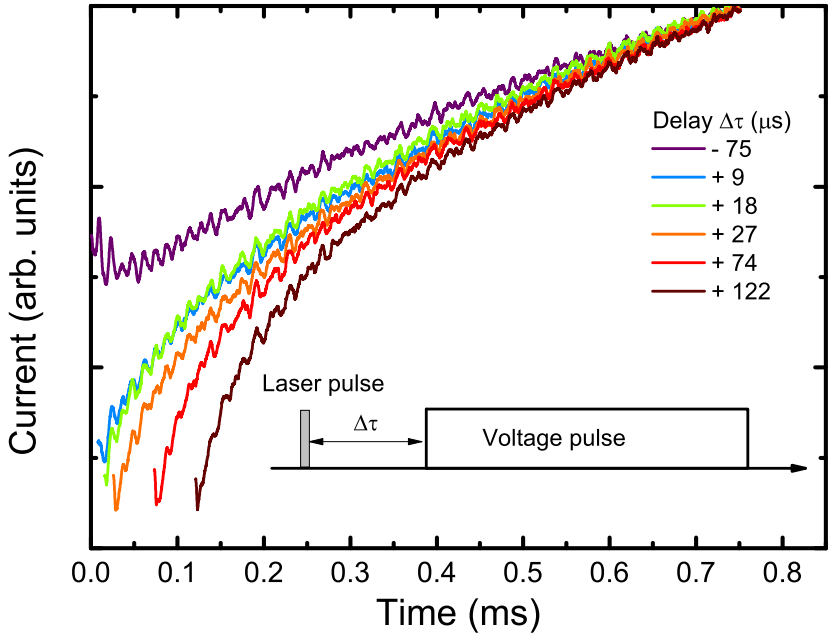

Figure 5.38: Raw photocurrent signal for various delay time between the voltage and laser pulse for a laser intensity of 40 μJ and 10 V at 147 K.

Besides that, the lateral electric field is the strongest along the direct line between the contacts. Thus, we are probably probing a thin layer at the surface. From this simulation, a very sharp increase of the current would result which is not the case in the presented experimental curves. The relaxation dynamics or cooling process are very fast and related to an extreme drop of the photocurrent within 1 μs. Afterwards, it asymptotically approaches zero. By comparing the experimental results with the theoretical ones, it is clear that the amplitudes and time constants of the signals are different. Only in the case of the long relaxation process a thermal effect contributes to the photocurrent signal. Furthermore, the simulation does not reveal any current oscillations, which supports that the system is driven instead into a metastable condition different from a simple heating scenario. However, it is also possible that a cooling process drives the system into a quenched regime, where two states compete with each other, leading to the oscillating current.

In the following, we will perform a discourse about the possible origin of the current oscillations. By that, we want to identify some similarities to previous observations in other material classes and try to disclose their origin in this way. We have seen that in the previous paragraph the resonance frequencies are not a function of the voltage or the laser intensity and only vary slightly with temperature. In contrast, the amplitude changes linearly with the laser intensity and voltage.

The first idea to explain the oscillations could be an artificial effect which is caused by the experimental setup. The arguments against this opportunity are:

- In Sec. 5.4.3 and Appx. D.4.4 the results of electrically induced phase transitions in α-(BEDT-TTF)$_2$I$_3$[23] are presented and in none of these studies oscillations were observed, although the same setup was used. Furthermore, the present case differs from the shape of the oscillations in VO_2 that resemble the charging and discharging of a capacitor.

23 Photoconductivity measurements in α-(BEDT-TTF)$_2$I$_3$ are not presented in this thesis.

- In addition, the pure time-dependent current signal without illumination does not contain any trace of these oscillations, as displayed in Fig. 5.33. Also, an electric parasitic signal of the laser system which couples to the photocurrent signal can be excluded, since the laser has been running during the whole experiment.

- The setup arrangement is not the origin of the oscillations because the exchange of the external load resistor did not reveal any modification of the interference pattern and its resonance frequency. Furthermore, also the pulse generator as well as the oscilloscope were exchanged, resulting in the same outcome.

- In Fig. 5.38 the photocurrent signal is shown for different voltage pulses delayed to the laser pulse. The signals were overlapped with each other at 0.8 ms. The oscillations persist also for voltage pulses after the irradiation, but with a smaller amplitude. Moreover, the oscillations appear still at the same position which implies a relation to the light pulse. Amazingly, the current curves reveal a gap between each other. This indicates that without an external electric field, the excited free electrons and holes, as well as the excitons are not separated from each other and hence, recombine. In the case of a pure thermally induced effect the current dynamics or the resistance, respectively, would be independent of the applied voltage and would reveal the same temporal behavior.

In summary, it can be excluded that the setup or one of its parts cause this phenomenon.

The next question is: was a similar effect detected in other experiments with and without illumination?

1. In the early 60's and 70's in transport measurements on silicon with two Schottky contacts low current oscillations in the kHz regime were recorded, which were ascribed to double current injection at the contacts [217]. However, the frequency could be varied by changing the voltage bias or temperature and the oscillations occur only above a critical threshold field [218].

2. The well-known creation of hot or non-equilibrium electrons in semiconductors as GaAs [81] leads to electric field-dependent charge carrier velocities, causing a negative-differential resistance (NDR). One of the related phenomena is the famous Gunn effect [79], yielding current oscillations in the microwave regime. In this case, the frequency can be tuned by the sample length or by the applied voltage.

3. Similar to the NDR current oscillations in pure semiconductors, self-oscillating (photo-)currents were observed in superlattice structures, consisting of two different direct semiconductors as GaAs-AlAs [219]. Due to the different energy levels in the quantum wells and the tunneling effect between the layers, a negative differential velocity regime is created as a function of the external electric field. The electric field reveals a spatial variation within the superlattice structure. Thereby, the different regions separated by domain walls get unstable and hence, cause the oscillations. The resonance frequency can be tuned by the bias voltage or laser power. [220, 221]

4. Current oscillations occur very often in nonlinear transport studies in various organic conductors [47, 222, 223, 224, 225]. There, they are often related to sliding charge density waves or electrically induced insulator-metal transitions accompanied by a bistability. More details can be found in Sec. 3.2 and Sec. 5.4.3.[222].

5. It is known that ferroelectric materials reveal a modification of the polarization by light stimulation, which can be detected by photoconductivity measurements [87]. Here, the detected signal is composed in general of three different components [226, 227, 228]. i.) A fast decay of the excited states within a few microseconds. ii.) A pyroelectric signal which can last for milliseconds. iii.) Piezoelectric oscillations are superimposed on the decaying current due to the thickness variation of the sample by sound waves. Since the Fabre salts are charge-ordered ferroelectric salts they resemble the behavior of well-known inorganic ferroelectric, such as $LiNbO_3$.

6. Above a certain threshold field voltage (in the range of a few hundred 100 $mVcm^{-1}$) oscillations occur in charge-density systems CDW [31] like $NbSe_3$, TaS_3 or $K_{0.3}MoO_3$ which are attributed to the collective sliding of the charge density wave. There, the resonance frequency reveals a dependence on the applied voltage and temperature. However, only a few photoconductivity studies[24] were conducted on CDW materials [229, 230]. In these, it was observed that the threshold voltage between the creeping and sliding state of the CDW can be raised by increasing the light intensity.

As already discussed at the end of the respective paragraphs, the first four opportunities can be disregarded as a possible origin of the current oscillations. Since $(TMTTF)_2SbF_6$ can be regarded as a one-dimensional charge-ordered ferroelectric, it is not surprising that the temporal dynamics of its photocurrent resembles those of illuminated inorganic ferroelectric crystals. For these, the current oscillations are related to the speed of sound in the bulk material. In our case this would lead with a sample length of l=2 mm and a resonance frequency of 77.5 kHz to the sound velocity $c_{\text{sound}} = f \times l$ of 155 ms^{-1}. However, organic salts have a speed of sound of about 2500 ms^{-1} [231, 232], which is one order of magnitude larger. From that we conclude that the origin of the oscillations are not light-induced sound waves.

As an alternative, the charge-ordered state of $(TMTTF)_2SbF_6$ can be considered as a $4k$-CDW which should start to slide above a certain electric threshold field, but this is not the case for $(TMTTF)_2SbF_6$. The here applied electric fields were a few Volts per cm. This is much more than typically needed for classical CDW systems [31], but two orders of magnitude smaller than the threshold fields in α-$(BEDT\text{-}TTF)_2I_3$ (see Sec. 5.4.3). Furthermore, a single particle excitation does not lead to weakened "pinning" of the CDW and causes in principle an increase of the threshold field. Therefore, photo excitation is not enhancing the sliding of the CDW in commonly known systems. Additionally, the resonance frequency of the depinned $4k$-CDW should exhibit a dependence on the external voltage, as observed in other CDW materials, such as $NbSe_3$, but not in the present case. However, this is the first photoconductivity study on a charge-ordered one-dimensional material ($4k$-CDW). In this regard, we suggest

24 Mainly measured by the lock-in technique which does not directly provide the time-dependent behavior of the photocurrent.

that our observations are caused by photo-induced fluctuations of the charge-ordered state which alter the current flow of the single particles and hence, the photocurrent.

5.1.9 *Summary and conclusion*

In the previous chapter we have presented comprehensive investigation of several quasi-one-dimensional organic members of the Fabre family[25]. We have performed theoretical calculations of the band structure, optical excitations as well as of the vibrational normal modes of the differently charged free TMTTF molecule. The three different salts TMTTF$_2X$ with X=PF$_6$, AsF$_6$, and SbF$_6$ reveal two bands at the Fermi surface, which originates from the dimerzation of the two TMTTF molecules in the unit cell. By that the system is half-filled leading dependent on the on-site Coulomb repulsion eventually to the opening of a Mott gap, which is the case in the present system. The band dispersion only varies slightly for different anions. However, the band width increases with decreasing anions size. This causes an increase of the hopping integral t i. e. an enhanced conductivity, which can be experimentally verified by DC transport measurements. Moreover, by a comparison of the calculated band structure of different anions with the temperature-dependent band structure of TMTTF$_2$SbF$_6$, we were able to impressively demonstrate that cooling has the same effect as decreasing the anion size (applying chemical pressure). This means that by cooling t increases and the compounds become more conducting. This happens indeed from room temperature down to temperatures between 200 K and 250 K, where the conductivity exhibits a minimum. At lower temperatures, the conductivity starts to decrease, which is ascribed to the opening of the Mott gap due to the dominating U. Since the DFT simulations do not take the correlation effects properly into account, we state that the on-site and inter-site Coulomb repulsion U and V defines the physical properties. Therefore, the systems cross over into an insulating phase, in which the dimerization of the cationic molecular building blocks is lifted and the charge is unequally distributed between the molecular sites. By that the materials become quarter-filled. This cannot be described in the standard framework of the DFT theory. The simulations show that the materials are metallic along the molecular stacking direction. The theoretically determined conductivity ratios between the different crystallographic axis agree very well with the literature values. Furthermore, we assert that not only the mid-infrared range reveals a temperature-dependence, but also the VIS range. We suggest that future studies have to focus on this spectral range, as they can deliver important information about the redistribution of the spectral weight and the impact of U and V. We also propose that strong modifications of the spectral features for this range will appear at the charge order phase transition, as the configuration of the molecular orbital is affected by the charge redistrubtion. Hints for that were found recently in an x-ray photoemission study on Fabre salts [233]. A direct comparison of the theoretical and experimental spectra reveals that almost all electronic features are reproduced correctly in the calculations.

In the second part of this chapter, we have performed the first comprehensive investigation of the temperature-dependent optical properties along all crystallographic axis of the TMTTF$_2X$: X=PF$_6$, AsF$_6$, SbF$_6$, and ReO$_4$ compounds [2, 11].

25 All samples were synthesized at the 1. Physical Institute.

In general, the b- and c-direction does not reveal any strong electronic feature, but instead a clear view on the vibrational features of the cations and anions. By our theoretical normal mode analysis, we could successfully ascribe most of the features to the molecular vibrations. By that we could identify charge sensitive modes, which we used to determine the temperature-dependent evolution of the charge disproportionation with a very high precision. Interestingly, it seems that an almost linear relation exists between T_{CO}, charge disproportionation $\delta\rho$, anion size and hence the distance between the molecular building block. The charge disproportionation as well as the transition temperature increase with increasing anion size. In the case of the non-centrosymmetric anion ReO_4, the charge imbalance changes two times, once at the charge order transition at about 230 K and a second time at the anion transition at 157 K to +0.63 e. We ascribe that to the enhanced charge localization of the charge carriers due to the tetramerization triggered by the anion ordering. Furthermore, with increasing T_{CO} a crossover from a second to a first order transition occurs for the symmetric anions. Hence, we expect for the new member $TMTTF_2TaF_6$ of the Fabre salt family that the transition temperature will be significantly higher than 160 K and the transition of the first-order kind.

In literature it is controversially discussed, whether a spatial rearrangement of the anion acts as a precursor of the charge order phase transition. Clear evidence is still missing, as x-ray scattering experiments influence too much the charge order phase. Since molecular vibrations are sensitive to every change of the molecular environment as well as to any modification of the atomic bonds within the molecule, we have examined specific vibrational features, especially the infrared active modes of the anions in order to clarify this question. However, we could not observe any temperature-dependent modification of the ν_3 (t_{1u}) mode for the symmetric anions. Solely, for the ν_3 (t_2) mode of the ReO_4 anion, a change of the line width appears at the anion transition, simultaneously with the appearance of a second weak vibrational shoulder. In addition, we examined the temperature-dependence of the vibrational modes of the TMTTF molecule which contains the methyl end groups CH_3 that interact with the anions. Similar to the anion modes, no feature reveals a correlation with the charge order transition. The only modification which appears takes place above 200 K and is related to the thermal contraction of the sample, well-known for other organic systems.

In addition, we have examined the stacking direction (a-direction) of the TMTTF molecules. The corresponding spectra are dominated by the electronic excitations, superimposed by the emv-coupled vibrational modes. We could demonstrate that in the charge ordered phase overtones of strongly emv-coupled modes get activated. This can be attributed to the anharmonic molecular energy potential PES being enhanced by the unequal charge distribution. For the future studies these features can be used to record the charge order phase transition.

Moreover, in all the optical spectra a very broad and intense feature appears, which can be assigned to an electronic excitation across the Mott and charge order gap, i. e. a transfer of a charge carrier from one molecular site to the neighboring site. From the fits the resonance frequency as well as the plasma frequency of the electronic excitation were determined, yielding no modification at T_{CO} for the compounds with centro-symmetric anions. Additionally, the derived transfer integral t increases on cooling, since the intermolecular distance shrinks. From that it can be deduced that the next-nearest Coulomb repulsion V must vary stronger with temperature than t. In contrast, for ReO_4 the resonance

aas well as the plasma frequency for ReO_4 exhibit a strong jump at T_{AO} due to the first-order nature of the transition and the enlargement of the energy gap. However, only a small modification can be noticed at T_{CO}.

Besides the static optical study, also the reaction of the Fabre salts on electric fields and light pulses were examined. While no interesting effect on short electric pulses could be observed, $(TMTTF)_2SbF_6$ shows a temporal photoconductivity signal. While it overall decays within milliseconds after photo excitation, two further shorter time scales are detected in the microsecond range. Very interestingly, an oscillation is superimposed on top of the photocurrent, which contains several frequencies in the kHz regime that reveal a dependence on temperature. From a discourse of photoconductivity phenomena and current oscillations, we finally conclude that this is a new exotic effect which is attributed to the interaction of the excited single particles and the charge ordered state.

5.2 δ-(EDT-TTFCONME$_2$)$_2X$, X=BR AND ASF$_6$

The main goal of this study is to gain information about the organic non-dimerized and one-dimensional compounds δ-(EDT-TTF-CONMe$_2$)$_2X$, X=Br and AsF$_6$[26] by infrared spectroscopy and compare them in regard to the Fabre salts. Here, the focus is on the different coupling mechanism between the lattice and the intramolecular vibrations and the electronic system. Thereby, it is of great interest to know the charge disproportionation between the molecular sites in the unit cell as a function of temperature. Additionally, the question arises whether the structural transition can be observed in the infrared spectra and delivers further information about the interaction of the individual molecular fragments with the surrounding. Furthermore, in this chapter the infrared spectra of both compounds, which were measured in a temperature range from 300 K to 10 K as well as along all three crystallographic axes, are compared with the results of quantum chemical *ab initio* calculations covering band structure, optical spectra and normal mode analysis. The experimentally resolved vibrational modes are assigned by the help of theoretical calculated resonance frequency of the normal modes of the positively charged and neutral EDT-TTF-CONMe$_2$ molecule. Furthermore, the features appearing in the spectra along the stacking direction will be discussed and interpreted in detail on the basis of the optical conductivity regarding the electronic excitation and the emv-coupled modes. An extended part of the presented results have been published in the two publications [4] and [12] which are presented in Sec. 5.2.3.

5.2.1 *Physical properties*

[27]In the previous chapter 5.1.2 we have already seen and learned about the Fabre salts that the physical properties of low-dimensional compounds can be tuned by electron-electron-correlation: the on-site Coulomb repulsion U, the nearest-neighbor interaction V and by the transfer integral t. This consideration is valid for the present conductors as well. The ground state is defined by the two ratios U/t and V/t, and the band filling, and determine whether a metal-insulator transition MIT [26] occurs or not. In general, two main possibilities are known so that a MIT appears:

- the opening of a Mott-gap due to the localisation of the charge carriers which is triggered by a large ratio of U/t
- or due to an imbalance of the charge carriers on the different molecular or atomic sites leading to a so-called charged-ordered state because of a large V/t.

One of the best known and recently treated examples for an MIT are the Fabre salts, (TMTTF)$_2X$ (X=TaF$_6$, SbF$_6$, AsF$_6$, PF$_6$, ClO$_4$, Br, etc.). In Sec. 5.1.2 it was shown that upon cooling they undergo a transition from a dimerized and hence, half-filled phase to an insulating charge-ordered phase. A profound understanding of the driving force of the charge order could stimulate the development and synthesis of new chemical compounds and hence, the design of new molecular

26 The abbreviations EDT$_2$AsF$_6$ and EDT$_2$Br for δ-(EDT-TTF-CONMe$_2$)$_2$AsF$_6$ and, respectively δ-(EDT-TTF-CONMe$_2$)$_2$Br are used in the text.

27 Passages in the following paragraph are analogously quoted from the publication [5].

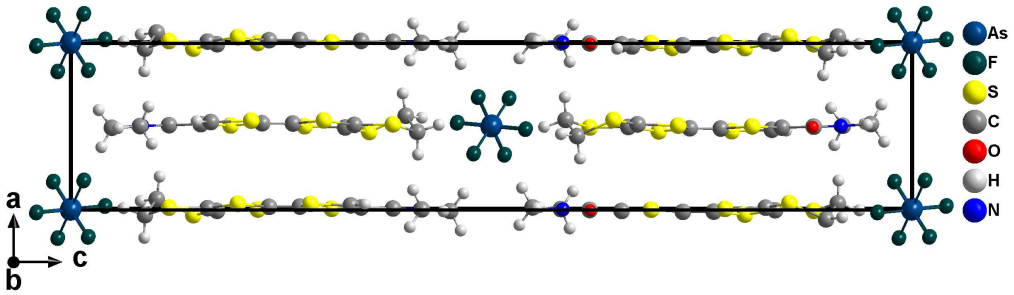

Figure 5.39: Crystal structure of δ-(EDT-TTF-CONMe$_2$)$_2$AsF$_6$ with viewing direction along the b-direction. The distance between the individual EDT-TTF-CONMe$_2$ molecules is constant.

electronic circuits. An often controversially discussed topic is the question, if the dimerization of the molecules along the stacking direction positively influences or destabilizes the charge order [172, 234, 235]. Therefore, it is of great interest to examine perfect quarter-filled materials without any dimerization and hence any Umklapp scattering process. In 2003, the materials δ-[(EDT-TTF)-CONMe$_2$]$_2$AsF$_6$ and δ-(EDT-TTF-CONMe$_2$)$_2$Br were synthesized in the group of P. Batail [236, 237]. These compounds δ-(EDT-TTF-CONMe$_2$)$_2X$, X=Br and AsF$_6$ undergo a second-order structural transition from the space group P_{2nn} to the $P2_1/a$ monoclinic crystal structure at 190 K, which is additionally twinned [237]. In Fig. 5.39 the unit cell of EDT$_2$AsF$_6$ is depicted with viewing direction along the b-axis. One EDT-TTF-CONMe$_2$ molecule resides on a crystal site with a four times multiplicity. The EDT-TTF-CONMe$_2$ molecules in Fig. 5.43 have exactly the same distance from each other along the stacking direction. At room temperature the methyl- und ethylene end groups are strongly disordered (not shown here) [237]. The disorder reduces with decreasing temperature. In the unit cell each molecular site carries a half of a hole leading in total to a full and a quarter-filled band. C^{13} NMR and x-ray diffraction experiments [237, 238] demonstrate a charge-ordered state at RT in both materials. From the NMR spin-lattice relaxation rate the derived charge imbalance is 0.8 e between two adjacent molecules. Furthermore, the charge alternates along all three crystal axes. It was verified that the charge disproportionation of both materials exists down to 10 K and probably also in the AFM phase. This observation explains the insulating behavior observed in the transport measurements.

Instead of applying hydrostatic pressure the AsF$_6$ anion can be substituted by a Br atom which is equivalent to applying a pressure of about 7 kbar [238]. In Fig. 5.40 the unified p-T phase diagram is displayed which was constructed out of pressure-dependent NMR and transport data. It reveals striking similarities to the well-studied phase diagram (see Fig. 5.3) of the (TMTTF)$_2X$ (X = TaF$_6$, SbF$_6$, AsF$_6$, PF$_6$, Br and ClO$_4$ with M = S or Se) family which is shown in Sec. 5.1.2 [239]. EDT$_2$AsF$_6$ resides on the left side of the graph at -7 kbar which is already deep in the CO-Phase at RT and by cooling an AFM transition occurs at about 10 K. The situation is similar for EDT$_2$Br which is already charge-ordered at RT with an additional AFM phase at low temperatures. With increasing pressure the

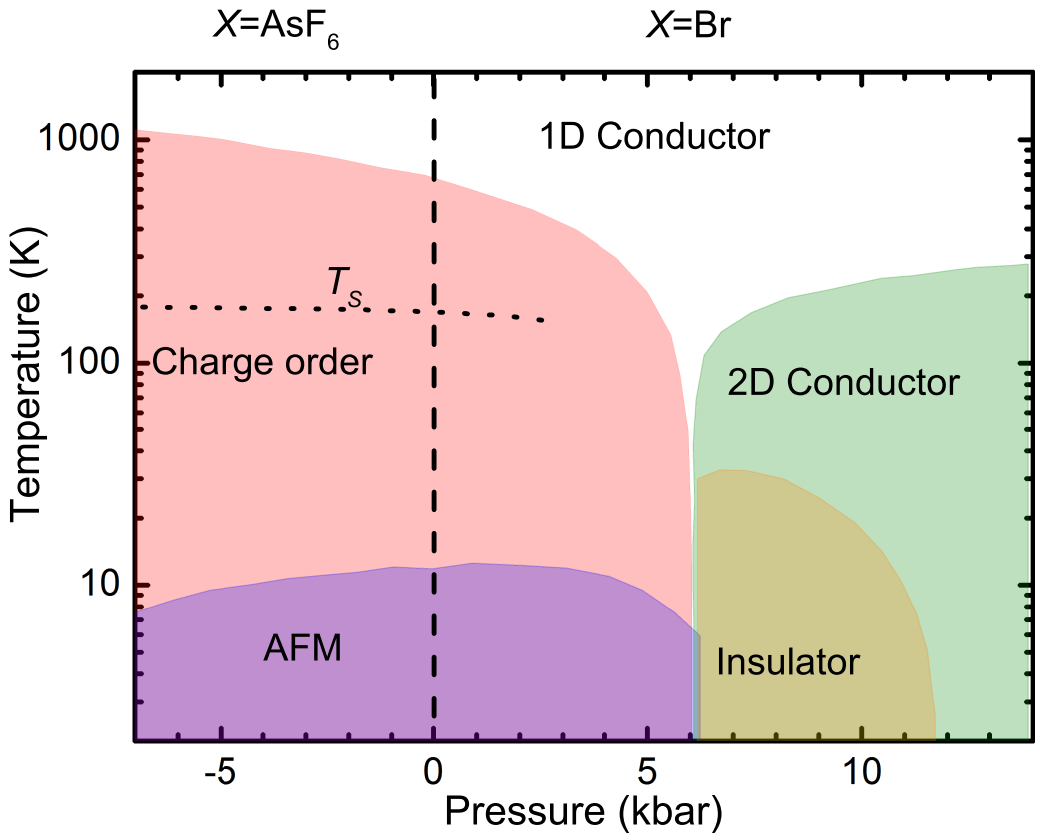

Figure 5.40: p-T phase diagram of EDT_2AsF_6 and EDT_2Br. At normal conditions both compounds are in the CO state. The ground state is antiferromagnetic. With increasing pressure the CO is suppressed and a transition in a two-dimensional metal occurs revealing an insulating state at low temperatures which vanishes above a pressure of 12 kbar.

transition temperature of the CO phase decreases within 4 kbar till 6 kbar very fast and vanishes in the case of EDT_2Br at a pressure of 6 kbar completely. From the measurements of the DC conductivity along the b-direction can be concluded that a crossover from a one-dimensional to a two-dimensional metal takes place, exhibiting a T^2 Fermi-liquid behavior of the conductivity. At lower temperatures at around 30 K a transition into a Peierls-like insulating states appears which is suppressed above a pressure of $P = 12$ kbar. At higher pressures, in contrast to the Fabre or Bechgaard salts, no superconducting state was observed.

5.2.2 *Ab initio calculations: band structure, optical spectra and normal modes*

Parallel to the experimental measurements theoretical calculations of the band structure, the optical spectra, and the molecular vibrations were performed. For the band structure as well as for the optical spectra PBE-functionals [130] in connection with norm-conserving pseudopotentials were used. The cutoff energy of the wave function was set to 40 Ry whereas the cutoff energy of the electron density was 160 Ry. For the self-consisting calculation a 8x8x4 large Monkhorst grid[142] was applied. As the DFT calculations do not take into account any correlation effects, the compounds were treated as metals. Therefore, a smearing value of 0.005 Ry was used. This is also the reason why no band gap can be observed as the Mott energy gap bases on electron-electron

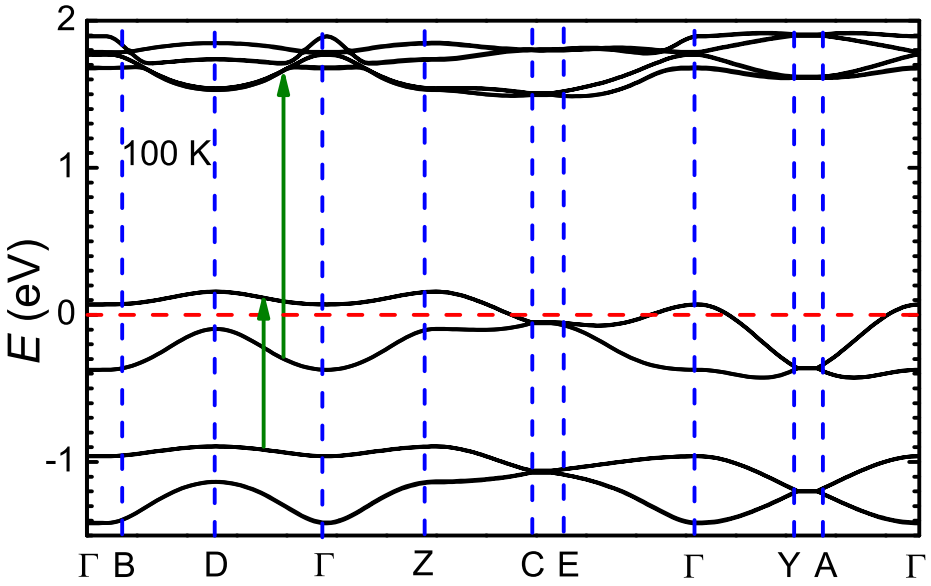

Figure 5.41: Band structure of δ-(EDT-TTF-CONMe$_2$)$_2$AsF$_6$ between -1.5 eV and 2.0 eV along the k path: $\Gamma\,(0,0,0) \rightarrow B\,(0,0,0.5) \rightarrow D\,(0,0.5,0.5) \rightarrow \Gamma(0,0,0) \rightarrow Z\,(0,0.5,0) \rightarrow C\,(0.5,0.5,0) \rightarrow E\,(0.5,0.5,0.5) \rightarrow \Gamma(0,0,0) \rightarrow Y\,(0.5,0,0) \rightarrow A\,(0.5,0,0.5) \rightarrow \Gamma(0,0,0)$. The two bands at the Fermi energy are quarter-filled in the whole. Due to the intersection of the Fermi energy the compound exhibits strong anisotropic band structure. The vertical green arrows exemplary mark the different transition.

correlation. The band structure in Fig. 5.41 were calculated for the monoclinic crystal structure of EDT$_2$AsF$_6$ [237] at a temperature of 150 K along the k-path: $\Gamma \rightarrow B \rightarrow D \rightarrow \Gamma \rightarrow Z \rightarrow C \rightarrow E \rightarrow \Gamma \rightarrow Y \rightarrow A \rightarrow \Gamma$. The nomenclature of the k points complies with the definition suggested in Ref. [240] of the monoclinic space group which is in opposite to the chosen labeling in Ref. [237] of the orthorhombic phase with the space group P_{2nn}. The band structure consists of four filled bands due to the fact that there are four molecules in the unit cell. The systems are one-dimensional and the EDT-TTFCONMe$_2$ molecules are separated along the c-direction which leads to the case that there are two completely bands at around -1 eV and one completely as well as one half-filled HOMO band close to the Fermi surface. Therefore, only the two bands close to the Fermi energy have to be considered. The band dispersion is different from the band structure of the Fabre salts which is shown in Sec. 5.1.3 because there, the two bands in the whole are half-filled due to the dimerization[28]. In the case of EDT$_2$AsF$_6$ there is no dimerization gap present because of the equal stacking. This is reflected in the degeneracy of the bands at some high symmetric points [25] and therefore, regarding the two bands as one band it is a pure quarter-filled system. The largest dispersion appears along the $\Gamma \rightarrow Y$ path which is along the stacking direction (a-direction), in which the π-orbital overlap is the strongest and intersects the Fermi energy. Along the b-direction the band is unoccupied and does not cut the Fermi energy. Indeed, the E_F is intersected along the $Z \rightarrow C \rightarrow E \rightarrow \Gamma$ path meaning that the Fermi surface is distorted along the b- and c-direction and the system is quasi one-dimensional. The distance of the bands at the Γ point is 440 meV and agrees with the results of 423 meV of the Hückel calculations from Ref. [237]. The bandwidth between the Z point and

28 As a reminder: the lower band is completely filled whereas the upper band is half-filled.

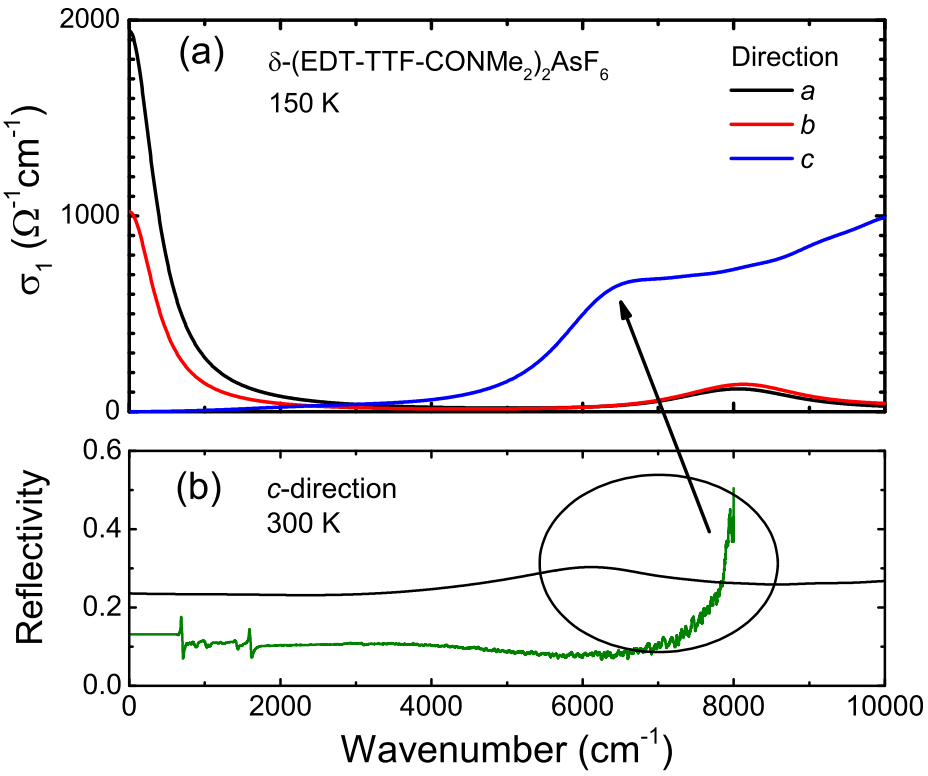

Figure 5.42: (a) Calculated optical conductivtiy $\sigma_1(\nu)$ of EDT_2AsF_6 along all three crystallographic directions from 0 cm^{-1} to 10000 cm^{-1} at 150 K. EDT_2AsF_6 should be a two-dimensional conductor according to the calculation since for the a- and b-direction a Drude-like behavior exists at low frequencies. The c-direction is dominated by interband transitions at above 6000 cm^{-1}. (b) Reflectivity of EDT_2AsF_6 measured along the c-direction up to 8000 cm^{-1}. Above 7000 cm^{-1} the reflectivity sharply increases from 0.1 to 0.4 indicating the onset of an interband transition. The simulated reflectivity spectrum (black solid line) resembles this behavior with the resonance centered at about 6000 cm^{-1}.

the Γ point is about 266 meV for the lower band and 87 meV for the upper band. Since the next occupied bands are located at -1 eV the first interband transition can be expected to occur at about 8000 cm^{-1}. The next highest excitation is from the highest occupied band to the LUMO at 1.7 eV. These transitions also include the excitation between the cation and the anion as known from the Fabre salts (see Sec. 5.1.3).

OPTICAL SPECTRA In Fig. 5.42 (a) the optical conductivity of EDT_2AsF_6 is illustrated for all three crystallographic axes in the frequency range from 0 cm^{-1} und 10000 cm^{-1}. For the calculations the aforementioned parameters from the previous calculation of the band structure were used. The sampling of the k-space results from 200 equally distributed k points. The interband transitions were broadened with a Lorentz function with a width of 1600 cm^{-1} while the free carriers (Drude) experience a broadening of 400 cm^{-1}. Due to the band structure the a- and b-direction reveal a Drude- and herewith, a metallic behavior at low frequencies. Due to the anion layer the EDT-TTF-$CONMe_2$ are spatially separated along the c-direction whereby the molecular orbitals do not overlap leading to an insulating behavior and hence, to the very low conductivity below 2000 cm^{-1}. The anisotropy in the resistivity for $\nu \rightarrow 0\,cm^{-1}$ between

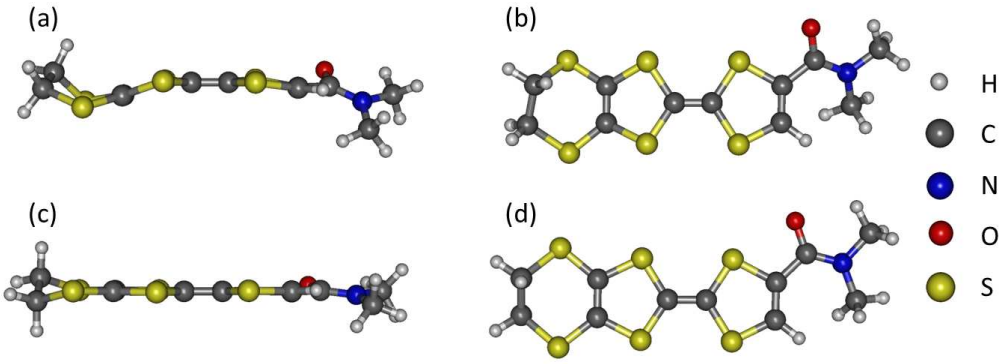

Figure 5.43: (a) The neutral EDT-TTF-CONMe$_2$ molecule reveals a bended S-like structure. (b) The corresponding top view shows a slightly deformed ring system. (c) In contrast the positive charged EDT-TTF-CONMe$_2$ is flat from the side whereas from the top the molecular structure is less distorted (d). Adapted from Peterseim et al. [4].

the a- and b-direction is about 1:2 and for a and c 1:40000. In comparison to that transport measurements reveal an anisotropy ratio of about 1:10000 between the a-direction and the b- and c-direction. To remind, the calculation does not take into account any correlation effects and hence, the CO phase is not considered. From the experimental data it is obvious that all directions are insulating due to the CO gap. At higher energies several distinct interband transitions appear in all spectra which are located above 6000 cm^{-1}. They can be assigned to the excitation from HOMO-1 to LUMO. The excitation is the strongest in the c-direction. Therefore, in Fig. 5.42 (b) the measured reflectivity for $E \parallel c$ is depicted in comparison to the theoretical spectra in which an increase of the reflectivity can be observed above 6000 cm^{-1}. A measurement error due to a poor polarization of the infrared light can be excluded and the measurement of the perpendicular direction does not reveal any increase of the signal in this range. Furthermore, other measurements with the same setup and with other organic compounds do not show such an increase of the reflectivity. From the calculation it can be deduced that for an accurate KKT the examined frequency range has to be extended not only to low frequencies, for instance to the far and far-far infrared range, but also to the frequency range above 8000 cm^{-1}(1 eV) up to the VIS or UV region.

VIBRATIONS [29]One can take from Fig. 5.42 (b) that the electronic excitations below 3500 cm^{-1}are enriched by further excitations. Similar to the Fabre salts these features can solely be assigned to the intramolecular vibrational modes. To perform a precise assignment of the individual modes and to draw conclusions from various interactions, DFT calculations have been conducted, which are described in Sec. 4.5.2, to calculate the normal modes of the EDT-TTF-CONMe$_2$ molecule for the positive and neutral charged state. Therefore, the software package Gamess-US [123, 124] was used. For the optimization of the structure and determination of the vibrational modes the molecule structure from the published x-ray data [237] was extracted. In Fig. 5.43 the EDT-TTF-CONMe$_2$ molecules are displayed which reveal no symmetry wherefore the C_1 symmetry was used for the calculation. That is why all 84 molecular vibrations are infrared- and Raman-active simultaneously. The well-established standard functional B3LPY

29 Passages in the following paragraph are analogously quoted from the publication [4].

[132] together with the 6-31G(d) basis set were applied for the optimization and the subsequent calculation of the normal modes. No negative resonance frequencies were found proofing that the equilibrium state was determined. For a better comparison of the theoretical determined resonance frequencies with the experimental ones they have been multiplied by two different scaling factors: for modes above 1300 cm^{-1} a factor of 0.9679 was applied and for lower frequencies a value of 1.01[30]. Previous calculations, for example in Sec. 5.1.3 and in Ref. [2, 210], have shown that the scaling factors for the used basis set deliver a good agreement with the experimental values (see Fig. 5.44). The resonance frequencies and intensities are summarized in Tab. A.2.

Fig. 5.43 shows the two equilibrium geometries of the cation and the neutral EDT-TTF-$CONMe_2$ molecule. In the case of the neutral molecule (see Fig. 5.43 (a) and (c)) the structure has almost an S-shape and is strongly distorted. In contrast, the structure of the cation is planar. This effect was also demonstrated in our calculations of the equilibrium molecule structure of the TMTTF molecule, which supports previous observations of other organic molecules, for instance BEDT-TTF [180], and DMTTF [178, 179, 180, 202]. Since the charge per molecule in the crystal is +0.5 e due to the charge transfer between the cation and the anion, it is assumed that the molecular structure resides between the boat and flat state and should be slightly bended. Going one step further it was also implied that the bended shape of the molecule body plays an important role on the charge transport and on the superconductivity on the basis of electron-phonon-coupling.[180]

A distance of 1.350 Å and 1.391 Å for the inner C=C double bonds was determined for the neutral molecule and the cation, respectively, which is almost in perfect accordance with the experimental x-ray data of 1.354 and 1.392 Å [237]. The difference in bond lengths confirms the enormous charge disproportionation of 9:1. Furthermore, the x-ray measurements [237] for both compounds show that the CH_2 and CH_3 endgroups of the EDT-TTF-$CONMe_2$ molecules capture at room temperature two different molecular arrangements. From the calculation one knows that the structure of the two different charged states differs extremely in the methyl groups (see Fig. 5.43 (a) and (c)). Therefore, this could be an additional hint of the presence of a CO phase at room temperature because the cation and the neutral molecule alter in the unit cell which cannot be really resolved by the scattering experiments. This is especially enhanced at room temperature as there is still enough space in the molecule cavity to capture two positions. At lower temperatures the unit cell volume shrinks and hence, the molecule is forced to capture an average configuration. Similar observations could not be made in other systems like $TMTTF_2X$ or α-$(BEDT\text{-}TTF)_2I_3$ which have a charge-ordered state as well, occurring at much lower temperatures. Note, the effect is not a simple thermal fluctuation phenomena of the individual atoms around their atomic position in the molecule which in general occurs quite often at elevated temperatures.

30 These parameters were derived for the triplet basis set 6-311+G(d,p) [137] which is closely related to the applied one in this thesis.

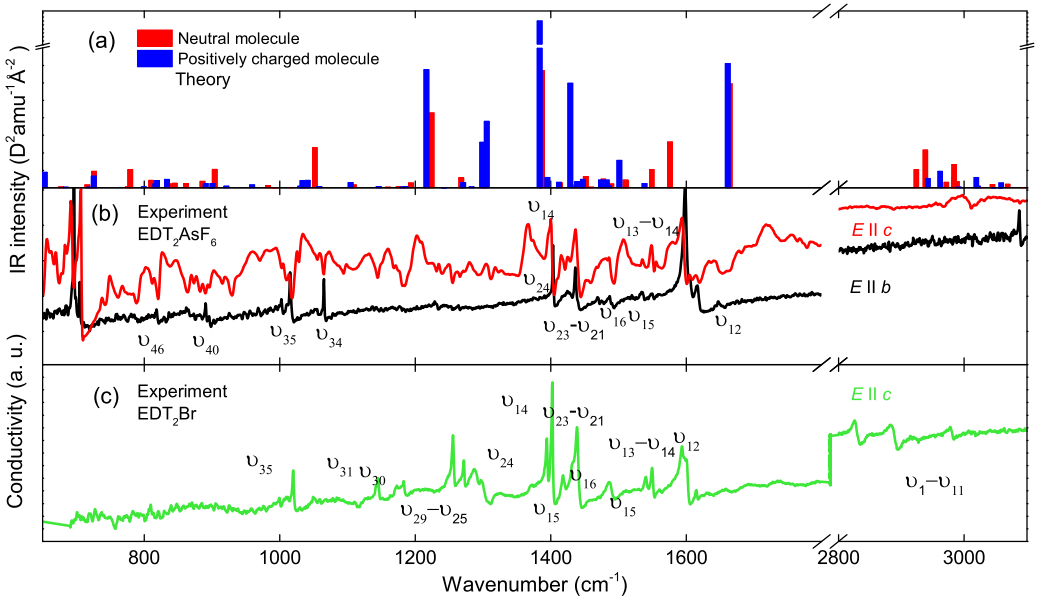

Figure 5.44: (a) Calculated resonance frequency and infrared intensity of the normal modes of the positively charged (blue bars) and neutral (red bars) EDT-TTFCONMe$_2$ molecule. (b) The optical conductivity of EDT$_2$AsF$_6$ for $E \parallel c$ at $T = 12$ K (red curve) and $E \parallel b$ at 8 K (black curve). (c) illustrates the optical conductivity of EDT$_2$Br along the crystallographic c-axis at 10 K (green curve). Published in [4].

5.2.3 *Infrared measurements*

[31]Since the maximal overlap of the molecular orbitals of the EDT-TTF-CONMe$_2$ occurs along the a-direction, the spectra with $\vec{E}_{IR} \parallel a$ mainly provide information about the electronic excitation [12]. This is reflected in the broad features and the high optical conductivity of both materials which is depicted in Fig. 5.47. In comparison to the a-direction the reflectivity and optical conductivity spectra of the b- and c-direction confirm the one-dimensionality of these compounds. Similar to the TMTTF$_2X$ family in Sec. 5.1.4 the spectra provide information about the molecular vibrations, the charge imbalance and the interaction of the molecules with its surrounding. In Fig. 5.44 the low conducting spectra of EDT$_2$AsF$_6$ for $\vec{E}_{IR} \parallel c$ and b and the spectrum of EDT$_2$Br along the c-axis are compared with each other. In general, for the KKT the reflectivity data of the b- and c-direction were extrapolated for $\nu \to 0$ cm^{-1} with a constant value as the compounds are insulating for the studied temperatures. For the high frequency part a ω^{-4} function up to 500000 cm^{-1}were applied for the extrapolation. We have compared the theoretical intensity and resonance frequency of the cation and the neutral EDT-TTFCONMe$_2$ molecules in (a) with the experimentally determined vibrational features in Fig. 5.44 (b) and (c). The theoretical intensity and fundamental frequency are in good accordance with the detected values within the error bars of the calculation. In Tab. A.2 of the Appx. A all frequencies and intensities are listed up. Concerning the labeling of the modes in all following sections it is referred to this table. One of the strongest modes is the ν_{12} vibration at about 1600 cm^{-1}. It contains the stretching of the C=O bond. It reveals a splitting of 6 cm^{-1} for EDT$_2$AsF$_6$ and 8 cm^{-1} for EDT$_2$Br appearing below 100 K for both compounds. The splitting is caused by the charge disproportionation between

31 The following section is correspondingly quoted from the following publication [4].

two different cation sites. At higher temperatures it cannot be detected because of the broad line width of about 9 cm^{-1}.

When vibrations contain the C=C double bonds, they are very sensitive to the molecular charge. As it was mentioned in Sec. 5.1.6 a linear relation between the charge and the resonance frequency can be assumed which holds for several materials such as the TTF molecule [241], TMTTF [2, 177] or BEDT-TTF [19]. As soon as the modes are emv-coupled, this assumption breaks down [193, 242]. The calculations reveal several modes obeying a clear frequency shift as soon as the charge of the (EDT-TTF)-$CONMe_2$ molecules varies. According to the calculation, the ν_{13}, ν_{14}, and ν_{15} modes experience a shift to lower frequencies of about 40, 165 and 82 cm^{-1} if the charge is reduced from the neutral to cationic state. By tracing the resonance frequency of the ν_{14} and ν_{15} modes, the charge imbalance between the two neighboring molecules can be determined. The resonance frequency was determined by fitting all vibrational features with several Fano functions (see Appx. F). Although in the b- and c-direction no strong electronic background is present, the features exhibit a slight asymmetric shape indicating a weak coupling. The derived charge imbalance is about 0.8 and 0.82 e for EDT_2AsF_6 and respectively, 0.82 as well as 0.75 e for EDT_2Br. The difference between the individual values is caused by the weak coupling of the vibrations to the electronic background (emv) leading to a deviation from the linear relation between molecular charge and resonance frequency. The ν_{15} mode reacts sensitive to thermal variations since the mode contains the bending H-C-H bonding of the methyl group. They form a molecular cavity around the anion whose volume diminishes on cooling. Nevertheless, the outcome is in excellent accordance with previous NMR experiments [237]. They estimate that the charge disproportion is 0.8 e. Furthermore, we cannot observe any temperature-dependent charge redistribution at all temperatures below 300 K and hence, confirming the phase diagram. The spectrum of the c-direction of EDT_2AsF_6 shows a high SNR, as depicted in Fig. 5.44. It is caused by the low reflectivity and the small thickness of the sample. Therefore, the backside of the sample backscatters the incident light which interferes with the reflected light from the top surface. This leads to the inference pattern in the spectrum.

Temperature-dependent optical conductivity and reflectivity of b- and c-direction

[32]As aforementioned, most of the vibrational modes shift to higher frequencies and their line width narrows upon cooling. The ν_{15} and ν_{21} modes undergo the largest temperature-dependent shift. These vibrations contain the bending of H-C-H bonds, as partly stated in the previous paragraph. The optical conductivity of EDT_2AsF_6 and EDT_2Br along the c-direction is displayed for various modes and different temperatures in Fig. 5.45. The modes undergo a clear shift upon cooling. To analyze qualitatively the slightly asymmetric resonances, the spectra were fitted for all measured temperatures with Fano functions (see Sec. F), because we assume a weak coupling to the electronic background. The ν_{15}, ν_{21}, ν_{22}, and ν_{23} modes are presented in Fig. 5.46. The ν_{21} mode resides at 1430 cm^{-1} in the case of EDT_2AsF_6 and at 1434 cm^{-1} for EDT_2Br at room temperature. Cooling leads to a blue shift of this mode of about 8 cm^{-1} for EDT_2AsF_6 and 6 cm^{-1} for EDT_2Br respectively. The ν_{15} mode reveals the same behavior

32 The following section is correspondingly quoted from the following publication [4].

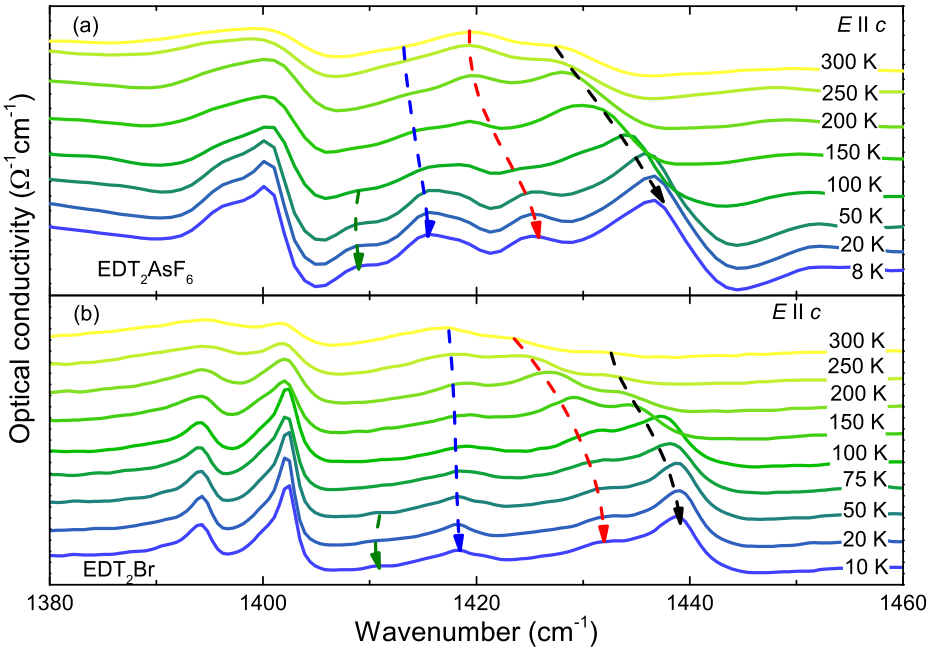

Figure 5.45: (a) and (b) shows the optical conductivity of EDT_2AsF_6 and EDT_2Br in the spectral range from 1380 cm^{-1} to 1450 cm^{-1} for temperatures between 300 K and 8 K for $E \parallel c$. The ν_{21} and ν_{15} mode (black and red arrow) reveal a blue shift to higher energies and becomes narrower for both materials. In contrast the ν_{22} mode (blue arrow) undergoes only a small modification. The ν_{23} mode (green arrow) appears solely below $T = 50$ K. For clarification we have shifted the spectra by constant values. Published in [4].

and is located at 1421 cm^{-1} for EDT_2AsF_6 and 1425 cm^{-1} for EDT_2Br with a total shift of 5 cm^{-1} and 9 cm^{-1}, respectively.

As mentioned at the beginning of this chapter, the compounds exhibit a structural transition at $T_S = 190$ K [237]. The unit cell parameter γ continuously changes between 190 K and 120 K. In the case of EDT_2AsF_6 only the structure data in the monoclinic phase at 100 k are available. However, for EDT_2AsF_6 ESR experiments indicate a structural transition since a modification of the line width and the spin susceptibility at $T_S \approx 190$ K were observed. As soon as the transition sets in, the resonance frequencies shift to higher energies below 200 K and asymptotically approach a constant value below 100 K. These observations demonstrate that the structural phase transition influences the cavity of the anion and hence, the ethyl- and methyl groups of the cation which becomes noticeable in the modification of the resonance frequency. Structural examinations of the bond length and bond angles of the cation support this interpretation as they demonstrate that the distance of C_{Me}-H $\cdots$ Br (see therefore Fig. 5.46 (b)) and the angle between the individual molecular fragments C_{Me}-H $\cdots$ Br changes below the transition [237]. One can conclude from the collected data that both compounds reveal a structural phase transition below 200 K.

OPTICAL MEASUREMENTS OF THE STACKING DIRECTION

[33]The temperature-dependent optical conductivity of EDT_2AsF_6 and EDT_2Br for the stacking-direction is illustrated in Fig. 5.47 (a) and (b). Since both com-

33 The following section is correspondingly quoted from the following publications [4] and [12].

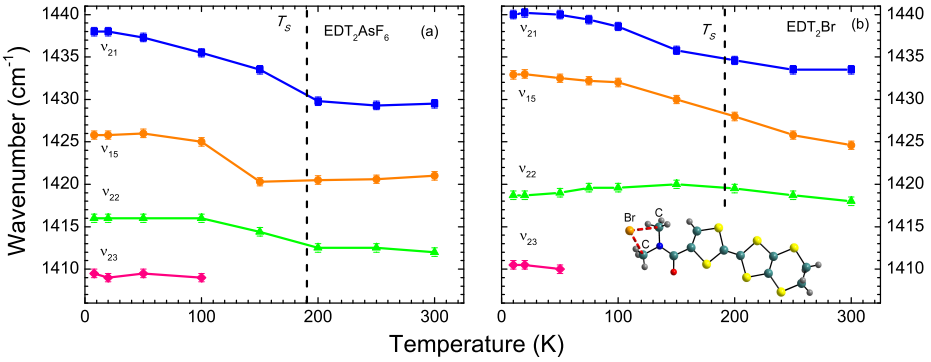

Figure 5.46: The resonance frequency of the ν_{21} (blue), ν_{15} (orange), ν_{22} (green), and ν_{23} (purple) modes is plotted as a function of temperature between 300 K and 10 K. All modes undergo a strong blue shift below the structural transition at T_S= 190 K. The EDT-TTFCONMe$_2$ molecule with the Br anion is illustrated in (b). The red dashed line reflects the connecting line between the methyl end group of the EDT-TTFCONMe$_2$ molecule and the atomic anion. Published in [4].

pounds are insulating along the stacking direction a constant extrapolation for the KKT was applied for the low frequency part whereas at about 6000 cm^{-1}a function with ω^{-2} was used up to 500000 cm^{-1}. For EDT$_2$AsF$_6$ two narrow and strong maxima can be observed at all temperatures at 699 and 719 cm^{-1}(tagged by the hearts in Fig. 5.47). Next to them several side maxima can be found at 696 and 712 cm^{-1}. The peak at 699 cm^{-1}corresponds to the resonance frequency of the odd $\nu_3(t_{1u})$ mode of the AsF_6^- anion whose resonance is typically found at 700 cm^{-1}in the gaseous phase [185]. In accordance with the Fabre salts from Sec. 5.1.1, the ν_3 mode becomes nondegenerated due to the Wyckoff position with the symmetry C_1 which breaks up the single vibrational resonance into different spectral features. Similar to the Fabre salts, no modification of the features could be detected on cooling. The peak at 719 cm^{-1} in EDT$_2$AsF$_6$ is assigned to the ν_{48} out-of plane O-C-C bending mode since it appears at 714 cm^{-1} in EDT$_2$Br as well and can therefore not be ascribed to any anion mode.

In Fig. 5.47 several dip-like patterns can be observed and are marked by the vertical lines. These characteristics were already observed in the previous chapter 5.1.4 in the optical spectrum of the Fabre salts in the charge ordered state. Similar observations were made in α-(BEDT-TTF)$_2$I$_3$ [192] (see Sec. 5.4.2).

Especially the origin of the antisymmetric modes, located at 1890 cm^{-1} and at 2880 cm^{-1} is not clear which is similar to the situation in the Fabre salts (see Sec. 5.1.4). Based on the model of Yamamoto et al. [194] which was explained in detail in Sec. 5.1.4 the ratio of the two parameters

$$A_{CT} = \left| \frac{g g^{(2)} \delta n_{eg}^2}{\sqrt{2} E_{eg}} \right| \text{ and } A_{CD} = \left| \frac{g^3 \delta n_{eg}^2 \delta \rho}{\sqrt{2} E_{eg}^2} \right| \tag{5.17}$$

was calculated and displayed in Fig. 5.47. For the calculation of the ratio A_{CD}/A_{CT}, emv-coupling constant of the ν_3 (a_g) mode of the BEDT-TTF molecule g_i = 132 meV [198] was used since the dimension of both molecule matches. This is a good approximation for the modes containing C=C double bonds and originating from the TTF molecule. One knows from Sec. 5.1.4 that the g_i values

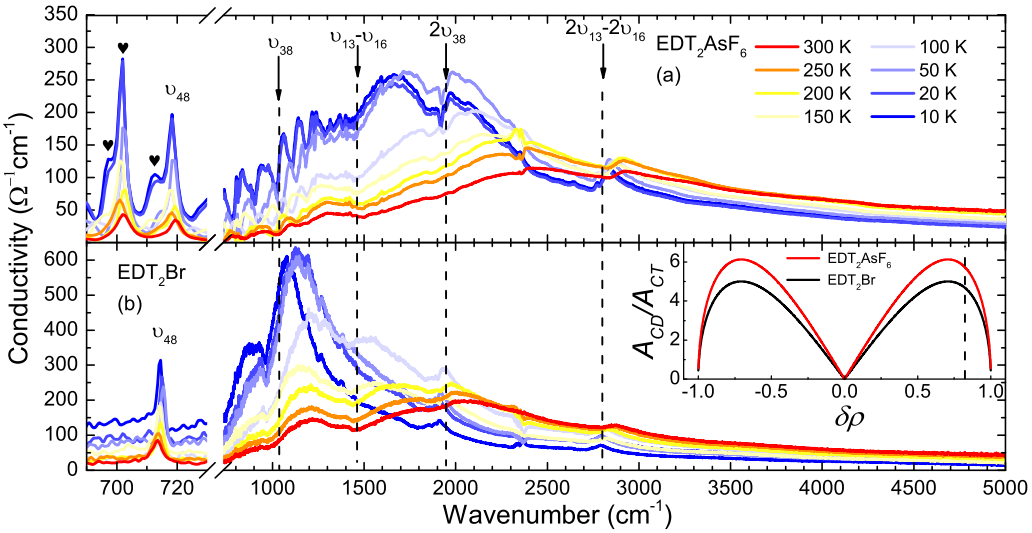

Figure 5.47: Temperature evolution of the optical conductivity of EDT_2AsF_6 (a) and EDT_2Br (b) along the a-direction from 300 K to 10 K. The features at 702 cm^{-1} (black hearts) are ascribed to the ν_3 (t_{1u}) mode of the AsF_6 anion whose degeneracy is lifted due the crystal symmetry. The inset in (b) displays the ratio between A_{CD} and A_{CT} coefficient as a function of $\delta\rho$ for both compounds (EDT_2AsF_6 (red) and EDT_2Br (black)) derived from Eq. 5.17. The dashed lines highlight the fundamental modes and their corresponding first overtones. Published in [4].

for TTF-based molecules are very similar.[34] The quadratic coupling constant g_2 was derived from Eq. 5.12 presented in Sec. 5.1.4.

The energy gap E_{eg} is related to the transfer integral t along the stacking direction which was determined by the Hückel method: 87 meV for EDT_2Br at 150 K [237] and 71 meV in the case of EDT_2AsF_6 at 300 K [236]. In the lower panel of Fig. 5.47 the ratio A_{CD}/A_{CT} of both materials is displayed for different charge imbalance $\delta\rho$ values. A_{CD} dominates for $\delta\rho$ above 0.1 e. The charge disproportionation is $\delta\rho \approx 0.8e$ for both examined compounds, so that A_{CD}/A_{CT} almost reaches the maximum. Therefore, the spectral antiresonances solely appear because of the unequally distributed molecular charge.

By that finding and the theoretical calculation presented in Sec. 5.2.2, the experimentally observed overtones can be assigned to their fundamental modes. The dip at 1970 cm^{-1} is related to the ν_{38} mode located at 970 cm^{-1} (experiment) and 992 cm^{-1} (calculation), respectively. Furthermore, the feature residing at 2900 cm^{-1} correlates with the overtones of the ν_{13}, ν_{14}, ν_{15}, and ν_{16} modes[35]. In the embedded graph of Fig. 5.48 one can trace very well the modification of the coupling constant q of the modes ν_{13} - ν_{16} which is caused by the strong shift of the mid-infrared band upon cooling. The coupling constant is a measure for the symmetry of the resonance. The sign indicates the position of the emv-coupling modes referring to the broad mid-infrared band. Such a strong modification of the sign has never been observed before.

The strong temperature-dependent evolution of the mid-infrared band and its physical meaning and causes will be discussed in the following paragraph. In Fig. 5.47 the maximum of the electronic transition in both compounds shifts

34 g_i weakly changes with increasing molecule size: from 117 meV for TTF [197] to 120 meV for TMTTF [191] and 132 meV for BEDT-TTF [198].

35 The calculated resonance frequencies of the corresponding modes are 1576 cm^{-1}, 1549 cm^{-1}, 1511 cm^{-1} and 1511 cm^{-1} for the uncharged molecule).

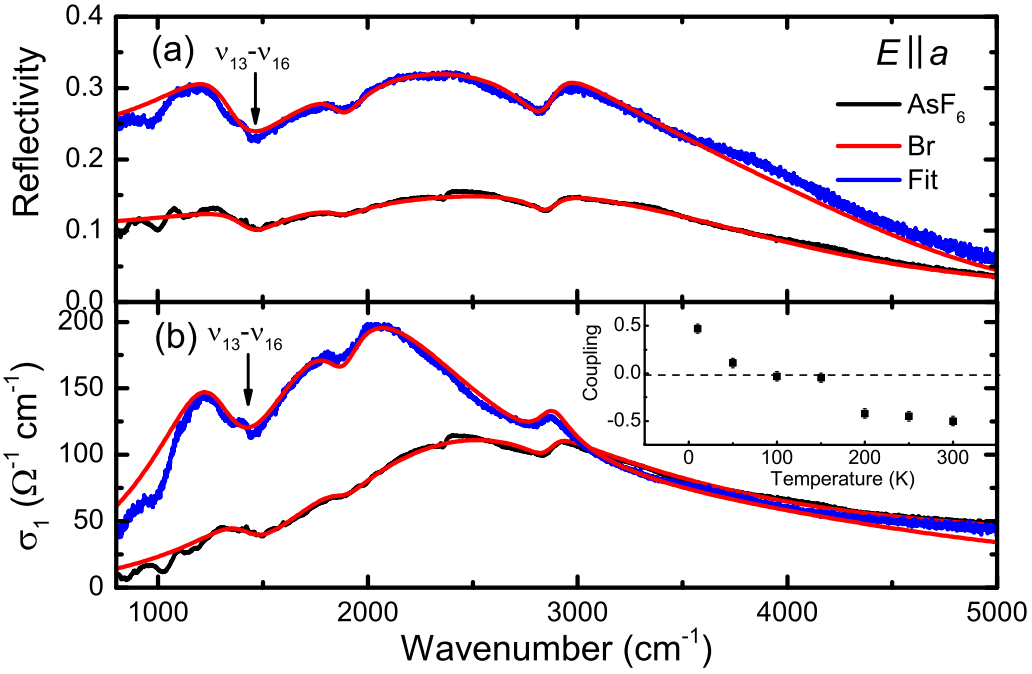

Figure 5.48: (a) Reflectivity of EDT_2AsF_6 (black) and EDT_2Br (blue) at RT in comparison to the fitted reflectivity (red) between 800 $cm^{-1}$and 5000 cm^{-1}. (b) Kramers-Kronig consistent optical conductivity $\sigma_1(\nu)$ of EDT_2AsF_6 (black) and EDT_2Br (blue) derived from the reflectivity data in (a). The inset shows the coupling parameter q of the ν_{13} - ν_{16} modes as a function of temperature for EDT_2Br.

towards lower frequencies with decreasing temperature. Similar temperature-dependent effects can be observed in other one-dimensional charge-ordered organic conductors, however not as extreme. In the case of the dimerized Fabre salts the electronic excitation undergoes a red shift with decreasing temperature. A similar effect occurs in the $(DI\text{-}DCNQI)_2Ag$[243] salt, but the shift is weaker. However, in $(EDO\text{-}TTF)_2PF_6$ [244] this feature shifts to higher energies.

In the considered salts the distance between the molecules along the stacking direction alters under cooling and correlates with the shift of the maximum. The reflectivity and optical conductivity data can be fitted by a single Lorentz function for the mid-infrared band and three Fano functions for the emv-coupled modes depicted in Fig. 5.48. The position of the mid-infrared band is plotted as a function of temperature in Fig. 5.49. For EDT_2AsF_6 and EDT_2Br the maximum linearly decreases with the temperature. To understand this trend the underlying physics must be understood. In a simple picture this band corresponds to an excitation of a charge transfer between a charge-rich and charge-poor molecular site. In 2006 Mayr and Horsch [245] suggested another explanation for the optical excitation. They assumed in their model that in a one-dimensional quarter-filled system in the charge-ordered state a pair of domain walls can be excited as it is depicted in the inset of Fig.5.50 (a). They examined the optical conductivity as a function of temperature and the ratio of t/V.

$\sigma_1(\nu)$ is presented for t/V =0.02 and 0.05 in Fig. 5.50. For a ratio of t/V =0.02 a broad band appears at $\nu/V = 0.04$ which corresponds to the excitation of the domain walls (DW). Below the band a sharp excitonic excitation can be observed which disappears with increasing t/V. Simultaneously, the maximum shifts to lower energies and becomes more asymmetric. As the nearest-neighbor

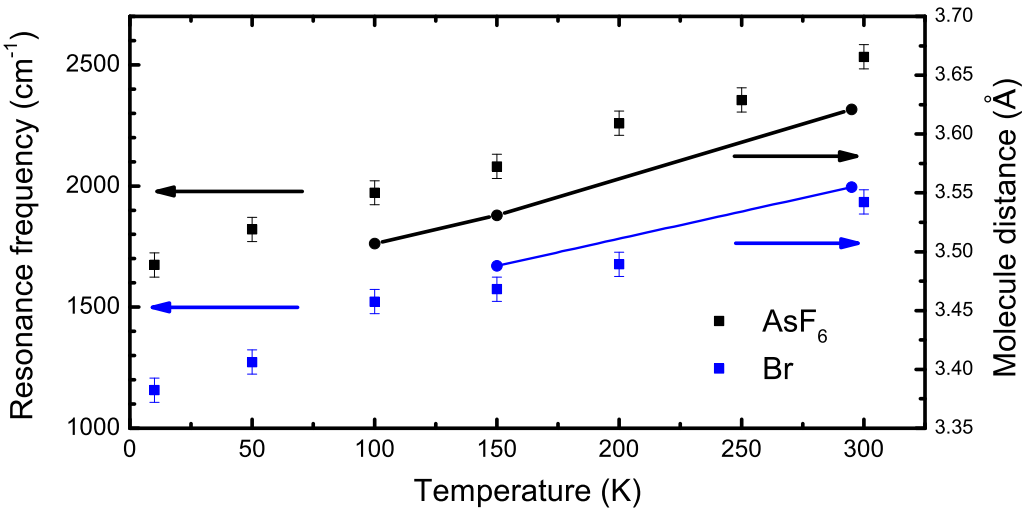

Figure 5.49: Illustrated is the temperature-dependent shift of the resonance frequency of the electronic excitation for both salts EDT$_2$Br and EDT$_2$AsF$_6$. Additionally, the distance of two neighboring EDT-TTFCONMe$_2$ molecules along the a-direction, derived from the structural data, is shown as a function of temperature.

interaction V is in general temperature-independent and therefore, can be considered as constant. However, the transfer integral t varies with temperature and depends on the orientation and strongly on the distance of the molecules to each other. The distance of the molecules reduces with decreasing temperature (see Fig. 5.49) whereas t increases. From this it follows that the ratio t/V as well increases and according to the DW model the maximum of the broad bands undergoes a red shift or the band gap becomes smaller. V can take values, for instance in the case of the organic molecule BEDT-TTF between 0.5 eV and 0.9 eV [246]. EDT$_2$AsF$_6$ has a transfer integral of $t = 0.071$ eV [236] at RT and for EDT$_2$Br $t = 0.087$ eV [237] at 150 K. In Fig. 5.50 (b) the energy gap is plotted as function of t/V. For comparison t/V for EDT$_2$AsF$_6$ and EDT$_2$Br is highlighted with V= 0.9 eV by the dotted vertical lines. Hence, the theoretical position of the maximum for EDT$_2$AsF$_6$ must be at 1790 cm^{-1}, experimentally a value of 2533 cm^{-1}was derived. In the case of EDT$_2$Br the maximum must be located at 1532 cm^{-1}which coincides very well with the experimentally detected result of 1574 cm^{-1}. Between 300 K and 10 K the maximum shifts about 35% for EDT$_2$AsF$_6$ and 41% for EDT$_2$Br. The difference of the transfer integrals of EDT$_2$AsF$_6$ and EDT$_2$Br is about 20% whereas the position of the maxima differs by 38%. In the DW model t/V must be doubled to achieve a shift of the maximum of about 50%. For the DW calculations and for the assumption of the ratio t/V it was supposed that V is constant which is usually valid. The model of the optically excited DW qualitatively agrees with the observations made. Although the interaction of the molecules in the adjacent chains is weak, an influence of the interstack interaction on the DW excitation cannot be fully excluded. This effect is not included in the model. Furthermore, a precise analysis of V is very important to accurately determine the position of the compounds in the Fig. 5.50 (b). In addition, the phase diagram has to be extended with compounds on the left side of EDT$_2$AsF$_6$ similar to the Fabre salts. A possible route would be releasing chemical pressure by substituting, for instance AsF$_6$ by the X =SbF$_6$ or X =TaF$_6$. Thereby, the distance between the cations enlarges and hence, t diminishes. This opens the opportunity to study the excitation of an exciton at small

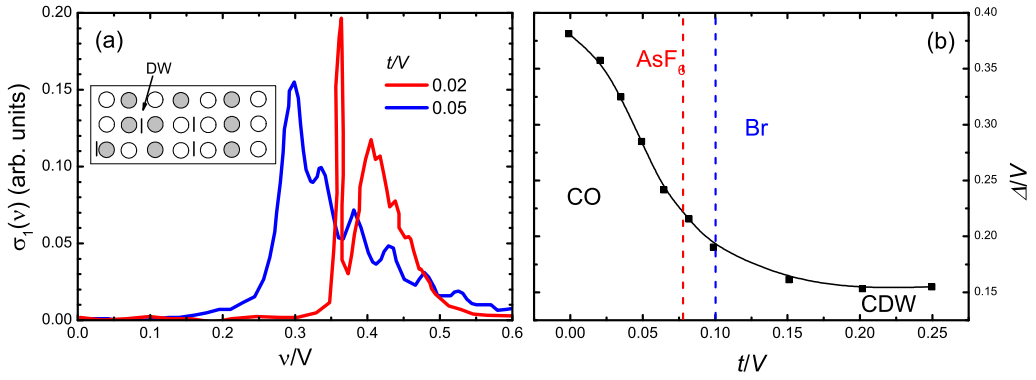

Figure 5.50: (a) Optical conductivity as a function of ν/V for a one-dimensional charged-ordered system for $t/V = 0.02$ and 0.05. The broad band corresponds to the excitation of two DWs. For 0.02 an excitonic resonance shows up and disappears with increasing t/V. A schematic illustration of the optical creation of a DW pair is presented in the inset. (b) The band gap Δ/V as a function of t/V. There is a crossover from a CO to a CDW state for $t/V > 0.15$ which could correlate with exotic insulating state at high hydrostatic pressure. The red and blue dotted lines mark the ratio t/V for EDT_2AsF_6 and EDT_2Br . For EDT_2AsF_6 $t = 0.071$ eV at 300 K and for EDT_2Br $t = 0.087$ eV[237] at 150 K was used. For V, a value of 0.9 eV [246] was assumed. Extracted from Ref. [245].

t/V. A further confirmation of the validity of the model is the existence of the second insulating phase above 7 kbar which might be a CDW. With increasing hydrostatic pressure t increases and under the assumption that V stays constant the gain of t results in a transition in accordance with the model of Ref. [245] from a charge-ordered into charge-density-wave state. The phase diagram of $(DI\text{-}DCNQI)_2Ag$[247] exhibits a striking analogy to the EDT-TTFCONMe$_2$ compounds. $(DI\text{-}DCNQI)_2Ag$ also reveals a transition from CO to CDW. Beside the modulation of the transfer integral due to thermal contraction, no further thermal effect could be observed in the experimental data by the model predicted as the studied temperature range is too small. With respect to the derived data optical measurements under hydrostatic pressure are very important since with increasing pressure the transfer integral also alters. Here, EDT_2Br is especially recommended as initial material as it reveals a transition into a second insulating state above 7 kbar and below 30 K which is probably a CDW phase.

5.2.4 *Summary and conclusion*

Both compounds EDT_2AsF_6 and EDT_2Br were optically studied by FTIR spectroscopy. The reflectivity was measured along all three crystallographic axis and the optical conductivity was calculated by KKT. The low reflectivity of the b- and c-direction confirms the quasi one-dimensional character of the materials. By analyzing the corresponding temperature-dependent conductivity spectra quantitatively, the interaction of the methyl groups and the related vibrations could be connected with the structural transition at $T = 190$ K. Furthermore, no thermal drift of the charge sensitive vibrational modes could be observed. The individual experimental resolved features could be assigned to the intramolecular vibrations of the EDT-TTFCONMe$_2$ molecule due to DFT based normal mode analysis. By comparing the resonance frequency of the separated charge sensitive modes with the theoretical ones the charge imbalance $\delta\rho$ of both compounds

could be determined. At RT, both materials have a charge disproportionation of about 0.8 e which stays constant down to 10 K. The results are in full accordance with previous NMR measurement data recorded below 200 K. Additionally to the normal mode analysis, the band structure of EDT$_2$AsF$_6$ was calculated. At the Fermi energy the band structure consists of a completely filled band and a half-filled band leading to a pure quarter-filled system altogether. The largest dispersion appears along the a-axis while along the other directions the bands are very flat and hence, without any dispersion. This reflects the quasi one-dimensional character of the compounds. The calculation of the optical conductivity along all axis reveals that they are not purely one-dimensional. The a-direction exhibits the highest conductivity whereas the b-direction reveals by a factor of two smaller conductivity. However, the DFT method does not adequately consider correlation effects. The simulation of the optical spectra exhibits a feature above 6000 cm^{-1}which can be related to an electronic excitation. This band can be correlated to the steep increase of the experimental reflectivity above 6000 cm^{-1}. Concerning this observation it is very important for future studies that the NIR and VIS spectral ranges have to be examined in detail. Moreover, the optical conductivity of EDT$_2$AsF$_6$ and EDT$_2$Br is dominated by interband transitions appearing as broad bands located at about 2000 cm^{-1}. Strong asymmetric resonances - overtones and sum frequencies - are superimposed on the electronic band. Their existence is an evidence for the CO phase, especially, as it is already fully developed at RT. These modes are enhanced and become activated due to anharmonicity of the molecular energy potential in the CO state. The resonance frequency of the electronic band shifts strongly with temperature. The effect can be explained by the excitation of DWs by light leading to the same spectral shape. By cooling, the molecule distance alters whereas the transfer integral t is modified leading to the aforementioned red shift of the resonance. The observation agrees well with the theoretical model and is to our best knowledge the best example for the excitation of domain walls. Regarding the model it is highly recommended to perform pressure-dependent optical studies to tune t in a controlled way. As well by substituting the anions by other, perhaps by anti-symmetric anions, the chemical pressure should be varied in a similar way as in the Bechgaard and Fabre salts. Because of the existence of the CO at RT and in regard to possible future technical applications this family of materials has to be studied more in detail, concerning the electric-induced switching behavior and nonlinear conductivity. Furthermore, it must be clarified if the domain walls can be optically excited by irradiating the sample with MIR or VIS light and hence, controlling the conducting behavior.

5.3 TTF-CA

5.3.1 *Scope of the project*

This chapter presents and summarizes several efforts to study and understand the nature of the ground state of TTF-CA and photo-induced states. Therefore, extended theoretical calculations were performed where the band structure, the vibrational modes of the molecules contained in the crystal and the optical spectra were determined. The theoretical results were compared with our experimental ones and placed in context to the current state of knowledge. As we have grown high quality samples in our laboratory, a short introduction into the various methods to grow the samples is given. The quality of the crystals were examined by x-ray scattering and transport experiments. The temperature-dependent optical infrared spectra were studied extensively and are discussed in detail in one of the upcoming sections. One of the main parts of this chapter is dedicated to the examination of the photo-induced phase transition at the vicinity of thermally-induced phase transition. The observed temporal dynamics of the photo-induced states is attributed to the random-walk of neutral-ionic domain walls which is strongly supported by our simulation of a random-walk annihilation process of domain walls on a one-dimensional chain. Several parts of the presented results were published in various articles [5, 248].

5.3.2 *Physical properties of TTF-CA*

TTF-CA consists of the two organic molecules, tetrathiavulvalene (TTF, $C_6S_4H_4$) and chloranil (CA, $C_6Cl_4O_2$), whose molecular structure is depicted in Fig. 5.51 (a). It was firstly synthesized in 1979 [252]. The main goal was to create an organic compound with a high electric conductivity which can compete with conventional metals. At present several synthesis methods exist which are described in detail in Sec. 5.3.3. In all cases the stoichiometric ratio of the starting materials is 1:1. At room temperature two equivalent TTF and CA molecules are contained in the monoclinic unit cell. The CA is the acceptor molecule (A) while TTF is the electron donator (D). Therefore, a charge transfer takes place between them. In the unit cell both the TTF and CA molecules are arranged parallel to their molecular plane in a distance of 3.70 Å [249]. Thereby, they are shifted and rotated slightly towards each other, leading to a maximum overlap of the molecular orbitals. The molecules, TTF and CA are alternating and equally spaced along the a-direction, as depicted in Fig. 5.51 (c) and (d). First studies on the crystal structure and the bond lengths of the C=C double bond of TTF and CA as well as the C=O bonds in CA reveal that the molecules are almost neutral at room temperature; caused by a small charge transfer between TTF and CA [253] which can be attributed to the large intermolecular distance of 3.70 Å[249]. Indeed, infrared measurements have shown that the charge transfer is $\rho = 0.2\ e$ [199, 254] at room temperature. Therefore, this state is referred to as the neutral phase. Due to the small charge transfer the crystals glimmer greenish and transparent because the total absorption and reflection spectrum is composed of the single spectrum of the quasi-neutral TTF^0 and CA^0 molecules whose electronic excitations in the visible range are blue shifted. This is why it is often called the green phase in literature. The color can be used to check the quality of the crystals (see Fig. 5.55), besides the green phase a so-called black phase exists which

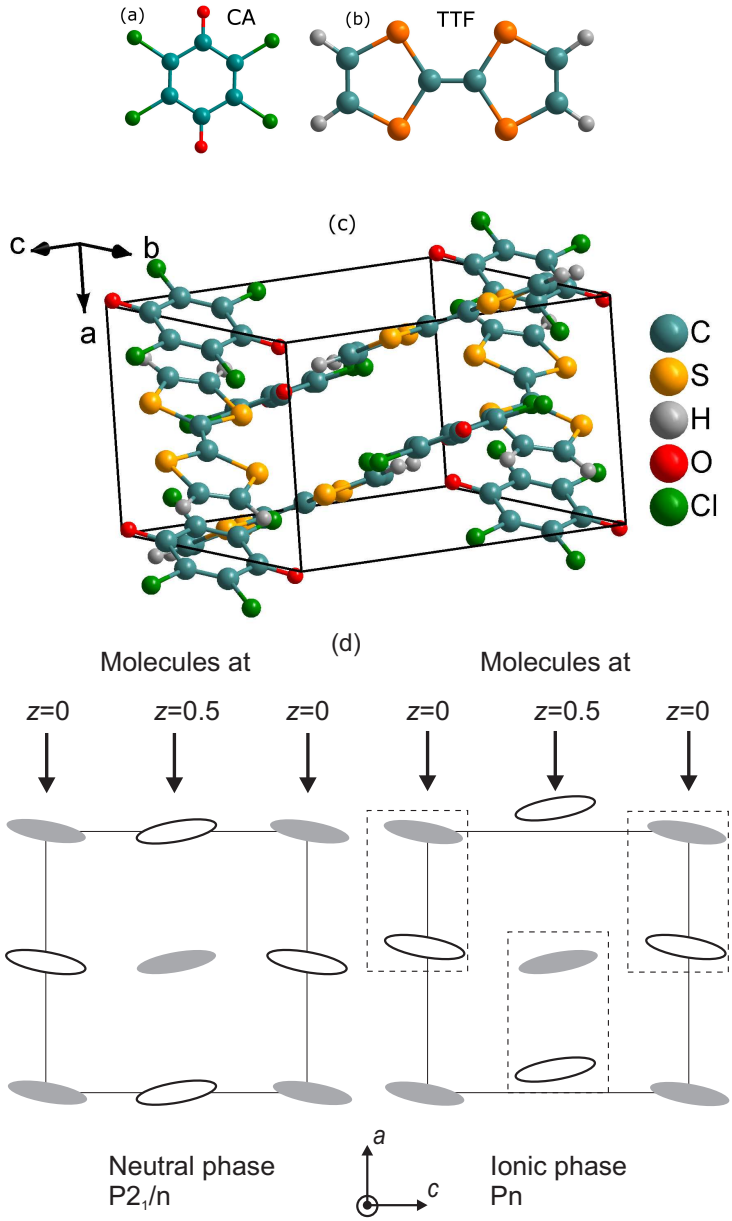

Figure 5.51: (a) Chloranil molecule (CA, $C_6Cl_4O_2$, color of the material: yellow). (b) Tetrathiafulvalene (TTF, $C_6S_4H_4$, color of the solid: orange).
(c) Monoclinic unit cell of TTF-CA at room temperature. The TTF and CA molecules are ordered along the crystallographic a-axis [249]. Due to the crystal symmetry and the position of the molecules two equalivent TTF and CA molecules are contained in a unit cell.
(d) At room temperature the space group of the unit cell is $P2_1/n$ and the CA and TTF molecules are stacked equally spaced along the a-axis. A further stack is located at $z = c = 0.5$, respectively, at which the TTF-CA pairs are tilted opposite to the a-axis. Lower right: in the ionic phase the TTF and CA molecules dimerize along the a-direction. By the charge transfer of about $\rho = 0.6$ e electric dipoles are formed along the stacking direction, resulting in a loss of the two-fold screw axis 2_1 [250, 251].

exhibits different physical properties, for instance the absence of the neutral to ionic phase transition.

Upon cooling the charge transfer increases slightly from 0.2 e to 0.3 e [199, 249, 254, 255]. At T_{NI}=82 K a phase transition occurs at which the space group is lowered from $P2_1/n$ to Pn, detected by structural resolving techniques. By

that, two symmetry operations, the point inversion and the screw rotation along the b-direction, are lost, which is deflected in the abrupt appearing of the $(0k0)$ reflections, as plotted in Fig 5.52 (a). Due to thermal contraction the unit cell shrinks and at the phase transition the cell parameters b and c jump to lower values. Furthermore, the TTF and CA molecules dimerize along the a-axis in the low temperature phase, at which the initial distance of 3.70 Å decreases to 3.504 Å and 3.685 Å [249], as it is depicted in Fig. 5.51 (c), respectively. Also, the ionicity ρ increases from 0.3 e to about 0.6 e [199, 249, 254, 255], which was consistently determined by infrared, Raman and x-ray studies. The strong dimerization and the charge transfer lead to the creation of strong electric dipoles between the TTF and CA molecules. This was proven by dielectric measurements where it was observed as a sharp feature in ϵ_1 at the transition temperature T_{NI}. In Fig. 5.52 (b) the real part ϵ_1 of the complex dielectric function ϵ_1 is displayed as a function of temperature for 100 Hz and 100 kHz. At the transition temperature T_{NI}, ϵ_1 rises steeply and diverges for both frequencies; corresponding to a transition from a paraelectric to a ferroelectric state, at which ϵ_1 follows a Curie-Weiss law above the critical temperature T_{NI}. The feature between 100 and 200 K for 100 Hz is attributed to solitons and neutral-ionic domains walls, which will be described in detail in the subsequent sections.

In Fig. 5.52 (c) the temperature-dependent behavior of the specific heat C_p is illustrated which diverges similar to ϵ_1 at the phase transition and proves that it is a first-order transition.

How does the electric conductivity behave at the vicinity of the neutral-ionic transition? And does TTF-CA reveal metallic behavior?

Fig. 5.52 (d) displays the resistivity ρ_{DC} along the stacking direction of one of our grown TTF-CA single crystals. The specific resistance in the neutral phase is $\rho = 3 \cdot 10^6$ Ωcm yielding an insulating behavior at ambient conditions. Previous DC-measurements from Mitani et al. [258] result values between 10^5 and 10^6 Ωcm which is in very good agreement with our results. Upon cooling, the resistivity increases linearly in a log-plot of $\frac{1}{T}$, corresponding to a thermal activated behavior of a band insulator, for instance a semiconductor. By assuming a band insulator, the resistivity follows an Arrhenius development $\rho(T) = \rho_0 \exp\left(\frac{\Delta}{T}\right)$, at which Δ is the temperature-independent energy gap, or activation energy, respectively. According to our calculations in the neutral phase the activation energy is 0.12 eV (1276 K) which is close to the literature values lying between 0.095 eV and 0.065 eV [89, 256, 258]. In the Inset 5.52 (e) of Fig. 5.52 (d) the derivative of the logarithmic resistivity is illustrated. The slope of the decreases upon cooling. At the transition to the ionic phase, the resistivity reduces by one-order of magnitude to increase afterwards again. Below the transition the activation energy Δ is only 0.065 eV and agrees excellently with literature.

How can one understand the neutral-ionic phase transition physically? How can the conductivity be increased at the phase transition? And what is the origin of the anomaly in the real part of the dielectric function ϵ_1 above T_{NI}?

In general, the total energy [259, 260]

$$E_{tot}(\rho) = (I - A)\rho - \alpha\langle\frac{e^2}{d_{Dim}}\rangle\rho^2 \tag{5.18}$$

of a donor-acceptor crystal, as TTF-CA, depends on the ionicity ρ. The first term $I - A$ describes the energy which is necessary to ionize a D-A pair at which I is the ionization energy of D and A is the electron affinity of A. It competes

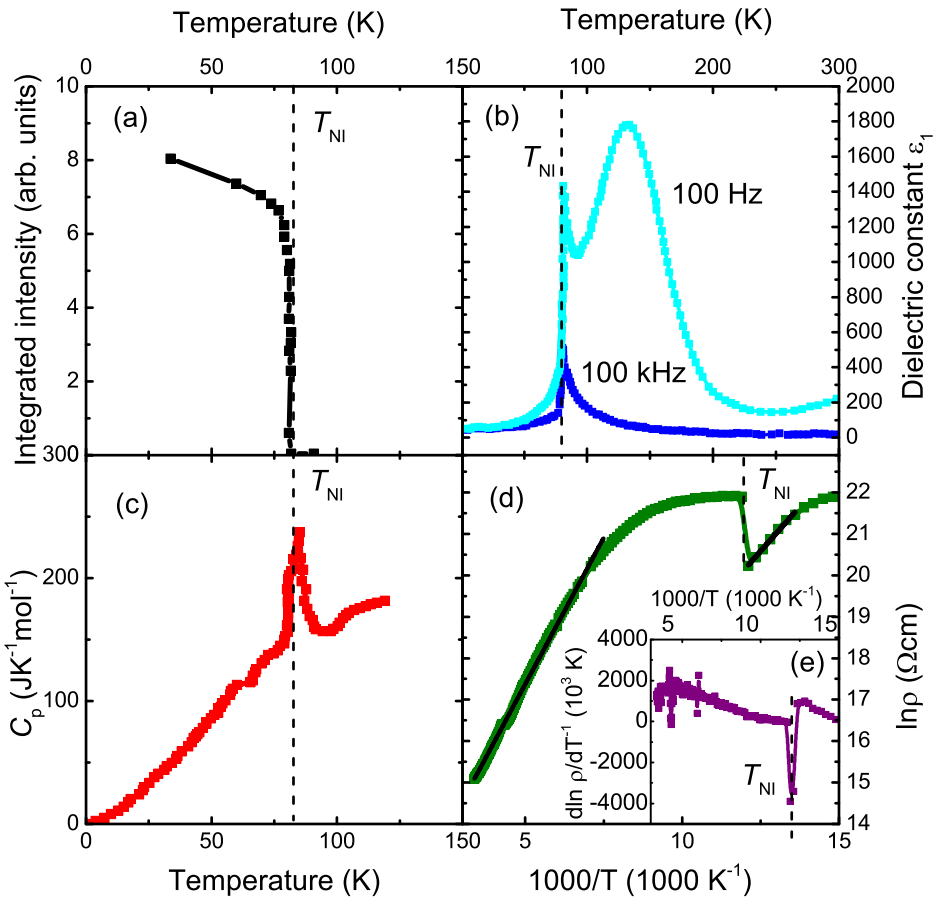

Figure 5.52: (a) Temperature-dependent $(0k0)$-reflection [249], occurring after the loss of the twofold screw axis which is caused by the break of symmetry and the structural phase transition.
(b) Temperature evolution of the real part ϵ_1 of the dielectric function, recorded at a frequency of 100 Hz (light blue) and 100 kHz (dark blue). ϵ_1 diverges for all frequencies at the critical temperature T_{NI} and marks a first order para- to ferroelectric transition [256]. The feature, appearing between 100 and 200 K for 100 Hz, is attributed to the excitation of neutral-ionic domain walls.
(c) The specific heat capacity C_p of TTF-CA diverges similar as ϵ_1 at the phase transition; being an evidence of a first-order phase transition [257].
(d) Arrhenius plot of the resistivity ρ_{DC} (green) of TTF-CA along the stacking direction. Above the transition it behaves as a classic band insulator with an activation energy of $\Delta = 0.12$ eV.

with the Madelung energy $\alpha\langle\frac{e^2}{d_{Dim}}\rangle$, which is set free, if the lattice becomes ionic. d is the distance between the acceptor and the donor molecule which varies with temperature, e the electron charge and α the Madelung constant. $E_{tot}(\rho)$ is minimal for the case $\rho = 0$, if $I - A > \alpha\langle\frac{e^2}{d_{Dim}}\rangle$ and for the case $\rho = 1$, if $I - A < \alpha\langle\frac{e^2}{d_{Dim}}\rangle$. When $I - A < \alpha\langle\frac{e^2}{d_{Dim}}\rangle$, then a transition from a neutral to ionic phase takes place. This means that in the D-A crystal the terms, $I - A$ and $\alpha\langle\frac{e^2}{d_{Dim}}\rangle$, compete with each other. In the case of TTF-CA, the ionization energy of TTF is $I = 6.2 - 6.8$ eV [261, 262, 263, 264] and the electron affinity of CA is $A = 2.8$ eV [265], resulting in $I - A = 3.7$ eV with $I = 6.5$ eV for TTF. Tanaka et al. [266] calculated for TTF-CA a Madelung energy of $\alpha\langle\frac{e^2}{d_{Dim}}\rangle = 3.59$ eV, leading to an energy difference between the Madelung energy and $I - A$ of about 0.1 eV. Therefore, TTF-CA is in the neutral phase under ambient conditions. As visible in

Table 5.7: Unit cell parameter TTF-CA for 300 K and 40 K. Le Cointe et al. [249], Mayerle et al. [253].

Parameter	TTF-CA (300 K)[253]	TTF-CA (40 K)[249]
a (Å)	7.41	7.19
b (Å)	7.621	7.54
c (Å)	14.571	14.44
α (°)	90	90
β (°)	99.2	98.6
γ (°)	90	90
V (Å^3)	812.35	774.03
Z	2	2
M (g mol^{-1})	900.74	900.74
ρ (g cm^{-3})	1.82	1.93
Space group	$P2_1/n$	Pn

Eq. 5.18, the Madelung energy is a function of the intermolecular distance d_{Dim} between D and A. Thus, by cooling and the related thermal contraction as well as by hydrostatic pressure, the Madelung energy can be increased and becomes larger than $I - A$. This leads to a transition from the neutral to the ionic phase occurring at T_{NI}=81.5 K.

Due to the thermal shrinking of the unit cell parameter a, as listed in Tab. 5.7, the molecule distance d_{Dim} decreases and induces the phase transition at T_{NI}=81.5 K. Under consideration of the energy it can be reasoned that it is possible to induce this transition at room temperature by applying hydrostatic pressure. Transport studies under pressure by Mitani et al. [267] reveal exactly this behavior. A pressure of $p = 11$ kbar induces the ionic phase at $T = 295$ K. With decreasing temperature less pressure is necessary to trigger the transition. The down and up turn of the conductivity at ambient pressure (see Fig. 5.52 (b)) becomes broader and shifts to higher temperatures. The conductivity increases exponentially as well with the pressure. The strong increase of the conductivity is attributed to the increase of the number of neutral-ionic domain walls (NIDW) in the neutral phase. However, this is also valid for the ionic phase. Model calculation [268, 269, 270] reveal that NIDW can also be excited at room temperature and their concentration decreases with decreasing temperature. However, the simulation confirms the influence of the NIDW on the transport properties and on the pressure-induced phase transition. The NIDWs are also responsible for the feature in the dielectric function [256] above the phase transition, the electric transport [267] and the nonlinear conductivity [89]. This was originally theoretically predicted by Nagaosa [268, 268] and quantitatively theoretically confirmed by Soos and Painelli [270], by taking into account the interaction of the lattice and the molecular vibrations with the electronic system. Additionally, several different energetically low-lying excitations exist in the neutral as well as in the ionic phase. Besides the excitation of NIDWs, also polarons, spin-solitons [271, 272], and charged solitons can be excited.

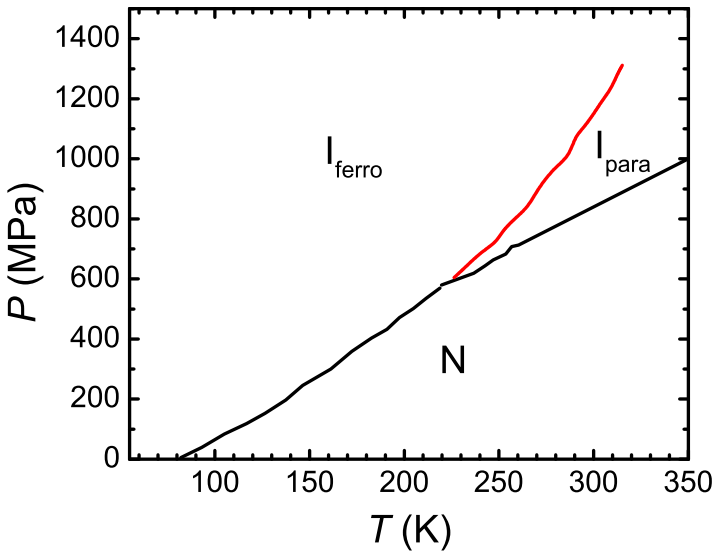

Figure 5.53: The *P*-*T*-phase diagram of TTF-CA exhibits in a pressure range from 0 MPa to 1500 MPa and in a temperature range between 0 K and 350 K three different phases (I_{ferro}: ferroelectric ionic phase, I_{para}: paraelectric ionic phase, N: neutral phase). The phase diagram resembles the characteristic of a solid-liquid-gas-phase diagram. Adapted from [250]

In Fig. 5.53 the *P*-*T*-phase diagram is depicted which is composed out of different measurements, i.e. electric transport [267], optical measurements [248, 260, 273, 274, 275, 276, 277, 278], neutron scattering experiments and ^{35}Cl NQR [279, 280]. The phase diagram reveals similarities to a solid-liquid-gas-phase diagram with a triple point at 210 K and 500 MPa where all three phases coexist. For low pressure and at room temperature TTF-CA resides in the neutral, non-dimerized phase (N). For lower temperatures ($T_{NI} = 81.5\,K$ and $P_{NI} = 0\,MPa$) a crossover into the ionic, dimerized phase (I_{ferro}) occurs. At 300 K the ionic phase can be induced by applying a pressure of about 800 MPa. However, this state (I_{para}) is not dimerized. A pressure of more than 1200 MPa induces the transition to the dimerized, ferroelectric state. The physical nature of I_{para} is discussed controversially in literature. Studies on the crystal structure [249] indicate that it must be a paraelectric phase. Infrared data [277] on single crystals of TTF-CA under hydrostatic pressure suggest that in the paraelectric phase two different ionic states are present. In contrast, most recent infrared measurements [248] on TTF-CA powder, examining the whole *P*-*T*-space, show clearly that in this specific phase two different ionic configurations do not exist. However, to finally make a conclusion on this "exotic" state, it will be necessary to perform polarized infrared studies on single crystals under high pressure.

5.3.3 *Crystal growth*

Different crystal growth techniques are available to synthesize charge transfer salts. Within this framework of this thesis, there is only enough space to give a rough overview about the methods. Therefore, the more interested readers are referred to Ref. [281] and [282].

For the synthesizes of TTF-CA the plate sublimation method or the slow cooling of an oversaturated solution of TTF and CA in an organic solvent, i.e. acetonitrile are preferably used. The first one, however, yield high quality films. A first

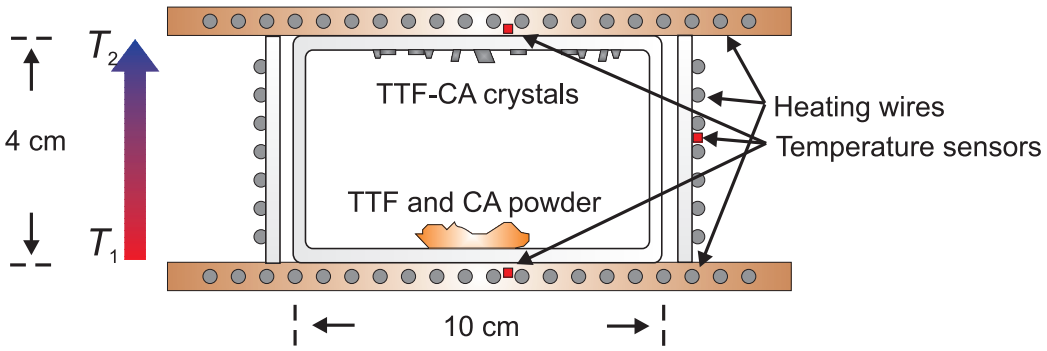

Figure 5.54: Schematic setup of the plate sublimation. It consists of two copper plates with incorporated meander-like thermocoax wires. A PT-1000 temperature sensor (red square) is placed in the center of each plate to check their temperature. The so-called French cheese box is located between the two plates and is surrounded by a glass ring. A third thermocoax wire is helically glued on the ring with Stycast. The temperature is controlled by a third PT-1000 in the center of the ring as well. During the growth process a temperature gradient is set between the two plates of about $\Delta T = T_2 - T_1$. The starting powder material is placed on the bottom of the glass box. The TTF-CA crystals grow on the colder top part of the glass box.

single crystal for the study was produced by A. Girlando and M. Massimo from the University of Parma. They used the cooling method of an oversaturated solution. Though, the crystals are thin and needle-like. Thus, optical measurements were even with the infrared microscope impossible. Since the supply with large crystals is complicated and the growth process consumes a lot of time. As a consequence, a project was started to synthesize the crystal in our laboratories with the cooling method. Therefore, the commercially available starting material, TTF and CA, from Sigma-Aldricht with a purity of 99.7 % was used without further purification. Both materials were solved in a molar ratio of 1:1 at room temperature in C_2H_3N (acetonitrile). The first attempts were performed under ambient conditions by which the solvent evaporates very fast. By that, the solvent level decreases and small TTF-CA crystals crystallizes at the walls of the glass recipient. The shape of the grown crystal is needle-like and very thin. The long axis is along the a-direction. Better results were achieved by decreasing the evaporation rate of the solvent. Thus, the glass vessel is put in refrigerator at 7°C. Thereby the crystallization process is slowed down and hence, the crystal becomes wider and longer. Furthermore, this method has the advantage that the whole process takes place in the dark. So, any photochemical reaction during the synthesis is avoided [282] which can disturb the growth process. For the planned experiments these crystals were not sufficient large enough.

The aforementioned plate sublimation technique provides naturally grown single crystals [281] of very high purity and quality. There, they grow trapezoidal in the a- and b-direction (see Fig. 5.55). That is why, we choose this method which was originally developed by N. Karl at the university of Stuttgart. The apparatus to grow the crystal was built according to the description in Ref. [281]. In Fig. 5.54 the setup of the plate sublimation is illustrated schematically. The centerpieces of the setup are two cooper plates which contain equally layed thermocoax wires to heat them up. By that, it is guaranteed that the temperature is homogeneous distributed on the plate. The temperature is controlled by built-in PT-1000 temperature sensors. To establish a one-dimensional temperature gradient between the two plates, a glass pipe was placed between the plates to ensure

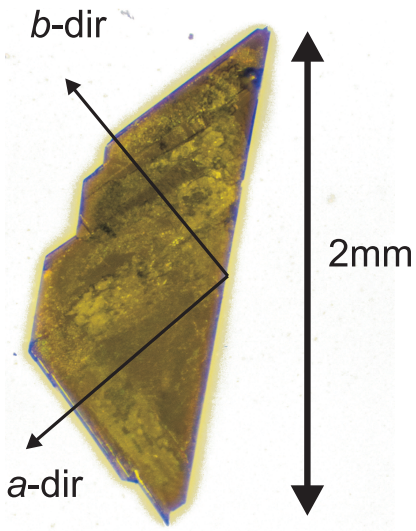

Figure 5.55: Photograph of a naturally grown TTF-CA single crystal which was grown by the plate sublimation method. The shape is trapezoidal with a dimension of 1 mm × 2 mm. The a- and b-direction are perpendicular to the short edges of the crystal. The crystallographic axis are determined by polarized infrared measurements.

a fixed distance between them. The glass tube was helically wrapped with thermocoax wires and equipped with a further PT-1000 sensor for the temperature control as well. The glass tube ensures that the temperature of the side wall of the inner glass vessel, the so-called "French cheese box", is higher than the top part, avoiding any formation of the crystals at the wall. Three self-developed temperature controller ensured the selected temperature and thermal stability over several days or weeks. The temperature of the different components was controlled by that independently of each other. The "French cheese-box" was filled with TTF and chloranil (CA) in a ratio of 1:1. Afterwards, the box was evacuated. First efforts with different pressures of argon gas failed and lead only to very small and thin crystals. We recognized that the growth process is significantly improved when the pressure in the vessel is about 10^{-3} mbar without any inert gas as argon. The opening of the glass box was sealed by melting the glass. Afterwards, it was placed between the two plates in the inner part of the outer glass tube. Additionally, the whole setup was isolated by glass wool to avoid any temperature fluctuation during the lasting for days crystal growth. Since vibrations are a crucial issue concerning the crystal growth, the whole setup was, therefore, placed on heavily damped plates. To evaporate and remove possible impurities on the surface of the glass vessel, the temperature was set everywhere to $T_1 = T_2 = 78\,\mathrm{C}°$. Afterwards, the growth process was stimulated by setting the temperature T_2 of the upper plate to 70 C° so that the temperature difference between the two plates is $\Delta T = 8\,\mathrm{K}$. Thereby, the fast growth of seed crystal is initialized. After a few hours, the temperature of the upper plate is reduced to 76°C ($\Delta T = 6\,\mathrm{C}°$). After 2 to 6 weeks the crystals can be harvested by breaking the sealed glass box. Finally, the samples were stored in an exsiccator for protection against water and kept in a refrigerator due to the high vapor pressure of TTF. As depicted in Fig. 5.55, the crystal glimmers greenish under light corresponding to the expected green phase of TTF-CA. Besides the TTF-CA crystals also red and orange tetrathiafulvalene (TTF) crystals grow due to the high vapor pressure of TTF.

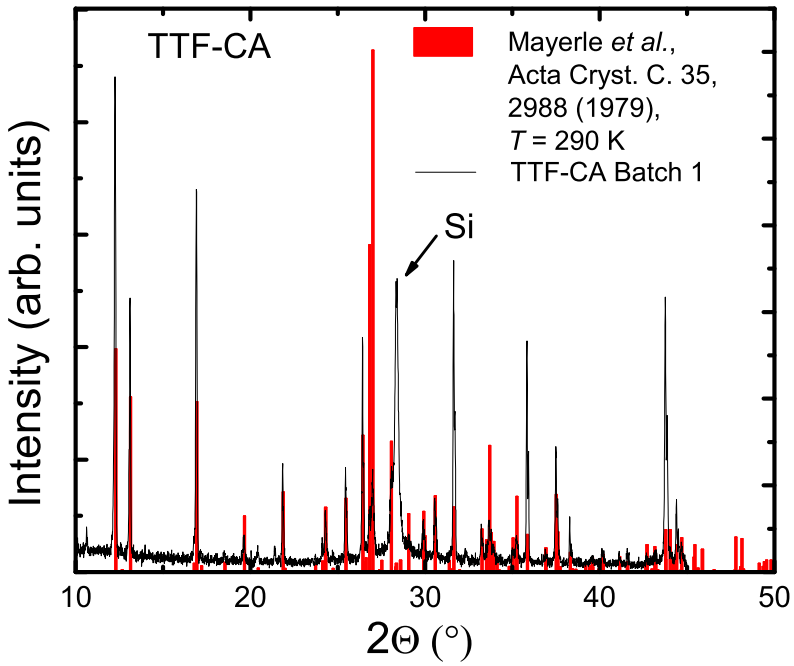

Figure 5.56: Comparison of the experimental powder diffractogram (black) of TTF-CA (Batch 1) with the simulated diffractogram (red) calculated from the crystal structure Mayerle et al. [253]. The broad maximum at $2\Theta = 28.4\,^\circ$ can be attributed to the silicon substrate.

The setup can be used in principle for the synthesis of further kinds of charge transfer salts, for instance TTF-TCNQ, TTF-BA. Furthermore, the method can be optimized concerning the growth process. One idea would be to reduce the number of surface defects on the glass walls by etching or cooling down one specific point on the top part of the glass vessel extremely to stimulate the growth of only a few large single crystals.

The quality of the crystals is checked by electric transport measurements (see Sec. 5.3.2, Fig. 5.52 (d)), optical studies (see Sec. 5.3.5) and x-ray powder diffraction. In Fig. 5.56 the room temperature diffractogram of the synthesized TTF-CA crystals are compared with the simulated one derived from the structural data Mayerle et al. [253]. The simulation was performed with the visualization software Diamond which is capable of generating diffraction spectra from crystallographic data. The positions of the experimental diffraction maxima (black) agree very well with the simulated values (red). The absolute intensities deviate from each other because of the sample preparation. In our case the crystals were possibly not milled uniformly, by what several crystal directions are not taken into account precisely enough. The maximum located at $2\Theta = 28.4\,^\circ$ cannot be ascribed to TTF-CA powder and is caused by the silicon carrier material. Due to the results of the structural examination it can be clearly concluded that the crystals have the right crystal structure. This is confirmed by further upcoming experimental results presented within this thesis.

5.3.4 *Ab-initio calculations: band structure, optical spectra and normal modes*

The optical spectra in the mid-infrared deliver comprehensive information about the electronic, intra- and intermolecular physical properties of solid state materials. At first, we want to concentrate on the intramolecular vibrations occurring

Table 5.8: Calculated resonance frequencies (in cm^{-1}), infrared intensities (D^2amu^{-1} $Å^{-2}$) and emv coupling constants g_i[254] in meV. The following abbreviation are used: Int.: infrared intensity.

		CA^0			CA^-				
Label	Symmetry	ν_{calc}	ν_{scaled}	Int.	ν_{calc}	ν_{scaled}	Int.	$\Delta\nu$	g_i
ν_1	a_g	1754.1	1696.22	-	1548.51	1497.41	-	-199	67
ν_2		1630.2	1576.24	-	1608.16	1555.09	-	-21	83
ν_3		970.94	990.07	-	982.53	1002	-	12	95
ν_{10}	b_{1u}	1757	1699	349.46	1565.35	1513.7	288.1	-185	
ν_{11}		1086.54	1050.68	415.77	1117.9	1081	203.72	30	
ν_{12}		899.07	916.78	25.31	892.53	910.12	159.74	-7	
		TTF^0			TTF^+				
Label	Symmetry	ν_{calc}	ν_{scaled}	Int.	ν_{calc}	ν_{scaled}	Int.	$\Delta\nu$	g_i
ν_2	a_g	1621.92	1568.39	-	1551.15	1499.96	-	-68	16
ν_3		1.576	1524.41	-	1427.75	1380.63	-	-144	115
ν_4		1.125	1088	-	1130	1092.71	-	5	10
ν_{14}	b_{1u}	1598.57	1545.82	23.07	1532	1481.43	111.48	-64	
ν_{15}		1124.65	1087.54	3.15	1130.92	1094	0.12	6	

in TTF-CA. To ascribe the observed vibrational features to the corresponding molecular vibrational modes and to determine the ionicity of TTF-CA from the resonance frequency of specific modes, DFT-calculations in connection with a normal mode analysis were performed. Therefore, the EDF2-functional [136] in combination with the 6-311G*(d,p) basis set was used. The calculations were performed with the software package Spartan [283]. The molecule structure of TTF, TTF^+ with the point group C_{2v} and CA, CA^- with the symmetry D_{2h} were optimized in respect to the total energy of the system to find the equilibrium molecular structure. The subsequent calculation did not reveal any negative or imaginary frequency, indicating that the energy minimum is reached. For the modes with a frequency above 1000 cm^{-1} a correction factor of 0.967 was applied whereas for the modes below 1000 cm^{-1} 1.0197 [139] was employed. In Tab. A.3 and A.4 all resonance frequencies and intensities of CA, CA^-, TTF, and TTF^+ are listed. The results agree well with previous calculations [261, 284, 285]. However, less precise DFT-methods as basis sets were used. For both molecules the vibrational modes can be classified according to the D_{2h} [241] symmetry as follows:

$$\Gamma_{CA} \Rightarrow 6a_g + 1b_{1g} + 3b_{2g} + 5b_{3g} + 2a_u + 5b_{1u} + 5b_{2u} + 3b_{3u} \quad (5.19)$$

$$\Gamma_{TTF} \Rightarrow 7a_g + 2b_{1g} + 3b_{2g} + 6b_{3g} + 3a_u + 6b_{1u} + 6b_{2u} + 3b_{3u} \quad (5.20)$$

Thereby, a_g, and b_{3u} from the point group D_{2h} correlate with a_1 from C_{2v}, a_u, and b_{3g} with a_1, b_{2u}, b_{1g} with b_1 and b_{2g} and b_{1u} with b_2. Similar to the TMTTF, BEDT-TTF, and EDT-TTFCONMe$_2$ molecules, the structure of TTF is in the neutral state bent meaning the C-H bonds point out of the molecule plane. That is why, we assumed in the calculation that the point group of TTF is C_{2v}. Yet, the structure of TTF is planar in the condensed phase and thus, it is valid that we

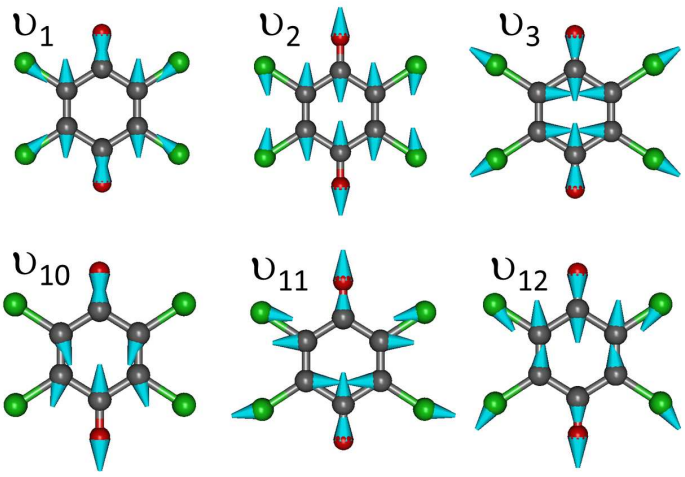

Figure 5.57: In the upper row the symmetric a_g-modes ν_1, ν_2, and ν_3 of CA are visualized. The ungerade b_{1u}-modes ν_{10}, ν_{11}, and ν_{12} are listed in the lower row.

imply D_{2h}. The labeling of the modes in Tab. 5.8 are according to Ref. Girlando et al. [286] and Bozio et al. [241].

The calculations reveal an inner distance of the C=C double bonds in TTF^0 of 1.346 Å, which agrees very well with the experimentally determined value of d=1.35 Å in the gaseous phase [285]. In contrast, this bond length in the crystal is d=1.3639 Å [249] at room temperature. This is caused by the interaction with the neighboring molecules which deform the molecule frame. In addition, the actual charge state of TTF in the crystal at ambient conditions is not zero. This is the reason why the bond length increases in comparison to the vacuum value. The calculated double bond length of TTF^+ is increased to d=1.395 Å due to the π-orbital of the C=C bond and resembles very well the behavior of TTF-CA (d=1.3875 Å [287]) in the ionic phase at low temperatures. For CA in TTF-CA at 300 K the bond length of the C=O bond is 1.214 Å while the C=C bond length is 1.352 Å. The calculation yields for the neutral molecule 1.205 Å and 1.346 Å, respectively. In the ionic phase the distance of both bonds increases to 1.2378 Å and 1.366 Å. The theoretically derived values of CA^{-1} resemble this trend excellently with 1.24 Å and 1.369 Å.

In Tab. 5.8 the most important vibrational modes are listed with their resonance frequencies, infrared intensities and for the symmetric emv coupled modes their emv-coupling constants g_i for the neutral as well as the positively charged TTF and CA molecule. Only the gerade and infrared-inactive a_g and ungerade infrared-active b_{1u} modes are listed. The symmetric a_g modes become infrared-active when they are connected to the electronic background via emv coupling (for a more detailed description see Sec. F). This appears in the case of TTF-CA only in the ionic phase, since the TTF and CA molecules are dimerzed along the stacking direction. The appearance of these modes in the spectrum along the a-direction is a clear evidence for the ionic phase transition and is later used to determine the transition temperature, or in the case of the photo-induced process, to identify the transition into the neutral phase. The strongest coupling to the electronic background reveals the ν_3 mode of TTF and exhibits, therefore, the largest modification of the intensity in the IR spectrum.

The largest shift of the resonance frequency as a function of ionicity are observed for the ν_1 and ν_{10} modes of CA with a decrease of the frequency of

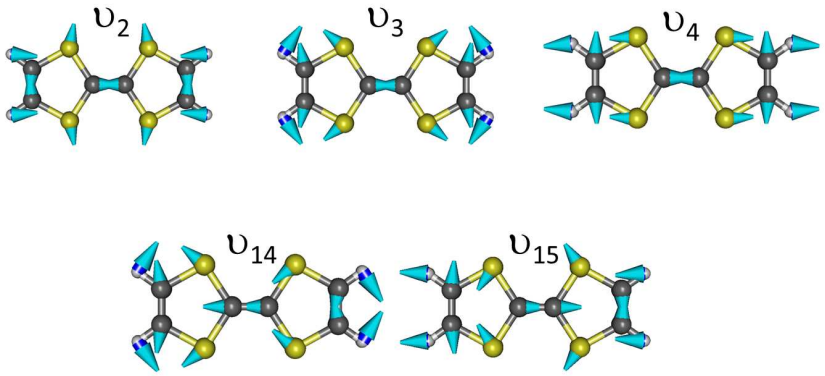

Figure 5.58: In the upper row the gerade a_g modes ν_2, ν_3, and ν_4 of TTF are depicted. The ungerade b_{1u} mode ν_{14} and ν_{15} are displayed in the second row.

-199 $cm^{-1}$and -185 cm^{-1}, respectively. In TTF the most sensitive modes are the ν_3 and ν_{14} which shift by -144 $cm^{-1}$and -64 cm^{-1}. To determine the ioncity, the symmetric modes can be excluded since they are not visible in the neutral phase. By that, only the antisymmetric vibrations can be used for that purpose. From the calculations it can be deduced that the ν_{10} mode of the CA molecule is the best choice concerning the intensity and total frequency shift. This is based on the fact that the electron density effects the bond length of the C=C and C=O bonds the most, being included in the vibration of the ν_{10} mode, and hence, it is very sensitive to any modification of the molecular charge. Furthermore, the oxygen atom is deflected along the C=O axis against the molecule body, leading to a large dipole moment. Therefore, this resonance is later used to determine the charge state of the molecules above and below the phase transition.

In Fig. 5.57 in the first row the vibrational a_g modes of CA are displayed, being symmetric to symmetry operations of the point group D_{2h}, together with the antisymmetric, infrared-active b_{1u} mode. Similar to that, the most important modes of the TTF molecules are depicted in Fig. 5.58. There, the electron density is as well the largest on the C=C double bond which has the largest impact on any modification of the PES. Although vibrations of the outer methyl groups take place, they have only little influence on the dipole moment.

For the band structure calculations we used the DFT method in connection with pseudopotentials and plane waves, implemented in the software suite Quantum Espresso [122]. In the framework of this theoretical consideration the GGA PBE-functional [130] together with ultrasoft pseudopotentials [141] for all atomic types is employed. The cutoff-energy of the wave function was set to $E_{\text{Wave}} = 30\,\text{eV}$. The selected electron density cutoff-energy was fixed to $E_\rho = 450\,\text{eV}$. For the self-consistent calculation an equally-spaced Monkhorst-grid [142] (6) was generated. The band structure was determined along the k-path: $\Gamma(0,0,0) \rightarrow Z(0,0,0.5) \rightarrow \Gamma(0,0,0) \rightarrow Y(0,0.5,0) \rightarrow U(0,0.5,0.5) \rightarrow \Gamma(0,0,0) \rightarrow X(0.5,0,0) \rightarrow S(0.5,0.5,0) \rightarrow \Gamma(0,0,0)$. In Fig. 5.59 the band structure in an energy range from -2 eV to 3 eV is depicted for the ionic and neutral phase of TTF-CA. Between -0.5 eV and 0.5 eV the VB and CB are located, which are separated from each other by a band gap of 0.02 eV at 300 K and 0.23 eV at 15 K. Each of the single bands are split into two bands due to the slightly interacting neighboring TTF-CA-chains within the unit cell. The HOMO of the TTF molecule contributes to the two lower bands whereas the upper bands are dominated by the LUMO of the CA molecule.

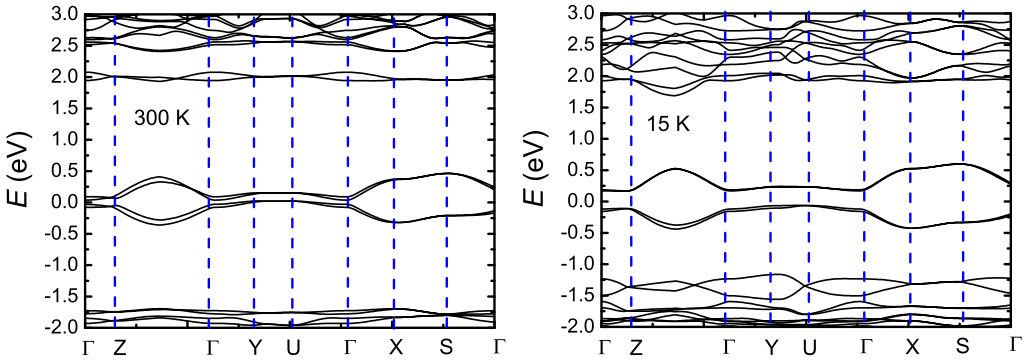

Figure 5.59: Band structure of TTF-CA at 300 K (a) and 15 K (b) along the selected k-path in an energy range from -2 eV to 3 eV : $\Gamma\,(0,0,0) \rightarrow Z\,(0,0,0.5) \rightarrow \Gamma(0,0,0) \rightarrow Y\,(0,0.5,0) \rightarrow U\,(0,0.5,0.5) \rightarrow \Gamma(0,0,0) \rightarrow X\,(0.5,0,0) \rightarrow S\,(0.5,0.5,0) \rightarrow \Gamma(0,0,0)$The band gaps are 0.02 eV at 300 K and 0.23 eV at 15 K.

The energy dispersion along $\Gamma \rightarrow X$ is obviously maximum along the stacking direction (a-axis). The band width W of the CB is about $W = 4t = 410$ meV at 300 K and temperature-independent. The VB reveals a band width of $W = 4t =$ 300 meV and increases to 360 meV upon cooling. Along the other directions the dispersion is very weak meaning that TTF-CA is a one-dimensional system. The optical measurements, depicted in Fig. 5.60, show that an extensive maximum is located at about 0.6 eV (4800 cm^{-1}) which is caused by the excitations from the VB to the CB in the regions where the energy difference of the two states Δ=E_{CB}-E_{VB} is almost constant over a wide range [81]. This means that the joint density of states becomes extremely large in this energy range and area in the k-space which resembles the behavior of an M_0 van-Hove singularity in one dimensions with a minimum in the energy difference Δ.[36]. This causes a maximum in the JDOS and hence, in the optical conductivity. The VB and CB are well separated from the other bands that is why TTF-CA can be considered as a two band system by neglecting the lifting of the degeneracy of the VB and CB. The energy difference to the lower bands is about 1.3 eV and decreases to 0.7 eV at low temperatures. This is similar to the upper band whose distance reduces from 1.5 eV at 300 K to 1.1 eV at 15 K. Therefore, it is not surprising that in the visible range strong modifications of the optical properties of TTF-CA occur by going from the neutral to the ionic phase.

Additionally to the band structure, we theoretically determined the optical conductivity according to Eq. 4.20 for all crystallographic directions by calculating the electronic transition of 200 equally spaced k-points in the Brillouin zone. In this case, we used norm-conserving PBE pseudo potentials at which the band gap was determined to 0.11 eV at 300 K and 0.28 eV at 15 K. They agree very well with previous calculations [288], based on LDA, but their results are closer to the experimentally determined 0.6 eV. It is, however, well known that especially the LDA functional underestimates the experimental band gap more than the GGA functional, as PBE.

36 Definition of the joint density of state JDOS: $D(E_{VB}) \propto \int \frac{dS_k}{\nabla_k \Delta E}$. Special interesting points of the JDOS are positions in the k-space where the energy difference E_{CB}-E_{VB}=ΔE becomes stationary and varies only slightly in a large region of the k-space, meaning that the deviation in the denominator $\nabla_k \Delta E$ tends to zero and thus, JDOS diverges.[81]

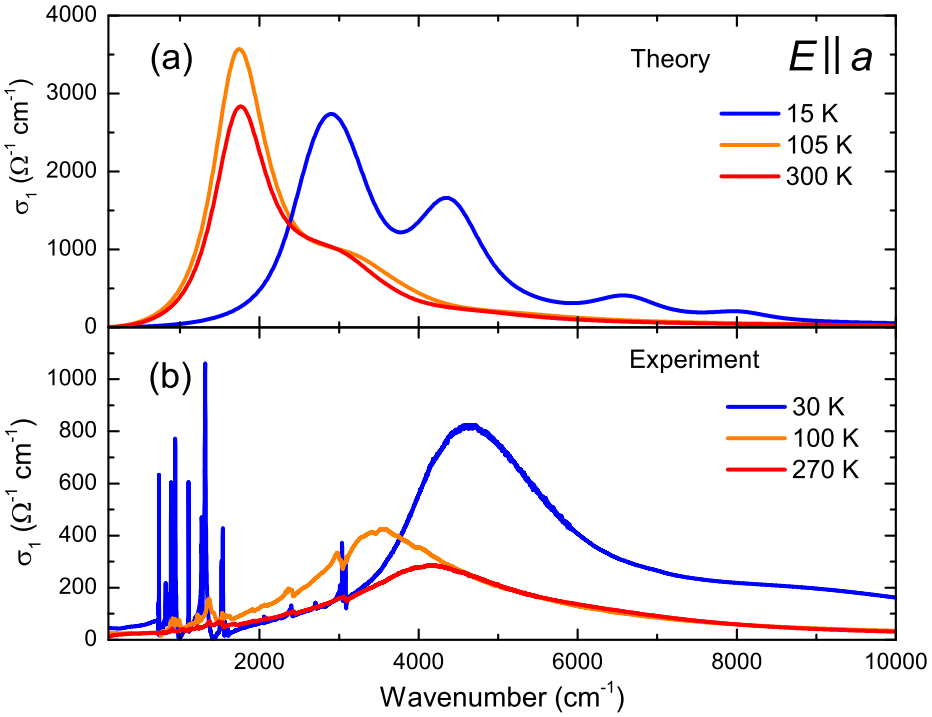

Figure 5.60: (a) Optical conductivity $\sigma_1(\nu)$ of TTF-CA at 15 K (blue), 105 K (orange) and 300 K (red) along the stacking direction. The calculations were performed with the method described in Sec. 4.5. Various electronic transitions between the lower valence bands and the unoccupied conduction band are visible. (b) Experimentally determined optical conductivity $\sigma_1(\nu)$ of TTF-CA at 30 K, 100 K, and 270 K. In the range between 3000 cm^{-1} and 10000 cm^{-1} the electronic excitations are located while the sharp features below 3000 cm^{-1} can be ascribed to intramolecular vibrations.

In Fig. 5.60 the theoretically calculated optical conductivity $\sigma_1(\nu)$ is compared with the experimentally received conductivity in a frequency range from 0 cm^{-1} (-experiment: 500 cm^{-1}) to 10000 cm^{-1} for $E \parallel a$. The transitions were folded for a better comparison with a Lorentz function with the width of 800 cm^{-1} (0.1 eV). At room temperature the maximum in Fig. 5.60 (a) is located at 1700 cm^{-1} (0.22 eV) and does not shift with temperature till 100 K. Below the phase transition the maximum is suddenly located at higher energies at 2900 cm^{-1} (0.36 eV) which is related to the increase of the band gap in the ionic phase. Besides that, further maxima exist which originate from transitions between the VB and CB with a large JDOS due to a constant ΔE between the bands, for instance at the symmetric X or S points. The temperature-dependent shift of the spectra agrees qualitatively very well with the optical study. Only the absolute positions of the resonance frequencies of the experiments are located higher, between 1400 cm^{-1} and 2400 cm^{-1}, which can be attributed to the underestimation of the gap by the DFT method. Furthermore, it can be supposed that the experimental mid-infrared interband transition is composed of several excitations which are rendered by the simulation. They are added up to this one broad feature. One strong proof for it is the long tail above 6000 cm^{-1} in the case of the spectra at 30 K indicating the fact that more electronic excitations are involved in this optical band. This probably explains the wavelength-dependent generation efficiency in photo-induced

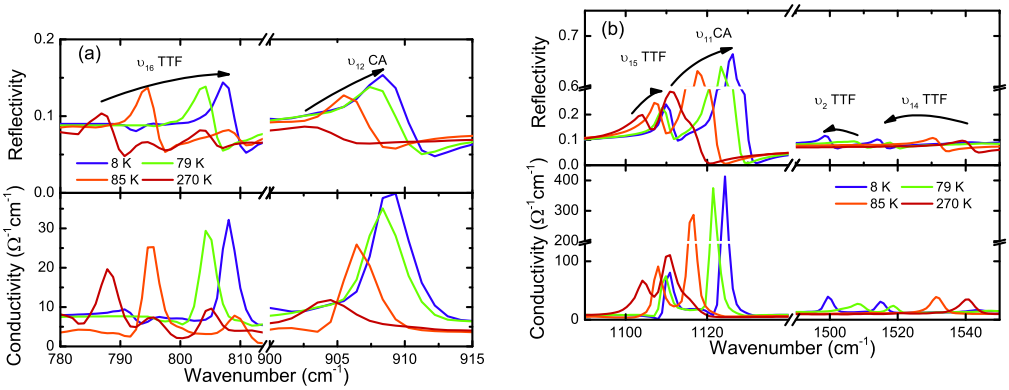

Figure 5.61: (a) Reflectivity and optical conductivity of TTF-CA as a function of temperature in the frequency range from 780 cm^{-1} to 920 cm^{-1}. The first mode can be assigned to the b_{1u} ν_{14} of TTF. The neighboring maximum belongs to the antisymmetric ν_{12}-mode of CA, as listed in Tab. 5.8. (b) Between 1000 cm^{-1} and 1550 cm^{-1} four modes appear whose resonance frequency shifts with decreasing temperature. The strongest intensity has the ν_{11} mode of CA at 1120 cm^{-1} while the antisymmetric modes of TTF are barely noticeable.

phase transition in TTF-CA as up to now less is discussed about the composition of this band. Above the phase transition a slight red shift of the interband transition of about 600 cm^{-1} takes place with decreasing temperature which is related to the thermal contraction of the crystal similar to hydrostatic pressure. The sharp features below 3000 cm^{-1} can be related to intramolecular modes of the TTF and CA molecules and do not influence the electronic excitations. In the experimental spectra no more feature could be detected in the examined spectral range, indicating the excitation of solitons or NIDW.

5.3.5 *Infrared measurements*

Additionally, the samples were further optically characterized along the crystallographic a- and b- axis. One goal was to compare the temperature-dependent reflectivity data with the photo-induced measurements and by that derive the induced state. As mentioned previously in Sec. 5.3.4, the spectra along the stacking directions contain information about the molecular vibrations of the single molecules within the unit cell as well as about electronic excitations. In contrast, no inter- and intraband transitions occur along the b-direction and enable a clear view on the infrared-active molecular vibrational modes. The following paragraph is dedicated to the optical properties of the a- and b-axis and their temperature-dependent behavior.

b-direction

Due to the absence of electronic excitations, the odd modes of TTF and CA can be observed without any problems with light polarized parallel to the b-axis. The b_{1u}-modes appear mainly for $E \parallel b$, since their dipole moment is oriented along the long molecular axis (compare therefore Fig. 5.57 and 5.58). However, because of the arrangement of the molecules in the unit cell, also vibrational modes with

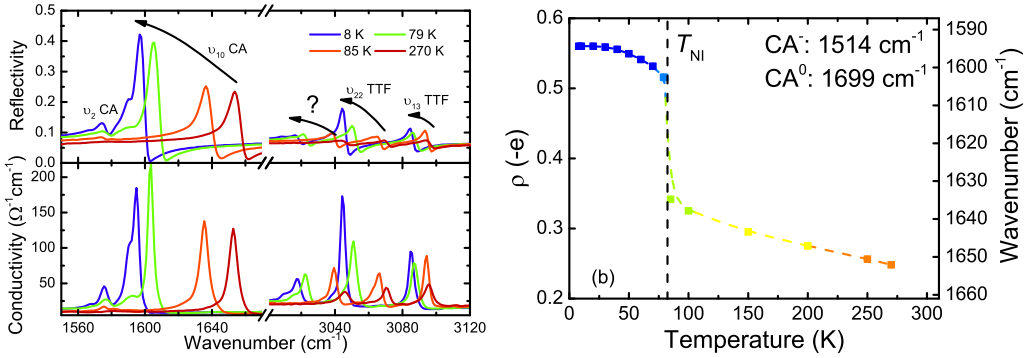

Figure 5.62: (a) Reflectivity and optical conductivity of TTF-CA for four different temperatures between 1550 cm^{-1} and 1670 cm^{-1}. The first mode is ascribed to the charge sensitive, ungerade b_{1u} ν_{10} mode of CA. The neighboring satellite peak belongs to the symmetric ν_2-mode of CA. (b) Temperature-dependent evolution of the resonance frequency of the ν_{10}-Mode. From Eq. 5.21 and the calculated values in Tab. A.3 the ionicity of CA can be determined. At the phase transition the molecular charge jumps from 0.34 e to 0.51 e and increases moderately.

the symmetry b_{2u} can be found whose dipole moment is within the molecular plane, but perpendicular to the long molecular axis.

In Fig. 5.61 (a) and (b) details of the reflectivity and optical conductivity are displayed for four different temperatures. The KKT-transformation were performed by extrapolating the low frequency range with a constant value. For the extrapolation above 6000 cm^{-1} up to 500000 cm^{-1} a ω^{-4}-decay was applied. The data are a composition of own measurements and Ref. [289].

The average reflectivity for the b-axis is 10%. Between 750 cm^{-1} and 920 cm^{-1} two modes are located. The energetically lower resonance at about 800 cm^{-1} can be ascribed to the ν_{16}-mode of TTF which blue shifts on cooling and undergoes a jump of 10 cm^{-1} at the phase transition. The intensity increases slightly as well, as predicted by the theoretical calculations (see therefore Tab. A.4). At RT at higher frequencies further weak maxima can be recognized which we assort to the ν_{25} b_{2u}-mode of TTF [241], which should theoretically appear at 802 cm^{-1} accordingly to Tab. A.4 which is shifted due to the ionicity in this case to 805 cm^{-1}. In the ionic phase a weak satellite peak appears above the ν_{16}-Mode at about 820 cm^{-1} (not shown here) as well. The ν_{12}-mode of CA located at about 905 cm^{-1} shifts a bit to higher energies and gains intensity. The calculations predict a minimal increase of a factor of six. In conclusion, for both considered modes the total shift is moderate.

In Fig. 5.61 (b) the frequency range between 1050 cm^{-1} and 1550 cm^{-1} is visualized. The frequency band at 1100 cm^{-1} is dominated by the ν_{11}-mode of CA which is accompanied by the ν_{15}-mode of TTF. Both modes experience a positive shift of a few wavenumbers on cooling. Especially, the ν_{11} vibration hardens. In the range of 1500 cm^{-1} only one feature exists at 1540 cm^{-1} in the neutral phase which is related to the ν_{14} mode of TTF. In the ionic phase it is located at 1520 cm^{-1}. In addition, a further mode appears at 1510 cm^{-1} and 1500 cm^{-1}, which can be ascribed to the symmetric ν_2 mode of TTF, which are infrared-active due to emv-coupling in the modified crystal field below the phase transition. However, it can be as well assigned to a combination or higher harmonic mode which becomes allowed due to the altered PES of the molecules.

In the spectral ranges illustrated in Fig. 5.62 the ν_{10} and ν_2-Mode of CA are shown. The ν_2 mode appears only in the ionic phase and does not exhibit any temperature dependence and therefore, we suppose a symmetric mode becoming infrared-active due to the dimerization below T_{NI}. In contrast, the antisymmetric ν_{10} mode reveals a strong shift with decreasing temperature and hence, a change of the molecular ionicity. Furthermore, the intensity increases strongly below the phase transition. Therefore, this mode is absolutely the first choice to determine the charge state of the molecule within the different phases. For the antisymmetric mode is generally known as in the previous chapters, that a linear relation between the molecular charge and the resonance frequency holds. Girlando et al. [290] have shown that for the symmetric a_g-mode the resonance frequency changes nonlinearly with charge per molecules by what it is not appropriate to determine the ionicity.

By the help of the resonance frequency of the ν_{10} mode of CA and the calculated values from Tab. A.3 for ν_{10} and the equation:

$$\rho_t = \frac{\nu_0 - 1699\,\mathrm{cm}^{-1}}{185\,\mathrm{cm}^{-1}} \tag{5.21}$$

the molecular charge ρ_t can be derived at which the resonance frequency of a neutral CA molecule is 1699 cm^{-1}, while the total difference between the positive charged and neutral CA molecule is -185 cm^{-1}. In the neutral phase the charge changes from 0.25 e to 0.35 e at 85 K on cooling. Thus, the charge transfer increases slightly with decreasing temperature. Below 85 K at 81.5 K the charge is suddenly redistributed so that ρ_t jumps to 0.52 e. This abrupt change is a direct hallmark of a first-order transition. Further typical behavior is the appearance of hysteresis between the cooling and heating cycle which, indeed, we have observed in our optical measurement by a very slow cooling rate (not presented here). The difference between the coercive temperatures is 3 K. This observation agrees very well with previous measurement of the heat capacity and the crystal structure [291].

The methyl vibrations of the TTF molecule are located mainly in the range of 3000 cm^{-1}which is illustrated in the right frame of Fig. 5.62 (a). There, several resonances can be observed which are connected to different vibrational states of CH_3. Two of three of the modes can be assigned, in accordance to the values in Tab. A.4, to ν_{22} (b_{2u}) and ν_{13} (b_{1u})-modes. The third maximum cannot be ascribed to a specific vibration. However, it can be supposed that it is the emv-coupled a_g or the second harmonic of the ν_{14}-mode.

To analyze the spectra quantitatively, we fitted resonances in the optical conductivity $\sigma_1(\nu)$ as well as the reflectivity $R(\nu)$ simultaneously with Fano functions (for more details it is referred to Appx. F). The temperature-dependent evolution of all resonance frequencies is depicted in detail in Fig. 5.63. All shown modes reveal without exception a slight shift within the neutral phase, but at T_{NI} their frequency changes suddenly marking the phase transition. Below the transition it saturates at a fixed value below 20 K. This is originally caused by the thermal contraction of the unit cell enhancing the charge transfer on cooling. This behavior is in strong contrast to the behavior of the Fabre-salts (see Sec. 5.1.4) whereas the transition of the charge ordered state evolves continuously indicated by the charge imbalance. Moreover, several features reveal a positive shift instead of a negative one which can only be predicted by a previously performed calculation. The sign of the frequency shift depends on the intermolec-

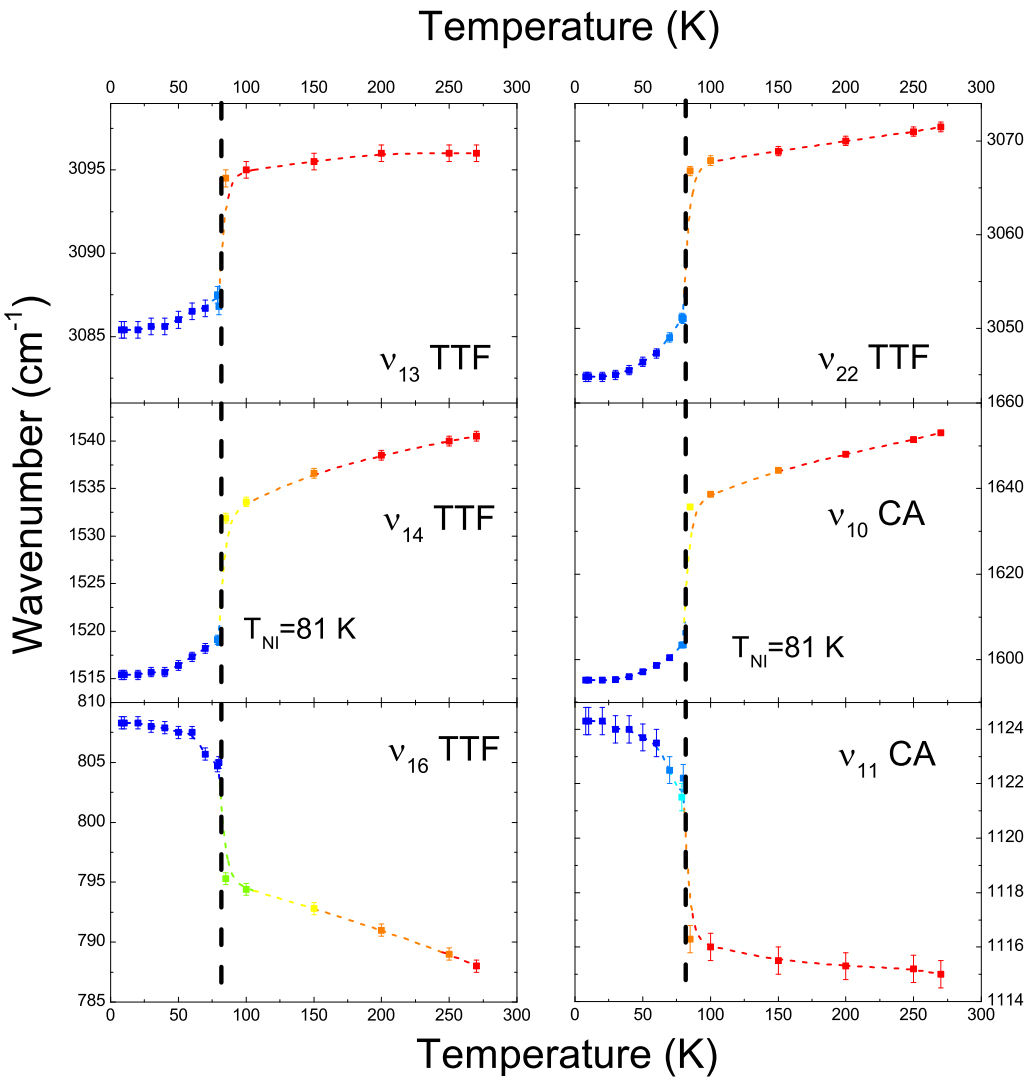

Figure 5.63: In the single graphs the vibrational frequency of all modes observed in the *b*-direction are depicted.

ular forces and bond lengths which are a function of the charge distribution within the molecule, therefore depending on the charge state of the molecule. In principle, every mode can be used to determine the ionicity. However, the ν_{10} mode of CA has some unbeatable advantages to other modes: i.) The total shift between the neutral and positive charged molecules is with -185 $\frac{\text{cm}^{-1}}{e}$ extremely large. ii.) The infrared intensity, corresponding to the calculation, is the largest. iii.) The relation between charge and frequency is linear.

a-direction

In the framework of this thesis we also studied the spectrum for $E \parallel a$ for various temperatures above and below the phase transition. Since TTF-CA is insulating in the neutral phase, one would in general extrapolate the low frequency part with a constant value. However, we know that below 200 cm^{-1} very strong lattice vibrations [292] exist which have a strong impact on the reflectivity and lift it up to almost 0.6. Therefore, an effective reflectivity function was used as an extrapolation in this frequency range resembling exactly this behavior. It consists

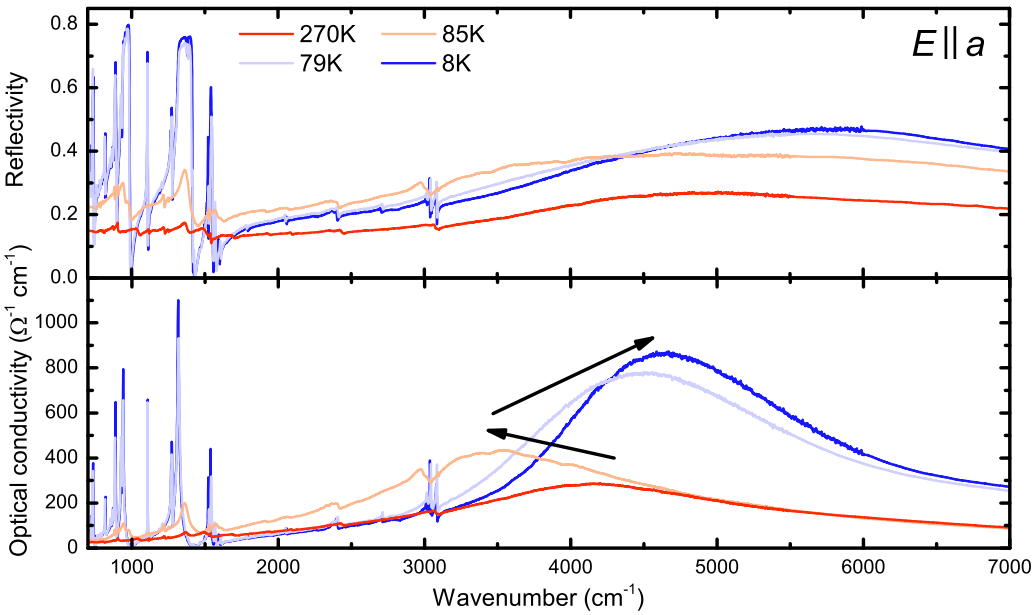

Figure 5.64: Reflectivity and optical conductivity of TTF-CA for $E \parallel a$ from 295 K to 8 K between 700 cm^{-1} and 7000 cm^{-1}. The spectrum is divided into the regions: i.) From 700 cm^{-1} to 3200 cm^{-1} intramolecular modes dominate and ii.) in the higher frequency range the feature originates from electronic excitations.

of an averaged spectrum of the far-infrared measurement [292]. For the high frequency part, a ω^{-4} extrapolation was employed up to 500000 cm^{-1}.

In Fig. 5.64 the reflectivity and the optical conductivity of TTF-CA along the stacking direction is exemplary plotted for a few temperatures between 700 cm^{-1} and 7000 cm^{-1}. The most prominent feature is the charge transfer band whose maximum at RT is located at 4000 cm^{-1} and shifts about 500 cm^{-1} to 3500 cm^{-1} at 85 K on cooling. After the transition the maximum jumps to 4500 cm^{-1} due to the hybridization of the TTF and CA orbitals in the ionic phase and therewith the related charge transfer by what the ionicity is increased as well. For further cooling the maximum moves barely observable about 100 cm^{-1} to 4600 cm^{-1}. Additionally, the intensity rises drastically. The absolute values agree very well with previous measurements [293]. As shown in Sec. 5.3.4, the broad band consists of several narrower bands expressed in the experimental spectrum as a shoulder connected to the maximum at higher frequencies. We attribute this to the excitation of an interdimer transition [293]. Similar observations were made earlier in charge transfer salt K-TCNQ [294] and related to the excitations into the conduction band. This interpretation is conform with our calculation that it is a transition from the HOMO/ VB to the LUMO/CB.

To make a precise statement, the spectra were fitted for the electronic excitation with a Lorentz function and the molecular vibrations with Fano functions (see Sec. F and F). From the mid-infrared band the transfer integral t and the charge transfer ρ_t can be determined by the following relation [295] starting with the oscillator strength $f_{Osc.}$:

$$f_{Osc.} = \frac{\omega_p^2 m \epsilon_0}{4\pi N e^2} \tag{5.22}$$

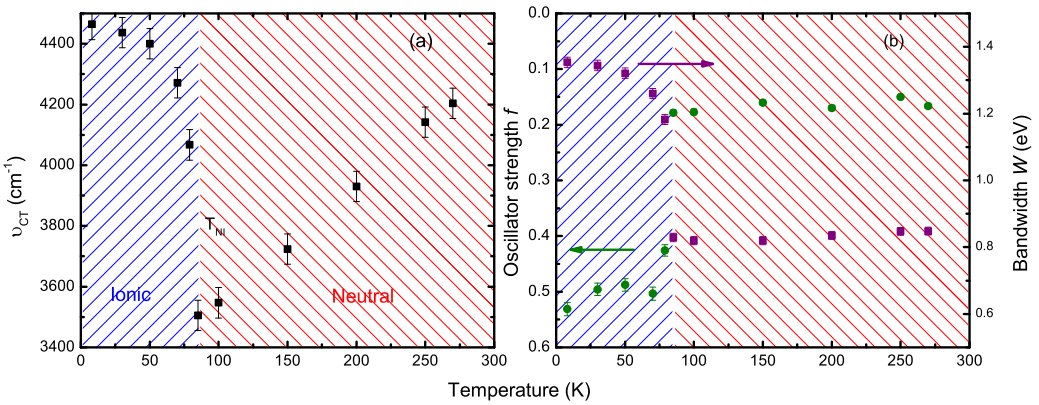

Figure 5.65: (a) Resonance frequency of the charge transfer band of TTF-CA as a function of temperature. (b) Temperature dependence of the oscillator strength of the charge transfer band (left scale) and the bandwidth for different temperatures (right scale).

with N the number of Dimer pairs in the unit cell and the plasma frequency ω_p of the resonance. The charge transfer ρ_t is related to the transfer integral t via the charge transfer band ω_{CT} and the following formula:

$$\rho_t = \frac{3et^2}{2(\hbar\omega_{CT})^2}. \tag{5.23}$$

By using the charge transfer ρ_t determined in the previous section from the ν_{10} mode and the resonance frequency of the mid-infrared band ω_{CT}, depicted in Fig. 5.65 in cm^{-1} the transfer integral t can be deduced. We suppose that on cooling t only varies slightly since ρ_t increases and ω_{CT} decreases in the neutral phase to jump abruptly at the phase transition accordingly to the behavior of ρ_t and ω_{CT}. From t the bandwidth $W = 4t$ can be estimated with values of about 0.8 eV in the neutral phase and 1.3 eV at 8 K. If we compare these values now to the total bandwidth of the calculated bands in Sec. 5.3.4, which is 0.7 eV at RT and 1 eV at 15 K, they match nicely and reproduce the properties of the material accurately. The temperature-dependent behavior is illustrated in Fig. 5.65 (b) together with the oscillator strength $f_{Osc.}$. The oscillator strength reflects very well the trend of the mid-infrared band intensity which gains drastically on strength from 0.1 to 0.6 and thus, dominates the optical response in this frequency range.

In Fig. 5.66 (a) and (b) the reflectivity and the optical conductivity are depicted in the frequency range from 1650 cm^{-1} to 750 cm^{-1} for 8 K and 270 K. In this energy range the intramolecular modes of the TTF and CA molecules, which are the most interesting ones, can be found [241, 254, 286]. Along the a-direction the symmetric a_g as well as the infrared-active b_{3u} modes of CA and TTF can be observed whereas the first one is only infrared active due to the emv-coupling. Because of the electronic coupling to the charge transfer band each mode is modeled by a Fano function. In the case of the b_{3u} modes the vibrational frequency appears below 700 cm^{-1} and thus, not arises in the studied regions. Above the phase transition in the neutral phase the TTF and CA molecules are not dimerized since the distance between them is constant with 3.70 Å, why the a_g modes are only slightly infrared-active and the optical conductivity is low.

In the ionic phase the point inversion symmetry is lost and the molecules become dimerized, by what the intermolecular distance alters and the intensity of

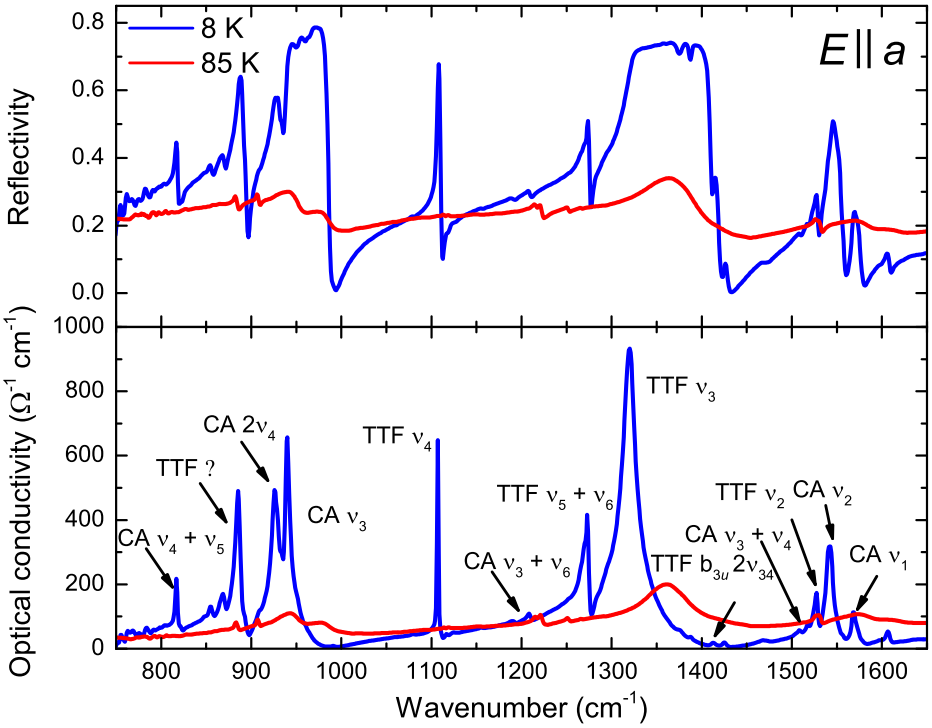

Figure 5.66: (a) Reflectivity of TTF-CA for 8 K (blue) and 85 K (red) between 750 cm^{-1} and 1650 cm^{-1}. (b) Corresponding optical conductivity is illustrated. The maximum is mainly caused by emv-coupled modes which gain intensity in the dimerized ionic phase.

a_g modes is enhanced enormously. This extreme gain can be used as a fingerprint for

- the dimerization of the TTF and CA molecules,
- the increase of the ionicity,
- and the transition in the ionic phase related to it.

First, we have assigned the features to the corresponding vibrational modes. Starting with the lowest energy the first maximum is located at 816 cm^{-1} and can be ascribed to the combination of the $\nu_4 + \nu_5$ (a_g) modes. In the harmonic approximation such coupling between different modes is not allowed due to the selection rules because due to the strong interaction between the molecules in the ionic phase the PES are strongly deformed and become therefore anharmonic which causes the selection rules to be lifted.[37] For combination modes as well as for overtones, the original modes with the symmetry a_g lead in the case of the direct product $a_g \otimes a_g$ again to an a_g symmetric mode which stays by that symmetric and infrared-active via emv-coupling. In the most cases the intensity of the

37 Beginning with a symmetry consideration the molecules are in the D_{2h} symmetry group in gaseous phase with 8 irreducible representations, as the single molecules in the ionic and in the neutral phase occupy the Wyckoff-position 2a and 4e, respectively. Therefore, they have only the site symmetry C_1 as well as C_i. To receive the actual symmetry of the molecular vibration within the crystal, the site symmetry must be correlated with C_{2h} symmetry of the unit cell. It is noteworthy that the symmetry group of the site position is a subgroup of the unit cell space group and the free molecule symmetry. Thus, the intramolecular vibrations have the following symmetry representatives a_g, b_g, a_u, and b_u, where only the last two ones are infrared-active. The a_g-symmetry of the D_{2h} symmetry group stays conserved in this case.

higher order modes is strongly reduced in comparison to the fundamental one. The resonance frequency is lower than the sum or product of the fundamental mode due to the anharmonicity of the PES.

The next strong feature is at 885 cm^{-1}. An antisymmetric mode can be excluded as the intensity increases in the ionic phase and the spectral shape is antisymmetric, indicating an emv-coupled mode. From our calculations we cannot assign it to a fundamental a_g mode, combination mode or overtone with the corresponding resonance frequency. The satellite peaks at lower energy are very weak and do not appear in the neutral phase. Therefore, they are also emv-coupled modes. As an origin also symmetric modes with the b_{1g}, b_{2g}, and b_{3g} are possible. Since these modes are in accordance to the symmetry of the unit cell, they can have the a_g symmetry and by that become visible along the a-direction.

Two modes in the range from 900 cm^{-1} to 1000 cm^{-1} are from the second harmonic of the ν_4 and ν_3 modes of the CA molecule. At 1100 cm^{-1} a very sharp feature is located which is not existing above T_{NI} and is attributed according to Tab. A.4 to the symmetric ν_4 (a_g) mode of the TTF molecule. Between 1100 cm^{-1} and 1300 cm^{-1} several weak and narrow bands can be discovered. The strongest is settled at 1208 cm^{-1} and correlates with the combination mode of $\nu_3 + \nu_6$ of CA. The combination mode of $\nu_5 + \nu_6$ of TTF is located 1270 cm^{-1}. The maximum with the largest intensity is caused by the ν_3 mode of the TTF molecules located at 1320 cm^{-1}. This is not surprising since the coupling parameter g_i with 115 meV is the largest. Close to this mode several weak features are connected whereas one of them corresponds to the strongly infrared-active, odd ν_{34} (b_{3u}) mode. At 1507 cm^{-1} the combined mode of $\nu_3 + \nu_4$ of CA appears. The three following features at 1527 cm^{-1}, 1540 cm^{-1}, and 1570 cm^{-1} accord to the ν_2 of TTF, ν_2 of CA and the ν_1 mode of CA. These trident-like structure is induced by the small coupling constant of the TTF's modes. From Tab. 5.8 it can be deduced that g_i of CA decreases with rising frequency. By that the intensity of the ν_1 of CA is weaker than the intensity of the ν_2 mode.

In the neutral phase these modes are only very weak due to the absence of dimerization. Nevertheless, the strongest coupled modes can be observed, for example the ν_3 mode of CA at 978cm^{-1} or the ν_3 of TTF at 1360 cm^{-1}.[38]

Since several overtones and combination modes are found in the energy range below 1700 cm^{-1}, we can assume that several weak features must appear above 1700 cm^{-1}, which are depicted in Fig. 5.67. Indeed, aside from the fundamental vibrations of the C-H bonds of TTF at 3100 cm^{-1} several asymmetric resonances occur between 1650 cm^{-1} and 3000 cm^{-1}. The weakest resonance at 1783 cm^{-1} is the second harmonic of the ν_3 mode of CA. The fundamental mode ν_4 mode of TTF, which is situated at 1108 cm^{-1}, causes an overtone at 2050 cm^{-1} as well. The broad feature at 2400 cm^{-1} originates from the ungerade ν_1 vibration of the CO_2 which is present in the atmosphere. The asymmetric resonance located at 2714 cm^{-1} accords to the overtone of the ν_3 mode of TTF. As aforementioned, the strongest resonances above 3000 cm^{-1} are correlated to modes involving the C-H bonds of TTF. The weak sidebands are assigned because of the low intensity to the second harmonic of the ν_1 and ν_2 modes of CA and the ν_2 mode of TTF.

38 Noteworthy, Masino et al. [296] could show by comparison of infrared and Raman spectra that not only intramolecular modes are coupled, but also intermolecular Peierls mode can couple via the modulation of the charge transfer band to the intramolecular modes.

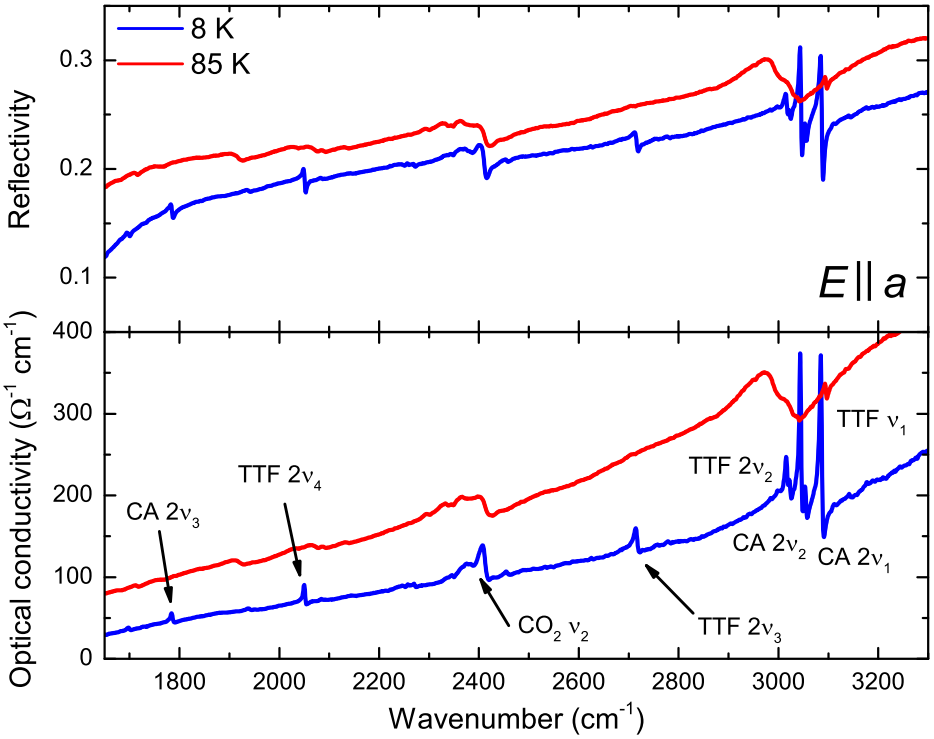

Figure 5.67: (a) Reflectivity of TTF-CA for 8 K (blue) and 85 K (red) in a frequency range from 1650 cm^{-1} to 3300 cm^{-1}. (b) Corresponding conductivity for the same temperatures. The peaks at 3200 cm^{-1} originate from the C-H vibration of the TTF molecule. The weak resonances belong mainly to higher harmonic vibrations of both molecules, CA and TTF.

5.3.6 *Photo-induced phase transition in TTF-CA*

[39]In the following we studied the photo-induced non-equilibrium state of TTF-CA. In recent ultrafast pump-probe experiments were performed to examine the photo-induced phase transition PIPT occurring in TTF-CA in the femto- and picoseconds time range. The studies were mainly restricted to low temperatures (~ 4 K) or very close to the phase transition ($T \leqslant T_{NI}$).

Mainly the charge transfer band with its maximum located at 0.65 eV was excited in the pump-probe experiments while the probing range was predominant the visible spectral range [69, 297]. To the best of our knowledge there is solely one study in the infrared spectral range [298]. The main results were that a ionic-neutral phase transition and vice versa can be induced by photo excitation. As aforementioned in Sec. 5.3.2, the phase transition is accompanied by a break of the symmetry which can be detected by structural resolving techniques.

Indeed, Guérin et al. [299] performed a time-resolved x-ray diffraction experiment in which they could detected the formation of a neutral phase in the ionic matrix. The photo-generated state was stable up to 2.5 ns, demonstrating that the induced state is very robust and long-living.

The ionic-neutral photo-generated phase transition in TTF-CA [63] is the archetype for a PIPT since it was observed almost 25 years ago. Although many studies were undertaken, there are sill many open questions:

39 The following section is correspondingly quoted from Ref. [5].

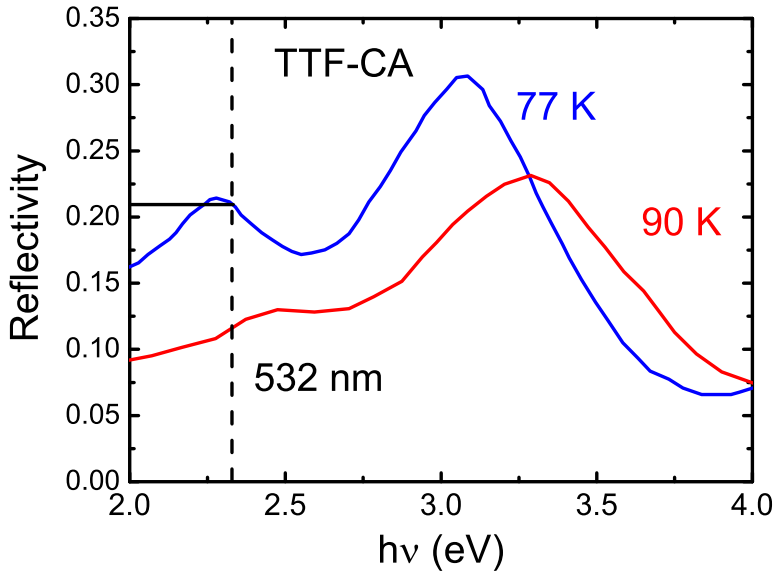

Figure 5.68: Reflectivity of TTF-CA in the ionic (blue) and neutral (red) phase between 2.0 eV and 4.0 eV. The dashed line marks the photon energy of the exciting laser. (Adapted from [63].)

- the dependence of the PIPT on external parameters such as excitation wavelength, photon flux, and enviromental temperature (between 4 K and T_{NI}),
- the relaxation process of the induced state/domains and the relaxation time,
- response of the infrared spectrum after a photo excitation with a photon energy higher than 1.44 eV.

Therefore, we concentrated on the micro- and millisecond time range and on the mid-infrared spectral range in this study. For the excitation, laser pulses with a photon energy of 2.33 eV were used. How can we understand or imagine the PIPT in TTF-CA? That is why we are going to explain the involved creation steps of the metastable phase in detail.

In Sec. 3.1 we have introduced the basic concepts of photo-induced phase transitions PIPT in general. TTF-CA is the model system of organic salts for PIPT. The first observations of a PIPT were made in 1990 by Koshihara et al. [63]. There, the crystal at 77 K was excited by a pulsed laser with an unknown excitation energy. At the same time, the reflectivity was probed perpendicular to the stacking direction, as visualized in Fig. 5.68, in the spectral range from 1.5 to 4 eV (from 12000 $cm^{-1}$to 32000 cm^{-1}). The maxima at 3.3 eV (26600 cm^{-1}) and 2.5 eV in the neutral phase can be assigned to the intramolecular excitation of $TTF^{+\rho}$. The maxima shift due to the increasing ionicity below T_{NI} to lower energies. A similar conclusion can be drawn from the consideration of the band structure, in which the distance of the bands below the VB and the bands above the CB is reduced below the phase transition (see Sec. 5.3.4). The excitations of the anion CA are above 4.0 eV. The modification of the reflectivity can be used to determine the present state of TTF-CA. A comparison of the modification of the reflectivity between the thermodynamic equilibrium above (90 K) and below (77 K) the transition with the photo-induced change of the reflectivity, indeed, reveal a transition from the ionic phase to the neutral one. The state decays within

Table 5.9: Electronic transitions of TTF^+, TTF^0, CA^-, and CA^0 correlated with the corresponding experimentally determined excitation energy in $cm^{-1}$and eV. The relative intensities are in brackets.

Transition	Excitation energy TTF^+[306][40]	Excitation energy TTF^0[307, 308] [41]
1	17300/2.14(0.27)	22200/2.76(0.02)
2	20300/2.51(weak)	27100/3.37(0.16)
3	23000/2.85(1.00)	31600/3.92(0.89)
4	29600/3.67(0.52)	33000/4.09(1.00)
Transition	Excitation energy CA^-	Excitation energy CA^0
1	22300/2.77(-)[309, 310]	27200/3.37(-)[311]
2	23700/2.94(-)[309, 310]	34800/4.32(-)[311]
3	31100/3.86(-)[309]	

a few milliseconds. Measurements of the static photoconductivity let suppose that neutral domains, which are separated by NIDWs from the ionic phase, are generated and the NIDWs contribute with their fractional charge state to the photocurrent. The activation energy of the photocurrent [63] is $\Delta_{Photo} = 0.09\,eV$ and corresponds exactly to the activation energy of the dark current. From that we can deduce that the conductivity contributions in both cases are thermally activated or optically excited NIDWs, respectively.

Based on this pioneer work numerous studies [69, 300, 301, 302, 303] of the PIPT were stimulated aiming to examine the creation process of the neutral domains in the ionic phase. Mostly only two temperatures were studied; one very close to the transition (~ 78 K) and for a very low temperature (~ 4 K). It turned out that close to the phase transition the conversion efficiency is significantly larger at the same photon density. Beside temperature, the dependence of the PIPTs on the photon energy was examined in the NIR range. It was demonstrated that the laser pulses with a photon energy E_{Photon} between 0.65 eV and 1.55 eV must exceed a certain threshold intensity [301, 302, 304] to induce the neutral domains. The photon energy corresponds in this case the energy ω_{CT} of the charge transfer band/exciton (CT) which we have identified in the spectrum as a broad maximum at 5200 cm^{-1}(0.65 eV). A successive decrease of E_{Photon} beginning from 1.55 eV leads to a decrease of the threshold intensity [302], which does not drop to zero E_{Photon}. The situation changes when the intramolecular, vertical electronic transition of CA^- and especially of TTF^+ is excited. The four lowest electronic transitions in TTF^+ and TTF^0 are listed in Tab. 5.9 causing four different bands in the visible spectral range which are located in TTF-CA in the ionic phase between 2 eV and 4.5 eV [294, 305]. From Tab. 5.9 it is apparent that the position strongly depends on the ionicity ρ_t. Therefore, these features can be used to determine the critical temperature of the phase transition. In the case of TTF the transition bands undergo a redshift between 3400 $cm^{-1}$and 8600 cm^{-1} in comparison to the gas phase.[42] In Fig. 5.68 it is depicted that the

42 Due to the interaction of the molecules with their environment, for instance with neighboring molecules in the crystal or in a solvent, a so-called solvent shift of crystal shift [312] is induced causing most of the interband transitions to shift to lower energies. The magnitude of the shift depends on the type of solvent and affects differently on the energy levels [15]. Thus, the listed values for the neutral and charged state of the molecules are solely guided values and can vary.

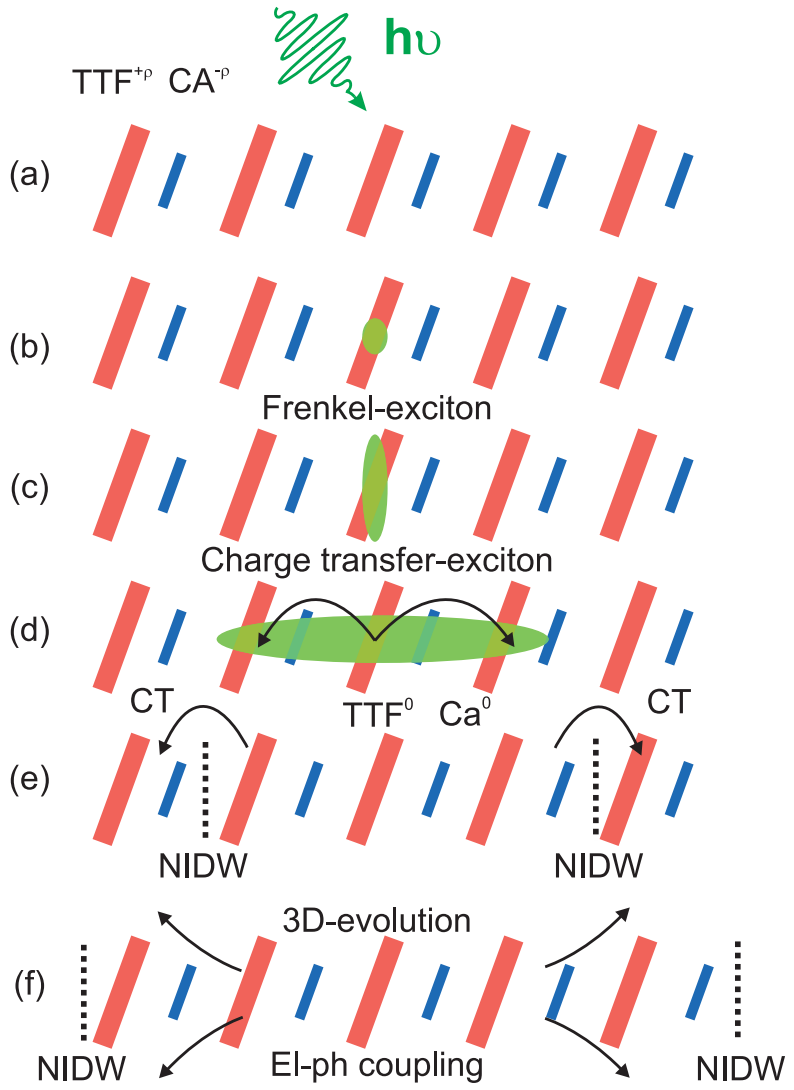

Figure 5.69: (a) Illustration of a 1D-chain of dimerized $TTF^{+\rho}$ and $CA^{+\rho}$ pairs in the ionic phase in TTF-CA. A $TTF^{+\rho}$ molecules is excited with a laser pulse with the photon energy $E_{Photon}=h\nu$. (b) Vertical excitation of the HOMOs of $TTF^{+\rho}$ according to the Frank-Condon-principle in the LUMO of $TTF^{+\rho}$. The excitation is strongly localized to the molecule. (c) Creation of excitons, for instance Frenkel-excitons, which are delocalized across the whole molecules. (d) Via different relaxation processes and channels charge transfer excitons are created which triggers to the transition of the neutral phase. (e) The dimerization is suppressed and the charge between the molecules is redistributed. A neutral domain is created in the ionic host matrix which is separated by NIDWs. (f) Afterwards the neutral domains extend along the 1D-chain. By electron-phonon-coupling also neighboring ionic chains are converted into neutral regions and a 3D domain is established.

temperature-dependent shift of the two maxima is about 1600 cm^{-1}in TTF-CA. This corresponds, under the assumption of a linear relation between the excitation energy and the molecular charge and the usage of Tab. 5.9, a change of the molecular charge of 0.25 e and 0.2 e, respectively, which is in perfect agreement with values derived from the resonance frequency of the ν_{10} (b_{1u}) mode.

The PIPT measurements, where the second harmonic (19000 cm^{-1} ~ 2.35 eV) of a pulsed Nd:YAG laser is used, only one of the first transitions of TTF^{+} is excited. A further look manifests in Tab. 5.9 that this assumption is absolutely correct since all intermolecular transitions of CA^{-} lie above the photon energy E_{Ph} =

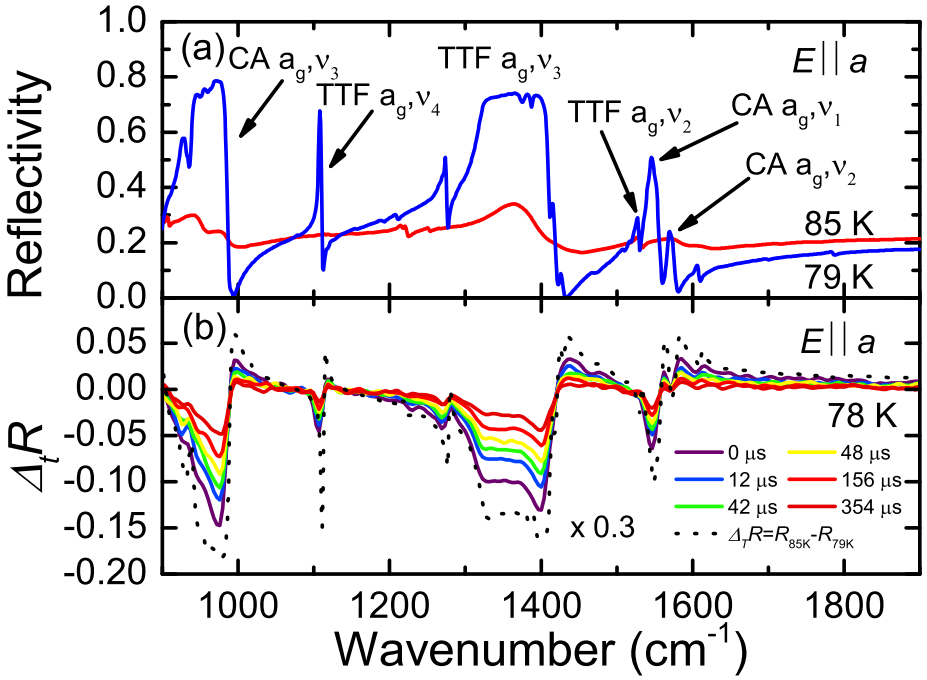

Figure 5.70: (a) Reflectivity of TTF-CA along the stacking direction in a frequency range from 900 cm^{-1} to 1900 cm^{-1} for 79 K (red) and 85 K (blue). The a_g modes become strongly enhanced due to the dimerized TTF and CA pairs in the ionic phase. (b) The temporal sequence of the reflectivity change $\Delta_t R = R(t) - R(0)$ (solid lines) after photo excitation is depicted for various times and directly compared to the static reflectivity difference $\Delta_T R = R_{85K} - R_{79K}$ (dashed line). (Reprinted with permission from Ref. [5].)

2.35 eV. It should be stated that also excitations from lower lying bands into the VB are possible, which are not included into this consideration. As one of the first, Suzuki et al. [301] have compared the dependence of the conversion efficiency on the photon energy (ses Fig. 5.72) and stated that by excitation of intramolecular transitions no threshold intensity occurs to create neutral domains.

In Fig. 5.69 the optical generation of neutral domains is schematically illustrated. (b)-(c) In the case of the intramolecular excitations Frenckel-excitons [15, 312] are created, which are electron-hole pairs which are in contrast to Wannier-excitons (occuring in anorganic semiconductors as silicon) that are strongly localized on the excited molecules. The Frenckel-excitons decay via various decay channels into several charge transfer excitons [74] (d)-(e) and lead by that to a phase transition. The participating processes are named in Sec. 3.1. While in this case several CT are created, in the direct excitation of the charge transfer band only one CT is created which is not enough to establish a macroscopic, metastable domain extended over several D^0A^0 pairs. First, with a sufficient number of photons which create a CT by that a multiplicative, non-linear effect is established, formating metastable domains. By the creation of the 1D, neutral, non-dimerized region NIDWs formed between the neutral and ionic parts. The excitation energy of the NIDW is about 0.1 eV [256, 267] and corresponds to the activation energy of 0.12 eV and 0.065 eV in the ionic phase, determined within this thesis.

In the generation process of NIDW besides the excitation wavelength, the excitation energy [69] plays an important role since also soliton states with a spin can be created on which time-dependent measurements will focus in the future.

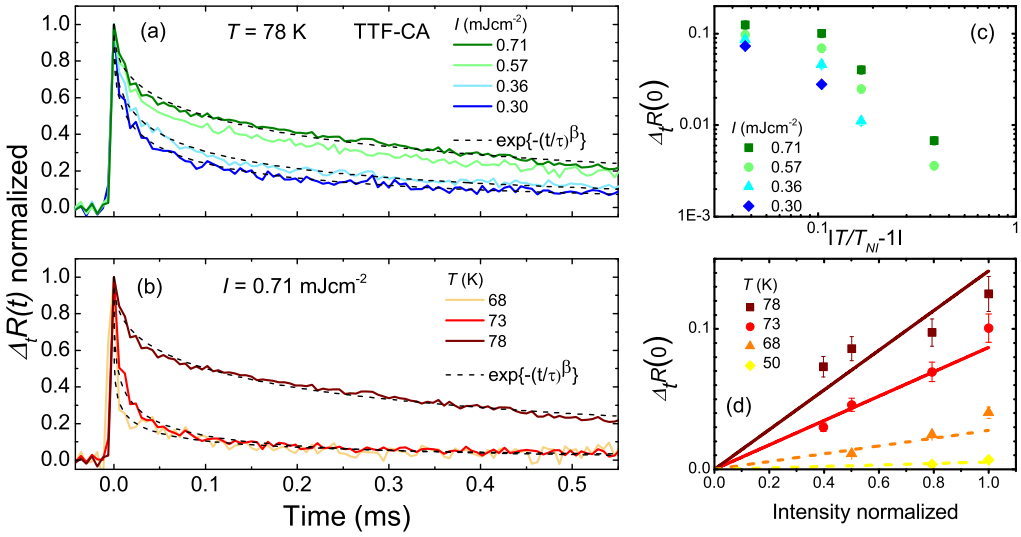

Figure 5.71: (a) and (b) Normalized $\Delta_t R(t)$ for various laser intensities recorded at 1390 cm^{-1} for $T = 78$ K and for different temperatures for 0,71 $\frac{mJ}{cm^2}$. The time profile can be successfully fitted by a KWW function $\exp\{-(t/\tau)^\beta\}$ (dashed linies). (c) Absolute value of $\Delta_t R$ for different laser intensities and temperatures observed immediately after the photo excitation. (d) $\Delta_t R$ as a function of the normalized laser intensity for temperatures between 50 K and 78 K. (Adapted with permission from Ref. [5].)

Theoretical calculations have shown that the activation energy is between 25 meV [268, 269] and 56 meV [270]. According to Soos and Painelli [270] the term "domain" can be used above a total length of 30 DA-pairs [43].

Afterwards, the electronic system couples to the crystal lattice and exciting phonons [303] via electron-phonon coupling and hence, creates shock-waves. They can convert neighboring chains into neutral domains. The total conversion process is finished after several hundred picoseconds. In ultrafast pump-probe experiments it was observed that the life time can range in the millisecond time range.

EXPERIMENTAL CONFIGURATION For the time-resolved study the second harmonic light pulse ($\lambda = 532$ nm, pulse length: 8 ns) of an Nd:YAG laser was used to excite the TTF-CA crystal. The time-dependent response of the infrared reflectivity signal was detected by an FTIR spectrometer operating in the Step-Scan mode, which is describe in detail in Sec. 4.1.3.

PHOTO-INDUCED PHASE TRANSITION The static reflectivity of TTF-CA for $E \parallel a$ in the ionic and neutral phase (T=85 K and 79 K) is presented in Fig. 5.70 (a). As discussed in Sec. 5.3.5 the symmetric a_g modes become infrared activated in the ionic phase due to the dimerization of the molecules along the a-direction. This effect is a unique property of the ionic phase and thus it can be utilized to measure the vanishing of the ionic state [303].

In Fig. 5.70 (a) the time-dependent behavior of the reflectivity change $\Delta_t R = R(t) - R(0)$ at $T = 78$ K and for a laser pulse intensity of 0.71 mJ/cm^2 is directly compared with the static reflectivity change $\Delta_T R = R_{85K} - R_{79K}$. By photo excitation $\Delta_t R$ becomes negative within a short time which is below the experimental time resolution of 6 µs. The direct comparison of the $\Delta_t R$ shape and the static

43 This term we will be used in this manuscript nevertheless for domains larger than five DA-pairs.

reflectivity change $\Delta_T R$ reveal that the ionic phase was not only dissolved, but also a transition into a neutral state was induced. Within several hundreds of microseconds the signal $\Delta_t R$ relaxes back to zero which means that the ionic phase is reestablished. Moreover, no change of the spectral shape with the elapsed time and laser pulse intensity could be detected.

$\Delta_T R$ was scaled by a factor of 0.33 to reach the same value as the maximum value of $\Delta_t R$ immediately after the photo excitation. The difference of the absolute values originated from the different penetration depth of the visible light (~200 nm)[44] is by a factor of 10-times smaller than the penetration depth of the infrared light.

To trace the temporal evolution of the PIPT in dependence of the pump intensity and the sample temperature, we have chosen the very intense ν_3 (a_g) mode of TTF residing at 1390 cm^{-1}since we have asserted that the temporal evolution is the same for the whole spectra. The normalized $\Delta_t R(t)$ is represented in Fig. 5.71(a) for different pulse intensities. Several temporal regimes can be recognized:

1. at the beginning the signal decays very fast
2. and at the end it flattens out.

At the vicinity of T_{NI} the first component decays faster with decreasing laser intensity. In literature the time-dependent signal is in general fitted by a simple single or double exponential function [74]. However, in this case it only can be nicely modeled by a stretched-exponential function, which is also called Kohlrausch-William-Watt (KWW) function [313, 314] $\Delta_t R(t) \propto \exp\left\{-(t/\tau)^\beta\right\}$, as depicted in Fig. 5.71(a) and (b). The fitting parameters β and τ are a function of the laser intensity and decreases from 0.35 to 0.42 and from 3.4×10^{-5} to 2.4×10^{-4} s with decreasing laser intensities. As stated earlier, the behavior of the PIPT in a larger temperature range below T_{NI} is of great interest. Therefore, the temporal behavior was examined in a temperature between 68 K and 78 K.

In Fig. 5.71(b) $\Delta_t R(t)$ is displayed for 68 K, 73 K, and 78 K. Far below T_{NI}, the temporal dynamics of the reflectivity drops very fast within the first 20 µs and approaches asymptotically a constant value which is in contrast to the temporal profile at the vicinity (T=78 K) of T_{NI} which constantly diminishes. Similar to the dependence of the fitting parameters on the laser intensity the effective recombination time τ as well as the stretching exponent decrease from 2.4×10^{-4} s to 3.2×10^{-6} s and from 0.42 to 0.23, respectively, with decreasing sample temperature.

The total change of $\Delta_t R(0)$ is depicted on a logarithmic scale for the normalized temperature $|\frac{T}{T_{NI}} - 1|$ and for various laser intensity in Fig. 5.71(c). Typically for a PIPT [74], $\Delta_t R(0)$ diverges closely to the phase transition temperature and decreases exponentially independently on the laser intensity. The temperature dependence behavior of $\Delta_t R(0)$ is in accordance with previous experiments [69]. The actual absolute values can be higher since the first nanoseconds of the phase transition are not captured due to the limited time resolution.

$\Delta_t R(0)$ is a linear function of the laser intensity, which is visualized in Fig. 5.71(d). We do not recognize any saturation of the signal and no threshold value

44 The penetration depth was determined from the reflectivity in the visible range depicted in Fig. 5.68 by fitting the spectra with three Lorentz functions. From the optical conductivity $\sigma_1(\nu)$ and $\sigma_2(\nu)$ the penetration depth $\delta_d(\nu)$ can be deduced from the equation $\delta_d(\omega) = \sqrt{\frac{2}{\omega\nu_0}}((\sigma_1^2(\omega) + \sigma_2^2(\omega))^2 + \sigma_2(\omega))^{-0.5}$.

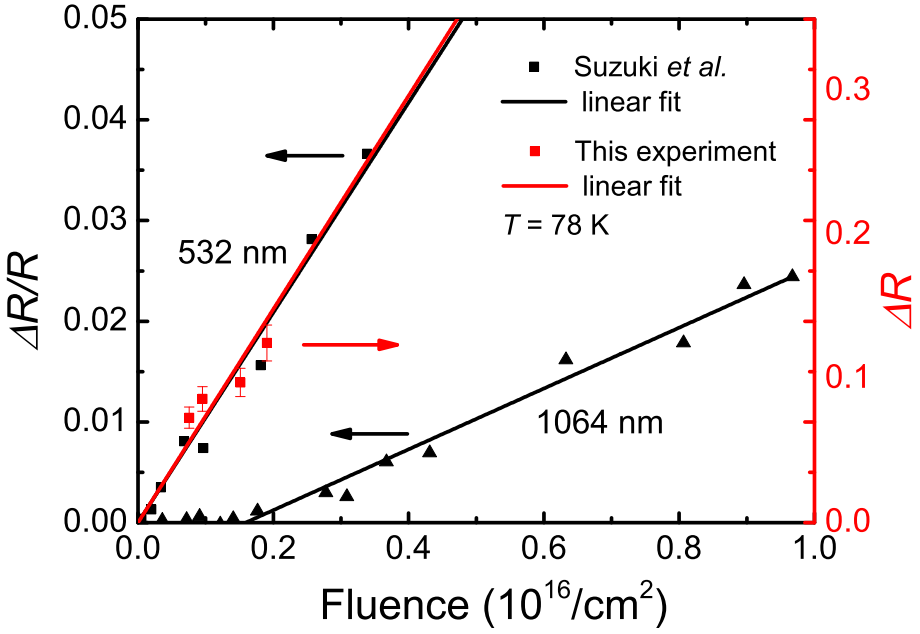

Figure 5.72: Comparison of the results from our study recorded at 1390 cm^{-1} and 78 K with an excitation energy of 2.33 eV (532 nm) with the variation of the reflectivity at 24200 cm^{-1} from Ref. [301] recorded 3 µs after the photo perturbation detected as well at 78 K for two different excitation energies (532 nm and 1064 nm).

for the laser intensity. Therefore, a thermally induced phase transition can be excluded in general. A comparison with previous measurements, which are presented in Fig. 5.72, reveals that the observed linear behavior of $\Delta_t R(0)$ agrees very well with the study of Ref. [301]. There, the change of reflectivity was measured at 24200 cm^{-1}. By that we can deduce that in the present case $\Delta_t R(0)$ rises with increasing laser intensity as well and does not exhibit any saturation which as well contradicts a thermally induced transition. What one can see in Fig. 5.72 is that when the charge transfer band is excited by light with an excitation wavelength of 1064 nm a threshold intensity has to be exceed to initialize the multiplication effect.

From the laser beam penetrated volume $V = \pi r^2 \delta_d(532\,\mathrm{nm}) \approx 5.6 \cdot 10^{-14}\,\mathrm{m}^3$ the number of excited dimers $N_{\mathrm{Dimer}} = \frac{2V}{V_{Unitcell}} = 1.4 \cdot 10^{15}$ can be calculated via the volume of the unit cell $V_{\mathrm{Unit\,cell}} = 812 \cdot 10^{-30}\,\mathrm{m}^3$. The factor of 2 originates from the fact that two dimers are in the unit cell. The laser pulse with the highest intensity I_{L} yields a photon number of $N_{\mathrm{Photon}} = \frac{\pi r^2 I_{\mathrm{L}}}{E_{\mathrm{Photon}}} = \frac{E_{\mathrm{p}}}{E_{\mathrm{Photon}}} = 5.4 \cdot 10^{12}$ with the pulse energy E_{p} and the photon energy E_{Photon}. This results in 25 $D^{+\rho_t}A^{-\rho_t}$ transferred dimer pairs per photon. This exactly corresponds for a photon energy of E_{Photon}=2.33 eV a conversion energy of 0.09 eV per dimer which perfectly agrees with the energy to generate a NIDW.

HEATING EFFECT To exclude a thermal effect as the origin of the phase transition, we have applied various thermodynamic models to determine the impact of a thermally induced transition. The experiment was designed in such a way that heat accumulation can be completely neglected since the repetition rate was set to 20 Hz which is in comparison to Ref. [315] by a factor of 50 smaller. Furthermore, the selected laser intensities are minimum five times smaller. To make a precise prediction of the sample temperature, the models have been refined

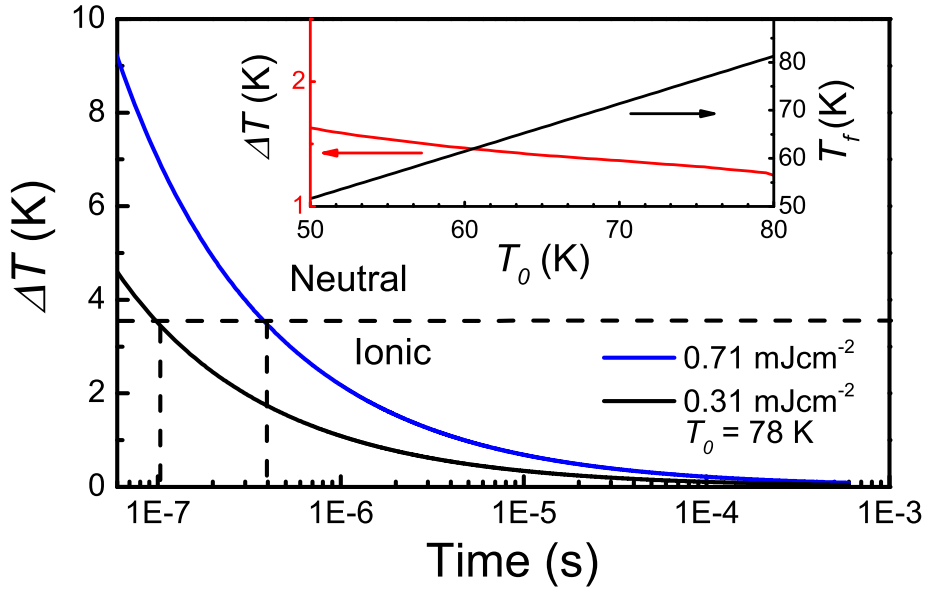

Figure 5.73: Time-dependent behavior of the surface temperature of TTF-CA, determined from Eq. 5.25, after irradiation with the lowest and highest laser intensity at $T_0 = 78$ K. The surface temperature drops below T_{NI} after 500 ns and is below the transition temperature T_{NI} (highlighted by the black dashed vertical line). Therefore, any thermally induced effect can be excluded as the origin of the made spectral observation since it would be far below our time resolution. The detail shows the absolute change (black) and the relative (red curve) temperature modification, T_f and ΔT, below T_{NI} derived from Eq. 5.24, respectively. (Adapted with permission from Ref. [5].)

and only the penetrated volume was considered, instead of the whole sample volume which is oversimplified, but very often applied to determine the sample temperature after photo excitation [315].

To address this question, we have first calculated the absolute temperature variation by neglecting any temperature-dependence to receive an upper limit of the sample surface temperature. The temperature raise can be determined by solving the following thermodynamic equilibrium equation. There, we assumed that the whole laser pulse energy is converted into thermal energy :

$$E_p = n \int_{T_0}^{T} C_p(T) \mathrm{d}T \tag{5.24}$$

with C_p(T) the temperature-dependent heat capacity in units of $\frac{J}{mol\,K}$, E_p the pulse energy, and $n = \frac{\delta_{therm} A \rho}{M_{mol}}$ the amount of substances which is warmed up in units of mol. It was assumed that the total energy is absorbed at the surface. n is a function of the thermal diffusion length $\delta_{therm} = \sqrt{\frac{t_p \lambda_{therm} M_{mol}}{\rho C_p}}$, which is on the scale of micrometer, with the irradiated area $A = 2.8 \cdot 10^{-3}$ cm^2, the density ρ, the molar mass M_{mol} of TTF-CA and $t_p = 6\,\mu$s after the time point the laser pulse hits the sample surface. As a value for the thermal conductivity, λ_{therm}= 0.02 W/cmK from the Bechgaard salt $(TMTSF)_2PF_6$ recorded at $T = 50$ K [316] is used. In the inset of Fig. 5.73 the results are displayed from Eq. (5.24). The relative temperature change ΔT after the irradiation of the sample with the laser energy E_p increases from $\Delta T = 1.2$ K at $T = 80$ K to $\Delta T = 1.6$ K at 50 K. It is noteworthy that the temperature stays below the transition temperature $T_{NI} = 81.5$ K.

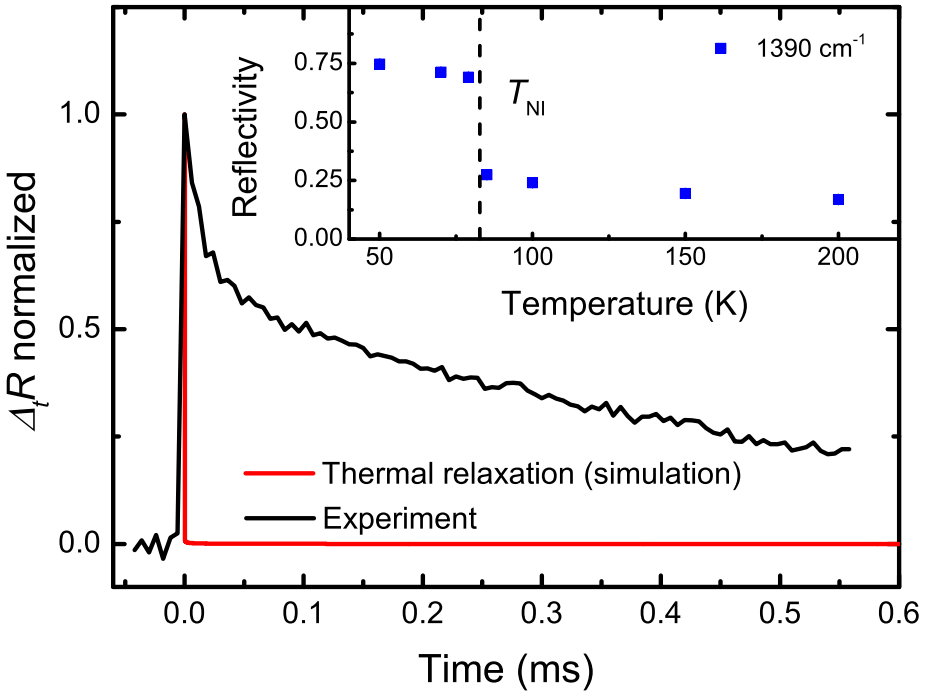

Figure 5.74: Comparison of the thermally-induced reflectivity change $\Delta_t R$ (red) with the observed photo-induced reflectivity change (black). Their decay characteristics is completely different from each other. In the inset the reflectivity of the ν_3 mode at 1390 cm^{-1} is displayed as a function of temperature. The reflectivity jumps at T_{NI} due to the enhanced infrared intensity of the emv-coupled mode in the ionic state. (Adapted with permission from Ref. [5].)

The time-dependent evolution of the temperature was comprehensively theoretically studied by Bechtel [317]. An exact description of the equation can be found in Appx. E. When solely the sample surface was heated up by the laser beam, the change of the surface temperature $\Delta T(t)$ can be derived from the following equation:

$$\Delta T(t) = \frac{2Q_p(1-R)}{\lambda}\frac{(\kappa\tau_p)^{0.5}}{\pi^{0.5}}((t\tau_p^{-1})^{0.5} - (t\tau_p^{-1}-1)^{0.5}) \tag{5.25}$$

We know that the penetration depth $\delta_d(\nu)$ for $\nu = 2.33$ eV is about 200 nm which is much smaller than the sample thickness of 200 µm. Therefore, we can assume that solely the surface is heated up. From Fig. 5.68 the reflectivity $R = 0.21$ at 2.33 eV was determined. The thermal diffusivity was accordingly derived from the equation:

$$\kappa = \frac{\lambda_{therm}}{\rho C_p(T_0)}. \tag{5.26}$$

Further parameters are the laser pulse width of τ_p=8 ns and the radiant photon flux Q_p.

The temporal evolution of $\Delta T(t)$ decays with $\sqrt{t}$, as displayed in Fig. 5.73 for T close to T_{NI}. Under the assumption that the whole pulse energy is converted at the surface directly in heat, the surface temperature shots up across T_{NI}. Afterwards it drops within 500 ns below the transition temperature. Since a thermal induced transition would recover within a four order of magnitudes faster time scale, we exclude that a heating effect is solely responsible for the spectral modification.

Furthermore, we varied also the laser intensity Q_p by more than a factor of three and λ_{therm} between 0.12 W/Kcm (value for TTF-TCNQ [318] at 40 K) and 0.001 W/Kcm (for α-(BEDT-TTF)$_2$I$_3$[319] in the charge ordered phase) in Eq. 5.25. However, we cannot observe any significant changes in the temperature drop which can be correlated with our measured data.

We also went one step forward and calculated on the basis of our reflectivity data and its temperature-dependent behavior at 1390 cm^{-1} the reflectivity change in dependence of the temporal evolution of the temperature variation. In Fig. 5.74 the experimental observed change of the reflectivity is compared with the calculated thermally induced one. It is obvious that the thermally induced transition signal would vanish within 500 ns, whereas our detected signal persists at least several hundreds of microseconds.

Concluding, the temporal dynamic cannot be explained by a simple cooling mechanism. Furthermore, it is suggested that the initialization and relaxation process are of an electronic origin.

One-dimensional random walk: electronically driven transition

The concept of an electronically induced phase transition [216] has already been introduced at the beginning of this Sec. 5.3.6. There, we suggested that the creation of a domain can be considered as the excitation of NIDW pairs which are the lowest excitation state in TTF-CA. Based on this concept, we assume that after the NIDWs are generated, they perform a one-dimensional random-walk and annihilate after two NIDWs meet each other.

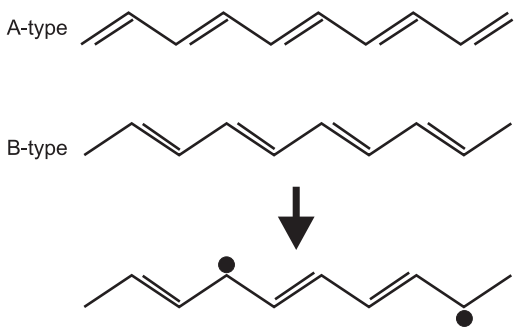

Figure 5.75: A- and B-type of *trans*-polyacetylene. The ground state is degenerated. By photon excitation, solitons and anti-solitons are created in the polymer chain which move along the chain and annihilate when they meet each other.

This process is analog to the creation and annihilation of soliton-anti-soliton pairs in *trans*-polyacetylene and MX chain compounds [320, 321]. The two possible binding configurations of the ground state of *trans*-polyacetylene are depicted in Fig. 5.75 which are energetically degenerated. The photon-generated soliton pairs can move freely along the chain as long as no traps or impurities capture them. However, when an anti-solition meets a soliton, they recombine. By applying a voltage a photocurrent [322, 323] can be detected, which decays nonlinearly and not exponentially, and provides information about the transport mechanism. Furthermore, time-dependent optical absorption measurements deliver further information of the lifetime of the generated particles [324]. There, the temporal evolution of the measured quantities can be described theoretically by a one-dimensional random-walk model which includes an annihilation process. With increasing temperature the photocurrent as well as the absorption signal decay faster, since with raising kinetic energy the probability to find a recombination partner increases. The same consideration holds for increasing the laser intensity, as with increasing density of solitons the possibility for annihilation increases as well.

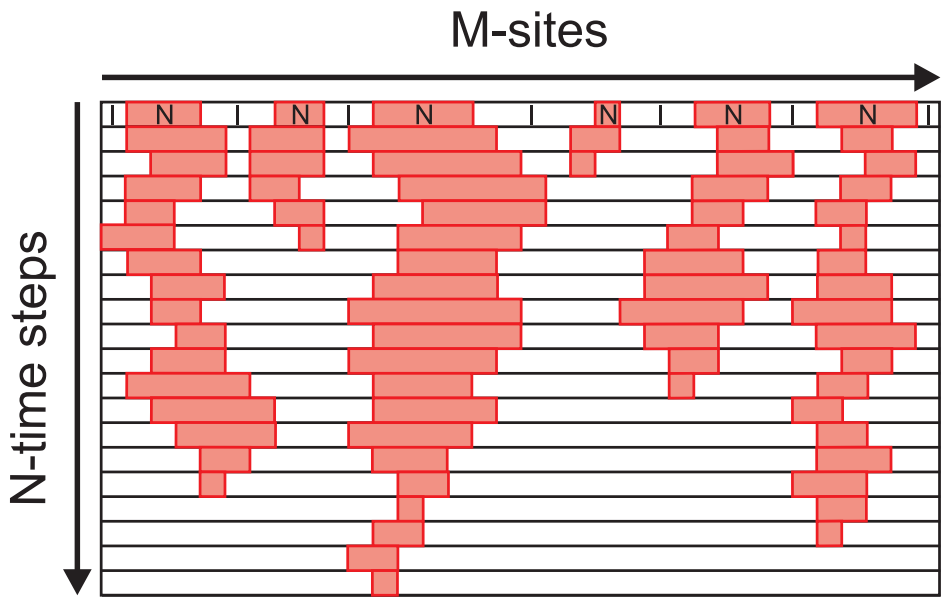

Figure 5.76: Schematic illustration of a random-walk annihilation process of NIDWs along a one-dimensional chain with the length M. Neutral domains (red) are embedded in the ionic phase (white) separated from each other by NIDWs. After several time steps the neutral domain collapses which is the same for the annihilation of two NIDWs.

The diffusion random-walk annihilation process of equal particles, which we consider in the present case as the NIDWs, was theoretically studied for finite, closed and infinite chains. For a detailed description we refer to Ref. [321, 325, 326, 327, 328, 329]. In the theoretical consideration one of the most interesting parameters is the survival probability $S(t)$ which follows a $\frac{1}{\sqrt{t}}$ evolution in an infinite chain. For a large chain there exists a crossover from a power law of $S(t)$ to an exponential behavior of $S(t)$ for small finite rings. To model the temporal dynamics present in Fig. 5.71, we modeled a random-walk annihilation process on a closed ring, which consists of $M = 5 \times 10^4$ sites, and determined $S(t)$. For that we applied the direct method described in detail in Ref. [330]. Any three and two-dimensional interactions with the neighboring chains, traps as well as external fields were neglected.

The average distance $L(0)$ is a function of $\frac{1}{N(0)}$ where $N(0)$ is the initial randomly distributed number of NIDWs on the closed ring. Immediately after the creation process, $L(0)$ is the size of the neutral domains. To decrease the noise level in $S(t)$, especially for $L(0) > 100$ since the reaction is very low for each time step, it was averaged over 10 simulations. The probability for the NIDWs to jump to one of the neighboring sites was set to 50%. When two NIDWs occupy the same site, they annihilate and are removed from the simulation. The survival probability $S(t)$ is defined as follows :$L(t)/L(0) = N(t)/N(0)$. Here, $S(t)$ corresponds to the time-dependent reflectivity change $\Delta_t R(t)$.

In Fig. 5.77 (a) $S(t)$ is displayed as a function of the experimentally adjusted time scale for various initial domain sizes $L(0)$. By comparing the simulated decay profile of $S(t)$ and $\Delta_t R(t)$ with experimental ones, it is obvious that they agree very well. The lifetime of initially large domains is long since $S(t)$ drops slowly whereas small domains decay faster since the NIDWs annihilate process takes place on a shorter time scale since the spacing between the NIDWs is smaller. Similar to $\Delta_t R(t)$, a KWW function models the temporal profile of $S(t)$ excellently, as depicted in Fig. 5.77(a).

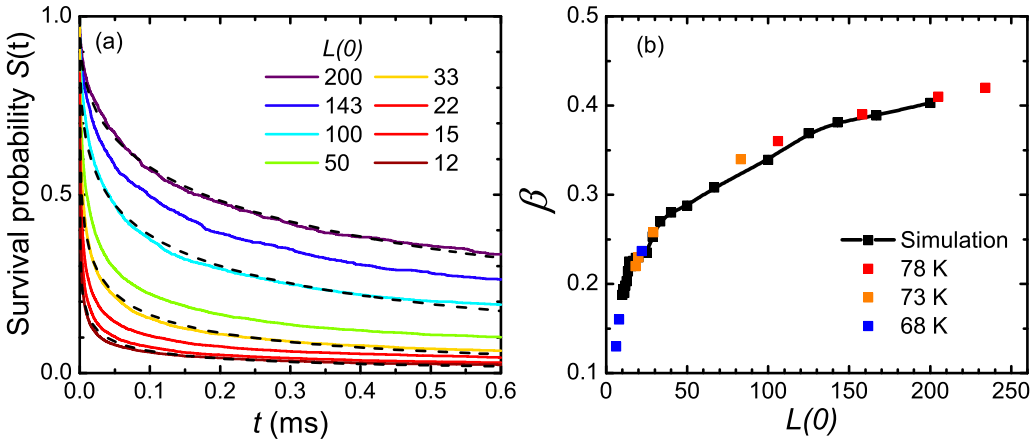

Figure 5.77: (a) Survival probability $S(t)$ of a domain wall pairs on a one-dimensional chain as a function of time for different average domain sizes $L(0)$. The signal can be very well modeled by a KWW-function (dotted line). (b) Fit parameter β as a function of $L(0)$ derived from the fit of the KWW function to the simulated (black lines and dots) and the experimental $S(t)$ curve (colored squares). (Reprinted with permission from Ref. [5].)

In Fig. 5.77, the experimental and the simulated β parameters are plotted as a function of the initial domains size. From that by a direct comparison of the results we can conclude that the domains range over 230 D^0A^0 pairs for the highest laser intensity whereas in contrast for the lowest laser power the domain size is about 100 D^0A^0. This difference is explained by the fact that at the vicinity of the phase transition temperature T_{NI} the potential energy surface PES reveals several separated, but energetically equal minima [270], as illustrated in Fig. 5.78. Furthermore, we assume that at the beginning of the growth process several domains can merge leading to large domains, also a coupling to neighboring stacks cannot be excluded. Additionally, for smaller photon flux the initial domain is smaller since the number of merging processes is reduced. By cooling the domain size reduces continuously from 80 D^0A^0 at $T = 73$ K to 20 D^0A^0 for 68 K, respectively. This can be explained in the picture of the PES, displayed in Fig. 5.78. At lower temperatures the minimum of the ionic phase is below the energy minimum of the neutral phase and hence stable. Additionally, the weak local minimum of the neutral phase is only separated from the ionic phase by a small energy barrier which supports a very fast relaxation process [216]. Also the possibility to end up in the neutral phase is reduced since the PES of the ground and excited state have changed their shape. By that the route to reach the neutral state becomes much difficult.

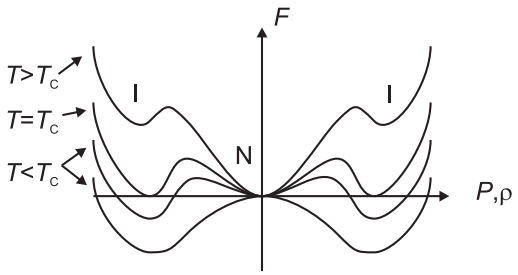

Figure 5.78: The free energy of a first order transition is depicted as a function of the order parameter (for instance polarization, ionicity) for various temperatures at the vicinity of the phase transition. At the transition several minima exist.

The simulation does not take into account some influencing parameters such as coupling to adjacent stacks, i.e. higher dimensions, or pinning centers, for example impurities. Also the hopping rate was set to 50% for both directions

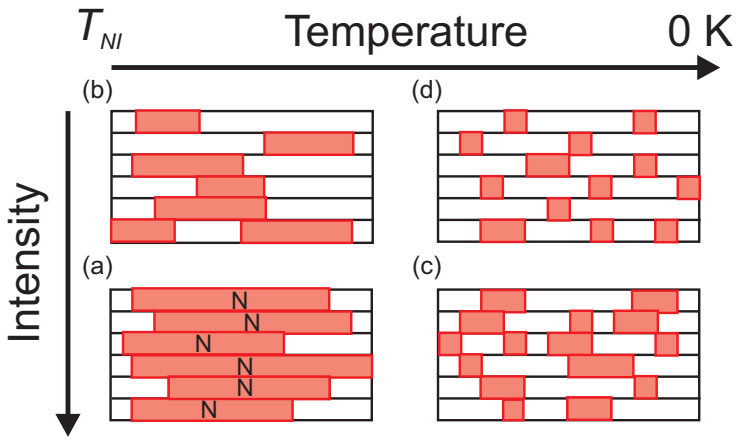

Figure 5.79: (a) Size of the photo-generated domains at vicinity of T_{NI} and high laser power. (b) Reduced domain dimension at reduced laser intensity. At lower temperatures the domain size is smaller and is almost independent of the laser intensity, as shown in (c) and (d). (Reprinted with permission from our publication [5].)

along the stack which can deviate in reality. However, the theoretical calculations are a very good approach to describe the experimental observations.

5.3.7 *Summary and conclusion*

In summary, in this section we have examined the mixed-stacked organic charge transfer salt TTF-CA which is well-known in the scientific community for its neutral-ionic phase transition at T_{NI}=81.5 K. The ionic phase is marked by a strong dimerization of the TTF and CA pairs and abrupt change of the molecular ionicity. Therefore, in a previous step a setup was constructed in the course of this thesis which allows to grow single crystals of TTF-CA and other mixed-stack compounds. The high quality of the single crystal was confirmed by x-ray diffraction measurements and transport studies which reveal the characteristic dip of the resistivity below the phase transition. Furthermore, comprehensive theoretical calculations on the basis of DFT of the band structure and for the first time of the optical properties were performed and compared with experimental results which yields very good agreement within the error bars and reveal the same temperature dependence. Also, the gap feature is reproduced precisely and argues that the mid-infrared band consists of several transitions. Additionally to that, the resonance frequency and infrared intensity of vibrational modes were theoretically calculated and used to assign the vibrational features.

Besides the transport and x-ray measurements, an extensive optical study of the a- and b-direction was performed where the temperature-dependent evolution of the vibrational frequency was examined. By taking a closer look we could observe several modes which exhibit a distinguish jump at the neutral-ionic phase transition. By using the shift of the ν_{10} (b_{1u}) mode of the CA molecules it was possible to determine the temperature dependence of the ionicity.

Furthermore, by exciting the TTF-CA crystal with short laser pulses, a phase transition could be induced below T_{NI}. The time-dependent reflectivity variation was probed by infrared light. The measured spectrum resembles the shape of the reflectivity difference $\Delta_T R$ between the spectrum above and below T_{NI}. This implies that neutral, one-dimensional and metastable domains are created in the ionic phase. The observed characteristic time scale is between the microsecond

and millisecond range. It was shown that the decay profile can be successfully fitted by a KWW function. A one-dimensional random-walk annihilation process of metastable neutral-ionic domain walls NIDW, which was numerical simulated, explains excellently the made observations.

By a comparison of the experimental and theoretical KWW parameter β the domain size was estimated which leads to the expansion of the established concept of the photo-induced domain size, as depicted in Fig. 5.79. At low temperatures, the domain size is in general smaller and decreases with decreasing laser intensity (see Fig. 5.79(c) and (d)). By approaching the transition temperature T_{NI}, the domain size rises (see Fig. 5.79(a) and (b)) due to the valance instability at the vicinity of the phase transition, as exemplary displayed in Fig. 5.78.

However, the photo-induced creation of NIDW can lead to a significant time-dependent photocurrent which should be examined in future studies. In this context, the influence of electric fields on the NIDW can become interesting. Furthermore, photo-created spins can be detectecd by time-resolved ESR experiments. This study should not be restricted to TTF-CA and should be extended to other mixed-stacked compounds such as TTF-TCNQ.

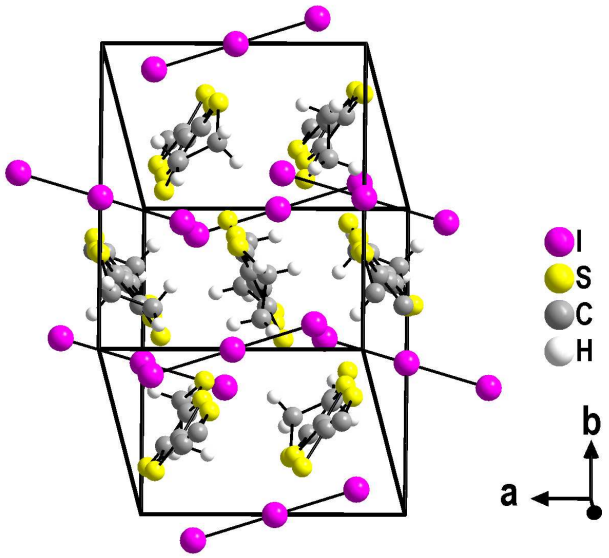

Figure 5.80: Drawing of the α-(BEDT-TTF)$_2$I$_3$ unit cell with orientation along the c'-direction. The unit cell contains four BEDT-TTF and two I$_3$ molecules. The cations are arranged in a herringbone-like structure within the ab-plane separated from each other along the c'-direction by the anions.

5.4 TWO-DIMENSIONAL ORGANIC CONDUCTORS

The following chapter is dedicated to the two-dimensional salts. We have investigated the model system α-(BEDT-TTF)$_2$I$_3$ which reveals a metal-insulator phase transition at 136 K. Firstly, we performed a theoretical characterization of the compound by DFT calculations as in the previous chapters. In this context, we have determined the band structure in the metallic as well as in the insulating state. Furthermore, the optical properties are compared with our experimental results, which agree very well. Besides the theoretical and optical measurements, standard transport studies were performed and beyond that the electrically induced phase transition was examined in great detail by time-resolved transport and infrared methods. In a further step, we applied a model of non-equilibrium charge carriers to our observations explaining our observation excellently. We have published a few results in Ref. [331] and at least one further publication is scheduled [13].

5.4.1 α-(BEDT-TTF)$_2$I$_3$

α-(BEDT-TTF)$_2$I$_3$ is one of the first two-dimensional conductors with a very high conductivity of about 100 Ω^{-1}cm^{-1} at RT which was synthesized for the first time in 1984 [332] while searching for an organic room temperature superconductor and at least to significantly raise the critical temperature by increasing the dimensionality of the system. The unit cell consists of four BEDT-TTF molecules. Two of them are connected with each other by an inversion center and the other two are unequal, as depicted in Fig. 5.80 and Fig. 5.81. The layers formed by the BEDT-TTFs are separated along the c'-direction by two I$_3$ anions per unit cell creating a two dimensional sheet system. The crystal symmetry close to RT is P-1. The room temperature conductivity in the ab-plane is very high between 10 and 100 Ω^{-1}cm^{-1} for the a- and b-direction, respectively. The resistivity ratio

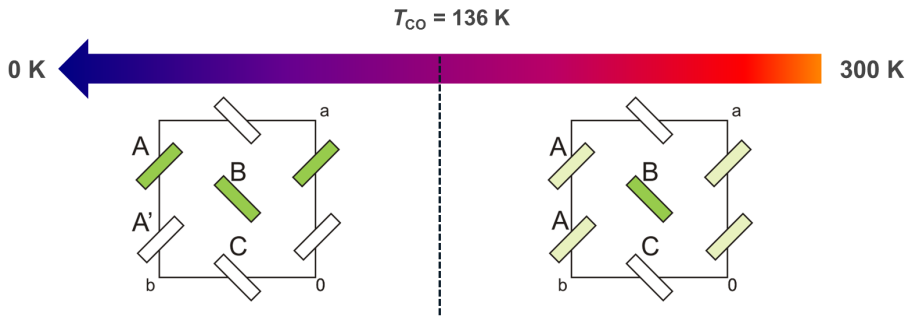

Figure 5.81: Illustration of the development of the charge disproportionation and crystal symmetry in α-(BEDT-TTF)$_2$I$_3$ when cooling from RT to 0 K. The ab-plane is displayed with the four BEDT-TTF molecules labeled with **A**, **B**, and **C**. The **A** molecules are connected with each other by a point inversion on their connecting line. The opacity of the green color represents the charge imbalance between the molecules. At RT there is an imbalance between molecule **B** and **C**. Below T_{CO} the point inversion is lost and the **A** molecules become inequivalent. A stripe-like charge order pattern develops along the b-direction. The anions are not displayed for a better clarification.

is $\rho_a : \rho_b = 2 : 1$ which indicates the quasi-two-dimensional character of this material [192, 332]. This is caused by the larger size of the BEDT-TTF molecules in comparison to the TMTTF molecules in the Fabre salts as well as by the orientation of the molecules to each other within the plane. Therefore, the molecular overlap is optimal. In contrast, the resistivity perpendicular to the ab-plane is larger by a factor 1000. Each I_3 anion receives one electron from two BEDT-TTF molecules leading to a half charge per cation. Therefore, the system can be considered as a quarter-filled system as the Fabre (neglecting the dimerization) or the EDT-TTFCONMe$_2$ salts (see Sec. 5.1.2 and Sec. 5.2). Thus, holes are considered as the main charge carriers detected by thermopower and Hall effect measurements although our theoretical calculations (see Sec. 5.4.2) as well as previous calculations [333, 334] reveal a semi-metallic behavior at room temperature since the Fermi surface intersects the VB and CB leading to hole and electron pockets. On the first approximation, the anions play a secondary role since their energy levels are far below or above the Fermi energy. However, it is supposed that their arrangement and position in the crystal cavity, formed by the cation layers, influences the physical properties and triggers the MIT in α-(BEDT-TTF)$_2$I$_3$.

On cooling the resistivity shoots up over several order of magnitudes in a narrow temperature range at 136 K. This first order metal-insulator transition was demonstrated as well in heat capacity measurements revealing a diverging behavior at the transition temperature [335]. The nature of the insulating state has been unclear for a long time. NMR [336] and x-ray scattering studies [56] reveal a charge disproportionation between the molecular sites indicating the development of a long range horizontal charge order below T_{CO}=136 K. However, also a signature of the CO transition was observed above the transition. The creation of the CO can be dedicated to electron-electron interactions in the form of on-site Coulomb interaction U as well as nearest neighbor interaction V as the driving forces for the MIT [173]. Recently, DFT calculations on the basis of GGA functional could as well determine the metal and the insulating state as well as the charge imbalance between the molecular sites [334]. Therefore, the amount of influence of the electron-electron interactions on the physical properties is questionable.

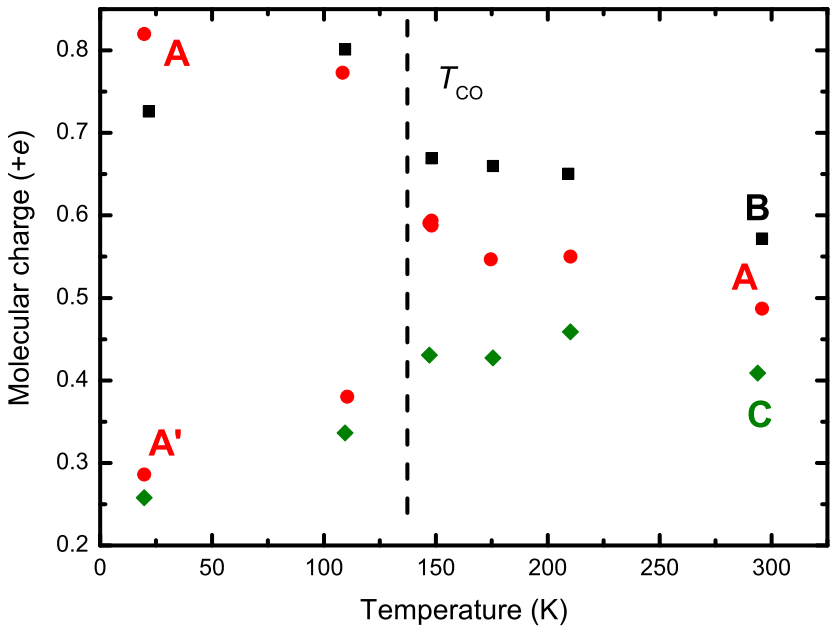

Figure 5.82: Temperature evolution of the molecular charge of the BEDT-TTF$^{+\delta}$ molecules. Above T_{CO} three different charged molecular sites, **A**, **B**, and **C**, can be identified whereas below T_{CO} four inequivalent molecules reside in the unit cell due to the symmetry breaking. The vertical dashed line marks the transition temperature of T_{CO}=136 K. (Adapted from [56].)

As displayed in Fig. 5.81, the space group is reduced from P-1 to P1 whereby all inversion centers are lost. Thus, four inequivalent BEDT-TTF molecules are in the unit cell where the two **A** molecules are transformed into **A** and **A**$'$. By that the charge form a stripe pattern along the b-direction. The charge disproportion was estimated by infrared [192, 337, 338], Raman measurements [339], and x-ray scattering experiments [56] revealing a change of +0.82 e (**A**), +0.29 e (A$'$), +0.73 e (B), and +0.26 e (C) on the molecular site, as shown in Fig. 5.82. The charge ordering leads to a ferroelectric state which was probed by second harmonic generation of light [57, 195, 340] which is a direct proof of the loss of the inversion symmetry. These studies have also shown that different ferroelectric domains exist in a single crystal separated by domain walls from each other. Indications of an influence of cooling rate and pressure on the amount of domains and their size was found, although a systematic study is still missing and necessary.

Recent dielectric measurements detect two modes with a dielectric strength $\Delta\epsilon$ between 400 and 5000 for the a- and b-direction indicating a strong ferroelectric response with no temperature dependence below T_{CO}. The first mode is present at all temperatures and is ascribed to a CDW which is screened by activated charge carriers since the relaxation time follows the temperature-dependence of the DC conductivity. The second mode appears on further cooling below 75 K. It is suggested that this response is caused by solitons and domain walls which are fixed to pinning centers.

There is still an ongoing discussion about the electronic nature of the insulating state. Optical measurements point towards a Wigner crystal (charge ordering). x-ray measurements [56] interpret their results as a $2k_F$ bond CDW, rather than a CO resembling the theoretical results of Θ-(BEDT-TTF)$_2X$ system [341].

Besides these interesting findings and physical ground states, α-(BEDT-TTF)$_2$I$_3$ attracted attention of the research community because of photo-induced phase

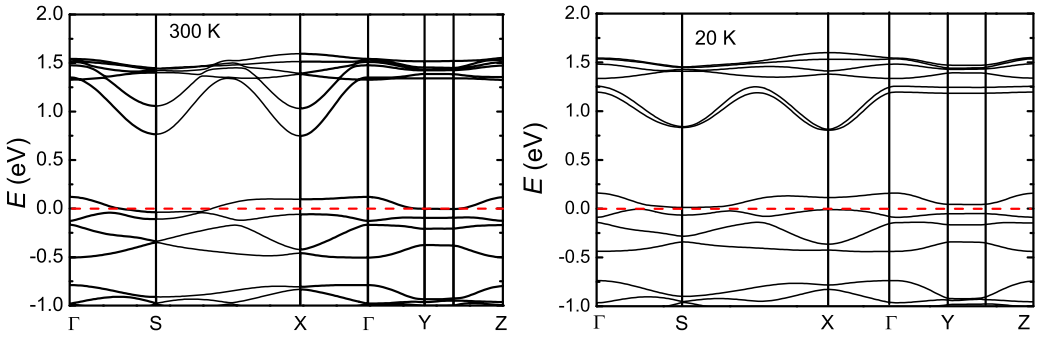

Figure 5.83: Band structure of α-(BEDT-TTF)$_2$I$_3$at 300 K and 20 K along the k-path: $\Gamma(0,0,0) \rightarrow S(-0.5,0.5,0) \rightarrow X(0.5,0,0) \rightarrow \Gamma(0,0,0) \rightarrow Y(0,0.5,0) \rightarrow$ Z$(0,0,0.5)$.

transition phenomena [50, 342, 343], photoconductivity [344, 345] connected with a memory effect [211, 346] (an overview can be found in Ref. [9] and [214]), nonlinear conductivity and zero-gap state [334, 347, 348] under pressure. Since the discovery of massless Dirac fermions in the 2D material graphene due to the Dirac cones it was intensively searched for bulk materials with similar properties. This was finally achieved and proven by transport studies of α-(BEDT-TTF)$_2$I$_3$ under hydrostatic pressure [349, 350]. By applying pressure, the MIT is suppressed and the resistivity stays almost constant down to 2 K. Surprisingly, the charge carrier density decreases by six orders of magnitudes whereas contrarily the mobility increases simultaneously by the same order of magnitude to 3×10^5 cm^{2}V^{-1}s^{-1}. While the Dirac cones are symmetrical in graphene and located at high symmetry points, the Dirac cone is tilted in α-(BEDT-TTF)$_2$I$_3$ and is located at a nonspecific point in the k-space. Recent measurements demonstrate the presences of massive carriers [351] with a two order of magnitudes smaller mobility than the Dirac fermions which originates from a parabolic hole band crossing the Fermi energy under hydrostatic pressure at the X-point in the k-space (see therefore Fig. 5.83).

5.4.2 *Ab initio calculations: band structure and optical spectra*

Similar to the Fabre salts, TTF-CA and EDT-CONMe$_2$, we have performed extended DFT calculations to determine its band dispersion along a specific path as well as the electronic excitation which we compare directly to our experimental results. In the case of α-(BEDT-TTF)$_2$I$_3$ we have resigned on the determination of the molecular motions of the BEDT-TTF molecule in dependence of the molecular charge since it has already been intensively studied. Therefore, we have used the Quantum Espresso software suite [122] with a GGA PBE functional [131] in combination of plane wave function. The cut-off energy for the plane waves and electronic density was set to 30 Ry and 120 Ry, respectively. The self-consistent energy calculations were performed on a regularly spaced grid of 8×8×4 Monkhorst grid [142]. Since α-(BEDT-TTF)$_2$I$_3$ is metallic at room temperature, a smearing factor of 0.05 Ry was selected. The crystal structures determined from x-ray scattering experiments were taken from Ref. [56] at 20 K and Ref. [352] at 300 K. They are used without any optimization of the unit cell parameters or the atomic positions.

In Fig. 5.83 the band structure of α-(BEDT-TTF)$_2$I$_3$ is depicted in an energy range from -1 eV to 2 eV along the $\Gamma(0,0,0) \rightarrow S(-0.5,0.5,0) \rightarrow X(0.5,0,0) \rightarrow$

$\Gamma(0,0,0) \rightarrow Y(0,0.5,0) \rightarrow Z(0,0,0.5)$. Three regions with several bands can be identified in the displayed energy range. The upper band located between 1 eV and 1.5 eV are attributed to the LUMO bands of the BEDT-TTF molecules. Due to the fact that the unit cell contains four molecules, four bands are found at the Fermi energy. Two are well separated from the Fermi energy whereas the upper band intersects the Fermi edge. From that, we conclude that α-(BEDT-TTF)$_2$I$_3$ is according to our results a metal with electrons as major carriers which is in agreement to previous calculations where they also found electron pockets [334, 348] and additionally also small hole pockets. The difference between the calculations can be ascribed to numerical errors in the calculations since the difference are on the meV regime as well as on the (unrelaxed) used crystal structures leading to small deviations. On cooling in the charge ordered state, a small indirect gap opens with 21 meV (direct gap 55 meV) separating the upper bands from each other. This is in perfect agreement with the theoretically derived values from Ref. [334] with 30 meV and 60 meV, respectively, which is as well in accordance with the energy gap determined from transport and optical experiments with 40 meV (b-axis) and 80 meV (a-axis) and 75 meV [192]. The total bandwidth W is about 0.6 eV which is in agreement with the values from the tight-binding model [348].

In both figures, between the S- and X-point, the contact point of the quasi Dirac cone is indicated. It is to emphasize that the evolution of the Dirac band structure is a delicate affair since small variations of the temperature as well as the strength of the applied pressure and its manner can influence the band dispersion. While in graphene the energy range with linear dispersion extends over 1 eV [353], for α-(BEDT-TTF)$_2$I$_3$ it is less than 100 meV. Taking into account the smearing of the density of states at high temperature, the contribution of the Dirac fermions to the optical conductivity is only possible at high pressures and very low temperatures. However, even in this case the Fermi energy intersects other parts of the band structure and, hence the Drude component of the ordinary charge carriers can obscure the view on the Dirac fermions.

Here, we focus on the theoretically and experimentally derived optical conductivity. We want to mention that in comparison to the previous chapter we have additionally performed an extended and comprehensive set of measurements of the optical properties of α-(BEDT-TTF)$_2$I$_3$ in the ab-plane. Nevertheless, we are not going to provide an extensive explanation and interpretation of the spectra since there are already many published studies on that field [192, 338, 354, 355]. Therefore, we have decided to limit this part to the framework of this thesis and show the optical conductivity and reflectivity in comparison to our theoretically determined data. The reflectivity data were collected between 300 K and 20 K. To determine the optical conductivity, we have first extended the reflectivity of the a- and b-direction with published data from Ref. [192] to 10 cm^{-1}and extrapolated it with a constant value to zero for the insulating state and a Hagen-Rubens for the high-temperature metallic phase. For the high frequency range we have extrapolated it from 6000 cm^{-1}to 500000 cm^{-1}with a constant value to 40000 cm^{-1}and above with a ω^{-4} function. The optical response of α-(BEDT-TTF)$_2$I$_3$ was derived from DFT calculations after a self-consistent energy run with parameters and settings mentioned in the previous paragraph. The vertical electronic transitions were calculated on 200 equally distributed k-points in the Brillouin zone. The interband transitions were folded with Lorentzian functions of 100 meV width and the intraband transition with a 10 meV broad Gaussian function, respectively.

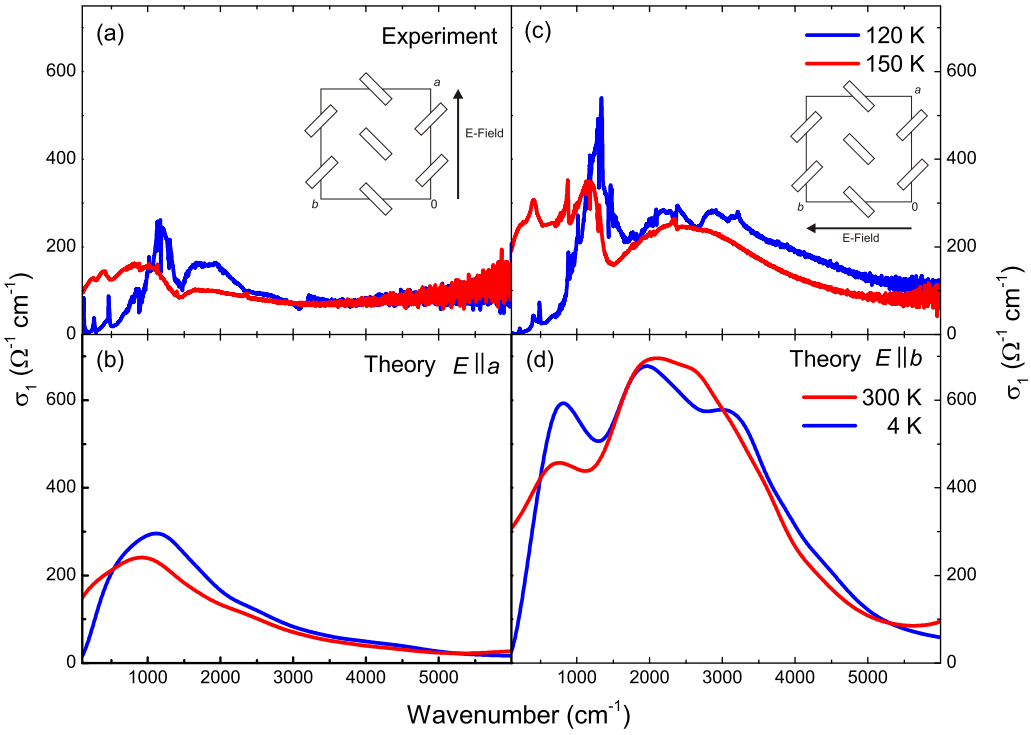

Figure 5.84: (a) Measured optical conductivity of α-(BEDT-TTF)$_2$I$_3$ along the a-direction for 150 K (above T_{CO}, red) and 120 K (below T_{CO}, blue). (b) Theoretically calculated optical conductivity at 300 K (red) and 4 K (blue). (c) Measured optical conductivity of α-(BEDT-TTF)$_2$I$_3$ along the crystallographic b-axis for 150 K (above T_{CO}, red) and 120 K (below T_{CO}, blue). (d) Corresponding simulated optical conductivity for $E \parallel b$ at 300 K (red) and 4 K (blue). The temperature dependence as well as the spectral dependence of the optical conductivity is excellently reproduced by the DFT calculations. Noteworthy, the calculations take into account solely electronic excitations. The experimental spectra show apart the electronic transitions as well as vibrational features which should not be mixed up with the electronic ones.

In Fig. 5.84 the measured optical conductivity for $E \parallel a$ and $E \parallel b$ is compared to the simulated optical conductivity in a frequency range from 100 cm^{-1}to 6000 cm^{-1}at 150 K and 120 K for the experiment and at 300 K and 4 K in the case of the simulation. In 5.84 (a) the spectra along the a-direction have an average conductivity of about 100 Ω^{-1}cm^{-1} above 2000 cm^{-1}. Below it is dominated by a broad mid-infrared band which is disturbed by emv-coupled modes of the BEDT-TTF molecules. For 150 K the conductivity is 100 Ω^{-1}cm^{-1} for $\omega \to 0$ cm^{-1}and marks the metallic character. Below T_{CO} the optical conductivity drops to zero and an energy gap opens at about 500 cm^{-1} which is a hallmark of the MIT. The temperature-dependent evolution and shape of the theoretically determined spectra amazingly resembles the same temperature-dependent characteristic. The metallic and the insulating optical response is described very precisely. Also, the absolute values agree very well with the experimental values, solely the vibrational modes are missing since they are not included in the model. From theory we know that several interband transitions contribute to the mid-infrared band.

In contrast to the a-direction, the optical conductivity along the b-axis is at least by a factor of 2 larger. It reveals as well a broad electronically originated mid-infrared band with emv-coupled vibrational modes superimposed on top of it. In the metallic state the conductivity is around 200 Ω^{-1}cm^{-1} below

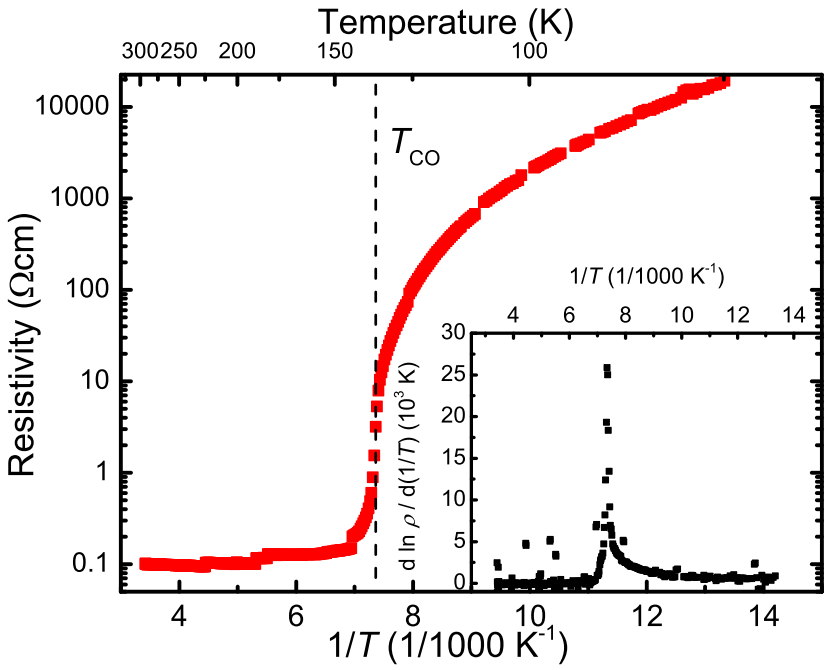

Figure 5.85: Resistivity of α-(BEDT-TTF)$_2$I$_3$ as a function of $1/T$ between 300 K and 75 K. The dashed vertical line marks the metal-insulator transition which is characterized by an abrupt and steep increase of the resistivity of several orders of magnitude. In the inset the derivative of the logarithm of the resistivity is plotted as a function of $1/T$. The transition manifests as a sharp peak deflecting a first-order transition.

1000 cm^{-1}and does not reach zero. At 120 K it drops by several orders of magnitude which is related to the opening of an energy gap indicating the MIT. This is accompanied by a transfer of spectral weight from low frequencies (< 1000 cm^{-1}) to high frequencies (> 1000 cm^{-1}). The calculated spectra in (d) shows as well as a metallic behavior at room temperature. The mid-infrared band is composed of several excitations between different bands. Due to the small broadening of 100 meV they can be distinguished, but should not be mixed up with the vibrational features of the emv-coupled modes. At low temperatures the spectrum reveals an energy gap and the conductivity jumps to zero. As aforementioned, the determined direct gap value is about 55 meV (440 cm^{-1}) which is obscured by the broadening of the interband transition.

In summary, the spectral shape of the optical response is very good reproduced. Furthermore, the absolute values agree very well, also the conductivity ratio between the spectra accords with the observed values. Furthermore, also the opening of the isotropic gap is modeled accurately.

5.4.3 *Electrically-induced phase transition in α-(BEDT-TTF)$_2$I$_3$*

The electrically induced phase transition in α-(BEDT-TTF)$_2$I$_3$ was studied along the a-direction by measuring the electronic response and the variation of the reflectivity along the a- and b-direction. In a first step the transport characteristic was measured for the crystallographic a-direction with the four-point method (see Sec. 4.2 and Fig. 5.86).

In Fig. 5.85 the temperature dependence of the specific resistivity is plotted as a function of the reciprocal temperature between 300 K and 75 K. At high

temperatures, the resistivity reveals almost no change on cooling, but at about 136 K it increases very steeply over several orders of magnitude.

Above 100 K it increases exponentially with decreasing temperature. In the inset, the derivative of the logarithmic resistivity is depicted as a function of $1/T$. The transition is marked by a very sharp and narrow, peak-like feature which indicates the first-order character of the transition. Above 100 K the derivative flattens and stays constant, resembling a thermally activated behavior which yields an activation energy $\Delta E_{\text{Akt.}}$=60±1 meV which agrees perfectly with the literature values [192].

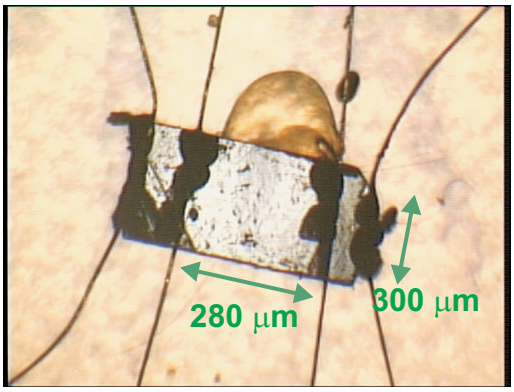

Figure 5.86: Photograph of the cut α-(BEDT-TTF)$_2$I$_3$ sample with four carbon paints contacts and the gold wires. The sample was glued to the ground plate by GE. The inner distance was 280 µm (green) and the width was about 300 µm (green) at a sample thickness of 80 µm.

Below T_{CO} short voltage pulses with a length of 10 ms were applied to the sample along the a-direction with a repetition rate of 2 Hz to avoid any accumulation of heat. The distance between the inner and the outer contacts was 280 µm and 600 µm, respectively. The sample cross section was 2.4×10^{-4} cm^2. The sample was cut to receive a perfect cuboid. At the vicinity of the phase transition, four contacts have been used for the measurement, where on the outer ones the voltage was created and the time-dependent voltage drop across the sample was measured via the inner contacts by an oscilloscope. At low temperatures the contact and sample resistance have exceeded the resistance of the oscilloscope which would lead to a wrong voltage signal. Therefore, we have solely used the two inner contacts and measured the circuit current through the voltage drop across the load resistor. The load resistance was set between 1 KΩ and 100 kΩ. As a reminder the load resistor is not effecting the switching behavior as it is kept very low and smaller than the sample resistance. Moreover, it is only implemented to protect the sample from current burst and to measure the total current. The experimental setup is described in detail in Sec. 4.2.

In Fig. 5.87 different source voltages and their corresponding load voltage is depicted at 79 K. At low source voltages U_{S}, for instance 30 V, the total voltage drop across the load resistor U_{L} is flat and only reveals an overshot at the beginning of the pulse due to the contact and sample capacitance forming an RC circuit. In contrast, the source voltage U_{S} does not exhibit any alternation during the pulse for all shown voltages. This behavior indicates that our voltage source is not disturbed by any phase transition of the sample. When the voltage is increased continuously, the voltage drop U_{L} increases slightly within the pulse, which we attribute to a small thermally induced change of the contact resistance and the sample resistance. U_{S} is proportional to the total current $I_{\text{Tot.}} = \frac{U_{\text{S}}}{R_{\text{L}}}$. Above a certain threshold field E_{th} the current $I_{\text{Tot.}} \propto U_{\text{L}}$ jumps immediately within a few microseconds to a high conducting state resembling the switching behavior of VO_2 under an electric field (see in Appx. D). In the high conducting state the current increases slightly which was as well observed in

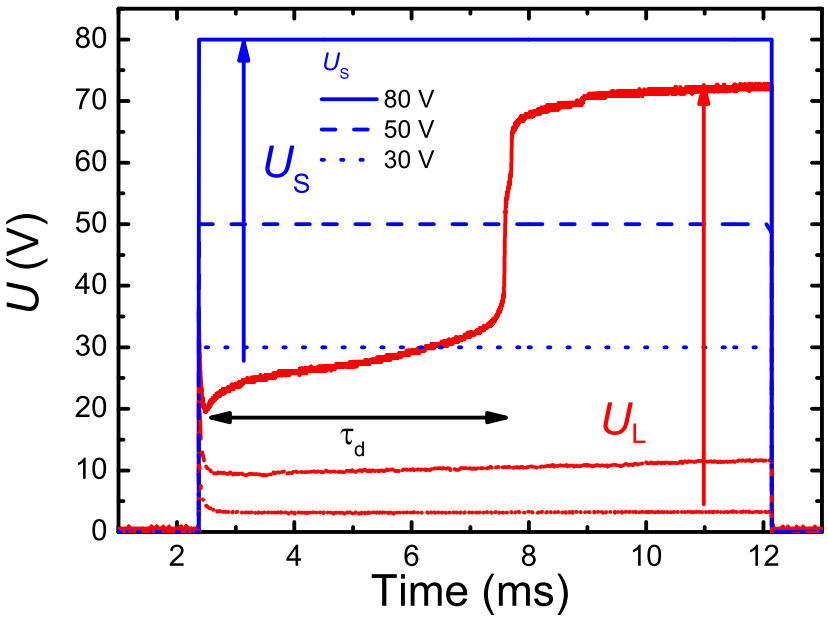

Figure 5.87: Time-dependence of U_S and U_L at 79 K for α-(BEDT-TTF)$_2$I$_3$ along the a-direction. Above a certain threshold field the sample switches from a low conducting, insulating state into a high conducting state which is marked by a steep increase of the total circuit current $I_{Tot.} = \frac{U_L}{R_L}$.

other studies [223, 356] and can be ascribed to thermal variations of the contact resistance.

The observation is in general in good agreement with our previous measurements [331] which were only performed at 125 K and deviates in some points from other studies [223, 356]. It was observed for a contact distance shorter than 200 µm that current oscillations[45] occur, but only in the constant current mode [223]. However, it was stated that the oscillations were absent in the constant voltage as in our measurements. We have shown in Ref. [331] that the oscillations (in the current mode) are caused by the current source which is destabilized by the switching. Nevertheless, the oscillations are attributed to a sliding of the charge order parallel to the horizontal charge order (a-direction), as depicted in Fig. 5.81, since a voltage-dependence of the oscillation frequency and shapiro steps were detected which are characteristics for a sliding CDW (see Sec. 2.4). However, the oscillations were also observed perpendicular to the BEDT-TTF layers although they are separated from each other by the anions which contradicts the idea of a sliding CDW. Up to now, no systematic study was performed on the influence of external parameters, as load resistor or capacitance, on the current oscillations as in the case of VO_2 (see Appx. D). Nevertheless, such switching and oscillations were also observed in other organic conductors [47].

In Fig. 5.88 the time dependence of the sample resistance is depicted as a function of the applied electric field exemplary at 125 K and 79 K. The sample resistance was determined via the relation

$$R_{sam} = \frac{U_S - U_L}{I_{Tot.}} = R_L \left(\frac{U_S}{U_L} - 1 \right) \tag{5.27}$$

At 125 K the sample resistance is about 19 kΩ. At low electric source field the current flow is low and therefore, the noise high and the signal is strongly

45 Also for current applied along the b-direction.

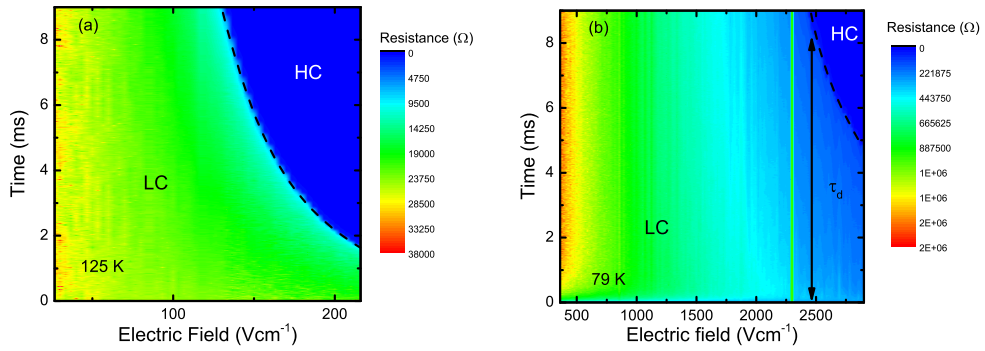

Figure 5.88: (a) Contour plot of the time-dependent sample resistance at 125 K in a time frame of 10 ms for different electric fields created by the pulse generator. (b) Similar contour plot as (a) recorded at 79 K. It is visible that with increasing voltage the delay time τ_d decreases.

disturbed. In the considered time frame the resistance jumps very abruptly from the insulating state into a high conducting state above a certain threshold field which is marked by the change of the color from green to blue in Fig. 5.88. The initial resistance value is reduced by two orders of magnitude to about 200 Ω. Furthermore, as also visible in Fig. 5.87, the switching appears with a certain delay time τ_d which decreases nonlinearly with increasing electric field. For 79 K, it behaves in a similar way although the total resistance is much higher at about 1 MΩ which decreases slightly due to the nonlinear behavior of the contact resistance with increasing electric field, which was as well observed in our previous studies [331]. Furthermore, the electric field must be increased significantly to induce the high conducting state. Its resistivity value is two orders of magnitude smaller than the insulating values as in the case of 125 K.

In the following, we have calculated the current-voltage characteristic, J and E_{Sam} between 130 K to 71 K, which is displayed in Fig.5.89. The current density was determined from the simple equation $J = \frac{I_{\mathrm{Tot.}}}{A}$ with A_{sam} the cross section of the sample in cm^2. The electric field which drops across the sample as determined from $E_{\mathrm{Sam}} = \frac{(U_{\mathrm{S}} - U_{\mathrm{L}})}{d}$ with d the contact distance, U_{S} the source voltage, and U_{L} the voltage drop across R_{L}. The values for J and E_{Sam} were extracted at the end of the voltage pulse at 9 ms. The J curves exhibit a regime of a negative differential resistance NDR where the current jumps to a much higher value while the E_{Sam} drops to a very low value. This curve reveals a so-called S-shape which is in contrast to an N-curve where the current drops to smaller values with increasing electric field (see therefore Sec. 3.2) due to a reduction of the carrier mobility. The NDR appears above a certain threshold field E_{th} which increases with decreasing temperature. Before the NDR regime the current density increases linearly reflecting ohmic behavior. In our context, this means that the conductivity must be increased significantly by generating high mobility carriers.

From Fig. 5.89, we have extracted the threshold electric field E_{th} and the threshold current density J_{th} and plotted the parameter as a function of temperature in Fig. 5.90. E_{th} increases linearly with decreasing temperature below T_{CO} where it is zero. This is in agreement with measurements in the current mode which were solely performed below 100 K [223, 356] and agrees with observations in other organic materials [95]. There, the threshold field E_{th} rises continuously as well.

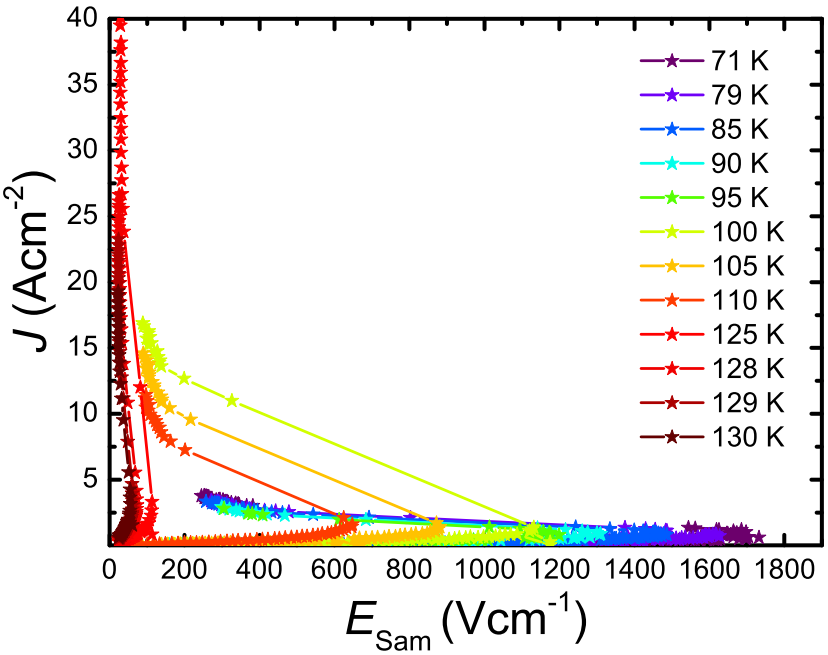

Figure 5.89: Current density J as a function of the electric field E_{Sam} between 130 K and 79 K. For all temperatures a negative differential regime (NDR) can be observed whose threshold electric field increases with decreasing temperature.

When we compare our threshold fields to other systems, then we discover i.) in comparison to CDW materials [31] it is by several orders of magnitudes larger since the electric fields are typically below 1 Vcm^{-1} and ii.) for an avalanche or dielectric breakdown found in semiconductors or insulators the fields are in general above 1 MVcm^{-1}. Additionally, in the case of CDW the threshold field has to follow $E_{\mathrm{Th}} \propto \exp(-T/T_0)$ [357] in contrast to dielectric breakdown where it behaves like $E_{\mathrm{Th}} \propto \exp(T_0/T)$. However, this is obviously not the case in our present study since it behaves linearly. From that, we can conclude that nonlinear transport behavior in charge-ordered materials play a special role and cannot be simply classified within the previous mentioned phenomena.

In contrast to that, the threshold current density reveals a nonlinear behavior which seems to start diverging at the transition temperature and approaches at lower temperature a fixed value similar to the results in Ref. [356]. From these values, we calculate the threshold power density P_{th}=$E_{\mathrm{th}} \times J_{\mathrm{th}}$ which is presented in Fig. 5.90 (b). Interestingly, the necessary power for the switching increases steeply below T_{CO}=136 K and to stay almost constant below 120 K. This temperature dependence resembles the behavior of the resistivity of Fig. 5.85 where the largest modification occurs in a narrow temperature range between 136 K and 120 K which we ascribe to the opening of the energy gap. As previously stated, it reveals below 110 K only an activated behavior. We relate the temperature dependent evolution of the threshold power density to the opening of the gap and its temperature behavior.

As this effect can also be caused by Joules heating we dedicate the following paragraph to this issue. To answer this profound question we performed a comprehensive calculation to determine the actual temperature of the sample while applying the voltage pulse when the whole pulse energy is consumed by the sample. In a first step, we have calculated the thermal power which stems to 100 % from the electric current and field. Therefore, we calculated

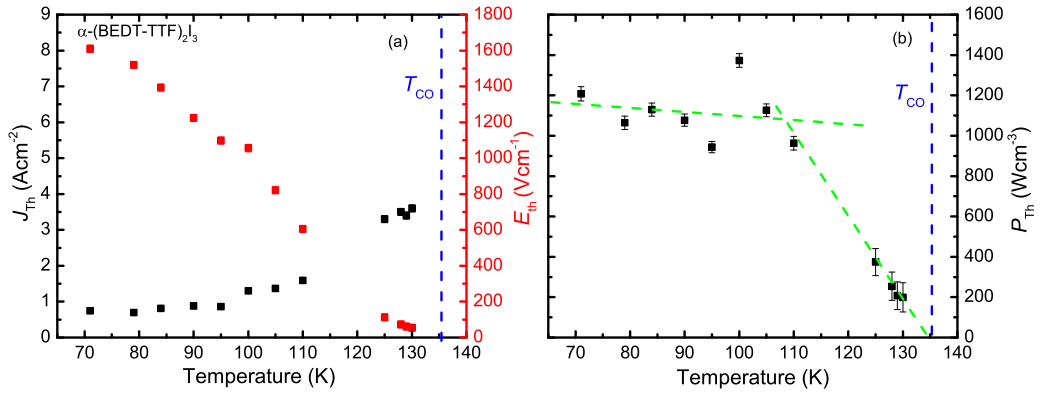

Figure 5.90: (a) Temperature dependence of the threshold current density J_{th} (black) and threshold electric field E_{th} (red). (b) Power density P_{th} below the transition temperature. The green dotted curves are to guide the eyes. The blue dashed vertical lines mark the transition temperature.

$P(t) = U_{\text{Sam}}(t) \times I_{\text{Tot.}}(t)$ from the measured values and determined the energy input in the sample by integrating the power over each time step.

By that we receive the stored energy in the crystal at each time point while the voltage pulse is applied. To estimate the sample temperature we used the following relation:

$$Q(T_i) = n \int_{T_0}^{T_i} C_p(T)\,dT \tag{5.28}$$

with $Q(T_i)$ the energy at the temperature T_i and n the amount of substance determined from the sample volume, molar mass, and density. T_0 is the initial temperature, T_i is a certain temperature above T_0 and C_p is the heat capacity from Ref. [335]. By comparing the calculated input energy with the energy determined from Eq. 5.28 we have estimated the temperature of the sample.

In Fig. 5.91 (a) and (b) the temporal dynamics of the heating power is displayed during the pulse for different applied electric fields for 125 K and 79 K. At both temperatures the power increases with increasing electric field. At high fields the switching sets in, highlighted by the dashed line. At the transition the heating power increases substantially since the current increases more than the voltage drops. Furthermore, the power drops after the switching has finished due to the very low sample resistance in the high conducting state HCP.

In Fig. 5.91 (c) and (d) we illustrate the corresponding sample temperature derived by the previously introduced method. It is noteworthy that we have neglected any heat dissipation to the sample holder which starts to take place already in the first microsecond of the voltage pulse in this consideration. Thus, the determined sample temperature is an upper limit which will be lower in reality. In the case of 125 K, the temperature raises from 125 K to 130 K which is still below the phase transition temperature of T_{CO}=136 K. However at a later time point within the pulse the temperature climbs above T_{CO} according to our calculation. While for 125 K the temperature can exceed the transition temperature of 136 K, the temperature just increases maximally to 96.5 K for 79 K which is absolutely far below T_{CO}. The switching appears at a sample temperature of 92 K for 79 K.

Therefore, we can conclude that at least far below T_{CO}=136 K we can exclude that the switching from the low-conducting to high conducting state is caused

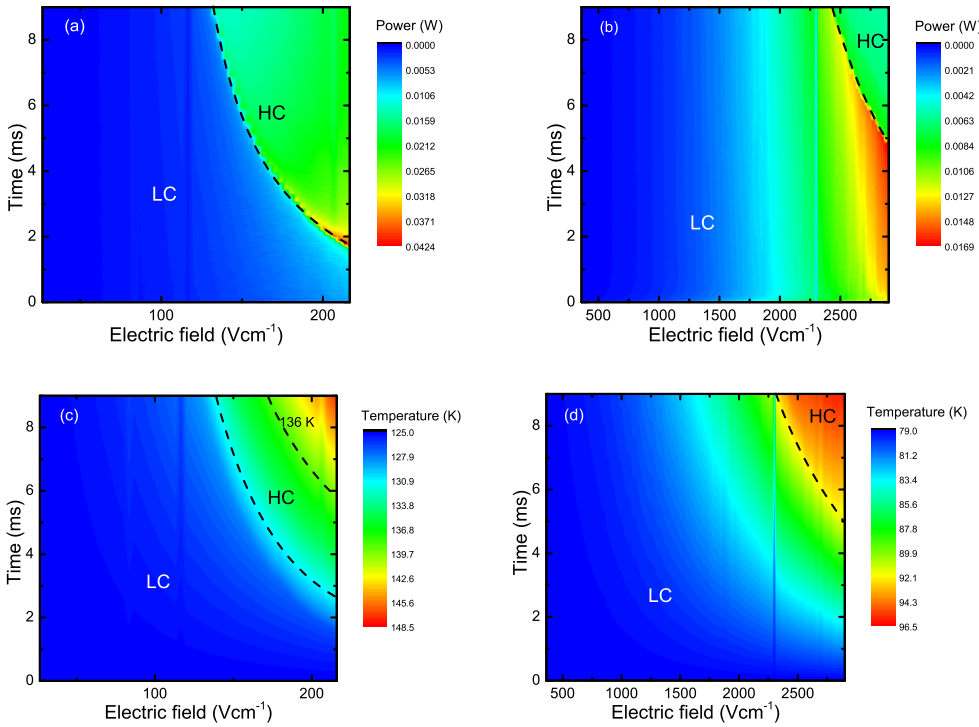

Figure 5.91: (a) and (b) heating power as a function of time and external electric field at 125 K and 79 K. (c) and (d) sample temperature during the voltage pulse as a function of time and external field derived from the comparison of the electric energy with the consumed energy via the heat capacity. The first dashed line marks the position of the phase transition whereas the second line in (c) marks the thermal crossing of T_{CO}=136 K.

by Joules heating. However, for 125 K and closer to T_{CO} it remains unclear if the transition is driven electronically or thermally.

To draw a more conclusive picture, we have additionally performed time-resolved infrared measurements by employing the technique introduced in Sec. 4.1.3. The previous experimental parameters were kept the same. The time resolution was set to 20 µs and 1000 time steps were recorded for 20 ms. The data were acquired 1 ms before the voltage pulse was initialized. To improve the SNR, it was averaged over 20 scans. The spectral resolution was 4 cm^{-1} and the recorded frequency range was from 800 cm^{-1} to 3900 cm^{-1}. Before, we performed several standard Rapid-Scan measurements with infrared light polarized parallel to the a- and b-direction below and above T_{CO}=136 K to compare them with our time-dependent reflectivity data.

The reflectivity spectrum is visualized in Fig. 5.92 for 137 K, 130 K, and 120 K for $E \parallel a$ and $E \parallel b$. The a-direction reveals a maximum reflectivity of about 40 % in the metallic phase and 35 % in the insulating state. At the phase transition the reflectivity drops to 30 % at 750 cm^{-1} indicating the opening of an energy gap which is accompanied by a transfer of spectral weight from low to high energies marking the localization of the charge carriers. Similarly, the reflectivity along the b-direction experiences as well as a sudden drop of the reflectivity at low frequencies from 0.5 to 0.4 due the vanishing of the Drude component which extends up to the mid-infrared range. By that, the metal-insulator transition can be easily identified by the optical response of the ab-plane. Aside

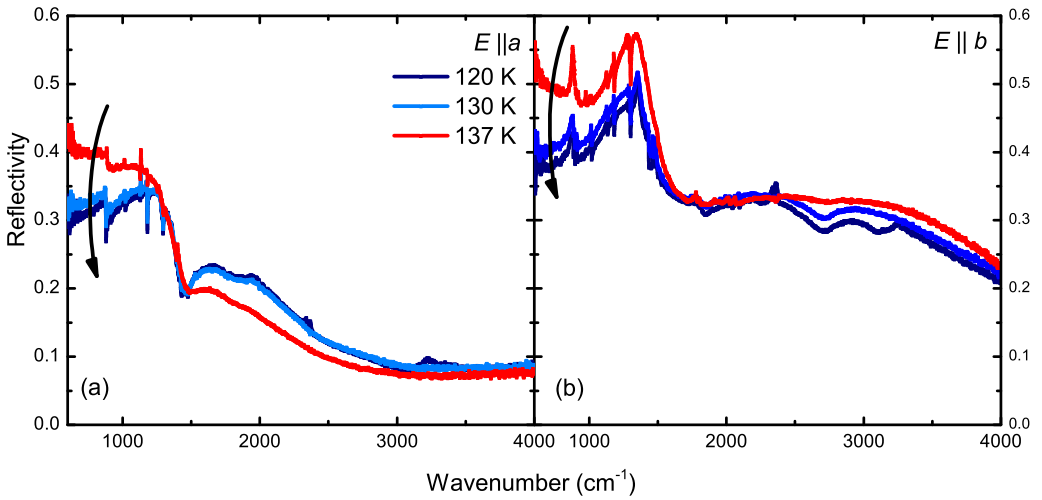

Figure 5.92: (a) Reflectivity spectrum of α-(BEDT-TTF)$_2$I$_3$ along the a-direction below and above T_{CO}=136 K. (b) Corresponding reflectivity spectrum of α-(BEDT-TTF)$_2$I$_3$ for the a-direction. Below 1500 cm^{-1}the reflectivity drops of about 10 % to 0.3 and 0.4 for the a- and the b-direction, respectively, which is a fingerprint of the metal-insulator transition. For the a-direction the reflectivity increases above 1500 cm^{-1}due to the spectral weight transfer from the low to the high energy part.

from that, the dip-like structure located at around 2800 cm^{-1}is attributed to an overtone of the ν_4 (a_g) mode of the BEDT-TTF molecules activated by the charge ordering. This agrees with the observations we made in the Fabre salts and δ-(EDT-TTFCONMe$_2$)$_2X$ compounds (see Sec. 5.1.4 and Sec. 5.2).

Since the time-resolved measurements were performed in the AC-mode, we have recorded the change of reflectivity $\Delta_t R(\nu, t)$. Therefore, we have calculated the reflectivity difference $\Delta_T R$ between various temperatures above and below T_{CO} which is depicted in Fig. 5.93. While $\Delta_T R$, for instance 120 K - 80 K, exhibits almost no modification besides a slight modification of the energy gap in the charge ordered phase, spectral changes are strongly pronounced between the two phases (between 137 K - 80 K). Not surprisingly, it is the same case for the spectrum with $E \parallel b$ where the vanishing charge carriers lead to change in the low frequency part.

In this context, we show in Fig. 5.94 (a) and (b) the time- and frequency-dependent change of the reflectivity at 125 K for the a- and b-direction for an electric field of 216 Vcm^{-1}. As a reminder, the electric field was applied parallel to the crystallographic a-axis. The recorded time window is 20 ms and the initially recorded infrared spectrum was 1 ms before the voltage pulse was applied to the sample. In both directions in the first 5 ms we do not observe any modification in the spectrum. It is to note that 4 ms have elapsed after the pulse. The starting and end point of the pulse is marked by the dotted horizontal line. Afterwards, we see a positive increase of the spectrum below 1500 cm^{-1}and a drop of the signal between 1500 cm^{-1}and 2500 cm^{-1}for the a- and b-direction, respectively. Surprisingly, the voltage pulse stops at about 11 ms, whereas the signal is still increasing and lasts until the end of the pulse. This indicates an influence of the electric field on the material in excess of the pulse duration. It seems that the initiated modification lasts over the recorded time frame. The vertical stripes in the spectrum are due to instabilities of the interferometer mirror during the Step-Scan run.

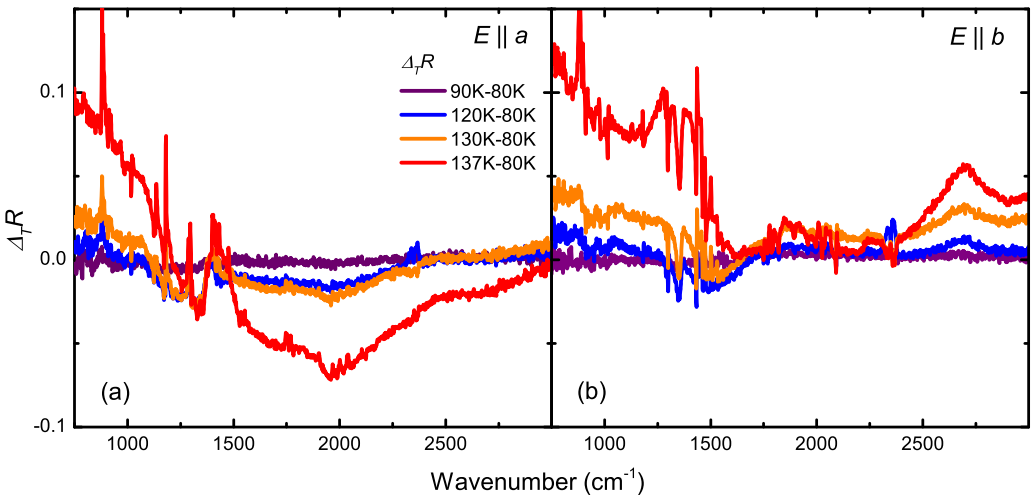

Figure 5.93: (a) and (b) Frequency-dependent reflectivity difference $\Delta_T R$ between 80 K and 90 K (purple), 120 K (blue), 130 K (orange) and 137 K (red) for $E \parallel a$ and $E \parallel b$, respectively.

To perform a detailed analysis of the time dependence of the reflectivity, we have extracted spectra and time slices at the position marked by the black arrows in Fig. 5.94. The results are displayed in Fig. 5.95. In Fig. 5.95 (a) and (c) $\Delta_t R(t)$ is shown for 6 different time points. Before the voltage pulse is created (~ 0.5 ms)[46], no change of the reflectivity can be detected. At 2 ms (after 1 ms of the pulse has passed) a small, almost not recognizable signal appears which stays constant until 4 ms. However, at 125 K the electrically-induced switching occurs at 2.7 ms (~1.7 ms) extracted from Fig. 5.88. From that we cannot correlate the phase transition (~1.7 ms) detected in the resistivity drop of the sample with the change of the reflectivity at 5 ms (~4 ms). Therefore, we have to deal with two different effects. By taking a closer look at the spectral shape of $\Delta_t R(\nu, t)$ after 5 ms (~4 ms) and compare them with the reflectivity difference $\Delta_T R$ from Fig. 5.93 then we immediately recognize that they agree with the difference spectra at 137 K and 80 K. This indicates that when the pulse is applied, the crystal is transferred into the metallic phase after 4 ms .

The time-dependent behavior of the spectra, depicted in Fig. 5.95 (c) and (d), confirms our observations and conclusions. Before the pulse, the signal is flat and increases slightly after 1 ms (~0 ms) corresponding to the onset of the voltage pulse. Afterwards it stays constant over the electrically-induced switching point at 2.7 ms (~1.7 ms) and rises linearly after 5 ms (~4 ms). In both directions it increases linearly over the endpoint of the pulse, saturates at about 15 ms and consequently decreases linearly, which is best visualized along the b-direction. Summarizing and concluding:

1. No observable changes before the voltage pulse.

2. Very small temporal changes of the spectrum occur within the first 5 ms (~4 ms) which we attribute to a fractional transfer of the sample into a metallic phase. Spatially-resolved Raman studies of a current induced phase transition under steady-state conditions confirm this picture [96].[47].

46 Value in brackets correspond to the elapsed time after the pulse was created.

47 Mori et al. [96] could observe a modification of the spectral intensity of a emv-coupled mode of the BEDT-TTF molecules which was ascribed to the modification of the electronic background and

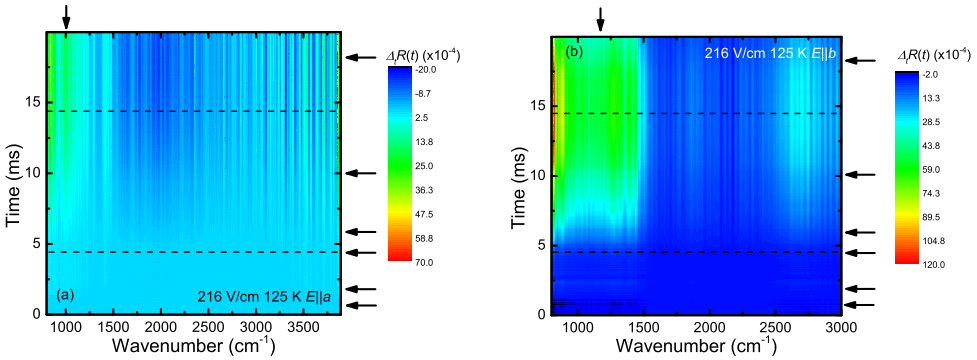

Figure 5.94: (a) and (b) show a contour plot of the reflectivity change $\Delta_t R(\nu, t)$ along the a- and b-direction at 125 K after applying an electric field of 216 Vcm^{-1}along the a-axis lasting for 10 ms. The recorded time was 20 ms and the spectral window is from 800 cm^{-1}to 3000 cm^{-1}, respectively. The dashed horizontal lines mark the onset and end of the voltage pulse whereas the arrows mark the position where the spectra and the time slices were extracted from the frequency- and time-dependent spectrum and displayed in Fig. 5.95.

However, the switching from low to high conducting state cannot be correlated with the temporal dynamics of the sample resistivity. Therefore, we interpret the modification of the reflectivity in the following that a few spatial limited areas undergo a thermally-induced phase transition since the current scatters at some inhomogeneously distributed impurities and cracks within the sample leading to local heating.[48]

3. Although the sample is already in the highly conducting (metallic-like) state according to the transport measurements, a modification of the reflectivity takes place after 5 ms and grows further until 15 ms at which the pulse is switched off at 11 ms(~10 ms). We suggest that the system is in a highly conducting state due to an excited electronic system (" excited" or "hot" charge carriers) which couples to the lattice subsystem to which the energy is transfered with a certain delay time. This leads to a heating up of the sample across the phase transition causing the reflectivity change. First indications for that are provided by our calculation where we assume that the whole electric energy is completely converted into heat and the sample temperature crosses T_{CO}.

4. The excited charge carriers relax back into their initial ground state via releasing the energy to the lattice system. Therefore, $\Delta_t R(\nu, t)$ first saturates while the thermal energy is further transferred to the sample holder. By that the energy flow is balanced. After all energy is stored into the lattice subsystem, which further transfers heat to the sample holder (heat sink) which leads finally to a linear decrease of the reflectivity signal. This explains also the results of our electric pump-probe experiments in Ref. [331]

therefore, to an electrically-induced metallic state. In contrast, a temperature sensitive vibrational mode of the I_3 anion does not reveal any modification. However, studies on the switching mechanism of VO_2 under similar experimental conditions reveal a heating effect [358] (see Appx. D). Therefore, measurements under steady current flow are a delicate task.

48 Recently, we have observed a sample-dependent variation of the AC- and DC response of the organic spin-liquid system κ-(BEDT-TTF)$_2$Cu$_2$(CN)$_3$ which we attribute to the sample impurity and growth conditions what induces disorder in the systems [359].

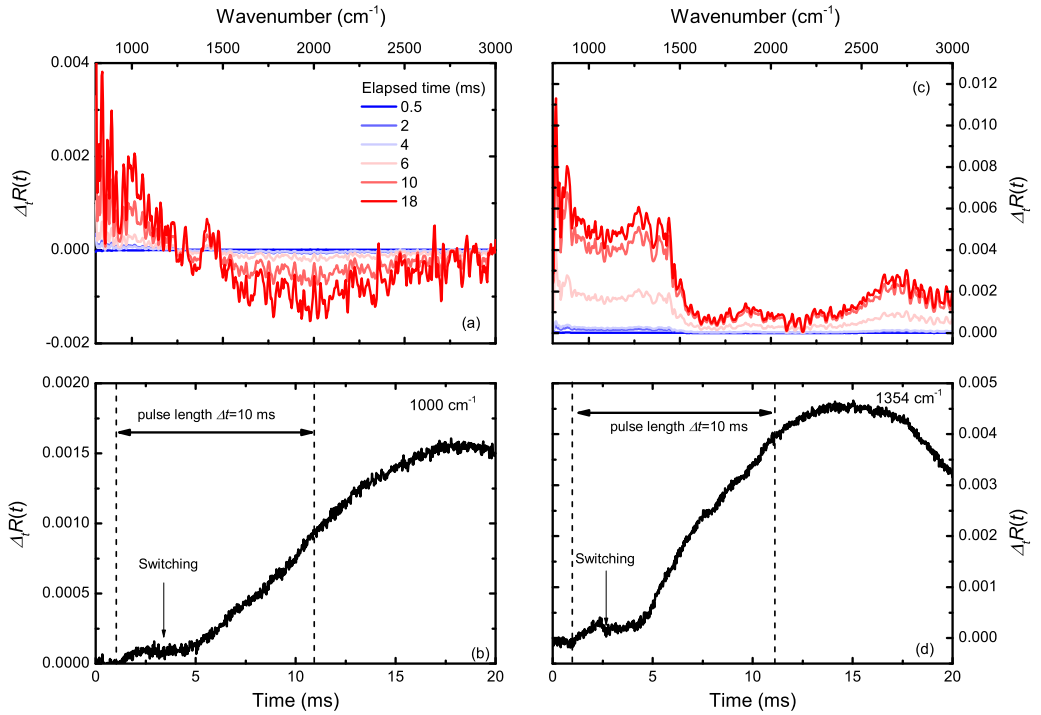

Figure 5.95: (a) and (c) illustration of $\Delta_t R(\nu, t)$ of the a- and b-direction for different times at 125 K extracted from Fig. 5.94 in a frequency range from 800 cm^{-1} to 3000 cm^{-1}. After 10 ms the spectral shape resembles the reflectivity modification $\Delta_T R$ of the thermal phase transition, for instance going from 80 K to 137 K. (b) and (d) Time profile of the spectrum taken at 1000 cm^{-1} and 1354 cm^{-1} between 0 ms and 20 ms. Only a very slight change of the reflectivity occurs in the spectrum which stays constant after the high conducting state is induced. After a delay time of a few millisecond the signal rises linearly until it saturates after the voltage pulse is switched off and decays linearly. The vertical dotted lines mark the start and end point of the voltage pulse.

where the resistivity recovers in an exponential manner within a few milliseconds after the highly conducting state was initialized by a 3 ms long voltage pulse.

5. The linear decrease of the reflectivity after 17 ms suggests that Newtonian cooling is present with

$$Q_{\text{Cool}} = -\lambda_{\text{therm}}(T_{\text{L}} - T_0) \tag{5.29}$$

with T_{L} the lattice temperature, the environment temperature T_0 and thermal conductivity λ_{therm}. [49]

Now, we consider the switching behavior far below T_{CO} at 79 K. Therefore, we have plotted the frequency- and time-dependent spectra $\Delta_t R(\nu, t)$ for $E \parallel a$ and $E \parallel b$ under an electric field strength of 2900 Vcm^{-1} in Fig. 5.96. The voltage pulse arrives at the sample at 1 ms (~0 ms). In both spectra, a change can be recognized with the onset of the pulse.[50] However, at this point of time a negative change occurs between 800 cm^{-1} and 3000 cm^{-1} which is obviously different from the observed change at 125 K, depicted in Fig. 5.94. It persists until the end of the record time, although it starts to decay after 12.5 ms which is 4 ms after the voltage pulse is switched off.

49 We neglect in this consideration energy transfer due to thermal radiation.
50 It is to emphasize that we used here the same color code as in Fig. 5.94.

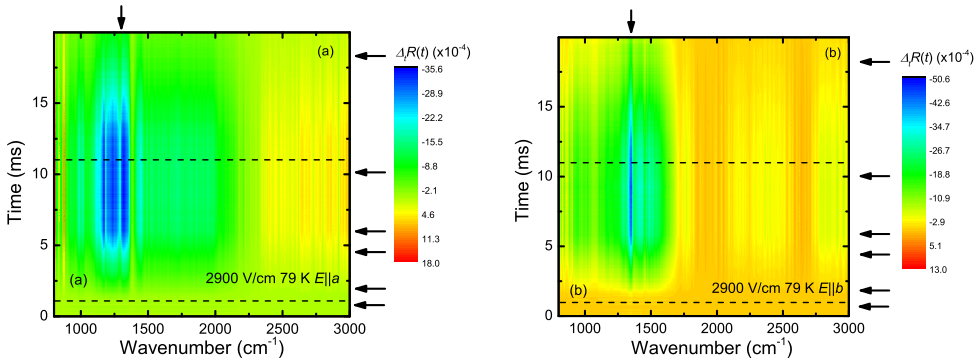

Figure 5.96: a) and (b) show a contour plot of the reflectivity change $\Delta_t R(\nu, t)$ along the a- and b-direction at 79 K after applying a pulsed electric field of 2900 Vcm^{-1} along the a-axis in a frequency range from 800 cm^{-1} to 3000 cm^{-1} for 20 ms. The dashed horizontal lines mark the onset and end of the voltage pulse whereas the arrows mark the position where the spectra and the time slices were extracted from the frequency- and time-dependent spectrum shown in Fig. 5.97.

In Fig. 5.97 the frequency-dependent $\Delta_t R(\nu, t)$ is plotted for different times between 800 cm^{-1} and 3000 cm^{-1} extracted from Fig. 5.96. Before the voltage pulse arrives at the sample, the signal is completely flat. However, it starts to increase linearly from the beginning of the voltage pulse at 1 ms and drops after 12.5 ms. The spectra differ significantly from the previously shown spectra at 125 K and reveal a reduction of the electronic band intensity and the emv-coupled modes in the case of the a- and b-direction, respectively. This behavior corresponds in comparison to $\Delta_T R$ to a small increase of the sample temperature of only a few degrees Kelvin, for instance for 80 K-90 K, as depicted in Fig. 5.93. Especially, the energy gap is not shrinking which would be expressed by a positive signal below 1000 cm^{-1}. This is in excellent agreement with our estimation of an upper limit of the sample temperature caused by Joule heating which predicts a maximum temperature of 96.5 K in the HCP state and hence, still far below T_{CO}=136 K. Therefore, we believe that no thermally induced phase transition is responsible for the switching from the LCP to the HCP and suppose that the temperature raise of the lattice is less than 10 K.

Fig. 5.97 (b) and (d) show the temporal dynamic of the reflectivity change for the a- and b-direction at 1334 cm^{-1} and 1354 cm^{-1} between 0 ms and 20 ms. As mentioned previously, the signal is zero at the beginning and decreases linearly after the onset of the voltage pulse which is in clear contrast to the behavior at 125 K. Precisely at the resistivity switching from LCP to HCP at 5.5 ms the signal is constant which means that an energy and, hence temperature balance between the electron system, the lattice system and the environment (sample holder) is established. After the voltage pulse the electronic system, thus excited charge carriers, decays back and the energy is transferred to the lattice system while the infrared signal stays still high and exceeds the voltage pulse length. Finally, the lattice system is cooled down linearly in accordance with Newtonian cooling, presented in the previous paragraph. Summarizing:

1. The signal increases linearly with the onset of the pulse. The lattice system absorbs the energy of the electronic system.

2. Saturation of the signal due to steady state and HCP. Balance between the electronic and lattice system.

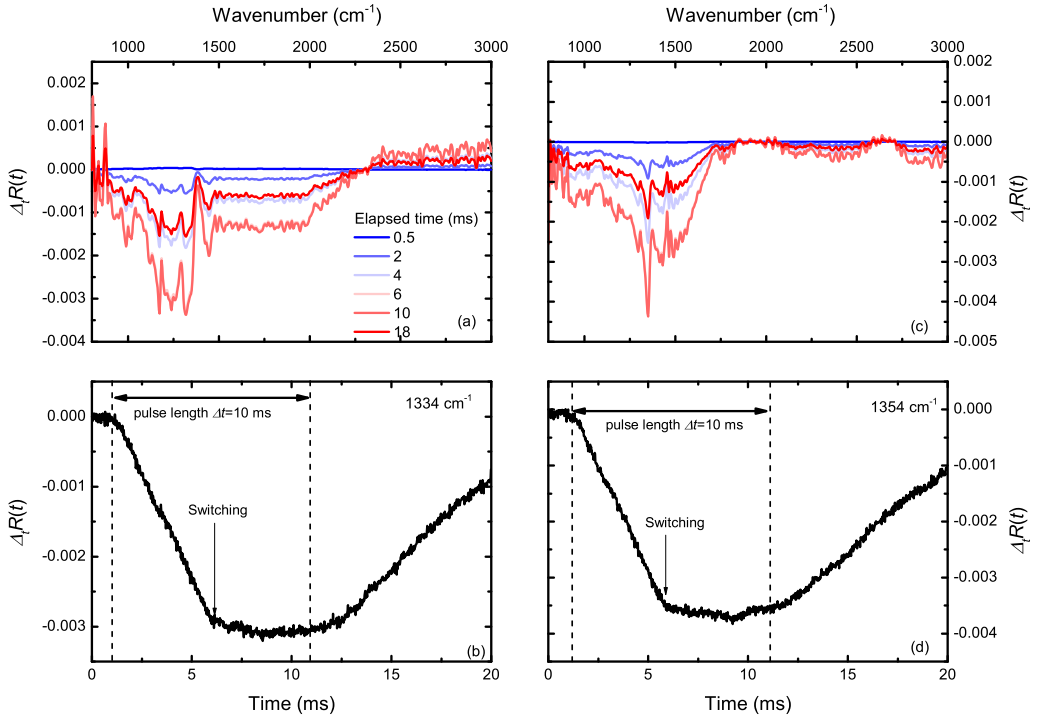

Figure 5.97: (a) and (c) illustration of $\Delta_t R(\nu, t)$ for different times at 79 K extracted from Fig. 5.96 between 800 cm^{-1} and 3000 cm^{-1} for the a- and b-direction. The spectral shape is completely different from Fig. 5.95 and means that the sample is still in the insulating state by comparing them with the spectra displayed in Fig. 5.93. (b) and (d) temporal profile of the spectrum taken at 1334 cm^{-1} for the a-direction and 1354 cm^{-1} for the b-direction, respectively. The signal decreases continuously after the pulse is switched on, marking the heat transfer to the crystal lattice. After switching from the LCP to the HCP at about 5.5 ms the signal is constant and decays afterwards with a smaller slope. The vertical dotted lines mark the start and end point of the voltage pulse.

3. Decay of the signal due to cooling process of the lattice via energy transfer to the environment.

MODEL In Ref. [331] we have suggested that the electrically induced switching from LCP to the HCP is caused by the collective excitation of solitons and domain walls. However, up to now it is unclear how the solitons are generated by an electric field. In the case of domain walls it is experimentally demonstrated for ferroelectric materials that they are generated at the contacts and move towards the counter contact [87]. It is an open question if they could be generated at crystal imperfections or impurities leading to a persisting high conducting state. Furthermore, moving domain walls exposed to a pulse of high electric field pulse lead to a high conducting state at the beginning of the pulse that drops down to zero after a certain delay time which is opposite to our observation where the HCP is established at the end of the pulse (read Ref. [87] and references there within).

We suggest another explanation here which is also known under the keyword "hot" electrons or non-equilibrium charge carriers [80, 81, 360]. It is well-known from inorganic semiconductor materials where the excited unoccupied state exhibits different valleys, for instance two different minima in the conduction band

with two different effective charge carrier masses $m^\star$ which lead to two different charge carrier mobilities μ_1 and μ_2, since

$$\mu_n = \frac{q\tau_{Sc}}{m^\star} \tag{5.30}$$

with μ_n the charge carrier mobility, q the charge per carrier, the scattering rate τ_{Sc} and the effective mass $m^\star$. In general, in inorganic materials μ_2 of the high-lying energy level is much larger due to the wide-open parabolic shape of the band dispersion. Therefore, μ_2 is reduced leading to a N-shaped J-$\vec{E}$ characteristic. In the present case we assume here that $\mu_2 \gg \mu_1$. The current density J depends on the electric field as follows [80, 81]:

$$J = q(n_1\mu_1 + n_2\mu_2)E \tag{5.31}$$

with the charge carrier concentration n_1 and n_2, the mobilities μ_1 and μ_2, and the electric field $\vec{E}$[51]. The two charge carrier concentrations are related via:

$$n_2 = n_1\, e^{\frac{-\Delta E}{kT_e}} \tag{5.32}$$

with ΔE the charge separation between the two levels. Importantly, the energy separation between the low and high-mobility state must be smaller than the energy band gap Δ between the VB and CB, otherwise carriers can be excited from the VB into the CB. In our case the energy gap is about 60 meV which corresponds to 700 K whereas the valleys of the CB have an energy difference smaller than 20 meV and thus the first condition is fulfilled. The occupation ratio of the two states, as reflected in Eq. 5.32, is controlled by an effective electron temperature T_e [52] [80, 361] which is not related to the lattice temperature.

The principle idea of the model is illustrated in Fig. 5.98. The sample receives an electric input power which depends on the temperature-dependent conductivity of the sample and quadratically on the electric field $E_{Sam}(t)$, which drops across the sample contacts. In a further step, the electron system gains energy by the input power which depends on its heat capacity and leads to an effective electron temperature T_e. In addition to that, the electron system is coupled to the lattice subsystem through a parameter $\lambda_{therm,e}$ considering the thermal heat conductivity between the electronic and the lattice system which gives rise to a lattice temperature T_L. As the sample is connected to the environment, the energy dissipates to its surroundings. Here, we neglect the latter one in our consideration.

We approach this problem by solving the equation of energy conservation to determine the electron temperature:

$$nC\frac{dT_e}{dt} = P - K \tag{5.33}$$

The left term reflects the increase of electron temperature T_e with time. The first term $P = \sigma(T_e)E_{Sam}^2$ on the right-hand side expresses the energy rise of the electrons whereas the second term $K = -\lambda_{therm,e}(T_e - T_L)$ corresponds to the energy transfer from the electron system to the lattice subsystem[53]. The last term corresponds to the experimental situation where the reflectivity change,

51 We consider that the electric field points along one dimension

52 This is the reason why the excited carriers are also called "hot" electrons.

53 For our calculations we set the lattice temperature T_L equal to the environment temperature T_0

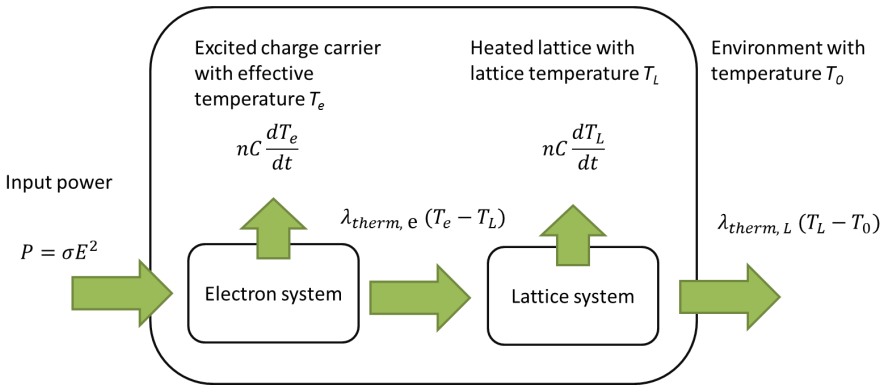

Figure 5.98: Schematic energy flow diagram of the "hot" electron model. The electric power is first stored in the electron system causing an increase of the electron temperature T_e. The coupling to the lattice subsystem is responsible for heating up the lattice and to increase the lattice temperature T_L. According to Ref. [96].

respectively, the sample temperature is constant, as depicted in Fig. 5.97 (b) and (d). There, we have already assumed a linear Newtonian cooling. This proposed two-state model was first successfully applied by Mori et al. [96] and Ozawa et al. [95] for two different organic conductors, (TMET-TTP)$_4$PF$_6$ and β″-(BEDT-TTF)$_3$(HSO)$_2$, respectively, which are of activated as well as of the transition type[54].

We have solved Eq. 5.33 numerically by first calculating the right side and subsequently, determining T_e from the left side for each time step of the voltage pulse. The time resolution was 2 µs for a pulse width of 10 ms which corresponds to the experimental parameters. $\sigma(T_e)$ were taken from Fig. 5.85 which was interpolated for the simulation in the considered temperature range. We assumed for nC=0.2 JK^{-1}cm^{-3} and $\lambda_{therm,e}$=40 WK^{-1}cm^{-3} throughout the manuscript which is in agreement with other studies [95, 96]. The only free parameter was the value of the load resistance which was adjusted accordingly to the experimental value. It was increased from 1 kΩ to 100 kΩ.

In Fig. 5.99 the time dependence of the C-, P-, and K-terms are plotted for 125 K (250 Vcm^{-1}) and 80 K (3000 Vcm^{-1}). The electric power is transferred to the electronic system at the beginning of the voltage pulse whereas the cooling term increases slowly in the case of 125 K. Before the switching point, the electric power as well as the stored energy in the electric system diverge and drop afterwards to a fixed value. The C-term (left term) decreases slowly to zero since the cooling term approaches the electric power term P initializing the steady-state. In the case of 80 K, the power term behaves similarly to 125 K, only the cooling K-term reaches immediately the value of the electric input P-term after the resistivity switching by what the energy of the electronic system drops down to zero.

The electron temperature T_e is displayed in Fig. 5.100 for 125 K and 80 K. For 125 K the electron temperature increases nonlinearly at the beginning and reveals step-like modification of the slope at the phase transition located at 2 ms and increases sub-linearly up to 160 K at the end of the pulse. In contrast to that

54 Activated type: the conductivity follows an activated behavior. Transition type: the conductivity reveals a sharp increase at the phase transition.

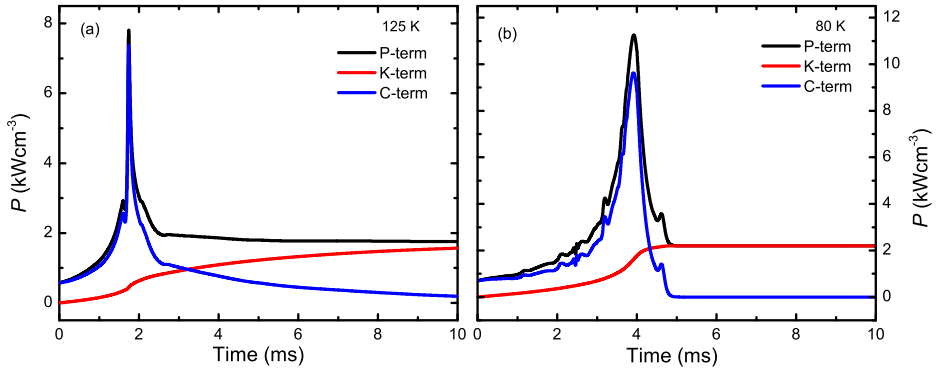

Figure 5.99: (a) and (b) show the time dependence of the input power term P (black), cooling power K-term (red), and the power gain of the electronic system (blue).

the temperature rises steeply up to 134 K at 85 K, which is below the transition temperature T_{CO} and stays constant.

From Ref. [335] we know that the heat capacity is 0.5 $JK^{-1}g^{-1}$ below T_{CO}. The values used in the simulation was 0.2 $JK^{-1}cm^{-3}$ for the electron system which corresponds with the density of α-(BEDT-TTF)$_2$I$_3$ of 2.2 gcm^{-3} to 0.09 $JK^{-1}g^{-1}$ which is five times smaller than the total heat capacity. In general, the specific heat of the lattice/phonons follows a T^3 power law whereas the specific heat of the electrons increases linearly with temperature. The specific heat of the phonons dominates the total specific heat above 10 K [362] implying that the lattice heat capacity is much larger than the electron heat capacity confirming our assumption. Mori et al. [96] suggested that the lattice heat capacity is independent of the electron one and the following simplified equation for the energy conservation can be applied with the total specific heat $C_{\text{total}} = C_e + C_L = 5C_e$:

$$nC_e(T_e - T_L) = nC_L(T_L - T_0) \tag{5.34}$$

$$\frac{C_e}{C_L} = \frac{(T_L - T_0)}{(T_e - T_L)} = \frac{1}{4} \tag{5.35}$$

with the initial and environmental temperature T_0. From this formula we have estimated the time dependence of the lattice temperature of α-(BEDT-TTF)$_2$I$_3$ for 125 K and 80 K which is displayed in Fig. 5.100. Parallel to electron temperature the lattice temperature increases slightly from 125 K to 132 K at 10 ms which is still below 136 K. However, as stated in the experimental part, we assume that due to some scattering centers the lattice temperature can locally outreach the transition temperature of 136 K which leads to the metallic signal in our reflectivity data. Furthermore, this model also explains why the reflectivity still increases after switching since the lattice temperature T_L increases continuously as well after the switching. While for 125 K we have observed a metallic transition, depicted in Fig. 5.95, the reflectivity for 80 K just indicates a small increase of the lattice temperature of less than 10 K. Indeed, our simulation reveals an increase of the lattice temperature and saturates when the switching from the LCP to the HCP sets in, which is in perfect agreement with our optical observation where the signal stays constant until the pulse is switched off.

Up to now, only the time-dependent behavior of the power and the different temperatures were discussed. Therefore, to compare our experimental results better with the simulation, the calculated current density is displayed in Fig. 5.101 for 125 K and 80 K for various external electric fields from 0 to 250 Vcm^{-1}

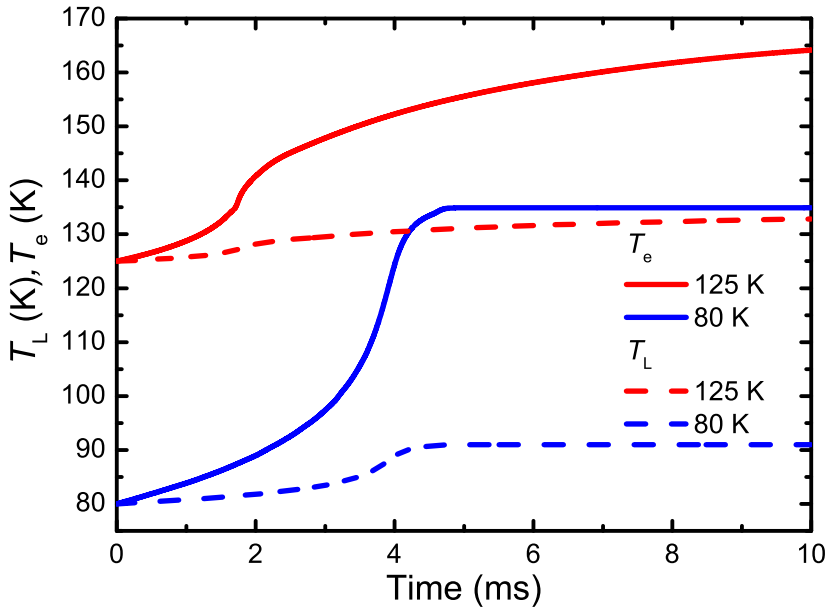

Figure 5.100: The electron temperature T_e (solid, red and blue) and the lattice temperature T_L (dashed, red and blue) are depicted as a function of time for 125 K and 80 K for an external electric field of 250 Vcm^{-1} and 3000 Vcm^{-1} respectively.

and from 0 to 3000 Vcm^{-1}, respectively. For a better understanding of Fig. 5.101 and comparison with Fig. 5.88, the current density is inversely proportional to the sample resistance. A very sharp jump of the current density occurs at electric fields higher than 100 Vcm^{-1} deflecting a transition from a low conducting state LCP to a high conducting state HCP which is in excellent accordance with the experimental observation. Also the field-dependent behavior of the delay time τ_d resembles the experimental behavior excellently. The switching occurs in the simulation already at 2000 Vcm^{-1}.

The small deviations of the simulation to the experiment can have multiple reasons: i.) The contact resistance is not taken into account in our 2-point measurement influencing $E_{Sam}(t)$ and its temperature dependence. ii.) Also, we have supposed a temperature independent nC_p and $\lambda_{therm,e}$ which is probably not the case in reality which can effect the experimental outcome slightly. In spite of the minor deviations, we can conclude that the two-state model perfectly reflects our experimental findings.

Additionally, the J-$\vec{E}$ characteristic was determined to see if the nonlinear conductivity and the NDR is reproduced as well. The result is depicted in Fig. 5.102 for the temperatures between 79 K and 129 K[55]. The overall behavior is the same as in Fig. 5.89 resembling an S-shaped current-voltage curve. All temperatures reveal a linear regime at low electric fields exhibiting a turning point which marks the threshold field E_{th} and current density J_{th}. Further, the J-$\vec{E}$ curves cross over into the NDR regime and finally, above a certain current density it increases further, but much steeper than for lower electric fields, indicating that the final state is different from the initial state at low fields. However, small deviations from the experiment can be found, for instance, the current density values after the NDR are higher than in the experiment (see Fig. 5.89). Also, the position of the turning points are located at higher fields. We attribute these differences

55 For 71 K no conductivity values were determined.

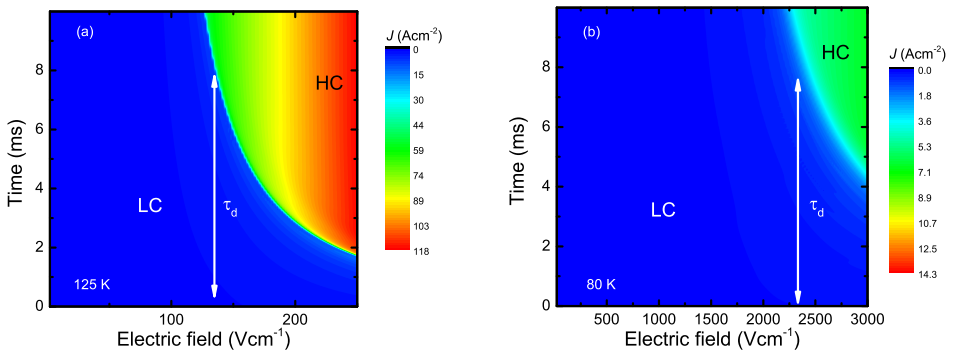

Figure 5.101: The current density J is presented as a function of time and electric field for 125 K and 80 K. The arrow indicates the delay time τ. The low conducting state (blue area) is characterized by a low current density while in the high conducting part (green-red) the current density is extremely high.

to the unknown contact resistance in the experiment which is in series to the sample and load resistance and affects $E_{\mathrm{Sam}}(t)$ and J, directly. Nevertheless, the agreement of the simulation with the experiment is excellent.

The threshold current J_{th} and threshold field E_{th} were extracted from the J-$\vec{E}$ curve and plotted as a function of temperature in Fig. 5.103. A similar picture to the experimental one manifests. The threshold field increases in a quadratic manner whereas in the experiment it reveals a linear way. The current density decays linearly on cooling while in the experiment it flattens at low temperatures. However, the threshold power density increases steeply close to the phase transition and crosses over in regime with a smaller slope which resembles the development of the energy gap. Moreover, the increase of E_{th} at low temperatures can also be attributed to the decrease of the occupation number of the CB on cooling.

We have seen that the two-state model excellently describes the electrically-induced phase transition and explains qualitatively and, impressively, also the quantitative behavior of the experimental values. It does not only support the time-resolved transport measurements, but also explains in detail the made observations in the time-dependent reflectivity study. It confirms that we have to deal with an electronic system being linearly coupled to the crystal lattice. Furthermore, we made a precise estimation of the lattice temperature T_{L} which is different from the electronic system and agrees nicely with estimate sample temperature derived from the comparison of time-dependent reflectivity with the steady-state spectra. The two-state model can also explain the occurrence of the current oscillations[56] [95, 222]. For certain combinations of the heat capacity nC and the thermal conductivity $\lambda_{\mathrm{therm,e}}$, the system can be driven in chaos and bistable states where nonlinear dynamics occur, which eventually leads to current oscillations [47].

56 We have uncovered that in the case of the current-driven switching the oscillations are caused by the instability of the current source and does not appear for voltage sources.

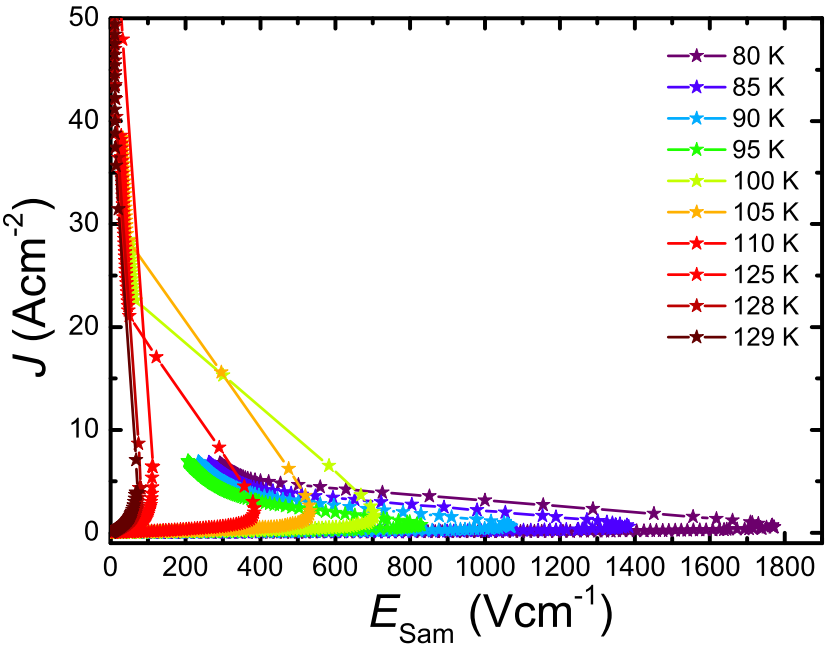

Figure 5.102: Simulated J-$\vec{E}$ characteristic between 0 Vcm^{-1} and 1900 Vcm^{-1} from 129 K to 80 K. All curves exhibit a nonlinear regime with an NDR. On cooling, the threshold current decreases while the threshold electric field rises.

5.4.4 *Summary and conclusion*

In summary, we have performed theoretical calculations of the band structure and the optical spectra of α-(BEDT-TTF)$_2$I$_3$ in the metallic and charge-ordered, insulating state for all crystallographic directions. The band structure calculation yields a metallic state with electrons as the majority charge carrier. However, previous calculations with relaxed molecules and unit cell parameters have predicted a semi-metallic behavior with very small hole and large electron pockets [334]. Since the bandwidth is small and any change of the structure and temperature can shift the Fermi energy, it is not definitely clear which are the majority carriers since hall measurements suggest that holes are the major carriers [332, 363]. The low temperature insulating phase reveals a band gap of about 55 meV which agrees perfectly with the results from optical and transport studies. Although electron-electron correlations drive the transition into the charge ordered state, they are only included to a certain fraction in DFT. This points towards the idea that correlation effects are not that much important to drive the system into the charge-ordered phase. Moreover, the band dispersion does not exhibit any strong modification at the first order transition.

To support our calculation, the frequency-dependent reflectivity was recorded between 300 K and 10 K from 800 $cm^{-1}$to 6000 cm^{-1}. By a Kramers-Kronig transformation we could determine the optical conductivity of the a- and b-axis. Thus, we compared the optical data with the theoretically determined optical spectra which yields a very good agreement. The transfer of the spectral weight due to the phase transition is accurately demonstrated by the theoretical simulation. The relative intensity between the optical conductivity along the a- and b-direction and the spectral shape is reproduced very well. Also, the in-plane DC resistivity of a : b=2:1 is determined correctly. From that, we can conclude that a possible observation of Dirac fermions under high pressure will be a difficult

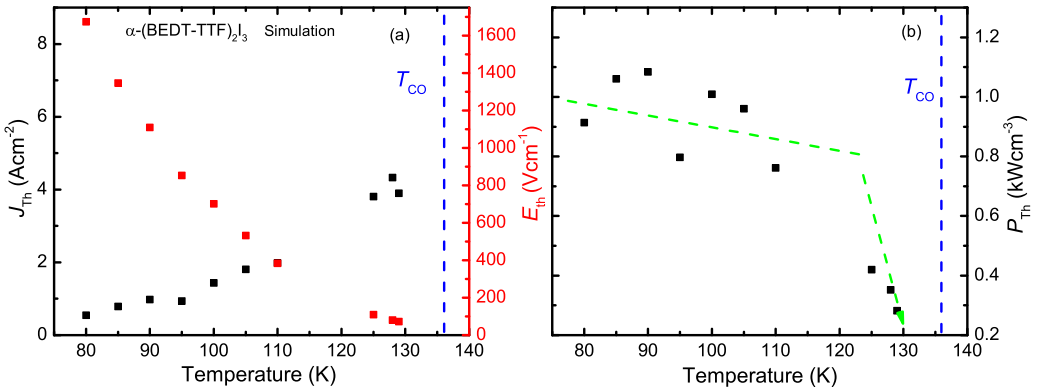

Figure 5.103: (a) Simulated threshold electric field (red) and current density (black) plotted as a function of temperature below T_{CO}. (b) Temperature dependence of the threshold power P_{th} determined from the product of E_{th} and J_{th}. The vertical dotted line marks the phase transition temperature of 136 K.

task since they can be masked by normal charge carriers of neighboring k-points intersecting the Fermi surface.

The reflectivity data were also used to allocate the transition temperature by tracing the reflectivity drop at low frequencies due to the opening of the band gap and by observing vibrational overtones, appearing solely in the charge ordered phase, above 1600 cm^{-1}.

Additionally, standard transport measurements were conducted to determine on the one hand the phase transition temperature T_{CO}=136 K and the energy gap Δ=60 meV.

We have examined the electrically-induced resistivity switching from a low conducting LCP to a high conducting HCP state in α-(BEDT-TTF)$_2$I$_3$. Thus, we applied an electric field parallel to the a-direction over a wide temperature range below T_{CO}=136 K by employing a time-resolved transport method. This was demonstrated by time-resolved transport measurements. The drop of the resistivity is about 2 orders of magnitude. The J-$\vec{E}$ curve reveals an S-like shape without any recovery of the initial conductivity behavior. The most impressive feature is the NDR regime where the electric field across the sample drops drastically. We could not find any hints for current oscillations whose appearance we attribute to the instability of the used current sources and the forming of conducting filaments for small contact distance [360]. The threshold electric field increases on cooling while the threshold current density diminishes leading to a threshold power density which moderately increases at low temperatures. To support our observations and to finally disentangle the origin and nature of the induced metallic state, we have performed time-resolved reflectivity measurements which, indeed, reveal at the vicinity of the phase transition a metallic state resembling the characteristics of the high temperature metallic phase. In contrast, at 80 K the reflectivity modifications are completely different indicating a slight temporal heating of the sample of about 10 K to 90 K. Simulation of the temperature rise due to Joules heating could not reproduce the experimental findings satisfactorily and the preliminary conclusion is that the transition must be driven electronically.

To explain our findings, we have employed the two-state model which describes the generation of "hot" charge carriers. Therefore, we have solved the equation of energy conservation numerically and determined from the solution

all relevant experimental parameters. The temporal resistivity behavior as a function of the electric field could be precisely reproduced within the framework of the model. Moreover, the NDR is as well modeled and the derived threshold values agree very well with the experimental ones. By employing an effective electron temperature T_e, we could also make an estimation of T_L which agrees excellently with our experimental assumption of the sample temperature.

We have demonstrated that the switching into a HCP is caused by the excitation of charge carriers with a higher mobility. Here, the question arises if the enhanced mobility is somehow related to the linear band dispersion found in α-(BEDT-TTF)$_2$I$_3$. The tilted Dirac cone is only predicted for high pressure. Nevertheless, the linear dispersion can be present as well in the insulating phase. Furthermore, the temperature-dependence of the resistance normalized to the room temperature values under pressure exhibit exactly the same slope as the resistance at ambient pressure [364, 365]. Since Dirac fermions are made responsible for the conductivity behavior under pressure, we propose, that they also contribute to the metallic state at ambient conditions. Here, we want to refer again to Ref. [351] where two different charge carriers contribute to the conductivity with two orders of magnitude different mobility. Could this also be the case for the excited electrons in the conduction band?

Thus, we suggest for future research that the band dispersion has to be studied theoretically more closer and from that the anisotropic effective charge carrier mass as well as the velocity has to be determined. Although optical measurements under pressure are a very difficult task, the far-infrared range and below has to be examined to gain more insight in the electronic structure of the system.

Part V

SUMMARY AND OUTLOOK

6 CONCLUSION AND OUTLOOK

In the framework of this thesis several investigations were performed on the ground as well as the non-equilibrium state of one- and two-dimensional organic conductors by a variety of experimental and theoretical methods.

By one of the up to now most comprehensive optical studies of the one-dimensional organic Fabre salts $(TMTTF)_2X$ (X=PF_6, AsF_6, SbF_6, and ReO_4) all crystallographic axis were optically examined in the mid-infrared range [2] (see Sec. 5.1.4). Most impressively, the charge disproportion [2, 11] occurring in the charge order phase could be determined by infrared spectroscopy with much higher precision compared to other techniques. For $(TMTTF)_2PF_6$, the temperature dependence of the charge disproportionation follows a meanfield-like behavior; with increasing anion size and hence, increasing transition temperature T_{CO}, it becomes more first-order like. Additionally, in ReO_4 a further charge redistribution was detected in the anion ordered phase. This was only possible by a normal mode analysis of the molecular constitutions, giving us the possibility to assign each vibrational feature in the spectrum and the dependence of the resonance frequency on the molecular charge.

Furthermore, the anion modes are non-degenerated and split due to the low crystal symmetry. They do not reveal any modification above T_{CO}. Therefore, an influence of the anion molecules on the charge order phase transition as a precursor can be rejected, in accordance with other structural resolving methods which fail to resolve any precursor behavior. This outcome does also agree with the temperature evolution of the vibrational modes which contain the end groups of the TMTTF molecule.

The spectrum along the stacking direction is dominated by electronic excitations which are disturbed by emv-coupled modes. We could attribute up to now unassigned vibrational features to vibrational overtones and combination modes which become visible mainly in the charge ordered phase. By determining the nonlinear terms of the emv-coupling, we could relate to the enhancement and activation of these modes to the charge ordering and determine the related anharmonicity of the molecular potential energy surface. This is a further proof that vibrational overtones can be used to detect charge ordered phases in organic conductors. From fits to the optical spectra the main information about the electronic excitations could be determined as, for example, the transfer integral t. However, no clear alternation of the mid-infrared band was detected, meaning that the charge ordering does not significantly affect the occupation and shape of the electronic bands at the vicinity of the Fermi surface. The transfer integral reveals a linear increase due to cooling, which is in accordance with the variation of the unit cell parameters. It means that the compounds become more metallic with decreasing temperature which is in contradiction with the experimental observations. By considering the Hubbard model it becomes clear that the next-nearest Coulomb repulsion V must vary stronger with temperature than the transfer integral in order to explain the experimental observations.

In addition, extensive DFT calculations based on structural data were performed to calculate the band structure of Fabre salts with centro-symmetric anions at various different temperatures. From the band structure we could see that with decreasing anion size the bandwidth and hence, the kinetic energy become larger, which directly influences the intermolecular spacing between the TMTTF molecules. This is in full agreement with an increase of conductivity with diminishing anion size from SbF_6 to PF_6. Additionally, the temperature dependent band structure behaves in the same way as applying chemical pressure. With decreasing temperature the total bandwidth W increases; as it is proportional to the transfer integral, we could verify this with our optical results. The temperature trend of the experimental t agrees excellently with the theoretical one, which also rises on cooling. However, the calculations cannot reproduce the charge order as well as the Mott/dimerization gap which is located above 200 K, because electron-electron correlations are mainly neglected in DFT calculations. This points again towards correlation effects playing a crucial role in developing the ground states.

Besides the optical study, the response of the compounds to short electric fields and laser pulses were studied. Only in the case of $(TMTTF)_2SbF_6$ a temporal photocurrent was detected in the CO phase, which vanishes on the millisecond time scale. Even more interesting is the fact that the photocurrent oscillates on a characteristic frequency of several kHz, which resembles the behavior of a sliding CDW. Such a phenomenon has never been detected before neither in an organic nor inorganic compound. We attribute these oscillations to an interaction of the charge order state with the excited single particle.

Besides the band structure, we also calculated the optical spectra for$(TMTTF)_2X$: X=PF_6, AsF_6, and SbF_6 along all three crystallographic axis, which are to our best knowledge[1] the first of their kind. The optical spectra of the a- and b-direction are dominated by a Drude feature at low energies which is in agreement with our band structure calculations. A comparison of the theoretical DC conductivity ratios and the experimental ones [59] yield a very good agreement; solely the absolute values deviate from each other. Furthermore, we could as well simulate the mid-infrared bands of all directions located between 2000 cm^{-1} and 7000 cm^{-1} in full agreement with our experimental data. Moreover, the temperature shift of the mid-infrared bands could be reproduced, which is also the case for the electronic excitations in the visible range. This energy range should be a playground for future studies. Therefore, these calculations can be used in future to make a first prediction for the optical spectra of organic compounds.

While the Fabre salts are dimerized systems and not purely quarter-filled materials, we have also studied the one-dimensional compounds EDT_2AsF_6 and EDT_2Br optically [4, 12]. Our theoretical calculations reveal that the systems are in contrast to the Fabre salts purely quarter-filled (see Sec. 5.2). Furthermore, they seem to be more two- than one-dimensional. However, the theoretical and experimental optical spectra deliver hints about an electronic excitation along the c-direction. With the help of normal mode analysis the vibrational features and the charge sensitive modes were identified. Indeed, we can support the results of NMR data that the charge ordered phase is already established at room temperature with a record charge imbalance of 1:9. This is further confirmed by the

1 This statement is as well valid for the other calculations of the other compounds discussed within this thesis.

presence of strong vibrational overtones. Specific modes reveal a modification of the resonance below 200 K, indicating a change of the molecular environment which we ascribe to the structural transition.

The behavior of the electronic excitations are similar to the Fabre salts. Their temperature evolution can be ascribed to the excitation of domain walls in the charge ordered phase [12], consistent with theoretical predictions [245].

In a next chapter, the self-synthesized, mixed-stacked organic compound TTF-CA was chosen to study the photo-induced ionic-neutral phase transition. Additionally, the compound was theoretically examined in order to determine the vibrational features and the electronic excitations. Our determined band structure agrees with previously performed calculations [288] and also reflects the experimentally determined temperature evolution of the band gap accurately. By a direct comparison of theoretical and experimental spectra, we derived that the typically observed MIR feature actually consists of several bands. Motivated by theoretical predictions, the temperature dependence of the optical response was measured by light polarized in the ab-plane. A sudden jump of certain vibrational features mark the first-order phase transition from the neutral to the ionic phase. By a closer examination of the ν_{10} mode of the CA molecule we derived the ionicity of the molecules in the specific phases. From the charge transfer band we could determine bandwidth W, which is in accordance with the calculated band structure.

Photo-excitation of TTF-CA in the ionic phase (< 81.5 K) leads to an immediately strong modification of the spectral response, which we identify as a photo-induced transition into the neutral phase [5]. The temporal spectral change was detected by the Step-Scan FTIR technique which was applied for the first time to study solid state materials. This technique was combined with a home-made experimental setup.

Surprisingly, the relaxation rate follows a non-exponential behavior which can be fitted by a so-called Kohlrausch-William-Watt function that decays on the microsecond range. This unique study extends from previous ones in several points: i.) the time range, ii.) the experimental technique, and iii.) the spectral range. This untypical relaxation behavior is nicely described by a one-dimensional annihilation random walk process. From the results of our simulation we were able to estimate the average emerging domain size as a function of temperature and laser pulse energy.

Finally, the two-dimensional organic conductor α-(BEDT-TTF)$_2$I$_3$ moved into the focus of this thesis, since it reveals a pronounced charge order transition at 136 K. In a first approach, the optical properties were examined by FTIR spectroscopy and compared with the optical conductivity derived from DFT calculations. Although it is assumed that in this compound electron-electron correlations play a very important role to develop the charge ordered phase. We deduce that correlations are not the dominating factor for this compound. Indeed, the calculated optical spectra are in full agreement with the experiment, predicting the metallic as well as the insulating state, the position of the electronic bands, and amplitudes without the assumption of any correlations.

Furthermore, we examined nonlinear conductivity phenomena [331] in the CO state. In this context it was always the question whether the phenomenon

is comparable to the sliding of a CDW or to the melting of the CO. A switching behavior from the low conducting CO state to the high conducting metallic-like state was observed with the switching time being a function of the electric field and temperature. Related to that a negative differential resistance can be observed, whose threshold electric fields increase while the threshold current decreases with dropping temperature. From thermodynamic consideration we can exclude a thermally induced phase transition. To answer the open questions in situ time-resolved infrared measurements were performed which reveal a modification of the optical spectra along the a- and b-direction. The temporal behavior of the spectral response correlates with the electrically induced switching. By applying a model for non-equilibrium charge carriers it was possible to simulate the electric switching as well as to explain the time-dependent optical spectrum. We find that the switching in this material is due to electrically induced non-equilibrium charge carriers, from which a fraction of their energy is transferred to the lattice. This causes a rise in the system's temperature and significant changes in the spectrum. This further supports the high agreement of the simulated and experimental data.

In summary, this work treats main aspects of the charge carrier dynamics of organic compounds. In this framework, numerical as well as theoretical models as DFT were used to calculate their physical properties and relate them to optical studies. The theoretical calculations yield satisfying and good results, especially for the optical spectra. However, the results can be further refined by methods including correlation effects.

Furthermore, externally induced phenomena such as electrically and photo-induced switching were investigated by novel methods such as the Step-Scan technique. We are very optimistic that the present results will stimulate further studies on the field of externally induced effect as photoconductivity measurements by the step-scan technique. For instance, we suggest a closer look on Θ-(BEDT-TTF)$_2$$MM'(SCN)_4$, MM'=CsCo, CsZn, RbCo, and RbZn compounds, where it is of interest whether the charge order gets melted by a high electric field. In this context, the impact of light on the magnetic properties of organic conductors as well as on molecular crystals should be extended by using ESR and Squid technology in combination with laser systems. Furthermore, we suggest studies of the optical properties of the CO state on the nanometer scale by a (time-resolved) near-field optical microscope to detect whether the transition is spatially uniform. The thesis has also proven that the combination of experiment and theory can deliver important information and insights on the physical properties of organic conductors. Therefore, we are confident that this thesis will trigger a wide variety of further interesting studies on the interesting research field of organic conductors and beyond.

Part VI

DEUTSCHE ZUSAMMENFASSUNG

7

DEUTSCHE ZUSAMMENFASSUNG

Schon seit Anbeginn der Menschheitsgeschichte ist die stetige Weiterentwicklung von alltäglichen Gegenständen wie Werkzeugen und Waffen die Grundlage für die stetige Evolution des Menschen. Beginnend mit der Verwendung von einfachen Steinen und Naturmaterialien als Waffen und Werkzeuge in der Steinzeit hat die Menschheit schon vor über 14000 Jahren damit begonnnen, ihre Instrumente und Werkzeuge kontinuierlich zu verbessern, was durch äußere Faktoren wie den natürlichen Selektionsdruck begünstigt wurde. Diese Entwicklung wurde meistens durch die Verwendung effektiverer und effizienterer Materialien sowie verbesserter Verarbeitungstechniken erreicht, wie zum Beispiel durch die Entwicklung von Schmelz- und Formtechniken für Metalle. Auf dieser Grundlage basierte das Fundament der Macht antiker Hochkulturen wie des römischen Reiches und führte zur Ausbildung einer hochtechnologischen Gesellschaft.

Bis zur Mitte des 19. Jahrhunderts war das Forschungsinteresse hauptsächlich auf die Untersuchung von Metallen beschränkt. Jedoch wurde durch die kontinuierlichen Entwicklung der Chemie zu Beginn des 20. Jahrhunderts eine systematische Untersuchung verschiedener Materialarten eingeleitet, wodurch eine große Anzahl neuer Materialien und Legierungen entdeckt wurden. Während am Anfang der Materialwissenschaft und der Physik die Forschung daran interessiert war, die mechanischen Eigenschaften zu verbessern, änderte sich dies mit dem physikalischen Verständnis des Elektromagnetismus und seiner Wechselwirkung mit Materie, wodurch sich vollständig neue Anwendungsgebiete eröffneten. Dies trieb die Erforschung und chemische Behandlung von Halbleitern wie Silizium entscheidend an. Heutzutage ist Silizium immer noch das wichtigste Material in der Halbleiter- und Elektronikindustrie. Parallel zu dieser Entwicklung wurden im Verlauf der letzten 60 Jahre tausend verschiedene organische Verbindungen wie Polymere, organische Halbleiter, Fullerene, Nanoröhrchen, Graphen und organische Leiter neben einer Vielzahl anorganischer Materialien in den Laboratorien geschaffen, die sich zum Teil im alltäglichen Leben wiederfinden. Somit kann man sagen, dass der Siegeszug organischer Elektronik gegenüber der Siliziumtechnologie gerade erst begonnen hat.

In diesem Zusammenhang wurde sehr schnell das Potential organischer Materialien erkannt. Die physikalischen Eigenschaften organischer Materialien lassen sich im Rahmen klassischer Bandtheorien nicht genau beschreiben, da die theoretischen Vorhersagen die experimentellen Beobachtungen nicht bestätigen. Der Grund dafür ist das komplexe Zusammenspiel von Elektron-Elektron- und Elektron-Gitter-Wechselwirkungen, die den Grundzustand dieser Materialien bestimmen. Dadurch weisen sie verschiedene magnetische und nichtmagnetische Zustände auf, die durch externe Parameter wie Druck, Temperatur sowie elektrische und magnetische Felder aktiv kontrolliert werden können. Diese Manipulierbarkeit eröffnet vollkommen neue Einsatzmöglichkeiten im Bereich der Elektronik.

Aber warum sind organische Leiter so interessent? Hierfür gibt es mehrere eindeutige Gründe:

1. Die Ausgangsmaterialien sind sehr günstig und einfach herzustellen.
2. Die Materialzusammensetzung kann schnell und einfach verändert werden und somit auch die physikalischen Eigenschaften der Produkte.
3. Die Endprodukte weisen eine sehr hohe Qualität bezüglich ihrer Reinheit auf.
4. Sie sind sehr empfindlich auf äußere Einflüsse wie zum Beispiel Druck oder Licht.
5. Ihre physikalischen Eigenschaften können eine starke Anisotropie aufweisen. Dadurch lassen sich Effekte in 1D, 2D sowie 3D untersuchen und mit theoretischen Modellen vergleichen.
6. Die Wechselwirkung von Elektronen miteinander und mit dem Kristallgitter kann in dieser Materialklasse sehr gut untersucht und durch chemische Modifikation variiert werden.

Aufgrund ihrer besonderen und vielfältigen Eigenschaften wurden im Rahmen dieser Arbeit folgende Ziele verfolgt:

1. Durchführung detaillierter und umfassender Untersuchungen der Grundzustände mittels optischer Spektroskopie und Transportmessungen.
2. Theoretische Berechnungen der Bandstrukturen, der Molekülschwingungen und der optischen Eigenschaften.
3. Aufbau von Experimenten zur Untersuchung zeitabhängiger Effekte, die sich im Ladungstransport sowie in den optischen Eigenschaften bemerkbar machen.
4. Untersuchung der Wechselwirkung organischer Leiter mit elektrischen Feldern und kurzen Lichtimpulsen, um neue induzierte Effekte und ihre charakteristische Zeitskala zu entdecken. Dabei stand die Abhängigkeit der Phänomene von der Umgebungstemperatur, der elektrischen Feldstärke sowie Lichtintensität im Fokus.
5. Besseres physikalisches Verständnis der Grundzustände durch den Vergleich der Daten im thermodynamischen Gleichgewicht mit den Ergebnissen des induzierten Zustands.

Jedoch besitzen organische Leiter auch Nachteile:

1. Sie sind wenig temperaturstabil (> 370 K).
2. Ihre mechanische Belastbarkeit ist gering.

Dies macht experimentelle Untersuchungen schwierig. Im Rahmen dieser Arbeit wurden verschiedene ein- und zweidimensionale organische Leiter durch unterschiedliche experimentelle und theoretische Methoden eingehend und systematisch untersucht. Die Konzentration lag dabei zum einen auf den leicht dimerisierten eindimensionalen organischen Fabre Salzen $TMTTF_2X$ (for example X=PF_6, AsF_6, ClO_4). Zum Anderen wurden die kürzlich synthetisierten organischen Salze δ-(EDT-TTFCONMe$_2$)$_2$AsF$_6$ und δ-(EDT-TTFCONMe$_2$)$_2$Br, das

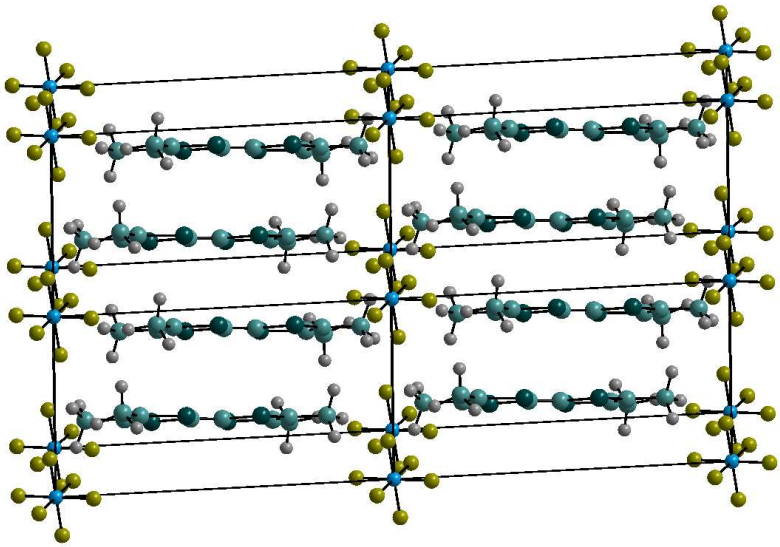

Figure 7.1: Exemplarische Darstellung der Kristallstruktur des eindimensionalen organischen Leiters $(TMTTF)_2PF_6$. Die organischen Moleküle (graue, dunkelblaue Atome) bilden Schichten, die durch die Anionen (hellblaue, gelbe Atome) voneinander getrennt sind. [1]

sehr bekannte Ladungstransfersalz TTF-CA sowie das zweidimensionale organische α-$(BEDT\text{-}TTF)_2I_3$ Salz untersucht.

Im Allgemeinen bestehen organische Leiter aus zwei verschiedenen organischen sowie anorganischen Molekülen bzw. Atomen. Innerhalb des Kristalls formen die organischen Komponenten Schichten, die durch anorganische Moleküle bzw. Atome voneinander getrennt sind (s. Abb. 7.1). In der Einheitszelle findet ein Elektronentransfer zwischen den organischen Molekülen und den anorganischen Anionen statt. Die untersuchten Verbindungen sind vorwiegend dreiviertel gefüllte Systeme. Die überlappenden Molekülorbitale der organischen Moleküle bestimmen die physikalischen Eigenschaften und wegen ihrer starken Anisotropie auch die Dimensionalität des Materials. Organische Leiter reagieren empfindlich auf Elektron-Gitter-Wechselwirkungen. Da die Bandbreite sehr schmal ist und somit die Elektronendichte sehr hoch, spielt Elektron-Elektron-Wechselwirkung ebenfalls einen sehr wichtige Rolle.

Diese Wechselwirkungen führen zu einer großen Anzahl von verschiedener Grundzustände, die am Besten durch Infrarotspektroskopie untersucht werden können:

1. Die Bandlücken und Transferenergie für $(TMTTF)_2X$, α-$(BEDT\text{-}TTF)_2I_3$ und TTF-CA kann gemessen werden.

2. Die molekulare Ladungsverteilung kann genau bestimmt werden.

Innerhalb dieser Studie wurden die elektrodynamischen Eigenschaften dieser Verbindungen untersucht. Insbesondere im Falle der Fabre Salze $TMTTF_2X$ mit X=PF_6, AsF_6, SbF_6 und ReO_4 wurde die bisher umfangreichste optische Untersuchung durchgeführt [2]. In diesem Zusammenhang wurden die beobachteten spektralen Merkmale aufgrund einer Normalmodenanalyse molekularen Vibrationsmoden zugeordnet. Dadurch war es möglich, die Temperaturabhängigkeit der Ladungsverteilung zwischen den einzelnen molekularen Gitterplätzen mit

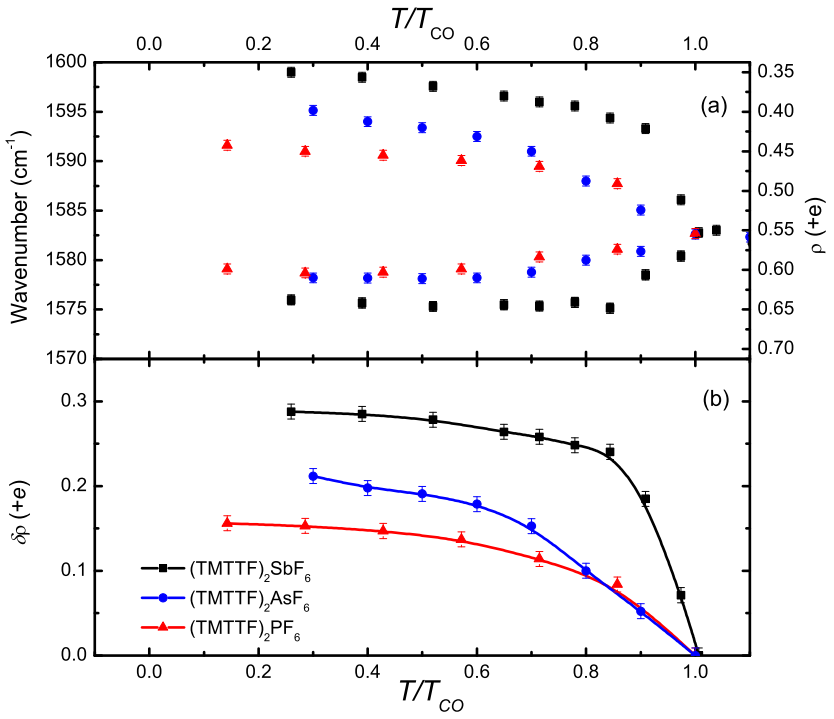

Figure 7.2: (a) Resonanzfrequenz einer ladungsempfindlichen Schwingungsmode verschiedener untersuchter Fabre Salze als Funktion der normierten Temperatur T/T_{CO}. (b) Aus der Resonanzfrequenz bestimmte Ladungsverteilung als Funktion von T/T_{CO} für drei verschiedene $(TMTTF)_2X$ Saze mit X=PF_6, AsF_6 und SbF_6 mit T_{CO}=67 K, 102 K und 157 K.

sehr hoher Genauigkeit zu bestimmen (s. Abb. 7.2). Mit zunehmender Übergangstemperatur T_{CO} findet ein Übergang von der zweiten in die erste Ordnung statt. Daraus lässt sich ableiten, dass das neueste Mitglied in der Fabre Familie $TMTTF_2TaF_6$ mit T_{CO}=174 K [3] einen reinen Übergang 1. Ordnung zeigen wird. Darüberhinaus werden den lokalen Minimas in den Spektren entlang der stark reflektierenden Richtung Obertöne und Kombinationsmoden emv-gekoppelter Molekülschwingungen zugeordnet. Deren Intensität wird durch die Asymmetrie des Molekülpotentials in der ladungsgeordneten Phase maßgeblich beeinflusst. Mit diesem wichtigen Ergebnis liefert diese Arbeit eine weitere Erkennungsmöglichkeit eines Ladungsordnungsübergangs in organischen Leitern.

Insgesamt beschreiben die DFT Berechnungen dieser Arbeit die Bandstruktur, die elektronischen Anregungen und die Anisotropie der optischen Eigenschaften der Fabre Salz sehr gut. Ausgehend von der Bandstruktur konnten gezeigt werden, dass eine Variation der Temperatur einen ähnlichen Effekt hat wie das Anlegen von hydrostatischen beziehungsweise chemischen Drucks. Die simulierten optischen Spektren zeigen neben einer starken Verschiebung der optischen Merkmale im MIR Bereich ebenfalls eine Veränderung der Spektren im sichtbaren Spektralbereich. Dieser Bereich sollte bei zukünftigen optischen Studien gezielt mituntersucht werden. Obwohl die Berechnungen im Rahmen der Genauigkeit mit den experimentellen Ergebnissen gute Übereinstimmungen erzielen, konnte gezeigt werden, dass im Falle eindimensionaler System wie der Fabre Salze Elektron-Elektron-Wechselwirkungen eine wichtige Rolle bei der Ausbildung der physikalischen Eigenschaften spielen. Durch eine komplexe Fit-

prozedur wurde die Temperaturabhängigkeit der Transferintegrale t bestimmt, welche tendenziell mit den Ergebnissen von Hückel Berechnungen übereinstimmen.

Ergebnisse dieser Arbeit sind die ersten Photoleitfähigkeitsmessungen an Fabre Salzen, für die ein neuer experimenteller Aufbau entwickelt und in den bestehenden optischen FTIR- und Transportaufbau integriert wurde. Dieser erlaubt es, die zeitliche Dynamik des Photostroms zu messen. Im Falle von SbF_6 wurde ein zeitlich abfallender Photostrom unterhalb von T_{CO} beobachtet, welcher zusätzlich mit oszillierendem Signal überlagert ist. Es konnte nachgewiesen werden, dass der ozillierende Strom, welcher durch die bisher bekannte Photostromeffekte nicht erklärt werden konnte, eine intrinsische Eigenschaft der Verbindung ist. Dies wird der Wechselwirkung einzelner angeregter Ladungsträger zugeschrieben, die mit dem kollektiven ladungsgeordneten Zustand interagieren, welcher dadurch destabilisiert wird und somit zu dem gezeigten Schwingungsverhalten des Photostroms führt.

Während in den Fabre Salzen $2k_F$ Umklappstreuungen auftreten können, die zum Öffnen einer Mott-Energielücke aufgrund des halben gefüllten Bands führt, ist diese Art von Streuprozess in den eindimensionalen Verbindungen δ-(EDT-TTFCONMe)$_2X$ mit X=Br und AsF_6 nicht vorhanden, da die organischen Moleküle gleichmäßig angeordnet sind. Dadurch sind die Bänder zu einem Viertel gefüllt. Wir zeigen innerhalb dieser Thesis die Temperaturabhängigkeit der optischen Eigenschaften für alle Kristallachsen. In den optischen Spektren zeigt sich die niedrige Dimensionalität der Materialien, was durch theoretische Berechnungen der optischen Anregungen eindeutig bestätigt wird [12]. Die beobachteten Vibrationsmoden wurden durch eine Normalmodenanalyse der freien neutralen und positiv geladenen EDT-TTFCONMe$_2$ Moleküle den Molekülschwingungen zugeordnet, wodurch die molekulare Ladungsverteilung bestimmt wurde. Dabei wurde entdeckt, dass diese schon bei Raumtemperatur existiert und zudem mit einem Verhältnis von 1:9 sehr groß ist. Des Weiteren war es uns möglich, den strukturellen Phasenübergang, der unterhalb von 200 K auftritt, durch die Verschiebung bestimmter Resonanzfrequenzen zu beobachten [4]. Im Fall der gut leitenden Kristallrichtung schreiben wir das Mitinfrarotband der optischen Anregung von Domainwänden zu.

TTF-CA unterscheidet sich von den zuletzt vorgestellten organischen Verbindungen, da die kationischen und anionischen Moleküle abwechselnd entlang der Kristallachsen angeordnet sind. Bei Raumtemperatur ist die Verbindung neutral und die Ladung gleichmäßig auf die Gitterplätzen verteilt, wobei durch Abkühlen bei T_{NI}=81.5 K ein Phasenübergang erster Ordnung in einen ionischen Zustand auftritt. Die qualitativ hochwertigen Kristalle wurden in einem eigens dafür entwickelten Aufbau, welcher auf der Sublimationstechnik basiert, gezüchtet. Es wurden theoretische DFT Berechnungen durchgeführt, woraus die Bandstruktur und die elektronischen Anregungen berechnet wurden, die sehr genau die Energielücke sowie das Temperaturverhalten der optischen Anregungen zeigen.

Eine der detailliertesten optischen Untersuchungen im Bereich des Mittelinfraroten wurde hierbei durchgeführt, wodurch wir die Veränderung der Molekülionizität sowie die Breite der Energiebänder bestimmen konnten. Dafür wurden wiederum DFT Simulationen eingesetzt, um die Vibrationsmoden genau zu bestimmen.

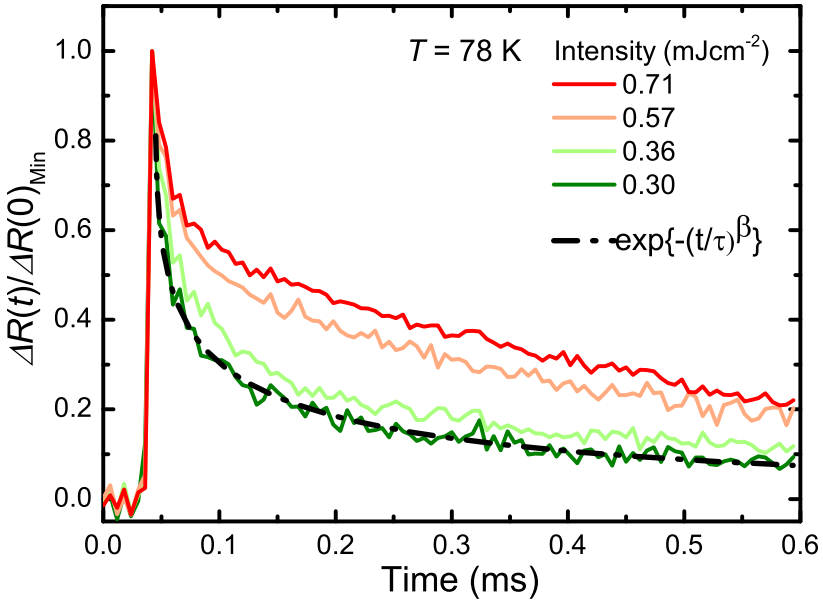

Figure 7.3: Zeitliche Dynmaik des normierten Reflektionssignals von TTF-CA nach der optischen Anregung mit einem Laserpuls der Wellenlänge 532 nm bei einer Temperature von 78 K für unterschiedliche Laserintensitäten. Die gestrichelte schwarze Linie stellt examplarisch die Anpassung einer Kohlrausch-Williams-Watt Funktion $e^{-(\frac{t}{\tau})^{\beta}}$ an die experimentellen Daten dar. (Nachgedruck mit Erlaubnis von Ref. [5].)

In diesem Zusammenhang haben wir erstmalig die Step-Scan Technik eingesetzt, um die zeitabhängige optische Antwort eines Festkörpers auf die Anregung durch einen Laserpuls zu untersuchen. Im Falle von TTF-CA wurde der photo-induzierte Phasenübergang in der ionischen Phase durch zeitaufgelöste Infrarotspektroskopie im Mikro- und Millisekundenbereich [5] untersucht. Das Reflektionsspektrum nach der Photoanregung ähnelt dem Spektrum der neutralen Phase. Die zeitliche Entwicklung des Signals kann nicht durch eine einfache Exponentialfunktion beschrieben werden, sondern nur durch eine Kohlrausch-Williams-Watt Funktion, wie sie in Abb. 7.3 dargestellt ist. Der Relaxationsprozess kann durch einen eindimensionalen Random-Walk-Annihilationsprozess von neutralen-ionischen Domänenwänden beschrieben und erklärt werden, was durch numerische Simulation, die während dieser Arbeit durchgeführt wurde, bestätigt wird. Dadurch ist man ebenfalls in der Lage, die induzierte Domänengröße abzuschätzen, welche von Temperatur und Laserintensität abhängt.

Neben den eindimensionalen organischen Leitern wurde auch das zweidimensionale organische Material α-(BEDT-TTF)$_2$I$_3$ untersucht, das einen Metall-Isolator Übergang bei 136 K aufweist. Der isolierende Zustand wird dabei begleitet von einer ungleichen Verteilung der Ladungsträger auf die molekularen Gitterplätzen. Überraschenderweise konnte auf Grundlage von temperaturabhängigen Strukturdaten der metallische und der ladungsgeordneten Zustand durch DFT erfolgreich berechnet werden, obwohl im Allgemeinen davon ausgegangen wird, dass starke Korrelationseffekte eine wichtige Rolle bei der Ausbildung der isolierenden Phase spielen. Ein weiterer Aspekt dieser Arbeit ist die erfolgreiche Untersuchung des elektrisch induzierten Isolator-Metall-Übergangs, welcher durch einen neuen experimentellen Aufbau charakterisiert wurde. Dieser Versuch erlaubt es, die Transporteigenschaften zeitaufgelöst zu detektieren. Dadurch sind wir in der Lage, das Schalten der Probe von einem niedrig- in einen

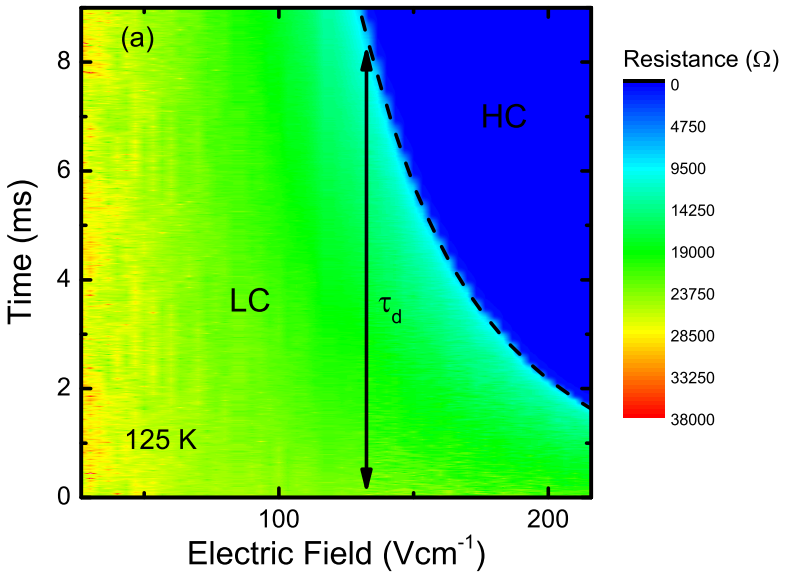

Figure 7.4: Konturplot des zeitabhängigen Probenwiderstands von α-(BEDT-TTF)$_2$I$_3$ für verschiedene elektrische Felder in der isolierenden Phase. Es wurden zur Anregung Spannungspulse mit einer Länge von 9 ms angelegt. Der gelbgrüne Bereich entspricht dem niedrigleitenden Zustand, wobei das blaue Gebiet den hochleitenden Zustand widerspiegelt. Mit zunehmenden elektrischen Feldern nimmt die Schaltzeit τ_d nicht linear zu.

hochleitenden Zustand nach Anlegen eines kurzen Spannungspulses nachzuweisen (s. Abb. 7.4). In diesem Zusammenhang wurde ein nichtlinearer Transporteffekt mit einem negativ differentiellen Widerstandsbereich beobachtet. Zusätzlich wurde zeitaufgelöste Infrarotspektroskopie eingesetzt, um eine Veränderung des Mittelinfrarotspektrums aufgrund des elektrisch induzierten Phasenübergangs zu verfolgen. Tatsächlich konnten wir eine Änderung des Infrarotspektrums in einen metallischen Zustand in der Nähe des Phasenübergangs feststellen. Im Gegensatz dazu konnte für Temperaturen unterhalb von 110 K nur eine unmerkliche Veränderung der Probentemperatur nachgewiesen werden. Diese schwache Veränderung beweist, dass sich die Probe noch im isolierenden Ausgangszustand befindet. Den induzierten Schaltvorgang schreiben wir der Anregung von Ladungsträgern zu, die sich nicht im thermodynamischen Gleichgewicht befinden. Dies wird durch unsere numerischen Simulationen "heißer" Elektronen bestätigt und hervorragend erklärt. Dadurch sind wir in der Lage, die Gittertemperatur theoretisch zu bestimmen, die von der Elektronentemperatur verschieden ist. Dabei stimmt die theoretisch bestimmte Gittertemperatur ausgezeichnet mit der Temperaturabschätzung aus den Infrarotmessungen überein.

Zusammenfassend lieferten die verwendeten theoretischen Methoden und Berechnungen wichtige Informationen über den Einfluss von Elektron-Elektron-Wechsel-wirkungen und die Anisotropie des elektronischen Systems der verschiedenen untersuchten Materialien. Durch die sehr gute Übereinstimmung mit unseren experimentellen Untersuchungen sind sie ein sehr geeignetes Mittel, um optische Spektren organischer Leiter vorherzusagen. Außerdem wurde die Normalmodenanalyse zur Identifizierung und Zuweisung von molekularen

Schwingungen eingesetzt und etablierte sich dadurch als probates Mittel zur Identifikation molekularer Schwingungen.

Ein weiterer Meilenstein dieser Dissertation war die erstmalig erfolgreiche Anwendung der zeitaufgelösten Step-Scan Technik zur Untersuchung von angeregten Festkörpern. Des Weiteren wurde diese Technik mit den experimentellen Aufbauten zur Messung der zeitabhängigen Leitfähigkeit kombiniert, um den Einfluss von Spannungs- und Lichtpulsen auf die Proben umfassend zu untersuchen. Dies eröffnet uns die einzigartige Möglichkeit, die Proben außerhalb des Gleichgewichtszustands in einem Zeitraum von Mikro- bis in den Minutenbereich zu untersuchen, was von der klassischen ultraschnellen Pump-Probe Spektroskopiemethoden nicht erreicht werden kann. Dadurch konnten neue Effekte und deren Zusammenspiel mit äußeren Parametern entdeckt, untersucht und erklärt werden. In diesem Zusammenhang wurden Grundlagen für zukünftige Experimente zur Erkundung der möglichen Anwendung von organischen Leitern in der molekularen Elektronik, wie zum Beispiel flüchtige Speicher oder optische Schalter, geschaffen.

Für zukünftige Forschungsprojekte bietet es sich auf Grundlage der Ergebnisse dieser Dissertation an, gleichzeitig theoretisch als auch experimentell zur Untersuchung von unerforschten organischen Verbindungen zu arbeiten. Diese Arbeit kann als Motivation für zukünftige Studien auf dem Gebiet organischer Leiter wegweisend sein.

Die Dissertation unterteilt sich wie folgt in mehrere Kapitel:

1. In den ersten beiden Kapiteln wird eine generelle Einführung in die Materialklasse der organischen Leiter gegeben und diese in Zusammenhang zu anderen organischen Materialien gestellt. Des Weiteren werden die physikalischen Grundzustände und ihre theoretischen Modelle vorgestellt. Die letzten Abschnitte widmen sich den Nichtgleichgewichtszuständen wie zum Beispiel photoinduzierten Phasenübergängen.

2. Während der Dissertation wurden viele unterschiedliche Experimente und theoretische Techniken eingesetzt, die in Kapitel 2 im Detail vorgestellt werden. Ein weiterer Fokus dieses Kapitels liegt auf der Dichtefunktionaltheorie, die zur Berechnung der Bandstruktur, der optischen Spektren sowie der molekularen Vibrationsmoden eingesetzt wurde.

3. Das Hauptkapitel ist den experimentellen Ergebnissen gewidmet, das entsprechend nach der Dimensionalität der untersuchten Materialien aufgeteilt ist. Dieses beginnt mit den eindimensionalen Fabre Salzen $(TMTTF)_2X$, X = PF_6, AsF_6, SbF_6 und ReO_4. In diesem Zusammenhang werden auch die Ergebnisse der Untersuchung der neuen organischen Salze δ-$(EDT\text{-}TTFCONMe_2)_2X$, X = Br und AsF_6 vorgestellt. Das Überkapitel eindimensionaler organischer Salze wird von den Ergebnissen aus den Untersuchungen von TTF-CA abgeschlossen.

   Jedes materialspezifische Kapitel beinhaltet eine Diskussion der theoretischen Ergebnisse und einen Vergleich mit den experimentellen Resultaten. Hierbei werden die umfangreichen optischen Untersuchungen im Detail vorgestellt und interpretiert. Die letzten Unterkapitel beinhalten Untersuchungen eletrischer sowie lichtinduzierter Phänomene, die schließlich durch theoretische Modelle genau beschrieben werden.

Neben den erwähnten eindimensionalen Systemen wurde auch der zweidimensionale organische Leiter α-(BEDT-TTF)$_2$I$_3$ untersucht. Der Schwerpunkt liegt hierbei zum einen auf den theoretischen Berechnungen der elektronischen Eigenschaften, dem Vergleich mit den experimentellen Ergebnissen und zum anderen auf der umfangreichen Untersuchung und Interpretation des elektrisch induzierten Schaltvorgangs in einen hochleitenden Zustand.

4. Das letzte Hauptkapitel beinhaltet eine kurze Zusammenfassung der Ergebnisse und der dabei gewonnen Erkenntnisse. Auf dieser Grundlage wird ein Ausblick in die zukünftige Entwicklung der Materialklasse organischer Leiter und der Anwendbarkeit von theoretischen Modellen und Nichtgleichgewichtszuständen gegeben.

5. Neben dem Aufbau der komplexen Experimente und Untersuchungen organischer Kristalle wurden weitere umfassende Projekte auf dem Gebiet von Flüssigkristallen und korrelierten Übergangsmetalloxiden hier im speziellen VO_2 durchgeführt, die im Anhang vii ausführlich erläutert sind. Hier finden man auch zahlreiche Tabellen von Resonanzfrequenzen der molekularen Vibrationsmoden und simulierte optische Spektren der untersuchten organischen Salze.

Part VII

APPENDIX

A

NORMAL MODE ANALYSIS

A.1 TMTTF

Table A.1: Calculated frequencies (cm^{-1}) and IR intensities (D^2 amu^{-1} $Å^{-2}$) of $TMTTF^0$ and $TMTTF^+$. The experimental values are extracted from [177]. Published in Dressel et al. [2].

		$TMTTF^0$				$TMTTF^+$			
Symmetry	Label	$\nu_{Exp.}$	$\nu_{calc.}$	ν_{scaled}	Int	$\nu_{Exp.}$	$\nu_{calc.}$	ν_{scaled}	Int.
A_g	ν_1	2,923	3,142	3,041	0.4127		3,167	3,056	0.1161
	ν_2		3,034	2,937	0.0291		3,054	2,956	0.0994
	ν_3	1,639	1,690	1,636	0.0036	1,567	1,622	1,570	0
	ν_4	1,538	1,596	1,545	0.0036	1,418	1,492	1,444	0.0021
	ν_5	1,432	1,502	1,454	0.2444		1,447	1,400	0
	ν_6		1,434	1,388	0.006		1,436	1,391	0.0015
	ν_7	1,092	1,103	1,114	0.051	1,104	1,101	1,112	0
	ν_8	934	940	949	0.018	941	936	945	0.0008
	ν_9	560	553	558	0.013	566	563	569	0
	ν_{10}	494	495	500	0.0197	523	524	530	0
	ν_{11}	277	313	316	0.036	298	311	314	0.0018
	ν_{12}	217	211	213	0.0114	228	222	224	0
B_{1g}	ν_{20}		3,083	2,984	0.238		3,111	3,011	0.0353
	ν_{21}		1,482	1,434	0.0246		1,479	1,431	0.0656
	ν_{22}		1,063	1,073	0.005		1,063	1,074	0.001
	ν_{23}		507	512	0.0006		511	516	0.0002
	ν_{24}		176	178	0.0652		151	153	0.0002
	ν_{25}		145	147	0.005		121	122	0.0002
B_{2g}	ν_{37}		3,082	2,983	0.2187		3,113	3,013	0.0361
	ν_{38}		1,488	1,440	0.4105		1,487	1,439	0.0418
	ν_{39}		1,047	1,057	0.0014		1,048	1,058	0.0024
	ν_{40}		517	522	0.1132		507	512	0.0001
	ν_{41}		261	263	0.0009		296	299	0.0004
	ν_{42}		151	153	0.0206		98	99	0
	ν_{43}		60	61	0.0684		73	74	0.0018
B_{3g}	ν_{55}		3,133	3,032	0.12		3,158	3,057	0.0079
	ν_{56}		3,031	2,934	0.0205		3,052	2,953	0.0651
	ν_{57}		1,493	1,445	0.0343		1,484	1,436	0.1928
	ν_{58}		1,417	1,371	0.0015		1,419	1,374	0.0453
	ν_{59}		1,188	1,200	0.0004		1,194	1,207	0
	ν_{60}		1,118	1,129	0.0305		1,126	1,136	0
	ν_{61}		985	995	0.0032		1,038	1,049	0

		TMTTF^0				TMTTF$^+$			
Symmetry	Label	$\nu_{Exp.}$	$\nu_{calc.}$	ν_{scaled}	Int	$\nu_{Exp.}$	$\nu_{calc.}$	ν_{scaled}	Int.
	ν_{62}		743	751	0.0072		763	770	0
	ν_{63}		473	478	0.0007		474	479	0
	ν_{64}		385	389	0.0073		387	391	0
	ν_{65}		246	259	0.0111		236	239	0.0002
A_u	ν_{13}		3,082	2,983	0.4242		3,111	3,011	0.0447
	ν_{14}		1,483	1,435	0.1007		1,480	1,432	0.0551
	ν_{15}		1,064	1,074	0.0028		1,063	1,073	0.0003
	ν_{16}		505	510	0.0016		501	506	0
	ν_{17}		177	179	0.0298		147	149	0.0006
	ν_{18}		145	146	0.0226		117	118	0.0034
	ν_{19}		66	67	0.0011		43	43	0.0054
B_{1u}	ν_{26}	2,912	3,142	3,041	0.8701	2,923	3,166	3,065	0.1837
	ν_{27}	2,848	3,034	2,936	1.7466	2,848	3,053	2,956	0.2383
	ν_{28}	1,627	1,682	1,628	0.208	1,547	1,602	1,551	8.6833
	ν_{29}	1,437	1,502	1,454	0.3773	1,438	1,491	1,443	0.0307
	ν_{30}	1,374	1,433	1,387	0.001		1,437	1,391	0.0857
	ν_{31}	1,090	1,101	1,112	0.6616	1,095	1,096	1,108	0.0616
	ν_{32}	935	941	950	0.0842	935	930	939	1.2806
	ν_{33}	780	778	786	0.9168	828	821	829	0.6553
	ν_{34}	556	545	551	0.0573	557	551	556	0.1366
	ν_{35}	439	435	440	0.356	468	476	480	0.5027
	ν_{36}	236	307	310	0.076		306	309	0.0039
B_{2u}	ν_{44}	2,990	3,132	3,032	0.25	2,973	3,159	3,057	0.028
	ν_{45}	2,848	3,032	2,934	1.955	2,853	3,052	2,954	0.1876
	ν_{46}	1,437	1,493	1,445	0.403	1,438	1,484	1,436	0.2372
	ν_{47}	1,385	1,418	1,372	0.015	1,399	1,420	1,374	0.0894
	ν_{48}	1,183	1,192	1,203	0.5125	1,185	1,197	1,209	0.075
	ν_{49}		1,109	1,120	0.3985		1,109	1,120	0.2273
	ν_{50}		853	861	0.0333	875	907	917	0.1686
	ν_{51}	747	745	753	0.0224	768	764	771	0.0041
	ν_{52}		479	484	0.11		483	488	0.0384
	ν_{53}	332	337	341	0.13	359	345	348	0.0466
	ν_{54}		80	81	0.06		83	84	0.0093
B_{3u}	ν_{66}		3,083	2,984	0.4		3,112	3,012	0.0566
	ν_{67}		1,488	1,441	0.4328		1,487	1,439	1.02
	ν_{68}		1,048	1,058	0.0021		1,049	1,059	0.0188
	ν_{69}		277	280	0.1603		323	326	0.1897
	ν_{70}		274	278	0.02038		279	282	0.0463
	ν_{71}		150	151	0.115		76	76	0.0142
	ν_{72}		34	35	0.0667		46	47	0.069

A.2 (EDT-TTF)-CONME$_2$

Table A.2: Calculated frequencies (in cm^{-1}) and infrared intensities (given in units of D^{2}amu^{-1} Å^{-2}). The direction of observation is noted in brackets behind the experimental values. The following abbreviation is used: Int.: Intensity. Published in Peterseim et al. [4].

	EDT_2AsF_6	EDT_2Br	(EDT-TTF)-CONMe$_2^0$			(EDT-TTF)-CONMe$_2^+$		
Label	Experimental	Experimental	ν_{calc}	ν_{scaled}	Int.	ν_{calc}	ν_{scaled}	Int.
ν_1			3249	3145	0.037	3283	3177	0.271
ν_2	-	-	3196	3094	0.025	3209	3106	0.018
ν_3	-	-	3171	3069	0.212	3160	3059	0.267
ν_4	-	-	3146	3045	0.181	3159	3058	0.005
ν_5	-	-	3128	3028	0.01	3148	3047	0.003
ν_6	-	-	3088	2989	0.358	3122	3022	0.084
ν_7	3011(*c*)	2980 (*c*)	3083	2984	1.326	3120	3019	0.581
ν_8	-	-	3082	2983	0.562	3095	2995	0.017
ν_9	-	-	3070	2972	0.308	3091	2992	0.036
ν_{10}	-	2890 (*c*)	3036	2938	2.16	3060	2962	0.941
ν_{11}	-	2830 (*c*)	3021	2924	1.027	3040	2942	0.537
ν_{12}	1599/1605 (*b,c*)	1592/1600 (*c*)	1720	1664	5.939	1716	1661	7.101
ν_{13}	1551(*c*)	1549 (*c*)	1628	1576	2.62	1589	1538	0.233
ν_{14}	1536/1404 (*c*)	1538/1403 (*c*)	1601	1549	1.041	1430	1384	31.029
ν_{15}	1488/1421 (*b,c*)	1490/1428 (*c*)	1561	1511	0.412	1476	1429	5.98
ν_{16}	-	-	1561	1511	0.434	1551	1502	1.57
ν_{17}	-	-	1539	1489	0.218	1535	1486	0.128
ν_{18}	-	-	1527	1478	0.5	1532	1483	0.441
ν_{19}	-	-	1523	1474	0.269	1523	1474	0.439
ν_{20}	-	-	1509	1460	0.028	1493	1445	0.323
ν_{21}	1438 (*b,c*)	1440 (*c*)	1500	1452	0.638	1496	1447	0.48
ν_{22}	1419 (*b,c*)	1416 (*c*)	1482	1435	0.149	1487	1439	0.345
ν_{23}	1409 (*c*)	1410 (*c*)	1460	1414	0.270	1459	1412	0.316
ν_{24}	1396 (*b,c*)	1395 (*c*)	1433	1387	6.697	1441	1395	0.585
ν_{25}	-	1300 (*c*)	1345	1302	0.64	1349	1306	0.3805
ν_{26}	-	-	1310	1268	0.047	1326	1283	0.064
ν_{27}	-	1290 (*c*)	1290	1303	1.866	1286	1299	2.61
ν_{28}	-	1272 (*c*)	1255	1268	0.57	1258	1271	0.291
ν_{29}	-	1256 (*c*)	1212	1224	4.277	1204	1216	6.748
ν_{30}	-	1173/1184 (*c*)	1206	1218	0.146	1230	1243	0.002
ν_{31}	-	1146 (*c*)	1181	1193	0.269	1174	1185	0.073
ν_{32}	-	-	1164	1175	0.073	1169	1181	0.037
ν_{33}	-	-	1149	1160	0.034	1134	1146	0.074
ν_{34}	1064 (*b*)	-	1098	1109	0.163	1094	1105	0.288
ν_{35}	1015/1002 (*b,c*)	1020/1000 (*c*)	1042	1052	2.292	1032	1041	0.431
ν_{36}	-	-	1027	1037	0.021	1020	1030	0.09
ν_{37}	1000 (*b,c*)	1000 (*c*)	1007	1017	0.021	1024	1034	0.4

	EDT_2AsF_6	EDT_2Br	(EDT-TTF)-$CONMe_2^0$			(EDT-TTF)-$CONMe_2^+$		
Label	Experimental	Experimental	ν_{calc}	ν_{scaled}	Int.	ν_{calc}	ν_{scaled}	nt.
ν_{38}	-	-	983	992	0.001	1048	1059	0.068
ν_{39}	-	-	973	983	0.129	950	959	0.157
ν_{40}	896/891 (*b*)	-	895	904	1.06	891	899	0.0001
ν_{41}	-	-	877	886	0.367	882	891	0.2489
ν_{42}	-	-	853	862	0.245	912	921	0.087
ν_{43}	-	-	837	845	0.256	892	901	0.235
ν_{44}	-	-	829	837	0.221	825	834	0.476
ν_{45}	-	-	802	810	0.425	808	816	0.223
ν_{46}	819 (*b*)	-	771	779	1.034	811	819	0.397
ν_{47}	-	-	768	776	0.054	791	799	0.057
ν_{48}	719 (*a*)	714 (*a*)	719	726	0.948	719	726	0.671
ν_{49}	-	-	709	716	0.163	712	719	0.029
ν_{50}	-	-	671	677	0.062	677	684	0.042
ν_{51}	-	-	641	647	0.516	647	653	0.881
ν_{52}	-	-	617	623	0.075	640	646	0.0228
ν_{53}	-	-	550	556	0.024	524	529	0.0272
ν_{54}	-	-	524	529	0.299	524	529	0.013
ν_{55}	-	-	508	513	0.019	499	504	0.072
ν_{56}	-	-	483	488	0.023	509	514	0.011
ν_{57}	-	-	461	465	0.022	474	479	0.003
ν_{58}	-	-	452	456	0.093	477	481	0.746
ν_{59}	-	-	444	448	0.061	453	458	0.036
ν_{60}	-	-	418	422	0.133	433	438	0.009
ν_{61}	-	-	408	412	0.407	413	417	0.676
ν_{62}	-	-	369	373	0.007	357	361	0.003
ν_{63}	-	-	349	352	0.012	342	346	0.192
ν_{64}	-	-	340	343	0.07	333	3336	0.001
ν_{65}	-	-	332	335	0.085	297	300	0.173
ν_{66}	-	-	309	312	0.007	311	314	0.044
ν_{67}	-	-	272	274	0.008	314	317	0.048
ν_{68}	-	-	265	267	0.027	271	274	0.01
ν_{69}	-	-	251	254	0.205	279	282	0.351
ν_{70}	-	-	250	253	0.104	264	266	0.021
ν_{71}	-	-	227	229	0.061	231	233	0.117
ν_{72}	-	-	195	197	0.03	219	221	0.049
ν_{73}	-	-	177	179	0.011	193	195	0.015
ν_{74}	-	-	154	156	0.028	161	163	0.006
ν_{75}	-	-	140	141	0.023	141	143	0.162
ν_{76}	-	-	132	134	0.006	127	129	0.007
ν_{77}	-	-	117	118	0.023	100	101	0.001
ν_{78}	-	-	91	92	0.039	106	107	0.02
ν_{79}	-	-	76	77	0.009	65	65	0.012
ν_{80}	-	-	67	68	0.066	54	54	0.007

	EDT_2AsF_6	EDT_2Br	(EDT-TTF)-CONMe$_2^0$			(EDT-TTF)-CONMe$_2^+$		
Label	Experimental	Experimental	ν_{calc}	ν_{scaled}	Int.	ν_{calc}	ν_{scaled}	nt.
ν_{81}	-	-	52	52	0.064	46	47	0.117
ν_{82}	-	-	41	42	0.058	48	49	0.051
ν_{83}	-	-	38	38	0.011	33	33	0.061
ν_{84}	-	-	18	18	0.068	24	25	0.006

A.3 CA

Table A.3: Calculated frequencies (in cm^{-1}) and infrared intensities (given in units of D^2amu^{-1} $Å^{-2}$). The following abbreviation is used: Int.: infrared intensity.

		CA^0			CA^-			
Label	Symmetry	ν_{calc}	ν_{scaled}	Int.	ν_{calc}	ν_{scaled}	Int.	$\Delta\nu$
ν_1	a_g	1754.1	1696.22	-	1548.51	1497.41	-	-199
ν_2		1630.2	1576.24	-	1608.16	1555.09	-	-21
ν_3		970.94	990.07	-	982.53	1002	-	11.82
ν_4		486.36	495.94	-	496.35	506.13	-	10.18
ν_5		317.71	323.97	-	320.91	327.23	-	3.26
ν_6		200.04	203.98	-	201.04	205	-	1.02
ν_9	b_{1g}	322.03	328.37	-	328.8	335.3	-	6.92
ν_{15}	b_{2g}	801.56	817.35	-	771.93	787.13	-	-29.93
ν_{16}		441.79	450.49	-	390.53	398.22	-	-52.27
ν_{17}		96.76	98.66	-	120.16	119.02	-	21.5
ν_{23}	b_{3g}	1215.35	1175.25	-	1301.89	1258.92	-	83.68
ν_{24}		829	845.33	-	807.37	823.28	-	-22.06
ν_{25}		733.82	748.28	-	724.12	738.4	-	-10
ν_{26}		337.27	343.92	-	325.54	331.96	-	-12
ν_{27}		263.81	269	-	275.46	281	-	11.88
ν_7	a_u	573.15	584.44	-	559.45	570.47	-	-13.96
ν_8		69.76	71.13	-	75.07	76.54	-	5.36
ν_{10}	b_{1u}	1757	1699	349.46	1565.35	1513.7	288.1	-185.31
ν_{11}		1086.54	1050.68	415.77	1117.9	1081	203.72	30.32
ν_{12}		899.07	916.78	25.31	892.53	910.12	159.74	-6.67
ν_{13}		460.13	469.2	5.27	436.92	445.53	0.66	-23.66
ν_{14}		205.26	209.3	0.03	205.46	209.51	1.44	0.21
ν_{18}	b_{2u}	1590.76	1538.26	254.54	1465	1416.57	0.27	-121.7
ν_{19}		1202.63	1162.94	120.02	1099.8	1063.5	97.81	-99.44
ν_{20}		723.56	737.81	206.15	686.72	700.25	155.1	-37.56
ν_{21}		380.92	388.42	3.11	360.35	367.45	0.16	-20.97
ν_{22}		214.24	218.46	0.23	213.82	218.04	0.73	-0.43
ν_{28}	b_{3u}	756.16	771.05	27.3	732.12	746.54	17.92	-24.51
ν_{29}		199.7	203.62	2.88	201.47	205.44	2.76	1.82
ν_{30}		69	70.33	1.68	86.8	88.5	3.12	18.17

A.4 TTF

Table A.4: Calculated frequencies (in cm^{-1}) and infrared intensities (given in units of D^2amu^{-1} $Å^{-2}$). The following abbreviation is used: Int.: infrared intensity.

		TTF^0			TTF^+			
Label	Symmetry	ν_{calc}	ν_{scaled}	Int.	ν_{calc}	ν_{scaled}	Int.	$\Delta\nu$
ν_1	a_g	3226.47	3120	-	3236.63	3129.82	-	9.83
ν_2		1621.92	1568.39	-	1551.15	1499.96	-	-68.43
ν_3		1.576	1524.41	-	1427.75	1380.63	-	-143.78
ν_4		1.125	1088	-	1130	1092.71	-	4.72
ν_5		722.50	736.73	-	737.72	752.25	-	15.52
ν_6		466.1	475.28	-	501.95	511.84	-	36.56
ν_7		248.6	253.5	-	262.21	267.38	-	13.88
ν_{11}	b_{1g}	849	865.71	-	875.55	892.8	-	27.1
ν_{12}		419.08	427.34	-	435.66	444.24	-	16.91
ν_{19}	b_{2g}	632.63	645.09	-	688.56	702.13	-	57.03
ν_{20}		498.9	508.73	-	513.54	523.65	-	14.92
ν_{21}		93.78	95.63	-	154.6	157.6	-	61.96
ν_{28}	b_{3g}	3206	3100.2	-	3220.42	3114.15	-	14
ν_{29}		1289.96	1247.4	-	1298.58	1255.72	-	8.34
ν_{30}		967.9	986.97	-	1021.58	987.87	-	0.9
ν_{31}		796.98	812.68	-	824.12	840.36	-	27.68
ν_{32}		612.32	624.38	-	627.6	639.96		15.56
ν_{33}		305.94	311.97	-	301.15	307.08	-	-4.88
ν_8	a_u	848.96	865.68	-	873.54	890.74	-	25.06
ν_9		415.72	423.91	-	424.94	433.31	-	9.40
ν_{10}		92.4	94.22	-	65.36	66.64	-	-27.57
ν_{13}	b_{1u}	3226.5	3120.03	0.5	3236.64	3129.83	28.57	9.8
ν_{14}		1598.57	1545.82	23.07	1532	1481.43	111.48	-64.38
ν_{15}		1124.65	1087.54	3.15	1130.92	1094	0.12	6.06
ν_{16}		764.21	779.27	26.39	812	828	36.55	48.72
ν_{17}		720.14	734.33	9.13	726.8	741.15	7.63	6.82
ν_{18}		434.26	442.82	20.44	468.17	477.4	14.72	34.58
ν_{22}	b_{2u}	3206.9	3101.04	4.1	3220.6	3114.31	30.46	13.27
ν_{23}		1287.6	1245.11	0.02	1294.56	1251.84	8	6.73
ν_{24}		823.4	839.62	7.7	868.33	885.44	7	45.82
ν_{25}		786.91	802.41	56	823.81	840.04	26.51	37.63
ν_{26}		621.37	633.61	2.76	636.68	649.27	1.19	15.61
ν_{27}		114.31	116.56	0.58	123.45	125.88	0.28	9.32
ν_{34}	b_{3u}	633	645.46	160.31	690.13	703.73	164.7	58.27
ν_{35}		243.12	247.91	1.64	332.33	338.87	3.93	90.97
ν_{36}		51.44	52.45	3.69	101.27	103.27	4.85	50.81

B

OPTICAL SPECTRA OF TTF-CA, $(TMTTF)_2SBF_6$, α-$(BEDT\text{-}TTF)_2I_3$, δ-$(EDT\text{-}TTFCONME_2)_2ASF_6$, AND VO_2

B.1 TTF-CA

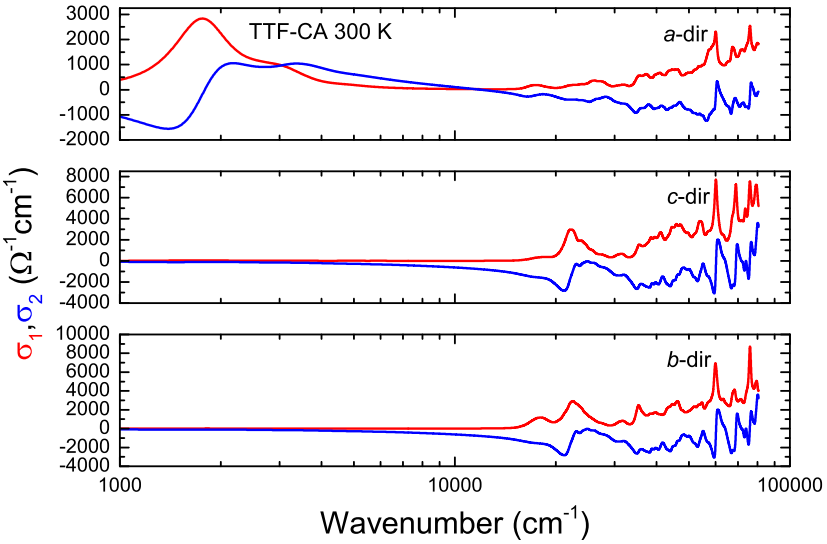

Figure B.1: Optical conductivity σ_1 and σ_2 of TTF-CA calculated after the method described in Sec. 4.5 for all three crystallographic axis. For the calculation the structural data [249] of TTF-CA at 300 K were used.

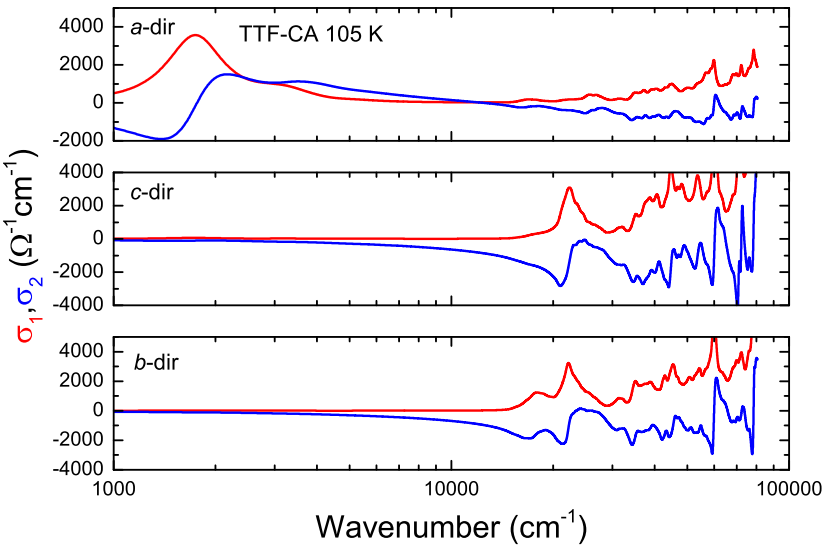

Figure B.2: Optical conductivity σ_1 and σ_2 of TTF-CA calculated after the method described in Sec. 4.5 for all three crystallographic axis. For the calculation the structural data [287] of TTF-CA at 105 K were used.

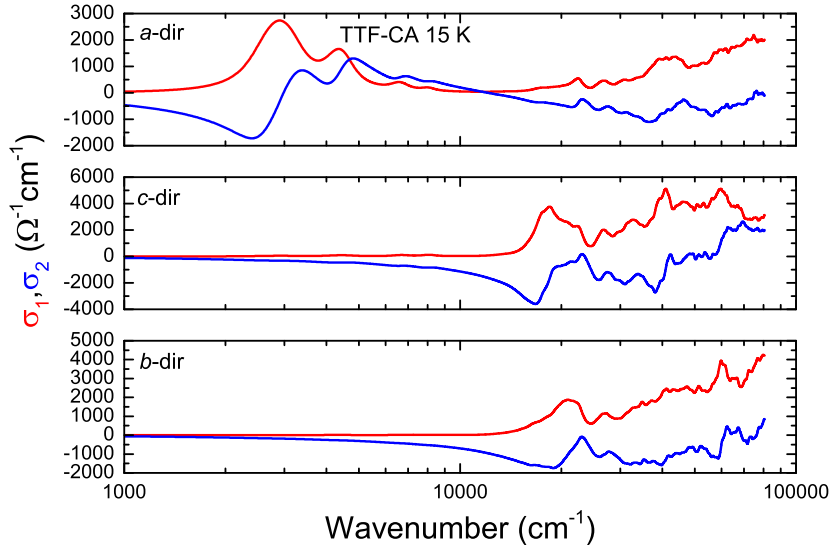

Figure B.3: Optical conductivity σ_1 and σ_2 of TTF-CA calculated after the method described in Sec. 4.5 for all three crystallographic axis. For the calculation the structural data [287] of TTF-CA at 15 K were used.

B.2 (TMTTF)$_2$SbF$_6$

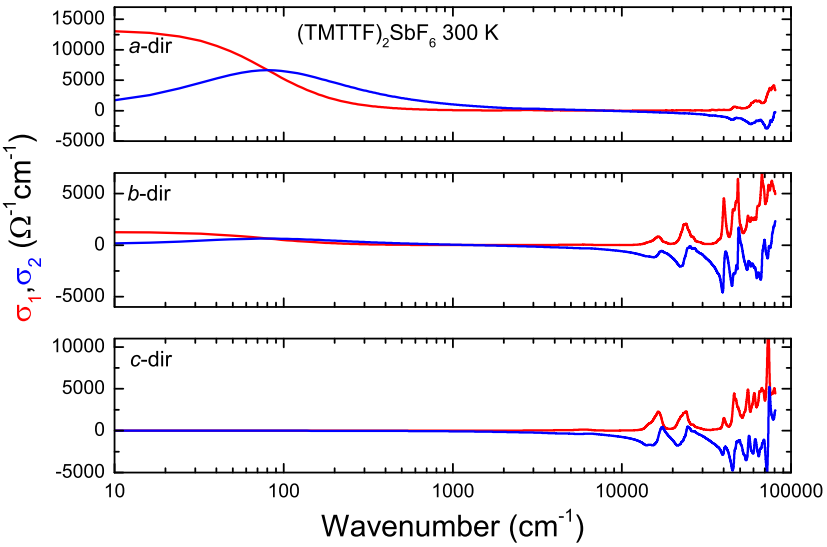

Figure B.4: Optical conductivity σ_1 and σ_2 of (TMTTF)$_2$SbF$_6$ at 300 K calculated with the method presented in Sec. 4.5. The structural data were kindly provided by [174].

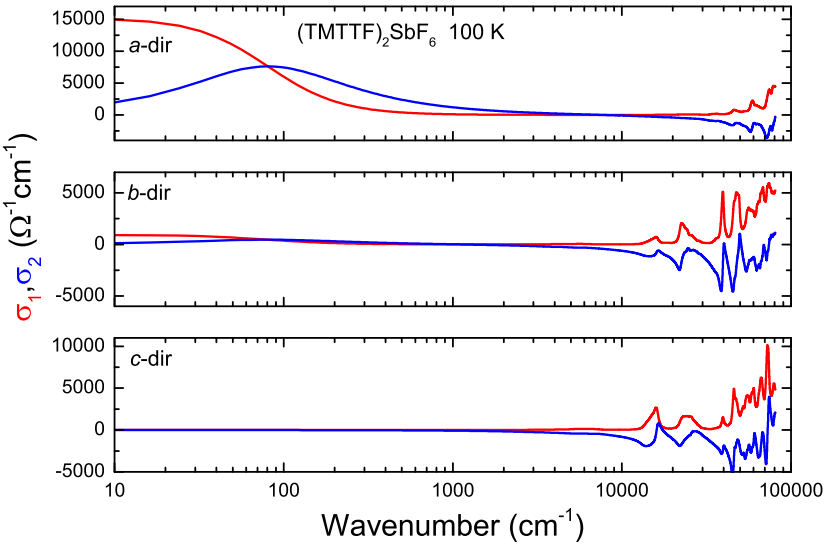

Figure B.5: Optical conductivity σ_1 and σ_2 of (TMTTF)$_2$SbF$_6$ at 100 K calculated with the method presented in Sec. 4.5. The structural data at 100 K were provided by [174].

B.3 α-$(BEDT\text{-}TTF)_2I_3$

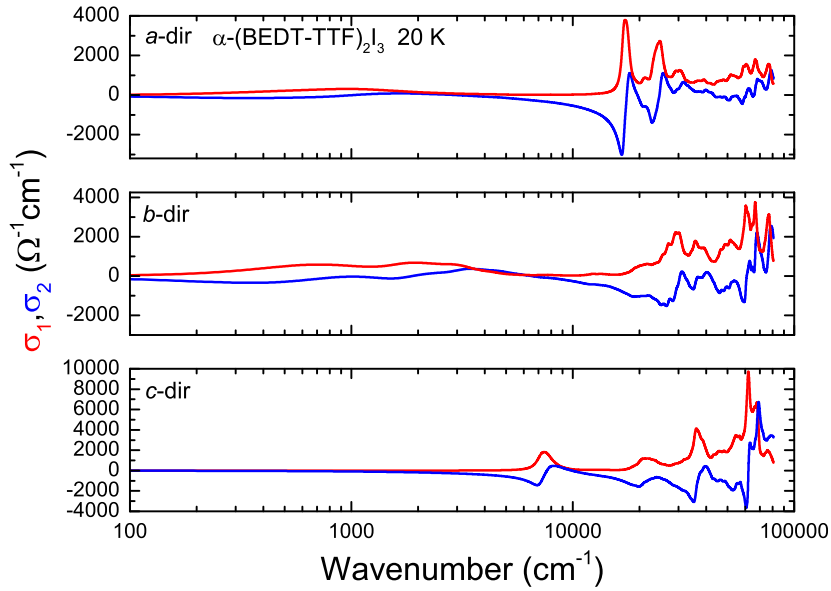

Figure B.6: Optical conductivity σ_1 and σ_2 of α-$(BEDT\text{-}TTF)_2I_3$ calculated after the method described in Sec. 4.5 for all three crystallographic axis. For the calculation the structural data [56] of α-$(BEDT\text{-}TTF)_2I_3$ at 20 K were used.

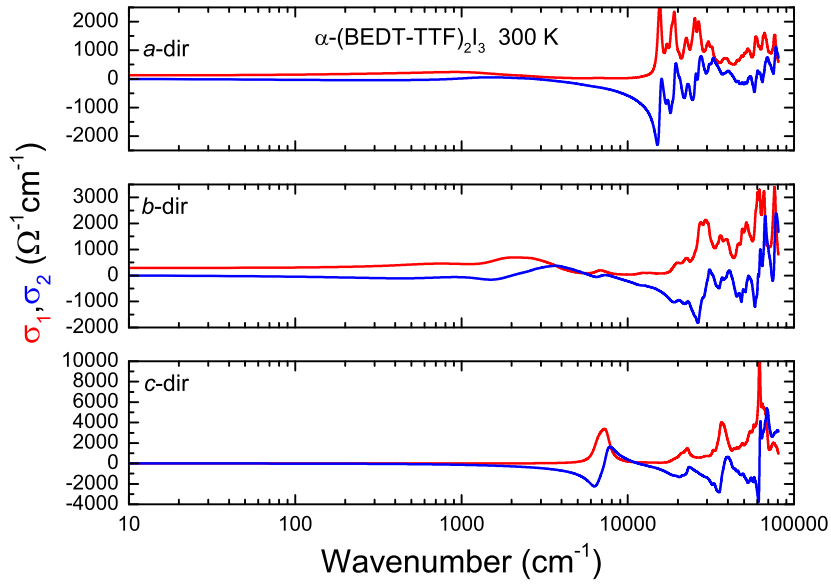

Figure B.7: Optical conductivity σ_1 and σ_2 of α-$(BEDT\text{-}TTF)_2I_3$ calculated after the method described in Sec. 4.5 for all three crystallographic axis. For the calculation the structural data [352] of α-$(BEDT\text{-}TTF)_2I_3$ at 300 K were used.

B.4 δ-(EDT-TTFCONME2)2ASF6

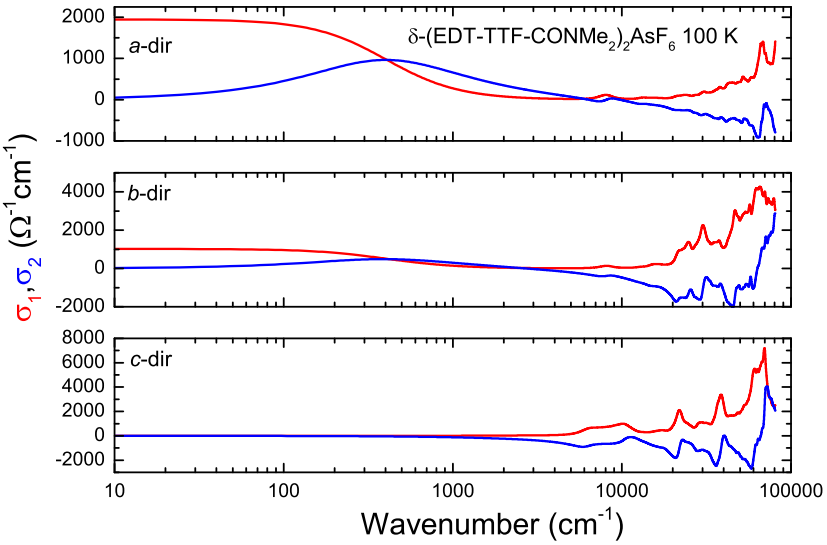

Figure B.8: Optical conductivity σ_1 and σ_2 of EDT_2AsF_6 calculated after the method described in Sec. 4.5 for all three crystallographic axis. For the calculation the structural data [237] of EDT_2AsF_6 at 150 K were used.

B.5 VO_2

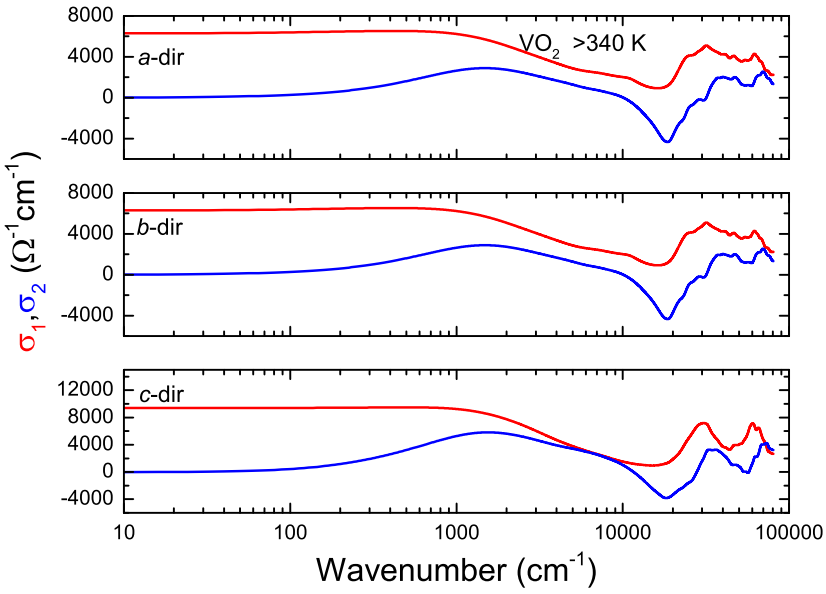

Figure B.9: Optical conductivity σ_1 and σ_2 of VO_2 calculated after the method described in Sec. 4.5 for all three crystallographic axis. For the calculation the structural data [366] of VO_2 at 360 K were used.

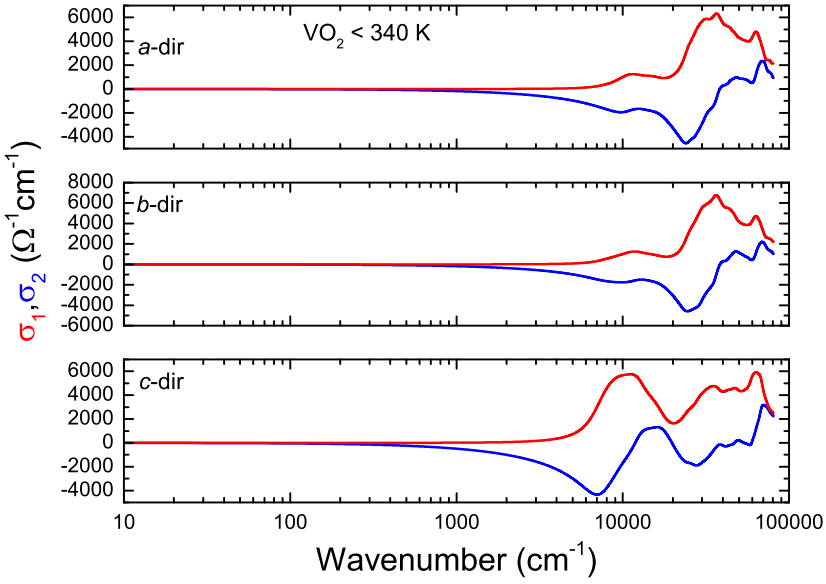

Figure B.10: Optical conductivity σ_1 and σ_2 of VO_2 calculated after the method described in Sec. 4.5 for all three crystallographic axis. For the calculation the structural data [367] of VO_2 at 300 K were used.

C

ELECTRIC-INDUCED SWITCHING OF LIQUID CRYSTALS

C.1 MAIN GOALS OF THE PROJECT

Liquid crystals short LCs are mainly used in the display industry due to the possibility to manipulate their orientation by applying an electric field and their birefringent property. They basically consist of complex organic molecules whose vibrational modes can be used on the one hand as an identification characteristic and on the other hand to determine the molecular orientation of molecules. The conducted experiments should meet several purposes: gaining information about the orientation of the molecules, the switching and relaxation behavior of the LCs, and to get familiar with the capabilities and the handling of the Step-Scan technique. Therefore, a liquid crystal cell filled with the LC Felix 017/100 has been developed and constructed in cooperation with the Institute of Physical Chemistry and the Institute for Large Area Microelectronics. One of the main feature of the LCs cell is its transparency in the infrared spectral range. The used materials were first optically characterized and tested. Ensuring polarization-dependent, static and time-resolved transmission measurement were performed to study the electric-induced switching behavior.

C.2 LIQUID CRYSTALS

As aforementioned, LCs can be primarily found in electronic displays. The polarization state of the transmitted light through the LCs can be controlled by changing the orientation of the molecules. The LCs can be aligned by applying an electric field which couples to the electric dipole moment of the organic molecules whereby the force constrains the molecule in a new direction. Therefore, the LC-cell, consisting of two transparent windows and the LC in between, is placed between two crossed polarizers. If no voltage is applied, LCs form a helical structure between the two cell windows thus the incoming, polarized light is rotated so that it can pass the analyzer. As soon as a voltage is applied, the LCs (dipole moment) reorient due to the electric field, accordingly no light will be transmitted. The brightness can be tuned by the amplitude of the applied voltage. LCs usually consist of organic molecules which belong to the thermotropic or the lyotropic class[1]. Thermotropic LCs have the properties of a liquid at high temperatures, but on cooling they undergo different phases which are called mesophases. They can exist between the liquid high temperature and the crystalline low temperature phase.

$$\text{Crystalline phase} \underset{T_{\text{crystal}}}{\rightleftharpoons} \text{Liquid crystal phases/mesophases} \tag{C.1}$$

$$\underset{T_{\text{melt}}}{\rightleftharpoons} \text{Melt or isotropic phase} \tag{C.2}$$

1 The phase of the thermotropic LCs depends on the temperature whereas the state of the lyotropic LCs can be controlled by the amount of solvent in the mixture.

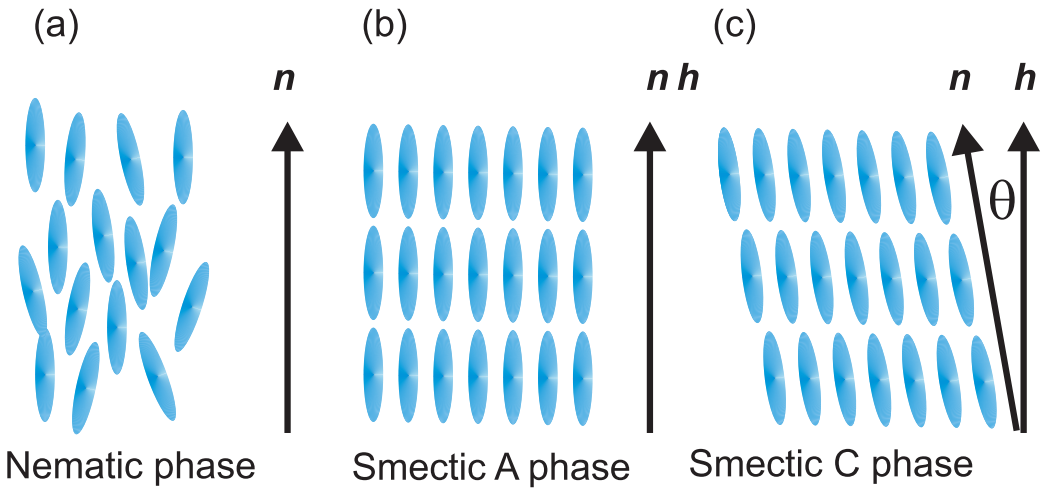

Figure C.1: (a) Nematic phase of LCs. (b) Smectic A phase in which the director $\vec{n}$ is parallel to the layer normal vector $\vec{h}$. (c) Smectic C phase: the director and the normal vector enclose the angle Θ.

In the mesophases the LCs can take different orientational and/or positional long-range order which can be divided in two large subclasses depicted in Fig. C.1.

- Nematic phase: the molecules are oriented along a certain vector, the so called director $\vec{n}$, and form mostly small domains. The center of mass of the molecules is randomly spatial spread and shows only a short-range order (see Fig. C.1 (a)). This type of LC is employed in liquid crystal displays LCD because of their helix structure.

- Smectic phase: in principle it is an extension of the nematic phase as position long-range order additionally appears leading to the creation of molecule layers along one direction. One differs between two types: the smectic A phase (Fig. C.1 (b)) in which the layer normal vector $\vec{h}$ is parallel oriented to $\vec{n}$, and the smectic C phase (Fig. C.1 (c)), where $\vec{h}$ is tilted against $\vec{n}$ by a certain angle Θ. The smectic C phase typically appears at lower temperatures than the A phase.

The molecules consist of a rigid body and flexible end groups. They are responsible for the transitions from the liquid melt to the crystalline state and determine also the transition temperatures. Most of the LCs reveal in the ordered state an anisotropic refraction index and are birefringent. Furthermore, the molecules can have end groups which are opposite charged leading to a permanent electric dipole moment making the whole system ferroelectric. By applying an electric field the director $\vec{n}$ is reoriented a certain period of time τ_{or}. If the field is switched off, the molecules relax slowly back into their initial position with a relaxation time τ_{reor}. Free LCs create small randomly oriented volumes. By a special treatment of the surface of the substrate all the molecules are forced to oriented along the same director $\vec{n}$. The surface must be rubbed uniaxial to achieve such kind of effect whereby the molecules are oriented along the rubbing direction as soon as they come in contact with the surface.

Different experimental methods are used for the characterization of LCs. The most established techniques are the polarisation microscopy and the X-ray diffraction method providing information about the director $\vec{n}$, the structure and the

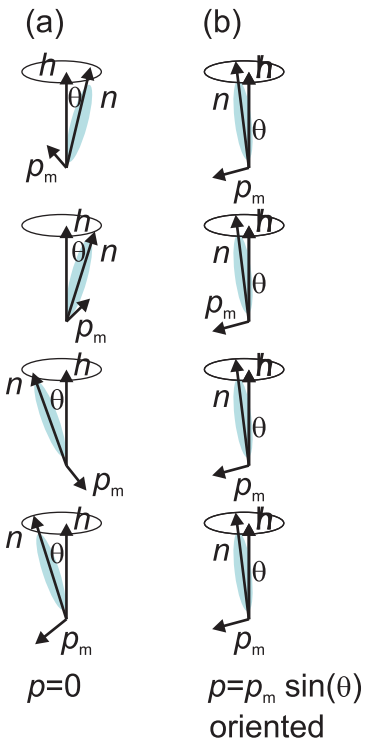

Figure C.2: (a) Chiral smectic phase (SmC*): the director $\vec{n}$ successively precedes around the stacking normal vector $\vec{h}$ in a helix manner. The angle Θ is the same for all layers. The spontaneous polarization $\vec{p}_m$ is perpendicular to the director and the normal vector. The total polarization $\vec{p}_{total}$ is zero. (b) Oriented smectic C phase: all directors $\vec{n}$ are directed towards the same direction. That is why the polarization $\vec{p}_m = p_m \cdot (\vec{h} \times \vec{n}) = p_m \sin\Theta$ can adopt two possible values.

orientation of the LCs. By the classic polarization microscopy which uses visible light, polarized infrared spectroscopy can deliver important hints about the alignment of certain molecular fragments in an electric field. The intramolecular vibrational modes of the organic molecules must have an electric transition dipole moment μ_e to become infrared-active. The transition is most effectively excited if the dipole moment μ_e is aligned parallel to the electric field vector $\vec{E}_{IR}$ of the irradiated infrared light. In these molecules several vibrational modes exist which can be assigned to different parts of the molecules. By static and time-resolved polarization-dependent measurements one gains on the one hand information about the orientation of the individual molecular building blocks in static positions and on the other hand about the temporal evolution of the electric switching process and, hence one can make statements about the rotation of the different molecular constituents with the electric field. For that reason an infrared polarization spectrometer was built to exactly study this effect.

C.3 EXPERIMENTAL SETUP

C.3.1 *Liquid crystal cell*

The FELIX 017/100 mixture from the Clariant company in Germany was used as the ferroelectric LC. It was provided by Florian Schörg from the Institute of Prof. Dr. Giesselmann (Institut of Physical Chemistry, University Stuttgart). The physical parameters of FELIX 017/100 can be found in Tab. C.1. The FELIX mixture undergoes several phases upon cooling starting with the isotropic melt above 85°C, below it crosses over to the nematic phase that ends at 77°C. It is followed by the smectic A phase (SmA*) which exists in a small temperature range of 5°C. Below 73°C the chiral smectic C phase (SmC*) extends to -28°C, below FELIX starts to freeze out and captures a crystalline structure. The chiral SmC* phase differs from the aforementioned SmC phase where the director $\vec{n}$ is

Table C.1: Parameter of the liquid crystal mixture FELIX 017/100 [115, 369].

Temperature	η (Pa·s)	Θ (°)	$\vec{p}_m$ ($\frac{nC}{cm^2}$)	K (N)
35	0.08	14	47	$5 \cdot 10^{-12}$

twisted along the stacking direction $\vec{h}$ with a fixed angle Θ and the LCs create a helix structure which is displayed in Fig. C.2 (a). The spontaneous electric polarization $\vec{p}_m = p_m \cdot (\vec{h} \times \vec{n}) = p_m \sin\Theta$ is thereby perpendicular to the director vector $\vec{n}$ and the layer normal vector $\vec{h}$ with the absolute value p_m. However, the helix structure leads to the case that the individual electric dipole moments of the overlapping layers sum up to zero and, hence the total polarization is zero. By the uniaxial rubbed surface, the LCs are aligned parallel to each other which is depicted in Fig. C.2 (b). The whole procedure is well-known under the term SSFLC and was originally developed by Clark and Lagerwall [368]. Two energetically equal configurations exist after the alignment whereas the total polarization p_m is arranged into opposite directions. But in both cases the polarization is perpendicular to the surface with the same tilting angle $\pm\Theta$. An applied electric field can now induce the transition in one of the two polarization states by changing the orientation of the molecule.

First of all, the liquid crystal cell (see Fig. C.3 (a) and (b)) was constructed and manufactured which is not transparent in the visible, but in the infrared spectral range. The standard window material like glass or plastic could not be used. Normally, KBr is used as a window material in the infrared range, but it is strongly hygroscopic, becomes very fast unclear and in contact with air intransparent. In contrast calcium florid CaF_2 is heavily solvable and stable at air. Therefore, it is the ideal choice. CaF_2 is transparent in a frequency range from 1000 cm^{-1} to 50000 cm^{-1} [370] which almost corresponds to the transmissions region of KBr which ranges from 400 cm^{-1} to 40000 cm^{-1} [370]. Most of the

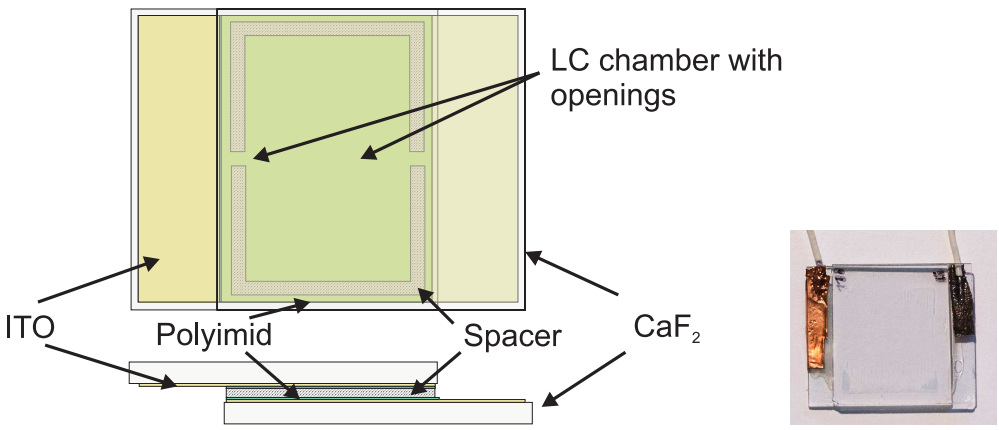

Figure C.3: Left: Side- and top view of the used liquid crystal cell which mainly consists of two CaF_2 plates (light gray, transparent). A thin film of ITO was sputtered onto the plates (bright brown). Polyimid (green) was deposited by the spin-coating process on top of the ITO layer and serves as an orientation layer for the LCs. UV-glue in connection with small plastic spheres (shaded area) with a diameter of $d = 5\,\mu m$ keeps the two windows at a fixed distance together. Right: Picture of the used liquid crystal cell. On the left and right side one can see the copper contact pads. The sample compartment of the LC can be recognized by the help of the contours.

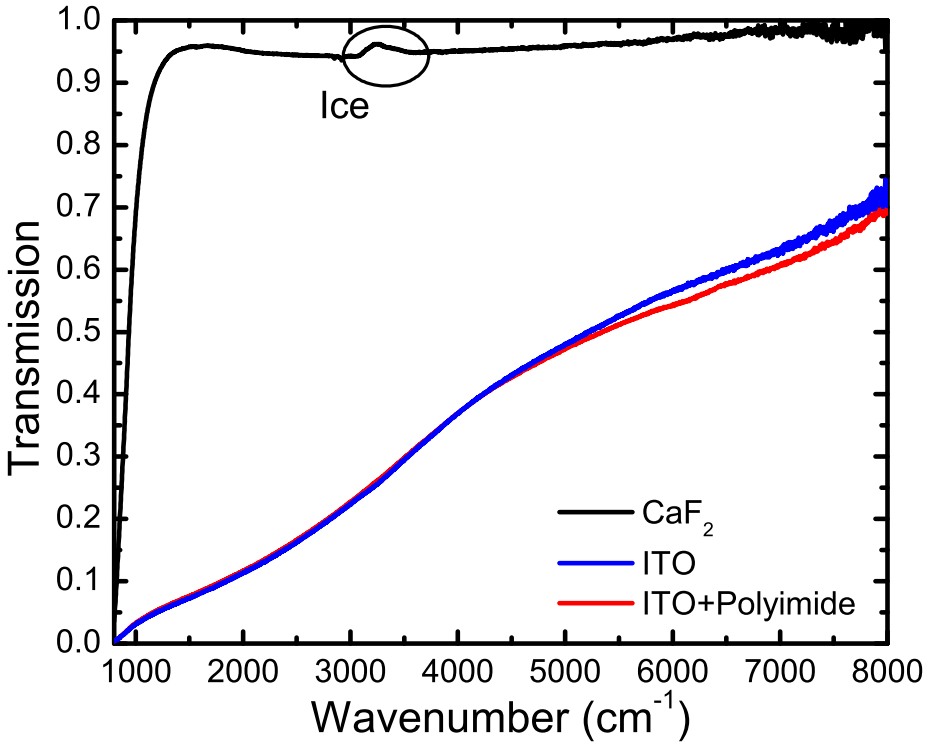

Figure C.4: Transmission spectrum of CaF_2(black) at room temperature in a frequency range from 800 $cm^{-1}$to 8000 cm^{-1} in comparison to CaF_2 coated with ITO (blue) and CaF_2 in combination with ITO and polyimid (red). In the frequency regime above 5000 $cm^{-1}$the red and the blue curve only differ slightly from each other. The feature which is marked by a circle originates from condensed water and ice on the window of the MCT detector.

interesting vibrational modes, for example the C=C double bonds, appear above 1000 cm^{-1}. Therefore, the robust CaF_2 was the first choice also because of the hygroscopic property of KBr. For the cell, plates with a dimension of 20×20 cm^2 and a thickness of $d = 0.1$ mm were polished optically to get the optimal surface quality for the optical experiments. They were supplied by the company Korth Kristall GmbH. First, transmission measurements on single CaF_2 plates with a thickness of $d = 0.1$ cm, illustrated in Fig. C.4, were conducted. A spectral range from 800 $cm^{-1}$to 8000 $cm^{-1}$was examined, thereby one notices that CaF_2 let pass more than 90 % of the infrared light in that frequency region. Note, that it was also tried to use the semiconducting material Germanium (Ge) as a window material. However, the high refraction index n = 4 of Ge leads (KBr: 1.5 and CaF_2: 1.4) to a strong back reflection signal and to a low transmission of less than 50 %. Therefore, Ge discards as a window material. Both CaF_2 windows have been sputtered with a thin film of ITO in the clean room of the Institute of Large Area Microelectronic under the supervision of Eberhard Kurz. ITO is mainly used in the industry as an electrode material for displays because it unifies two very important properties: it is lucent over a broad energy range as well as it is conductive. However, optical measurements in Ref. [371] reveal that the transmission rapidly decreases below 5000 $cm^{-1}$from 60 % to 10 % and below 2000 cm^{-1}ITO is almost nontransparent. The measurements with ITO on CaF_2, shown in Fig. C.4, reveal a similar behavior: the transmission drops continuously and almost linear with decreasing wavenumber. In the interesting range of the C=C double bond vibrations the transmission is between 5 % and 20 %

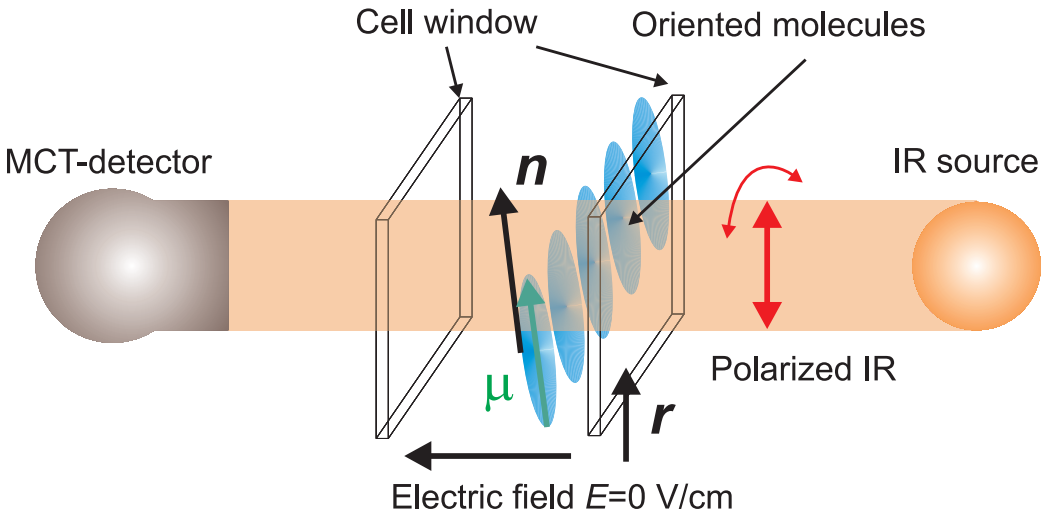

Figure C.5: Schematic diagram depicting the position of the liquid crystal cell in the spectrometer and the principle experimental arrangement. The molecule, illustrated as blue ellipsoids, are oriented along the rubbing direction $\vec{r}$ and point into the direction of the director $\vec{n}$. The red arrow determines the polarization direction of the infrared light $\vec{E}_{\mathrm{IR}}$. $\vec{E}$ is the direction of the applied electric field which is perpendicular to the window surface. μ_e describes the transition dipole moment of the molecular vibration which does not have to correlate with the direction of $\vec{n}$.

which is enough to successfully perform the experiment as the expected changes are large.

For the preorientation of the LCs a very thin film of polyimide was deposited on top of the ITO layer by using the spin-coating technique which was rubbed afterwards unidirectional. As soon as the LC molecules were placed on the surface, they align themselves along the rubbing direction [372]. The possibility of the system to transmit light in the relevant frequency range was not limited by the polyimide[115]. It is somehow surprising that no significant features of polyimide, which also consists of organic molecules, do not appear in the spectrum which is represented in Fig. C.4. The reason for that is the very low concentration of polyimide. Earlier measurements [111, 115, 373] with an analog cell configuration could not as well prove traces of polyimide in the infrared spectrum.

In the following the cell structure was constructed with a CAD program which is depicted in Fig. C.3 (a). Both plates have been clued together with a UV glue which was mixed with small macroscopic plastic spheres with a diameter of $d = 5\,\mu\mathrm{m}$. The spheres serve as a spacer to keep the windows on a constant distance. A picture as well as a schematic drawing of the cell can be seen in Fig. C.3 (a) and (b). After the glue was cured, the cell was heated up above 80°C so that the LC-mixture transformed in the isotropic phase with a reduced viscosity. The LC was sucked in the chamber due to the capillary action . The capillary force was created because of the small distance between the cell windows and the two openings (see Fig. C.3 (a)). Afterwards, the temperature of the melt was slowly lowered so that a single domain was formed. The distance of the two plates was not constant and reduces to the center of the cell causing the creation of Newton's rings. This happens because of the large dimension of the sample chamber. The interference rings occur because of the constructive and nonconstructive interference of the reflected or transmitted light on the inner

boundary surface of the cell. Finally, the contact wires were made out of copper and fixed on the exposed ITO side areas with indium.

C.3.2 *(Time-resolved) polarization-dependent spectroscopy*

To study the switching process, the liquid crystal cell was mounted on a standard Bruker sample holder. The transmission measurements have been performed under vacuum in the sample chamber of the Bruker Vertex 66v/s FTIR spectrometer. By pumping the spectrometer the distance of the plates was altered because the residual enclosed air between the CaF_2 cell expands. This leads to a temporal variation of the transmitted infrared signal during the pumping process, but the infrared signal stabilizes after a few minutes. The electric connections have been connected to a Philips-PM 5768B pulse generator to switch the LCs. The generator sends during the measurement simultaneously to the switching voltage pulse a second TTL signal to the spectrometer to start the data acquiring process. In front of the cell a polarizer was placed to polarize the incident infrared light which is illustrated in Fig. C.5.

The incident light hits the cell and is absorbed by the oriented molecule. The extenuated light is recorded by the MCT detector. The absorption becomes maximal if the $\vec{E}_{IR}$ vector of the infrared light is aligned parallel to the electronic transition dipole moment μ_e of the molecular vibrational mode. As soon as the external electric field $\vec{E}$ is switched on, a force acts the LC. In general, the switching process takes a few microseconds τ_{or} until most of the molecules are reoriented. The new orientation of the molecules and its director $\vec{n}$ lead to change of the direction of the transition dipole moment μ_e leading to an increase or decrease of the absorption signal.

C.4 INTERACTION OF LIQUID CRYSTALS WITH AN ELECTRIC FIELD

If the electric field is switched on, the directors from Fig. C.2 (b) spin collectively in one direction and therefore, the azimuthal angle Φ changes. The switching velocity and -time can be derived from the equation of motion [374, 375, 376]:

$$\eta\dot{\chi}(t,z) = -I\ddot{\chi}(t,z) + K\nabla^2\chi(t,z) - pE\sin\chi(t,z) \tag{C.3}$$

η is the damping of the motion caused by the viscosity of the liquid, χ the angle between the electric field and the polarization of the LC, I the moment of inertia of the density, and K[2] the Frank-elasticity constant whereas we only consider $\chi(t,z)$ with z as a coordinate which is along the direction perpendicular to cell windows. Typical material-specific values are for the damping $\gamma = \frac{\eta}{I} = 10^{15}\,\frac{1}{s}$, with a viscosity $\eta = 0.1\,\text{Pa s}$ and $I = 1\cdot10^{-16}\,\frac{kg}{m}$, which is very large so that the total system is strongly overdamped. Therefore, the term $-I\ddot{\chi}(t,z)$ can be neglected, so the Eq. C.3 reduces to:

$$\eta\dot{\chi} = K\nabla^2\chi - pE\sin\chi. \tag{C.4}$$

For small angles χ we derive the following solution

$$\chi = \chi_0\, e^{\frac{t}{\tau}}\cdot\sin\frac{\pi z}{d} \tag{C.5}$$

2 K is on the order of $5\cdot10^{-12}$ N.

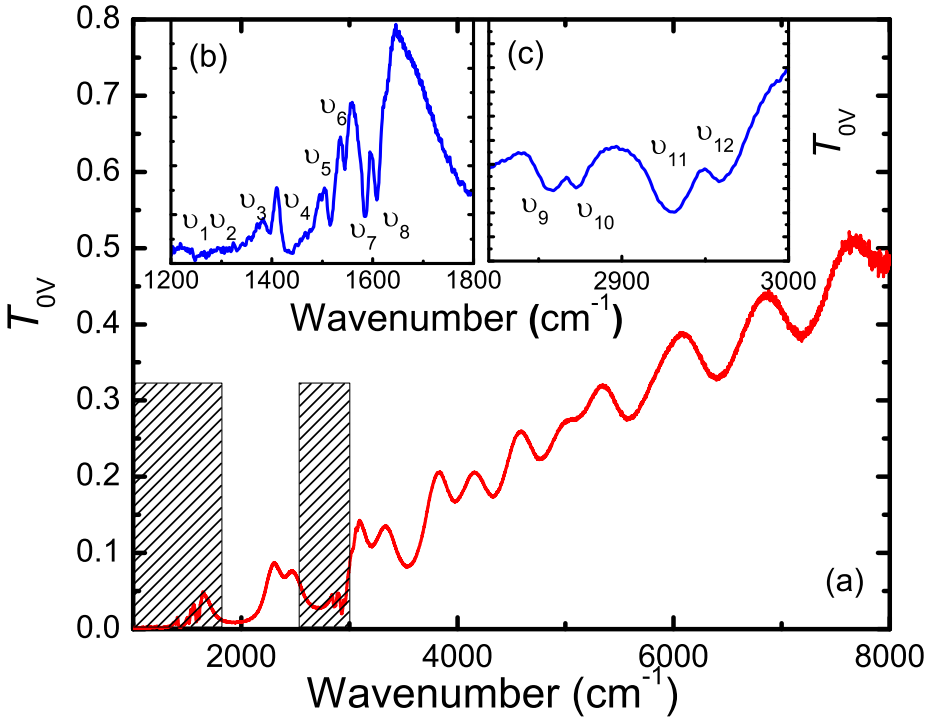

Figure C.6: (a) Transmission spectrum of FELIX at room temperature in a frequency range from 800 cm^{-1} to 8000 cm^{-1}. The oscillations originate from interference effects caused by multi-reflections within the liquid crystal cell. (b) Detail view of the frequency region from 1200 cm^{-1} to 1800 cm^{-1} which shows mainly resonance features of the vibrations of the molecular body. (c) The inset shows the feature of the methyl vibrations which are located at 2850 cm^{-1} and 2950 cm^{-1}.

with d as the spacing between the two cell windows. Thus, we obtain two time constants, the rise or switching time

$$\tau_{or} = \frac{\eta}{pE - K\frac{\pi^2}{d^2}} \tag{C.6}$$

and, respectively, after switching of the $\vec{E}$ field, the fall time

$$\tau_{reor} = \frac{\eta d^2}{K\pi^2} \tag{C.7}$$

defining the time until the molecules are relaxed back in their initial position.

The switching time is $\tau_{or} = 170\,\mu s$ for the here examined material resulting from the specific parameters [115]($\eta = 8 \cdot 10^{-6}\,Ns\,cm^{-2}$, $p_m = 47\,nC\,cm^{-2}$, the electric field strength $E = 10\,KVcm^{-1}$, whereas the last term in the denominator can be neglected). With the elastic constant $K = 5 \cdot 10^{-12}\,N$ and a cell thickness of $d = 5\,\mu m$ the relaxation time is $\tau_{reor} = 40\,ms$.

C.5 RESULTS

Infrared measurements

Fig. C.6 (a) shows the transmission spectrum of the liquid crystal cell filled with FELIX in a frequency range from 800 cm^{-1} to 8000 cm^{-1}. The most noticable feature are wiggles dominating the whole spectrum. They emerge from the

Table C.2: Comparison of the observed resonance frequencies of the FELIX LC mixture with the measured values of Huang and Shih [115] in cm^{-1}.

Labeling	resonance frequency (this measurement)	resonance frequency [115]
ν_1	1243	1252
ν_2	1269	1281
ν_3	1395	1393
ν_4	1439	1439
ν_5	1516	1514
ν_6	1546	-
ν_7	1584	1584
ν_8	1606	1608
ν_9	2858	2853
ν_{10}	2874	-
ν_{11}	2931	2926
ν_{12}	2956	2956

multiple reflection and interference of the infrared light after passing through the cell. As the distance between the plates is about $d = 5$ µm, light with the wavelength λ satisfying the condition $\lambda = 2 \cdot n \cdot d$ interferes constructively. The dips in the spectrum between 1000 cm^{-1} and 1700 cm^{-1} (Fig. C.6 (b)) as well as between 2800 cm^{-1} and 3000 cm^{-1} (Fig. C.6 (c)) can be assigned to the vibrational modes of the LC. As FELIX is a mixture of different molecules and its exact composition is not known, no precise and unique assignment can be performed. However, from the position of the resonance frequency conclusions can be drawn about the involved molecular bonds and their location in the molecule. The features $\nu_9 - \nu_{12}$ located between 2800 cm^{-1} and 3000 cm^{-1} can be assigned to the stretching of the CH_2- and CH_3 end group. The modes from 1606 cm^{-1} to 1516 cm^{-1} labeled with $\nu_4 - \nu_8$ are connected with the vibrations of the C=C double bonds belonging to the center part of the molecules. The features at 1439 cm^{-1} and 1395 cm^{-1} can be referred to the wiggling and torsion of the CH_3 group. The low-lying resonances at 1269 cm^{-1} and 1243 cm^{-1} belongs to an asymmetric stretch oscillation of the C-O-C bond. The position of the detected features perfectly coincides with the resonance frequencies determined by Huang and Shih [115].

Polarization-dependent infrared measurements

Fig. C.7 (a) shows a change of the infrared intensity $\Delta S = S_{5V} - S_{0V}$ between 5 V and 0 V in a frequency region from 1000 cm^{-1} to 1800 cm^{-1} and 2800 cm^{-1} to 3000 cm^{-1}. All measurements were performed at 25°C. By applying the electric field, a strong modification of the intensity could be observed in the whole spectral range due to the rearrangement of the LC molecules. From the fact that the intensities decrease or increase one can deduce that two different-oriented transition dipole moments exist. The first of them belongs to the vibrational mode of the rigid body of the molecule and the other one points out from the molecule axis related to the end groups. The angle dependence of the change in the in-

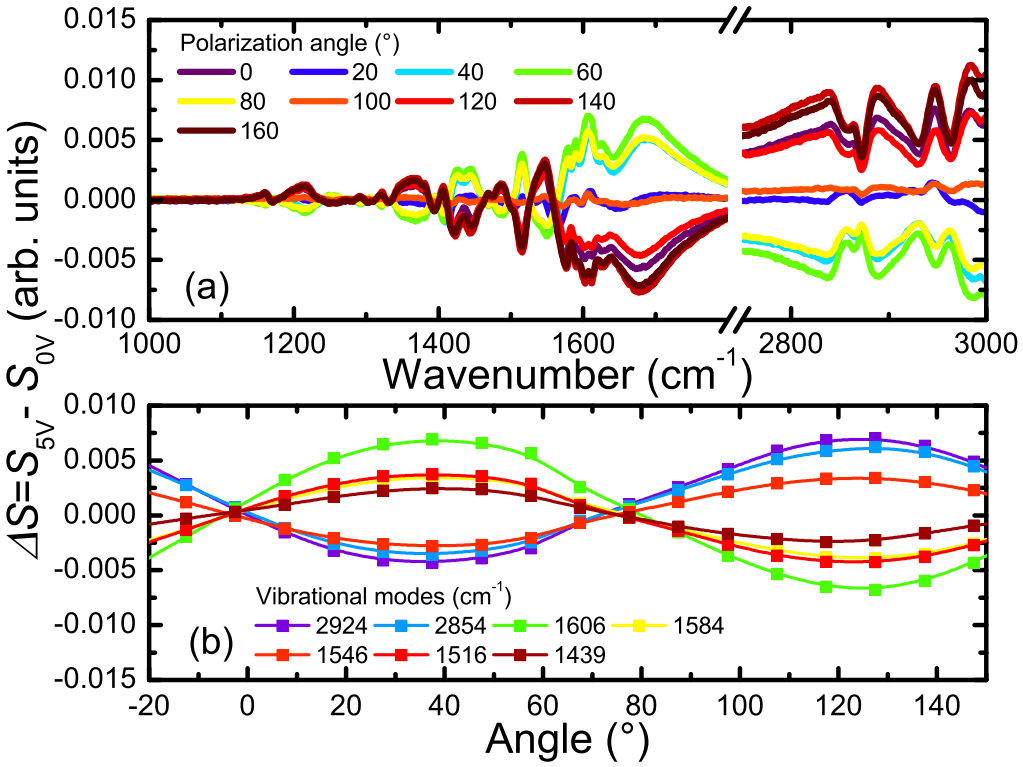

Figure C.7: (a) Spectra of the alternation of the detected light intensity $\Delta S = S_{5\,V} - S_{0\,V}$ for different polarization states of the incident light in range from 1000 cm^{-1} to 1800cm^{-1} as well as from 2800 cm^{-1} to 3000 cm^{-1}. From the modification of the spectra it can be concluded that the LC reacts on the external applied electric field. (b) Polarization-dependent measurement of the change of the transmitted intensity after creating 5 V on the two windows for seven different vibrational modes. The maximal change of the transmission appears at 40°, for instance, followed by a minimum at 120°. The characteristic of the intensity variation obeys a sinusoidal function.

frared intensity from the polarization state of the infrared light is depicted in Fig. C.7 (b) for the strongest and most important modes. All modes reveal a strong dependence of the polarization angle. The modes containing the CH_2 and CH_3 bonds exhibit a minimum at 40° and at a distance of 90° a maximum at 130°. The minimum of the modes belonging to the molecule body are slightly shifted and can be found at 120°. For instance, the green curve in Fig. C.7 (b) should be examine more closely. It belongs to a vibrational mode with an aligned dipole moment parallel to the central molecular frame. At 40° it reaches a maximum for a voltage of 5 V, this means that the dipole moment rotates away from the electric field vector of the infrared light. Hence, the transmitted intensity increases at this specific wavelength. In contrast, the intensity of the dipole moments related to the end groups of the molecule is reduced because the transition dipole moments are aligned parallel to $\vec{E}_{\mathrm{IR}}$.

Time-dependent electric-induced switching of liquid crystals

The switching process of the LC cell was studied at a temperature of 25°C under vacuum at a polarization angle of 45°. Different voltages between 4 V and 6 V were created between the two plates. The time-dependent infrared signal was

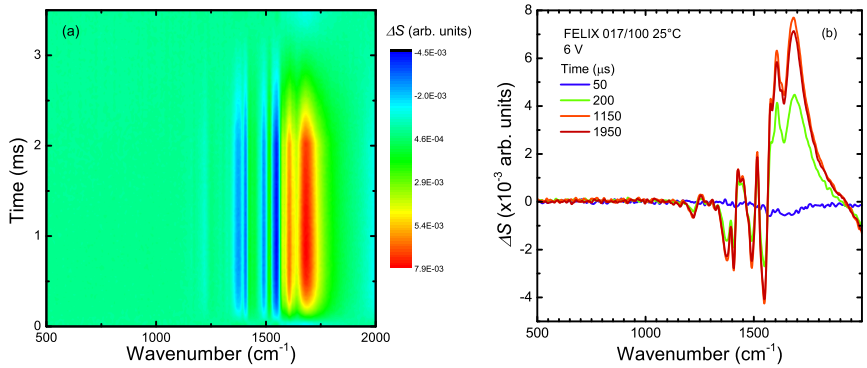

Figure C.8: (a) Contour plot of switching process of the LC cell for an electric field pulse of the strength $E = 12\,\mathrm{kVcm^{-1}}$ with a pulse width of 2 ms in a frequency range from 500 $\mathrm{cm^{-1}}$ to 2000 $\mathrm{cm^{-1}}$. In a region from 1200 $\mathrm{cm^{-1}}$ to 1800 $\mathrm{cm^{-1}}$ several features can be recognized, they correspond to an increase or decrease of the signal which depends on the orientation of their transition dipole moment. (b) Spectra at four different points in time after applying the voltage pulse. The spectrum (blue), recorded 50 µs before the pulse is applied, exhibits almost no change and is flat. Several features appear at time 200 µs which can be ascribed to various vibrational modes (see text). The signal saturates after 1150 µs and shows no further variation of the intensity.

detected with the Step-Scan technique which is described in detail in Sec. 4.1.3. For the phase correction the phase from a standard FTIR measurement was used.

The contour plot of $\Delta S(\nu, t)$ is presented in Fig. C.8 for 6 V from 500 $\mathrm{cm^{-1}}$ to 2000 $\mathrm{cm^{-1}}$. The rectangular voltage pulse had a width of 2 ms with a repetition rate of 30 Hz and the signal was recorded for a period of 4 ms. To improve the SNR, the signal was averaged over five spectra. The time resolution was set to 25 µs and the spectral resolution was 2 $\mathrm{cm^{-1}}$.

The extreme values of $\Delta S(\nu, t)$ are displayed in blue or in red in the contour plot. The transition dipole moments μ_e which are aligned parallel to $\vec{E}_{IR}$ lead to a reduced and, hence to a negative signal whereas in contrast for a positive μ_e is turned away from $\vec{E}_{IR}$. This becomes more obvious in Fig. C.8 where spectra at different times are plotted. 50 µs before the pulse is created, no variation of the vibrational modes and no shift can be observed. However, after applying the voltage pulse, the spectrum dramatically alters and exactly reveals the same feature as in Fig. C.7 (a) which marks the final state. Also the absolute values of the change are the same. Below 1000 $\mathrm{cm^{-1}}$ no changes appear which is similar to the observation in Fig. C.6 (a) and C.7 (a). The reason for that is the ITO layer which absorbs a large fraction of the incident light. The switching process is completed after about 1 ms and the signal stays constant over a period of 800 µs.

To determine the rise and fall time, the temporal evolution of $\Delta S(\nu, t)$ of five vibrational modes were used. The change of the intensity of the ν_8 mode is plotted as a function of time in Fig. C.9 for three different voltages. While the voltage pulse features a rectangular shape with a rise time of less than 10 ns, the infrared signal reacts slowly and requires several hundreds of microsecond until it saturates. The molecules react with a delay on turning-on of the electric field due to the temperature-dependent viscosity of the LCs. The switching time τ_{or} diminishes with rising voltage whereas the amplitude increases slightly. However, the signal overshoots at the beginning for 6 V and relapses back to the value of the 5 V pulse. The rise time can be determined by fitting the experimental data

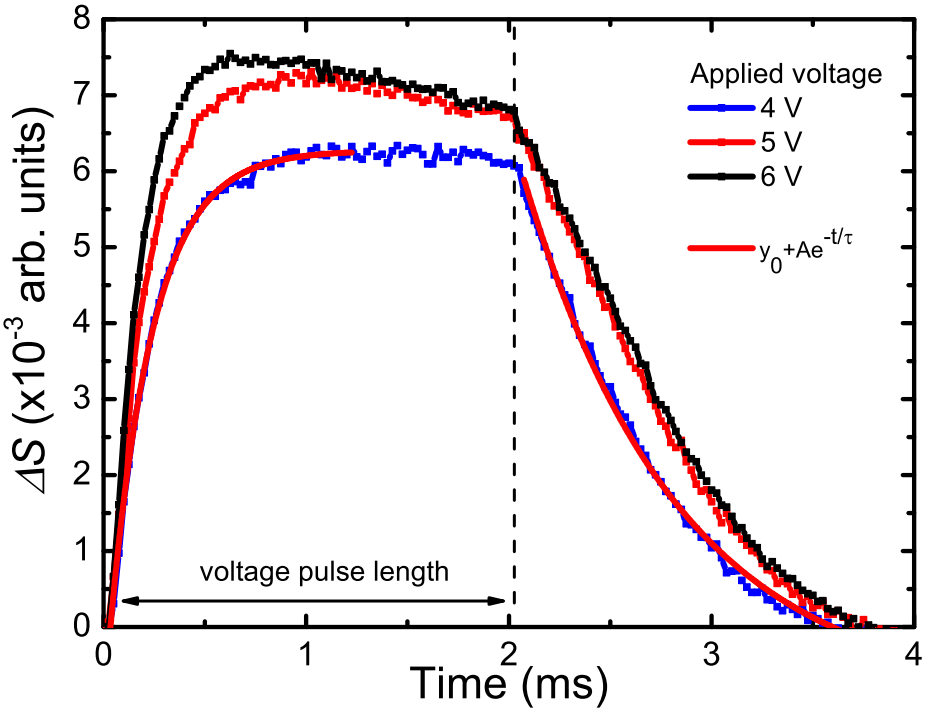

Figure C.9: The variation of the intensity $\Delta S(\nu, t)$ is displayed for the resonance frequency 1606 cm^{-1} for three different voltages. The rise of the signal as well as the drop can be fitted well by a single exponential function $y_0 + A\exp(-t\tau^{-1})$. The signal increases with increasing voltage. At the same time the switching speed increases. In contrast to that the relaxation process retards with rising voltage.

with a single exponential function $y_0 + A \cdot \exp(-t/\tau)$. The assigned values of τ_{or} are shown in Fig. C.10 as a function of the applied voltage. At the end of the pulse the signal relaxes slowly back to its initial values within 2 ms and is at least by a factor of four larger than the rise time τ_{or}. τ_{reor} can be ascertained as well from the temporal evolution of the recovery process by a single exponential function.

At a voltage of 4 V almost all vibrational modes reveal a switching time τ_{or} between 210 µs and 230 µs; with increasing voltage this range enlarges to maximum 70 µs for 6 V whereas the values are between 190 µs and 120 µs. The various time constants mean that constituents of the molecules react differently on the electric field. From the graph one can derive that the vibrational modes related to the molecule body (ν_8-mode) rotate slower than the ones (ν_4-mode) which are connected to the end groups. The theoretically calculated value for τ_{or}= 170 µs derived from Eq. C.6 agrees very well with the determined τ_{or} which is of about 200 µs. The reason for the small discrepancy can be that the real distance of the spacer plates slightly differs from the assumed thickness of 5 µm or that the used material specific parameters η and $\vec{p}_m$ for the calculation of τ_{or} exhibit an error. These parameters strongly depend on temperature. Furthermore, a $1/E$ characteristic of the rise time cannot be observed as the total number of studied voltages as well as the range are too small. Therefore, it seems that the time constant decreases linearly. Probably, τ_{or} exhibits the expected field dependence and the divergent behavior for smaller voltages.

As it was expected from the theoretical calculations of τ_{reor} in Sec. C.4 the relaxation times in Fig. C.10 (b) are larger than the switching time. A time con-

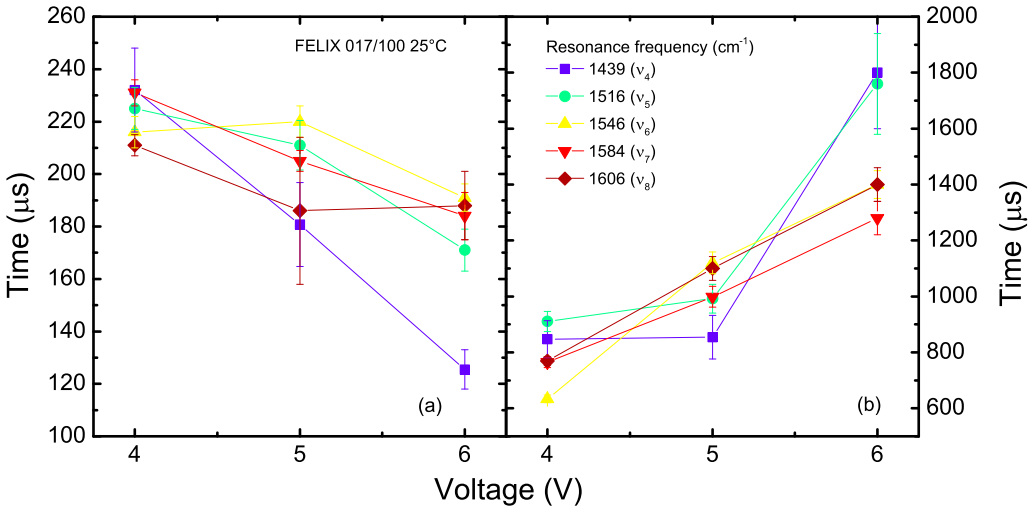

Figure C.10: (a) Rise time τ_{or} for five different resonance frequencies. With increasing voltage the switching time decreases continuously. (b) Whereas the relaxation time τ_{reor} deceases but no direct dependence on the voltage can be discovered. For 6 V τ_{reor} reveals a larger variance.

stant of 40 ms was predicted what is by a factor of 70 larger than the measured values. Furthermore, the relaxation rate is a function of the applied voltage but according to Eq. C.7 it should be independent of any external parameter. One possible explanation therefor is the stronger tilting of the molecules with increasing voltage as well as the total amount of realigned molecules increases as well. Thereby, the layer of oriented molecules increases which leads to a kind of self-stabilization effect resulting in the extended decay. For this reason, the relaxation rate τ_{reor} is not a function of the intrinsic elastic constant K, but also of the external electric field.

C.6 SUMMARY

With the help of the Institute of Physical Chemistry and the Institute of Large Area Microelectronic at the University of Stuttgart it was possible to manufacture a liquid crystal cell consisting of CaF_2 windows which can be switched by applying a voltage to the sputtered ITO layer on the windows. The whole cell is transparent for infrared light. The first optical characterization has revealed that the transmitted intensity starting from 90 % at 8000 cm^{-1} for pure CaF_2 drops down to 70 % after the deposition of ITO and even down to 5 % at 1000 cm^{-1} for CaF_2 with ITO and polyimide. The LC cell with a thickness of $d = 5\,\mu m$ exhibited a very good transmission performance although disturbing artifacts in the form of interference fringes appeared. As a testing material the ferroelectric LC mixture FELIX 017/100 was chosen which exhibits several mesophases which can be controlled by setting the temperature. Several vibrational modes of the LC molecules were observed in the transmissions spectra. The modes can be assigned to the different corresponding molecule fragments by their resonance frequency occurring between 1000 cm^{-1} and 3000 cm^{-1}. Polarization-dependent measurements of the transmission variation for 5 V reveal that the LC molecules rotate and reorient under the influence of an external electric field leading to an angle-dependent variation of the transmitted light intensity. Thereby, it was

discovered that the various parts of the molecule obey the same behavior under the influence of an electric field. The whole molecule reacts like a stiff body. The switching behavior of the LC was studied by creating short voltage pulse on the two windows. There, two different time constants τ_{or} and τ_{reor} could be verified. The first one is the so-called switching or rise time τ_{or} which is in the range of 200 µs and seems to decrease with increasing electric field linearly. A comparison of the theoretical switching time with the experimental one reveals a very good agreement. In contrast, the second time constant or the relaxation time which is between 600 µs and 1.8 ms, differs notably from the theoretical value of 40 ms. One of the major reasons are the used temperature-dependent parameters for the calculation for which no exact values are available. Additionally, the relaxation time shows an unexpected dependence on the applied voltage. In total the reaction time of the LC is about $\tau_{rea.} = \tau_{or.} + \tau_{rel.} \approx 1 - 2\,\text{ms}$ what is in accordance with literature values.

For future projects dealing with liquid crystal cells several improvements can be made:

- the cell construction can be improved by decreasing the cell volume. The advantage is that the distance of the two windows over the whole sample compartment is constant.
- the distance can be scaled down suppressing constructive interference effects of the incident light and, hence the interference pattern in the infrared spectrum
- the electrode material ITO can be deposit thinner or totally replaced by another material, for instance aluminum tin oxide (AZO)

A further widespread study of different types of LCs and their switching behavior would deliver many important information about relevant physical quantities, for instance about the spontaneous polarization $\vec{p}_m$, the rotational viscosity η or the elastic constant K. The measurements were performed at a temperature of 25°C, but it would be more interesting to study the switching as a function of temperature as the LCs undergo several phase transitions. Concerning the Step-Scan technique, with this experiment it was proven that it is possible to perform time-resolved infrared measurements with a time resolution in the microsecond range and with a spectral resolution of 2 cm^{-1}. Also changes of the infrared intensity of about 10^{-3} can be resolved which makes it possible to study time-resolved effects in correlated materials.

D

VO_2: VANADIUM DIOXIDE

D.1 INTRODUCTION

Most of the transition metal oxides exhibit a rich phase diagram with various electronic and magnetic states. The phases can be tuned and controlled by external parameters such as temperature, pressure, doping, chemical as well as isovalent substitution, or a magnetic or electric field. Since several decades this material class has been a very active research area, especially, because of the emerging MIT or IMT transitions. Besides the interest to understand the physical mechanism triggering the phase transition [26] it is of interest to use the MIT transition in technical applications. The goal is to build new electronic devices which are not based on silicon. This IMT or MIT transition can be triggered by short electric or optical pulses, opening the opportunity to build fast FETs, volatile memory devices, oscillators, sensors or optical switches. In this sense VO_2 is a special material as the IMT phase transition is located at 340 K. Consequently, it is very close to room temperature and hence, easy to access. Additionally, nowadays high quality thin films and single crystals can be manufactured including different types of doping. Over the last two decades several experiments have shown that VO_2 can be used to build new electronic devices [377]. Hence, VO_2 is close to being employed in several applications. Thus, VO_2 is a very interesting material due to its physical properties and to manipulate these by external parameters.

Therefore, two different kinds of films were studied which only differ in the chosen substrate (SiO_2/Si and Al_2O_3). First of all, the surface quality was checked by an AFM microscope, the transition temperature and thermal hysteresis were determined by transport measurements and the optical properties of the films were characterized. In addition, DFT calculations of the band structure and the optical spectra were performed and compared with the experimental results and the literature values. To study the non-equilibrium properties of the VO_2 films induced by short electric pulses, gold contacts were evaporated on top of the film. For these samples the switching behavior between the insulating and metallic state as well as the appearing current oscillations were studied by time-resolved transport measurements. In the framework of this thesis the first time- and spectral resolved optical measurements of the electric-induced transition are presented in this chapter. This opens the unique opportunity to compare the time-dependent optical data with static reflectivity measurements and with the time-resolved transport observations. Here, the goal was to find out if the high conductivity state is due to an induced metallic state or due to a "hot electron" effect which is well-known from semiconductors. A further question is whether the time constant of the optical experiment correlates with the values from the time-resolved conductivity measurements. This opens new perspectives on the underlying physical process being responsible for the (induced) insulator-metal transition.

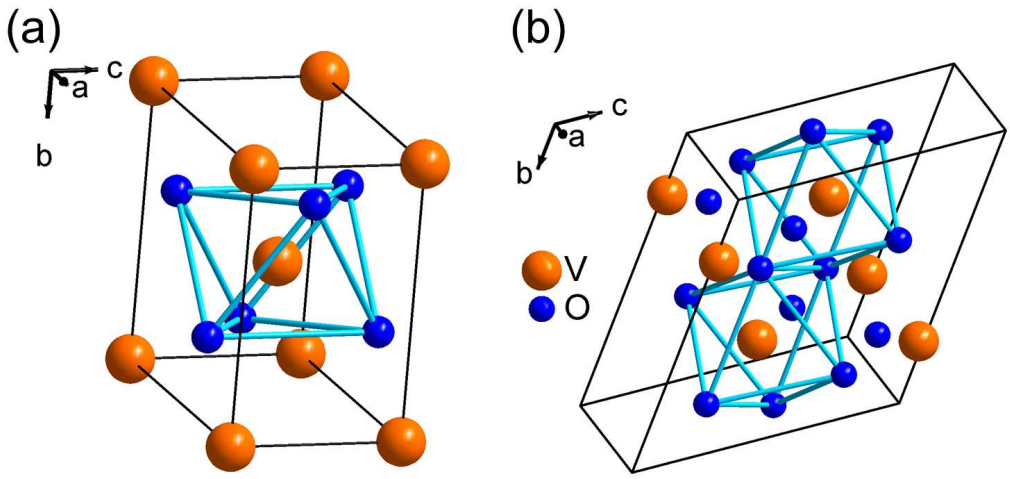

Figure D.1: (a) Crystal structure of VO_2 in the rutile phase with the space group $P4_2/mnm$. The vanadium atoms are surrounded in octahedral manner by six oxygen atoms. (b) In the monoclinic insulating phase Phase VO_2 exhibits a $P2_1/c$ crystal structure. Due to the phase transition the unit cell is doubled.

D.2 PHYSICAL PROPERTIES OF VO_2

Different compositions of vanadium oxides V_xO_y [378] exist and all of them exhibit a thermal induced insulator-Metal transition. One of the most famous oxides is VO_2 which strongly differs from the other vanadium oxides as its ground state is nonmagnetic. The IMT occurs at a transition temperature of 340 K which is accompanied by a modification of the crystal structure going from the monoclinic low temperature phase (M1, $P2_1/c$, C_{2h}^5, No. 14) to the rutile high temperature phase (R, $P4_2/mnm$, D_{4h}^{14}, No. 136). Both crystal structures are presented in Fig. D.1 (a) and (b). In the rutile phase the vanadium atoms are symmetrically surrounded by six oxygen atoms. In the monoclinic structure the octahedral lattice gets distorted and the original position of the vanadium atoms is shifted leading to an antiferroelectric zigzag structure.

The $3d$-state of vanadium is energetically located above the $2p$-level of the oxygen atoms. Because of the crystal field splitting the degeneracy of the d-state is lifted and splitted into the e_g^σ- and t_{2g}-state. Thereby, the energy of the e_g^σ-state is higher than the t_{2g}-state and is unoccupied. The t_{2g}-band is further separated into an a_{1g}-state and the energetically higher lying e_g^π-state. In Fig. D.2 the band structure of the rutile and monoclinic phase is schematically sketched according to the model of Goodenough [379] for VO_2. In the rutile phase the a_{1g}-band crosses the Fermi energy, therefore VO_2 is metallic. Corresponding to Goodenough the phase transition is triggered by the p-d-overlap between the vanadium and the oxygen atoms causing a splitting of the a_{1g} state and the opening of a band gap as depicted in the right illustration of Fig. D.2. The experimentally determined optical band gap between the highest occupied a_{1g} and the lowest unoccupied a_{1g} and e_g^π-band [380, 381, 382, 383, 384] is about 0.6 eV which depends on the sample quality of VO_2. The $2p$-band of the oxygen atoms is located below the a_{1g}-band in an energy range from -1.6 eV to -8 eV in accordance with the DFT calculations performed in this thesis (see Sec. D.4.2) and Ref. [385]. Beside Goodenough's model based on classical molecule orbitals and assuming that VO_2 is a band isolator at room temperature, there are considerations

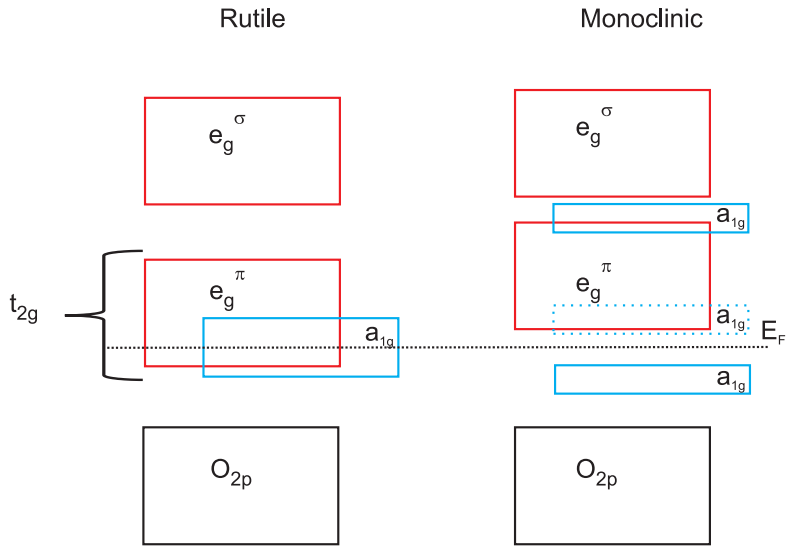

Figure D.2: Schematic band structure of VO_2 of the rutile and monoclinic phase. In the rutile phase the t_{2g}-band intersects the Fermi energy while it splits in the monoclinic phase due to the shift of the vanadium atoms in the octahedral cage and hence, an energy gap opens.

of Zylbersztejn [386] that electron-electron correlations play a crucial role and trigger the phase transition. Compared to these, electron-phonon interactions are negligible [387]. A further counterargument for a Peierls effect is the huge optical band gap of 0.6 eV which is too large being caused by electron-phonon interaction.

Various theoretical calculations ranging from semi-empirical to self-consistent methods verified Goodenough's suggested arrangement of the orbitals which is supported by UPS [383] and XPS [382, 383, 388] studies. However, *ab-initio* calculations [389] on the basis of LDA functional yielded a half metal behavior for the monoclinic phase which disagrees with the experimental observations. This discrepancy between theory and experiment can be attributed to the LDA functional which in general systematically underestimates the band gap. The gap could be reproduced by introducing the on-site Coulomb potential U in combination with LDA. This can be accounted as evidence for electron-electron correlations defining the physical properties. Presented in Sec. D.4.2 the on GGA functional based DFT calculations determine exactly the optical gap in the monoclinic phase and supports the model of a classical band isolator similar to the case of α-(BEDT-TTF)$_2$I$_3$ in Sec. 5.4.1.

Up to now, the origin of the physical properties and phase transition of VO_2 is not clarified and there is still an ongoing discussion in the scientific community whether it is a classic band insulator/semiconductor as silicon, a Mott-insulator in which electron-electron interactions dominate or even a Peierls insulator. Related to that issue, it is still an open question whether the electronic transition is induced by the structural transition or vice versa.

During the last decades many experimental studies were performed on VO_2 and delivered extensive information about the crystal structure, the electronic system and its controllability. For instance, it was shown that the phase transition can be controlled by temperature, but also by pressure [390, 391], doping [392], electric field or optical excitation [65] , in particular the last two methods offer manifold possibilities concerning technical applications. Different optical

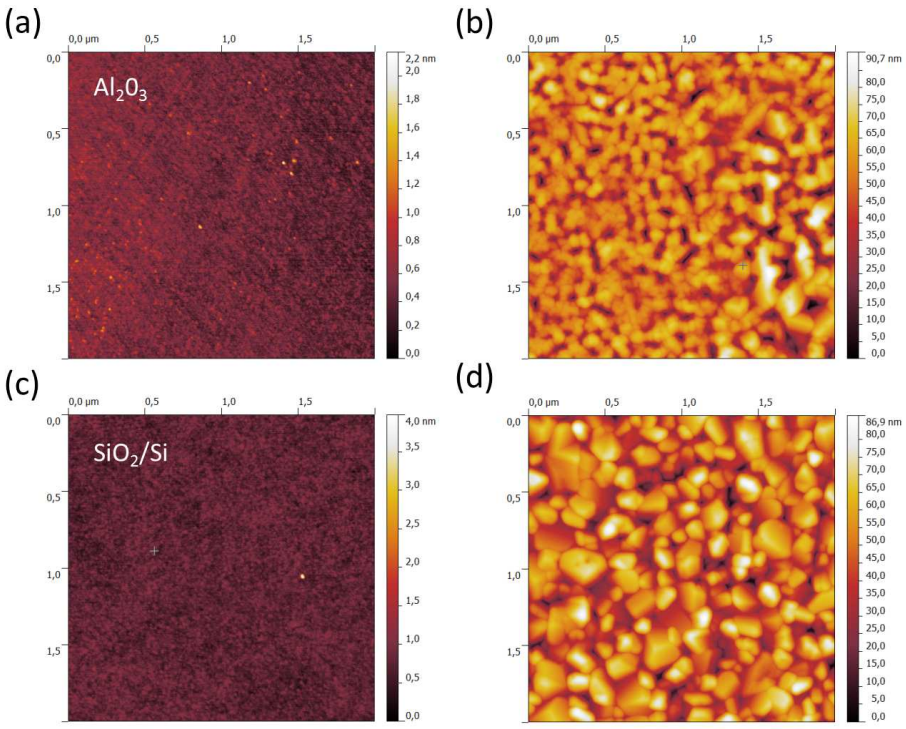

Figure D.3: The pictures, (a) and (c), present the AFM pictures of the substrates while (b) and (d) depict the VO_2-films on the corresponding substrates.(a) AFM $2 \times 2\,\mu m^2$ picture of a clean Al_2O_3 surface. The maximal height of the surface defects is about 1 nm. The white dots are small impurity particles which are distributed randomly on the surface. They have a maximum height of 2 nm. (b) The AFM picture has a dimension $2 \times 2\,\mu m^2$. The Al_2O_3 substrate is covered by VO_2-islands whose average diameter is 89 ± 56 nm. The maximal difference of the particle height is 91 nm. (c) AFM $2 \times 2\,\mu m^2$ picture of a clean SiO_2/Si substrate. The maximal height is 1 nm. (d) The dimension of the AFM picture is $2 \times 2\,\mu m^2$. The average grain size is about 129 ± 67 nm and by a factor of 1.5 larger than the determined island size on sapphire.

studies[1] over an energy range of 4 eV[393] reveal an immense redistribution of the spectral weight which can be voted as a clear sign for the importance of electron-electron interaction. The same observations were already made by XAS and PE experiments and were related to correlation effects near the phase transition. Furthermore, the effective mass m^* [394, 395] of the free charge carriers diverges at the phase transition to a value of $m^*/m_e = 5$ and decreases in the metallic phase to one. The opening and closing of the band gap could also be observed in the present conductivity and optical measurements.

D.3 EXPERIMENTAL SETUP

VO_2-Deposition

For the fabrication of the VO_2 film a number of various techniques exist: the PLD method, CVD, sputtering technique, electron beam evaporation and sol-gel processing. Independent of the used technique the stoichiometry strongly de-

1 An overview of the recent optical measurements is given by Basov et al. [44] revealing that the spectrum is strongly altered at the phase transition which becomes obvious by the redistribution of the spectral weight SW(ν).

Table D.1: Overview of the average grain diameter of VO_2 on sapphire and SiO_2.

	Si_2	Al_2O_3
diameter (nm)	129 ± 67	89 ± 56

pends on the chosen substrate temperature $T_{Sub.}$, the crystal structure of the substrate, the defect concentration, and the multiple valence states of vanadium. The wrong stoichiometry or the false V/O ratio causes different physical properties of the film, for example a variation of the conductivity or a shift of the transition temperature [396, 397, 398]. A good indicator for high quality films is a change of the resistance at the IMT and should be better than three orders of magnitude. For VO_2 the oxygen concentration can only be between 7.8 % and 8.8 % and the substrate temperature must be above 550 °C [377]. Al_2O_3 and silicon with a 150 nm thick layer of silicon oxide were chosen as a substrate material.

The VO_2 films were fabricated at the University of Giessen at the 1. Physical Institute in the semiconductor group. This group has a lot of experience in the syntheses and fabrication of smart glasses or smart materials[2].

Before the sputtering process, the substrates were cleaned for 3 min in an acetone bath and afterwards in a methanol ultra sonic bath for further 3 min. The VO_2 films with a thickness of 200 nm on sapphire (orientation (c-axis)) and SiO_2/Si were created by the sputtering technique. Therefore, a pure vanadium target in a fixed oxygen atmosphere ($p = 2 \cdot 10^{-4}$ mbar $\sim$ 1.4 mTorr) was used. The substrate temperature was set to 650°C for all samples and the deposition process took 140 min. The final film thickness was checked by XRR afterwards.

D.4 RESULTS

D.4.1 *Film quality*

To check the film quality, the surface of the film was studied by a Bruker Dimension AFM microscope. The software program NanoScopeAnalysis of Veeco was applied for the evaluation of the pictures. To exclude any influence of the substrate on the film, the surface quality and the roughness of SiO_2/Si and sapphire were inspected. In Fig. D.3 (a) and (c) a $2 \times 2\,\mu m^2$ detail of the silicon oxide and sapphire surface is depicted. It is obvious that in both cases the surface is very flat and only a few impurities reside on the surface visible as white spots in the AFM picture. The average height variation is about 1 nm. Only single impurities or defects with a maximum height of 2 nm can be recognized. The AFM pictures confirm that the used cleaning method results in clean surfaces which are sufficiently enough to grow high quality films. A large $2 \times 2\,\mu m^2$ screen shot of the on sapphire grown VO_2 film is presented in Fig. D.3 (b). Several small islands and grain-like structures can be noticed on the surface. The height of the islands

2 The concept of smart materials in general means materials whose physical and chemical properties can be manipulated by external parameters such as temperature, pressure, light or electric field. A subtopic of the smart materials are the smart glasses which are applied for instance in technical optic as absorbers, polarizers or in architecture to regulate the incident light or the temperature in buildings.

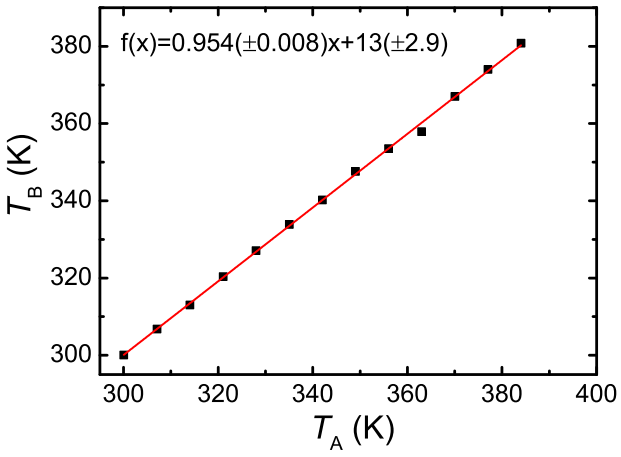

Figure D.4: Comparison of the recorded temperature of sensor T_A, controlling the heating plate, and sensor T_B which is located next to the sample. With increasing temperature the temperature difference between the two sensors increases. The temperature evolution obeys a linear behavior. Hereby, the determined parameters were further used for calibration of the temperature-dependent measurements.

is in average 45 nm with an average diameter of 89 ± 56 nm. Thus, it can be assumed that the VO_2 film is completely closed with a total thickness of about 200 nm. In comparison to sapphire the VO_2 grains on the Si_2/Si substrate are by 30 % larger (depicted in Fig. D.3 (d)) and thereby, the number of islands is about 30% less than on the sapphire substrate. However, the average size is 129 nm and the maximum height is 90 nm, respectively. The film is completely closed as well. But which effect has the grain size on the properties of the film and what can we state about the quality?

Youn et al. [397] could show for VO_2 deposited on SiO_2 that with raising substrate temperature the grain size increases and a transition from an amorphous to a polycrystalline phase sets in. Furthermore, the width of the phase transition decreases with $T_{\text{Sub.}}$, accompanied by a sharpening of the resistance jump of by up to three orders of magnitude and an increase of the transition temperatures towards the value of VO_2 single crystals. Ruzmetov et al. [399, 400] support this observation, but with VO_2 on sapphire. Although, for both substrates the identical growth parameters have been used, VO_2-films reveal different morphologies due to the completely different crystal structure of the substrates. These lead to stress or strain in the crystal lattice of VO_2 and thus, to the formation of small crystals/grains whose sizes are statistically distributed. The width of the distribution defines the width of the transition and the hysteresis curve. This indicates that one can assume that the film of the amorphous SiO_2 should have a higher quality in the kind of a narrower transition and a higher transition temperature than the film on sapphire. Therefore, to gain further information the resistivity and optical characteristic were studied.

Transport measurements

For the temperature-dependent electrical conductivity measurements, the VO_2 films were glued on a brass plate with high temperature grease. The brass plate was equipped with heating wires making it possible to heat the sample up to 400°C. The temperature was measured by a standard PT-1000 temperature ele-

ment which was placed directly next to the sample and fixed with GE. By measuring the resistance of the temperature sensor continuously, a Lakeshore 340 temperature controller varies the voltage on the heating wires correspondingly. A control measurement of the temperature discrepancy between the controlling PT-1000 temperature element T_A and the T_B located next to the sample is presented in Fig. D.4. The slope of the curve is constant. As expected no difference occurs at room temperature, but it increases continuously up to 7.6 K at 390 K. That is why all measurement were scaled on the sample temperature. The electrical conductivity was measured in the two contact-configuration. Therefore, two 500 nm thick gold stripes were evaporated on top of the VO_2 film as an intermediate layer and as contact pads. The golden wires were fixed on the gold contacts with silver paint. The channel width was 30 µm with a total length of 1 mm. A Keithley 2611 source meter was used to apply the current and the voltage drop was recorded by a Keithley 2812A Nanovoltmeter (see Fig. 4.9). In the insulting state a current of 10 nA was created while in the metallic phase it was increased to 1 µA.

Fig. D.5 (a) depicts the specific resistance of VO_2 on Al_2O_3. It decreases slightly from 3.4 Ωcm at 310 K to 1.6 Ωcm at 330 K. The values agree well with the results of Ref. [396] for the same growth conditions, for instance they measured 1 Ωcm at 323 K. Above the transition, the resistance drops by three order of magnitude to $2.6 \cdot 10^{-3}$ Ωcm confirming the expected high quality of the film. Berglund and Guggenheim [401] quantified a resistance between $2 \cdot 10^{-4}$ Ωcm and $5 \cdot 10^{-4}$ Ωcm in the metallic phase whereas Griffiths [396] recorded values of around $1 \cdot 10^{-3}$ Ωcm. The here determined value of $2.6 \cdot 10^{-3}$ Ωcm at 360 K is in well agreement with the literature values. Furthermore, the phase transition is accompanied by a thermal hysteresis with the transition temperature for the cooling cycle being lower than for the heating cycle. The occurrence of a hysteresis is typical for a first order phase transition. While the resistivity ρ in the metallic state is temperature-independent. It obeys an exponential dependence in the insulating phase. This can be easily seen in the Arrhenius plot of fig. D.5 (a): in this graphical representation with $1/T$ the resistivity shows a linear behavior as function of reciprocal temperature meaning an activated behavior of the conductivity which can be described by the following formula:

$$\sigma(T) = \frac{1}{\rho(T)} = \sigma_0 e^{\frac{\Delta E_{\text{Akt}}}{kT}} = q_{\text{en}} N_c \mu_n e^{\frac{\Delta E_{\text{Akt}}}{kT}} \tag{D.1}$$

with the charge q_{en}, the major charge carrier concentration N_c, charge carrier mobility μ_n, activation energy $\Delta E_{\text{Akt.}}$, Boltzmann constant k, and temperature T. From the constant slope in Fig. D.5 the activation energy $\Delta E_{\text{Akt}} = (0.256 \pm 0.004)$ eV can be determined which coincides with the literature value [401] and is by a factor of 2.5 smaller than the optical band gap. By fitting the derivative of the logarithm of ρ with a Gaussian function the transition temperature $T_{\text{Heat.}} = 336$ K and $T_{\text{Cool.}} = 342$ K can be derived from the position of the maximum. The width of the hysteresis $\Delta H = 6$ K is within the range of the literature values [399] which ranges from 4.5 K to 10 K. The transition temperature is in the upper limit of Ref. [396] and is a sign for the high quality of the film.

Already, the first Hall measurements [401, 402, 403] revealed that electrons are the major charge carriers in the metallic state as well as in the insulating phase. The charge carrier concentration [401, 404] is in the insulating phase about $N_c = n_e = 1 \cdot 10^{19}$ cm^{-3} and increases above the IMT by four orders of magnitude

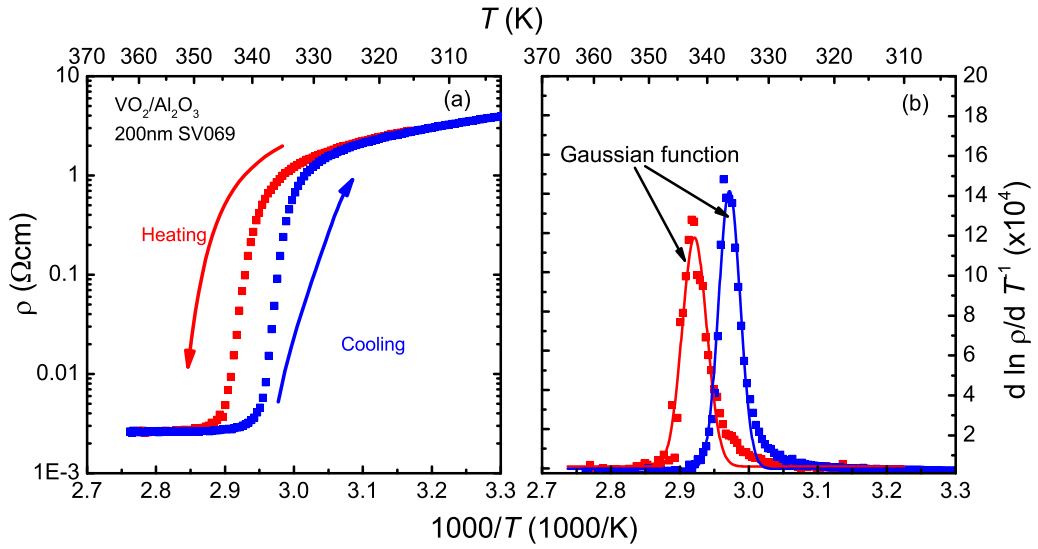

Figure D.5: (a) Temperature-dependent resistivity curve of VO_2 grown on sapphire in a $\frac{1}{T}$-plot in a temperature range from 313 K to 365 K. A clear hysteresis can be observed between the heating and cooling run. The resistivity drops/raises more than 3 orders of magnitude under heating or cooling, respectively. The resistivity in the metallic state is almost constant whereas in the semiconductor state the resistivity exponentially increases on cooling following an activated behavior. (b) Temperature-dependent plot of the derivative of log ρ versus $\frac{1}{T}$. The maximum of the derivative marks the transition temperature of the heating and cooling cycle. The transition temperature T_{MI} for heating is 342 K whereas for the cooling the maximum is at $T_{IM} = 336$ K. The change of the resistivity in the metallic state is small. In the semi-conducting state the derivative is constant which implies an activated behavior with $\rho \propto \exp\frac{\Delta E}{kT}$ for $T < T_{IM}$.

to $n_e = 1 \cdot 10^{23}\,\mathrm{cm}^{-3}$. The charge carrier mobility μ_n is independent of the temperature and only slightly diminishes from $\mu_n = 0.1\,\mathrm{cm}^2/\mathrm{Vs}$ to $0.07\,\mathrm{cm}^2/\mathrm{Vs}$.

For our film, from the logarithmic plot of the conductivity versus $1/T$ and the linear fit function $\ln(y) = a \cdot x + \ln(y_0)$, the number of charge carriers can be estimated from the intersection with the y-axis and the relation $\ln(y_0) = q\mu_n N_c$. For a mobility of $\mu_n = 0.1\,\mathrm{cm}^2/\mathrm{Vs}$ and $q_{\mathrm{en}} = 1.609 \cdot 10^{-19}\,\mathrm{C}$ one derives $N_c = 4.96 \cdot 10^{23}\,\mathrm{cm}^{-3}$, which is in good agreement with Hall measurements in the metallic phase. Furthermore, from the Hall experiments it can be argued that the conductivity σ is mainly dictated by the temperature-dependent charge carrier concentration. The carrier concentration is larger than the density of the vanadium anions ($3 \cdot 10^{22}\,\mathrm{cm}^3$) which can only be explained that in addition to electrons also holes contribute to the electric transport. The effective mass m^*/m_e, derived from transport measurements [401], is between 1 and 7 and hence, higher than the mass of free electrons. Optical studies of Qazilbash [394] yielded a temperature-dependent effective mass, which drops down to one in the metallic phase, and diverges at the transition to 5. This clearly indicates the increase of electron-electron interactions at the vicinity of the phase transition.

D.4.2 *Theoretical calculations of VO_2*

For the theoretical calculations performed in the framework of this thesis the cell parameter and atomic position of the monoclinic (M1) and the rutile phase (R) were taken from Ref. [367] and [366], respectively. The values are listed in Tab.

Table D.2: Table of the cell parameter of VO_2 for the monoclinic (M1) [367] and rutile (R) [366] phase.

Parameter	M1	R
a (Å)	4.5378	4.5546
b (Å)	5.7517	4.5546
c (Å)	5.3825	2.8514
α (°)	122.6460	90
β (°)	0	90
γ (°)	0	90
V (Å^3)	118.29	59.15
space group	$P2_1/c$ (14)	P 4_2/mnm (136)

D.2. In the rutile phase the oxygen atoms are located on a 4f Wyckoff position WP: $\pm(u,u,0), \pm(0.5+u, 0.5-u, 0.5)$ with $u = 0.3001$ Å. The vanadium atoms occupy a 2a Wyckoff position: (0,0,0), (0.5,0.5,0.5), thereby the unit cell contains two vanadium and four oxygen atoms. In contrast, in the monoclinic phase the vanadium atom and the two different oxygen atoms reside on a 4e WP position: $(\pm(x,y,z), \pm(x, 0.5-y, 0.5+z)$ corresponding to a doubling of the volume of the rutile unit cell.

The software package Quantum Espresso [122] based on DFT theory was applied to determine the band structure, the density of states, and the optical conductivity. For all atoms a norm-conserving GGA Perdew-Burke-Ernzerhof PBE [130, 131] functional was used as previous calculations [385] with the local density approximation LDA yield a metallic state for the monoclinic phase. It is expected that a calculation with a GGA functional yields an energy gap. For the insulating as well as for the metallic state the cut-off energy of the wave function and the electronic density was set to 40 Ry and 200 Ry, respectively. The Gaussian smearing factor of the density of states near the Fermi energy was 0.0005 Ry for the metallic band structure. For the k-space sampling in the reciprocal space an equally spaced Monkhorst grid was created with the size $16k \times 16k \times 16k$ for the metallic phase and $14k$x$14k$x $14k$ for the insulation state . For LTP the following k-path was chosen: $\Gamma \to Y \to C \to Z \to \Gamma \to B \to D \to Z \to \Gamma \to A \to E \to \Gamma$ and respectively for the HTP: $\Gamma \to X \to R \to Z \to D \to \Gamma \to R \to A \to \Gamma \to M \to A \to Z$. To calculate the optical spectra the subroutine introduced in Sec. 4.5 was used. Therefore, the optical quantities were determined for 504 equally distributed points in the Brillouin zone.

The resulting band structure in the rutile phase is depicted in Fig. D.6. Several groups of bands can be observed in an energy range from -2 eV to 8 eV. At the Γ point below the highest occupied bands appears at -1.7 eV which can be assigned in Goodenough's model to the O_{2p} band (blue shaded area in Fig. D.6). It extends roughly from -1.7 eV to -8.0 eV. This is in excellent agreement with findings of UPS [383] and PE [384] studies in which the O_{2p}-band was determined at 2 eV below the Fermi energy and spans to -8 eV. The first three bands in the range from -0.6 eV to 2.2 eV can be ascribed to the a_{1g}- and the e_g^π-band (green shaded area in Fig. D.6). Above them, the e_g^σ-band starts and extends to 6 eV

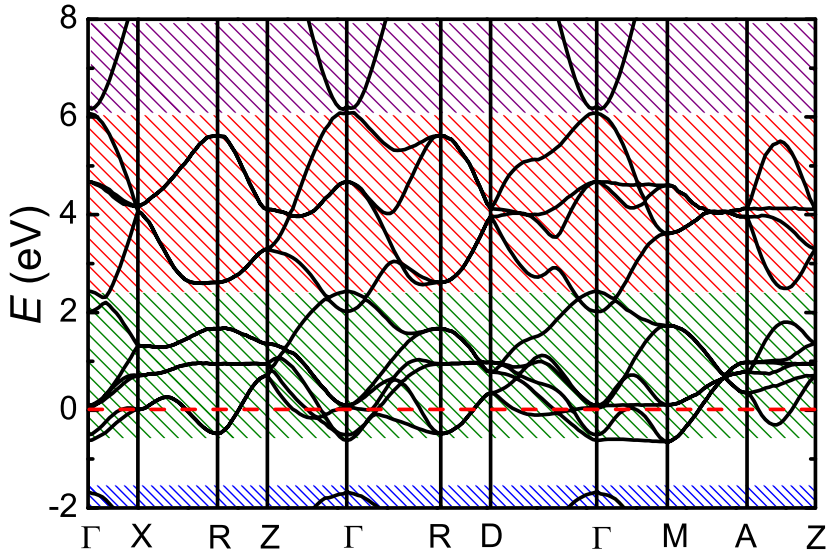

Figure D.6: Band structure of VO_2 in the rutile and metallic phase in an energy range from -2 eV to 8 eV. Details about the shaded area can be found in the text. (k-path: $\Gamma \rightarrow X \rightarrow R \rightarrow Z \rightarrow D \rightarrow \Gamma \rightarrow R \rightarrow A \rightarrow \Gamma \rightarrow M \rightarrow A \rightarrow Z$).

(red shaded area in Fig. D.6). At even higher energies, a band is partially visible and belongs to the s-band of the vanadium atoms (violet shaded area).

The band structure of the monoclinic phase is depicted in Fig. D.7. However, in the monoclinic phase a band gap of 0.68 eV occurs, in perfect agreement with the experimental determined value of 0.6 eV [380, 384, 405, 406]. Due to the large energy gap the IMT transition cannot be explained by Peierls effect or the Hubbard model which only respects one energy band. The lowest visible band can again be assigned to the O_{2p} band and is located at 1.4 eV below the Fermi edge. The band is shifted up by 0.3 eV in comparison to the metallic phase. The same ratio could be observed in PE experiments of Koethe et al. [384]. The next energetically higher band belongs to the a_{1g}- band and exhibits a bandwidth of 0.55 eV which is much narrower in comparison to the experimental value of 1.5 eV [383].

In order to better understand the temperature evolution of the optical spectra of VO_2 shown in Sec. D.4.3, the optical conductivity $\sigma_1(\nu)$ was derived from the DFT calculations for the metallic and insulating phase. This gives us the possibility to compare previous measurements from literature and our experimental data with theoretical determined spectra. Thus, the various optical features can be assigned to the excitations between the bands. The theoretical spectra in the HTP and LTP, and the experimental spectra[3] [380, 406] are displayed in Fig. D.8 in a frequency range from 0 cm^{-1} to 50000 cm^{-1}. For a better comparison with

3 The spectrum of Okazaki et al. [405] strongly differs from the spectra of Verleur et al. [380], and Qazilbash et al. [406]. One of the reasons might be the low film thickness of 10 nm which could lead to strain and tension in the film due to the lattice mismatch between TiO_2 and VO_2. Furthermore, at the interface of the materials electronic interactions can be enhanced and alter the optical spectrum. However, the most plausible explanation for the difference between the spectra above 25000 cm^{-1} is that the VO_2 film was not completely closed and the substrate was measured instead. This interpretation is supported by the in Ref.[405] observed strong resonance frequency $\mathbf{D}^\star$ at 30600 cm^{-1} which exactly agrees with the band edge of TiO_2 at 30240 cm^{-1} [407]. Therefore, the spectra is not shown in Fig. D.8.

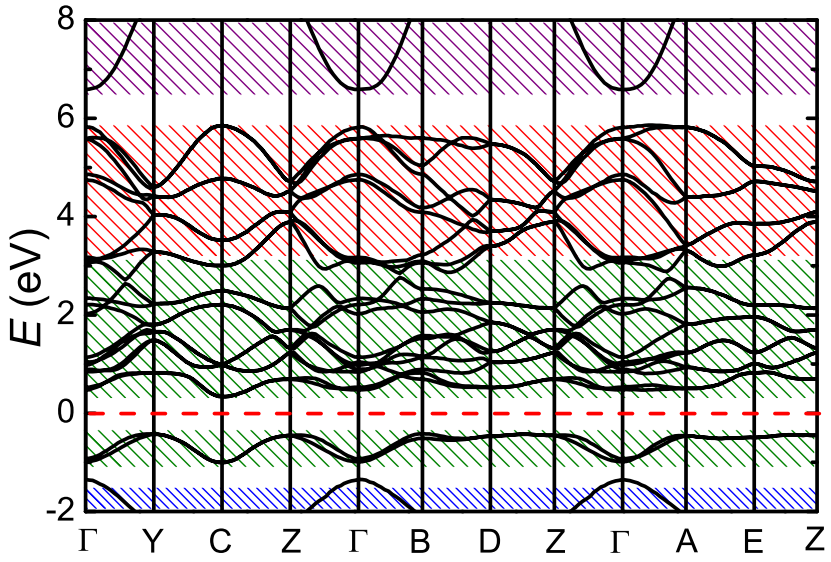

Figure D.7: Band structure of VO_2 at 295 K (blue) in the monoclinic M_1 phase in an energy range from -2 eV to 8 eV (see text for details about the shaded areas). The band gap is about 0.68 eV and agrees very well with the experimental results of 0.6 eV. (k-path: $\Gamma \rightarrow Y \rightarrow C \rightarrow Z \rightarrow \Gamma \rightarrow B \rightarrow D \rightarrow Z \rightarrow \Gamma \rightarrow A \rightarrow E \rightarrow \Gamma$)

the experimental data, the calculated conductivity are scaled by a factor of two for a better comparison.

It is difficult to compare film spectra with spectra of single-crystals. Studies of VO_2 single crystals are not shown as Verleur et al. [380] recognized that the reflectivity strongly depends on the sample and varies by about 10%. This observation was attributed to surface effects and cracks in the crystal which makes it difficult to compare single crystal spectra with film spectra. Therefore, we only consider film spectra. Most of the previous measurements were performed on VO_2 films with a thickness between 10 nm and 100 nm which were grown with different methods on the substrates sapphire and TiO_2. The films are polycrystalline which can be deduced from the AFM Fig. D.4.1. However, the film spectra can be reproduced very well within a sample. But due to the varying roughness of the surfaces the incident light can be scattered in different ways resulting in a wavelength-dependent modification of the reflectivity and hence, the absolute values of $R(\nu)$ and $\sigma_1(\nu)$ can differ slightly from sample to sample depending on the growth conditions. This explains the deviation between the measurements.

We are more interested in the position of the optical transitions and their origin than in the absolute values of the optical conductivity. In the metallic HTP the conductivity of all samples reveals below 10000 cm^{-1}a steep increase, caused by free charge carriers. This transition is labeled in Fig. D.8 (a) by the letter **A**. Depending on the samples and their quality, the experimental value for $\sigma(\nu \mapsto 0)$ ranges between 2300 $\Omega^{-1}cm^{-1}$and 6000 $\Omega^{-1}cm^{-1}$. In the case of the unscaled calculated spectrum it is 6300 $\Omega^{-1}cm^{-1}$and agrees well with the published data. Since the calculations do not consider any intrinsic broadening, the interband transitions were folded with a Lorentz function with a width of 0.4 eV in order to facilitate a better comparison of the experimental data and calculation. For the intraband transitions a width of 0.35 eV was chosen. Besides the artificial

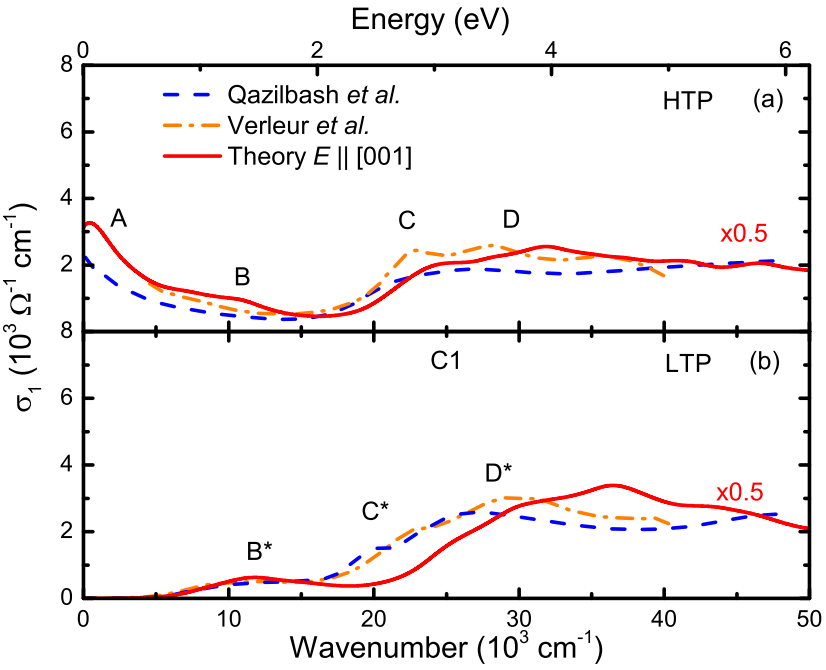

Figure D.8: (a) Theoretical spectrum (red solid line, scaled by a factor of two) for $E \parallel [001]$ in the HTP compared to the measured film spectra of Verleur et al. [380] (orange, dashed-dotted line) on sapphire and of Qazilbash et al. [406] (blue, dashed) on sapphire substrate. All spectra feature a rise of the conductivity below 10000 cm^{-1} indicating a Drude behavior. (b) In the LTP all spectra reveal a band gap of about 0.6 eV (5000 cm^{-1}) and a spectral redistribution.

broadening, the absolute value also depends slightly on the applied smearing factor which was set to a low value of 0.005 Ry (68 meV).

The peak **B** in Fig. D.8 (a) marks the interband transition which can be assigned to the excitation of the partially filled a_{1g} band into an unoccupied e_g^π-level. The transition takes place between the d_{yz}-orbital (part of the e_g^π band) of next neighboring vanadium atoms in the rutile plane and the $d_{x^2-y^2}$-orbital. The higher excitations, labeled with **C** and **D**, originate from the fully occupied O_{2p}-band in the higher unoccupied d-bands of vanadium. In more detail, the transition labeled with **C** (situated between 20000 cm^{-1} and 24000 cm^{-1}) corresponds to an excitation from O_{2p} to the a_{1g}-state; the feature **D** originates from the excitation of the O_{2p}-band in the unoccupied e_g^π-band whose theoretical resonance frequency is at 32000 cm^{-1} and appears as a broad shallow feature in the measurement [380, 393, 405] in a range from 25000 cm^{-1} to 31000 cm^{-1}. An alternative explanation would be the excitation of a charge transfer exciton.

The optical conductivity of the insulating phase is displayed in Fig. D.8 (b). In the spectra the band gap can be clearly recognized which is about 0.6 eV large. The theoretical value of 0.68 eV is in very good agreement with the experimental results. One should note, Verleur et al. [380] reported an additional feature that appears 0.3 eV inside the gap whose intensity is strongly sample-dependent. It was speculated whether this resonance is caused by impurities or by lattice mismatches. However, this feature is not present in the shown data. The local maximum, highlighted with $\mathbf{B}^\star$, can be related to the feature **B** in the metallic phase which is generated by the $a_{1g} \rightarrow e_g^\pi$ transition. In addition, PE experiments [384] have revealed that a fraction of the unoccupied a_{1g} band is also located below the e_g^π-level which was confirmed by CDMFT calculations. This transition should

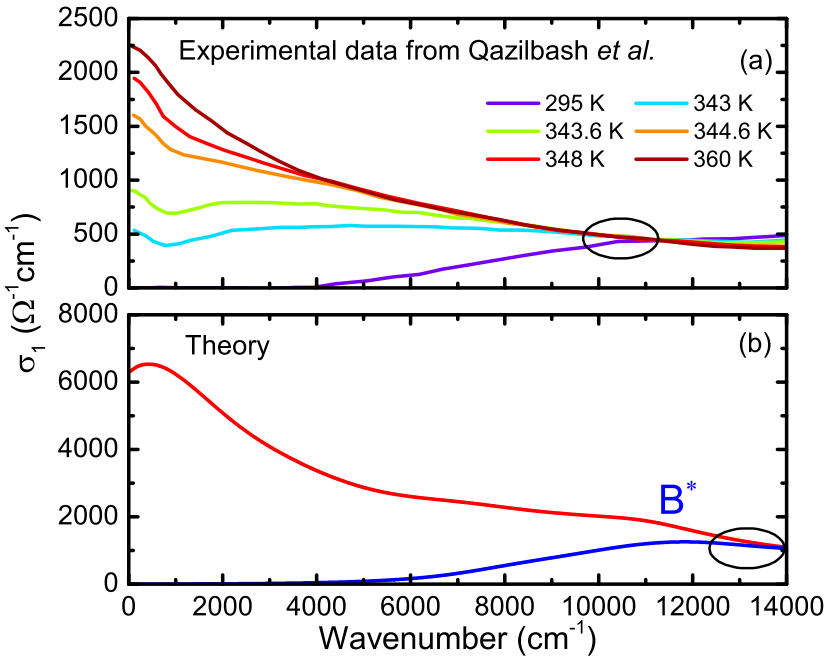

Figure D.9: (a) Infrared spectra of VO_2 in a temperature range from 295 K to 360 K and a frequency region from 0 cm^{-1} to 14000 cm^{-1}. In a small temperature window of 6 K a small Drude feature develops and initiates the phase transition into the metallic phase. (b) Theoretical spectra of VO_2 at 295 K (blue) and at 360 K (red). The simulated spectra reflect very well the evolution of the experimental data.

be strongest parallel to the rutile c-axis or along the one-dimensional vanadium atom chain and should not contribute to the in-plane response. The feature with **C*** which is located at 20000 cm^{-1}[406] and at 22000 cm^{-1}[380] as well as at 25000 cm^{-1} in the calculated spectra is caused by the transition from the a_{1g} in the e_g^π-band as well as a transition of the O_{2p}-band in the unoccupied bands of the vanadium atoms. There is an alternative interpretation which suggests that due to the narrow line width it is an excitation of a Frenkel-exciton between the vanadium atoms along the rutile c-axis. The excitation of the full O_{2p} in the a_{1g}-band is located between 25000 cm^{-1} and 30000 cm^{-1} for the experiments and at 35000 cm^{-1} in the case of the calculation.

In Fig. D.9 the experimental optical conductivity $\sigma(\nu)$[395] is compared for various temperatures with the theoretical conductivity of the rutile and monoclinic phase focusing on frequencies below 14000 cm^{-1}. Below the transition at about 343 K the B* feature can be clearly recognized at 12000 cm^{-1} in Fig. D.9 (a), which is described very well by the simulation. Moreover, both spectra reveal the same band gap. With increasing temperature the bands shift to lower energies whereas at 2000 cm^{-1} a further band develops. It can be caused by an interband transition. In the metallic phase this feature can contribute to that part of the spectrum. Simultaneously to the peak a minimum at 1000 cm^{-1} appears which can be ascribed to an opening of a pseudogap [394, 395]. The existence of a pseudogap is in general a sign that electron correlations play an important role in VO_2 [26]. Up to now, it is still under discussion whether the feature is caused by a pseudogap or an interband transition. The energy gap is filled up with increasing temperature by the transfer of spectral weight from the interband transition to the part of the free charge carriers. In the metallic phase the optical response of the free charge carriers dominates and leads to a higher optical conductivity

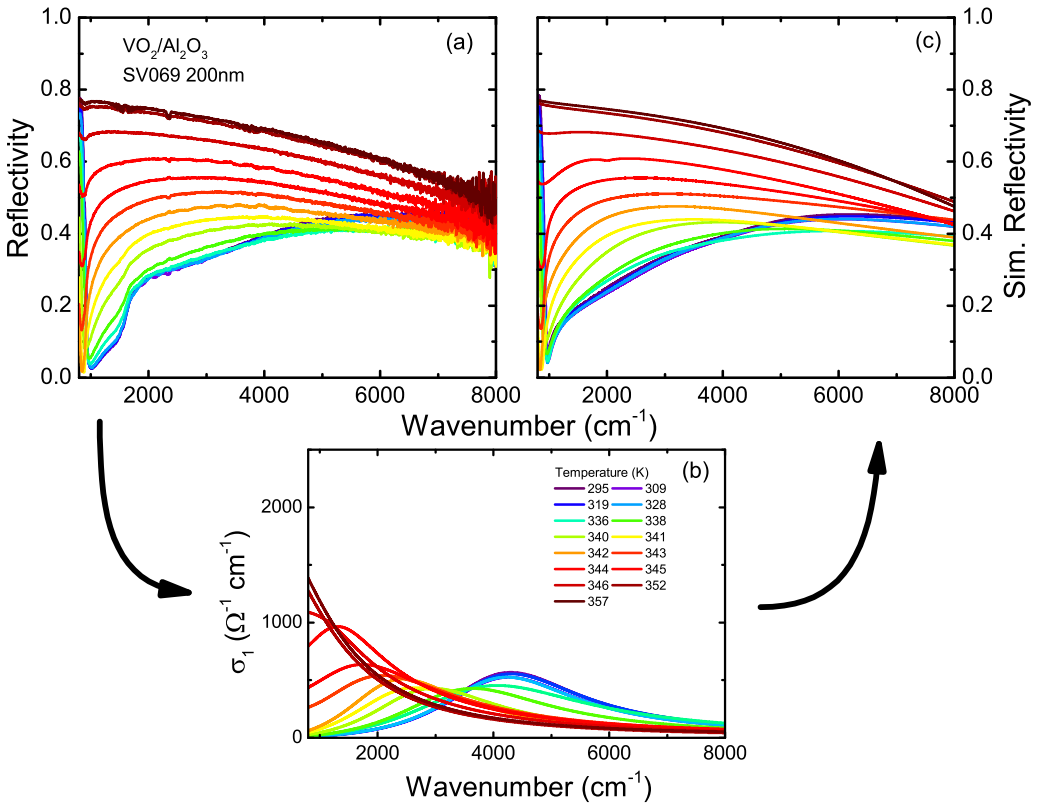

Figure D.10: (a) Temperature-dependent and non-polarized infrared spectra of VO_2 on a sapphire substrate. In the insulating state the reflectivity is in average 40 % above 2000 cm^{-1} and almost transparent at 1000 cm^{-1}. Lattice vibrations of Al_2O_3 appear at lower frequencies. With increasing temperature and crossing the phase transition the total signal rises up to $R = 0.75$. (b) Temperature-dependent optical conductivity of VO_2 which was determined by fitting experimental data according to the two-layer model. In the insulating phase the spectrum of VO_2 consists of one interband transition reflected by the Lorentz peak. In the metallic phase the optical response consists solely of a Drude-feature. (c) Modeled reflectivity of the VO_2/Al_2O_3-layer system determined from the optical conductivity of VO_2 (b) and the sapphire substrate.

at low frequencies. The temperature-dependent spectra in Fig. D.9 (a) intersect at one point, the so-called isobestic point[4], at about 11000 cm^{-1} which is very often observed in correlated systems [408, 409], but up to now not understood. The calculated spectra exhibit this specific point at a slightly higher frequency because of the superimposed interband transition on top of the Drude band. Thus, the intersection is shifted. In addition, the position of the intersection is also affected by the artificial broadening of the transition. For a more precise analysis, temperature-dependent structural-resolved data have to be collected at the phase transition, which could help to disentangle whether the interband transition shifts to lower frequencies.

D.4.3 *Temperature-dependent optical measurements*

Temperature-dependent unpolarized infrared measurement were performed for samples on both substrates SiO_2/Si and Al_2O_3 between 295 K and 360 K in a frequency range from 800 cm^{-1} to 8000 cm^{-1}. Therefore, the films were placed

4 Energy at which all spectra have the same absorption.

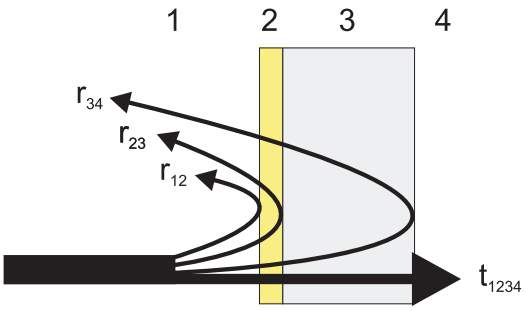

Figure D.11: Reflection and transmission behavior of a layered system which consists of layer 2 and 3 embedded in the material 1 and 4.

on the sample holder described in Sec. D.4.1 and investigated with an infrared microscope for normal incident infrared light. As a reference an aluminum mirror located next to the sample was used. In Fig. D.10 (a) the reflectivity of VO_2-film on sapphire is illustrated for various temperatures. Between 295 K and 336 K, the reflectivity curves overlap and basically do not show any temperature dependence.

Sapphire is optically transparent in a frequency range between 1500 cm^{-1} and 50000 cm^{-1} [370] with an an average reflectivity of 20%. Below 1000 cm^{-1} several phonons [410] exist, leading to a strong increase of the reflectivity in this specific range. The reflectivity has a minimum at 1010 cm^{-1} with $R = 0.025$ which shifts with increasing temperature to 850 cm^{-1}. A similar behavior was observed in Ref. [411] for a VO_2 film with a thickness of 180 nm and explained by the fact that there occurs a non-trivial phase shift of the multiple reflected beams in the VO_2-film. By the abnormal phase shift the radiation is absorbed within the film which is similar to an asymmetric Fabry-Perot resonator. In this case the film must have a minimum film thickness of a quarter wavelength. However, this effect originates from the combination of the temperature-dependent optical constants of the film and the steady optical constants of the substrate. That is why VO_2 is considered as a material for the development of thermally controlled absorber.

To determine the optical conductivity of VO_2 from the measured reflectivity the spectrum was fitted by a Drude function in the metallic phase and a Lorentz function in the insulating state. For the transition a combination of both functions was used. One difficulty which arises for any fitting approach is that the film consists of a 200 nm thick layer VO_2 and a 1 mm thick Al_2O_3 substrate. Therefore, the reflectivity is composed of a reflecting part of the VO_2-film and the sapphire substrate. According to Dressel and Grüner [103] for systems consisting of several layers the following formula of the complex reflection and transmission at the interface layer ij can be derived:

$$\hat{r}_{ij} = \frac{\hat{N}_i - \hat{N}_j}{\hat{N}_i + \hat{N}_j} \tag{D.2}$$

$$\hat{t}_{ij} = \frac{2\hat{N}_j}{\hat{N}_i + \hat{N}_j} \tag{D.3}$$

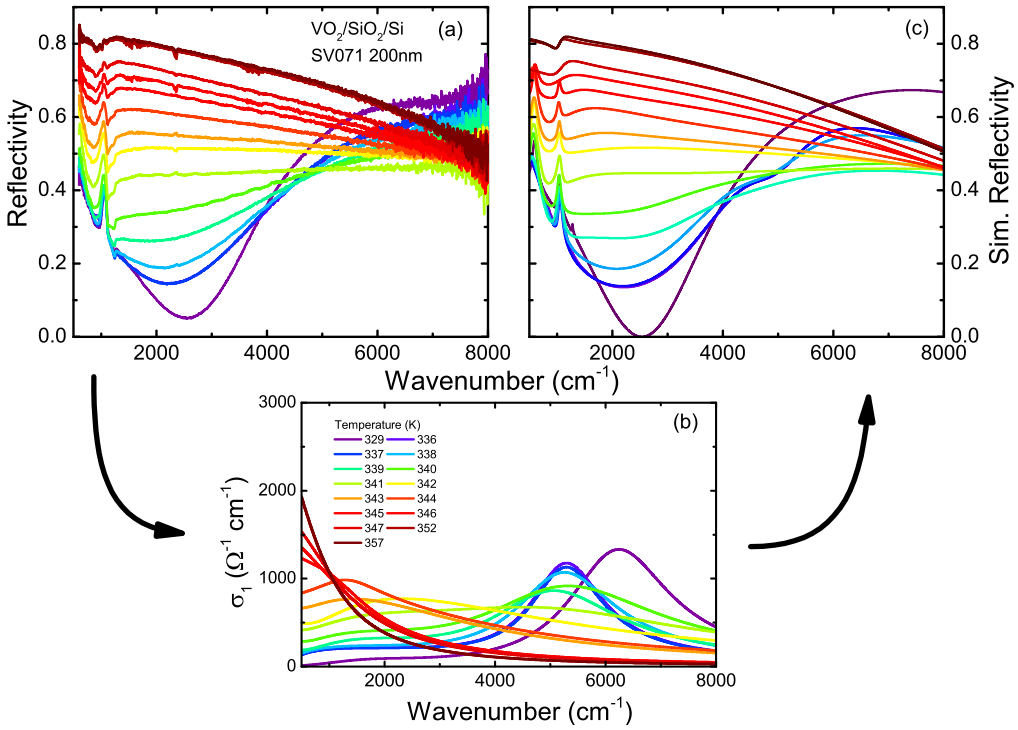

Figure D.12: (a) Reflectivity spectra of VO_2 on SiO_2/Si between 800 cm^{-1} and 8000 cm^{-1} in a temperature range from 330 to 360 K. The spectral shape deviates from the previous spectra of VO_2 on sapphire, caused by the optical properties of the substrate. The main reason that in SiO_2/Si a phonon resonance appears at about 1000 cm^{-1} which can be assigned to SiO_2. Above the transition temperature the spectra reveals the same high reflectivity as VO_2 on sapphire. (b) Temperature-dependence of the optical conductivity determined by fitting the reflectivity spectra. In the insulating phase the spectrum consists of two interband transitions depicted by two Lorentz peaks. In the metallic phase only one Drude component is present. (c) Modeled reflectivity of the VO_2/SiO_2/Si-layered system from the optical conductivity of the VO_2-film (b) and the silicon substrate.

which can be simplified for a system composed of two layers. Since the considered system consists of two parts embedded in the third medium, vacuum, the following equation accounts for the complex reflection coefficient $\hat{r}_{1234}$:

$$\hat{r}_{1234} = \frac{\hat{r}_{12} + \hat{r}_{23} \cdot e^{2i\Phi_2} + \hat{r}_{34} \cdot e^{2i(\Phi_2+\Phi_3)} + \hat{r}_{12}\hat{r}_{23}\hat{r}_{34} \cdot e^{2i\Phi_3}}{1 + \hat{r}_{12}\hat{r}_{23} \cdot e^{2i\Phi_2} + \hat{r}_{23}\hat{r}_{34} \cdot e^{2i\Phi_3} + \hat{r}_{12}\hat{r}_{34} \cdot e^{2i(\Phi_2+\Phi_3)}} \tag{D.4}$$

$\Phi_i = 2\pi d \frac{(n_i + ik_i)}{\lambda}$ is the complex angle, which depends on the layer thickness d, the wavelength λ, the refraction index n_i and the absorption index k_i of the layer material. The reflection R is derived from $R = \sqrt{|\hat{r}_{1234}|^2}$. Equation D.4 is implemented as a standard function in the fit-program WASF and was used to determine the optical functions of VO_2.

As only a limited spectral range was measured, the system consists of two different materials, and the higher optical excitations in VO_2 have a non negligible influence on the reflectivity. Hence, it is not possible to perform a Kramers-Kronig transformation. In that case the high frequency as well as the low frequency extrapolation would lead to wrong results. Therefore, only the reflectivity was fitted in order to determine the optical constants for VO_2. In the case of VO_2/Al_2O_3 the lattice phonon of the substrate located at 800 cm^{-1} was taken into account. In the insulating state an electronic interband transition is present

(see also depicted in Fig. D.11 (b)) which shifts to lower frequencies while approaching the phase transition; its maximum is located for the room temperature spectrum at 4300 cm^{-1} and moves to 1300 cm^{-1} at 343 K until it completely vanishes at higher temperatures. In Sec. D.4.2 it was demonstrated that VO_2 is a multiband system in which several valence bands contribute to the optical spectrum up to 6 eV. In the energy range of 1 eV (8000 cm^{-1}) the optical spectrum is dominated by the interband transition $a_{1g} \rightarrow e_g^\pi$ and $a_{1g} \rightarrow a_{1g}$. Qazilbash et al. [393] assume in their optical studies that the lowest transition takes places from a_{1g} to e_g^π whereas PE and CDMFT reveals that below the e_g^π band and above the Fermi energy a fraction of the a_{1g} band resides. Therefore, we suggest that the Lorentz function results from both, transition from a_{1g} to e_g^π, as well as the transition from $a_{1g} \rightarrow a_{1g}$ which shift with the temperatures to lower energies.

The filling up of the band gap at the phase transition was tracked in Ref. [394, 395] which is in accordance with an IMT of a Mott insulator. In Ref. [394, 395] the interband transition (B*) is located at 11000 cm^{-1}; it is claimed that the feature does not reveal any temperature dependence. However, the published optical conductivity data allows to draw an alternative conclusion:

- The corresponding band (B*) consisting of excitations from the occupied a_{1g} to the unoccupied a_{1g} and e_g^π in the insulating phase.
- The energetically lowest band (a_{1g} and e_g^π) shifts close to the phase transition to lower frequencies and reduces the band gap.
- Within the phase transition a Drude component develops filling up the energy gap between $a_{1g} \rightarrow a_{1g}$ transition leading to the pseudogap like feature. These observations correlate with the here observed modification of the interband transition at about 5000 cm^{-1} which shifts with rising temperature (see Fig. D.10 (b) and D.12 (b)) to lower energies.
- In the metallic phase the spectrum is solely dominated by the free charge carriers and the interband transition is screened.
- Due to the Drude response in the metallic state the light is completely reflected by the VO_2 film and the response of the substrates is suppressed.

To fit the reflectivity of VO_2 on SiO_2/Si, only the lattice vibration of the silicon dioxide was considered. Therefore, two Lorentz functions at 590 cm^{-1} and 1054 cm^{-1} were used. The resonance frequency of the Lorentz function agrees very well with the results of previous optical studies [370, 412]. In opposite to the previous system VO_2/Al_2O_3 one addition Lorentz function had to be applied in the insulating phase to model the interband transitions accurately (see Fig. D.12). A broad, weak Lorentz peak is located at 1500 cm^{-1} and the second stronger one at 5300 cm^{-1} and shifts to low frequencies at the phase transition. One of the reasons for the necessity of a lowest-lying excitation can be impurity-bound gap states within the band gap (see Sec. D.4.2). Moreover, interactions between the substrate with the VO_2, as well as the connected structural tensions due to the different lattice constants are possible sources for the modification of the band structure of VO_2 which leads to a change of the spectrum.

Concerning the free carrier a Drude component shows up with increasing temperatures, whereas the Lorentz function loses intensity and diminishes in the metallic phase.

In Fig. D.13 the parameters of the Drude peaks are shown for VO_2/Al_2O_3 in a temperature region from 295 K to 360 K, as well as for VO_2/SiO_2/Si in a range from 325 K to 360 K. By the appearance of the Drude feature the phase transition can be determined exactly which is about 342 K for sapphire and 336.5 K for SiO_2/Si. It is to note that the right pictures show an less extended temperature range due to the higher temperature resolution. In both samples the plasma frequency ν_p increases strongly whilst crossing the phase transition and reaches a constant value of 12000 cm^{-1}in the metallic phase. The literature value [395] of the plasma frequency ν_p is at 22000 $cm^{-1}$and hence, by factor of 1.8 higher. Similarly, the conductivity σ_{DC} increases as well at the transition, flattens above 350 K in the metallic phase, and approaches asymptotically a constant value. For SiO_2 it approaches 2000 $\Omega^{-1}cm^{-1}$, for Al_2O_3 2500 $\Omega^{-1}cm^{-1}$ corresponding very well to the result of Ref. [406]. The optical determined σ_{DC} are by a factor 5 too high in comparison to the values derived from the transport measurements in Sec. D.4.1. However, the results from the DC study is by a factor two too small as the film thickness was assumed with 200 nm, but probably the effective thickness is only about 100 nm due to the roughness of the surface (see Sec. D.4.1).

In contrast, the scattering rate τ^{-1} reveals a diverging/non-monotonous behavior. At the phase transition it diverges and increases for Al_2O_3 to 1800 cm^{-1}as well as for SiO_2 to 1500 cm^{-1} in the metallic phase it drops down by about 40% to 1100 cm^{-1} and 800 cm^{-1}, respectively. The rise of the scattering rate marks the percolation boundary, meaning the transition from metallic islands to a closed metallic film. The behavior of τ is similar to temperature evolution of the effective mass at the phase transition [395]. With a Fermi velocity V_F [413] of $0.24 \cdot 10^6$ m/s (from DFT+LDA calculations) a free mean path l_{free} of 7 Å at the transition and 20 Å in the metallic phase can be calculated from the estimated scattering rate. This supports a classical Boltzmann transport of the charge carriers. In case that the free mean path is larger than $l_{free} > 10$ Å the conductivity of a material can be described by the Boltzmann theory. But if $l_{free} < 10$ Å or even smaller the Boltzmann model breaks down. After the Ioffe-Regel-Mott-Limit IRML [414, 415] the free mean path is not allowed to be smaller than the lattice constant. However, optical and transport measurements [406, 413] reveal that l_{free} of VO_2 is smaller than the lattice constant in the metallic phase and hence, the IRML is violated. This is a typical behavior of a correlated system in which conventional models such as Drude model are not valid anymore.

The performed optical studies for the two different substrates reproduces qualitatively the known results. However, to our best knowledge no optical data were published up to now, about VO_2 on SiO_2/Si. In both compounds the phase transition from an insulating to a metallic state was observed very clearly in the spectra. The first interband transition in the LTP is located at 5300 $cm^{-1}$and lower in comparison to previous measurements. However, the band gap depends on the film quality and the amount of impurities leading to the discrepancy. A further hint is the jump of the conductivity of three orders of magnitude at the transition which is already good. But very good films achieve a change of four orders of magnitude being the case of the optical studies in Ref. [406]. While $\sigma_{DC}(\nu \mapsto 0)$ corresponds to the literature values, the determined scattering rates τ^{-1} deviates by a factor of three from the literature values. At the phase transition it diverges and drops in the metallic phase to 1100 cm^{-1} and to 800 cm^{-1}, respectively. One reason for the rather low values could be the limited examined

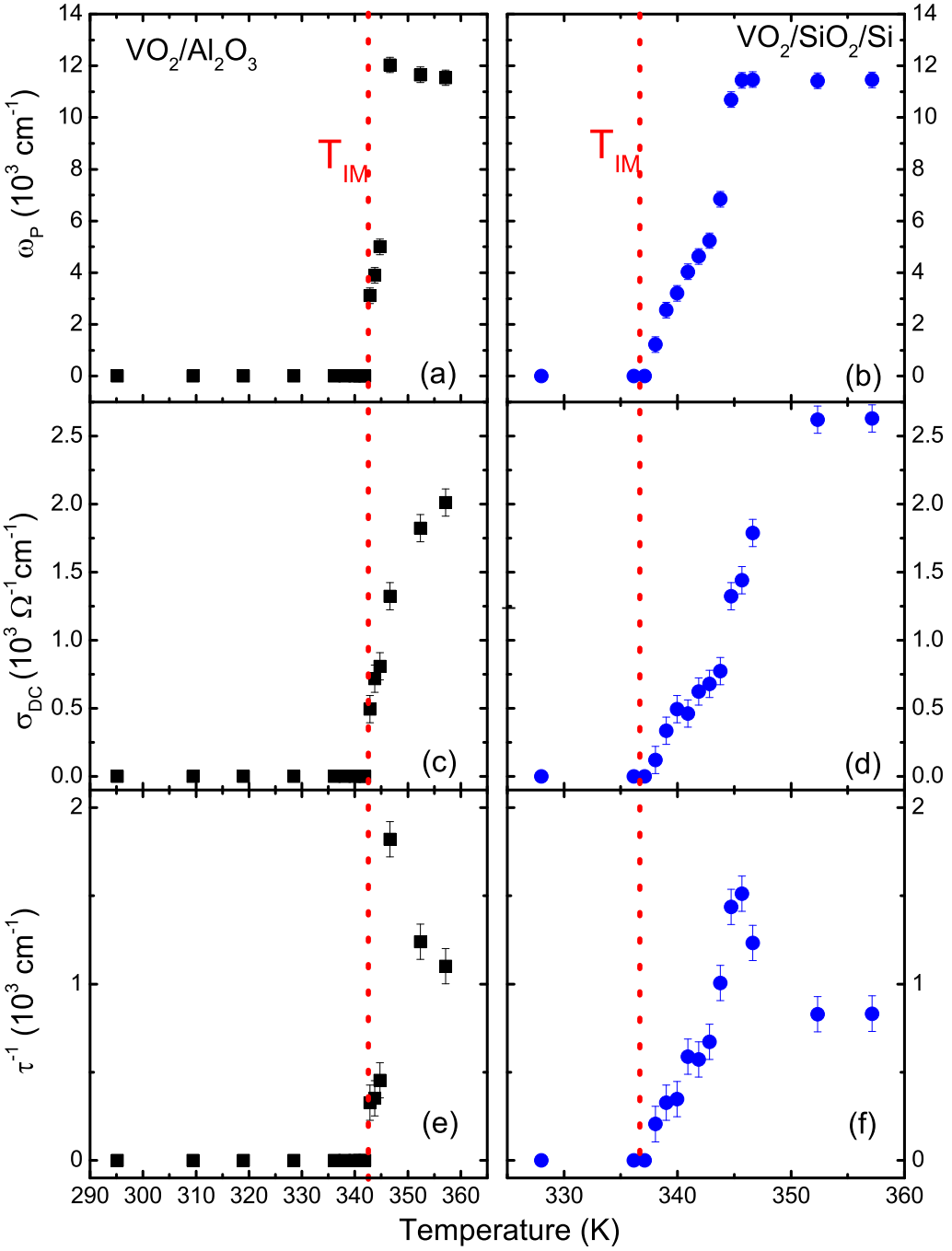

Figure D.13: Temperature evolution of the plasma frequency ν_p (a), σ_{DC} (b) and the scattering rate τ^{-1} (c) of VO_2/Al_2O_3 in a temperature range from 295 K to 360 K. Temperature evolution of the plasma frequency ν_p (d), σ_{DC} (e) and τ^{-1} (f) of $VO_2/SiO_2/Si$ in a temperature range from 325 K to 360 K. The red dashed lines mark the IMT.

frequency range as information is missing above 10000 cm^{-1}especially for the high frequency region.

D.4.4 *Electric-induced insulator-metal transition*

ELECTRIC-INDUCED PHASE TRANSITION Electric-induced phase transition in VO_2 and therewith related exotic phenomena, like bi-stability [416, 417] or negative differential conductivity [418], were observed in the early 70's. In the

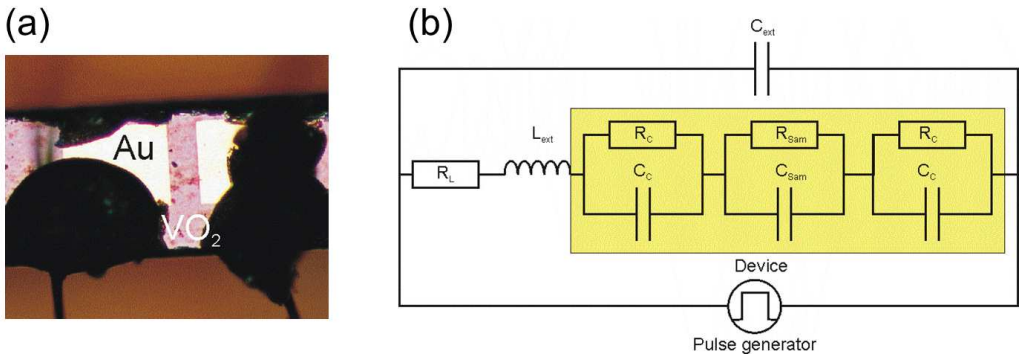

Figure D.14: (a) Picture of the VO_2 film with two gold contacts separated by a distance of 30 µm. The gold wires were glued on the contacts with silver paint. (b) Schematic circuit of the measurement arrangement containing the VO_2 sample as an electronic device. It consists of the film and contact resistance as well as several parasitic capacitance and inductances originating from the wires.

recent 10 years those effects became more interesting for the research community concerning a possible application in commercial and industrial products. However, up to now it is not clear whether the electric-induced transition can be ascribed to Joules heating or to a break down of the Mott state due to the modification of the on-site Coulomb repulsion U. Evidences for an electronically driven transition were provided by the groundbreaking study of Stefanovich et al. [419] which stimulated the study and the research on Mott-FET. VO_2 is a quite promising candidate that can revolutionize the silicon-based semiconductor industry one day, but before the physical origin of the effect has to be understood.

For our study of the electric-induced phase transition two 50 nm gold contacts were evaporated on a small stripe of VO_2 on a SiO_2 substrate (see Fig. D.14 (a)), with a distance of 30 µm. The width of the VO_2-channel was about 100 µm with a film thickness of 200 nm. The whole experimental setup accords with the schematic sketch in Fig. 4.10.

The main interest was to study the time-dependent switching process. While other groups have focused on the switching behavior under a constantly applied voltage or current, our main interest of our project was to study the time-dependent dynamics of the electrically-induced phase transition. Therefore, voltage pulses were applied to the film. This has the advantage that Joules heating plays a minor role and it can be clearly disentangled from electronic effects. In addition, fluorescence spectroscopy[358], which was used as a local probe, revealed that the switching from the insulating state into the metallic HCP state can be attributed to thermal heating.

An AV-1010-B pulse generator was used as a voltage source and a 1 kΩ load resistor was implemented in the circuit to protect the sample from current bursts. The total current was measured by the voltage drop across the load resistor and detected by a fast oscilloscope (R_L= 100 MΩ) which was also used to record the applied voltage pulse. The measurements were conducted for various temperatures above and below the phase transition. Therefore, the temperature was stabilized and the voltage amplitude successively increased up to a maximum value. The repetition rate was set to 10 Hz. The pulse length was set to 3 ms, with a total duty-cycle of 0.03, which is by a factor of 3 [420] and 17 [421], respectively, smaller than previous measurements. This low duty-cycle prevents an arising accumulation of heat.

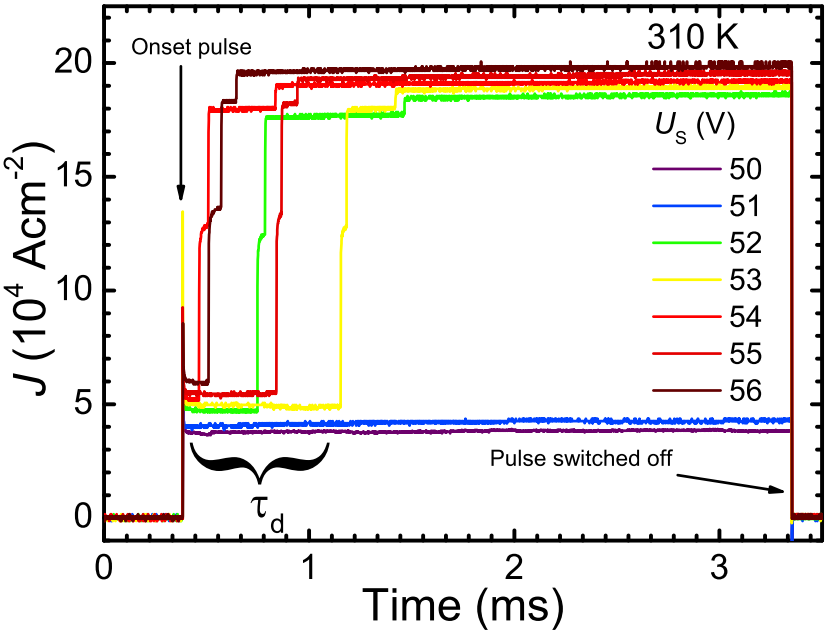

Figure D.15: Time-resolved current density of a VO_2-film at 310 K for different voltage amplitudes. The pulse length was 3 ms. Above 51 V the film switches into the high conducting state. Between the beginning of the pulse and the switching a so-called delay time τ_d elapses which decreases with increasing voltage.

In Fig. D.15 the time-dependent current density $J(t)$ at 310 K is depicted for various voltage values. At 50 V, the current density increases and reveals an overshoot at the beginning of the voltage pulse. This effect can be observed for all applied voltages. The overshoot of $J(t)$ can be attributed to the high sample resistance and a high contact capacitance. Afterwards, the signal fades away within 2 µs and the total system is in equilibrium. This time scale is surprisingly, as with a dielectric constant of $\epsilon(\nu \mapsto 0) \approx 50$ [422] at room temperature, a cross section of $A = 2 \cdot 10^{-11}\,\mathrm{m}^2$ and a contact resistance of $d = 30 \cdot 10^{-6}\,\mathrm{m}$, the sample's capacitance is on the order of 1 fF. This yields with a sample resistance of $R_{\mathrm{Sam}} = 1 \cdot 10^5\,\Omega$ a much smaller time constant for the decay of the overshoot of $\tau_{RC} = 10\,\mathrm{ps}$. The longer relaxation rate is probably related to the Au/VO_2-contacts[5]. For the remaining pulse period, the signal stays constant throughout the whole pulse. This means that the resistance of the sample does not change while the pulse is being applied. Also a slow increase of $J(t)$ with time could not be observed. This can be accounted as a sign that the film is not heated up during the pulse because in this case the current would increase according to the temperature-dependent conductivity of VO_2. A slow increase of the temperature would lead to a decrease of the resistance (see Fig. D.5) and hence, a rise of the

5 The gold contacts form Schottky-contacts at the interface. A barrier is created at the interface due to the difference of the working function $\Phi_{\mathrm{m,\,Au}} = 5{,}1\,\mathrm{eV}$ [80] of gold and the working function $\Phi_{\mathrm{m,\,VO_2}} = 4.9\,\mathrm{eV}$ [423] of VO_2. The barrier height is $\Phi_{Au/VO2} = \Phi_{\mathrm{m,\,Au}} - X_{\mathrm{VO_2}} = \Phi_{\mathrm{m,\,Au}} - (\Phi_{\mathrm{m,\,VO_2}} - \Phi_{\mathrm{n}}) = 0.5\,\mathrm{eV}$ [80], with $\Phi_{\mathrm{n}} = 0.3\,\mathrm{eV}$ as the difference between the Fermi energy, located in the middle of the band gap, and conduction band, and $X_{\mathrm{VO_2}}$ as the electron affinity of VO_2. The contact sheet is according to Ref. Sze and Ng [80]: $W_B = \sqrt{\frac{2\epsilon_0\,\epsilon(\nu\mapsto 0)\Psi_{Bi}}{q n_e}} \approx 1\,\mathrm{nm}$. With the in-build potential $\Psi_{Bi} = \Phi_{Au/VO2} - \Phi_{\mathrm{n}} = 0.2\,\mathrm{eV}$, the charge carrier concentration $n_e = 1 \cdot 10^{19}\,\mathrm{cm}^{-3}$ and $\epsilon(\nu \mapsto 0) = 50$ the capacitance is on the order of 10 pF leading to a time constant of 1 µs (with $R_{\mathrm{Sam}} = 100\,\mathrm{k}\Omega$). The result agrees very well with the observed relaxation time.

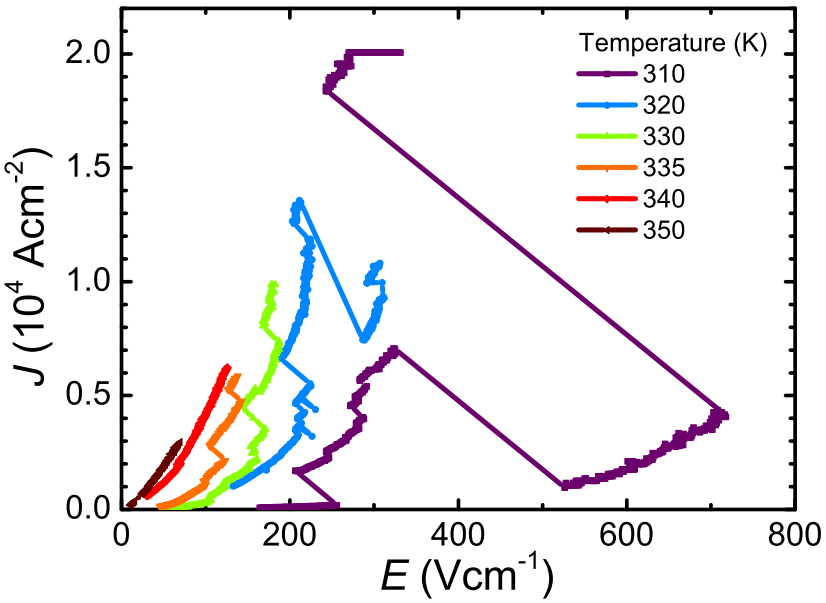

Figure D.16: Current density as a function of the applied electric field for various temperatures ranging from 310 K to 350 K. At low temperatures, a negative differential resistance regime NDR occurs.

current in the circuit. Finally, the current density drops down immediately to zero at the end of the voltage pulse.

If the voltage is increased above a certain critical value, the current jumps sharply into a high conducting state after a certain delay time τ_d. A similar behavior of the delay time τ_d was observed for VO_2-films on SiO_2 substrates in earlier measurements of Stefanovich et al. [419]. In contrast, VO_2-film on sapphire of Chae et al. [424] have revealed an instantaneously switching (<20 ns) to the high conducting state after creating a sufficiently large voltage. Taking a closer look at τ_d one recognizes that it is not a continuous function of U_S, but rather decreases with increasing U_S. Furthermore, jumps of τ_d could be observed. Therefore, we conclude that the formed filament is not stable from pulse to pulse, meaning that the current creates different path configurations.

The induced transition from the low-conducting state LCP to the high-conducting state HCP takes place within a microsecond in which the maximal time resolution is limited by the internal resistance of the oscilloscope which is about 500 ns. From that it can be expected that the switching happens on a nanosecond time scale as recorded in previous studies [419, 421, 424]. Until the film reaches its final state, the sample undergoes several short-living intermediate states which is reflected in the step-like structure of the current jump. This multi step behavior was also observed in other studies [421]. Its origin bases on the film morphology. The AFM pictures in Sec. D.4.1 show that the VO_2-layer consists of VO_2 islands of different size. They exhibit resistance values depending on their size, orientation, and shape. At a certain voltage one of these islands becomes conducting which can be caused by a thermally- or an electrically-induced effect. Thereupon, an avalanche-like process starts triggering the transition of further islands from the low conducting insulating state to the metallic one, until finally

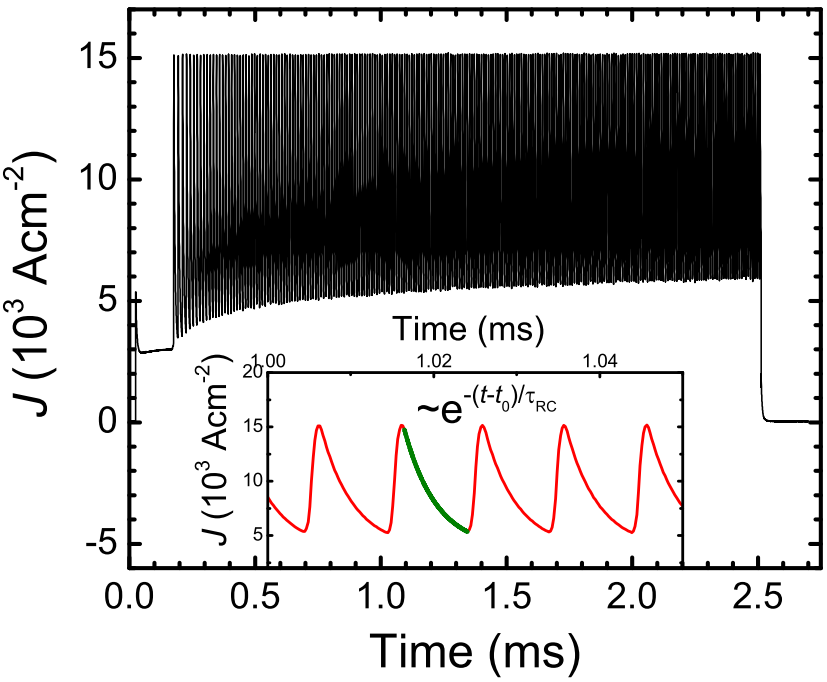

Figure D.17: Oscillations of the current density in a VO_2-film on sapphire after creating a voltage pulse of 2.5 ms width. The experiment was performed at room temperature. In the inset the oscillations are magnified in a time frame of 10 µs. The decaying edge can be fitted by $J(t) = J_0 + e^{-\frac{t-t_0}{\tau_{RC}}}$ (green line).

a conducting filament is formed. Based on a thermodynamical consideration,[6] the switching time as well as the delay time τ_d can be determined. With U_S=53 V and I=10 mA, we derived from an assumed channel width of 1 µm a value of τ_d= 1.2 ms. This result is on the same time scale and agrees very well with our observation. This is in conflict with the conclusion of Stefanovich et al. [419] that the delay time takes place on a two orders of magnitude faster time scale than the thermal-induced one.

A slow decay of the current as in previous studies [418] was not observed. This indicates that a thermally-induced effect can be excluded. Since dissipation of the thermal energy would lead to an increase of the resistance, whereas the current decreases at the same time. However, the final state depends slightly on the applied voltage U_S which means that by a higher electric field the VO_2-film is driven deeper into the metallic state.

In Fig. D.16 the current density $J(t)$ is plotted as a function of the internal electric field $E_{Sam}(t)$ for various temperatures, extracted 2.8 ms after the onset of the voltage pulse. The electric field in the sample can be calculated as follows:

$$E_{Sam} = \frac{U_{sam}}{d} = \frac{1}{d}(U_S - U_L) \tag{D.6}$$

whereas U_{Sam} is the applied voltage and d reflects the distance between the two contacts. The $J(E)$-curve at 350 K obeys the ohmic law, visible as it increases

6 From the heat balance equation:

$$P = \frac{C_p \cdot \Omega_V \cdot \rho}{\tau_d} \int_{T_0}^{T_{MI}} dT \tag{D.5}$$

with the heat power $P = I \cdot U_{Sam}$, the specific heat capacity C_p= 690 $\frac{J}{Kg\,K}$ and the density ρ= 4340 $\frac{kg}{cm^3}$, the delay time τ_d can be estimated.

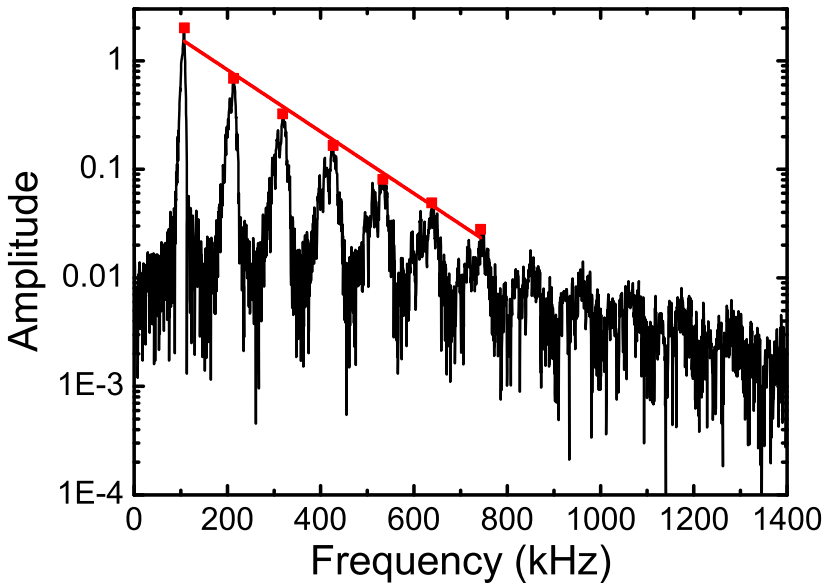

Figure D.18: Fast FT of the current signal in Fig. D.17 derived from a time range of 2.2 ms. The amplitude of the resonance frequency decays exponentially, confirmed by a linear fit (red line). The spectrum reveals similarities to the behavior of CDW-materials under the influence of an electric field.

linearly with the electric field which is typically for a metal. With decreasing temperature the resistance decreases and the current reveals a nonlinear behavior. Below the phase transition in the insulating phase, sharp jumps appear where the current increases steeply and the electric field drops. This leads to a S-shaped curve resulting in a negative differential resistance NDR (see also Sec. 5.4.3). Then the currents increase and reveal several further jumps. They can be related to the switching of VO_2-islands and the expansion of the conducting filament. Thereby, in principle several threshold fields E_{th} can be defined at which a switching occurs. With increasing temperature, E_{th} shifts to higher fields. Furthermore, a jump back to a smaller current value can be observed at 320 K and 310 K. This means that the current flow through the filament was too large and breaks down. Importantly, not the film is destroyed, but the contacts which cannot withstand the high load. By that, a higher voltage is necessary to create a new conducting path. In contrast, the film survives several thousands of switching cycles for a fixed voltage.

The volatile behavior of the current density depends according to Okimura et al. [421] on the dimensionality of the film. Narrower films with small contacts exhibit no jumps, as the growth of the filaments is limited by the size of the contact and hence, no shock-like increase of the current occurs. For the future, it is very important not to ensure only high quality films, but also very good contacts (suitable work function, dimension, low resistance and capacitance, etc.) to build reliable and high-power electronic devices.

CURRENT OSCILLATIONS A further study with voltage pulses were performed with a sample of VO_2 on Al_2O_3. The experimental setup is the same as before, despite contacts' distance of 60 µm, the contacts' width of 160 µm, the load resistance of $R_L = 10\,k\Omega$ and the pulse length of 2.5 ms.

Again, with increasing voltage a switching from the LCP to the HCP and a decreasing delay time τ_d can be observed. However, before the pure high conduct-

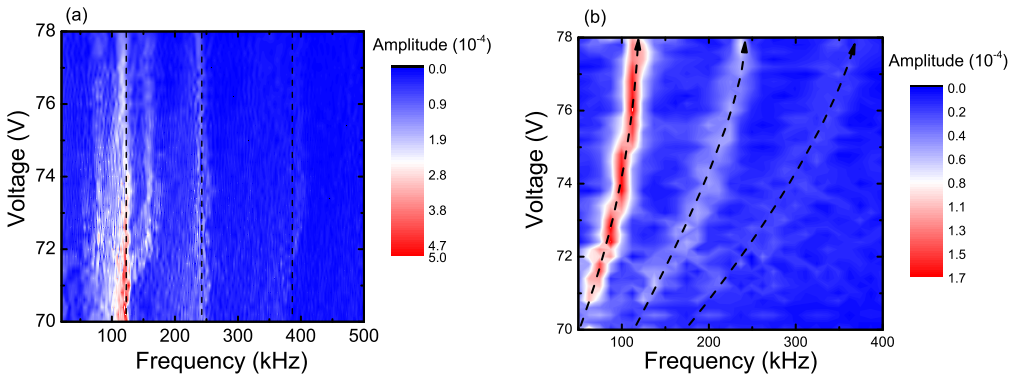

Figure D.19: (a) Contour plot of the amplitude of the resonance frequency dependent on the source voltage U_S. For the analysis all oscillations were taken into account. Several resonances occur which are marked by dashed lines. (b) Similar to (a), but only the first 200 µs were taken into account for the FT. The resonance frequency reveals a clear shift to higher frequencies with increasing voltage U_S.

ing state (HCP) is reached, strong oscillations of the current occur, as depicted in Fig. D.17. The current oscillates between the maximal current of the HCP-state and a minimal current which increases towards finite saturation value. This effect was first reported in Ref. [416] and [417]. However, they have detected only a rectangular oscillating signal with a resonance frequency of about 1 kHz.

In the inset of Fig. D.17 a 50 µs large detail of the oscillation is displayed. The begin of a period is dominated by a steep increase of the current while the relaxation process is much slower. The decay time is 4 µs determined by fitting the relaxation tail by an exponential decay function.

A fast Fourier transformation (FT)-analysis was performed to extract the frequency components from the oscillating signal. In Fig. D.18 the corresponding amplitude is plotted versus the frequency in a log-log plot. The fundamental frequency is 107 kHz, with more than 11 visible harmonics whose amplitude decays exponentially. A similar behavior can be observed in CDW-systems [31, 32] which is described in detail in Sec. 2.4. The CDWs exhibit a nonlinear increase of the current and a current oscillation as well after applying a small voltage. The fast FT of the time-dependent current in CDW-materials reveals the same behavior as illustrated in Fig. D.18. However, VO_2 can be considered as a Mott-Isolator, the physics of a charge density wave cannot be used to explain the phenomena. Several interpretations exist:

- Fisher [417] proposed the first interpretation for the current oscillations. He suggested that semiconducting domains are created at the contacts in the metallic matrix, which start to move with a certain velocity towards the opposite contact. However, the theoretical frequency of the domain movement was only a few Hertz at which the observed frequency is in the Kilohertz regime. Thus, this approach cannot be used to explain the effect satisfactorily.

- In Ref. [425, 426] the authors suggest another explanation where they consider the whole setup as an electronic circuit which consists of a load resistor R_L, the sample resistance R_{Sam}, and an external capacitance C_{Ext}. These parameters have the largest influence on the temporal behavior of

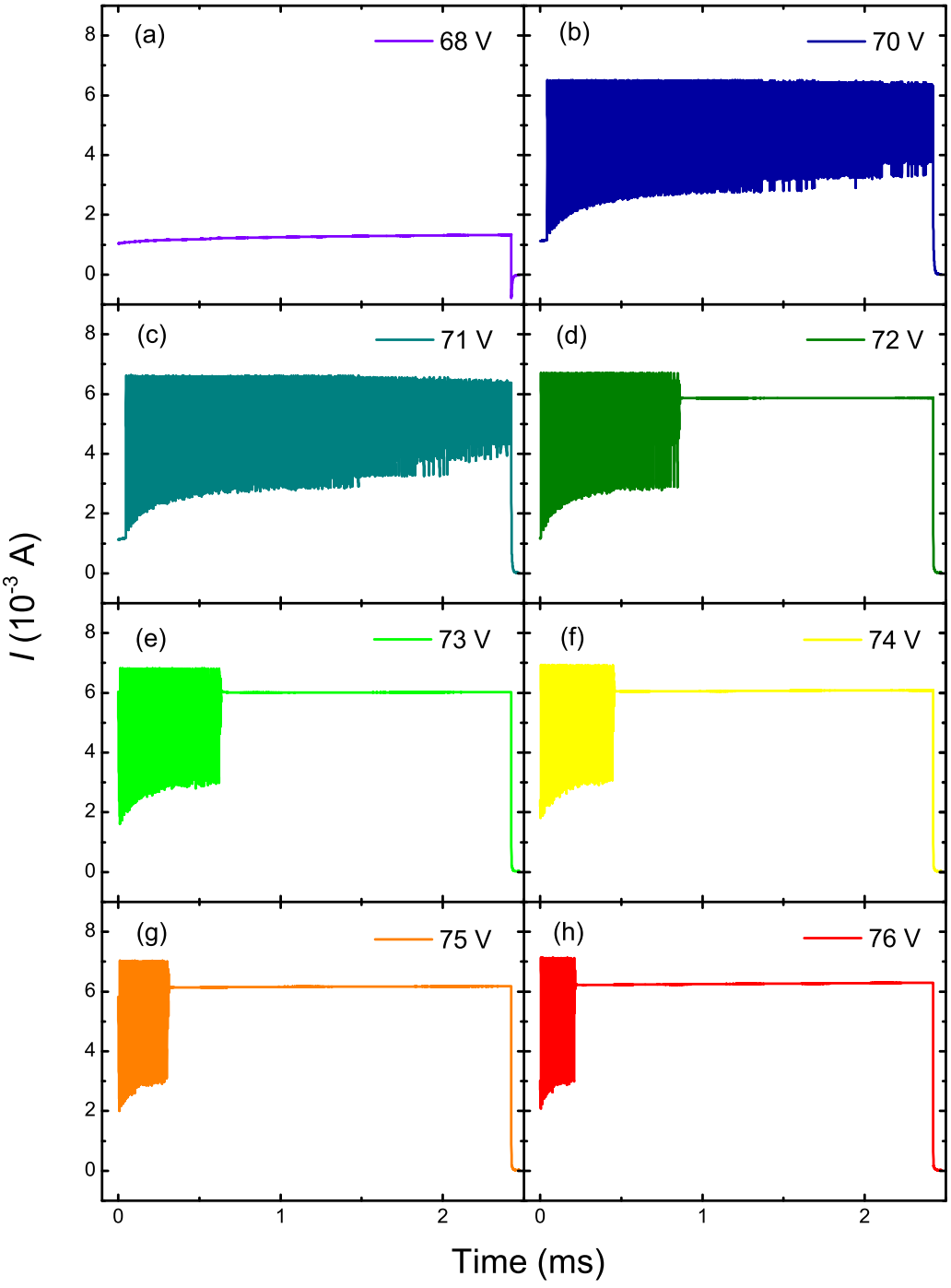

Figure D.20: Time-dependent current pulse $I(t)$ for different source voltages U_S. Below a threshold voltage U_{Th1} the current is constant (a), but above the oscillations appear ((b)-(c)). If the voltage is further increased, a metallic state is established after the oscillations are disappeared ((d)-(h)).

the current. However, the capacitance of the film C_{Sam} and the contact capacitance were completely neglected in the publications. Beaumont et al. [427] adapted this model successfully to studies on the oscillation characteristic. The current oscillations can be understood in the framework of Ref. [425, 426] as follows:

1. Above a threshold voltage U_{Th} the film, i.e. the individual VO_2-islands switch into a high-conducting state causing an abrupt increase of the

current. The maximal current is limited by the external load resistor R_L. Therefore, the current stays below a certain upper current limit I_{Th} so that the metallic state cannot be stabilized.

2. After the film is conductive the voltage U_{Sam} drops below the threshold voltage U_{Th1}. The film becomes insulating again. The dropping current charges the external capacitance, leading to a certain decay time τ_{RC}. In our case, a time constant τ_{RC}=4 µs was derived from the fit in the inset of Fig. D.17; its absolute value depends on external parameters like the load resistor R_L and the external capacitance C_{Ext}.
3. After that, the film is again insulating and the whole process is repeated, leading to oscillations.

- Another model includes the percolative nature of the phase transition where the insulating phase coexists with the metallic phase [428]. At the phase transition several metallic islands are formed; with deceasing temperature, they form macroscopic areas until the whole film is metallic. Driscoll et al. [428] performed simulations based on that assumption. They assumed a network of independent VO_2-islands which have different capacitive and resistive values. They studied the influence of a temperature increase on the electric current, but they could not reproduce the experimental observations satisfactorily. However, the behavior could be simulated accurately by assuming a electronically controlled transition. Furthermore, the increase of the minimum current in the oscillations could be nicely described by the model and assigned to a thermal effect.

In the contour plot D.19 (a) and (b) the amplitude of the oscillations is depicted for different voltages. Similar to Fig. D.18, Fig. D.19 (a) displays different resonance frequencies. Below the fundamental frequency f_0 at 120 kHz a weak resonance appears which are caused by initial oscillations at the beginning of the pulse. By increasing their source voltage U_S, the amplitude decreases and the resonance frequencies do not exhibit a shift. The Fast FT were hereby performed for the whole time interval (2.2 ms) where oscillations appear.

However, the pictures change if we take into account only the first 200 µs of the oscillations. The results are displayed in Fig. D.19 (b) where the amplitude of the single frequency components is plotted as a function of the applied voltage. With increasing voltage the resonance frequency shifts from initially 65 kHz to 117 kHz. The resonance frequency approaches asymptotically the threshold frequency of 125 Hz derived in Fig. D.19 (a). Driscoll et al. [428] and Kim et al. [426] have observed a similar shift. In the former publication the same asymptotic behavior was observed whereas in the latter case the resonance exhibits a linear evolution. The factors, which influence the maximal frequency f_0, are the external parameters R_L, L_{Ext}, and C_{Ext}, as the time constant τ_{RC} depends on them.

To our knowledge the presented measurements are the first with a pulse length longer than 100 µs. It is therefore not surprising that in comparison to the published results, further effects like the constant resonance frequency f_0 as a function of source voltage are observed. Up to now, it was assumed that f_0 can be tuned by U_S and hence, simple devices like clocks or internal frequency timer for computer chips can be built. This assumption is only valid for short pulses (< 100 µs) as we have shown in the last paragraph. In this context, more stud-

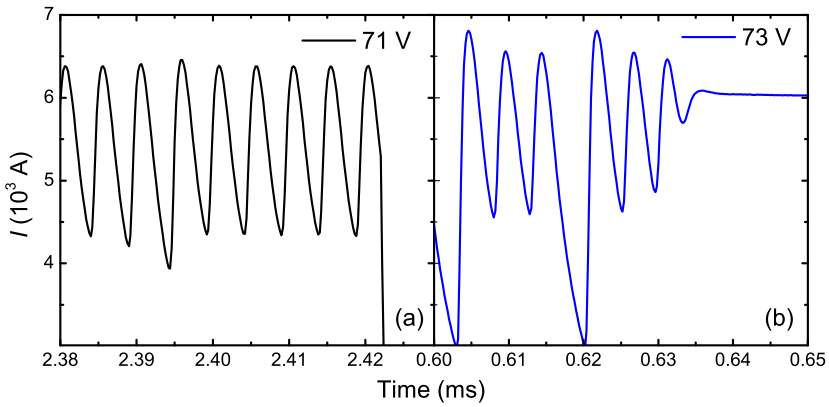

Figure D.21: (a) Current oscillations at the end of voltage pulse for an applied voltage U_S of 71 V. The phase transition is not completed. (b) Oscillations of the current for U_S = 73 V. After 640 µs the oscillations stop and the current reaches a constant value marking the established metallic phase.

ies are necessary on long voltage pulses which are more relevant for industrial applications. There, the main focus should be on the combination of different external parameters and their influence on the oscillations and switching behavior.

In Fig. D.20 (a)-(h) the temporal evolution of the current density $J(t)$ is plotted for various voltages U_S. Below the threshold voltage U_{Th1}=69 V the current is constant and drops to zero after the voltage pulse is switched off. Above U_{Th1} the current starts to oscillate which persists for the whole length of the pulse. In all cases the minimum current of the oscillations increases while the maximum current stays constant. This indicates a slow heating of the film. The sample resides in a bistable state where it switches between the insulating and conducting state. Only at even higher voltages, the oscillations cross over into the constant high conducting state. In this case, the constant value is lower than the maximal values of the oscillations. This is caused by an overshoot of the oscillating current which is similar to the overshoot at the onset of the pulse. With increasing voltage the number of oscillations diminishes until they are vanished completely above U_{Th2}. There, the metallic state is directly developed and increases only slightly with the applied voltage. In already published measurements [426, 428] the pulses (< 50 µs) were too short to actually record this voltage dependent behavior of the oscillations and the immediately transition into the high conducting states above U_{Th2}.

In Fig. D.21 (a) the oscillations shortly before the end of the pulse are visualized. At U_S=71 V the amplitudes and periods are constant and do not change. For slightly higher voltage (U_S=73 V) the frequency is not changing as well, but the amplitude fluctuates enormously (see Fig. D.21 (b)). This is caused by the electric-induced heat which cannot dissipate fast enough to the environment and substrate. Thus, the oscillations cannot reach their minimal current value of the initial temperature (295 K) anymore. In that case, the minimum current corresponds to the current at higher temperatures as well as close to the transition. This is the reason why it is inevitable that the phase transition is induced thermally above a certain U_{Th2}.

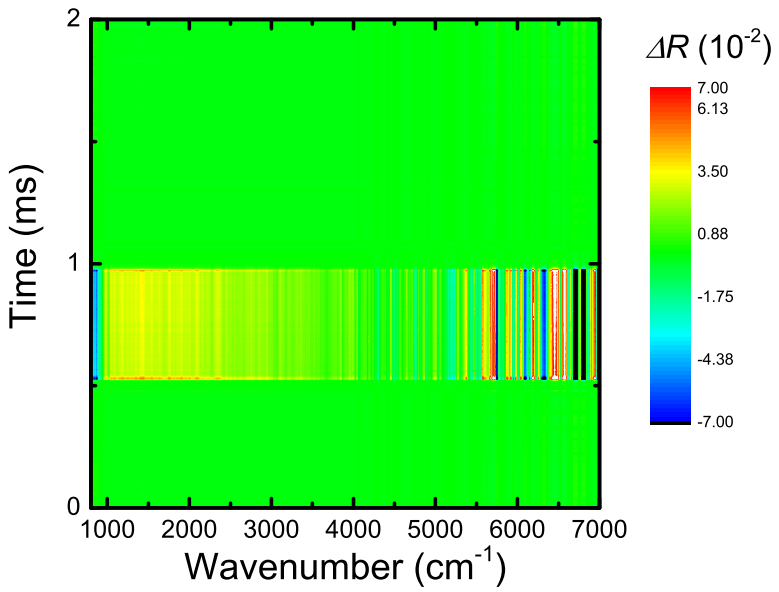

Figure D.22: Contour plot of $\Delta_t R(\nu, t)$ at 295 K for a time range from 0 ms to 2 ms as well as for a spectral range from 800 cm^{-1} to 7000 cm^{-1}. The signal was recored 500 µs before a voltage pulse U_S=100 V and τ=500 µs was applied. Therefore, no changes occur in this range. With the onset of the pulse $\Delta_t R(\nu, t)$ is strongly altered. The signal persists for the whole pulse length and drops afterwards back to its initial value. The strong fluctuations above 5000 cm^{-1} can be ascribed to a high noise level, due to the very small changes of $\Delta_t R(\nu, t)$.

D.4.5 *Time-resolved infrared spectroscopy of the electric-induced phase transition*

Additionally to the time-resolved transport measurements, the time-dependent change of the reflectivity was studied for VO_2 on Al_2O_3 when a short voltage pulse was applied. To the best of our knowledge, this is the first kind of investigation recording the temporal and spatial evolution of the spectrum. Therefore, the sample was placed below an IR-microscope (see Sec. 4.1.2). The time-resolved spectra were recorded by the Step-Scan technique. The time resolution was set to 6 µs with 500 recorded time points, corresponding to a time range of 3 ms. The signal was averaged over 20 scans to improve the SNR. The spectral resolution was 16 cm^{-1} for a spectral range from 800 cm^{-1} to 7000 cm^{-1}. The spectrometer served as control unit triggering the Avtech pulse generator which sends the 500 µs long voltage pulse with a delay of 500 µs to the sample. A serial load resistor R_L of 10 kΩ was placed in the circuit to protect the sample.

A contour plot of the time-dependent change of the reflection $\Delta_t R(\nu, t)$ within a time range of 2 ms is displayed in Fig. D.22. The recorded change of the intensity spectrum $\Delta S_{AC}(\nu, t)$ of the sample was divided by the spectrum of the light source $S_{Mi}(\nu)$ to calculate $\Delta_t R(\nu, t)$. While the first 500 µs no change can be observed, 20 µs after the pulse was created, a strong alternation of the spectrum sets in. In more detail, $\Delta_t R(\nu, t)$ is positive above 1000 cm^{-1} which corresponds to an increase of the reflectivity (yellow and orange color). Above 5000 cm^{-1} the noise strongly grows as the changes of $\Delta S_{AC}(\nu, t)$ are very small and fluctuates strongly for value close to zero. Below 1000 cm^{-1}, the reflectivity is reduced and hence, $\Delta_t R(\nu, t)$ is negative (blue color). When the voltage pulse is switched off

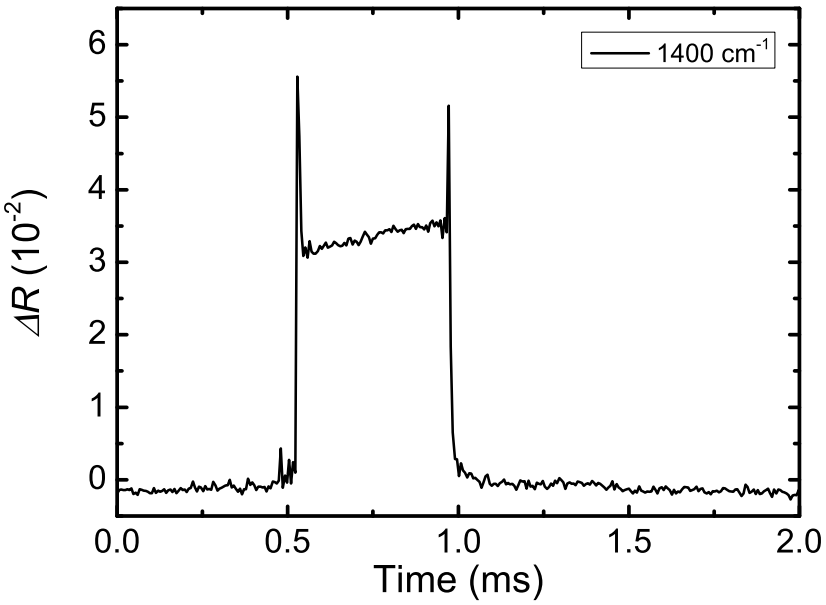

Figure D.23: Temporal evolution of $\Delta_t R(\nu, t)$ at $\nu = 1400$ cm^{-1}. The signal rises steeply at 500 µs and stays almost constant. At the end of the pulse, $\Delta_t R(\nu, t)$ drops down to zero. The overshoot of the signal is caused by a high excess current. This external, parasitic current is caused by the switching of the film and couples to the electric circuit of the spectrometer.

at 1 ms, $\Delta_t R(\nu, t)$ directly drops down to zero at 1 ms which correlates with the switch-off of the voltage pulse.

In Fig. D.23 the temporal evolution of $\Delta_t R(\nu, t)$ at 1400 cm^{-1}is depicted. The signal is almost zero at the beginning. The deviation can be ascribed to a small offset in the detector signal, which is negligible compared to the following strong modification of $\Delta_t R(\nu, t)$. The rise and fall times, τ_{rise} and τ_{fall}, respectively, are below the time resolution of 6 µs. They are probably on the same time scale as the time constants in the transport measurements in Sec. D.4.4. The overshoot is caused by an extreme rise of the current due to the switching of the film. This parasitic current peak induces fluctuations in the electronics of the spectrometer, the detector, and the A/D-converter. During the pulse the signal exhibits a slight increase which is an indicator for a thermal effect or for the enlargement of the filament dimension. It is obvious that $\Delta_t R(\nu, t)$ only persists as long as the voltage pulse is switched on. This is in strong contrast to a thermal-induced effect where the signal would drop down slowly in an exponential way.

Fig. D.24 (b) displays $\Delta_t R(\nu, t)$ at 900 µs in comparison to the thermal-induced change of the reflectivity $\Delta R(\nu)$ from the insulating to the metallic state (see Fig. D.24 (a)). Below T_{MI} the changes of $\Delta R(\nu)$ are very small, but above 340 K the modification are significant. The spectrum can be separated into two regions. In the energy range above 1000 cm^{-1}the signal is positive because of the metalization of the film, but negative below 1000 cm^{-1}with a minimum at 850 cm^{-1}. In the insulating state $\Delta R(\nu)$ displays this minimum due to the temperature-dependent optical constants of VO_2 in combination with the ones of Al_2O_3 [411]. It disappears due to the high reflectivity of VO_2 in the metallic phase. In principle, the positive as well as the negative region can be used as an identifier to disentangle which state is electronically induced in comparison to the thermal state. In order to determine the actually physical state, the ratio between the maximum and minimum value was calculated. $\Delta_t R(\nu, t)$ resembles in (a)

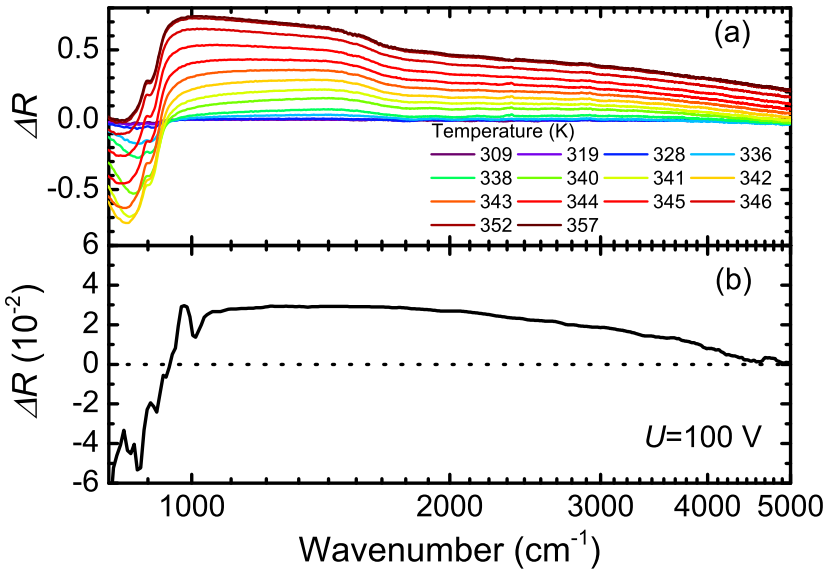

Figure D.24: Comparison between the change of the steady-state and time-resolved spectra. (a) Difference spectra between the reflection spectrum at 295 K and the spectra from 309 K to 357 K (substrate Al_2O_3). The increase of $\Delta R(\nu)$ above 1000 cm^{-1} is a fingerprint of the transition into the metallic phase. The minimum at 850 cm^{-1} originates from a combination of the temperature-dependent optical quantities [411] of the VO_2-film and the substrate. (b) Cross section of the contour plot in Fig. D.22 at 900 µs from 800 cm^{-1} to 5000 cm^{-1}. The shape of the spectrum accords perfectly with $\Delta R(\nu)$ from (a).

$\Delta R_{343\ K-295\ K}$ which is located at the vicinity of the thermally-induced phase transition.

When comparing the absolute values, it is apparent that $\Delta_t R(\nu, t)$ is by a factor of 10 smaller than the static change $R(\nu)$ for 343 K. As an area of 30×30 μm^2 was studied, we, therefore, conclude that the electronically-induced filaments have an average width of about 3 µm. This means that not the whole film is transformed. These results compare well with literature. In Fig. D.25 pictures of a VO_2-film with two gold contacts are illustrated. By applying a constant current, a conducting channel is formed. The width of the filament is on the micrometer scale which is in excellent agreement with our estimation of 3 µm.

Further spectral and spatial resolved methods were performed by other groups [429, 430] with constant voltage or current, but always without any time resolution. As aforementioned under these conditions heating is the reason for the transition. To the best of our knowledge, up to now only one time-resolved infrared measurement was performed on VO_2 [431]. The study concentrated on a VO_2-film on sapphire substrate measured at a synchrotron beamline at a sample temperature of 349 K (T_{MI}=359 K). The spatial resolution was 10 ×10 μm^2.

In this case, the time-dependent raw signal of the detector was only examined as a function of the distance from the contacts, but not the spectral evolution of the reflectivity. From that it was concluded that Joules heating must be the reason for the switching effect. This is based on rather poor arguments as neither the absolute temperature nor the actual state can be determined.

In contrast, our study proofs that due to the similarities between the difference in spectra the film is driven by the electric-field into an intermediate, high conducting state. There, electron correlations [395] dominate the physical properties, suggesting that the induced transition is of electronic nature.

D.5 SUMMARY AND CONCLUSION

Thin films of VO_2 grown on Al_2O_3 as well as on SiO_2/Si substrates were studied extensively with various methods. The main goal of the project was to examine the behavior of the films under the influence of strong electric fields which results in a switching into a so-called high conducting phase (HCP).

AFM-pictures of the films, shown in Sec. D.4.1 reveal an island-like growth for both substrates. The diameter of the islands is in average about 100 nm exhibiting a height of 90 nm. The beforehand determined film thickness was specified with 200 nm resulting in an effective thickness of about 100 nm deviated from the AFM measurements.

In our measurements presented in Sec. D.4.1 we observe a conductivity jump of three orders of magnitude at the transition temperature $T_{MI} \approx 343$ K. The width of the transition is about 6 K and agrees well with the literature values. The small width, large jump and the high transition temperature are criteria for high quality films. The estimated values for the activation temperature $\Delta E_{Akt.}$ and the charge carrier density N_C agree very well with literature values. The here presented theoretical calculations of the band structure based on the DFT-theory with a GGA-functional reproduce successfully that VO_2 is a metal in the rutile phase, but an insulator with an energy gap of about 0.65 eV in the monoclinic phase. The determined band structure is in full agreement with published data and supports Goodenough's suggested model of the orbital ordering. The calculated optical spectra agree qualitatively with the published data. Therefore, in Sec. D.4.3 we were able to assign the features in the measured reflectivity spectra to the corresponding calculated electronic excitations.

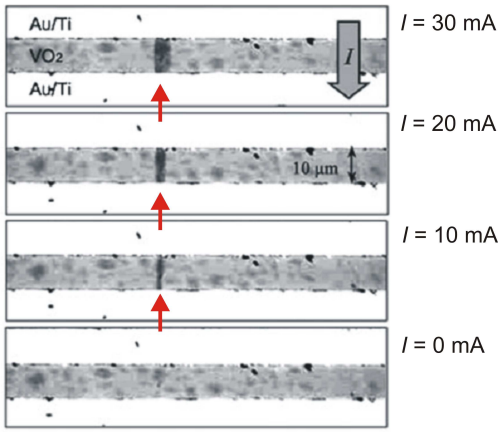

Figure D.25: Pictures of a VO_2-film between two Au-contact strips for four different currents I. With increasing current the conducting path broadens highlighted by an arrow. Adapted by [421].

The reflectivity spectra of the film were modeled in the framework of a two layer-system. Depending on the phase, Drude and/or Lorentz fits were performed. By plotting the parameters of the Drude feature as a function of temperature the phase transition can be traced and the transition temperature determined. The σ_{DC} agrees well with the literature values, but the plasma frequency ν_p deviates by a factor of 2 from the literature, probably to the limited frequency range and the interdependence results of ν_p on τ_{Sc}. γ_{Sc} diverges at the phase transition and drops to half of its maximum value, effecting the plasma frequency. The divergent behavior is attributed to correlation effects at the phase transition.

In the time-resolved transports measurements the film exhibits a switching from a low conducting initial state into a metallic high conducting state at temperatures below T_{MI}. Thereby, the voltage has to exceed a certain threshold values U_{Th1} to induce the transition. The switching is accompanied by a delay time τ_d which decreases with increasing source voltage U_S. Furthermore, avalanche-

like switching processes occur which become noticeable as a slope of the current $I(t)$. They result from the sudden enlargement of the conducting channel VO_2 and the switching of single VO_2-islands or island clusters.

The following arguments support a thermal effect as the reason for the switching:

- The delay time τ_d decreases with increasing voltage; this is expected for a thermal process, as the electric thermal power increases as well.
- It was shown experimentally that for constant currents and voltages the phase transition is thermally induced [358].
- The electric oscillations can be caused by repeated heating and cooling cycles of the VO_2-film when the applied voltage falls below a critical voltage U_{Th1}. As soon as the voltage exceeds a second threshold voltage U_{Th2} the system cannot cool down fast enough so that it remains in the metallic phase. Furthermore, the observed frequency components of the oscillation do not reveal any dependence on the source voltage when the whole pulse is considered.
- The filaments change their dimension between the contacts, leading to a multiple step behavior during the induced phase transition.
- The performed calculations of τ_d based on a simple thermodynamic model agree very well with our experimental observations [419].

Other arguments endorse an electronically induced effect:

- No modifications appear within the pulse and especially before the switching process. For a thermal effect the current would vary in the metallic phase.
- The switching process from the LTP-phase to the HTP-phase occurs within less than < 1 µs which is too fast for a thermal-induced effect. Such switching times are observed for electronic processes.
- For rather high voltages, the conducting filaments break down which can be attributed to the damage of the contacts; they cannot resist the high current load due to the large contact resistance.
- The oscillations, occurring within the first 100 µs, reveal a dependence on the applied voltage which indicates an electronic effect as the origin. This was successfully simulated by Damascelli et al. [432].
- The multi-step behavior can be also induced by an electronic effect when the VO_2-islands are switched individually.
- The time-resolved infrared measurement in Fig. D.23 reveals an abrupt increase (< 6 µs) and a drop of the reflectivity at the end of the voltage pulse. It does not show any slow relaxation of the signal which would indicate a thermal-induced state. The modification of $\Delta_t R(\nu, t)$ agrees with an hypothetically temperature change from 295 K to 343 K. This corresponds to the temperature range where the phase transition occurs and correlation effects play the major role.

There are several arguments for a thermal-induced, but also for an electric-induced transition. However, one can definitely conclude that going from a constant electric field to a short electric pulse of a few microseconds the impact of Joule heating diminishes and below the sub microsecond regime electronic effect must dominate (see Ref. Driscoll et al. [428]). However, our measurements were one of the first with a high time-resolution in transport and optical measurements, even shorter time scales are necessary. Especially, techniques with a temporal, spatial and spectral resolution like ultrafast near-field microscopy could deliver very important information about the nature of the high conducting state and the dimensions of the conducting filament. However, already extended infrared studies on the nanosecond time scale with the Step-Scan technique would be desirable to investigate the electric responds on pulses shorter than 10 µs.

From a technical perspective, it is even more important to gain information fabrication of high quality metal/VO_2-contacts. The studies performed in the framework of this thesis reveal that especially the contacts break down under high load, leading to their destruction. Therefore, one has to concentrate on the examination of possible contact materials (for example titanium with a working function of 4.3 eV), the morphology of the film and the influence of impurities on yielding ohmic contacts.

E

HEATING EFFECT BY LASER RADIATION

Starting point is the inhomogeneous heat conduction equation:

$$\vec{\nabla}^2 T(\vec{r},t) - \frac{\rho C_p}{\lambda_{\text{therm}}} \frac{\partial T(\vec{r},t)}{\partial t} = -\frac{Q_p(1-R)\alpha e^{-\alpha z} f(\vec{r}) q(t)}{\lambda_{\text{therm}}} \tag{E.1}$$

On the left side of the equation the first term is the spatial derivative of temperature describing the spatial heat flux, the second term reflects the time-dependent change of temperature which is normalized to the thermal diffusivity $\kappa = \frac{\lambda_{\text{therm}}}{\rho C_p}$. The right side considers the heat input due to a laser pulse with the temporal and spatial profile $q(t)$ and $f(\vec{r})$. In addition, the equation contains further intrinsic material parameters: the reflectivity $R(\nu)$, the irradiance Q_p and the absorption coefficient α. For $t > \tau_p$, a laser pulse with a constant pulse length of τ_p=8 ns and a spatial uniform profile with a diameter of $d = 600\,\mu\text{m}$ was assumed to determine the following dependence of temperature with distance z from the surface as function of time t by solving Eq. E.1:

$$\begin{aligned} \Delta T(z,t) = \frac{2Q_p(1-R(\nu))}{\lambda_{\text{therm}}} \sqrt{(\kappa\tau_p)} \\ \cdot \left[\sqrt{(t\tau_p)}\,\text{ierfc}\left(\frac{z}{2\sqrt{\kappa t}}\right) - \sqrt{(t\tau_p^{-1}-1)}\,\text{ierfc}\left(\frac{z}{2\sqrt{\kappa(t-\tau_p)}}\right)\right] \end{aligned} \tag{E.2}$$

with

$$\text{ierfc}(x) = \int_x^\infty \text{erfc}(y)\,\text{d}y \tag{E.3}$$

for z=0 the equation arises from Eq. 5.25 which was derived from Eq. E.1

$$\Delta T(t) = \frac{2Q_p(1-R(\nu))}{\lambda} \frac{(\kappa\tau_p)^{0.5}}{\pi^{0.5}} ((t\tau_p^{-1})^{0.5} - (t\tau_p^{-1}-1)^{0.5}) \tag{E.4}$$

for $\tau_p > t$. The temporal temperature profile for TTF-CA, derived from Eq. E.2, is plotted in Fig. E.1 for different positions z inside the sample. The used parameters correspond to the values in Sec. 5.3.6. With increasing distance from the sample surface the maximum of the temperature change shifts to later points in time. At a depth of 500 nm the maximum of the temperature change is located at 50 ns and resides below the transition temperature of 81.5 K. In a distance of 100 nm the temperature is above T_{NI}, but drops sharply after 100 ns below it.

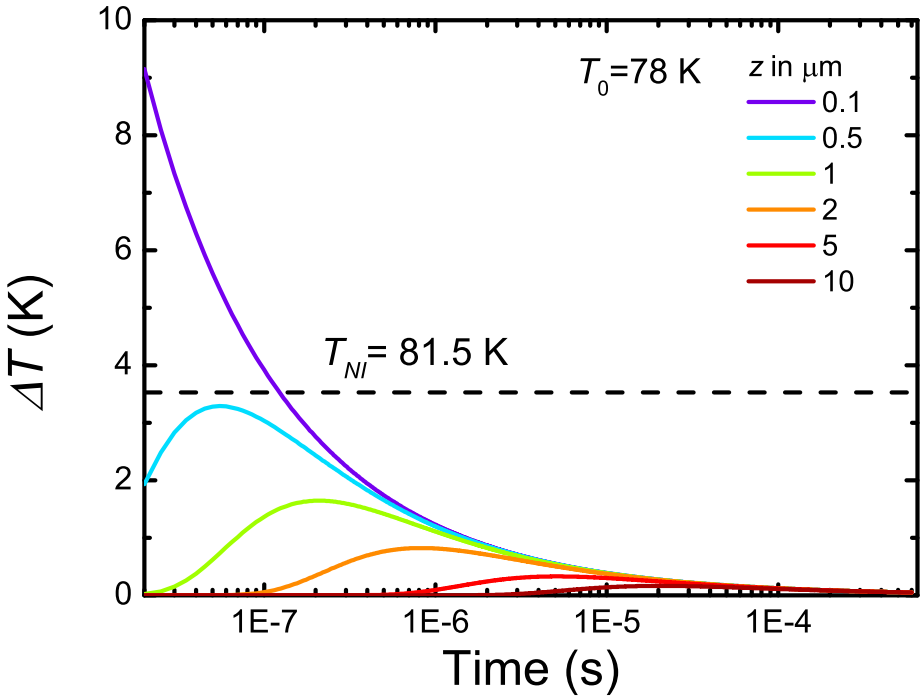

Figure E.1: Temporal evolution of the change of sample temperature of TTF-CA for a laser intensity of 0.71 mJ/cm^2 at 78 K derived from Eq. E.2. Starting from a depth of 500 nm the maximum of the temperature profile stays clearly below $T_{\mathrm{NI}} = 81.5$ K.

F

LIGHT-MATTER INTERACTION

DRUDE MODEL

In solid-state materials different kinds of electronic states can be excited depending on the electronic bands being empty, full, or partially occupied. Furthermore, this thesis is about solid-state compounds consisting of small building units which are mainly composed of organic and inorganic molecules. Aside the electronic states, described by the electronic bands in bulk material, they exhibit vibrational states which can be excited, for instance, by infrared light. Based on the electronic transitions generally one can distinguish between intra- and interband transitions. First of all, the intraband transitions will be treated. Especially in the case of metal they contribute a lot to the optical conductivity in the low frequency range. Starting from the Drude model[433] describing a non-interacting electron gas one can derive the following equation for damped charge carriers in an external electric field $\vec{E}(t) = \vec{E}_0 e^{-i\omega t}$:

$$m_e \frac{d\vec{r}^2}{dt^2} + \frac{m_e}{\tau_{Sc}} \frac{d\vec{r}}{dt} = -e\vec{E}(t). \tag{F.1}$$

The second term on the left side describes the damping of the charge carrier motion due to elastic scattering at impurities, phonons or defects. The strength of the damping depends on the relaxation rate τ_{Sc} which defines the elapsed time between two scattering events. After solving the differential equation one receives the following expression for the complex optical conductivity function $\hat{\sigma}(\omega)$:

$$\hat{\sigma}(\omega) = \frac{N_C e^2 \tau_{Sc}}{m_e} \frac{1}{(1 - i\omega\tau_{Sc})} = \frac{\sigma_{DC}}{(1 - i\omega\tau_{Sc})} \tag{F.2}$$

with the charge carrier density N_C and the charge carrier mass m_e . From equation F.2 the real and imaginary conductivity, $\sigma_1(\omega)$ and $\sigma_2(\omega)$, can be easily derived:

$$\sigma_1(\omega) = \frac{\omega_p^2 \tau_{Sc}}{4\pi} \frac{1}{1 + \omega^2 \tau_{Sc}^2} \tag{F.3}$$

$$\sigma_2(\omega) = \frac{\omega_p^2 \tau_{Sc}}{4\pi} \frac{\omega\tau_{Sc}}{1 + \omega^2 \tau_{Sc}^2}. \tag{F.4}$$

The parameter $\omega_p = \frac{N_C e^2}{m_e} = \frac{\sigma_{DC}}{\tau_{Sc}}$ is the plasma frequency and can be used to calculate the number of free charge carriers if the mass m_e is known. In this model the quantum mechanical nature of the charge carriers has been neglected and solely treated classically. If one includes the quantum mechanical consideration of Sommerfeld, the electron-electron interaction and other interaction processes, the extended form of the Drude equation F.2 is obtained in which the charge carrier mass m_e and the scattering time τ_{Sc} are replaced by a modified frequency-dependent effective charge carrier mass $m^\star$ and scattering time τ_{Sc}^*, respectively [103].

DRUDE-LORENTZ MODEL

In the case of interband transitions an electron is excited by a photon from the occupied valence band into the unoccupied conduction band, where a hole is created in the valence band. This kind of transition appears, for instance in systems with an energy gap like semiconductors or insulators, whose resonance energy is predominantly above the optical response of the free charge carriers. Here, the transition can occur directly or indirectly from the valence to the conduction band, but always under premise that ($E_L(\vec{k}) + \hbar\omega = E_V(\vec{k}')$) and momentum ($\vec{k} \pm \vec{q}_{Phonon} = \vec{k}'$) are conserved. The optical response can be derived from a classic model of a damped harmonic oscillator. Thereby, a similar equation of motion as the Eq. F.1 is used, but, however, with the additional appended term $D\vec{r}$ describing the fundamental resonance frequency of the harmonic system.

$$m_e \frac{d\vec{r}^2}{dt^2} + \frac{m_e}{\tau}\frac{d\vec{r}}{dt} + D\vec{r} = -e\vec{E}(t) \tag{F.5}$$

After solving the DE and further transformations the complex optical conductivity is

$$\hat{\sigma}(\omega) = \frac{Ne^2\tau}{m_e}\frac{\omega}{(\omega + i(\omega_0^2 - \omega^2)\tau)}. \tag{F.6}$$

Thereby, $\omega_0 = \sqrt{\frac{D}{m_e}}$ is the resonance frequency of the undamped harmonic oscillator, depending on m_e and on the restoring constant D, and the number of excited particles N. τ is the life time of the excited states and its reciprocal value corresponds to the line width of the resonance. Eq. F.6 can be separated into an imaginary and real part:

$$\sigma_1(\omega) = \frac{\omega_p^2}{4\pi}\frac{\omega^2}{\tau(\omega_0^2 + \omega^2)^2 - \frac{\omega^2}{\tau}} \tag{F.7}$$

$$\sigma_2(\omega) = -\frac{\omega_p^2}{4\pi}\frac{\omega(\omega_0^2 - \omega^2)}{(\omega_0^2 - \omega^2)^2 - \frac{\omega^2}{\tau^2}} \tag{F.8}$$

This model is not only valid for electronic excitations, but also for transitions between different vibrational levels.

FANO MODEL

In the early sixties Fano [434] presented his highly cited theoretical work about the inelastic scattering process of electrons from the $1s^2$ state in a helium atom into the 2s2p state. There he described the excitation of the electron from the s-orbital into the p-orbital which resides in an energetic point of view in a continuum of undisturbed states.

In the experimental excitation asymmetric resonances have been observed unexpectedly. Fano [434] could model this line shape with the help of his theory by taking into account the interaction of the excited state with a continuum of states.

Such a coupling of discrete states of any kind to a continuum is not observed only by scattering experiments, but also, for instance in organic conductors, where molecular vibrations interact with the electronic background coming from

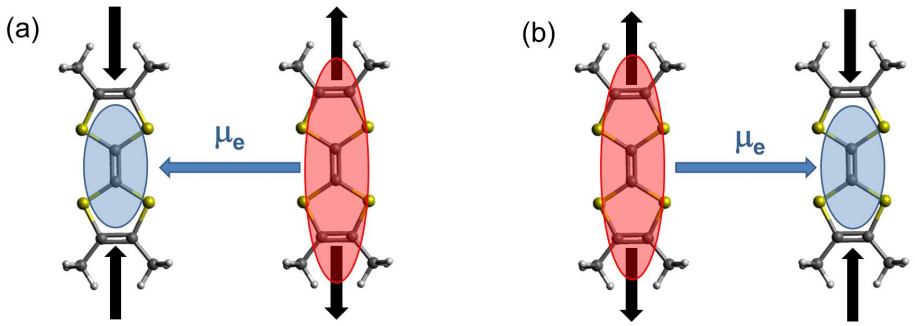

Figure F.1: (a) Both molecules oscillate out-of-phase, whereby the HOMOs are modulated accordingly (highlighted by the blue and red shaded areas). By the different charge density on the molecules an electric dipole μ_e along the connection axis between the molecules is induced. By this, infrared light can couple to the transition dipole moment. (b) After half of a period the modification of the HOMOs is the opposite. This corresponds to the picture that a charge is pumped forth and back between the two neighboring molecules.

broad electronic intra- and interband transitions. The results are the asymmetric Fano line shapes of the vibrational features which can be seen in the spectra of Sec. 5.1.4 and 5.3.5. This specific case is referred to as electron-molecular vibration (emv)-coupling where symmetric molecule oscillations modify the HOMO of the molecule and, therefore, become infrared-active. For simplicity we assume that a second molecule of the same type[1] is located parallel to the first one, forming a dimer. Both molecules vibrate with the same symmetric mode but with a phase shift of π, thus the modification of the HOMOs is as well shifted by π. In Fig. F.1 is depicted that by this an electric dipole moment is induced along the connecting line between both molecules. Because of the light mass of the electrons in comparison to the nucleus the temporal change of the HOMOs takes place instantaneously together with molecular vibrations so that the dipole moment changes with the same frequency as the resonance frequency of the molecular mode. This correlates with the idea that a charge is transferred from one molecule to the other and back again. Due to the phase shift this transition becomes infrared-active. Only gerade molecule modes can couple effectively to the HOMO whereas g_i specifies the coupling strength between the HOMOs and the molecular vibration and can be calculated as follows:

$$g = \frac{\partial E_{\mathrm{HOMO}}}{\partial Q_i} \tag{F.9}$$

with the energy of the HOMOs E_{HOMO} and the generalized normal coordinate Q_i of the symmetric vibration. In the case of TTF, TMTTF, BEDT-TTF and many other molecules the gerade modes containing the inner C=C double bonds modify the HOMO the strongest. This kind of excitation only occurs in relation with a broad electronic background whereas the vibrational features in the spectra cannot be modeled anymore by the Lorentz function. That is why the emv-coupled modes

1 In general, it does not have to be the same type of molecule.

have to be fitted with the so-called Fano function [432, 434] which contains several parameters:

$$\sigma_1(\omega) = \sigma_0 \frac{\gamma\omega[\gamma\omega(q^2-1) + 2q(\omega^2-\omega_0^2)]}{(\omega^2-\omega_0^2)^2 + \gamma^2\omega^2} \tag{F.10}$$

$$\sigma_2(\omega) = \sigma_0 \frac{\gamma\omega[(q^2-1)(\omega^2+\omega_0^2) - 2\gamma\omega]}{(\omega^2-\omega_0^2)^2 + \gamma^2\omega^2}. \tag{F.11}$$

γ is the line width, σ_0 the amplitude, ω_0 the resonance frequency and q the coupling strength.

G

KKT PROGRAM CODE

The Kramers-Kronig transformation KKT was implemented in the below-mentioned code by using the equation

$$\theta(\nu_i) = -\frac{\nu_i}{\pi}\int_0^\infty \frac{\ln R(\nu) - \ln R(\nu_i)}{\nu^2 - \nu_i^2}\, d\nu \tag{G.1}$$

proposed in Ref. [435]. Furthermore, the calculation of the optical constants is performed according to the description in Ref. [103]. The script can be executed in the mathematical software suite Scilab which is closely related to Matlab. Comparison of the calculations carried out with this code, the widely-used KK program, and the C based KKT program written by the bachelor student Andreas Abele shows only small differences in the high frequency part of the extrapolated region at which the differences on the measured spectral range are marginal and negligible. The small discrepancies between the different programs originate from the different numerical integration methods of the programs at which in the presented code the trapezoid method is applied. Therefore, it is important to chose a small step size for the numerical integration. This reduces the numerical errors. Furthermore, it is important that the high frequency extrapolation has to be carried at least up to 500000 cm^{-1}as the line shape of the spectral feature, for instance the phonon lines, can be influenced and thus falsified by a too small chosen frequency range.

```
global epsilon lightc
// Global parameters
epsilon=8.8542*10^(-12);
lightc=2.9979*10^8;
// For several files
for i=["filename_prefix_list"]
    temp=string(i)
    clear R omega Re
    // Directory
    dire='C:\test'
    chdir(dire)
    // File name
    R=fscanfMat(temp+"filename")
    // Wavenumber
    omega=R(:,1);
    // Reflectivity data
    Re1=R(:,2);
    // Size control
    if size(omega,1)>size(omega,2);
        omega=omega';
    end; if size(Re1,1)>size(Re1,2);
        Re1=Re1';
    end;
    Re=Re1;
    // Searching for negative values
    indnotRe=find(Re1<=0)
    Re(indnotRe)=[]
```

```
    omega(indnotRe)=[]
    f=scf(0);
    plot2d(omega,Re);
    // Size of the vectors
    g=size(omega,2)
    phi=zeros(size(Re));
    // Calculation of Phi,a: dumerator, b: denominator
    for j=1:g;
        omega1=omega
        a=(log(Re(1:g))-log(Re(j)));
        b=omega1(1:g).^2-omega1(j)^2;
        zerob=find(b==0)
        b(zerob)=[]
        a(zerob)=[]
        omega1(zerob)=[]
        c=a./b
        // Summation
        d=inttrap(omega1,c)
        phi(j)=(-1/%pi)*d*omega(j);
        clear omega1 a b
    end;
    // Calculation of the optical constants
    n=(1-Re)./(1+Re-2*sqrt(Re).*cos(phi));
    k=(2*sqrt(Re).*sin(phi))./(1+Re-2*sqrt(Re).*cos(phi));
    epsilon1=n.^2-k.^2;
    epsilon2=2*n.*k;
    sigma1=(4*%pi*epsilon*lightc*omega).*n.*k;
    sigma2=(2*%pi*epsilon*lightc*omega).*(1-(n.^2-k.^2));
    data=[omega' Re' phi' n' k' epsilon1' epsilon2' sigma1' sigma2']
    dataK=[omega' sigma1']
    f1=scf(1);
    plot2d(omega,phi);
    f2=scf(2);
    plot2d(omega,k)
    f3=scf(3)
    plot2d(omega,n)
    f4=scf(4);
    plot2d(omega,epsilon1);
    f5=scf(5);
    plot2d(omega,epsilon2);
    f6=scf(6);
    plot2d(omega,sigma1);
    f7=scf(7);
    plot2d(omega,sigma2);
   // Saving data
    fprintfMat(temp+"filename",data,'%25.10f');
    fprintfMat(temp+"filename",dataK,'%25.10f');
end
```

BIBLIOGRAPHY

[1] T. Granier, B. Gallois, L. Ducasse, A. Fritsch, and A. Filhol. *Synthetic Metals*, 24(4):343–356, 1988.

[2] M. Dressel, M. Dumm, T. Knoblauch, and M. Masino. *Crystals*, 2(4):528–578, 2012.

[3] F. Iwase, K. Sugiura, K. Furukawa, and To. Nakamura. *Journal of the Physics Society of Japan*, 78(10):104717, 2009.

[4] T. Peterseim, Á. Antal, M. Dressel, P. Batail, and N. Drichko. *The Journal of chemical physics*, 140(6):064504, 2014.

[5] T. Peterseim, P. Haremski, and M. Dressel. *Europhysics Letters (EPL)*, (109): 67003, 2015.

[6] W. Little. *Physical Review*, 134(6A):A1416–A1424, 1964.

[7] K. Bechgaard, K. Carneiro, M. Olsen, F. Rasmussen, and C. Jacobsen. *Physical Review Letters*, 46(13):852–855, 1981.

[8] T. Ishiguro, K. Yamaji, and G. Saito. *Organic Superconductors*. Springer-Verlag, 1990. ISBN 978-3-642-58262-2.

[9] T. Naito. *Molecular Electronic and Related Materials-Control and Probe with Light*. Transworld Research Network, Kerala, India, 2010 ISBN 978-8178954608.

[10] Peter Lunkenheimer, J. Müller, Stephan Krohns, Florian Schrettle, Alois Loidl, Benedikt Hartmann, Robert Rommel, M. de Souza, C. Hotta, John A. Schlueter, and M. Lang. *Nature Materials*, 11(9):755–758, 2012.

[11] T. Knoblauch and M. Dressel. *Physica Status Solidi (c)*, 9(5):1158–1160, 2012.

[12] Á. Antal, T. Knoblauch, M. Dressel, P. Batail, and N. Drichko. *Physical Review B*, 87(7):075118, 2013.

[13] T. Peterseim, T. Ivek, and M. Dressel. (to be published), 2016.

[14] Y. Kamihara, T. Watanabe, M. Hirano, and Hideo Hosono. *Journal of the American Chemical Society*, 130(11):3296–3297, 2008.

[15] M. Schwoerer and H. C. Wolf. *Organic molecular solids*. Physics textbook. Wiley-VCH, Weinheim, 2007. ISBN 9783527405404.

[16] H. Klauk. *Organic electronics*. Wiley-VCH-Verl., Weinheim, 1. ed., 1. reprint edition, 2007. ISBN 9783527312641.

[17] T. Mori, A. Kobayashi, Y. Sasaki, H. Kobayashi, G. Saito, and H. Inokuchi. *Chemistry Letters*, (6):957–960, 1984.

[18] N. Toyota, M. Lang, and J. Müller. *Low-dimensional molecular metals*, volume 154 of *Springer Series in Solid-State Sciences*. SPRINGER, Berlin and New York, ©2007. ISBN 978-3-540-49574-1.

[19] M. Dressel and N. Drichko. *Chemical Reviews*, 104(11):5689–5716, 2004.

[20] P. Monthoux, D. Pines, and G. G. Lonzarich. *Nature*, 450(7173):1177–1183, 2007.

[21] J. Merino and Ross H. McKenzie. *Physical Review Letters*, 87(23):237002, 2001.

[22] Richard M. Martin. *Electronic structure: Basic theory and practical methods*. Cambridge University Press, Cambridge, UK and New York, 2004. ISBN 9780521534406.

[23] F. Jensen. *Introduction to computational chemistry*. John Wiley & Sons, Chichester, England and Hoboken, NJ, 2nd ed edition, 2007. ISBN 978-0-470-01186-7.

[24] J. Hubbard. *Proceedings of the Royal Society A: Mathematical, Physical and Engineering Sciences*, 276(1365):238–257, 1963.

[25] H. Seo, M. Ogata, and M. Kuwabara. *Journal de Physique IV*, 114:29–34, 2004.

[26] M. Imada, A. Fujimori, and Y. Tokura. *Reviews of Modern Physics*, 70(4): 1039–1263, 1998.

[27] H. Seo and Hidetoshi Fukuyama. *Journal of the Physics Society Japan*, 66(5): 1249–1252, 1997.

[28] T. Mori. *Bulletin of the Chemical Society of Japan*, 73(10):2243–2253, 2000.

[29] A. C. Jacko, H. Feldner, E. Rose, F. Lissner, M. Dressel, Roser Valenti, and Harald O. Jeschke. *Physical Review B*, 87(15):155139, 2013.

[30] H. Seo, C. Hotta, and H. Fukuyama. *Chemical Reviews*, 104(11):5005–5036, 2004.

[31] G. Grüner. *Reviews of Modern Physics*, 60(4):1129–1181, 1988.

[32] G. Grüner. *Density waves in solids*, volume v. 89 of *Frontiers in physics*. Addison-Wesley Pub. Co., Advanced Book Program, Reading, Mass., 1994. ISBN 0-201-62654-3.

[33] L. Landau. *Soviet Physics JETP*, 3:920–925, 1957.

[34] N. F. Mott. *Reviews of Modern Physics*, 40(4):677–683, 1968.

[35] E. Wigner. *Physical Review*, 46(11):1002–1011, 1934.

[36] M. Dressel. *Naturwissenschaften*, 90(8):337–344, 2003.

[37] E. J. W. Verwey. *Nature*, 144:327–328, 1939.

[38] E. J. W. Verwey and P. W. Haayman. *Physica*, 8:979–987, 1941.

[39] Rao, C N R, Anthony Arulraj, A. K. Cheetham, and Bernard Raveau. *Journal of Physics: Condensed Matter*, 12(7):R83–R106, 2000.

[40] J. P. Attfield. *Solid State Sciences*, 8(8):861–867, 2006.

[41] J. M. Tranquada, B. J. Sternlieb, J. D. Axe, Y. Nakamura, and S. Uchida. *Nature*, 375(6532):561–563, 1995.

[42] N. Drichko, S. Kaiser, Y. Sun, C. Clauss, M. Dressel, H. Mori, J. Schlueter, E. I. Zhyliaeva, S. A. Torunova, and R. N. Lyubovskaya. *Physica B: Condensed Matter*, 404(3-4):490–493, 2009.

[43] S. Kaiser, M. Dressel, Y. Sun, A. Greco, J. A. Schlueter, Gard, G. L., and N. Drichko. *Physical Review Letters*, 105(20):206402, 2010.

[44] D. N. Basov, R. D. Averitt, D. van der Marel, M. Dressel, and K. Haule. *Reviews of Modern Physics*, 83(2):471–541, 2011.

[45] A. Asamitsu, Y. Tomioka, H. Kuwahara, and Y. Tokura. *Nature*, 388(6637): 50–52, 1997.

[46] Rao, C. N. R., Raju, A. R., V. Ponnambalam, Sachin Parashar, and N. Kumar. *Physical Review B*, 61(1):594–598, 2000.

[47] F. Sawano, I. Terasaki, H. Mori, T. Mori, M. Watanabe, N. Ikeda, Y. Nogami, and Y. Noda. *Nature*, 437(7058):522–524, 2005.

[48] T. Mori and T. Kawamoto. *Annu. Rep. Prog. Chem., Sect. C: Phys. Chem.*, 103: 134–172, 2007.

[49] T. Mori, I. Terasaki, and H. Mori. *Journal of Materials Chemistry*, 17(41):4343, 2007.

[50] S. Iwai, K. Yamamoto, A. Kashiwazaki, F. Hiramatsu, H. Nakaya, Y. Kawakami, K. Yakushi, H. Okamoto, H. Mori, and Y. Nishio. *Physical Review Letters*, 98(9):097402, 2007.

[51] M. Rini, R. Tobey, N. Dean, J. Itatani, Y. Tomioka, Y. Tokura, R. W. Schoenlein, and A. Cavalleri. *Nature*, 449(7158):72–74, 2007.

[52] J. C. Petersen, S. Kaiser, N. Dean, A. Simoncig, H. Y. Liu, A. L. Cavalieri, C. Cacho, Turcu, I. C. E., E. Springate, F. Frassetto, L. Poletto, S. S. Dhesi, H. Berger, and A. Cavalleri. *Phys. Rev. Lett.*, 107(17):177402, 2011.

[53] D. Fausti, R. I. Tobey, N. Dean, S. Kaiser, A. Dienst, M. C. Hoffmann, S. Pyon, T. Takayama, H. Takagi, and A. Cavalleri. *Science*, 331(6014):189–191, 2011.

[54] S. D. Chow, F. Zamborszky, B. Alavi, J. D. Tantillo, A. Baur, A. C. Merlic, and S. E. Brown. *Physical Review Letters*, 85(8):1698–1701, 2000.

[55] P. Monceau, F. Nad, M. J. Fabre, and T. Nakamura. *Journal of Low Temperature Physics*, 142(3-4):367–372, 2006.

[56] T. Kakiuchi, Y. Wakabayashi, H. Sawa, T. Takahashi, and To. Nakamura. *Journal of the Physics Society of Japan*, 76(11):113702, 2007.

[57] K. Yamamoto, S. Iwai, S. Boyko, A. Kashiwazaki, F. Hiramatsu, C. Okabe, N. Nishi, and K. Yakushi. *Journal of the Physical Socitey of Japan*, 77(7):074709, 2008.

[58] K. M. Shen, F. Ronning, D. H. Lu, F. Baumberger, N. J. C. Ingle, W. S. Lee, W. Meevasana, Y. Kohsaka, M. Azuma, M. Takano, H. Takagi, and Z. X. Shen. *Science*, 307(5711):901–904, 2005.

[59] B. Köhler, E. Rose, M. Dumm, G. Untereiner, and M. Dressel. *Physical Review B*, 84(3):035124, 2011.

[60] J. P. Pouget, P. Foury-Leylekian, P. Alemany, and E. Canadell. *Physica Status Solidi (b)*, 249(5):937–942, 2012.

[61] K. Ishikawa, K. Fukagai, T. Kanetake, T. Koda, Y. Tokura, and S. Koshihara. *Proceedings of the International Conference on Science and Technology of Synthetic Metals*, 28(3):D605–D612, 1989.

[62] S. y. Koshihara, Y. Tokura, Y. Iwasa, T. Koda, G. Saito, and T. Mitani. *Synthetic Metals*, 42(3):2351–2354, 1991.

[63] S. y. Koshihara, Y. Tokura, T. Mitani, G. Saito, and T. Koda. *Physical Review B*, 42(10):6853–6856, 1990.

[64] L. R. Testardi. *Physical Review B*, 4(7):2189, 1971.

[65] A. Cavalleri, T. Dekorsy, H. Chong, J. C. Kieffer, and R. W. Schoenlein. *Physical Review B*, 70(16):161102, 2004.

[66] A. Cavalleri, M. Rini, and R. W. Schoenlein. *Journal of the Physics Society of Japan*, 75(1):011004, 2006.

[67] S. Iwai, S. Tanaka, K. Fujinuma, H. Kishida, H. Okamoto, and Y. Tokura. *Phase Transitions*, 75(7-8):807–813, 2002.

[68] E. Collet, M. H. Lemée-Cailleau, M. Buron-Le Cointe, H. Cailleau, M. Wulff, T. Luty, S. y. Koshihara, M. Meyer, L. Toupet, P. Rabiller, and S. Techert. *Science*, 300(5619):612–615, 2003.

[69] H. Okamoto, Y. Ishige, S. Tanaka, H. Kishida, S. Iwai, and Y. Tokura. *Physical Review B*, 70(16):165202, 2004.

[70] H. Okamoto, K. Ikegami, T. Wakabayashi, Y. Ishige, J. Togo, H. Kishida, and H. Matsuzaki. *Physical Review Letters*, 96(3):037405, 2006.

[71] H. Okamoto, H. Matsuzaki, T. Wakabayashi, Y. Takahashi, and T. Hasegawa. *Physical Review Letters*, 98(3):037401, 2007.

[72] K. W. Kim, A. Pashkin, H. Schäfer, M. Beyer, M. Porer, T. Wolf, C. Bernhard, J. Demsar, R. Huber, and A. Leitenstorfer. *Nature Materials*, 11(6):497–501, 2012.

[73] J. Demsar, K. Biljaković, and D. Mihailovic. *Physical Review Letters*, 83(4): 800–803, 1999.

[74] K. Nasu. *Photoinduced phase transitions*. World Scientific, Singapore, 2004. ISBN 9812387633.

[75] K. Yonemitsu and K. Nasu. *Journal of the Physics Society of Japan*, 75(1): 011008, 2006.

[76] K. Yonemitsu and K. Nasu. *Physics Reports-Review Section of Physics Letters*, 465(1):1–60, 2008.

[77] W. Hu, S. Kaiser, D. Nicoletti, C. R. Hunt, I. Gierz, M. C. Hoffmann, M. Le Tacon, T. Loew, B. Keimer, and A. Cavalleri. *Nature Materials*, 13 (7):705–711, 2014.

[78] S. Kaiser, S. R. Clark, D. Nicoletti, G. Cotugno, R. I. Tobey, N. Dean, S. Lupi, H. Okamoto, T. Hasegawa, D. Jaksch, and A. Cavalleri. *Scientific reports*, 4: 3823, 2014.

[79] J. B. Gunn. *Solid State Communications*, 88(11-12):883–886, 1993.

[80] S. M. Sze and K. K. Ng. *Physics of semiconductor devices*. Wiley-Interscience, Hoboken, N.J, 3rd ed edition, 2007. ISBN 0-471-14323-5.

[81] P. Y. Yu and M. Cardona. *Fundamentals of semiconductors: Physics and materials properties*. Graduate texts in physics. SPRINGER, Berlin and London, 4th ed. edition, 2010. ISBN 3642007104.

[82] G. Dearnaley, A. M. Stoneham, and D. V. Morgan. *Reports on Progress in Physics*, 33(3):1129, 1970.

[83] T. W. Hickmott. *Journal of Applied Physics*, 35(7):2118, 1964.

[84] S. Yamanouchi, Y. Taguchi, and Y. Tokura. *Physical Review Letters*, 83(26): 5555–5558, 1999.

[85] S. Q. Liu, N. J. Wu, and A. Ignatiev. *Applied Physics Letters*, 76(19):2749, 2000.

[86] A. Sawa. *Materials Today*, 11(6):28–36, 2008.

[87] M. E. Lines and A. M. Glass. *Principles and applications of ferroelectrics and related materials*. International series of monographs on physics (Oxford, England). Clarendon Press, Oxford [England], 1979, ©1977. ISBN 0-19-852003-4.

[88] R. S. Potember, T. O. Poehler, and D. O. Cowan. *Applied Physics Letters*, 34 (6):405, 1979.

[89] Y. Tokura, H. Okamoto, T. Koda, T. Mitani, and G. Saito. *Physical Review B*, 38(3):2215–2218, 1988.

[90] R. Kumai, Y. Okimoto, and Y. Tokura. *Science*, 284(5420):1645–1647, 1999.

[91] K. Inagaki, I. Terasaki, H. Mori, and T. Mori. *Journal of the Physics Society of Japan*, 73(12):3364–3369, 2004.

[92] T. Mori, T. Kawamoto, I. Terasaki, T. Kakiuchi, and H. Sawa. *Physical Review B*, 75(23):235103, 2007.

[93] Y. Iwasa, T. Koda, Y. Tokura, S. y. Koshihara, N. Iwasawa, and G. Saito. *Applied Physics Letters*, 55(20):2111, 1989.

[94] Y. Iwasa, T. Koda, S. y. Koshihara, Y. Tokura, N. Iwasawa, and G. Saito. *Physical Review B*, 39(14):10441–10444, 1989.

[95] T. Ozawa, K. Tamura, Y. Bando, T. Kawamoto, T. Mori, and I. Terasaki. *Physical Review B*, 80(15):155106, 2009.

[96] T. Mori, T. Ozawa, Y. Bando, T. Kawamoto, S. Niizeki, H. Mori, and I. Terasaki. *Physical Review B*, 79(11):115108, 2009.

[97] A. A. Michelson. *American Journal of Science*, s3-22(128):120–129, 1881.

[98] A. A. Michelson and E. W. Morley. *American Journal of Science*, s3-34(203): 333–345, 1887.

[99] P. R. Griffiths and J. A. De Haseth. *Fourier transform infrared spectrometry*. John Wiley & Sons, Inc., Hoboken, N.J, 2nd ed edition, 2007. ISBN 0471194042.

[100] W. Herres and J. Gronholz. Understanding FT-IR data processing.

[101] P. R. Griffiths and J. A. De Haseth. *Fourier transform infrared spectrometry*, volume v. 171 of *Chemical analysis*. Wiley-Interscience, Hoboken, N.J, 2nd ed edition, 2007. ISBN 1621984524.

[102] E. D. Palik, E. J. Prucha, and I. P. Kaminow. *Handbook of optical constants of solids*. Academic Press, New York, 1985-98. ISBN 0125444206.

[103] M. Dressel and G. Grüner. *Electrodynamics of solids: Optical properties of electrons in matter*. Cambridge University Press, Cambridge and New York, 2002. ISBN 0521592534.

[104] V. Lucarini. *Kramers-Kronig relations in optical materials research*, volume v. 110 of *Springer series in optical sciences*. SPRINGER, Berlin and New York, 2005. ISBN 3540236732.

[105] T. J. Johnson, A. Simon, J. M. Weil, and G. W. Harris. *Applied Spectroscopy*, 47(9):1376–1381, 1993.

[106] Wolfgang U., A. Becker, Christoph Taran, and F. Siebert. *Applied Spectroscopy*, 45(3):390–397, 1991.

[107] B. Hessling, J. Herbst, R. Rammelsberg, and K. Gerwert. *Biophysical Journal*, 73(4):2071–2080, 1997.

[108] R. Rammelsberg, B. Hessling, H. Chorongiewski, and K. Gerwert. *Applied Spectroscopy*, 51(4):558–562, 1997.

[109] R. Rammelsberg, S. Boulas, H. Chorongiewski, and K. Gerwert. *Vibrational Spectroscopy*, 19(1):143–149, 1999.

[110] M. Schleeger, C. Wagner, M. J. Vellekoop, B. Lendl, and J. Heberle. *Analytical and Bioanalytical Chemistry*, 394(7):1869–1877, 2009.

[111] V. G. Gregoriou, J. L. Chao, H. Toriumi, and R. A. Palmer. *Chemical Physics Letters*, 179(5-6):491–496, 1991.

[112] N. Katayama, T. Sato, Y. Ozaki, K. Murashiro, M. Kikuchi, S. Saito, D. Demus, T. Yuzawa, and H. Hamaguchi. *Applied Spectroscopy*, 49(7):977–980, 1995.

[113] N. Katayama, M. A. Czarnecki, M. Satoh, T. Watanabe, and Y. Ozaki. *Applied Spectroscopy*, 51(4):487–490, 1997.

[114] A. L. Verma, B. Zhao, A. Bhattacharjee, and Y. Ozaki. *Physical Review E*, 63 (5, Part 1):051704, 2001.

[115] J. Y. Huang and W.-T. Shih. *Journal of Physics: Condensed Matter*, 18(32): 7593–7603, 2006.

[116] J. Shao, F. Yue, X. Lu, W. Lu, W. Huang, Z. Li, S. Guo, and J. Chu. *Applied Physics Letters*, 89(18):182121, 2006.

[117] J. Shao, W. Lu, F. Yue, X. Lu, W. Huang, Z. Li, S. Guo, and J. Chu. *Review of Scientific Instruments*, 78(1):013111, 2007.

[118] C. Rodig and F. Siebert. *Applied Spectroscopy*, 53(8):893–901, 1999.

[119] E. R. Henry and J. Hofrichter. [8] singular value decomposition: Application to analysis of experimental data. In Ludwig Brand, Michael L. Johnson, editor, *Methods in Enzymology : Numerical Computer Methods*, volume Volume 210, pages 129–192. Academic Press, 1992. ISBN 0076-6879.

[120] I. Noda and Y. Ozaki. *Two-dimensional correlation spectroscopy: Applications in vibrational and optical spectroscopy*. John Wiley & Sons, Chichester, West Sussex, England and Hoboken, NJ, 2004. ISBN 0471623911.

[121] N.V. Joshi. *Photoconductivity: Art: Science & Technology*. Taylor & Francis, 1990. ISBN 9780824783211.

[122] P. Giannozzi, S. Baroni, N. Bonini, M. Calandra, R. Car, C. Cavazzoni, D. Ceresoli, G. L. Chiarotti, M. Cococcioni, I. Dabo, A. Dal Corso, S. de Gironcoli, S. Fabris, G. Fratesi, R. Gebauer, Uwe G., C. Gougoussis, A. Kokalj, M. Lazzeri, L. Martin-Samos, N. Marzari, F. Mauri, R. Mazzarello, S. Paolini, A. Pasquarello, L. Paulatto, C. Sbraccia, S. Scandolo, G. Sclauzero, A. P. Seitsonen, A. Smogunov, P. Umari, and R. M. Wentzcovitch. *Journal of Physics: Condensed Matter*, 21(39):395502, 2009.

[123] M. S. Gordon and M. W. Schmidt. Advances in electronic structure theory. In *Theory and Applications of Computational Chemistry*, pages 1167–1189. Elsevier, 2005. ISBN 9780444517197.

[124] M. W. Schmidt, K. K. Baldridge, J. A. Boatz, Steven T. Elbert, M. S. Gordon, J. H. Jensen, S. Koseki, N. Matsunaga, K. A. Nguyen, S. Su, T. L. Windus, M. Dupuis, and J. A. Montgomery. *Journal of Computational Chemistry*, 14 (11):1347–1363, 1993.

[125] bwgrid (http://www.bw-grid.de), member of the german d-grid initiative, funded by the ministry for education and research (bundesministerium für bildung und forschung) and the ministry for science, research and arts baden-wuerttemberg (ministerium für wissenschaft, forschung und kunst baden-württemberg).

[126] John P. Perdew. Jacob's ladder of density functional approximations for the exchange-correlation energy. In *Density functional theory and its application to materials*, pages 1–20, 8-10 June 2000.

[127] A. D. Becke. *Physical Review A*, 38(6):3098–3100, 1988.

[128] C. Lee, W. Yang, and R. G. Parr. *Physical Review B*, 37(2):785–789, 1988.

[129] J. P. Perdew and Y. Wang. *Physical Review B*, 45(23):13244–13249, 1992.

[130] J. P. Perdew, K. Burke, and M. Ernzerhof. *Physical Review Letters*, 77(18): 3865–3868, 1996.

[131] J. P. Perdew, K. Burke, and M. Ernzerhof. *Physical Review Letters*, 78(7):1396, 1997.

[132] A. D. Becke. *The Journal of Chemical Physics*, 98(7):5648, 1993.

[133] A. D. Becke. *The Journal of Chemical Physics*, 98(2):1372, 1993.

[134] P. J. Stephens, F. J. Devlin, C. F. Chabalowski, and M. J. Frisch. *The Journal of Physical Chemistry*, 98(45):11623–11627, 1994.

[135] C. Adamo and V. Barone. *The Journal of Chemical Physics*, 110(13):6158, 1999.

[136] C. Y. Lin, M. W. George, and P. M. W. Gill. *Aust. J. Chem.*, 57(4):365–370, 2004.

[137] M. P. Andersson and P. Uvdal. *The journal of physical chemistry. A*, 109(12): 2937–2941, 2005.

[138] P. Carbonniere, T. Lucca, C. Pouchan, N. Rega, and V. Barone. *Journal of Computational Chemistry*, 26(4):384–388, 2005.

[139] J. P. Merrick, D. Moran, and L. Radom. *The journal of physical chemistry. A*, 111(45):11683–11700, 2007.

[140] L. Gisslén and R. Scholz. *Physical Review B*, 80(11):115309, 2009.

[141] D. Vanderbilt. *Physical Review B*, 41(11):7892–7895, 1990.

[142] H. J. Monkhorst and J. D. Pack. *Physical Review B*, 13(12):5188–5192, 1976.

[143] A. Kokalj. *Journal of Molecular Graphics and Modelling*, 17(3-4):176–179, 1999.

[144] A. Benassi. Pwscf's epsilon.x user's manual.

[145] M. Dressel, M. Dumm, T. Knoblauch, B. Köhler, B. Salameh, and S. Yasin. *Advances in Condensed Matter Physics*, 2012(4):1–13, 2012.

[146] J. L. Galigné, B. Liautard, S. Peytavin, G. Brun, J. M. Fabre, E. Torreilles, and L. Giral. *Acta Crystallographica Section B Structural Crystallography and Crystal Chemistry*, 34(2):620–624, 1978.

[147] D. Jérome, A. Mazaud, M. Ribault, and K. Bechgaard. *Journal de Physique Lettres*, 41(4):95–98, 1980.

[148] Xuefan Jiang and G. Y. Guo. *Solid State Communications*, 129(7):443–448, 2004.

[149] N. F. Mott and E. A. Davis. *Electronic processes in non-crystalline materials*. International series of monographs on physics. Clarendon Press and Oxford University Press, Oxford and New York, 2d ed edition, 1979. ISBN 0198512880.

[150] M. Dumm, A. Loidl, B. W. Fravel, K. P. Starkey, L. K. Montgomery, and M. Dressel. *Physical Review B*, 61(1):511–521, 2000.

[151] B. Salameh, S. Yasin, M. Dumm, G. Untereiner, L. Montgomery, and M. Dressel. *Physical Review B*, 83(20):205126, 2011.

[152] S. Fujiyama and T. Nakamura. *Journal of the Physical Socitey of Japan*, 75(1): 014705, 2006.

[153] F. Nad, P. Monceau, C. Carcel, and M. J. Fabre. *Journal of Physics-Condensed Matter*, 12(26):L435–L440, 2000.

[154] F. Nad and P. Monceau. *Journal of the Physical Socitey of Japan*, 75(5):051005, 2006.

[155] Jill C. Bonner and Michael E. Fisher. *Physical Review*, 135(3A):A640–A658, 1964.

[156] S. Yasin, B. Salameh, E. Rose, M. Dumm, Krug von Nidda, H.-A., A. Loidl, M. Ozerov, G. Untereiner, L. Montgomery, and M. Dressel. *Physical Review B*, 85(14):144428, 2012.

[157] D. Jérome. *Science (New York, N.Y.)*, 252(5012):1509–1514, 1991.

[158] F. Zamborszky, W. Yu, W. Raas, S. E. Brown, B. Alavi, A. C. Merlic, and A. Baur. *Physical Review B*, 66(8):081103, 2002.

[159] S. Hirose and A. Kawamoto. *Physical Review B*, 80(16):165103, 2009.

[160] To. Nakamura, K. Furukawa, and T. Hara. *Journal of the Physical Socitey of Japan*, 76(6):064715, 2007.

[161] C. Coulon and S. P. S. Parkin. *Physical Review B*, 31(6):3583–3587, 1985.

[162] C. Coulon, G. Lalet, J. P. Pouget, P. Foury-Leylekian, A. Moradpour, and M. J. Fabre. *Physical Review B*, 76(8):085126, 2007.

[163] M. Souza, P. Foury-Leylekian, A. Moradpour, J. P. Pouget, and M. Lang. *Physical Review Letters*, 101(21):216403, 2008.

[164] M. Souza, D. Hofmann, P. Foury-Leylekian, A. Moradpour, J. P. Pouget, and M. Lang. *Physica B: Condensed Matter*, 405(11, Suppl. S):S92–S94, 2010.

[165] R. Laversanne, C. Coulon, B. Gallois, J. P. Pouget, and R. Moret. *Journal de Physique Lettres*, 45(8):393–399, 1984.

[166] V. Vescoli. *Science*, 281(5380):1181–1184, 1998.

[167] F. Zwick, S. Brown, G. Margaritondo, C. Merlic, M. Onellion, J. Voit, and M. Grioni. *Physical Review Letters*, 79(20):3982–3985, 1997.

[168] S. Ejima, F. Gebhard, and S. Nishimoto. *Europhysics Letters (EPL)*, 70(4): 492–498, 2005.

[169] M. Nagasawa, F. Nad, P. Monceau, and M. J. Fabre. *Solid State Communications*, 136(5):262–267, 2005.

[170] F. Mila and X. Zotos. *Europhysics Letters (EPL)*, 24(2):133–138, 1993.

[171] K. Penc and F. Mila. *Physical Review B*, 49(14):9670–9678, 1994.

[172] Y. Shibata, S. Nishimoto, and Y. Ohta. *Physical Review B*, 64(23):235107, 2001.

[173] H. Seo, J. Merino, H. Yoshioka, and M. Ogata. *Journal of the Physical Society of Japan*, 75(5):051009, 2006.

[174] Eva Rose, 2014.

[175] E. Rose, C. Loose, J. Kortus, A. Pashkin, C. A. Kuntscher, S. G. Ebbinghaus, M. Hanfland, F. Lissner, Schleid Th., and M. Dressel. *Journal of Physics: Condensed Matter*, 25(1):014006, 2013.

[176] C. S. Jacobsen, D. B. Tanner, and K. Bechgaard. *Physical Review B*, 28(12): 7019–7032, 1983.

[177] M. Meneghetti, R. Bozio, I. Zanon, C. Pecile, C. Ricotta, and M. Zanetti. *The Journal of Chemical Physics*, 80(12):6210, 1984.

[178] A. Łapiński, L. Ouahab, and T. Imakubo. *Vibrational Spectroscopy*, 52(1): 22–30, 2010.

[179] A. Łapiński and A.I. Kotov. *Chemical Physics*, 326(2-3):551–562, 2006.

[180] E. Demiralp, S. Dasgupta, and W. A. Goddard. *Journal of the American Chemical Society*, 117(31):8154–8158, 1995.

[181] A. Painelli and A. Girlando. *The Journal of Chemical Physics*, 84(10):5655, 1986.

[182] K. Yamamoto and K. Yakushi. *J. Phys. IV France*, 114:153–155, 2004.

[183] T. Takahashi, Y. Nogami, and K. Yakushi. *Journal of the Physics Society of Japan*, 75(5):051008, 2006.

[184] J. C. Decius and R. M. Hexter. *Molecular vibrations in crystals*. McGraw-Hill, New York, 1977. ISBN 0070286159.

[185] K. Nakamoto. *Infrared and Raman spectra of inorganic and coordination compounds*. Wiley, Hoboken, N.J, 6th ed edition, 2009. ISBN 9780471743392.

[186] A. M. Heyns. *Spectrochimica Acta Part A: Molecular Spectroscopy*, 33(3-4): 315–322, 1977.

[187] C. Naulin and R. Bougon. *The Journal of Chemical Physics*, 64(10):4155–4158, 1976.

[188] N. Weinstock. *The Journal of Chemical Physics*, 59(9):5063, 1973.

[189] M. Akaber. PhD thesis, Universität Stuttgart, Stuttgart, 2006.

[190] M. M. Qazilbash, J. J. Hamlin, R. E. Baumbach, Lijun Zhang, D. J. Singh, M. B. Maple, and D. N. Basov. *Nature Physics*, 5(9):647–650, 2009.

[191] D. Pedron, R. Bozio, M. Meneghetti, and C. Pecile. *Molecular Crystals and Liquid Crystals Science and Technology. Section A. Molecular Crystals and Liquid Crystals*, 234(1):161–170, 1993.

[192] T. Ivek, B. Korin-Hamzić, O. Milat, S. Tomić, C. Clauss, N. Drichko, D. Schweitzer, and M. Dressel. *Physical Review B*, 83(16):165128, 2011.

[193] K. Yamamoto, K. Yakushi, K. Miyagawa, K. Kanoda, and A. Kawamoto. *Physical Review B*, 65(8):085110, 2002.

[194] K. Yamamoto, A. A. Kowalska, Y. Yue, and K. Yakushi. *Physical Review B*, 84(6):064306, 2011.

[195] K. Yamamoto, A. A. Kowalska, and K. Yakushi. *Phys. Status Solidi C*, 9(5): 1189–1192, 2012.

[196] M. J. Rice, V. M. Yartsev, and C. S. Jacobsen. *Physical Review B*, 21(8):3437–3446, 1980.

[197] R. Bozio and C. Pecile. *Journal of Physics C: Solid State Physics*, 13(33):6205–6218, 1980.

[198] M.E Kozlov, K. I. Pokhodnia, and A. A. Yurchenko. *Spectrochimica Acta Part A: Molecular Spectroscopy*, 45(4):437–444, 1989.

[199] C. S. Jacobsen and J. B. Torrance. *Journal of Chemical Physics*, 78(1):112–115, 1983.

[200] C. C. Homes and J. E. Eldridge. *Physical Review B*, 42(15):9522–9533, 1990.

[201] H. Kobayashi, A. Kobayashi, Y. Sasaki, G. Saito, and H. Inokuchi. *Bulletin of the Chemical Society of Japan*, 57(7):2025–2026, 1984.

[202] D. Jankowski, R. Swietlik, E. W. Reinheimer, and M. Fourmigué. *Journal of Raman Spectroscopy*, 42(7):1518–1527, 2011.

[203] K. Furukawa, T. Hara, and To. Nakamura. *Journal of the Physical Socitey of Japan*, 78(10):104713, 2009.

[204] J. Bardeen, Cooper, L. N., and Schrieffer, J. R. *Physical Review*, 108(5):1175–1204, 1957.

[205] Y. Nogami and T. Nakamura. *Journal de Physique IV*, 12:145, 2002.

[206] To. Nakamura, T. Hara, and K. Furukawa. *Journal of Low Temperature Physics*, 142(3-4):629–632, 2006.

[207] M. Dumm, M. Abaker, and M. Dressel. *Journal de Physique IV*, 131:55–58, 2005.

[208] M. Dumm, M. Abaker, M. Dressel, and L. K. Montgomery. *Journal of Low Temperature Physics*, 142:613–616, 2006.

[209] W. Yu, F. Zamborszky, B. Alavi, A. Baur, A. C. Merlic, and S. E. Brown. *Journal de Physique IV*, 114:35–40, 2004.

[210] A. Girlando. *The Journal of Physical Chemistry C*, 115(39):19371–19378, 2011.

[211] T. Iimori, T. Naito, and N. Ohta. *Chemistry Letters*, 36(4):536–537, 2007.

[212] T. Iimori, Toshio Naito, and N. Ohta. *The Journal of Physical Chemistry C*, 114(19):9070–9075, 2010.

[213] J. Tsutsumi, T. Yamada, H. Matsui, S. Haas, and T. Hasegawa. *Physical Review Letters*, 105(22):226601, 2010.

[214] T. Iimori and N. Ohta. *The Journal of Physical Chemistry C*, 118(14):7251–7260, 2014.

[215] N. Drichko, R. Hackl, and J. Schlueter. *Physical Review B*, 88(11), 2013.

[216] K. Nasu. *Relaxations of Excited States and Photo-Induced Structural Phase Transitions: Proceedings of the 19th Taniguchi Symposium, Kashikojima, Japan, July 18-23, 1996*, volume 124 of *Springer Series in Solid-State Sciences*. Springer Berlin Heidelberg, Berlin, Heidelberg, 1997. ISBN 3642607020.

[217] R. Kassing and E. Kähler. *Physica Status Solidi (a)*, 12(1):209–213, 1972.

[218] Nick Holonyak and S. F. Bevacqua. *Applied Physics Letters*, 2(4):71, 1963.

[219] J. Kastrup, R. Hey, K. H. Ploog, H. T. Grahn, L. L. Bonilla, M. Kindelan, M. Moscoso, A. Wacker, and J. Galán. *Physical Review B*, 55(4):2476–2488, 1997.

[220] M. Hosoda, H. Mimura, N. Ohtani, K. Tominaga, T. Watanabe, K. Fujiwara, and H. T. Grahn. *Applied Physics Letters*, 69(4):500, 1996.

[221] A. M. Tomlinson, A. M. Fox, J. E. Cunningham, and W. Y. Jan. *Applied Physics Letters*, 75(14):2067, 1999.

[222] T. Mori, Y. Bando, T. Kawamoto, I. Terasaki, K. Takimiya, and T. Otsubo. *Physical Review Letters*, 100(3):037001, 2008.

[223] K. Tamura, T. Ozawa, Y. Bando, T. Kawamoto, and T. Mori. *Journal of Applied Physics*, 107(10):103716, 2010.

[224] H. Wakita, T. Ozawa, Y. Bando, and T. Mori. *Journal of the Physical Socitey of Japan*, 79(9):094703, 2010.

[225] H. Kishida, T. Ito, A. Ito, and A. Nakamura. *Applied Physics Express*, 4(3):031601, 2011.

[226] A. M. Glass. *Journal of Applied Physics*, 41(11):4455, 1970.

[227] A. M. Glass and D. H. Auston. *Optics Communications*, 5(1):45–49, 1972.

[228] A. M. Glass and D. H. Auston. *Ferroelectrics*, 7(1):187–189, 1974.

[229] N. Ogawa, A. Shiraga, R. Kondo, S. Kagoshima, and K. Miyano. *Physical Review Letters*, 87(25):256401, 2001.

[230] Naoki Ogawa, Kenjiro Miyano, and Serguei Brazovski. *Physical Review B*, 71(7):075118, 2005.

[231] T. Tiedje, R. R. Haering, M. H. Jericho, W. A. Roger, and A. Simpson. *Solid State Communications*, 23(10):713–718, 1977.

[232] P. M. Chaikin, T. Tiedje, and A. N. Bloch. *Solid State Communications*, 41 (10):739–742, 1982.

[233] K. Medjanik, M. de Souza, D. Kutnyakhov, A. Gloskovskii, J. Müller, M. Lang, J. P. Pouget, P. Foury-Leylekian, A. Moradpour, H.-J. Elmers, and G. Schönhense. *The European Physical Journal B*, 87(11):50499, 2014.

[234] T. Giamarchi. *Physica B: Condensed Matter*, 230-232:975–980, 1997.

[235] V. Emery, R. Bruinsma, and S. Barišić. *Physical Review Letters*, 48(15):1039–1043, 1982.

[236] K. Heuzé, M. Fourmigué, P. Batail, C. Coulon, R. Clérac, E. Canadell, P. Auban-Senzier, S. Ravy, and D. Jérome. *Advanced Materials*, 15(15):1251–1254, 2003.

[237] L. Zorina, S. Simonov, C. Mézière, E. Canadell, S. Suh, S. E. Brown, P. Foury-Leylekian, P. Fertey, J. P. Pouget, and P. Batail. *Journal of Materials Chemistry*, 19(38):6980, 2009.

[238] P. Auban-Senzier, C. R. Pasquier, D. Jérome, S. Suh, S. E. Brown, C. Mézière, and P. Batail. *Physical Review Letters*, 102(25):257001, 2009.

[239] M. Dressel. *Naturwissenschaften*, 94(7):527–541, 2007.

[240] M. I. Aroyo, D. Orobengoa, G. de la Flor, E. S. Tasci, J. M. Perez-Mato, and H. Wondratschek. *Acta crystallographica. Section A, Foundations and advances*, 70(Pt 2):126–137, 2014.

[241] R. Bozio, I. Zanon, A. Girlando, and C. Pecile. *The Journal of Chemical Physics*, 71(5):2282, 1979.

[242] T. Yamamoto, M. Uruichi, K. Yamamoto, K. Yakushi, A. Kawamoto, and H. Taniguchi. *The Journal of Physical Chemistry B*, 109(32):15226–15235, 2005.

[243] K. Yamamoto, T. Yamamoto, K. Yakushi, C. Pecile, and M. Meneghetti. *Physical Review B*, 71(4):045118, 2005.

[244] O. Drozdova, K. Yakushi, K. Yamamoto, A. Ota, H. Yamochi, G. Saito, H. Tashiro, and D. Tanner. *Physical Review B*, 70(7):075107, 2004.

[245] M. Mayr and P. Horsch. *Physical Review B*, 73(19):195103, 2006.

[246] T. Koretsune and C. Hotta. *Physical Review B*, 89(4):045102, 2014.

[247] T. Itou, K. Kanoda, K. Hiraki, T. Takahashi, K. Murata, and T. Matsumoto. *Physical Review B*, 72(11):113109, 2005.

[248] A. Dengl, R. Beyer, T. Peterseim, T. Ivek, G. Untereiner, and M. Dressel. *The Journal of Chemical Physics*, 140(24):244511, 2014.

[249] M. Le Cointe, M. H. Lemée-Cailleau, H. Cailleau, B. Toudic, L. Toupet, K. H. Kraft, and N. Karl. *Physical Review B*, 51(6):3374–3386, 1995.

[250] M. Le Cointe-Buron, M. H. Lemée-Cailleau, H. Cailleau, and T. Luty. *Journal of Low Temperature Physics*, 111(3-4):677–691, 1998.

[251] M. Le Cointe, M. H. Lemée-Cailleau, H. Cailleau, and B. Toudic. *Organic Crystal Chemistry: Molecular Design, Structure, Reactivity, and Transformation*, 374(1–3):147–153, 1996.

[252] J. B. Torrance, J. J. Mayerle, V. Y. Lee, and K. Bechgaard. *Journal of the American Chemical Society*, 101(16):4747–4748, 1979.

[253] J. J. Mayerle, J. B. Torrance, and J. I. Crowley. *Acta Crystallographica Section B Structural Crystallography and Crystal Chemistry*, 35(12):2988–2995, 1979.

[254] A. Girlando, F. Marzola, C. Pecile, and J. B. Torrance. *The Journal of Chemical Physics*, 79(2):1075, 1983.

[255] A. Girlando, R. Bozio, C. Pecile, and J. B. Torrance. *Physical Review B*, 26 (4):2306–2309, 1982.

[256] H. Okamoto, T. Mitani, T. Komatsu, Y. Iwasa, T. Koda, and G. Saito. *Physical Review B*, 43(10):8224–8232, 1991.

[257] C. Ayache and J. B. Torrance. *Solid State Communications*, 47(10):789–793, 1983.

[258] T. Mitani, Y. Kaneko, S. Tanuma, Y. Tokura, T. Koda, and G. Saito. *Physical Review B*, 35(1):427–429, 1987.

[259] H. M. McConnell, B. M. Hoffman, and R. M. Metzger. *Proceedings of the National Academy of Sciences*, 53(1):46–50, 1965.

[260] J. B. Torrance, J. Vazquez, J. J. Mayerle, and V. Y. Lee. *Physical Review Letters*, 46(4):253–257, 1981.

[261] C. Katan. *The journal of physical chemistry. A*, 103(10):1407–1413, 1999.

[262] D. L. Lichtenberger, R. L. Johnston, K. Hinkelmann, T. Suzuki, and F. Wudl. *Journal of the American Chemical Society*, 112(9):3302–3307, 1990.

[263] N. Sato, H. Inokuchi, and I. Shirotani. *Chemical Physics*, 60(3):327–333, 1981.

[264] A. S. Batsanov, M. R. Bryce, J. N. Heaton, A. J. Moore, P. J. Skabara, J. A. K. Howard, E. Ortí, P. M. Viruela, and R. Viruela. *Journal of Materials Chemistry*, 5(10):1689, 1995.

[265] Cooper, C. D., Frey, W. F., and Compton, R. N. *The Journal of Chemical Physics*, 69(6):2367, 1978.

[266] S. Tanaka, S. Aoki, T. Nakayama, and S. Egusa. *Physical Review B*, 52(3): 1549–1565, 1995.

[267] T. Mitani, Y. Tokura, Y. Kaneko, K. Takaoka, T. Koda, and G. Saito. *Synthetic Metals*, 19(1-3):515–520, 1987.

[268] N. Nagaosa. *Journal of the Physical Socitey of Japan*, 55(10):3488–3497, 1986.

[269] N. Nagaosa and J. Takimoto. *Journal of the Physical Socitey of Japan*, 55(8): 2745–2753, 1986.

[270] Z. G. Soos and A. Painelli. *Physical Review B*, 75(15):155119, 2007.

[271] T. Kambe, Y. Nogami, K. Oshima, Y. Takahashi, H. Sakai, and S. y. Koshihara. *International Conference on Science and Technology of Synthetic Metals*, 103(1–3):1824, 1999.

[272] T. Mitani and G. Saito. *Physical Review Letters*, 53(8):842–845, 1984.

[273] Y. Tokura, H. Okamoto, T. Koda, and T. Mitani. *Solid State Communications*, 57(8):607–610, 1986.

[274] A. Girlando, C. Pecile, A. Brillante, and K. Syassen. *Solid State Communications*, 57(12):891–896, 1986.

[275] Y. Kaneko, S. Tanuma, Y. Tokura, T. Koda, T. Mitani, and G. Saito. *Physical Review B*, 35(15):8024–8029, 1987.

[276] H. Okamoto, T. Koda, Y. Tokura, T. Mitani, and G. Saito. *Physical Review B*, 39(15):10693–10701, 1989.

[277] M. Masino, A. Girlando, and A. Brillante. *Physical Review B*, 76(6):064114, 2007.

[278] K. Takaoka, Y. Kaneko, H. Okamoto, Y. Tokura, T. Koda, T. Mitani, and G. Saito. *Physical Review B*, 36(7):3884–3887, 1987.

[279] M. H. Lemée-Cailleau, M. Le Cointe, H. Cailleau, T. Luty, F. Moussa, J. Roos, D. Brinkmann, B. Toudic, C. Ayache, and N. Karl. *Physical Review Letters*, 79(9):1690–1693, 1997.

[280] T. Luty, H. Cailleau, S. y. Koshihara, E. Collet, M. Takesada, M. H. Lemée-Cailleau, M. Buron-Le Cointe, N. Nagaosa, Y. Tokura, E. Zienkiewicz, and B. Ouladdiaf. *Europhysics Letters*, 59(4):619–625, 2002.

[281] L. N. Demaniets. *Organic crystals ; Germanates ; Semiconductors*. SPRINGER, Berlin and Heidelberg and New York, 1980. ISBN 0387102981.

[282] J. R. Andersen, E. M. Engler, and K. Bechgaard. *Annals of the New York Academy of Sciences*, 313(1):293–300, 1978.

[283] Inc. Wavefunction. Spartan.

[284] P. Ranzieri, M. Masino, and A. Girlando. *The Journal of Physical Chemistry B*, 111(44):12844–12848, 2007.

[285] R. Liu, X. Zhou, and H. Kasmai. *Ab Initio and Ab Initio Derived Force Fields: State of the Science*, 53(8):1241–1256, 1997.

[286] A. Girlando, I. Zanon, R. Bozio, and C. Pecile. *The Journal of Chemical Physics*, 68(1):22, 1978.

[287] P. Garcia, S. Dahaoui, C. Katan, M. Souhassou, and C. Lecomte. *Faraday Discussions*, 135:217–235, 2007.

[288] V. Oison, C. Katan, and C. Koenig. *The journal of physical chemistry. A*, 105 (17):4300–4307, 2001.

[289] P. Haremski. Bachelor thesis, Universität Stuttgart, Stuttgart, 2013.

[290] A. Girlando, C. Pecile, A. Brillante, and K. Syassen. *Proceedings of the International Conference on Science and Technology of Synthetic Metals*, 19(1–3): 503–508, 1987.

[291] M. B.-L. Cointe, M. H. Lemée-Cailleau, H. Cailleau, B. Toudic, A. Moréac, F. Moussa, C. Ayache, and N. Karl. *Physical Review B*, 68(6):064103, 2003.

[292] A. Girlando, M. Masino, A. Painelli, N. Drichko, M. Dressel, A. Brillante, R. G. Della Valle, and E. Venuti. *Physical Review B*, 78(4):045103, 2008.

[293] C. S. Jacobsen. *The Journal of Chemical Physics*, 78(1):112, 1983.

[294] T. Sugano, K. Yakushi, and H. Kuroda. *Bulletin of the Chemical Society of Japan*, 51(4):1041–1046, 1978.

[295] M. Tanaka. *Bulletin of the Chemical Society of Japan*, 50(11):2881–2884, 1977.

[296] M. Masino, A. Girlando, and Z. G. Soos. *Chemical Physics Letters*, 369(3-4): 428–433, 2003.

[297] S. Iwai and H. Okamoto. *Journal of the Physics Society of Japan*, 75(1):011007, 2006.

[298] Y. Matsubara, Y. Okimoto, T. Yoshida, T. Ishikawa, S. y. Koshihara, and K. Onda. *Journal of the Physics Society of Japan*, 80(12):124711, 2011.

[299] L. Guérin, Eric Collet, M.-H. Lemée-Cailleau, M. Buron-Le Cointe, H. Cailleau, A. Plech, M. Wulff, S.-Y. Koshihara, and T. Luty. *Ultrafast Science with X-rays and Electrons*, 299(2–3):163–170, 2004.

[300] S. y. Koshihara, Y. Takahashi, H. Sakai, Y. Tokura, and T. Luty. *The Journal of Physical Chemistry B*, 103(14):2592–2600, 1999.

[301] T. Suzuki, T. Sakamaki, K. Tanimura, S. y. Koshihara, and Y. Tokura. *Physical Review B*, 60(9):6191, 1999.

[302] K. Tanimura and S. y. Koshihara. *Phase Transitions*, 74(1-2):21–34, 2001.

[303] S. Iwai, Y. Ishige, S. Tanaka, Y. Okimoto, Y. Tokura, and H. Okamoto. *Physical Review Letters*, 96(5):057403, 2006.

[304] K. Tanimura and I. Akimoto. *Journal of Luminescence*, 94-95:483–488, 2001.

[305] Y. Tokura, T. Koda, T. Mitani, and G. Saito. *Solid State Communications*, 43 (10):757–760, 1982.

[306] S. Hünig, G. Kießlich, H. Quast, and D. Scheutzow. *Justus Liebigs Annalen der Chemie*, 1973(2):310–323, 1973.

[307] F. Wudl, A. A. Kruger, M. L. Kaplan, and R. S. Hutton. *The Journal of Organic Chemistry*, 42(4):768–770, 1977.

[308] D. L. Coffen, J. Q. Chambers, D. R. Williams, P. E. Garrett, and N. D. Canfield. *Journal of the American Chemical Society*, 93(9):2258–2268, 1971.

[309] J. J. Andre and G. Weill. *Molecular Physics*, 15(1):97–99, 1968.

[310] N. Sakai, I. Shirotani, and S. Minomura. *Bulletin of the Chemical Society of Japan*, 44(3):675–679, 1971.

[311] A. Bieber and J. J. Andre. *Chemical Physics*, 5(2):166–182, 1974.

[312] M. Pope and C. E. Swenberg. *Electronic processes in organic crystals and polymers*, volume #56 of *Monographs on the physics and chemistry of materials*. Oxford University Press, New York, 2nd ed edition, 1999. ISBN 0195129636.

[313] R. Kohlrausch. *Annalen der Physik und Chemie*, (91):56–82,179–214, 1854.

[314] G. Williams and D. C. Watts. *Transactions of the Faraday Society*, 66:80, 1970.

[315] A. Nagahori, N. Kubota, and C. Itoh. *The European Physical Journal B*, 86(3): 109, 2013.

[316] D. Djurek, D. Jérome, and K. Bechgaard. *Journal of Physics C: Solid State Physics*, 17(23):4179–4192, 1984.

[317] J. H. Bechtel. *Journal of Applied Physics*, 46(4):1585, 1975.

[318] M. Salamon, J. Bray, G. DePasquali, R. Craven, G. Stucky, and A. Schultz. *Physical Review B*, 11(2):619–622, 1975.

[319] M. Matsukawa, K. Hashimoto, N. Yoshimoto, M. Yoshizawa, Y. Kashiwaba, and K. Noto. *Journal of the Physical Society of Japan*, 64(6):2233–2234, 1995.

[320] N. Kuroda, Y. Wakabayashi, M. Nishida, N. Wakabayashi, M. Yamashita, and N. Matsushita. *Physical Review Letters*, 79(13):2510–2513, 1997.

[321] Y. Tabata and N. Kuroda. *Journal of the Physics Society of Japan*, 78(3):034704, 2009.

[322] S. y. Koshihara, Y. Tokura, N. Sarukura, Y. Segawa, T. Koda, and K. Takeda. *Synthetic Metals*, 70(1-3):1225–1226, 1995.

[323] H. Bleier, S. Roth, Y. Shen, D. Schäfer-Siebert, and G. Leising. *Physical Review B*, 38(9):6031–6040, 1988.

[324] C. V. Shank, R. Yen, R. Fork, J. Orenstein, and G. Baker. *Physical Review Letters*, 49(22):1660–1663, 1982.

[325] V. Privman. *Nonequilibrium statistical mechanics in one dimension*. Cambridge University Press, Cambridge and New York, 1997. ISBN 9780521559744.

[326] D. C. Torney and H. M. McConnell. *The Journal of Physical Chemistry*, 87 (11):1941–1951, 1983.

[327] A. A. Lushnikov. *Physics Letters A*, 120(3):135–137, 1987.

[328] D. Balding, P. Clifford, and Green, N. J. B. *Physics Letters A*, 126(8–9):481–483, 1988.

[329] K. Sasaki and T. Nakagawa. *Journal of the Physics Society of Japan*, 69(5): 1341–1351, 2000.

[330] D. ben Avraham. *The Journal of Chemical Physics*, 88(2):941, 1988.

[331] T. Ivek, I. Kovačević, M. Pinterić, B. Korin-Hamzić, S. Tomić, T. Knoblauch, D. Schweitzer, and M. Dressel. *Physical Review B*, 86(24):245125, 2012.

[332] K. Bender, I. Hennig, D. Schweitzer, K. Dietz, H. Endres, and H. J. Keller. *Molecular Crystals and Liquid Crystals*, 108(3-4):359–371, 1984.

[333] T. Mori, A. Kobayashi, Y. Sasaki, H. Kobayashi, G. Saito, and H. Inokuchi. *Bulletin of the Chemical Society of Japan*, 57(3):627–633, 1984.

[334] P. Alemany, J. P. Pouget, and E. Canadell. *Physical Review B*, 85(19):195118, 2012.

[335] N. A. Fortune, K. Murata, M. Ishibashi, M. Tokumoto, N. Kinoshita, and H. Anzai. *Solid State Communications*, 79(3):265–269, 1991.

[336] Y. Takano, K. Hiraki, H.M Yamamoto, T. Nakamura, and T. Takahashi. *Journal of Physics and Chemistry of Solids*, 62(1-2):393–395, 2001.

[337] J. Moldenhauer, Ch. Horn, K. I. Pokhodnia, D. Schweitzer, I. Heinen, and H. J. Keller. *Synthetic Metals*, 60(1):31–38, 1993.

[338] Y. Yue, K. Yamamoto, M. Uruichi, C. Nakano, K. Yakushi, S. Yamada, T. Hiejima, and A. Kawamoto. *Physical Review B*, 82(7):075134, 2010.

[339] R. Wojciechowski, K. Yamamoto, K. Yakushi, M. Inokuchi, and A. Kawamoto. *Physical Review B*, 67(22), 2003.

[340] K. Yamamoto, A. A. Kowalska, and K. Yakushi. *Applied Physics Letters*, 96 (12):3327810, 2010.

[341] T. R. Clay, S. Mazumdar, and K. D. Campbell. *Physical Review B*, 67(11), 2003.

[342] H. Nakaya, F. Hiramatsu, Y. Kawakami, S. Iwai, K. Yamamoto, and K. Yakushi. *Journal of Luminescence*, 128(5-6):1065–1068, 2008.

[343] Y. Kawakami, T. Fukatsu, Y. Sakurai, H. Unno, H. Itoh, S. Iwai, T. Sasaki, K. Yamamoto, K. Yakushi, and K. Yonemitsu. *Physical Review Letters*, 105 (24):246402, 2010.

[344] N. Tajima, J. Fujisawa, N. Naka, T. Ishihara, R. Kato, Y. Nishio, and K. Kajita. *Journal of the Physical Socitey of Japan*, 74(2):511–514, 2005.

[345] T. Iimori, T. Naito, and N. Ohta. *Journal of Physical Chemistry C*, 113(11): 4654–4661, 2009.

[346] T. Iimori, T. Naito, and N. Ohta. *Journal of the American Chemical Society*, 129(12):3486+, 2007.

[347] S. Katayama, A. Kobayashi, and Y. Suzumura. *Journal of the Physical Society of Japan*, 75(5):054705, 2006.

[348] T. Mori. *Journal of the Physical Society of Japan*, 79(1):014703, 2010.

[349] N. Tajima, S. Sugawara, M. Tamura, R. Kato, Y. Nishio, and K. Kajita. *Europhysics Letters (EPL)*, 80(4):47002, 2007.

[350] N. Tajima, S. Sugawara, R. Kato, Y. Nishio, and K. Kajita. *Physical Review Letters*, 102(17):176403, 2009.

[351] M. Monteverde, Goerbig, M. O., P. Auban-Senzier, F. Navarin, H. Henck, C. R. Pasquier, C. Mézière, and P. Batail. *Physical Review B*, 87(24):245110, 2013.

[352] T. J. Emge, P. C. W. Leung, M. A. Beno, H. H. Wang, J. M. Williams, M.-H. Whangbo, and M. Evain. *Molecular Crystals and Liquid Crystals*, 138(1): 393–410, 1986.

[353] A. H. Castro Neto, F. Guinea, Peres, N. M. R., Novoselov, K. S., and Geim, A. K. *Reviews of Modern Physics*, 81(1):109–162, 2009.

[354] K. Yakushi, H. Kanbara, H. Tajima, H. Kuroda, G. Saito, and T. Mori. *Bulletin of the Chemical Society of Japan*, 60(12):4251–4257, 1987.

[355] M. Dressel, A. Schwartz, G. Grüner, and L. Degiorgi. *Physical Review Letters*, 77(2):398–401, 1996.

[356] F. Itose, T. Kawamoto, and T. Mori. *Journal of Applied Physics*, 113(21): 213702, 2013.

[357] K. Maki. *Physical Review B*, 33(4):2852–2854, 1986.

[358] A. Zimmers, L. Aigouy, M. Mortier, A. Sharoni, S. Wang, K. G. West, J. G. Ramirez, and I. K. Schuller. *Physical Review Letters*, 110(5):056601, 2013.

[359] M. Pinterić, M. Čulo, O. Milat, M. Basletić, B. Korin-Hamzić, E. Tafra, A. Hamzić, T. Ivek, T. Peterseim, K. Miyagawa, K. Kanoda, J. A. Schlueter, M. Dressel, and S. Tomić. *Physical Review B*, 90(19):195139, 2014.

[360] D. M. Kroll. *Physical Review B*, 9(4):1669–1706, 1974.

[361] H. Jain and A. K. Raychaudhuri. *Applied Physics Letters*, 93(18):182110, 2008.

[362] F. Pobell. *Matter and methods at low temperatures*. SPRINGER, Berlin and New York, 3rd rev. and expanded ed edition, 2007. ISBN 978-3-540-46356-6.

[363] N. Tajima, M. Tamura, Y. Nishio, K. Kajita, and Y. Iye. *Journal of the Physics Society of Japan*, 69(2):543–551, 2000.

[364] H. Schwenk, F. Gross, C.-P. Heidmann, K. Andres, D. Schweitzer, and H. Keller. *Molecular Crystals and Liquid Crystals*, 119(1):329–335, 1985.

[365] N. Tajima, S. Sugawara, Masafumi Tamura, Y. Nishio, and K. Kajita. *Journal of the Physical Society of Japan*, 75(5):051010, 2006.

[366] D. McWhan, M. Marezio, J. Remeika, and P. Dernier. *Physical Review B*, 10 (2):490–495, 1974.

[367] J. M. Longo, P. Kierkegaard, C. J. Ballhausen, U. Ragnarsson, S. E. Rasmussen, E. Sunde, and N. A. Sørensen. *Acta Chemica Scandinavica*, 24:420–426, 1970.

[368] N. A. Clark and S. T. Lagerwall. *Applied Physics Letters*, 36(11):899, 1980.

[369] L. S. Li and J. Y. Huang. *Journal of Physics D: Applied Physics*, 42(12):125413, 2009.

[370] E. D. Palik, editor. *Handbook of Optical Constants of Solids, Author and Subject Indices for Volumes I, II, and III*. Academic Press, 2009. ISBN 008052771X.

[371] P. K. Biswas, A. De, N. C. Pramanik, P. K. Chakraborty, K. Ortner, V. Hock, and S. Korder. *Materials Letters*, 57(15):2326–2332, 2003.

[372] K. Sakamoto, R. Arafune, N. Ito, S. Ushioda, Y. Suzuki, and S. Morokawa. *Japanese Journal of Applied Physics*, 33(Part 2, No. 9B):L1323–L1326, 1994.

[373] A. Verma, B. Zhao, S. Jiang, J. Sheng, and Y. Ozaki. *Physical Review E*, 56 (3):3053–3060, 1997.

[374] N. A. Clark, M. A. Handschy, and S. T. Lagerwall. *Molecular Crystals and Liquid Crystals*, 94(1-2):213–233, 1983.

[375] M. A. Handschy, K. M. Johnson, G. Moddel, and L. A. Pagano-Stauffer. *Ferroelectrics*, 85(1):279–289, 1988.

[376] J. W. Goodby, editor. *Handbook of liquid crystals*. Wiley-VCH, Weinheim, 2nd completely revised and enlarged ed edition, 2014. ISBN 978-3-527-32773-7.

[377] Z. Yang, S. Hart, C. Ko, A. Yacoby, and S. Ramanathan. *Journal of Applied Physics*, 110(3):033725, 2011.

[378] H. Katzke, P. Tolédano, and W. Depmeier. *Physical Review B*, 68(2):024109, 2003.

[379] J. B. Goodenough. *Journal of Solid State Chemistry*, 3(4):490–500, 1971.

[380] H. Verleur, A. Barker, and C. Berglund. *Physical Review*, 172(3):788–798, 1968.

[381] W. Rosevear and W. Paul. *Physical Review B*, 7(5):2109–2111, 1973.

[382] C. Blaauw, F. Leenhouts, F. van der Woude, and G. A. Sawatzky. *Journal of Physics C: Solid State Physics*, 8(4):459–468, 1975.

[383] S. Shin, S. Suga, M. Taniguchi, M. Fujisawa, H. Kanzaki, A. Fujimori, H. Daimon, Y. Ueda, K. Kosuge, and S. Kachi. *Physical Review B*, 41(8): 4993–5009, 1990.

[384] T. C. Koethe, Z. Hu, M. W. Haverkort, C. Schüßler-Langeheine, F. Venturini, N. B. Brookes, O. Tjernberg, W. Reichelt, H. H. Hsieh, H.-J. Lin, C. T. Chen, and L. H. Tjeng. *Physical Review Letters*, 97(11):116402, 2006.

[385] V. Eyert. *Annalen der Physik*, 11(9):650–704, 2002.

[386] A. Zylbersztejn. *Physical Review B*, 11(11):4383–4395, 1975.

[387] D. Paquet. *Physical Review B*, 22(11):5284–5301, 1980.

[388] M. Demeter, M. Neumann, and W. Reichelt. *Surface Science*, 454-456:41–44, 2000.

[389] R. M. Wentzcovitch. *Physical Review Letters*, 72(21):3389–3392, 1994.

[390] M. Marezio, D. McWhan, J. Remeika, and P. Dernier. *Physical Review B*, 5 (7):2541–2551, 1972.

[391] J. P. Pouget, H. Launois, and T. M. Rice. *Physical Review Letters*, 35(13): 873–875, 1975.

[392] J. B. Goodenough and H. Hong. *Physical Review B*, 8(4):1323–1331, 1973.

[393] M. M. Qazilbash, A. A. Schafgans, Burch, K. S., S. J. Yun, B. G. Chae, Kim, B. J., Kim, H. T., and D. N. Basov. *Physical Review B*, 77(11):115121, 2008.

[394] M. M. Qazilbash. *Physical Review B*, 79(7):075107, 2009.

[395] M. M. Qazilbash, M. Brehm, B. G. Chae, P. C. Ho, G. O. Andreev, B.-J. Kim, S. J. Yun, A. V. Balatsky, M. B. Maple, F. Keilmann, H.-T. Kim, and D. N. Basov. *Science (New York, N.Y.)*, 318(5857):1750–1753, 2007.

[396] C. H. Griffiths. *Journal of Applied Physics*, 45(5):2201, 1974.

[397] D. H. Youn, H.-T. Kim, B. G. Chae, Y.-J. Hwang, J.-W. Lee, S. L. Maeng, and K.-Y. Kang. *Journal of Vacuum Science & Technology A: Vacuum, Surfaces, and Films*, 22(3):719, 2004.

[398] J. Narayan and V. M. Bhosle. *Journal of Applied Physics*, 100(10):103524, 2006.

[399] D. Ruzmetov, S. D. Senanayake, and S. Ramanathan. *Physical Review B*, 75 (19):195102, 2007.

[400] D. Ruzmetov, K. T. Zawilski, V. Narayanamurti, and S. Ramanathan. *Journal of Applied Physics*, 102(11):113715, 2007.

[401] C. Berglund and H. Guggenheim. *Physical Review*, 185(3):1022–1033, 1969.

[402] I. Kitahiro, T. Ohashi, and A. Watanabe. *Journal of the Physics Society of Japan*, 21(11):2422, 1966.

[403] D. H. Hensler. *Journal of Applied Physics*, 39(5):2354, 1968.

[404] D. Ruzmetov, G. Gopalakrishnan, J. Deng, V. Narayanamurti, and S. Ramanathan. *Journal of Applied Physics*, 106(8):083702, 2009.

[405] K. Okazaki, S. Sugai, Y. Muraoka, and Z. Hiroi. *Physical Review B*, 73(16): 165116, 2006.

[406] M. M. Qazilbash, K. Burch, D. Whisler, D. Shrekenhamer, B. G. Chae, H. Kim, and D. N. Basov. *Physical Review B*, 74(20):205118, 2006.

[407] K. Vos and H. J. Krusemeyer. *Journal of Physics C: Solid State Physics*, 10(19): 3893–3915, 1977.

[408] S. Miyasaka, Y. Okimoto, and Y. Tokura. *Journal of the Physics Society of Japan*, 71(9):2086–2089, 2002.

[409] M. Eckstein, M. Kollar, and D. Vollhardt. *Journal of Low Temperature Physics*, 147(3-4):279–293, 2007.

[410] A. Barker. *Physical Review*, 132(4):1474–1481, 1963.

[411] M. A. Kats, D. Sharma, J. Lin, P. Genevet, R. Blanchard, Z. Yang, M. M. Qazilbash, D. N. Basov, S. Ramanathan, and F. Capasso. *Applied Physics Letters*, 101(22):221101, 2012.

[412] H. Ibach, H. D. Bruchmann, and H. Wagner. *Applied Physics A Solids and Surfaces*, 29(3):113–124, 1982.

[413] P. Allen, R. Wentzcovitch, W. Schulz, and P. Canfield. *Physical Review B*, 48 (7):4359–4363, 1993.

[414] A. F. Ioffe and A. R. Regel. *Prog. Semicond.*, (4):237, 1960.

[415] N. F. Mott. *Philosophical Magazine*, 26(4):1015–1026, 1972.

[416] Y. Taketa, F. Kato, M. Nitta, and M. Haradome. *Applied Physics Letters*, 27 (4):212, 1975.

[417] B. Fisher. *Journal of Applied Physics*, 49(10):5339, 1978.

[418] J. Duchene. *Applied Physics Letters*, 19(4):115, 1971.

[419] G. Stefanovich, A. L. Pergament, and D. Stefanovich. *Journal of Physics-Condensed Matter*, 12(41):8837–8845, 2000.

[420] K. Okimura and J. Sakai. *Japanese Journal of Applied Physics*, 46(No. 34): L813–L816, 2007.

[421] K. Okimura, N. Ezreena, Y. Sasakawa, and J. Sakai. *Japanese Journal of Applied Physics*, 48(6):065003, 2009.

[422] Z. Yang, C. Ko, V. Balakrishnan, G. Gopalakrishnan, and S. Ramanathan. *Physical Review B*, 82(20):205101, 2010.

[423] A. Sohn, H. Kim, D.-W. Kim, C. Ko, S. Ramanathan, J. Park, G. Seo, B.-J. Kim, J.-H. Shin, and H.-T. Kim. *Applied Physics Letters*, 101(19):191605, 2012.

[424] B. G. Chae, H. Kim, D. H. Youn, and K. Y. Kang. *Physica B: Condensed Matter*, 369(1-4):76–80, 2005.

[425] Y. W. Lee, B.-J. Kim, J. W. Lim, S. J. Yun, S. Choi, B. G. Chae, G. Kim, and H.-T. Kim. *Applied Physics Letters*, 92(16):162903–3, 2008.

[426] H.-T. Kim, B.-J. Kim, S. Choi, B. G. Chae, Y. W. Lee, T. Driscoll, M. M. Qazilbash, and D. N. Basov. *Journal of Applied Physics*, 107(2):023702, 2010.

[427] A. Beaumont, J. Leroy, J. C. Orlianges, and A. Crunteanu. *Journal of Applied Physics*, 115(15):154502, 2014.

[428] T. Driscoll, J. Quinn, M. Di Ventra, D. N. Basov, G. Seo, Y. W. Lee, H.-T. Kim, and D. R. Smith. *Physical Review B*, 86(9):094203, 2012.

[429] S. Kumar, M. D. Pickett, J. P. Strachan, G. Gibson, Y. Nishi, and R. S. Williams. *Advanced materials (Deerfield Beach, Fla.)*, 25(42):6128–6132, 2013.

[430] J. S. Lee, M. Ortolani, U. Schade, Y. J. Chang, and T. W. Noh. *Applied Physics Letters*, 90(5):051907, 2007.

[431] J. S. Lee, M. Ortolani, A. Ginolas, Y. J. Chang, T. W. Noh, and U. Schade. *Physica C: Superconductivity*, 460-462:549–550, 2007.

[432] A. Damascelli, K. Schulte, D. van der Marel, and A. A. Menovsky. *Physical Review B*, 55(8):R4863–R4866, 1997.

[433] P. Drude. *Annalen der Physik*, 306(3):566–613, 1900.

[434] U. Fano. *Physical Review*, 124(6):1866–1878, 1961.

[435] G. Andermann, A. Caron, and D. A. Dows. *Journal of the Optical Society of America*, 55(10):1210, 1965.

LIST OF FIGURES

LIST OF TABLES

ACRONYMS

A/D analog-to-digital

AC alternating current

AZO aluminum tin oxide

AFM atomic force microscope

Al_2O_3 sapphire

AO anion ordering

BCS Barden-Cooper-Schrieffer theory

BEDT-TTF Bis(ethylenedithio)tetrathiafulvalene

BMS beam splitter

BZ Brillouin zone

CA chloranil

CAD computer-based construction

CaF_2 sodium fluoride

CB conduction band

CDMFT cluster dynamical mean field theory

CDW charge density wave

C_2H_3N acetonitril

CO charge order

CT charge transfer exciton

CVD chemical gas phase deposition

DC direct current

DFT density functional theory

DE differential equation

DOS density of states

DW domain wall

EDT-TTFCONMe$_2$ EDT-TTFCONMe$_2$

emv electron-molecular vibration

ESR electron spin resonance

FET field-effect-transistor

FFT Fast-Fourier transformation

FT Fourier transformation

FTIR Fourier transform infrared

Ge Germanium

GE General Electric varnish

GGA generalized gradient approximation

HOMO highest occupied molecular orbital

HCP high conducting state

HTP high temperature phase

IMT insulator-metal-transition

IR infrared

IRML Ioffe-Regel-Mott-Limit

ITO Indium tin oxide

JDOS joint density of states

KBr sodium bromide

KKT Kramers-Kronig transformation

KWW Kohlrausch-Williams-Watt

LC liquid crystal

LCD liquid crystal display

LCP low-conducting state

LDA local density approximation

LSDA local spin density approximation

LTP low temperature phase

LUMO lowest unoccupied molecular orbital

MIR mid-infrared light

MCT Mercury-Cadmium-Telluride

MIT metal-insulator-transition

NDR negative differential resistance

NIDW neutral-ionic domain wall

NIR near-infrared spectral range

NQR nuclear quadrupole resonance

NMR nuclear spin resonance

OD optical density

PBE Perdew-Burke-Enzerhof

PC photo current

PES potential energy surface

PE photoemission

PIPT photo-induced phase transition

PLD pulsed laser deposition

PP pseudopotential

PV photovoltaic

QE Quantum Espresso

RPA random phase approximation

RT room temperature

SC superconductivity

SDW spin density wave

SiO_2 silicon dioxide

SNR signal-to-noise ratio

SP spin-Peierls

SSFLC surface-stabilized ferroelectric liquid crystal

STM scanning tunneling microscope

SVD singular value decomposition

SW spectral weight

TiO_2 titanium dioxide

TMTSF tetramethyltetraselenafulvalene

TMTTF tetramethyltetrasulfurfulvalene

TTF tetrathiafulvalene

TTF-CA tetrathiafulvalene-chloranil

TTF-TCNQ tetrathiafulvalene 7,7,8,8-tetracyanoquinodimethane

TTL transistor-transistor logic

UPS ultraviolet photoelectron spectroscopy

UV ultraviolet

VB valence band

VIS visible light

VO_2 vanadium dioxide

WASF Asf-for Windows

WP Wyckoff position

XAS x-ray absorption spectroscopy

XPS x-ray photoelectron spectroscopy

XRR x-ray reflectrometry

ZINDO semi-empirical quantum chemical method

ZPD zero path difference

GLOSSARY

A_{sam} sample cross section, [cm^2]. 186

A_{CD} cubic charge disproportionation term. 89, 90, 91, 92, 134, 135

A_{CT} cubic charge transfer term. 89, 90, 91, 92, 134

C_{Ext} external capacity, [F]. 277, 279

C_{Sam} capacity of the sample, [F]. 277

C_p specific heat capacity, [$\frac{J}{Kg\,K}$]. 17, 18, 32, 142, 170, 188, 199, 274

d	contact distance, [m]. 186, 275
d_{Dim}	intradimer distance, [m]. 94, 96, 142, 144
D	restoring constant, [Nm^{-1}]. 289, 290
E_{p}	laser pulse energy, [J]. 169, 170
$E_{\mathrm{Sam}}(t)$	time-dependent electric field across the sample, [Vcm^{-1}]. 196, 199, 275
E_{Sam}	electric field across the sample, [Vcm^{-1}]. 186
E_{th}	electric cutoff field, [Vcm^{-1}]. 17, 184, 186, 187, 199, 200, 202, 275, 323
E_{CB}	energy of the conduction band, [eV]. 151
E_{VB}	energy of the valence band, [eV]. 151
E_{eg}	energy difference between ground and excited state, [eV]. 89, 135
E_{F}	Fermi energy, [eV]. 20, 77, 126
E_{Photon}	photon energy, [eV]. 164, 169
E_{HOMO}	energy of the HOMO, [eV]. 291
$\vec{E}$	electric field, [Vcm^{-1}]. 196, 199, 200, 202, 244, 245, 246, 323
E_{ion}	ionization energy, [eV]. 9, 10, 31
E_{A}	electron affinity, [eV]. 9, 10
E_{B}	residual energy, [eV]. 10
E_{cut}	cutoff energy of the wave function, [eV]. 57, 58, 59, 63

$E_{\text{cut},\rho}$ cutoff energy of the electron density , [eV]. 57, 58, 63

$\vec{E}_{\text{IR}}$ electric field of the infrared light, [Vcm^{-1}]. 130, 240, 244, 245, 247, 249

f_0 fundamentel frequency, [Hz]. 279

$f_{\text{Osc.}}$ oscillator strength. 158, 159

g_i emv-coupling constant, [eV]. 89, 91, 92, 134, 148, 150, 161, 290

g g-tensor. 71, 105

g_{P} electron-phonon coupling constant, [eV]. 15, 16

g_2 quadratic coupling constant, [eV]. 89, 134

$\vec{h}$ layer normal vector, [m]. 239, 240, 241

$\mathbf{H}$ Hesse matrix. 63

$I(\delta)$ light intensity, [Jm^3]. 37, 38, 42

I_{Th} cutoff current, [A]. 278

$I_{\text{D}}(t)$ time-dependent dark current, [A]. 53

$I_{\text{Ill}}(t)$ time-dependent illumination current, [A]. 53

$I_{\text{Ph}}(t)$ time-dependent photocurrent, [A]. 53

$I_{\text{Tot.}}$ total circuit current, [A]. 184

$I(t)$ time-dependent current, [A]. 277, 284

I_{L} laser intensity, [Jcm^{-2}]. 169

I momentum of inertia. 245

$J(t)$ time-dependent current density, [Acm^{-2}]. 272, 275, 280

$J(E)$ current density as function of the electric field, [Acm^{-2}]. 275

J current density, [Acm^{-2}]. 186, 196, 199, 200, 202, 323

J_{th} threshold current density, [Acm^{-2}]. 186, 187, 199, 200, 202, 323

k Boltzmann constant, [JK^{-1}]. 259

k_{F} Fermi wave vector, [cm^{-1}]. vii, 14, 15, 18, 21, 114, 179, 217

K elasticity constant. 242, 245, 250, 252

$L(0)$ initial domain size. 173

L_{Ext} inductance, [H]. 279

m_{e} electron mass, [kg]. 16, 289, 290

$m^{\star}$ effective mass, [kg]. 16, 18, 195, 196, 289

M_{mol} molar mass, [kg mol^{-1}]. 170

n_1 carrier concentration of type 1, [cm^{-3}]. 196

n_2 carrier concentration of type 2, [cm^{-3}]. 196

n amount of substance, [mol]. 19, 32, 170, 188, 199, 242

δn_{eg} transfer matrix element. 89

$n(r)$ charge density, [cm^{-3}]. 14, 16

$\vec{n}$ director vector, [m]. 239, 240, 241, 244, 245

N_C charge density, [cm^{-3}]. 284, 289

N_c charge carrier concentration, [cm^{-3}]. 259

q coupling strength. 135, 196, 292

q_{en} charge carrier, [e]. 259

q_{AO} wave vector of the anion ordering, [m^{-1}]. 23

Q_p radiant flux density, [Wcm^{-2}]. 171, 287

$\vec{p}_m$ spontaneous polarization, [Cm]. 240, 242, 250, 252

$\vec{p}_{total}$ total polarization, [Cm]. 240

P power, [W]. 32, 274

P_{th} threshold power, [W]. 187, 202, 323

r_c cutoff radius, [Å]. 59, 60, 59

R_L load resistance, [Ω]. 49, 50, 51, 52, 53, 186, 272, 276, 277, 278, 279, 281

R_{Sam} sample resistance, [Ω]. 272, 277

$R_{Sam,D}$ dark sample resistance, [Ω]. 53

$R_{Sam,Ill}$ illuminated sample resistance, [Ω]. 53

$R(\nu)$ reflectivity. 43, 44, 156, 263, 283, 287, 322

$S_{Mi}(\nu)$ intensity spectrum of the light source. 281

$S(t)$ survival probability. 172, 173, 322

$S(\nu)$ light spectrum. 37, 38

$S_{Sam}(\nu)$ sample spectrum. 42

t transfer integral, [eV]. vii, 12, 19, 21, 26, 74, 89, 90, 91, 92, 94, 96, 107, 110, 121, 122, 124, 135, 136, 138, 158, 159, 207, 216

T temperature, [K]. 171, 259

T_{Cryo} cryostat temperature, [K]. 43

T_{f} final temperature, [K]. 168

T_{Sam} sample temperature, [K]. 43

T_{MI} transition temperature of the metal-insulator transition, [K]. 259, 282, 283, 284

T_{S} structural transition temperature, [K]. 132

T_0 initial temperature, [K]. 32, 188, 193, 196, 198

T_{e} electron temperature, [K]. 32, 196, 197, 198, 202, 323

T_{i} temperature at time i,[K]. 188

T_{I} kinetic energy of the atomic nuclei, [eV]. 56

T_{L} lattice temperature, [K]. 193, 196, 198, 200, 202, 323

T_{P} Peierls transition temperature, [K]. 15

T_{CDW} transition temperature of the charge density wave, [K]. 16, 17

T_{NI} transition temperature of the neutral-ionic phase transition, [K]. viii, 141, 142, 144, 155, 156, 161, 162, 163, 168, 171, 173, 175, 176, 217

T_{CO} transition temperature of the charge ordering, [K]. vii, 21, 69, 70, 69, 71, 72, 88, 92, 93, 94, 96, 99, 105, 106, 107, 109, 110, 112, 113, 112, 115, 121, 122, 177, 178, 179, 181, 184, 186, 187, 188, 189, 190, 192, 193, 197, 198, 202, 207, 214, 215, 217, 323

T_{AO} transition temperature of the anion ordering, [K]. 69, 70, 69, 70, 87, 88, 94, 96, 99, 106, 107, 108, 122

$u(r)$ lattice distortion, [Å]. 16

U on-site Coulomb repulsion, [eV]. 12, 13, 12, 19, 20, 19, 20, 21, 26, 27, 74, 92, 94, 121, 124, 178, 271

U_{23} voltage drop between the inner contacts, [V]. 48

U_{L} voltage drop across the load resistance, [V]. 48, 52, 184, 186, 323

U_{S} source voltage, [V]. 48, 52, 51, 53, 184, 186, 274, 275, 277, 279, 280, 284, 323, 325

U_{Sam} voltage drop across the sample, [V]. 275, 279

U_{Th} cutoff voltage, [V]. 278

U_{Th1} 1st cutoff voltage, [V]. 277, 279, 280, 284, 285

U_{Th2} 2nd cutoff voltage, [V]. 280, 285

v_{Mi} mirror velocity, [ms^{-1}]. 38, 44

V nearest-neighbor interaction, [eV]. 12, 13, 21, 22, 26, 31, 74, 94, 110, 121, 122, 124, 136, 178, 207

V_{m} unit cell volume, [m^3]. 94, 96

V_{F} Fermi velocity, [ms-1].270

$\mathcal{V}_{xc}$ exchange-correlation term, [eV]. 56

$\mathcal{V}_{II}$ Coulomb interaction term of the nuclei, [eV]. 56

W bandwidth, [eV]. 15, 20, 19, 20, 151, 159, 180, 207, 209

α absorption coefficient, [cm^{-1}]. 287

β	stretching parameter. 168, 173, 176
γ	line width, [cm^{-1}]. 292
γ_{Sc}	scattering rate, [cm^{-1}]. 24, 284
$\delta\rho$	charge imbalance, [e]. 87, 88, 89, 90, 89, 90, 91, 92, 105, 107, 108, 121, 134, 135, 138, 321
$\delta_d(\nu)$	penetration depth, [m]. 168, 171
δ	path difference, [m]. 37, 38
$\Delta\nu$	spectral resolution, [cm^{-1}]. 39
$\Delta R(\nu)$	static change of the reflectivity. 282, 283
$\Delta_t R$	time-dependent change of the reflectivity. 167, 168, 171
$\Delta_t R(t)$	reflectivity as a function of time. 167, 168, 173, 190
$\Delta_t R(\nu, t)$	time-dependent change of the reflectivity as a function of wavenumber and time. 190, 191, 192, 193, 280, 281, 282, 283, 285, 322
$\Delta_T R$	temperature-dependent change of the reflectivity. 167, 168, 175, 190, 193
$\Delta S_{AC}(\nu, t)$	time-dependent AC-spectrum. 281
$\Delta S(\nu, t)$	change of the spectrum. 45, 249
ΔT	temperature change, [K]. 168, 170
$\Delta T(t)$	time-dependent temperature change, [K]. 170, 171
$\Delta E_{Akt.}$	activation energy, [eV]. 184, 259, 284
Δ	energy gap, [eV]. 15, 16, 17, 107, 142, 151, 196, 202
ΔE	charge transfer energy, [eV]. 9

Δt time resolution, [s]. 45

$\Delta\epsilon$ dielectric permittivity strength. 179

$\epsilon(\nu)$ complex dielectric permittivity. 43

ϵ_1 real part of the dielectric permittivity. 70, 69, 141, 142

ϵ_2 imaginary part of the dielectric permittivity. 70

η viscosity, [Pa s]. 242, 245, 250, 252

$\theta(\nu)$ phase, [°]. 43, 44, 45

κ thermal diffusivity, [$m^2\ s^{-1}$]. 287

λ wavelength, [nm]. 37, 246

λ_{therm} thermal conductivity, [$Wm^{-1}K^{-1}$]. 32, 170, 171, 193

$\lambda_{therm,e}$ thermal conductivity of the electron system, [$Wm^{-1}K^{-1}$]. 196, 199

μ_1 mobility of charge carrier type 1, [$cm^2V^{-1}s^{-1}$]. 195, 196

μ_2 mobility of charge carrier type 2, [$cm^2V^{-1}s^{-1}$]. 195, 196

μ_n charge mobility, [$cm^2V^{-1}s^{-1}$]. 196, 259

μ_e dipole moment, [Debye]. 240, 244, 245, 249, 290

ν_p plasma frequency, [cm^{-1}]. 24, 269, 284

ρ density, [$\frac{kg}{cm^3}$]. 170, 259, 274

ρ_t molecular charge, [e]. 156, 158, 159, 164

ρ_{DC} resistivity, [Ωcm]. 142

$\sigma(\nu)$ complex optical conductivity, $[\Omega^{-1}cm^{-1}]$. 43

$\sigma_1(\nu)$ real part of the optical conductivity, $[\Omega^{-1}cm^{-1}]$. 128, 135, 136, 152, 156, 168, 263, 322

$\sigma_2(\nu)$ imaginary part of the optical conductivity, $[\Omega^{-1}cm^{-1}]$. 168

σ_{DC} DC part of the optical conductivity, $[\Omega^{-1}cm^{-1}]$. 18, 20, 31, 269, 270, 269, 284

σ_0 amplitude of the conductivity, $[\Omega^{-1}cm^{-1}]$. 292

τ_d delay time, [s]. ix, 31, 32, 185, 198, 218, 272, 274, 276, 284, 285

τ_{rise} rise time, [s]. 282

τ_{fall} fall time, [s]. 282

τ_{RC} time constant of the RC circuit, [s]. 272, 279

τ_p pulse width, [s]. 287

τ_{Sc} scattering rate, $[s^{-1}]$. 20, 196, 284, 289

τ^*_{Sc} effective scattering rate, $[s^{-1}]$. 18, 289

τ life time, [s]. 168, 199, 270, 280, 290

τ_{or} orientation time, [s]. 240, 245, 249, 250, 251

τ_{reor} relaxation time, [s]. 240, 249, 250, 251

Φ Phase. 16

$[\chi_S]_V$ spin susceptibility at constant volume, $[m^{-3}mol^{-1}]$. 70, 69, 70

$\Psi(\vec{r})$ wave function. 56

ω_0 resonance frequency, [Hz]. 290, 292

ω_{CT} resonance frequency of the charge transfer band, [Hz]. 93, 94, 158, 159, 164

ω_p plasma frequency, [Hz]. 93, 94, 96, 108, 158, 289

COLOPHON

This document was typeset using the typographical look-and-feel `classicthesis` developed by André Miede. The style was inspired by Robert Bringhurst's seminal book on typography "*The Elements of Typographic Style*". `classicthesis` is available for both LaTeX and LyX:

http://code.google.com/p/classicthesis/

Happy users of `classicthesis` usually send a real postcard to the author, a collection of postcards received so far is featured here:

http://postcards.miede.de/

Final Version as of March 2, 2016 (`classicthesis`).

ACKNOWLEDGMENTS

At that point I want to thank all the people who not only contributed, but also supported me over the last years:

- First of all, I want to thank my supervisor Prof. Dr. Martin Dressel who gave me the unique chance to work on the fascinating field of organic conductors. You had always an open ear to my new ideas, encouraged me and gave me the possibility to realize them.
- I would like to thank Prof. Dr. Jörg Wrachtrup to review my thesis and for providing me the laser system without which it would not be possible to accomplish this thesis.
- Especially, I would like to thank my supervisors Neven Barišić who introduced my to the broad research field of solid state materials. Dan Wu for her valuable time and the extensive discussions. It was always a great pleasure to work with you and the whole infrared group. Tomislav Ivek, you have always supported me over the last two years of my thesis. You introduced me in the field of dielectric spectroscopy and conductivity measurements. Our discussions were always enlightening and I enjoyed our fantastic stay in Zagreb.
- Bruno, I thank you for your hints, ideas and open ear throughout the last years. I really enjoyed my time with you as a tutor.
- I am so deeply grateful for Gabi Untereiner's and Agnes Schmidt's help. Gabi without your help and your steady hands I would never measured one of those fragile organic crystals. I already miss our chats and coffee breaks. Thank you Agni for your unresting help and support with the administrative work.
- Helga, you are godsend for the institute. I always enjoyed your presence and our talks.

I want to thank all my collaborators and colleagues who supported, helped and accompanied me through the last years:

- Silvia Tomic for here nice hospitality during my stay in her group at the Institute of Physics in Zagreb.
- I would like to thank Prof. Dr. Alberto Girlando and Dr. Matteo Massimo from the University of Parma for all discussion about molecular vibrations and for the help with the quantum chemical calculations.
- I would like to thank Natalia Drichko and Agnes Antal for the nice and successful collaboration on one-dimensional conductors.
- Marc Dietrich and Dr. Angelika Polity from the Institute of Functional Thin Layers of the University of Giessen for manufacturing and providing the VO_2 films.

- Florian Schörg from the Institute of Physical Chemistry - Giesselmann Group - for providing the liquid crystals. Eberhard Kurz from the Institute for Large Area Microelectronics for helping me for building up the crystal cell and introducing me to the clean room.
- I want to acknowledge the financial support of the Carl-Zeiss Stiftung and the computing time of the BW-Grid.
- Sina and Rebecca, we went through all the ups and downs. Rebecca, we have quite often not the same opinion, however I liked your company and perception. Sina, I absolutely enjoyed our joint time at the institute and all our Klatsch und Tratsch meetings in our office. I am pretty sure that our friendship will persist over our time at the institute.
- Eva, I always enjoyed our profound discussion about physics. I always appreciate that you wanted to understand each aspect of a physical problem.
- I would like to thank Ralph Hübner for his advice and help with the quantum chemical calculations and for finding the missing hydrogen atoms.
- My bachelor students Patrica Haremski, my Hiwis Avaise Mohammed and Parmida Shabestari. I hope that you learned lot during our joint time. I wish you the best for your future.
- Anja, David, Andrej, Conrad, Eric, Uwe, Stefano, Andrea and many more. I really enjoyed my time here with you. You all made things easier when things went wrong. And all other former members of the "Infrarats".
- Anja Peterseim, I appreciate that you have proofread my thesis. I am so infinite grateful that you have invested so much of your valuable time. Also I would like to thank Andrej for reading my thesis and commenting on it. Particularly, Sina, thank you for your great and helpful comments and hints.
- Furthermore, all my colleagues and institute members who made the atmosphere so great and pleasant at the institute.
- All the people in the mechanical and electronic workshop who used all their knowledge and skills to manufacture all the mechanical parts and electronic instruments which helped me to successfully accomplish my thesis.

Finally, I want to thank my parents who always supported me during my study in Freiburg and of course during my thesis in Stuttgart. Furthermore, all my friends from back home which I could not meet so often as I would have. My wife Linda, I want to thank you for your incredible support over the last years and all the encouraging and motivating impulses. You had so much patience with me for which I am so indescribable thankful.

DECLARATION OF ORIGINALITY

I hereby declare that this thesis and the work reported herein was composed by and originated entirely from me. Information derived from the published and unpublished work of others has been acknowledged in the text and references.